

Lecture Notes in Physics

Editorial Board

H. Araki, Kyoto, Japan
R. Beig, Vienna, Austria
J. Ehlers, Potsdam, Germany
U. Frisch, Nice, France
K. Hepp, Zürich, Switzerland
R. L. Jaffe, Cambridge, MA, USA
R. Kippenhahn, Göttingen, Germany
H. A. Weidenmüller, Heidelberg, Germany
J. Wess, München, Germany
J. Zittartz, Köln, Germany

Managing Editor

W. Beiglböck
Assisted by Mrs. Sabine Lehr
c/o Springer-Verlag, Physics Editorial Department II
Tiergartenstrasse 17, D-69121 Heidelberg, Germany

Springer

Berlin
Heidelberg
New York
Barcelona
Budapest
Hong Kong
London
Milan
Paris
Santa Clara
Singapore
Tokyo

The Editorial Policy for Proceedings

The series Lecture Notes in Physics reports new developments in physical research and teaching – quickly, informally, and at a high level. The proceedings to be considered for publication in this series should be limited to only a few areas of research, and these should be closely related to each other. The contributions should be of a high standard and should avoid lengthy redraftings of papers already published or about to be published elsewhere. As a whole, the proceedings should aim for a balanced presentation of the theme of the conference including a description of the techniques used and enough motivation for a broad readership. It should not be assumed that the published proceedings must reflect the conference in its entirety. (A listing or abstracts of papers presented at the meeting but not included in the proceedings could be added as an appendix.)

When applying for publication in the series Lecture Notes in Physics the volume's editor(s) should submit sufficient material to enable the series editors and their referees to make a fairly accurate evaluation (e.g. a complete list of speakers and titles of papers to be presented and abstracts). If, based on this information, the proceedings are (tentatively) accepted, the volume's editor(s), whose name(s) will appear on the title pages, should select the papers suitable for publication and have them refereed (as for a journal) when appropriate. As a rule discussions will not be accepted. The series editors and Springer-Verlag will normally not interfere with the detailed editing except in fairly obvious cases or on technical matters.

Final acceptance is expressed by the series editor in charge, in consultation with Springer-Verlag only after receiving the complete manuscript. It might help to send a copy of the authors' manuscripts in advance to the editor in charge to discuss possible revisions with him. As a general rule, the series editor will confirm his tentative acceptance if the final manuscript corresponds to the original concept discussed, if the quality of the contribution meets the requirements of the series, and if the final size of the manuscript does not greatly exceed the number of pages originally agreed upon. The manuscript should be forwarded to Springer-Verlag shortly after the meeting. In cases of extreme delay (more than six months after the conference) the series editors will check once more the timeliness of the papers. Therefore, the volume's editor(s) should establish strict deadlines, or collect the articles during the conference and have them revised on the spot. If a delay is unavoidable, one should encourage the authors to update their contributions if appropriate. The editors of proceedings are strongly advised to inform contributors about these points at an early stage.

The final manuscript should contain a table of contents and an informative introduction accessible also to readers not particularly familiar with the topic of the conference. The contributions should be in English. The volume's editor(s) should check the contributions for the correct use of language. At Springer-Verlag only the prefaces will be checked by a copy-editor for language and style. Grave linguistic or technical shortcomings may lead to the rejection of contributions by the series editors. A conference report should not exceed a total of 500 pages. Keeping the size within this bound should be achieved by a stricter selection of articles and not by imposing an upper limit to the length of the individual papers. Editors receive jointly 30 complimentary copies of their book. They are entitled to purchase further copies of their book at a reduced rate. As a rule no reprints of individual contributions can be supplied. No royalty is paid on Lecture Notes in Physics volumes. Commitment to publish is made by letter of interest rather than by signing a formal contract. Springer-Verlag secures the copyright for each volume.

The Production Process

The books are hardbound, and the publisher will select quality paper appropriate to the needs of the author(s). Publication time is about ten weeks. More than twenty years of experience guarantee authors the best possible service. To reach the goal of rapid publication at a low price the technique of photographic reproduction from a camera-ready manuscript was chosen. This process shifts the main responsibility for the technical quality considerably from the publisher to the authors. We therefore urge all authors and editors of proceedings to observe very carefully the essentials for the preparation of camera-ready manuscripts, which we will supply on request. This applies especially to the quality of figures and halftones submitted for publication. In addition, it might be useful to look at some of the volumes already published. As a special service, we offer free of charge L^AT_EX and T_EX macro packages to format the text according to Springer-Verlag's quality requirements. We strongly recommend that you make use of this offer, since the result will be a book of considerably improved technical quality. To avoid mistakes and time-consuming correspondence during the production period the conference editors should request special instructions from the publisher well before the beginning of the conference. Manuscripts not meeting the technical standard of the series will have to be returned for improvement.

For further information please contact Springer-Verlag, Physics Editorial Department II, Tiergartenstrasse 17, D-69121 Heidelberg, Germany

J.P. De Greve R. Blomme H. Hensberge (Eds.)

Stellar Atmospheres: Theory and Observations



Lectures Held at the
Astrophysics School IX

Organized by the European Astrophysics Doctoral Network
(EADN) in Brussels, Belgium, 10–19 September 1996



Springer

Editors

J.P. De Greve
Astronomy Group
Vrije Universiteit Brussel
Pleinlaan 2
B-1050 Brussels, Belgium

R. Blomme
H. Hensberge
Royal Observatory of Belgium
Ringlaan 3
B-1180 Brussels, Belgium

Cataloging-in-Publication Data applied for.

Die Deutsche Bibliothek - CIP-Einheitsaufnahme

Stellar atmospheres : theory and observations ; lectures held at the Astrophysics School IX in Brussels, Belgium, 10 - 19 September 1996 / J. P. DeGreve ... (ed.). Organized by the European Astrophysics Doctoral Network (EADN). - Berlin ; Heidelberg ; New York ; Barcelona ; Budapest ; Hong Kong ; London ; Milan ; Paris ; Santa Clara ; Singapore ; Tokyo : Springer, 1997
(Lecture notes in physics ; Vol. 497)
ISBN 3-540-63477-0

ISSN 0075-8450

ISBN 3-540-63477-0 Springer-Verlag Berlin Heidelberg New York

This work is subject to copyright. All rights are reserved, whether the whole or part of the material is concerned, specifically the rights of translation, reprinting, re-use of illustrations, recitation, broadcasting, reproduction on microfilms or in any other way, and storage in data banks. Duplication of this publication or parts thereof is permitted only under the provisions of the German Copyright Law of September 9, 1965, in its current version, and permission for use must always be obtained from Springer-Verlag. Violations are liable for prosecution under the German Copyright Law.

© Springer-Verlag Berlin Heidelberg 1997
Printed in Germany

The use of general descriptive names, registered names, trademarks, etc. in this publication does not imply, even in the absence of a specific statement, that such names are exempt from the relevant protective laws and regulations and therefore free for general use.

Typesetting: Camera-ready by the authors/editors
Cover design: *design & production* GmbH, Heidelberg
SPIN: 10643834 55/3144-543210 - Printed on acid-free paper

Preface

Advance in science builds upon the continuous exchange of ideas, and the confrontation of theory and experiment or observation. Both should be executed by researchers with a vast knowledge of the physics and mathematics involved.

The Summer Schools of the European Astrophysical Doctoral Network aim at contributing to this in providing doctoral students in astrophysics with opportunities to enrich their knowledge in particular fields in a truly international setting. Young scientists from all over Europe (and abroad!) gather for two weeks, study and work together, and enjoy the multicultural atmosphere. Future collaboration across the border may find its roots in the lively atmospheres of the Schools.

The 1996 School dealt with the atmospheres of stars, the various theories that describe their structure and the interactions with the interior of the stars as well as with the interstellar environment, and the observations that support, modify and sometimes contradict these theories.

The School aimed at 4 goals:

- To offer an insight into problems related to stellar atmospheres for both cool and hot stars, at a high-quality level.
- To offer opportunities to deal with modern technologies in analysing observational data versus theoretical modelling.
- To learn to appreciate teamwork.
- To work and live in an international, multicultural environment.

Forty-three students attended the 1996 School, 11 females and 32 males. They came from 15 different countries. Three participants came from outside the European Union. Although a majority had a research interest in the topic of the School, Ph.D. students in all possible subdisciplines attended, their interest ranging from cosmology, over galactic structure, stellar evolution to helioseismology.

Each morning, two of the eight lecturers presented their views on one of the topics in the field. This volume contains all the lectures presented at the School. In the afternoon, practical (computer) projects with observational data were organized at the Royal Observatory of Belgium. The content of these projects was designed by the lecturers. The students learnt to work

with different astrophysical data analysis packages. To ensure multicultural cooperation the participants were thoroughly mixed in the project teams. The following projects were offered to the students: the infrared continuum and excess of hot stars (Lamers & Bjorkman), the Sobolev method with exact integration for P Cygni profiles (Fullerton), analysis of ROSAT data (Schmitt), spectrum synthesis (Hubeny). Each team of students had to choose two projects.

A cheese and wine evening, offered by the university, was organized for students and participants. The students themselves organized a dining-out evening (with a little help from the local organization), attended by practically all students and lecturers. Coffee breaks and common lunches added to familiarize us with one another.

Important parts of the program were the Show and Tell parts, which took up almost 5 hours. Students presented their own research topic and their interest in it in 5-minutes talks (with one or two transparencies), followed by a few questions.

The organization of the School is impossible without the financial help of various bodies. We take the opportunity to thank the European Commission that financed the larger part of the School, more specifically through the ERASMUS and the Human Capital and Mobility Programmes. We also thank the authorities of the Vrije Universiteit Brussel and the Royal Observatory of Belgium for their hospitality, services and financial support. The university provided favourable conditions for housing and meals. We also appreciated very much the financial support from the Swedish government and from the Fund for Scientific Research of Flanders (F.W.O.).

One of us (J.P.D.G.) heartedly thanks Vincent Icke, the organizer of the previous School in Leiden, for the valuable preliminary information on the organization. It helped me getting things on the move much easier. And the T-shirt still fits me well, Icke. Special thanks go to Tom Ray, secretary of the EADN, whose extensive advice and support definitely helped me through some tough moments, and to Koen Vyverman, whose organizational talent contributed much to the smooth and pleasant running of the School.

The enthusiasm of both lecturers and students, and the many lively discussions, made this School a truly European experience.

This publication was made possible thanks to the interest of Springer-Verlag, through Prof. W. Beiglböck.

Brussels, August 1997

Jean-Pierre De Greve

Ronny Blomme
Herman Hensberge

Table of Contents

Stellar Atmospheres Theory: An Introduction

I. Hubeny	1
1 Fundamental Concepts	1
1.1 What Is a Stellar Atmosphere, and Why Do We Study It?	1
1.2 Basic Structural Equations	3
1.3 LTE Versus Non-LTE	5
2 Radiative Transfer Equation	7
2.1 Intensity of Radiation and Related Quantities	8
2.2 Absorption and Emission Coefficient	9
2.3 Phenomenological Derivation of the Transfer Equation	11
2.4 Optical Depth and the Source Function	12
2.5 Elementary Solutions	13
2.6 Moments of the Transfer Equation	15
2.7 Lambda Operator	17
2.8 Diffusion Approximation	19
3 Radiative Transfer with Constraints; Escape Probability	20
3.1 Two-Level Atom	20
3.2 Escape Probability	27
4 Numerical Methods	29
4.1 Formal Solution of the Transfer Equation	29
4.2 Linear Coupling Problems	32
4.3 Accelerated Lambda Iteration	34
4.4 Non-linear Coupling Problems	37
5 Model Atmospheres	39
5.1 Definition and Terminology	39
5.2 Basic Equations of Classical Stellar Atmospheres	42
5.3 LTE-Grey Model: A Tool to Understand the Temperature Structure	46
5.4 LTE and NLTE Model Atmospheres	50
5.5 Line Blanketing	52
6 Using Model Atmospheres to Analyse Observed Spectra	57
6.1 A Scheme of Spectroscopic Diagnostics	57
6.2 Spectrum Synthesis	60
6.3 Spectrum Fitting	62

6.4	Determination of Fundamental Stellar Parameters	64
Stellar Wind Theories		
	Henny J.G.L.M. Lamers	69
1	Introduction	69
2	Basic Concepts of Wind Theories	70
2.1	The Mass Continuity Equation	70
2.2	The Momentum Equation	70
2.3	The Energy Equation	71
3	Isothermal Winds Driven by Gas Pressure	72
3.1	The Critical Point of the Momentum Equation	72
3.2	The Velocity Law of Isothermal Winds Driven by Gas Pressure	75
3.3	The Density Structure of Isothermal Winds Driven by Gas Pressure	76
3.4	The Mass Loss Rate of Isothermal Winds Driven by Gas Pressure	77
4	Isothermal Winds with an Outward Force	78
5	The Effect of Energy Input on a Stellar Wind	79
6	A Wind with an $f \sim r^{-2}$ Force	81
7	The Five Laws of Stellar Wind Theory	83
8	Mass Loss Mechanisms	84
8.1	Coronal Winds	84
8.2	Dust Driven Winds	84
8.3	Line Driven Winds	85
8.4	Pulsation Driven Wind Theory	85
8.5	Sound Wave Driven Winds	85
8.6	Alfvén Wave Driven Wind Models	86
8.7	Magnetic Rotating Winds	87
8.8	Summary of Wind Theories	87
Cool Star Winds and Mass Loss: Theory		
	Erwin Sedlmayr and Jan Martin Winters	89
1	General Overview	89
2	Basic Characteristics of Late-Type Stars	91
2.1	HR Diagram Characteristics	91
2.2	Shell Characteristics	92
3	Self-consistent Description of Dust Forming Circumstellar Shells	94
3.1	Chemistry of the Circumstellar Shell	95
3.2	Dust Nucleation and Growth	102
4	Modeling of Dust Shells Around Late-Type Giants	111
4.1	Basic Equations	112
4.2	External Parameters	117
4.3	Stationary Dust Driven Winds	118

4.4	Dynamical Models for Dust Forming Shells Around Long-Period Variables	123
5	Conclusions	129

Cool Stars Winds and Mass Loss: Observations

	Thibaut Le Bertre	133
1	Introduction	133
2	Presentation of AGB Stars	134
2.1	The Evolution Towards the AGB	134
2.2	The Life on the AGB and Beyond	135
3	Evidence for Mass Loss in the Optical Range	137
3.1	Spectroscopy	137
3.2	Imagery	140
3.3	Polarimetry	140
4	The Infrared Range	141
4.1	Ground-Based Observations	141
4.2	IRAS	143
5	The Radio Range	145
5.1	CO Emission	146
5.2	OH Maser Emission	147
5.3	Other Molecules	148
6	Present Developments	149
6.1	High Spatial Resolution in the Optical and IR Range	149
6.2	Laboratory Studies	150
6.3	Space Projects	151
6.4	Near-Infrared Surveys	152
7	Final Comments	154

The Theory of Line Driven Stellar Winds

	Henny J.G.L.M. Lamers	159
1	Introduction	159
2	Basic Concepts and Some Estimates	160
2.1	How Many Lines Are Needed to Drive a Wind?	161
3	Radiation Pressure Due to Lines	164
3.1	The Radiation Pressure Due to One Line	164
3.2	Radiation Pressure by an Ensemble of Lines	165
3.3	The Lines That Drive the Winds	167
4	The Theory of Line Driven Winds	169
5	The Correction for the Finite Size of the Star	173
5.1	The Effect of the Finite Disk on the Mass Loss Rate and Velocity	174
6	The Instability of Line Driven Winds	177
7	Comparison Between Observations and Predictions for O and B Stars	181

7.1	Comparison Between Observed and Predicted v_∞	181
7.2	Comparison Between Observed and Predicted \dot{M}	182
8	Conclusion	183

Observations of Hot-Star Winds

A.W. Fullerton	187
1 Introduction	187
2 Tracers of Stellar Winds	189
3 Spectroscopic Diagnostics	189
3.1 Scattering Versus ρ^2 Formation Processes	192
3.2 Dissecting the P Cygni Profile	193
3.3 Calculation of Line Profiles Formed in Stellar Winds	198
3.4 UV Resonance Lines	204
3.5 Optical Emission Lines	210
3.6 Time-Dependent Structure in Hot-Star Winds	215
4 Continuum Diagnostics	223
4.1 Free-Free Emission	223
4.2 Spectrum of Free-Free Emission from a Stellar Wind	225
4.3 Mass-Loss Rates from Continuum Observations	227
4.4 Nonthermal Radio Emission	229
4.5 The New Frontier: Spectroscopy in the Near and Far IR	231
5 Summary and Outlook	232

Circumstellar Disks

J.E. Bjorkman	239
1 Introduction	239
2 Disk Diagnostics	240
3 Theory of Circumstellar Disks	241
3.1 Accretion Disks	241
3.2 Outflow Disks	250
3.3 Time-Dependent Hydrodynamics	257
4 Radiation Transfer in Axisymmetric Systems	260
4.1 IR Excess Emission	262
4.2 Intrinsic Polarization	264
4.3 Spectral Line Profiles	270
5 Determination of Disk Geometry	274

Stellar Coronae

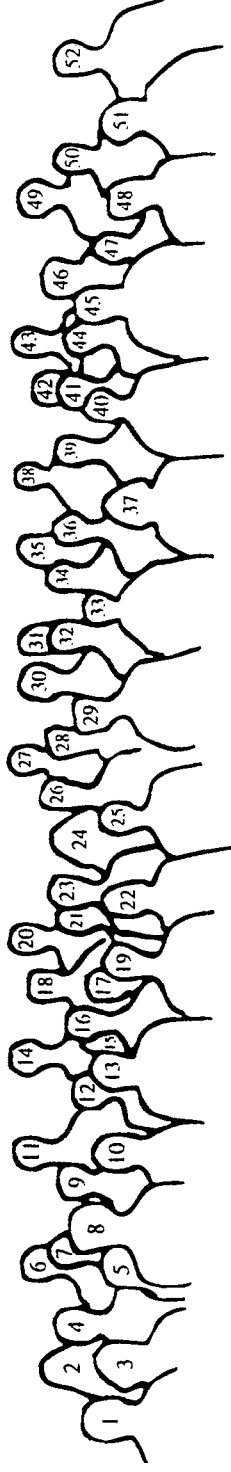
Jürgen H.M.M. Schmitt	277
1 Introduction	277
2 Basic Observational Results	282
2.1 The Solar–Stellar Connection	282
2.2 Which Stars Have Coronae?	283

2.3	The Sun in Perspective	285
2.4	Rotation-Activity Connection	285
2.5	Spectral Properties of X-Ray Coronae	289
2.6	Physical Properties of Stellar Coronae	291
3	Magnetically Closed Regions	300
3.1	Magnetically Open Regions	304
4	The Angular Momentum Problem	309
5	Magnetized Coronal Wind	310

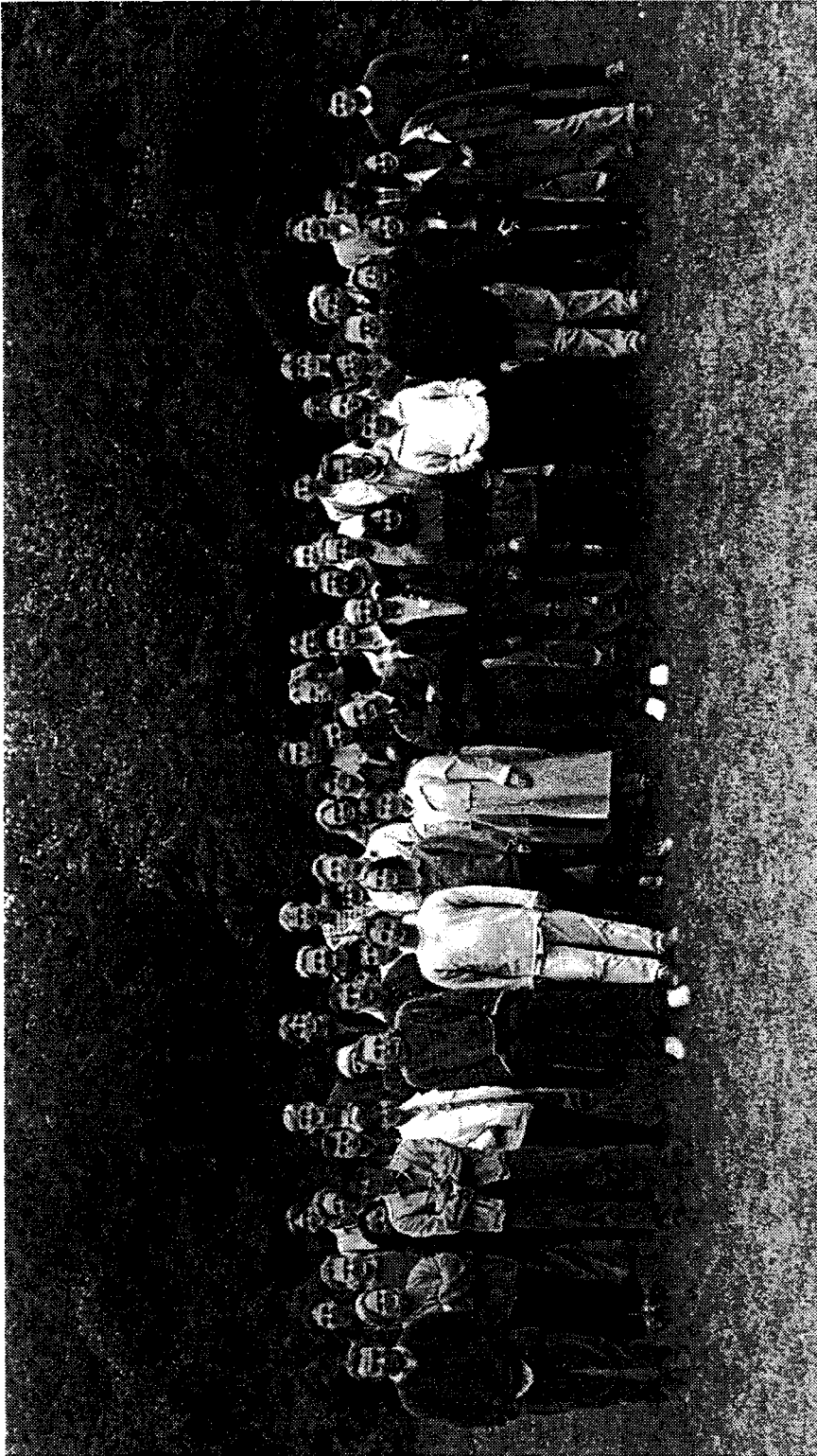
Atmospheres and Interior Models

J.P. De Greve	317
1 Why?	317
2 Recipe and Ingredients	318
2.1 Equations	318
2.2 Ingredients	318
2.3 Shooting (a Solution)	319
3 Evolution: From Wherefrom to Whereto, but Most of All: Why?	321
3.1 Masses Make All the Difference	321
3.2 Timescales	322
3.3 Convection and Other Mixings	323
3.4 Dredge-Up Phases in the Life of a Star	326
3.5 Anchored Shell Sources (the Node Theorem for Active Shell Sources)	327
3.6 Mass Motions of Different Shells	329
4 Thermal Pulses or Secular Stabilities of Shell Sources	330
4.1 Density Changes of a Nuclear Burning Zone	330
4.2 Shell Perturbation and Pressure Change	330
5 Cepheids (as an Answer to the Request of T. Le Bertre)	332
5.1 The Period-Density Relation	332
5.2 The Valve Mechanism	333
5.3 The Kappa Mechanism (Baker and Kippenhahn 1962)	333
6 Massive Stars ($M > 9 M_{\odot}$)	334
6.1 Mass Loss by Stellar Wind	335
6.2 Effects on the Position in the HRD	337
6.3 The Effect of Overshooting	338
6.4 Internal Mixing	338
6.5 Radius Correction for Hydrostatic Stars	339
6.6 New Models for Massive Stars	341

Subject Index	343
--------------------------------	------------



- | | | | | |
|-----------------------|--------------------------|-------------------------|--------------------------|---------------------------|
| 1. Koen Daems | 11. Klaus Schenker | 21. Leandro Machado | 31. Jean-Pierre De Greve | 41. Jurgen Schmitt |
| 2. Thomas Rivinius | 12. Elizabeth Humphreys | 22. Rita Loidl | 32. Sven De Rijcke | 42. Eswar Reddy |
| 3. Goedele Ruymackers | 13. Krzysztof Belczynski | 23. Alexander Heger | 33. Maurizio Manfre | 43. Neil McErlan |
| 4. Alex Fullerton | 14. Pieter Veen | 24. Yvonne Simis | 34. Jon Bjorkman | 44. Thibaut Le Bertre |
| 5. Gaitee Hussain | 15. Gwendolyn Meeus | 25. Véronique De Bruyne | 35. Jorge Sanz Forcada | 45. Yves Fremat |
| 6. Christopher Gill | 16. Nils Ryde | 26. Robert Voors | 36. Patrick Thoren | 46. Erwin Sedlmayr |
| 7. Bart Willems | 17. Maria Villamariz Cid | 27. Giovanni Catanzaro | 37. Maria Canullo | 47. Frau Sedlmayr |
| 8. Alain Hui-Bon-Hoa | 18. Yorick Vinck | 28. Kassios Mitrou | 38. Ignasi Ribas | 48. Eva Verdugo |
| 9. Darko Jevremovic | 19. Koen Malfait | 29. Thomas Lebzeller | 39. Olivier Varenne | 49. Alex Lobel |
| 10. Sophie Van Eck | 20. Kees Dullemond | 30. Peter Zaal | 40. Jean-Claude Bouret | 50. Stéphane Liberatore |
| | | | | 51. Konstantina Manolakou |
| | | | | 52. Carlos Allende Prieto |



Stellar Atmospheres Theory: An Introduction

I. Hubeny

Universities Space Research Association, NASA Goddard Space Flight Center,
Code 681, Greenbelt, MD 20771, USA
e-mail: hubeny@hrs.gsfc.nasa.gov

1 Fundamental Concepts

1.1 What Is a Stellar Atmosphere, and Why Do We Study It?

By the term stellar atmosphere we understand any medium connected physically to a star from which the photons escape to the surrounding space. In other words, it is a region where the radiation, observable by a distant observer, originates. Since in the vast majority of cases the radiation is the only information about a distant astronomical object we have (exceptions being a direct detection of solar wind particles, neutrinos from the Sun and SN 1987a, or gravitational waves), all the information we gather about stars is derived from analysis of their radiation.

It is therefore of considerable importance to develop reliable methods which are able to decode the information about a star contained in its spectrum with confidence. Having understood the physics of the problem and being able to carry out detailed numerical simulations will enable us to construct theoretical models of a stellar atmosphere and predict a stellar spectrum. This has important applications in other branches of astrophysics, such as i) derived stellar parameters can be used to verify predictions of the stellar evolution theory; ii) models provide ionizing fluxes for the interstellar medium and nebular models; iii) predicted stellar spectra are basic blocks for population syntheses of stellar clusters, starburst regions, and whole galaxies. Moreover, very hot and massive stars have special significance. They are very bright, and therefore may be studied spectroscopically as individual objects in distant galaxies. Reliable model atmospheres for these stars may therefore yield invaluable independent information about distant galaxies, like chemical composition, and, possibly, reliable distances.

This alone would easily substantiate viewing the stellar atmosphere theory as an independent, and very important, branch of modern astrophysics. Yet, in the global astrophysical context, there is another, and equally important, contribution of the stellar atmospheres theory. Stellar atmospheres are the best studied example of a medium where radiation is not only a *probe* of the physical state, but is in fact an *important constituent*. In other words, radiation in fact *determines* the structure of the medium, yet the medium is probed *only* by this radiation.

Unlike laboratory physics, where one can change a setup of the experiment in order to examine various aspects of the studied structures separately, we do not have this luxury in astrophysics: we are stuck with the observed spectrum so we should better make a good use of it. This is exactly what the stellar atmosphere theory is doing for almost a century now. Consequently, it is developed to such an extent that it provides an excellent methodological guide for other situations where the radiation has the dual role of a probe and a constituent. Examples of such astronomical objects are the interstellar medium, H II regions, and, in particular, accretion disks.

There has been a significant progress in the field of stellar atmospheres achieved in recent years. The progress was motivated by an unprecedented increase of quality of ground- and space-based observations, and by development of extremely fast and efficient numerical methods. However, despite of this progress, the stellar atmospheres theory is still far from being sufficiently developed. It is a mature field, yet it is now reaching qualitatively new levels of sophistication. In short, it is a field worth pursuing, offering as a reward a significant contribution to our knowledge about the Universe.

The main goal of this lecture is to provide a gentle introduction to the basic concepts needed to understand the fundamental physics of stellar atmospheres, as well as the leading principles behind recent developments. Particular emphasis will be devoted to the classical plane-parallel atmospheres in hydrostatic and radiative equilibrium. Topics which concentrate specifically on non-static phenomena (stellar winds), and on departures from radiative equilibrium (stellar chromospheres and coronae), are covered in other lectures of this volume.

There is no textbook that would fully cover the topics discussed in this lecture. The fundamental textbook of the field, Mihalas (1978), is still a highly recommended text, although it does not cover important recent developments, like for instance the ALI method. The third edition of the book is now in preparation, but it will take a couple of years before it is available. There is a recent textbook by Rutten (1995), distributed electronically, which covers both the basic concepts as well as some of the modern development, and is highly recommended to the beginner in the field. There are two books edited by Kalkofen which present a collection of reviews on various mathematical and numerical aspects of radiative transfer (Kalkofen 1984; 1987). A good textbook that covers both the theoretical and observational aspects of the stellar atmospheres is that by Gray (1992). Other related textbooks include Rybicki and Lightman (1979), Shu (1991), and an elementary-level textbook by Böhm-Vitense (1989). An old but excellent textbook on radiative transfer is Jefferies (1968). Besides these books, there are several excellent review papers covering various topics (e.g. Kudritzki 1988; Kudritzki and Hummer 1990), and several conference proceedings which contain many interesting papers on the stellar atmospheres theory – Properties of Hot Luminous Stars (Garmany 1990); Stellar Atmospheres: Beyond Classical Models (Crivellari,

Hubeny, and Hummer 1991); The Atmospheres of Early-Type Stars (Heber and Jeffery 1992); and Hydrogen-Deficient Stars (Jeffery and Heber 1996); to name just a few of the most important ones.

1.2 Basic Structural Equations

A stellar atmosphere is generally a plasma composed of many kinds of particles, namely atoms, ions, free electrons, molecules, or even dust grains, and photons. Typical values of temperature range from 10^3 K (or even less in the coolest stars) to a few times 10^5 K in the hottest stars (temperature is even higher, 10^6 - 10^7 K, in stellar coronae). Likewise, the total particle density ranges from, say, 10^6 to 10^{16} cm^{-3} . Under such conditions, the natural starting point for the physical description is the kinetic theory.

We start with very general equations, in order to emphasize a close connection of the stellar atmospheres theory and other branches of physics. We will then simplify these equations to the form which is used in most textbooks.

Specifically, the most general quantity which describes the system is the distribution function $f_i(\mathbf{r}, \mathbf{p}, t)$, which has the meaning that $f_i(\mathbf{r}, \mathbf{p}, t) d\mathbf{r} d\mathbf{p}$ is the number of particles of kind i in an elementary volume of the phase space at position \mathbf{r} , momentum \mathbf{p} , and at time t . The equation which describes a development of the distribution function is the well-known kinetic, or Boltzmann, equation, written as

$$\frac{\partial f_i}{\partial t} + (\mathbf{u} \cdot \nabla) f_i + (\mathbf{F} \cdot \nabla_{\mathbf{p}}) f_i = \left(\frac{Df_i}{Dt} \right)_{\text{coll}} , \quad (1)$$

where ∇ and $\nabla_{\mathbf{p}}$ are the usual nabla differential operators with respect to position and momentum components, respectively; \mathbf{u} is the particle velocity, and \mathbf{F} is the external force. The term $(Df/Dt)_{\text{coll}}$ is the so-called collisional term, which describes creations and destructions of particles of type i with the position $(\mathbf{r}, \mathbf{r} + d\mathbf{r})$ and momentum $(\mathbf{p}, \mathbf{p} + d\mathbf{p})$.

The kinetic equation provides a full description of the system. However, the number of unknowns is enormous. It should be realized that the individual particles are, in general, not just the atoms and ions, but in fact all the individual excitation states of atoms, ions, or molecules. According to the standard procedure, one simplifies the system by constructing equations for the *moments* of the distribution function, i.e. the integrals over momentum weighted by various powers of \mathbf{p} . I shall present only the final equations; the reader is referred to any standard textbook of the kinetic theory for a detailed derivation and an extensive discussion.

The resulting set of equations are the well-known hydrodynamic equations, namely the continuity equation,

$$\frac{\partial \rho}{\partial t} + \nabla \cdot (\rho \mathbf{v}) = 0 , \quad (2)$$

the momentum equation,

$$\frac{\partial(\rho \mathbf{v})}{\partial t} + \nabla \cdot (\rho \mathbf{v} \mathbf{v}) = -\nabla P + \mathbf{f} , \quad (3)$$

and the energy balance equation,

$$\frac{\partial}{\partial t} \left(\frac{1}{2} \rho v^2 + \rho \epsilon \right) + \nabla \cdot \left[\left(\frac{1}{2} \rho v^2 + \rho \epsilon + P \right) \mathbf{v} \right] = \mathbf{f} \cdot \mathbf{v} - \nabla \cdot (\mathbf{F}_{\text{rad}} + \mathbf{F}_{\text{con}}) . \quad (4)$$

Here, \mathbf{v} is the macroscopic velocity, ρ the total mass density, P the pressure, \mathbf{f} the external force, ϵ the internal energy, \mathbf{F}_{rad} the radiation flux, and \mathbf{F}_{con} the conductive flux. Equations (2) - (4) represent moment equations of the kinetic equation, (1), summed over all kinds of particles.

We may also write a zeroth-order moment equation for the individual kinds of particles, i.e. the conservation equation for particles of type i ,

$$\frac{\partial n_i}{\partial t} + \nabla \cdot (n_i \mathbf{v}) = \left(\frac{Dn_i}{Dt} \right)_{\text{coll}} , \quad (5)$$

where n_i is the number density (or the occupation number, or population) of particles of type i . One may also write momentum and energy balance equations for the individual particles if needed (e.g. if different kinds of particles have different macroscopic velocities). We will not consider these situations here.

The moment equations are still quite general. An application of those equations is discussed in other papers of this volume. Here, I will present a further significant simplification of the system, which applies for the case of a stationary (i.e. $\partial/\partial t = 0$), and moreover static ($\mathbf{v} = 0$) medium. Finally, we will consider a 1-D situation, i.e. all quantities depend on the z -coordinate only,

$$\left(\frac{Dn_i}{Dt} \right)_{\text{coll}} = 0 , \quad (6)$$

$$\nabla P = \mathbf{f} \implies \frac{dP}{dz} = -\rho g , \quad (7)$$

$$\nabla F_{\text{rad}} = 0 \implies F_{\text{rad}} = \text{const} \equiv \sigma T_{\text{eff}}^4 , \quad (8)$$

where σ is the Stefan-Boltzmann constant, and T_{eff} is the so-called effective temperature. The first equation is called the *statistical equilibrium* equation, the second one the *hydrostatic equilibrium* equation, while the last one, expressing the fact that the only mechanism that transports energy is radiation, is called the *radiative equilibrium* equation. (Notice that the conductive flux was neglected here, which is a common approximation in the stellar atmospheres theory. However, this approximation breaks down, for instance, in the solar transition region.)

What about convection, which we know may contribute significantly to the energy balance in certain types of stellar atmospheres? Convection is a

transport of energy by rising and falling bubbles of material with properties (e.g. temperature) different from the ambient medium. It is therefore, by its very nature, a non-stationary and non-homogeneous phenomenon. Putting $\mathbf{v} = 0$ and assuming a 1-D medium means, strictly speaking, that convection is a priori neglected. However, there are descriptions, like the mixing-length theory (see any standard textbook, like Mihalas 1978), that simplify the problem and cast it in the form of 1-D stationary equation, viz.

$$F_{\text{rad}} + F_{\text{conv}} = \sigma T_{\text{eff}}^4, \quad (9)$$

where the convective flux F_{conv} is a specified function of basic state parameters (temperature, density, etc.)

So far, we have specified the kinetic equation for particles. The same may be done for photons. Since, as explained above, photons have a special significance in stellar atmospheres, we will consider the kinetic equation for photons – the so-called *radiative transfer equation* – in the Sect. 2.

1.3 LTE Versus Non-LTE

It is well known from statistical physics that a description of material properties is greatly simplified if the thermodynamic equilibrium (TE) holds. In this state, the particle velocity distributions as well as the distributions of atoms over excitation and ionization states are specified uniquely by two thermodynamic variables. In the stellar atmospheres context, these variables are usually chosen to be the absolute temperature T , and the total particle number density, N , or the electron number density, n_e . From the very nature of a stellar atmosphere it is clear that it cannot be in thermodynamic equilibrium – we see a star, therefore we know that photons must be escaping. Since photons carry a significant momentum and energy, the elementary fact of photon escape has to give rise of significant *gradients* of the state parameters in the stellar outer layers.

However, even if the assumption of TE cannot be applied for a stellar atmosphere, we may still use the concept of *local thermodynamic equilibrium* – LTE. This assumption asserts that we may employ the standard thermodynamic relations not globally for the whole atmosphere, but *locally*, for local values of $T(\mathbf{r})$ and $N(\mathbf{r})$ or $n_e(\mathbf{r})$, despite the gradients that exist in the atmosphere. This assumption simplifies the problem enormously, for it implies that all the particle distribution functions may be evaluated locally, without reference to the physical ensemble in which the given material is found. Notice that the equilibrium values of distribution functions are assigned to *massive particles*; the radiation field is allowed to depart from its equilibrium, Planckian – (22), distribution function.

Specifically, LTE is characterized by the following three distributions:
– Maxwellian velocity distribution of particles

$$f(\mathbf{v})d\mathbf{v} = (m/2\pi kT)^{3/2} \exp(-m\mathbf{v}^2/2kT) d\mathbf{v}, \quad (10)$$

where m is the particle mass, and k the Boltzmann constant.

– Boltzmann excitation equation,

$$(n_j/n_i) = (g_j/g_i) \exp[-(E_j - E_i)/kT] , \quad (11)$$

where g_i is the statistical weight of level i , and E_i the level energy, measured from the ground state.

– Saha ionization equation,

$$\frac{N_I}{N_{I+1}} = n_e \frac{U_I}{U_{I+1}} C T^{-3/2} \exp(\chi_I/kT) , \quad (12)$$

where N_I is the total number density of ionization stage I , U is the partition function, defined by $U = \sum_1^\infty g_i \exp(-E_i/kT)$; χ_I is the ionization potential of ion I , and $C = (h^2/2\pi mk)^{3/2}$ is a constant ($= 2.07 \times 10^{-16}$ in cgs units). It should be stressed that in the astrophysical LTE description, the *same* temperature T applies to all kinds of particles, and to all kinds of distributions, (10) – (12).

Equations (10) – (12) define the state of LTE from the macroscopic point of view. Microscopically, LTE holds if all atomic processes are in *detailed balance*, i.e. if the number of processes $A \rightarrow B$ is exactly balanced by the number of inverse processes $B \rightarrow A$. By A and B we mean any particle states between which there exists a physically reasonable transition. For instance, A is an atom in an excited state i , and B the same atom in another state j (either of the same ion as i , in which case the process is an excitation/de-excitation; or of the higher or lower ion, in which case the term is an ionization/recombination). An illuminating discussion is presented in the textbook by Oxenius (1986).

In contrast, by the term non-LTE (or NLTE) we understand any state that departs from LTE. In practice, one usually means that populations of some selected energy levels of some selected atoms/ions are allowed to depart from their LTE value, while velocity distributions of all particles are assumed to be Maxwellian, (10), moreover with the same kinetic temperature, T .

One of the big issues of modern stellar atmospheres theory is whether, and if so to what extent, should departures from LTE be accounted for in numerical modeling. This question will be discussed in more detail later on (Sects. 3, 5). Generally, to understand why and where we may expect departures from LTE, let us turn to the microscopic definition of LTE. It is clear that LTE breaks down if the detailed balance in at least one transition $A \rightarrow B$ breaks down. We distinguish the *collisional transitions* (arising due to interactions between two or more massive particles), and *radiative transitions* (interactions involving particles and photons). Under stellar atmospheric conditions, collisions between massive particles tend to maintain the local equilibrium (since velocities are Maxwellian). Therefore, the validity of LTE hinges on whether the radiative transitions are in detailed balance or not.

Again, the fact that the radiation escapes from a star implies that LTE should eventually break down at a certain point in the atmosphere. Essentially, this is because detailed balance in radiative transitions generally breaks down at a certain point near the surface. Since photons escape (and more so from the uppermost layers), there must be a lack of them there. Consequently, the number of photoexcitations (or any atomic transition induced by absorbing a photon) is less than a number of inverse process, spontaneous de-excitations (we neglect here, for simplicity, stimulated emission).

These considerations explain that we may expect departures from LTE if the following two conditions are met: i) radiative rates in some important atomic transition dominate over the collisional rates; and ii) radiation is not in equilibrium, i.e. the intensity does not have the Planckian distribution. Later, we will show how these conditions are satisfied in different stellar types. However, some general features can be seen immediately. Collisional rates are proportional to the particle density; it is therefore clear that for high densities the departures from LTE tend to be small. Likewise, deep in the atmosphere, photons do not escape, and so the intensity is close to the equilibrium value. Departures from LTE are therefore small, even if the radiative rates dominate over the collisional rates.

2 Radiative Transfer Equation

As explained above, radiation plays a somewhat privileged role in the stellar atmospheres theory. This is the reason why we consider the radiative transfer equation separately from equations describing the material properties. The dominant role of radiation is also reflected in the terminology – the whole stellar atmosphere problem is sometimes referred to as a *solving the radiative transfer equation with constraints*, i.e. viewing all the material equations as mere “constraints”.

As discussed in the preceding section, one may view the radiative transfer equation as a kinetic equation for photons. In the astronomical literature, it is customary to start with a phenomenological derivation of the radiative transfer equation, and to show later that this equation is in fact equivalent to the kinetic equation.

It should be realized, however, that when viewing radiation as an ensemble of mutually non-interacting, massless particles – photons, and describing the interaction between radiation and matter in terms of simple collisions (interactions) between photons and massive particles, the wave phenomena connected with radiation are in fact neglected. This is a good approximation if i) the wavelength of radiation is much smaller than the typical distance between massive particles; and if ii) the particle positions are random. These conditions are well satisfied under the stellar atmospheric conditions: we deal with a hot plasma, so the particle positions are indeed random. For optical, UV, and even higher-frequency radiation, the wavelengths ($\lambda < 10^{-4}$ cm)

are indeed smaller than typical interparticle distances. For infrared and radio wavelengths, some wave phenomena (e.g. refraction) may actually play a role in the radiative transfer.

In the following, we will adhere to the photon picture, and neglect all the wave phenomena. A somewhat special case is the polarization of radiation. Polarization will also be neglected here, i.e. we assume an unpolarized radiation. We will see in other lectures (e.g., Bjorkman, this Volume), that polarization of radiation may actually play an important diagnostic role in certain stellar atmospheric structures (as an indicator of asymmetries of the medium). It is possible to extend the usual formalism of the transfer equation to account for polarization, by introducing a vector quantity (the so-called Stokes vector) instead of scalar intensity of radiation, and to write down the transfer equation in the vector form. We will not consider this case here; the interested reader is referred to standard textbooks – Chandrasekhar (1960); or recently Stenflo (1994); or excellent review articles (several papers in Kalkofen 1987).

2.1 Intensity of Radiation and Related Quantities

We start with phenomenological definitions. The *specific intensity*, $I(\mathbf{r}, \mathbf{n}, \nu, t)$, of radiation at position \mathbf{r} , traveling in direction \mathbf{n} , with frequency ν , at time t is defined such that the energy transported by radiation in the frequency range $(\nu, \nu + d\nu)$, across an elementary area dS , into a solid angle $d\omega$ in a time interval dt is

$$dE = I(\mathbf{r}, \mathbf{n}, \nu, t) dS \cos \theta d\omega d\nu dt, \quad (13)$$

where θ is the angle between \mathbf{n} and the normal to the surface dS (i.e. $dS \cos \theta = \mathbf{n} \cdot d\mathbf{S}$). The dimension of I is $\text{erg cm}^{-2} \text{ sec}^{-1} \text{ Hz}^{-1} \text{ sr}^{-1}$. The specific intensity provides a complete description of the unpolarized radiation field from the macroscopic point of view.

As pointed out above, there is a close connection between the specific intensity and the photon distribution function, f . The latter is defined such that $f(\mathbf{r}, \mathbf{n}, \nu, t) d\omega d\nu$ is the number of photons per unit volume at location \mathbf{r} and time t , with frequencies in the range $(\nu, \nu + d\nu)$, propagating with velocity c in direction \mathbf{n} . The number of photons crossing an element $d\mathbf{S}$ in time dt is $f(c \cdot dt)(\mathbf{n} \cdot d\mathbf{S})(d\omega d\nu)$. The energy of those photons is the same expression multiplied by $h\nu$, h being the Planck constant. Comparing this to the definition of the specific intensity, we obtain the desired relation between the specific intensity and the distribution function,

$$I = (ch\nu) f. \quad (14)$$

This relation makes it easy to understand the following expressions. Analogously as for massive particles, one defines various moments of the distribution function – i.e. the specific intensity in this case – which have a meaning of the energy density, flux, and the stress tensor.

From the definition of the distribution function, it is clear that the *energy density* of radiation is given by (dropping an explicit indication of the dependence on frequency, etc.)

$$E = \oint (h\nu) f d\omega = (1/c) \oint I d\omega , \quad (15)$$

because f is the number of photons in an elementary volume, and $h\nu$ the energy of each; we have to integrate over all solid angles. Similarly, the *energy flux* of radiation is given by

$$\mathbf{F} = \oint (h\nu) \cdot (c\mathbf{n}) f d\omega = \oint \mathbf{n} I d\omega , \quad (16)$$

because $c\mathbf{n}$ is the vector velocity.

The *radiation stress tensor* is defined by

$$\mathbf{P} = \oint (h\nu) \mathbf{n}\mathbf{n} f d\omega = (1/c) \oint \mathbf{n}\mathbf{n} I d\omega . \quad (17)$$

Finally, we mention that the *photon momentum density* [recall that the momentum of an individual photon is $(h\nu/c)\mathbf{n}$] is given by

$$\mathbf{G} = \oint (h\nu/c) \mathbf{n} f d\omega = (1/c^2) \mathbf{F} , \quad (18)$$

i.e., it is proportional to the radiation flux.

2.2 Absorption and Emission Coefficient

The radiative transfer equation describes the changes of the radiation field due to its interaction with matter. To describe this interaction, one first introduces several phenomenological quantities:

Absorption coefficient describes the removal of energy from the radiation field by matter. It is defined in such a way that an element of material, of cross-section dS and length ds , removes from a beam of specific intensity I (incident normal to dS into a solid angle $d\omega$), an amount of energy

$$dE = \chi(\mathbf{r}, \mathbf{n}, \nu, t) I(\mathbf{r}, \mathbf{n}, \nu, t) dS ds d\omega d\nu dt . \quad (19)$$

The dimension of χ is cm^{-1} , thus $1/\chi$ has a dimension of length, and it measures a characteristic distance a photon can travel before it is absorbed; in other words, the *photon mean free path*.

Emission coefficient describes the energy released by the material in the form of radiation. Analogously, it is defined such as an elementary volume of material, of cross-section dS and length ds , releases (into a solid angle $d\omega$, in direction \mathbf{n} , within a frequency band $d\nu$) an amount of energy

$$dE = \eta(\mathbf{r}, \mathbf{n}, \nu, t) dS ds d\omega d\nu dt . \quad (20)$$

The dimension of η is $\text{erg cm}^{-3} \text{hz}^{-1} \text{sec}^{-1} \text{sr}^{-1}$.

The absorption and emission coefficients are defined *per unit volume*. Sometimes, one defines the coefficients *per unit mass*, which are given by expressions (19) and (20) divided by the mass density, ρ .

The above coefficients are defined phenomenologically. To be able to write down actual expressions for them, we have to go to microscopic physics. In other words, we have to describe all contributions from microscopic processes that give rise to an absorption or emission of photons with specified properties. Detailed expressions will be considered later on (Sects. 3.1, 5.2). Here, we will discuss some general points:

i) Sometimes, one distinguishes two types of absorption, a “true absorption”, and a “scattering”. In the true absorption (also called “thermal absorption”) process, a photon is removed from the incident beam and is destroyed; while in the scattering process a photon is first removed from the beam, but is immediately re-emitted in a different direction and with (slightly) different frequency. This distinction is reflected in a notation,

$$\chi(\mathbf{r}, \mathbf{n}, \nu, t) = \kappa(\mathbf{r}, \mathbf{n}, \nu, t) + \sigma(\mathbf{r}, \mathbf{n}, \nu, t) , \quad (21)$$

where the first term on the right hand side, κ , refers to the true absorption, while the second term, σ , to the scattering. However, I stress that this distinction does not really have to do much with the absorption process – χ describes a removal of photon from the beam and does not have to care about what happens next. The distinction between the true absorption and scattering actually enters rather the proper formulation of the emission coefficient.

ii) It is known from the quantum theory of radiation that there are three types of elementary processes that give rise to an absorption or emission of a photon: 1) induced absorption – an absorption of a photon accompanied by a transition of an atom/ion to a higher energy state; 2) spontaneous emission – an emission of a photon accompanied by a spontaneous transition of an atom/ion to a lower energy state; and 3) stimulated emission – an interaction of an atom/ion with a photon accompanied by an emission of another photon with identical properties. In the astrophysical formalism, the stimulated emission is usually treated as negative absorption.

iii) In thermodynamic equilibrium, the microscopic detailed balance holds, and therefore the radiation energy absorbed in an elementary volume in an elementary frequency interval is exactly balanced by the energy emitted in the same volume and in the same frequency range. From the definition expressions for the absorption and emission coefficients, (19) and (20), it follows that in the equilibrium state, $\chi I = \eta$. Moreover, we know that in thermodynamic equilibrium the radiation intensity is equal to the Planck function, $I = B$, where

$$B(\nu, T) = \frac{2h\nu^3}{c^2} \frac{1}{\exp(h\nu/kT) - 1} . \quad (22)$$

We are then left with an interesting relation that in thermodynamic equilibrium, $\eta/\chi = B$, which is called *Kirchhoff's law*.

2.3 Phenomenological Derivation of the Transfer Equation

Having defined the basic phenomenological coefficients which describe the interaction of radiation and matter, a heuristic derivation of the radiative transfer equation is straightforward. We express a conservation of the total photon energy when a radiation beam passes through an elementary volume of matter of cross-section dS (perpendicular to the direction of propagation) and length ds (measured along the direction of propagation). Taking into account definitions of the specific intensity, (13), and the absorption and emission coefficients, (19) and (20), we obtain

$$\begin{aligned} & [I(\mathbf{r} + \Delta\mathbf{r}, \mathbf{n}, \nu, t + \Delta t) - I(\mathbf{r}, \mathbf{n}, \nu, t)] dS d\omega d\nu dt = \\ & [\eta(\mathbf{r}, \mathbf{n}, \nu, t) - \chi(\mathbf{r}, \mathbf{n}, \nu, t) I(\mathbf{r}, \mathbf{n}, \nu, t)] ds dS d\omega d\nu dt, \end{aligned} \quad (23)$$

which expresses the fact that the difference between specific intensities before and after passing through the elementary volume of pathlength ds is equal to the difference of the energy emitted and absorbed in the volume. The difference of intensities on the left hand side may be expressed as

$$\text{diff } I = \frac{\partial I}{\partial s} ds + \frac{\partial I}{\partial t} dt = \left(\frac{\partial I}{\partial s} + \frac{1}{c} \frac{\partial I}{\partial t} \right) ds. \quad (24)$$

Finally, $\partial I / \partial s$ may be written as $\mathbf{n} \cdot \nabla$, so we arrive at

$$\left(\frac{1}{c} \frac{\partial}{\partial t} + \mathbf{n} \cdot \nabla \right) I(\mathbf{r}, \mathbf{n}, \nu, t) = \eta(\mathbf{r}, \mathbf{n}, \nu, t) - \chi(\mathbf{r}, \mathbf{n}, \nu, t) I(\mathbf{r}, \mathbf{n}, \nu, t). \quad (25)$$

This is the general form of the radiative transfer equation. Let us now consider two important special cases.

1) for a one-dimensional planar atmosphere, $n_z = (dz/ds) = \cos \theta \equiv \mu$, where θ is the angle between direction of propagation of radiation, \mathbf{n} , and the normal to the surface. Further, let us assume a time-independent situation, $\partial / \partial t = 0$, so we obtain

$$\mu \frac{dI(\nu, \mu, z)}{dz} = \eta(\nu, \mu, z) - I(\nu, \mu, z) \chi(\nu, \mu, z), \quad (26)$$

where the intensity of radiation is now only a function of the geometrical coordinate z , frequency ν , and the directional cosine μ .

2) in spherical coordinates, the derivative along the ray, $\partial / \partial s$ is given by $\partial / \partial s = \mu(\partial / \partial r) + (1 - \mu^2)/r(\partial / \partial \mu)$, and the radiative transfer equation in a spherically symmetric medium is written as

$$\mu \frac{\partial I(\nu, \mu, r)}{\partial r} + \frac{1 - \mu^2}{r} \frac{\partial I(\nu, \mu, r)}{\partial \mu} = \eta(\nu, \mu, r) - I(\nu, \mu, r) \chi(\nu, \mu, r). \quad (27)$$

2.4 Optical Depth and the Source Function

Let us start with a simple 1-D transfer equation, written as

$$\mu \frac{dI_\nu}{dz} = \eta_\nu - \chi_\nu I_\nu , \quad (28)$$

where we drop an explicit indication of the dependence of I , η , and χ on the geometrical distance z and angle μ , and write, as is customary in the astrophysical literature, the frequency ν as a subscript. We divide the transfer equation by χ_ν , and obtain a very simple and advantageous form of the transfer equation,

$$\mu \frac{dI_\nu}{d\tau_\nu} = I_\nu - S_\nu , \quad (29)$$

where the *elementary optical depth* is defined by

$$d\tau_\nu \equiv -\chi_\nu dz , \quad (30)$$

and the *source function* is defined by

$$S_\nu \equiv \frac{\eta_\nu}{\chi_\nu} . \quad (31)$$

The absorption and emission coefficient are *local* quantities, therefore the definition of the source function, (31), applies for all geometries. The optical depth depends on the geometry; in case of a 3-D transfer, the most natural definition is the *optical depth along the ray*, defined by

$$d\tau = \chi(\mathbf{r}, \mathbf{n}, \nu) ds , \quad (32)$$

where ds is the elementary pathlength in the direction \mathbf{n} . In the case of a plane-parallel atmosphere, the relation between the optical depth in the direction μ (which we denote here as $\tau_{\mu\nu}$), and the “normal-direction” τ_ν defined by (30), is

$$d\tau_{\mu\nu} = d\tau_\nu / \mu . \quad (33)$$

What is the physical meaning of the optical depth and of the source function? The meaning of the optical depth is straightforward. In the absence of emissions, the transfer equation is simply $dI/d\tau = -I$, and the solution is $I(\tau) = I(\tau + \Delta\tau) \exp(-\Delta\tau)$, i.e. the optical depth is the e-folding distance for attenuation of the specific intensity due to absorption. In other words, the probability that a photon will travel an optical distance τ is simply $p(\tau) = \exp(-\tau)$. Since the absorption coefficient (e.g. in spectral lines) may be a sharply varying function of frequency, the (monochromatic) optical depth may also vary significantly with frequency. Sometimes one defines various frequency-independent optical depths, like those corresponding to the averaged absorption coefficient, either over the whole spectrum (a typical example being the Rosseland optical depth – see Sect. 2.8), or over a spectral line (see Sect. 3.1).

The meaning of the source function can also be easily understood. Let us write the number of photons emitted in an elementary volume (defined by an elementary area dS and an elementary path ds), to all directions. From the definition of the emission coefficient it follows that (assuming an isotropic emission for simplicity) $N_{\text{em}} = \eta ds (4\pi/h\nu) d\nu dt dS$, where the factor 4π comes from an integration over all solid angles, and $h\nu$ transforms energy (from the original definition of the emission coefficient) to the number of photons. Using the definition of the optical depth and the source function, we may rewrite the factor ηds as $\eta ds = (\eta/\chi)\chi ds = S(\tau)d\tau$. Consequently, the number of emitted photons is

$$N_{\text{em}} = S(\tau)d\tau \frac{4\pi}{h\nu} d\nu dt dS . \quad (34)$$

In other words, the source function is proportional to the *number of photons emitted per unit optical depth interval*.

For completeness, we mention that the number of photons *absorbed* per unit optical depth interval (from all solid angles) is analogously given by

$$N_{\text{abs}} = J(\tau)d\tau \frac{4\pi}{h\nu} d\nu dt dS , \quad (35)$$

which directly follows from (19); J being the mean intensity of radiation, defined by (48).

2.5 Elementary Solutions

In this section, we consider the simplest solutions of the 1-D plane-parallel transfer equation. For notational simplicity, we drop subscript ν indicating the frequency dependence.

a) *No absorption, no emission*, i.e. $\chi = \eta = 0$. The transfer equation reads $dI/dz = 0$, which has a trivial solution

$$I = \text{const} . \quad (36)$$

This expresses the obvious fact that in the absence of any interaction with the medium, the radiation intensity remains constant.

b) *No absorption, only emission*, i.e. $\chi = 0$, but $\eta > 0$. The solution is simply

$$I(z, \mu) = I(0, \mu) + \int_0^z \eta(z') dz' / \mu . \quad (37)$$

This equation is often used for describing an outgoing radiation from an optically thin radiating slab, like for instance a forbidden line radiation from planetary nebulae, or a radiation from the solar transition region and/or corona.

c) *No emission, only absorption*, i.e. $\eta = 0$, $\chi > 0$. The transfer equation now reads $\mu dI/d\tau = I$, and the solution is simply

$$I(0, \mu) = I(\tau, \mu) \exp(-\tau/\mu) . \quad (38)$$

d) *Absorption and emission*. We will now write a general formal solution of the transfer equation, i.e. for the case where both, absorption and emission, coefficients are different from zero, $\chi > 0$, $\eta > 0$. The solution is called “formal” because it is assumed here that both χ and η are *specified* functions of position and frequency. As we shall see later on, both coefficients may depend on the radiation field, so that in actual problems they may not be given a priori, without previously solving the general transfer problem. The formal solution reads

$$I(\tau_1, \mu) = I(\tau_2, \mu) \exp[-(\tau_2 - \tau_1)/\mu] + \int_{\tau_1}^{\tau_2} S(t) \exp[-(t - \tau_1)/\mu] dt/\mu . \quad (39)$$

e) *Semi-infinite atmosphere*. A special case of the formal solution (39) for emergent radiation (i.e. $\tau_1 = 0$) from a semi-infinite atmosphere ($\tau_2 = \infty$) reads

$$I(0, \mu) = \int_0^{\infty} S(t) \exp(-t/\mu) dt/\mu . \quad (40)$$

This equation shows that the specific intensity in a semi-infinite atmosphere is in fact a Laplace transform of the source function.

f) *Semi-infinite atmosphere with a linear source function*. Another special case of the general formal solution (39) is a emergent intensity from a semi-infinite atmosphere, with a source function being a *linear* function of optical depth, $S(\tau) = a + b\tau$. It is given by

$$I(0, \mu) = a + b\mu = S(\tau = \mu) . \quad (41)$$

This important expression is called the *Eddington-Barbier relation*. It shows that the emergent intensity, for instance in the normal direction ($\mu = 1$) is given by the value of the source function at the optical depth of unity. The values of emergent intensity for all angles μ between 0 and 1 then map the values of the source function between optical depths 0 and 1. Although in reality the source function does not have to be a linear function of optical depth, it can usually be well approximated by it in the vicinity of $\tau = 1$. Consequently, the Eddington-Barbier relation, (41), usually provides a good estimate of the emergent intensity.

g) *Finite homogeneous slab*. Finally, an expression for an emergent radiation ($\tau_1 = 0$) from a finite ($\tau_2 = T < \infty$) and homogeneous slab [i.e. $S(t) = S$ is constant], in the normal direction ($\mu = 1$), reads

$$I(0, 1) = S \cdot (1 - e^{-T}) . \quad (42)$$

In the special case $T \gg 1$, (42) becomes $I(0, 1) = S$, while for $T \ll 1$, we obtain $I(0, 1) = S \cdot T$. Both limiting expressions have a simple physical explanation. As we have shown above, the source function expresses a number of photons (or radiative energy) emitted per unit optical depth. In the optically thin case ($T \ll 1$), there is little absorption, so practically all created photons escape from the medium. Since the actual optical depth is T , the total emergent intensity is $S \cdot T$. In the optical thick case, we may roughly say that the photons created deeper than $\tau = 1$ are very likely absorbed, so the only photons which contribute to the emergent intensity are those emitted at optical depths $\tau \leq 1$. Consequently, the emergent intensity is $S \cdot 1$, i.e. S , regardless of the actual optical thickness of the slab.

2.6 Moments of the Transfer Equation

Analogously to the case of massive particles, we may define various moments of the photon distribution function, i.e. the specific intensity. By appropriately integrating the kinetic (i.e. transfer) equation we obtain relations between these moments. As was discussed in Sect. 2.1, the first three moments are the photon energy density, radiation flux, and the radiation stress tensor. Written synoptically, (see, e.g. the textbook by Shu 1991), we may write

$$\begin{pmatrix} cE_\nu \\ \mathbf{F}_\nu \\ c\mathbf{P}_\nu \end{pmatrix} = \oint \begin{pmatrix} 1 \\ \mathbf{n} \\ \mathbf{nn} \end{pmatrix} I_\nu d\omega . \quad (43)$$

Consequently, the moment equations are obtained by multiplying the transfer equation (25) by 1, \mathbf{n} , etc., and integrating over all solid angles. The first two moment equations read

$$\frac{\partial E_\nu}{\partial t} + \nabla \cdot \mathbf{F}_\nu = \eta_\nu - \chi_\nu c E_\nu , \quad (44)$$

$$\frac{1}{c} \frac{\partial \mathbf{F}_\nu}{\partial t} + c \nabla \cdot \mathbf{P}_\nu = -\chi_\nu \mathbf{F}_\nu , \quad (45)$$

Both these equations have the general structure of the moment equation of the kinetic equation, namely

$$\partial/\partial t(\text{density of quantity}) + (\text{gradient of its flux}) = (\text{sources} - \text{sinks}) . \quad (46)$$

In the astrophysical literature, one usually introduces moments as *angle-averaged*, rather than angle-integrated quantities. The first moments of the radiation intensity are usually denoted as J , H , K . We may synoptically write

$$\begin{pmatrix} J_\nu \\ \mathbf{H}_\nu \\ K_\nu \end{pmatrix} = \frac{1}{4\pi} \begin{pmatrix} cE_\nu \\ \mathbf{F}_\nu \\ c\mathbf{P}_\nu \end{pmatrix} = \frac{1}{4\pi} \oint \begin{pmatrix} 1 \\ \mathbf{n} \\ \mathbf{nn} \end{pmatrix} I_\nu d\omega . \quad (47)$$

In a plane-parallel approximation, all the moments are scalar quantities, and are given by

$$J_\nu = \frac{1}{2} \int_{-1}^1 I_\nu(\mu) d\mu , \quad (48)$$

$$H_\nu = \frac{1}{2} \int_{-1}^1 \mu I_\nu(\mu) d\mu , \quad (49)$$

$$K_\nu = \frac{1}{2} \int_{-1}^1 \mu^2 I_\nu(\mu) d\mu , \quad (50)$$

and the moment equations are written as

$$\frac{dH_\nu}{d\tau_\nu} = J_\nu - S_\nu , \quad (51)$$

and

$$\frac{dK_\nu}{d\tau_\nu} = H_\nu . \quad (52)$$

The system of moment equations is not closed, i.e. the equation for n -th moment contains the $(n+1)$ -th moment, etc. It is therefore necessary to come up with some kind of closure relation. In the stellar atmospheres theory, one defines the so-called Eddington factor, f^K , by

$$f_\nu^K \equiv K_\nu / J_\nu . \quad (53)$$

It is clear from the definition of moments that in the case of isotropic radiation, $I_\nu(\mu) = I_\nu$ being independent of angle, the Eddington factor $f^K = 1/3$. Assuming the Eddington factor to be specified, one may combine the two moment equations (51) and (52) together,

$$\frac{d^2(f_\nu^K J_\nu)}{d\tau_\nu^2} = J_\nu - S_\nu . \quad (54)$$

This equation is very useful. It effectively eliminates one independent variable, the angle μ , from the problem. Numerically, it replaces the original transfer equation, which is a first-order linear differential equation for the specific intensity $I_{\nu\mu}$, by a second-order but still linear differential equation for the mean intensity, J_ν . However, its simplicity is illusory. It cannot be used alone, even if the source function is given, since in general the Eddington factor is unknown unless the full solution of the transfer equation is known. However, this form of the transfer equation is very useful in certain numerical methods, as we will discuss later on. It should be realized that it can be used to advantage only in *iterative* methods; in which we use current values of J and K to determine the current Eddington factor f^K , and keep this factor fixed during the subsequent iteration step.

2.7 Lambda Operator

Let us first write down the general formal solution of the radiative transfer equation for a semi-infinite plane-parallel atmosphere, with no incoming radiation at the surface ($\tau = 0$),

$$I_\nu(\tau_\nu, \mu) = \int_{\tau_\nu}^{\infty} S_\nu(t) e^{-(t-\tau_\nu)/\mu} dt / \mu, \quad \text{for } \mu \geq 0, \quad (55)$$

$$I_\nu(\tau_\nu, \mu) = \int_0^{\tau_\nu} S_\nu(t) e^{-(\tau_\nu-t)/(-\mu)} dt / (-\mu), \quad \text{for } \mu < 0. \quad (56)$$

Recall that from the definition of the directional cosine μ follows that positive values of μ correspond to outward directions, while negative values of μ correspond to inward directions. The mean intensity of radiation is obtained by integrating (55) and (56) over μ , viz.

$$J_\nu(\tau_\nu) = \frac{1}{2} \int_0^\infty S_\nu(t) E_1(|t - \tau_\nu|) dt, \quad (57)$$

where E_1 is the first exponential integral. The general exponential integral is defined by

$$E_n(x) \equiv \int_1^\infty \frac{e^{-xt}}{t^n} dt, \quad (58)$$

The mean intensity may be synoptically expressed as an action of an operator, Λ , on the source function,

$$J_\nu(\tau_\nu) = \Lambda_{\tau_\nu} [S(t)], \quad (59)$$

where the Λ -operator is defined by

$$\Lambda_\tau[f(t)] = \frac{1}{2} \int_0^\infty E_1(|t - \tau|) f(t) dt, \quad (60)$$

The behavior of the kernel functions corresponding to the specific intensity, (55), which is a simple exponential, and for the mean intensity, which is the first exponential integral, (57), is displayed in Fig. 1. The width of the kernel decreases with decreasing μ , which is easily understood by realizing that a unit optical distance for a photon traveling with a certain angle with respect to the normal to the surface, μ , corresponds to a larger optical distance than for one traveling in the normal direction, because the distance is proportional to $1/\mu$. Similarly, the kernel for the specific intensity propagating in the normal direction ($\mu = 1$) is significantly wider than the kernel for the mean intensity. This is simply because the mean intensity contains contribution from all angles, i.e. the corresponding kernel is an average over all μ -dependent specific intensity kernels.

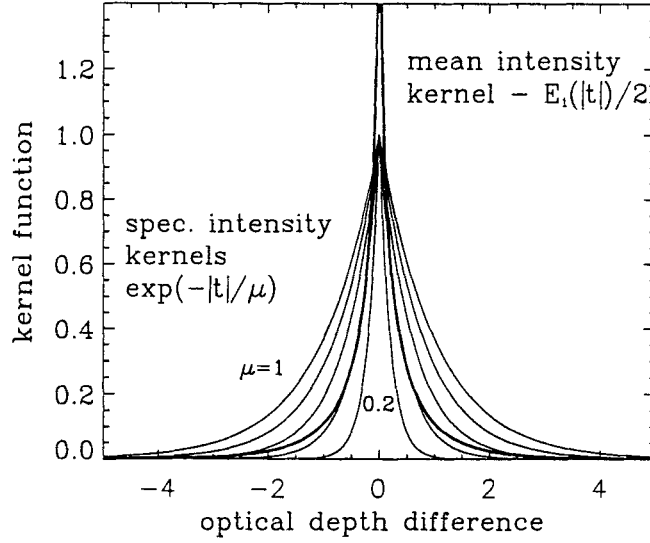


Fig. 1. Kernel functions for the specific intensity at various angles (thin lines for $\mu = 1, 0.8, 0.6, 0.4$, and 0.2), and for the mean intensity of radiation (thick line)

For practical purposes, (57) or (59) have to be replaced by a quadrature sum. Equation (59) can thus be written in the discretized form as

$$J_d = \sum_{d'=1}^D \Lambda_{dd'} S_{d'} , \quad (61)$$

where d denotes the depth index (we dropped the frequency index ν). The Λ -operator can thus be thought of as Λ -matrix, and the mean intensity as well as the source function at all depths as column vectors.

What is the meaning of the Λ -matrix? Let us take, quite formally, all elements of the source function vector to be zero except the i -th element which is taken to be 1, $S_d = \delta_{di}$. Then

$$\begin{pmatrix} J_1 \\ J_2 \\ \vdots \\ J_D \end{pmatrix} = \begin{pmatrix} \Lambda_{11} & \Lambda_{12} & \dots & \Lambda_{1D} \\ \Lambda_{21} & \Lambda_{22} & \dots & \Lambda_{2D} \\ \vdots & \vdots & \ddots & \vdots \\ \Lambda_{D1} & \Lambda_{D2} & \dots & \Lambda_{DD} \end{pmatrix} \times \begin{pmatrix} 0 \\ \vdots \\ 1 \\ \vdots \end{pmatrix} = \begin{pmatrix} \Lambda_{1i} \\ \Lambda_{2i} \\ \vdots \\ \Lambda_{Di} \end{pmatrix} . \quad (62)$$

In other words, the i -th column of the A matrix is a solution of the transfer equation with the source function given as a unit pulse function. Physically, the i -th column of A therefore describes how the pulse which originated at the i -th depth point spreads over all depths.

2.8 Diffusion Approximation

Deep in the atmosphere, the source function approaches the Planck function, $S_\nu \rightarrow B_\nu$, because virtually no photons escape, and thus the medium approaches the thermal equilibrium. Let us choose a reference optical depth, $\tau_\nu \gg 1$, and let us expand the source function for $t_\nu \geq \tau_\nu$ by a Taylor expansion,

$$S_\nu(t_\nu) = \sum_{n=0}^{\infty} \frac{d^n B_\nu}{d\tau_\nu^n} \frac{(t_\nu - \tau_\nu)^n}{n!} , \quad (63)$$

Substituting this expression to the formal solution, (55) and (56), we obtain

$$I_\nu(t_\nu, \mu) = \sum_{n=0}^{\infty} \mu^n \frac{d^n B_\nu}{d\tau_\nu^n} = B_\nu(\tau_\nu) + \mu \frac{dB_\nu}{d\tau_\nu} + \mu^2 \frac{d^2 B_\nu}{d\tau_\nu^2} + \dots . \quad (64)$$

By substituting this expression into definition equations for the moments, we obtain

$$J_\nu(\tau_\nu) = B_\nu(\tau_\nu) + \frac{1}{3} \frac{d^2 B_\nu}{d\tau_\nu^2} + \dots , \quad (65)$$

$$H_\nu(\tau_\nu) = \frac{1}{3} \frac{dB_\nu}{d\tau_\nu} + \dots , \quad (66)$$

$$K_\nu(\tau_\nu) = \frac{1}{3} B_\nu(\tau_\nu) + \frac{1}{5} \frac{d^2 B_\nu}{d\tau_\nu^2} + \dots . \quad (67)$$

These equations illustrate several features of the behavior of the radiation field at large depths. First, the mean intensity approaches the Planck function. Second, the radiation field is nearly isotropic, and the Eddington factor $f_\nu^K = K_\nu/J_\nu$ approaches $1/3$. Finally, the monochromatic flux is given as a derivative of the Planck function with respect to the optical depth. Since the Planck function is only a function of temperature, we may express the flux by means of the temperature gradient,

$$H_\nu = \frac{1}{3} \frac{dB_\nu}{d\tau_\nu} = -\frac{1}{3} \frac{1}{\chi_\nu} \frac{dB_\nu}{dz} = -\frac{1}{3} \frac{1}{\chi_\nu} \frac{dB_\nu}{dT} \frac{dT}{dz} . \quad (68)$$

Thus, at great depths the transfer problem reduces to this single equation. The name *diffusion approximation* comes from the similarity of this equation to other, material, diffusion equations, which are typically of the form

$$\text{flux} = (\text{diffusion coefficient}) \times (\text{gradient of the relevant quantity}) . \quad (69)$$

We may thus think of the term $(-1/3)(1/\chi_\nu)(dB_\nu/dT)$ as a *radiative diffusion coefficient*; or, because of a similarity of (68) to the heat conductivity equation, as *radiative conductivity*.

By integrating over all frequencies we obtain for the *total radiation flux* in the diffusion approximation

$$H = - \left(\frac{1}{3} \frac{1}{\chi_R} \frac{dB}{dT} \right) \frac{dT}{dz} . \quad (70)$$

where the averaged opacity is defined by

$$\frac{1}{\chi_R} \frac{dB}{dT} = \int_0^\infty \frac{1}{\chi_\nu} \frac{dB_\nu}{dT} d\nu , \quad (71)$$

which is the well-known *Rosseland mean opacity*. One may define many other averaged (mean) opacities by simpler expressions, but we see why the Rosseland opacity is defined by this seemingly strange expression – it yields the *exact total radiation flux* at large depths. Since the temperature in the atmosphere is in fact determined by the condition imposed on the total radiation flux, the Rosseland mean opacity yields the *correct temperature structure* deep in the atmosphere. It is also clear why the Rosseland opacity is the most appropriate one for the use in the stellar interior theory (de Greve, this Volume). Notice also that the integrand in the definition of Rosseland opacity contains $1/\chi$, i.e. the contribution to the integral is largest for the lowest monochromatic opacities. Indeed, for those frequencies the medium is most transparent, and therefore the monochromatic flux is largest. This again shows that the Rosseland mean opacity is the most appropriate one for describing the total radiation flux.

3 Radiative Transfer with Constraints; Escape Probability

3.1 Two-Level Atom

The simplest situation where we have a coupling of the radiative transfer equation and the statistical equilibrium equation is an idealized case of a two-level atom. Real atoms contain many energy levels, so that this approximation may seem at first sight to be grossly inadequate. However it actually provides a surprisingly good description of line formation in many cases of interest. And, more importantly, the case of the two-level atom has a significant pedagogical value because it provides an explanation of many elementary processes that are crucial to understand NLTE line formation. In other words, a good physical understanding of line formation in a two-level atom is a prerequisite to understanding of more complicated cases. Therefore, this model will be discussed here in certain detail.

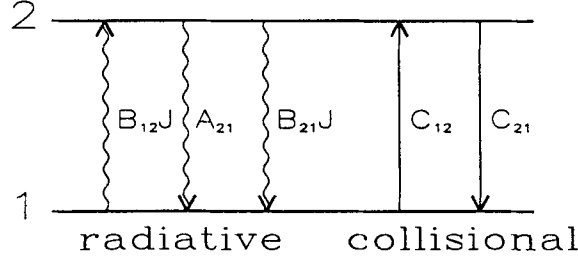


Fig. 2. Schematic representation of microscopic processes in a two-level atom

Let us first derive the expression for the source function. Figure 2 shows schematically the energy levels and all the elementary processes populating and depopulating the levels. The absorption and emission coefficients are given by

$$\kappa_\nu = \frac{h\nu_0}{4\pi} (n_1 B_{12} - n_2 B_{21}) \phi(\nu) , \quad (72)$$

and

$$\eta_\nu = \frac{h\nu_0}{4\pi} n_2 A_{21} \phi(\nu) , \quad (73)$$

where ν_0 is the line-center frequency, and B_{12} , B_{21} and A_{21} are the Einstein coefficients for absorption, stimulated emission, and spontaneous emission, respectively, for the radiative transitions between levels 1 and 2; n_1 and n_2 are populations (occupation numbers) of levels 1 and 2, respectively, and $\phi(\nu)$ is the *absorption profile*. The latter expresses the probability density that if a photon is absorbed (emitted) in a line 1–2, it has a frequency in the range $(\nu, \nu + d\nu)$. The profile coefficient is thus normalized to unity, $\int_0^\infty \phi(\nu) d\nu = 1$. We assume that there is no other absorption or emission mechanism present.

It is advantageous to introduce a dimensionless frequency, x , by

$$x \equiv \frac{\nu - \nu_0}{\Delta\nu_D} , \quad (74)$$

$\Delta\nu_D$ is the Doppler width, given by $\Delta\nu_D = (\nu_0/c)v_{\text{th}}$, with the thermal velocity $v_{\text{th}} = (2kT/m)^{1/2}$, m being the mass of the radiating atom. In the case of a pure Doppler profile (i.e. no intrinsic broadening of the spectral line;

the only broadening is due to the thermal motion of radiators), the absorption profile is given by

$$\phi(x) = \exp(-x^2)/\sqrt{\pi} . \quad (75)$$

In a more general case, where there is an intrinsic broadening of lines described by a Lorentz profile in the atomic rest frame (the most common types of intrinsic broadening being the natural, Stark, and Van der Waals broadening - see Mihalas 1978, or monograph by Griem 1974), the profile function is given by the Voigt function,

$$\phi(x) = H(a, x)/\sqrt{\pi}, \quad H(a, x) = \frac{a}{\pi} \int_{-\infty}^{\infty} \frac{e^{-y^2}}{(x-y)^2 + a^2} dy . \quad (76)$$

The Voigt function is a convolution of the Doppler profile (i.e. the thermal motions) and the Lorentz profile (intrinsic broadening). The parameter a is a damping parameter expressed in units of Doppler width, $a = \Gamma/(4\pi\Delta\nu_D)$, where Γ is the atomic damping parameter. For instance, for the natural broadening of a line originating in a two-level atom, $\Gamma = A_{21}$.

Opacity in the line may be written as

$$\kappa_x = \kappa \phi(x) , \quad (77)$$

and analogously for η_x . The optical depth corresponding to the frequency-independent opacity, κ , is called the *frequency-averaged opacity* in the line, and is often used in line transfer studies. Notice that this opacity is *not* equal to the line center opacity, $\kappa(0)$, but is related to it by, for instance for the Doppler profile, $\kappa(0) = \kappa/\sqrt{\pi}$.

A remark is in order. We use the same profile coefficient for absorption, stimulated emission, and spontaneous emission - all of them are given through $\phi(\nu)$. This is an approximation called *complete redistribution* (CRD), which holds if an emitted photon is completely uncorrelated to a previously absorbed photon. In other words, the absorbed photon is re-emitted, i.e. redistributed, *completely*, without any memory of the frequency at which it was previously absorbed. A more exact description, taking into account photon correlations, is called the *partial redistribution* (PRD) approach. A discussion of this approach is beyond the scope of the present lecture; moreover, PRD effects are important only for certain lines (e.g. strong resonance lines, like hydrogen $L\alpha$, Mg II h and k lines, etc.), and under certain conditions (rather low density). The interested reader is referred to several reviews (e.g. Mihalas 1978; Hubeny 1985).

The source function follows from (72) and (73),

$$S_\nu \equiv \frac{\eta_\nu}{\kappa_\nu} = \frac{n_2 A_{21}}{n_1 B_{12} - n_2 B_{21}} \equiv S^L , \quad (78)$$

which is independent of frequency, thanks to the approximation of CRD.

Next step is to determine the ratio n_2/n_1 which enters the source function. This is obtained from the statistical equilibrium equation, which states that

the number of transitions into the state 1 (or 2) is equal to the number of transitions out of state 1 (2). This equation reads

$$n_1 (R_{12} + C_{12}) = n_2 (R_{21} + C_{21}) , \quad (79)$$

where R 's are the radiative rates, and C 's the collisional rates. The radiative rates are given by

$$R_{12} = B_{12} \int_0^\infty J_\nu \phi(\nu) d\nu \equiv B_{12} \bar{J} , \quad (80)$$

$$R_{21} = A_{21} + B_{21} \int_0^\infty J_\nu \phi(\nu) d\nu \equiv A_{21} + B_{21} \bar{J} , \quad (81)$$

where the quantity \bar{J} is called the *frequency-averaged mean intensity* of radiation. We will view here collisional rates as known functions of electron density (since collisions with electrons are usually most efficient) and temperature; for details, refer e.g. to Mihalas (1978).

Using the well-known relations between the Einstein coefficients, $B_{21}/B_{12} = g_1/g_2$, and $A_{21}/B_{21} = 2h\nu_0^3/c^2$, and the relation between the collisional rates, $C_{21}/C_{12} = (n_1/n_2)^* = (g_1/g_2) \exp(h\nu_0/kT)$ (where $(n_1/n_2)^*$ denotes the LTE population ratio), we obtain after some algebra

$$S = (1 - \epsilon) \bar{J} + \epsilon B_{\nu_0} , \quad (82)$$

where

$$\epsilon = \frac{\epsilon'}{1 + \epsilon'} ; \quad \epsilon' = \frac{C_{21}(1 - e^{-h\nu/kT})}{A_{21}} . \quad (83)$$

In the typical case, $h\nu/kT \gg 1$ (since typical resonance lines, for which the two-level approximation is adequate, are formed in the UV region where the frequency is large), and therefore ϵ may be expressed simply as

$$\epsilon \approx \frac{C_{21}}{C_{21} + A_{21}} , \quad (84)$$

which shows that ϵ may be interpreted as a *destruction probability*, i.e. the probability that an absorbed photon is destroyed by a collisional de-excitation process (C_{21}) rather than being re-emitted (A_{21}).

Equation (82) is the fundamental equation of the problem. The first term on the right hand side represents the photons in the line created by scattering, i.e. by the emission following a previous absorption of a photon, while the second term represents the thermal creation of a photon, i.e. an emission following a previous collisional excitation.

Mathematically, the source function, (82), is still a *linear* function of the mean intensities. This is the case only for a two-level atom; in a general multi-level atom the source function contains non-linear terms in the radiation intensity. The two-level atom is thus an interesting pedagogical case: it contains a large-scale coupling of the radiation field and matter, yet the

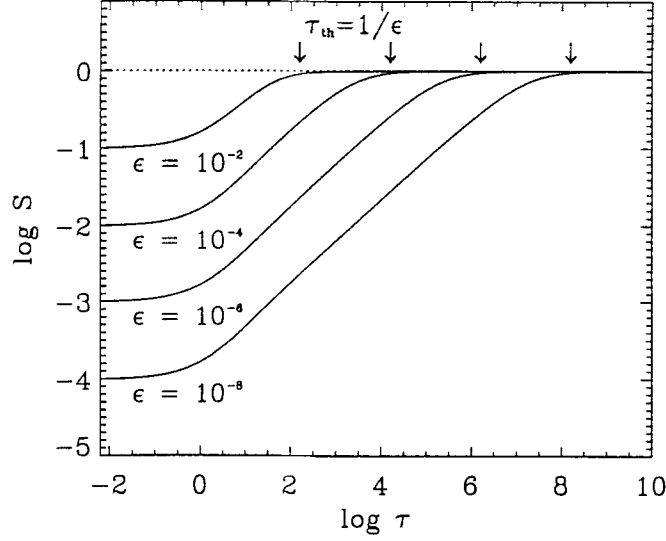


Fig.3. Source function for a two-level atom in a constant-property semi-infinite atmosphere, with $B = 1$ (which only states that the source function is expressed in units of B), and for various values of the destruction parameter ϵ ; $\epsilon = 10^{-2}, 10^{-4}, 10^{-6}, 10^{-8}$

coupling, although being non-local, is still linear, and therefore much easier to handle (and understand!) than in the general case.

By applying any of the numerical methods which are discussed in the next chapter, one can easily obtain a solution of the two-level atom problem. Let us take a standard example of line formation in a homogeneous semi-infinite slab. The homogeneity implies that all material properties (temperature, density, etc.) are independent of depth. In the context of the source function, (82), this means that ϵ , B , and $\phi(x)$ are depth-independent. The solution, first obtained by Avrett and Hummer (1965), is displayed in Fig. 3 for several values of the destruction parameter ϵ . It shows two interesting features:

i) The surface value of the source function is equal to $\sqrt{\epsilon} B$. Actually, this is a rather robust result, which is valid regardless of the type of the profile coefficient. Several rigorous mathematical proofs exist (see, e.g., monograph by Ivanov 1973); a physical explanation of this result was given by Hubeny (1987).

ii) The source function starts to deviate from the Planck function at a

certain depth; below this point it is essentially equal to B . This depth is called the *thermalization depth*, and is traditionally denoted as Λ . We use here the notation τ_{th} to avoid confusion with the Λ -operator. Figure 3 indicates that for a Doppler profile, $\tau_{\text{th}} \approx 1/\epsilon$. This indeed agrees with a more rigorous analytical study (Avrett and Hummer 1965; Ivanov 1973). These analyses moreover show that for a Voigt profile the thermalization depth is even larger, $\tau_{\text{th}} \approx a/\epsilon^2$.

Why does the source function decrease towards the surface? We know that in the case of a homogeneous medium the departures from LTE arise only because of the presence of the boundary through which the photons escape. Before the line photons “feel” the presence of the boundary (i.e. in large enough optical depths), all microscopic processes depicted on Fig. 2 are in detailed balance, so the LTE approximation holds. However, as soon as the photons start to feel the boundary, i.e. they start to escape from the medium through the boundary, the photo-excitations are no longer balanced by radiative de-excitations. Since the absorption rate depends on the number of photons present, while the spontaneous emission rate does not (we neglect for simplicity the stimulated emission), the number of radiative excitations drops below the number of de-excitations as soon as photons start to escape. The lower level will consequently start to be overpopulated with respect to LTE, while the upper level will be underpopulated. Since the source function measures the number of photons created per unit optical depth, and since the number of created photons is proportional to the population of the upper level (because this is the level from which the atomic transition accompanied by the photon emission occur), the source function has to drop below the Planck function.

Having understood that, we now face an intriguing question: Given that departures from LTE arise because of the presence of the boundary, how come that the thermalization depth, i.e. the depth where the departures of the source function from the Planck function set in, is so large? Recall that the optical depth τ in Fig. 3 is the frequency-averaged optical depth in the line. One might then expect that the presence of the boundary is felt by an “average” photon around $\tau \approx 1$, while the actual depth where photons feel the boundary is much larger (e.g. $\tau \approx 10^6$ for a typical value of $\epsilon = 10^{-6}$)!

The explanation hinges on the fact that an “average” photon is not the one which is responsible for the transport and escape of photons in a line. Let us follow a photon trajectory from the point of its thermal creation. Let us assume that the photon was created at a large optical distance from the boundary. The photon is created with a large probability of having the frequency near the line center, because this probability is given by the absorption profile, $\phi(x)$, which is a sharply peaked function of frequency around $x = 0$. Consequently, the monochromatic optical depth is large, and so the physical distance it travels before the next absorption (i.e. the geometrical distance corresponding to $\tau_x \approx 1$) is quite small. The same situation very likely oc-

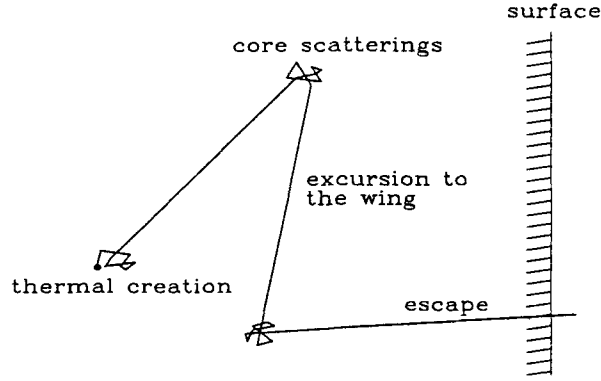


Fig. 4. Schematic representation of a trajectory of a photon in a gas of two-level atoms

curs after the next scattering. We are then left with the following picture of photon trajectory in the two-level atom case with complete redistribution (the trajectory for the case of partial redistribution is quite different!): The photon makes many consecutive scatterings with the frequency staying close to the line center; during these scatterings the photon practically does not move at all in the physical space. However, in a very infrequent event when it is re-emitted in the wing, the opacity it sees drops suddenly by orders of magnitude, and therefore it can travel a very large distance. The situation is depicted in Fig. 4. We see that the transfer in the core is inefficient; what really accomplishes the transfer are infrequent excursions of the photon to the line wings. This makes the photon transfer quite different from the massive particle transport: The particle mean free path remains of the same order of magnitude when a particle diffuses through the physical space, while the photon mean free path can change enormously. It is now clear why the thermalization depth is so large: it is determined by line-wing photons, whose mean free path is much larger than that of the core photons, which in turn define the mean optical depth τ .

It is also clear why the thermalization depth depends on the destruction probability ϵ . The total number of consecutive scatterings is of the order of $1/\epsilon$; if the photon does not escape before it experiences $1/\epsilon$ scatterings, it is destroyed by collisional processes, and therefore does not feel the presence of the boundary. These considerations are made more quantitative by the *escape probability* approach, which we shall consider in detail in the next subsection.

Finally, I mention that the source function for a line in a general multi-level atom can always be written in a form analogous to (82), viz. (see, e.g., Mihalas 1978)

$$S_{ij}^L = (1 - \epsilon_{ij}) \bar{J}_{ij} + \eta_{ij} , \quad (85)$$

where ϵ_{ij} and η_{ij} are the generalized destruction and creation terms, respectively; subscripts ij indicate that the quantities are appropriate for the transition $i \rightarrow j$. This approach is called the *equivalent-two-level-atom* (ETA) approach. The source function is formally a linear function of the mean intensity. However, it should be realized that the destruction and creation terms ϵ_{ij} and η_{ij} contain contributions from the transition rates in all transitions in and out of states i and j , which depend on the radiation field. Therefore, despite apparent linearity of equation (85), one has to solve a general multi-level atom problem by an iteration process. The ETA approach may or may not converge in actual situations, and is not recommended as a robust and universal method. Nevertheless, it may be useful in some applications (see, for instance, several papers in Kalkofen 1984 and 1987; or Castor et al. 1992).

3.2 Escape Probability

Let us first consider a probability that a photon with frequency ν and propagating in the direction specified by angle μ escapes in a single flight. This probability is given by

$$p_{\nu\mu} = e^{-\tau_{\nu\mu}} , \quad (86)$$

which follows from the very physical meaning of optical depth (see Sect. 2.4). The angle-averaged escape probability is given by

$$p_{\nu}(\tau_{\nu}) = \frac{1}{2} \int_0^1 e^{-\tau_{\nu}/\mu} d\mu = \frac{1}{2} E_2(\tau_{\nu}) , \quad (87)$$

where the integration only extends for angles $\mu \geq 0$, since photons moving in the inward direction ($\mu < 0$) cannot escape. Finally, the angle- and frequency-averaged escape probability for photons in one line is given by (adopting the x -notation, and writing x as a subscript)

$$p_e(\tau) = \int_{-\infty}^{\infty} \phi_x p_x(\tau_x) dx = \frac{1}{2} \int_{-\infty}^{\infty} \phi_x E_2(\tau \phi_x) dx . \quad (88)$$

Notice that at the surface, $p_e(0) = 1/2$, because a photon is either emitted in the outward direction, in which case it certainly escapes, or in the inward direction, in which case it does not escape (assuming an isotropic emission).

We may now quantify the considerations given in the previous subsection. We introduce the *photon destruction probability* by

$$p_d = \epsilon , \quad (89)$$

and we have the *photon escape probability*, p_e , defined above. Now, if $p_e \ll p_d$, photons are likely thermalized before escaping from the medium. In other words, the line photons do not feel the presence of the boundary, and therefore $S \approx B$. On the other hand, if $p_e \gg p_d$, photons likely escape before being thermalized, i.e. destroyed by a collisional process. It is therefore natural to define the thermalization depth τ_{th} , as

$$p_e(\tau_{th}) = p_d , \quad (90)$$

which indeed gives, by substituting the Doppler profile in (88), the expression $\tau_{th} \approx 1/\epsilon$.

The escape probability considerations are actually much more powerful than just to explain the value of thermalization depth. One may in fact construct approximate expressions for the source function as a function of depth. To demonstrate this, let us consider the following simple model: We know that \bar{J} measures the number of photons absorbed in a line per unit optical depth interval [which may be verified by integrating (35) over frequencies]. If we are far from the surface, all the photons emitted per unit optical distance, $S(\tau) d\tau$, either escape from the medium by a single flight (with a probability p_e), or are re-absorbed, more or less on the spot, with probability $1 - p_e$. This suggests that the number of photons absorbed at τ , i.e. $\bar{J}(\tau)$, should be given by

$$\bar{J}(\tau) = S(\tau) (1 - p_e) , \quad (91)$$

which gives us the desired approximate relation between the averaged mean intensity of radiation and the source function, without actually solving the transfer equation!

A very interesting point is that we can arrive, purely mathematically, to the same equation if we start with the integral expression (116) (see Sect. 4.2), and do the following trick: Since the kernel function $K_1(t)$ varies much more rapidly than $S(t)$, we may assume that the source function does not vary over the range where the kernel function varies appreciably. In other words, we may remove $S(t)$ from the integral in (116), and put $S(t) = S(\tau)$. One may easily verify that by integrating the kernel function K_1 over τ one obtains (91) with p_e given by (88).

Substituting (91) into the expression for the source function, (82), we obtain the following expression for the source function,

$$S(\tau) = \frac{\epsilon}{\epsilon + (1 - \epsilon)p_e} B , \quad (92)$$

which is traditionally called the *first-order escape probability approximation*. It describes very well the behavior of the source function at depths, but it fails to reproduce the $\sqrt{\epsilon}$ -law, since it yields for the source function at the surface $S(0) = 2\epsilon/(1 + \epsilon) B$, which may be quite different from $\sqrt{\epsilon} B$. The reason for this can be easily understood: any transfer of photons is neglected here, and the problem is reduced to just two mechanisms – a photon either

escapes in a single direct flight, or is thermalized. This so-called “dichotomous” model works well deep in the atmosphere, but fails in the outer layers of the atmosphere, where the transfer of photons is important.

Without going to any more details, I just mention that the so-called *second-order escape probability* formalism, which takes into account some aspects of the photon transport, was developed (for an illuminating discussion, see an excellent review by Rybicki, 1984). The resulting expression for the source function in a homogeneous atmosphere is

$$S(\tau) = \left(\frac{\epsilon}{\epsilon + 2(1 - \epsilon)p_e} \right)^{1/2} B, \quad (93)$$

which behaves very similarly to the first-order approximation at depths, but now yields the correct expression for the source function at the surface, $S(0) = \sqrt{\epsilon} B$.

Concluding, the escape probability approach is very useful and very powerful, because it is able to provide simple approximate relations between the source function and the mean intensity of radiation, based on simple physical arguments. It can therefore be used in cases where detailed numerical solutions are either too complicated and time consuming (like in the case of radiation hydrodynamic simulations, where the radiative transfer equation is solved in a huge number of time steps), or where a high accuracy of predicted emergent radiation is not required. However, one should always keep in mind that the escape probability methods are *inherently approximate*, and therefore one should be always aware of their potential limitations and inaccuracies. Finally, I stress that these methods were discussed here partly because of the above reasons, and partly because of their intimate relation to a class of modern numerical methods, called Accelerated Lambda Iteration (ALI) methods, which will be discussed in the next section.

4 Numerical Methods

There are several types of numerical method, depending on the degree of complexity of the problem at hand. In this section, we will consider numerical methods for treating three basic problems, ordered by increasing complexity, i) a formal solution of the radiative transfer equation – where the source function is specified; ii) a solution of linear line formation problems – the source function is a linear function of radiation intensity; and iii) a solution of general non-linear problems.

4.1 Formal Solution of the Transfer Equation

By the term formal solution we understand a solution of the transfer equation if the source function is fully specified. We have already shown the formal solution of the transfer equation, given by (39) for the general case; or by

(55) and (56) for a semi-infinite atmosphere. The related expression for the mean intensity is (57). In practice, we may replace the integral over optical depth by a quadrature sum, and calculate the radiation intensity by a simple summation.

Why, then, would we need to consider other numerical methods for this apparently trivial problem? The basic point is that the simple numerical quadrature is extremely inefficient from the point of view of computer time. This is because the kernel functions contain exponentials, which are very costly to compute. As we will see later on, the speed of modern numerical methods which solve a general coupled problem is in fact determined by the speed with which the individual formal solutions are accomplished. Therefore, we have to seek as efficient numerical schemes for performing a formal solution as possible.

There are essentially two classes of methods, namely those based on

1. the first-order form of the transfer equation; or
2. the second-order form of the transfer equation. The second-order method is usually called the Feautrier method, in honor of its originator (Feautrier 1964).

First-order methods. They were not used very much during the last two decades. However, they were revived recently by an ingenious adaptation of the Discontinuous Finite Element (DFE) method by Castor et al. (1992). This scheme now appears to be an extremely advantageous method, and will very likely be used more and more in the stellar atmosphere numerical work. I will present only a brief outline here; the interested reader is referred to the original paper.

Let us assume a given frequency ν and angle μ . Let us denote τ the monochromatic optical depth at frequency ν , along the ray specified by angle μ . In the following, we drop an explicit indication of frequency and angle variables. The intensity of radiation in the optical depth interval between two discretized depth points, (τ_d, τ_{d+1}) , is assumed to be given as a linear function of optical depth.

$$I(\tau) = I_d^+ \frac{\tau_{d+1} - \tau}{\Delta\tau_d} + I_{d+1}^- \frac{\tau - \tau_d}{\Delta\tau_d} . \quad (94)$$

To avoid confusion, I stress that we deal with the intensity in *one direction* only; the notation I^+ and I^- does not mean intensities in opposite directions, as it is usually used in the radiative transfer theory.

If $I_d^- = I_d^+$, the linear representation of intensity, (94), is a continuous function of frequency. However, the related numerical method would be quite inaccurate. The essence of the DFE method is to allow for step *discontinuities* at points τ_d , i.e. we consider generally $I_d^- \neq I_d^+$. Substituting (94) into the transfer equation (29), and performing analytic manipulations described in

Castor et al. (1992), one obtains final linear relations for the quantities I^+ and I^- , viz.

$$\frac{I_{d+1}^- + I_d^+ - 2I_d^-}{\Delta\tau_d} = S_d - I_d^- , \quad (95)$$

and

$$\frac{I_{d+1}^- - I_d^+}{\Delta\tau_d} = S_{d+1} - I_{d+1}^- . \quad (96)$$

By eliminating I_d^+ we obtain a simple linear recurrence relation for I_d^- ,

$$(\Delta\tau_d^2 + 2\Delta\tau_d + 2)I_{d+1}^- - 2I_d^- = \Delta\tau_d S_d + \Delta\tau_d(\Delta\tau_d + 1)S_{d+1} , \quad (97)$$

and I_d^+ follows from

$$(\Delta\tau_d^2 + 2\Delta\tau_d + 2)I_d^+ = 2(\Delta\tau_d + 1)I_d^- + \Delta\tau_d(\Delta\tau_d + 1)S_d - \Delta\tau_d S_{d+1} . \quad (98)$$

Finally, the resulting specific intensity at τ_d is given as a linear combination of the “discontinuous” intensities I_d^- and I_d^+ ,

$$I_d = \frac{I_d^- \Delta\tau_d + I_d^+ \Delta\tau_{d-1}}{\Delta\tau_d + \Delta\tau_{d-1}} . \quad (99)$$

Second-order, or Feautrier method. The basis of the method is to introduce the symmetric and antisymmetric averages of the specific intensity,

$$j_{\mu\nu} \equiv \frac{1}{2} [I(+\mu, \nu) + I(-\mu, \nu)] , \quad (0 \leq \mu \leq 1) , \quad (100)$$

$$h_{\mu\nu} \equiv \frac{1}{2} [I(+\mu, \nu) - I(-\mu, \nu)] , \quad (0 \leq \mu \leq 1) . \quad (101)$$

Considering separately the transfer equation (29) for positive and negative μ 's, and adding and subtracting these equations we obtain,

$$\mu (dh_{\mu\nu}/d\tau_\nu) = j_{\mu\nu} - S_\nu , \quad (102)$$

$$\mu (dj_{\mu\nu}/d\tau_\nu) = h_{\mu\nu} . \quad (103)$$

Using (103) to eliminate $h_{\mu\nu}$ from (102), we obtain

$$\mu^2 \frac{d^2 j_{\mu\nu}}{d\tau_\nu^2} = j_{\mu\nu} - S_\nu . \quad (104)$$

This equation is very similar to the moment equation (54); also the quantity $j_{\mu\nu}$ is very similar to the mean intensity J_ν . The essential difference between (54) and (104) is that (104) is a *closed* equation for the symmetrized intensity $j_{\mu\nu}$, which may therefore be solved in a single step if the source function is known.

Special care should be devoted to the boundary conditions. The specific intensity is specified for negative μ 's at the upper boundary, and for the positive μ 's at the lower boundary;

$$I(-\mu, \nu, \tau = 0) = I_{\mu\nu}^-, \quad (0 \leq \mu \leq 1) , \quad (105)$$

$$I(+\mu, \nu, \tau = \tau_{\max}) = I_{\mu\nu}^+, \quad (0 \leq \mu \leq 1) , \quad (106)$$

($\tau_{\max} = \infty$ for a semi-infinite atmosphere). Substituting (105) into (103), and using (101), we obtain

$$\mu (dj_{\mu\nu}/d\tau_\nu)_0 = j_{\mu\nu}(0) - I_{\mu\nu}^- , \quad (107)$$

$$\mu (dj_{\mu\nu}/d\tau_\nu)_{\tau_{\max}} = I_{\mu\nu}^+ - j_{\mu\nu}(\tau_{\max}) . \quad (108)$$

In most cases, the incoming intensity $I_{\mu\nu}^- = 0$. For a semi-infinite atmosphere, the diffusion approximation is usually used for the lower boundary condition,

$$I_{\mu\nu}^+ = B_\nu(\tau_{\max}) + \mu(\partial B_\nu/\partial \tau_\nu)_{\tau_{\max}} . \quad (109)$$

Equation (104), together with boundary conditions (107) and (108) is solved numerically by discretizing the depth variable. The discretized form may be written as (writing $u \equiv j_{\mu\nu}$),

$$-A_d u_{d-1} + B_d u_d - C_d u_{d+1} = S_d , \quad (110)$$

Detailed expressions for the elements A, B, C are given in the standard textbooks (e.g. Mihalas 1978). The resulting tridiagonal set of equations is solved by a straightforward Gaussian elimination, consisting in a forward-backward recursive sweep, namely

$$D_d = (B_d - A_d D_{d-1})^{-1} C_d, \quad D_1 = B_1^{-1} C_1 , \quad (111)$$

$$Z_d = (B_d - A_d D_{d-1})^{-1} (S_d + A_d Z_{d-1}), \quad Z_1 = B_1^{-1} S_1 , \quad (112)$$

followed by the reverse sweep,

$$u_d = D_d u_{d+1} + Z_d, \quad u_{ND+1} = 0 , \quad (113)$$

where ND is the number of discretized depth points.

4.2 Linear Coupling Problems

The second class of methods are those in which the source function is given as a known, *linear*, function of the specific intensities. A typical example is the line formation in a two-level atom, where the source function is given by (82). A more general case is the equivalent-two-level-atom source function, (85), with the creation and destruction terms η_{ij} and ϵ_{ij} assumed to be specified. In other words, this corresponds to solving the transfer problem for one line at a time.

Numerical solution can either be done by a *differential equation* approach, or by an *integral equation* approach.

The differential equation method. This consists in choosing discrete values of frequencies, $(x_i, i = 1, \dots, NF)$ and angles $(\mu_j, j = 1, \dots, NA)$, and to solve a coupled set of transfer equations written for all frequency-angle points,

$$\mu_j \frac{dI(x_i, \mu_j, \tau)}{d\tau} = \phi(x_i) [I(x_i, \mu_j, \tau) - S(\tau)] , \quad (114)$$

where the source function on the right hand side is given by (85), replacing the integrals over frequency and angle by a quadrature sum,

$$S = (1 - \epsilon) \frac{1}{2} \sum_{i=1}^{NF} \sum_{j=1}^{NA} w_i^x w_j^\mu \phi(x_i) I(x_i, \mu_j) + \eta , \quad (115)$$

where w_i^x and w_j^μ are the quadrature weights for the integration over frequencies and angles, respectively. The source function couples *all* frequencies and angles, but the main point is that the source function is a linear function of the specific intensities, (85). The system (114) is thus a system of *linear* differential equations. One may construct a column vector \mathbf{I} whose elements are values of specific intensity at given depth for all pairs of (x, μ) , and write all equations (114) as one differential equation for the vector \mathbf{I} . One may then apply the Feautrier method described above; equations (100) - (113) remain the same, only the meaning of u and the coefficients A, B, C will be different. u will represent a vector $(j_{\nu, \mu_j}, i = 1, \dots, NF, j = 1, \dots, NA)$ (i.e. the Feautrier intensities at all discretized frequency-angle points), and A, B, C will be $(NF \times NA) \times (NF \times NA)$ matrices. The resulting system of linear equations forms a block-tridiagonal system.

The integral equation method. This is based on expressing the averaged mean intensity \bar{J} as an integral over S , which easily follows from the formal solution of the transfer equation discussed in Sect. 2. By integrating (57) over frequencies, we obtain

$$\bar{J}(\tau) = \int_0^\infty S(t) K_1(|t - \tau|) dt , \quad (116)$$

where the kernel function K_1 is given by

$$K_1(s) = \int_0^\infty E_1(\phi_x s) \phi_x^2 dx . \quad (117)$$

The behavior of the kernel function depends on the type of the absorption profile. As can be intuitively expected, it has a narrower peak for the Doppler profile than for the Voigt profile. A useful numerical algorithm for computing the function K_1 was given by Hummer (1981).

Substituting (116) into (82) yields the following integral equation for the source function:

$$S(\tau) = (1 - \epsilon) \int_0^\infty S(t) K_1(|t - \tau|) dt + \epsilon B . \quad (118)$$

This equation was first solved more than three decades ago by Avrett and Hummer (1965). The equation was subsequently extensively studied analytically by the Russian analytical school. Many elegant analytical results are summarized in a monograph by Ivanov (1973); this book is recommended to anyone who intends to study the radiative transfer seriously.

The integral equation approach has several advantages and drawbacks. The advantage is that it deals with one simple integral equation for S , so in a sense it is formulated in the most efficient way since the knowledge of S represents the solution of the problem (individual specific intensities of radiation may then easily be obtained by the formal solution of the transfer equation). In other words, the coupling of radiation and material properties in the integral equation approach is fully contained in the function K_1 , which is calculated in advance, while in the differential equation approach the coupling is treated explicitly. Nevertheless, the differential equation approach may be reformulated in an efficient way by casting it in the form analogous to the integral approach (the so-called Rybicki variant of the Feautrier method – see Rybicki 1971). In any case, the integral equation approach suffers from a significant drawback, namely that in evaluating the kernel function (and in the formal solution of the transfer equation), one faces the task of evaluating a large number of exponentials, which are computationally very costly. Therefore, most of the actual numerical work in the radiative transfer is nowadays being done using the differential equation approach.

4.3 Accelerated Lambda Iteration

In the previous section, we saw that the two-level atom problem is a linear one, and thus may be solved in a single step, without any iterations. However, one pays a high price for that: one has to invert, at every discretized depth point, some auxiliary matrices whose dimension is given by the product of the number of discretized frequencies times the the number of discretized angles. [The situation may be alleviated by employing the so-called Variable Eddington Factor technique, developed by Auer and Mihalas (1970), which treats the angle coupling separately. The size of matrices is reduced but is still given by the number of frequencies, which may be large]. Generally, one should realize that *any method that describes a coupling of various quantities by means of a direct matrix inversion is fundamentally limited* in that the computer time scales as the cube of the number of quantities (i.e. the number of frequency points in our case).

Therefore, one needs faster schemes. How can this be accomplished? The clue is to realize that some part of the physical coupling is more important than others. In other words, not all the parts of the coupling should necessarily be treated on the same footing; it is more or less a numerical overkill to do so. So, this hints that the “important part” of the coupling should be treated exactly, while the rest may be treated iteratively.

Below, I demonstrate the method on an example of a two-level atom. However, the method is much more powerful, and can be applied to virtually any astrophysical radiative transfer problem. One such application will be mentioned in Sect. 5.4. We first recall that the two-level problem may be written, by substituting (60) into (82), as

$$S = (1 - \epsilon)\bar{\Lambda}[S] + \epsilon B , \quad (119)$$

(which is just another expression of the integral equation form 118). The frequency-averaged lambda operator is given by

$$\bar{\Lambda} = \int_0^\infty \Lambda_\nu \phi(\nu) d\nu , \quad (120)$$

with the frequency-dependent Lambda operator Λ_ν given by (60). In the following, I omit the bar over Λ for notational simplicity.

In a seminal paper Cannon (1973) introduced into astrophysical radiative transfer theory the *method of deferred corrections* (also called, somewhat inaccurately, *operator splitting*), long known in numerical analysis. The idea consists of writing

$$\Lambda = \Lambda^* + (\Lambda - \Lambda^*) , \quad (121)$$

where Λ^* is an appropriately chosen *approximate lambda operator*. The iteration scheme for solving (119) may then be written as

$$S^{(n+1)} = (1 - \epsilon)\Lambda^*[S^{(n+1)}] + (1 - \epsilon)(\Lambda - \Lambda^*)[S^{(n)}] + \epsilon B , \quad (122)$$

or, in a slightly different form whose importance becomes apparent later,

$$S^{(n+1)} - S^{(n)} = [1 - (1 - \epsilon)\Lambda^*]^{-1} [S^{\text{FS}} - S^{(n)}] , \quad (123)$$

where

$$S^{\text{FS}} = (1 - \epsilon)\Lambda[S^{(n)}] + \epsilon B . \quad (124)$$

Superscript FS stands for Formal Solution. In other words, (122) shows that the action of the exact Λ operator is split into two contributions: an approximate Λ^* operator which acts on the new iterate of the source function, and the difference between the exact and approximate operator, $\Lambda - \Lambda^*$, acting on the previous, known, iterate of the source function. The latter contribution may be easily evaluated by the formal solution.

If we choose $\Lambda^* = 0$, we recover the “ordinary” lambda iteration, which is straightforward, but is known to converge very slowly – see, e.g. Mihalas 1978; or Olson, Auer, Buchler (1986 – hereafter referred to as OAB). On the other hand, the choice $\Lambda^* = \Lambda$ represents the exact method, which is done without any iteration, but an inversion of the exact Λ operator may be costly. So, in order that Λ^* brings an essential improvement over both methods, it has to satisfy the following requirements: i) it has to incorporate all the *essential* properties of the exact Λ operator in order to obtain a fast convergence rate of the iteration process; but at the same time, ii) it must be

easy (and cheap) to invert. These requirements are generally incompatible, therefore the construction of the optimum Λ^* is a delicate matter.

The interesting history of the quest for the optimum Λ^* operator is summarized by Hubeny (1992). Let us stress that a numerically most advantageous approximate operator is a diagonal (i.e. local) operator Λ^* , in which case it represents a multiplication by a scalar value, and its inversion is a simple division. To understand that the term “diagonal operator” is equivalent to the term “local operator”, recall (61) and (62). These equations also explain why a good approximation for the exact Λ -matrix is its diagonal. Recall that the matrix element Λ_{ji} tells us what portion of photons created in an elementary interval around depth point i [i.e. $S(\tau_i)$] are being absorbed at depth point j [described by $J(\tau_j)$]. Most photons are absorbed very close to the point of their creation, so the diagonal term Λ_{ii} is much larger than the off-diagonal terms. In other words, approximating the exact Λ by a diagonal operator means replacing the kernel function for the mean intensity, (60) by a δ -function, which, as seen in Fig. 1, is quite reasonable. (These considerations also show that the next simplest approximation for the Λ -operator would be its tridiagonal part; here an interaction between a given depth and its immediate neighbors is taken into account.)

Equation (123) is particularly instructive. It shows that iteration is driven, similarly as the ordinary lambda iteration, by the difference between the old source function and the newer source function obtained by formal solution. However, unlike the ordinary lambda iteration, this difference is amplified by the “acceleration operator” $[1 - (1 - \epsilon)\Lambda^*]^{-1}$. To gain more insight, let us consider a diagonal (i.e. local) Λ^* operator. The appropriate Λ^* has to be chosen such as $\Lambda^*(\tau) \rightarrow 1$ for large τ (see below). Since in typical cases $\epsilon \ll 1$, the acceleration operator indeed acts as a large amplification factor. This interpretation was first introduced by Hamann (1985), who also coined the term “Accelerated Lambda Iteration” (ALI). The acronym ALI is also sometimes understood to mean “Approximate Lambda Iteration”. Other terms for ALI are *Operator Perturbation* (Kalkofen 1987), or *Approximate-Operator Iteration* (AOI; Castor et al. 1991, 1992). Finally, the term “accelerated Λ iteration” should not be confused with “acceleration of convergence”, discussed later on.

How do we know that Λ^* should approach unity at large depths? Here comes the intimate relation between the escape probability and the ALI methods, mentioned in Sect. 3.2. Recall that the escape probability formalism gives a relation between the mean intensity and the source function, namely $\bar{J} = (1 - p_e)S$. This is exactly what we need here – a local approximate relation between \bar{J} and S . We may thus put, as a reasonable choice, $\Lambda^* = 1 - p_e$, which indeed shows that Λ^* approaches unity for large τ . This escape-probability form of Λ^* may be used for numerical work, but modern approaches provided more efficient and robust ways to construct the approximate Λ^* operator.

I will not discuss here all possible variants of the Λ^* operator; the interested reader is referred to Hubeny (1992). I will only mention several important papers. First, Scharmer (1981) revived Cannon's original ideas, and constructed an ingenious Λ^* operator based on the Eddington-Barbier relation. Next, OAB have shown, using rigorous mathematics, that a nearly optimum Λ^* operator is a diagonal part of the true Λ operator. Olson and Kunasz (1987) showed that the tridiagonal and possibly higher multi-band parts of the lambda operator yield even more rapid convergence. Finally, Rybicki and Hummer (1991) used a formalism based on the Feautrier scheme, employing a very efficient algorithm for inverting a tridiagonal matrix, and demonstrated that the entire set of the diagonal elements of Λ can be found with an order of ND operations. This feature makes it the method of choice, since it avoids computing costly exponentials, a problem inherent to both previous approaches (OAB; Olson and Kunasz 1987).

Acceleration of Convergence. This is a highly technical topic, but is mentioned here because it has recently become an important ingredient of the ALI methods. Only a brief summary of the basic ideas is presented here. Any iterative scheme can be written in the form

$$\mathbf{x}^{(n+1)} = \mathbf{F} \cdot \mathbf{x}^{(n)} + \mathbf{x}^{(0)} , \quad (125)$$

where \mathbf{F} is called the *amplification matrix*. In the case of the linear transfer problem, (122), we have \mathbf{F} given by $\mathbf{F} = [1 - (1 - \epsilon)\Lambda^*]^{-1} [(1 - \epsilon)(\Lambda - \Lambda^*)]$, where $\mathbf{x}^{(n)}$ is an n -th iterate of the source function.

As it is well known from linear algebra, any iteration method where the $(n + 1)$ -th iterate is solely evaluated by means of the previous one converges only *linearly*. However, taking into account information from the earlier iterates, one may find faster schemes. I will not discuss these methods in any detail here, the interested reader is referred to the review papers by Auer (1987, 1991), or to the original papers cited therein. I just briefly mention that for the most popular scheme, the Ng acceleration, the general expression for the accelerated estimate of the solution in the n -th iteration is written

$$\mathbf{x}^{\text{acc}} = \left(1 - \sum_{m=1}^M \alpha_m \right) \mathbf{x}^{(n)} + \sum_{m=1}^M \alpha_m \mathbf{x}^{(n-m)} , \quad (126)$$

where the coefficients α are determined by a residual minimization. Practical expressions are given by OAB, Auer (1987, 1991), or Hubeny and Lanz (1992).

4.4 Non-linear Coupling Problems

To illustrate the basic problem of applying ALI in multilevel problems, let us first write down the expression for the radiative rates. For simplicity, let us

consider only lines; the treatment of continua is analogous. The net transition rate for any line $i \rightarrow j$ (i and $j \neq i$ represent any states of an atom), is

$$R_{ji}^{\text{net}} = n_j A_{ji} - (n_i B_{ij} - n_j B_{ji}) \bar{J}_{ij} , \quad (127)$$

The basic ALI equation, (121), gives for \bar{J}_{ij}

$$\bar{J}_{ij} = \Lambda^* [S^{\text{new}}] + (\Lambda - \Lambda^*) [S^{\text{old}}] . \quad (128)$$

Here the second term, which may be written as $\Delta \bar{J}_{ij}^{\text{old}}$, is known from the previous iteration. However, the first term contains S^{new} which is a complicated, and generally non-linear function of the “new” populations.

This is an unfortunate situation. By applying the ALI idea, we have succeeded to eliminate the radiation intensity from the rate equations, but at the expense of ending with a set of non-linear equations for the populations. We cope with this problem by one of the possible two ways:

1. *Linearization.* The usual way of solving the set of non-linear equations is by applying the Newton–Raphson method. This may be rather time consuming because each iteration requires to set up and to invert the Jacobi matrix of the system.
2. *Preconditioning.* This is an ingenious way to analytically remove inactive (scattering) parts of radiative rates from the rate equations, and to recover a linearity of the ALI form of the rate equations.

Let us demonstrate the idea of preconditioning on a simple case, where the total source function is given by the line source function $S_{ij} = n_j A_{ji} / (n_i B_{ij} - n_j B_{ji})$ (i.e., the case of non-overlapping lines and no background continuum). Let us further assume that we have a local (diagonal) approximate Λ^* operator (Λ^* is then a real number). The net rate (127) may be written, after some algebra,

$$R_{ji}^{\text{net}} = n_j A_{ji} (1 - \Lambda_{ji}^*) - (n_i B_{ij} - n_j B_{ji}) \Delta \bar{J}_{ij}^{\text{old}} , \quad (129)$$

which is indeed *linear* in the populations!

This is a very interesting expression. Notice first that the original net rate, (127), is represented by a subtraction of two large contributions, *all* emission minus all absorptions, while the result, the net rate, is rather small. Physically, this follows from the fact that most emissions (i.e. radiative transitions $j \rightarrow i$) are those which immediately follow a previous absorption of a photon (transitions $i \rightarrow j$), i.e. they are the part of a *scattering* process. In order to improve the numerical conditioning of the system of rate equations, we have to somehow eliminate the scattering contributions, i.e. to “precondition” the rates. An illuminating discussion of this topic is presented by Rybicki (1984).

In the ALI form of the net rate, (129), we see that deep in the atmosphere, $\Lambda^* \rightarrow 1$, so that the first term is indeed very small. Similarly, the second term is also small because $\Delta \bar{J}_{ij}$ is small. In other words, the radiative rates are

indeed preconditioned. In the context of the ALI approach, this idea was first used by Werner and Husfeld (1985); a systematic study was presented by Rybicki and Hummer (1991, 1992), who have extended it to the case of general overlap of lines and continua.

5 Model Atmospheres

5.1 Definition and Terminology

By the term *model atmosphere* we understand a specification of all the atmospheric state parameters as functions of depth. Since the problem is very complex, we cannot construct analytic solutions. Therefore, we discretize the depth coordinate and consider a finite number of depth points – this number is typically of the order of several tens to few hundreds. A model atmosphere is then a table of values of the state parameters in these discretized depth points.

Which are the parameters that describe the physical state of the atmosphere? The list of parameters depends on the type of the model, i.e. on the basic assumptions under which the model is constructed. Traditionally, the list of state parameters includes only massive particle state parameters (e.g. temperature, density, etc.), but not the radiation field parameters. This might seem to be in sharp contrast of what was being stated before, namely that radiation intensity is in fact a crucial parameter. It indeed is, and in fact the radiation intensity is an important state parameter in the process of constructing the atmospheric structure. But, when the system of all structural equations, which includes the radiative transfer equation, is solved, we do not have to keep the radiation intensity in the list of state parameters which has to be stored in the table representing the model. The point is that once all the necessary material properties are given, we may easily determine the radiation field by a formal solution of the transfer equation.

The terminology is sometimes ambiguous. Some astronomers, mostly observers, understand by the term “model stellar atmosphere” a table of emergent radiation flux as a function of wavelength. This is understandable, since for many purposes the predicted radiation from a star is the only interesting information coming out of the model. Let us take an example of a widely used Kurucz (1979, 1994) grid of model atmospheres. For each combination of input stellar parameters (T_{eff} , $\log g$, and metallicity), he publishes two tables; one is the “model atmosphere” in our definition, i.e. a relatively short table of values of temperature, electron density, etc., in all depth points; the second table is a table of emergent flux versus wavelength. In fact, many if not most workers use only this second table. A drawback of using the tabulated model flux is that it has a fixed wavelength resolution (in the case of Kurucz models, it is relatively coarse – 10 \AA), and thus cannot be used for purposes which require a high-resolution predicted spectrum. On the other

hand, from the genuine model, one may easily compute a spectrum of any resolution.

Below, I summarize the basic types of model stellar atmospheres.

I) Static models. These are models constructed under the assumption of hydrostatic equilibrium. Consequently, these models apply only to atmospheric layers that are indeed close to hydrostatic equilibrium, i.e. the macroscopic velocity is small compared to the thermal velocity of atoms. These layers are traditionally called *stellar photospheres*. Basic input parameters are the effective temperature, T_{eff} , the surface gravity, g (usually expressed as $\log g$), and chemical composition. Strictly speaking, one should give the values of abundances of all individual chemical species. In reality, one usually considers solar abundances, or some ratio of some or all abundances with respect to the solar one. If all elements but hydrogen and helium share the common abundance ratio with respect to the solar abundances, this ratio is called *metallicity*. There are some additional input parameters, like the microturbulent velocity, or, in the case of convective models, the mixing length (or some other parameters approximating the convection)

There are several basic types of models:

- LTE grey models. They are the simplest possible models, based on the assumption that the opacity is independent of frequency. They are not used any longer for spectroscopic work, but they are useful for providing an initial estimate in any iterative method for constructing more realistic models, and they are very useful for pedagogical purposes. For this reason, they will be discussed at length in the next section.
- LTE models. They are based on the assumption of LTE (see Sect. 1.3). Two state parameters, for instance temperature, T , and density, ρ , (or electron density, n_e), suffice to describe the physical state of the atmosphere at any given depth.
- NLTE models. This is a rather ambiguous term which encompasses any model which takes into account some kind of a departure from LTE. In early NLTE models, the populations of only few of the low-lying energy levels of the most abundant species, like H and He, were allowed to depart from LTE; the rest was treated in LTE. There are two basic kinds of NLTE models, or approaches to include NLTE effects:
 - Models solving for the full structure. The codes of general use include an early H-He model atmosphere code described by Mihalas et al. (1975), the Kiel code (Werner 1987); PAM (Anderson 1987), and a universal code TLUSTY (Hubeny 1988).
 - NLTE line formation (also called a restricted NLTE problem). Here, the atmospheric structure (temperature, density, etc.) is assumed to be known from previous calculations (either LTE or simplified NLTE), and is kept fixed, while only radiative transfer and statistical equilibrium for a chosen atom/ion is solved simultaneously. The

popular codes of this sort include DETAIL/SURFACE (Butler and Giddings 1985); MULTI (Carlsson 1986), and MALI (Rybicki and Hummer 1991).

- NLTE line-blanketed models. This is in fact a subset of the previous item. I consider it separately because these models represent a qualitatively new step in the model construction. They are models where NLTE is considered for practically *all* energy levels and transitions between them – lines and continua – that influence the atmospheric structure. The number of such lines may actually go to millions, so the problem is presently extremely demanding on the computer resources and ingenuity of the numerical methods used. In these models, it is no longer necessary to compute the atmospheric structure using simple atomic models, and recalculate NLTE line formation in individual atoms separately. These models will be discussed in more detail in Sect. 5.5.

II) Unified models. By definition, unified model atmosphere are those which relax the a priori assumption of hydrostatic equilibrium, and which thus treat the whole atmosphere ranging from an essentially static photosphere to a highly dynamical wind on the same footing. Ideally, this would mean solving self-consistently the set of hydrodynamic equations (2) - (4) and the radiative transfer equation. This is a tremendous task, which has not yet been even attempted to solve generally. Instead, one treats the hydrodynamic of the wind taking into account radiation in some approximate way (for instance, the line driven wind theory by Castor et al. 1975; or Pauldrach et al. 1986 – see Lamers, second contribution to this Volume). Once the basic hydrodynamic structure (essentially, the density and velocity as a function of radius) is determined, one solves in detail a NLTE radiative transfer, possibly together with the radiative equilibrium equation. This approach was pioneered by the Munich group (Gabler et al. 1989; Sellmaier et al. 1993), who also coined the term “unified models”. The name stresses a unification of a photosphere and wind; prior to this approach there were separate models for photospheres and for winds, so-called core-halo models.

Besides Munich models, there exists several other variants of unified model atmospheres. I do not present a review of these approaches (some topics are covered in other lectures (Lamers, this Volume; Fullerton, this Volume); I just briefly mention that various unified models are computed

- with or without self-consistent $T(r)$. That is, either the radiative equilibrium is solved exactly (e.g. Gabler et al. 1989; Hillier 1991); or the temperature structure is approximated for instance by the grey temperature structure (de Koter et al. 1993; Schaerer and Schmutz 1994);
- with or without Sobolev approximation in the wind;
- with or without metal line blanketing

5.2 Basic Equations of Classical Stellar Atmospheres

Let us summarize the basic equations of stellar atmospheres for the case of horizontally-homogeneous, plane-parallel, static atmosphere. This case is sometimes called the *classical stellar atmosphere problem*.

Radiative transfer equation. The most advantageous form of the transfer equation for the use in model atmosphere construction is either the usual first-order form, e.g. (29), which is then solved by the DFE method, or the second-order form with the variable Eddington factor,

$$\frac{d^2(f_\nu^K J_\nu)}{d\tau_\nu^2} = J_\nu - S_\nu . \quad (130)$$

It involves only the mean intensity of radiation, J_ν (which is a function of only frequency and depth), but not the specific intensity (which is in addition a function of angle μ). In fact, it is the mean intensity of radiation which enters other structural equations, and therefore the mean intensities, not specific intensities, are to be taken as the atmospheric state parameters. An obvious numerical advantage is that instead of dealing with $NF \times NA$ parameters describing the radiation field per depth (NF and NA being the number of discretized frequency and angle points, respectively) we have only NF parameters. A discretization of the depth variable, mentioned above, is done in such a way that depth points run from the “surface” depth, where $\tau_\nu \ll 1$ for all frequency points, to a depth where $\tau_\nu \gg 1$ for all frequencies (because the diffusion approximation, (109), is used for the lower boundary condition).

Hydrostatic equilibrium equation. This equation reads, recalling (7),

$$\frac{dP}{dz} = -\rho g , \quad (131)$$

where P is the total pressure. Introducing the Lagrangian mass m , defined as the mass in the column of a cross-section of 1 cm^2 above a given point in the atmosphere,

$$dm = -\rho dz , \quad (132)$$

we obtain for the hydrostatic equilibrium equation simply

$$\frac{dP}{dm} = g , \quad (133)$$

which, since g is constant in a plane-parallel atmosphere, has a trivial solution, $P(m) = mg + P(0)$. In fact, this is the reason why one usually chooses m as the basic depth variable of the 1-D plane-parallel atmospheres problem. Nevertheless, it should be kept in mind that the total pressure is generally

composed of three parts, the gas pressure, P_{gas} , the radiation pressure, P_{rad} , and the turbulent pressure, P_{turb} , i.e.

$$P = P_{\text{gas}} + P_{\text{rad}} + P_{\text{turb}} = NkT + \frac{4\pi}{c} \int_0^\infty K_\nu d\nu + \frac{1}{2} \rho v_{\text{turb}}^2 , \quad (134)$$

where v_{turb} is the microturbulent velocity. The hydrostatic equilibrium equation may then be written as (neglecting the turbulent pressure)

$$\frac{dP_{\text{gas}}}{dm} = g - \frac{4\pi}{c} \int_0^\infty \frac{dK_\nu}{dm} = g - \frac{4\pi}{c} \int_0^\infty \frac{\chi_\nu}{\rho} H_\nu d\nu . \quad (135)$$

We may think of the r.h.s. of this equation as the *effective gravity acceleration*, since it expresses the action of the true gravity acceleration (acting downward, i.e. towards the center of the star) minus the radiative acceleration (acting outward). In other lectures (Lamers, second contribution to this Volume) we saw that this is the term which is crucial in the radiatively-driven wind theory.

Radiative equilibrium equation. This expresses the fact that the total radiation flux is conserved, see (8),

$$\int_0^\infty H_\nu d\nu = \text{const} = \frac{\sigma}{4\pi} T_{\text{eff}}^4 . \quad (136)$$

This equation may be rewritten, using the radiative transfer equation, as

$$\int_0^\infty (\kappa_\nu J_\nu - \eta_\nu) d\nu = \int_0^\infty \kappa_\nu (J_\nu - S_\nu) d\nu = 0 , \quad (137)$$

Notice that (137) contains the *thermal* absorption coefficient κ_ν , not the total absorption coefficient χ_ν . This is because the scattering contributions cancel out. To illustrate this mathematically, let us take an example of electron scattering. The absorption coefficient for the process (see 141) is given by $n_e \sigma_e$; σ_e being the electron scattering (Thomson) cross-section. The emission coefficient is then given by $n_e \sigma_e J_\nu$. As it is seen from (137), these two contributions cancel. This is also clear physically, because an absorption followed immediately by a re-emission of a photon does not change the energy balance of the medium, and therefore cannot contribute to the radiative equilibrium equation.

Statistical equilibrium equations. These are also sometimes called *rate equations*. These are in fact equations (6), where the collisional term is written explicitly,

$$n_i \sum_{j \neq i} (R_{ij} + C_{ij}) = \sum_{j \neq i} n_j (R_{ji} + C_{ji}) , \quad (138)$$

where R_{ij} and C_{ij} is the radiative and collisional rate, respectively, for the transition from level i to level j . The l.h.s. of (138) represents the total number of transitions *out* of level i , while the r.h.s. represents the total number of transitions *into* level i from all other levels. The radiative rates are given by expressions analogous to those discussed for a two-level atom in Sect. 3.1 (notice that they depend on the radiation intensity), while the collisional rates are assumed to be given functions of temperature and electron density.

The set of rate equations for all levels of an atom would form a linearly dependent system. Therefore, one equation of the set has to be replaced by another equation. Usually, this is the *total number conservation* equation (or abundance definition equation), $\sum_i n_i = N_{\text{atom}}$, where the summation extends over all levels of all ions of a given species.

Two comments are in order. First, in practice there are only a limited number of levels of an atom/ion which are treated explicitly, i.e. for which the equation of the form (138) is actually written down and solved. These are usually low-lying levels. The remaining levels are typically treated in some approximate way, as, for instance, in LTE with respect to the ground state of the next ion (following Auer and Mihalas 1969), or with respect to the highest explicit level of the current ion. Another possibility is to express this contribution through the partition function (Hubeny 1988). In any case, the abundance definition equation has to be modified to read

$$\sum_{\text{explicit}} n_i + \sum_{\text{upper}} n_i = N_{\text{atom}} . \quad (139)$$

Second, the above abundance definition equation can replace the rate equation for *any* level. This level was usually taken, following Auer and Mihalas (1969), to be the ground state of the highest ion of the given species. However, a numerically more stable option is to choose a level which has the *highest population* of all the levels of the given species, as was suggested by Castor et al. (1992).

Charge conservation equation. This equation expresses the global electric neutrality of the medium,

$$\sum_i n_i Z_i - n_e = 0 , \quad (140)$$

where Z_i is the charge associated with level i (i.e. equal to 0 for levels of neutral atoms, 1 for levels for once ionized ions, etc.). The summation now extends over all levels of all ions of all species.

Auxiliary definition equations. There is a number of auxiliary expressions, like the definition equations of the absorption and emission coefficient,

$$\chi_\nu = \sum_i \sum_{j>i} [n_i - (g_i/g_j)n_j] \sigma_{ij}(\nu) + \sum_i \left(n_i - n_i^* e^{-h\nu/kT} \right) \sigma_{i\kappa}(\nu)$$

$$+ \sum_{\kappa} n_e n_{\kappa} \sigma_{\kappa\kappa}(\nu, T) \left(1 - e^{-h\nu/kT}\right) + n_e \sigma_e , \quad (141)$$

where the four terms represent, respectively, the contributions of bound-bound transitions (i.e. spectral lines), bound-free transitions (continua), free-free absorption (also called the inverse brehmstrahlung), and of electron scattering. Other scattering terms, like for instance the Rayleigh scattering, may also be added if appropriate to the problem at hand. Here, $\sigma(\nu)$ are the corresponding cross-sections; subscript κ denotes the “continuum”, and n_{κ} the ion number density. The negative contributions in the first three terms represent the stimulated emission (remember, stimulated emission is treated as negative absorption). There is no stimulated emission correction for the scattering term, since this contribution exactly cancels with ordinary absorption (for an illuminating discussion, see Shu 1991). Finally, notice that the relation between the bound-bound cross section $\sigma_{ij}(\nu)$ and previously introduced quantities (the Einstein coefficients and the absorption profile) is simply $\sigma_{ij}(\nu) = (h\nu_0/4\pi)B_{ij}\phi(\nu)$.

Analogously, the thermal emission coefficient is given by

$$\eta_{\nu} = (2h\nu^3/c^2) \left[\sum_i \sum_{j>i} n_j (g_i/g_j) \sigma_{ij}(\nu) + \sum_i n_i^* \sigma_{i\kappa}(\nu) e^{-h\nu/kT} + \sum_{\kappa} n_e n_{\kappa} \sigma_{\kappa\kappa}(\nu, T) e^{-h\nu/kT} \right] . \quad (142)$$

The three terms again describe the bound-bound, bound-free, and free-free emission processes, respectively.

These equations should be complemented by expressions for the relevant cross-sections, definition of LTE populations, and other necessary expressions. The resulting set forms a highly-coupled, highly non-linear system of equations. The equations and corresponding quantities that are determined by them are summarized in the Table 1.

Table 1. Summary of classical stellar atmosphere equations and state parameters

Equation	Corresponding state parameter
Radiative transfer	Mean intensities, J_{ν}
Radiative equilibrium	Temperature, T
Hydrostatic equilibrium	Total particle density, N
Statistical equilibrium	Populations, n_i
Charge conservation	Electron density, n_e

5.3 LTE-Grey Model: A Tool to Understand the Temperature Structure

Before discussing the methods and results of solving the full stellar atmosphere problem, it is very instructive to consider an extremely simplified case of the so-called LTE-grey model. Although these models have not been used to describe a real stellar atmosphere for more than four decades, they are still very useful because i) they provide a beautiful pedagogical tool to understand an interplay between radiative equilibrium and radiative transfer, thus to understand a behavior of temperature as a function of depth; and ii) they provide an excellent starting solution for iterative methods to construct more sophisticated models.

The basic assumption of these models is that the absorption coefficient is independent of frequency,

$$\chi_\nu \equiv \chi . \quad (143)$$

In reality, one uses some frequency-averaged opacity, usually the Rosseland mean opacity, (71). The other basic assumption is that of LTE, $S_\nu = B_\nu$. The radiative equilibrium equation thus reduces to

$$J = B , \quad (144)$$

where the quantities without the frequency subscript ν are understood as frequency-integrated quantities,

$$J = \int_0^\infty J_\nu d\nu ; \quad B = \int_0^\infty B_\nu d\nu = \sigma T^4 . \quad (145)$$

The second equation of the problem, the radiative transfer equation (actually, its second moment), reads

$$\frac{dK}{d\tau} = H \implies K(\tau) = H \cdot \tau + \text{const} , \quad (146)$$

because H is constant with depth, as follows from the radiative equilibrium. The constant in the above equation is equal to $K(0)$. Invoking, for simplicity, the Eddington approximation – $K = J/3$, and $K(0) = (2/3)H$ – we obtain (recall that the flux is given by $F = 4H$),

$$J(\tau) = \frac{3}{4} F \cdot \left(\tau + \frac{2}{3} \right) , \quad (147)$$

We know that the total flux, F , is specified through the effective temperature, $F = \sigma T_{\text{eff}}^4$. Combining (145) and (147) together, we obtain

$$T^4 = \frac{3}{4} T_{\text{eff}}^4 \left(\tau + \frac{2}{3} \right) , \quad (148)$$

There exists an elegant analytic solution of the general grey atmosphere problem which yields an analogous expression for the temperature as (148), only

the constant $2/3$ is replaced by a function $q(\tau)$, called *Hopf function*. It is a smoothly varying function of optical depth, with $q(0) = 0.577$; $q(\infty) = 0.71$, which is not very far from the Eddington approximation value.

An important point to realize is that the grey temperature structure follows just from the radiative transfer equation and the radiative equilibrium equation. The hydrostatic equilibrium equation does not enter this derivation. In other words, the temperature in a grey atmosphere, as a function of mean optical depth, does not depend on the surface gravity. However, the hydrostatic equation determines the relation between the averaged optical depth and the geometrical coordinate (m or z).

We see that the temperature is a monotonically increasing function of optical depth. Why this is so? It is easy to understand it in physical terms. The condition of radiative equilibrium stipulates that the *total* radiation flux is constant with depth in the atmosphere. However, the radiation flux measures the *anisotropy* of the radiation field (i.e. the flux would be zero for perfectly isotropic radiation). We know from the transfer equation, and in particular from the diffusion approximation, that the anisotropy decreases with increasing depth in the atmosphere. The only way how to maintain the constant flux in spite of decreasing anisotropy of radiation is to increase the total energy density of radiation (proportional to J), i.e. the temperature (recall that $J = S = B = \sigma T^4$).

The fact that the integrated J is equal to integrated B at all depths τ does not necessarily mean that the frequency-dependent J_ν has to be equal to B_ν for all frequencies. In fact, we should expect that there should be a frequency range for which $J_\nu > B_\nu$, i.e. $J_\nu - B_\nu > 0$; these regions may be called “heating” regions; while at the rest of frequencies $J_\nu < B_\nu$, i.e. $J_\nu - B_\nu < 0$; these regions may be called “cooling” regions. Remember, J is proportional to the number of photons absorbed per unit optical depth, while $S = B$ to the number of photons emitted per unit optical depth. Thus, for instance, $J_\nu > B_\nu$ means that more photons are absorbed than emitted at frequency ν ; the energy of extra absorbed photons must then increase the internal energy, i.e. the temperature, of the medium.

Which frequency regions are the heating ones, and which are the cooling ones? In the case of an LTE-grey atmosphere, the answer is easy. Let us first write down some useful expressions. From the general expression for the Planck function, (22), we may easily derive two limiting expressions: In the high frequency limit, $(h\nu/kT) \gg 1$, we obtain the *Wien* form,

$$B(\nu, T) \approx \frac{2h\nu^3}{c^2} \exp(-h\nu/kT) , \quad (149)$$

while the low-frequency limit, $(h\nu/kT) \ll 1$, is called the *Rayleigh-Jeans* tail,

$$B(\nu, T) \approx \frac{2k\nu^2}{c^2} T . \quad (150)$$

Another important expression is the Eddington-Barbier relation for the mean intensity at the surface, which may be derived from the Eddington-Barbier relation (41) integrated over angles,

$$J(0) = \frac{1}{2} S(\tau=1) . \quad (151)$$

Let us consider the surface layer of a grey atmosphere. If the frequency ν is “large”, i.e. in the Wien regime, then a decrease of the local temperature between $\tau = 1$ and the surface ($\tau = 0$), translates into a large decrease of $B_\nu(T(\tau))$, because for large frequencies the Planck function is very sensitive to T – see (149). In other words, B at the surface may be significantly (even orders of magnitude) lower than B at $\tau = 1$. Since the mean intensity at the surface is about one half of $B(\tau=1)$, it is clear that $J_\nu(0) > B_\nu(0)$ for these frequencies. The large frequencies are therefore the “heating” frequencies.

In contrast, for low frequencies (the Rayleigh-Jeans tail), B is linearly proportional to T . We know from the $T(\tau)$ relation for a grey atmosphere that $T(0) \approx 0.8 T(\tau=1)$. The factor $1/2$ from the Eddington-Barbier relation will now dominate, so we get $J_\nu(0) = (1/2) B_\nu(\tau=1) < B_\nu(0)$. Consequently, the low frequencies are the “cooling” frequencies. One can make these considerations more quantitative, but this is not necessary; the only important point to remember is that the high-frequency part of the spectrum is responsible for heating, while the low-frequency part is responsible for cooling.

Two-step grey model. The above considerations are interesting, but not particularly useful for a purely grey atmosphere. They are, however, very helpful if we consider an atmosphere with some simple departures from the greyness. Let us consider a *two-step grey* model, i.e. with the opacity given as a step function, $\chi_\nu = \chi$ (the original grey opacity) for $\nu < \nu_0$, and $\chi_\nu = a\chi$ for $\nu \geq \nu_0$, with $a \gg 1$, i.e. with a large opacity for high frequencies (one may visualize this as a schematic representation of a strong continuum jump, for instance the Lyman discontinuity). We will denote the original optical depth as τ^{old} , and the new one (for $\nu \geq \nu_0$), as τ_ν^{new} . Let us further assume that the frequency ν_0 is high enough to be in the range of “heating” frequencies.

What are the changes of the temperature structure with respect to the original grey temperature distribution implied by the opacity jump? We will consider separately the surface layers $\tau \approx 0$, and the deep layers.

The surface layers. Since the opacity for $\nu \geq \nu_0$ is much larger than the original opacity, we may neglect the contribution of the latter to the radiative equilibrium integral, so the modified radiative equilibrium equation becomes

$$\int_{\nu_0}^{\infty} J_\nu d\nu = \int_{\nu_0}^{\infty} B_\nu d\nu , \quad (152)$$

which, together with the Eddington-Barbier relation $J_\nu(0) = B_\nu(\tau_\nu^{\text{new}} = 1)/2$ yields for the new surface temperature, T_0 , the expression

$$(1/2) \int_{\nu_0}^{\infty} B_\nu (T(\tau_\nu^{\text{new}} = 1)) d\nu = \int_{\nu_0}^{\infty} B_\nu(T_0) d\nu , \quad (153)$$

from which follows that $T_0 < T(\tau_\nu^{\text{new}} = 1)$. Since the temperature at $\tau_\nu^{\text{new}} = 1$ must be close to the original temperature at the surface (recall that $\tau_\nu^{\text{new}} \gg \tau^{\text{old}}$), the new temperature at the surface is *lower* than the original surface temperature, which gives rise to the term *surface cooling* effect.

The above derivation was more or less a mathematical one. But, in physical terms, why do we get a cooling? This is simply because by *adding opacity in the heating portion* of the spectrum, we effectively suppress this heating. Therefore, we obtain a cooling. These considerations also suggest that by adding an additional opacity in the cooling, i.e. the low-frequency, part of the spectrum, we may actually get a *surface heating* of the atmosphere.

The deep layers. It is intuitively clear that the atmospheric layers which are optically thick in all frequencies will be little influenced by the additional opacity jump. However, an interesting region is the one which is opaque for large frequencies ($\nu \geq \nu_0$), (i.e. $\tau_\nu^{\text{new}} \gg 1$ for these frequencies), while still transparent for the original opacity, $\tau^{\text{old}} < 1$. Since the optical depth is large for $\nu \geq \nu_0$, $J_\nu \approx B_\nu$ for these frequencies, and therefore the monochromatic flux is close to zero. The condition of radiative equilibrium at those depths may be written as $J' = B'$, where the primed quantities are defined as partial integrals, e.g. $J' = \int_0^{\nu_0} J_\nu d\nu$, and analogously for B . From the radiative transfer equation and the Eddington approximation, we have $dJ'/d\tau = 3H$ (not H' ; or, better speaking, $H' = H$, because there is no flux for $\nu \geq \nu_0$). We may formally write $J' = \sigma' T^4$, and by repeating the same procedure as in deriving the original grey temperature structure, we obtain

$$T^4 = (3/4)(\sigma/\sigma') T_{\text{eff}}^4 (\tau + 2/3) . \quad (154)$$

We have $\sigma' < \sigma$, because $J' < J$. This is simply because the energy density of radiation for $\nu < \nu_0$ is smaller than the total energy density. Therefore, the new temperature is larger than the original one. Consequently, the phenomenon is called the *backwarming effect*.

Again, what is the explanation of this effect in physical terms? By adding opacity, the flux in the high-opacity part *drops*. Therefore, the flux in the rest must *increase* in order to keep the total flux constant. However, the only way how to accomplish it in LTE is to increase the temperature gradient, and therefore the temperature itself in the previously flat $T(\tau)$ region.

One may wonder why we spend so much time with an admittedly crude and unrealistic model, such as a simple two-step grey model. However, it should be realized that the above discussed phenomena of surface cooling and backwarming are quite general, and are not at all limited to a grey approximation. In any model, including sophisticated NLTE models (see Sect. 5.5), there are always frequencies which cause heating and those which cause cooling. Any process which changes opacity/emissivity in those regions changes the overall balance and therefore influences the temperature structure. In the NLTE models, there are typically several intervening or competing mechanisms, but the fundamental physics behind the temperature structure is basically the same as in the case of the grey model. Likewise, the mechanism of

backwarming is quite general. The beauty of the grey model is that one may describe all these phenomena by a simple analytical model.

5.4 LTE and NLTE Model Atmospheres

LTE models. Constructing LTE model stellar atmospheres is now a more or less standard procedure. It consists in solving simultaneously basic structural equations (130) - (142), where (138) is replaced by the Saha-Boltzmann distribution, (11) and (12). Consequently, the absorption and emission coefficients are known functions of temperature and electron density, i.e. they are given *locally*. Nevertheless, there is still a non-local coupling of radiation field and material properties via the radiative equilibrium equation (and, to a smaller extent also the hydrostatic equilibrium equation, via the radiation pressure term), which has to be dealt with.

I will not discuss this topic here in any detail. I just mention that the field of LTE model atmospheres is completely dominated by the Kurucz model grid (Kurucz 1979; 1994), and by his computer program ATLAS (Kurucz 1970; 1994). Yet, there are several independent computer programs, designed specifically for very cool stars – Gustafsson et al. (1975); Tsuji (1976); Johnson et al. (1977); Allard and Hauschildt (1995); to name just few.

NLTE models. Why do we expect that departures from LTE may be important in stellar atmospheres? As explained above, departures from LTE arise when the radiative rates dominate over the collisional rates. These conditions typically occur at high temperatures and low densities. The higher the effective temperature, and the stronger the radiation field, the deeper in the photosphere we may expect departures from LTE. We also anticipate that the departures will be largest at frequencies with highest opacities (EUV, cores of strong lines). When the opacity is large, the observed spectrum will be formed higher in the atmosphere where the density of the material is low. Therefore, NLTE models are most important for interpreting observed spectra of hot stars (O, B, A stars, typically $T_{\text{eff}} > 10\,000\text{ K}$) and of supergiants, i.e. the intrinsically brightest stars.

However, the most important point to realize is that *for a star of any spectral type, there is always a wavelength range, and correspondingly a layer in the atmosphere, where NLTE effects are important*. Yet, the meaning of the assessment “NLTE effects are important” is somewhat arbitrary. The point is that a precise definition of this term should in principle involve the desired accuracy of the predicted spectrum. For instance, if one requires an accuracy of, say, 10% in the predicted flux in the optical and UV spectrum for a main-sequence B star, then one may say that LTE models are sufficient. However, NLTE models would be necessary if one requires an accuracy of, say 2-5 %; and NLTE models would still be necessary if one requires an accuracy of 10-20% for the same star in the EUV spectrum range (wavelengths below the Lyman limit, i.e. 912 Å).

How one calculates NLTE model atmospheres? The realization that the nonlocal coupling of physical quantities is extremely important led Auer and Mihalas (1969) to develop the complete linearization (CL) method to solve the set of discretized structural equations. This is a very robust method based on the Newton-Raphson scheme. All equations are linearized and are treated on the same footing, allowing a fully consistent treatment of all couplings. The method has brought an enormous progress in the modeling, and in fact has opened a new era in the stellar atmospheres theory. However, a high price had to be paid. Because of the need to invert individual block matrices of the general Jacobi matrix of the system, the computer time increases with the cube of the number of unknowns. Therefore, it was possible to consider only a limited number of atomic levels and opacity sources (lines). Typically, about 10 to 15 energy levels were allowed to depart from their LTE populations; only a few lines were included explicitly, and the radiative transfer was solved at typically 100 frequencies. It also became clear very soon that dealing with millions of lines within this framework would be out of the question regardless of how rapidly the computer technology might progress.

However, already the early simplified NLTE models have demonstrated that departures from LTE form an essential feature in interpreting the spectra of hot stars (for a review, see Mihalas 1978, and Kudritzki and Hummer 1990). In the same period, the importance of metal line blanketing on the atmospheric structure was demonstrated numerically, and a widely used grid of LTE line-blanketed model atmospheres was constructed (Kurucz 1979). Since then, a debate ensued as to what kind of model atmospheres is more adequate: metal line-blanketed LTE models or NLTE models without blanketing? Models accounting for both metal line-blanketing effects and departures from LTE were then deemed an unreachable dream.

The dream had slowly started to come through in the 1980's with the advent of the ALI method. The first who applied the ALI idea to the model stellar atmosphere construction was Werner (1986; 1987; 1989). He has shown that the method has a great potential, because it effectively eliminates the radiation intensities from the set of model unknowns. One is therefore able to consider many more frequency points, and consequently many more atomic transitions, in the model construction. Moreover, the method was found to be more stable than the complete linearization method in many cases.

A disadvantage of the ALI scheme is that it sometimes converges rather slowly. This is easy to understand, since the information about changes in state parameters is lagged, i.e. is communicated to the rest of the state parameters only in the subsequent iteration. Nevertheless, the time per iteration is very small. Moreover, the speed of convergence can be accelerated by predicting better estimates of the solution using the acceleration of convergence techniques (see Sect. 4.3). In contrast, the CL method requires only a small number of iterations, because it is a global method with an almost quadratic convergence. The time per iteration may however be enormous.

What was therefore needed was a method which would combine the advantages of both these methods; namely the convergence rate (i.e. the number of iterations required to reach a given accuracy) being virtually as high as for the standard CL method, while the computer time per iteration is almost as low as for the standard ALI method. This was exactly what was achieved by developing the so-called hybrid complete linearization/accelerated lambda iteration (CL/ALI) method (Hubeny and Lanz 1995). The method formally resembles the standard complete linearization; the only difference being that the radiation intensity at selected frequency points is not explicitly linearized; instead, it is treated by means of the ALI approach.

5.5 Line Blanketing

The term line blanketing describes an influence of thousands to millions of spectral lines on the atmospheric structure and predicted emergent spectrum. The line blanketing influences not only the emergent spectrum (the so-called line blocking), but also, and more importantly, the atmospheric structure (the backwarming and the surface cooling effects). Although the ALI-based methods have opened the way to attack this problem, the enormous complexity of the iron-peak elements (i.e., we have to account for hundreds of energy levels and millions of line transitions per ion) still precludes using direct methods which were successfully used for light elements (He, C, N, O, etc.).

Statistical methods are therefore necessary. The idea is to avoid dealing with all individual energy levels of complicated metal species. Instead, several states with close enough energies are grouped together to form a so-called “superlevel”. The basic assumption is that all individual levels within the same superlevel share the same NLTE departure coefficient; in other words, the individual levels forming a superlevel are in Boltzmann equilibrium with each other. This idea was pioneered by Anderson (1989). The transitions between individual superlevels, called “superlines”, are treated by means of two possible approaches:

- *Opacity Distribution Functions* (ODF). The idea is to resample a complicated frequency dependence of the superline cross-section to form a monotonic function of frequency; this function is then represented by a small number of frequency quadrature points (Anderson 1989; Hubeny and Lanz 1995).
- *Opacity Sampling* (OS). The idea is a simple Monte Carlo-like sampling of frequency points of the superlevel cross-section (Anderson 1991; Dreizler and Werner 1993). The advantage of this approach is that it can easily treat line blends and overlaps; the disadvantage is that one has to be very careful to choose a sufficiently large number of frequency points, since otherwise the representation may be inaccurate. Indeed, the line cores, which represent the region of maximum opacity, are relatively narrow. Considering too few frequency points may easily lead to missing many important line cores.

These two approaches are illustrated in Fig. 5. We consider the superline between the superlevels 1 and 13 of Hubeny and Lanz (1995) model of Fe III. The detailed cross-section (upper panel) has been computed for some 16 000 internal frequency points. The dotted line in the middle panel represents the Opacity Sampling by 37 (equidistant) wavelength points, while the number of points is doubled for the full line. This shows that unless a large number of frequency points is considered, the OS representation may be quite inaccurate since practically all strong lines are missed. Finally, the lower panel shows the Opacity Distribution Function representation. With 24 points only, we have already a fairly accurate representation of the resampled cross-section to be used in model atmosphere construction.

The first NLTE model atmospheres including iron-line blanketing were presented by Anderson (1989), Anderson and Grigsby (1991), Dreizler and Werner (1993), and Hubeny and Lanz (1995). The strategy for computing line-blanketed model atmospheres is as follows. Hydrogen, helium, and the most important light metals (C, N, O, possibly others) are represented by detailed atomic models, and all the individual lines are treated separately. This involves of the order of 100 atomic levels, and up to 1 000 lines, which are represented by several thousands of frequency points. The heavy (iron-peak) metals are treated by means of the statistical, ODF or OS, approach. Since the dominant opacity is provided by iron and nickel, we either neglect all the other iron-peak elements, or group all of them together to form an averaged iron-peak element (as suggested first by Anderson 1989).

Finally, I will show how the line blanketing influences the temperature structure of an atmosphere. As an example, let us take a model with $T_{\text{eff}} = 35\,000$ K, and $\log g = 4$, which corresponds to a main-sequence O-star. Figure 6 shows the temperature as a function of depth (expressed as column mass in g cm^{-2}). We consider several NLTE model atmospheres, a) H-He LTE model, b) H-He NLTE model, c) NLTE model with light elements only (H-He-C-N-O-Si); and d) fully blanketed NLTE model (H-He-C-N-O-Si-Fe-Ni). All models consider all lines originating between explicit levels of all species that are taken into account.

The behavior of temperature is easily explained by a reasoning analogous to that put forward in the preceding subsection. The frequency region above the Balmer limit (i.e. $\lambda < 3648 \text{ \AA}$) is the “heating region”. Therefore, adding an opacity there causes a surface cooling. This explains the cooling in LTE H-He model (caused mainly by the hydrogen and He II Lyman and Balmer lines), and also the additional cooling in the H-He-C-N-O-Si model (which is caused mainly by the C IV resonance doublet at $\lambda 1550 \text{ \AA}$). Similarly, the additional opacity in the heating region causes the heating of deeper layers, the so-called backwarming effect. Indeed, it is clearly seen that while the lines of light elements cause only a modest backwarming (in the layers at $\log m \approx -1$ and deeper), the Fe and Ni lines, being quite numerous, cause an appreciable heating in these layers.

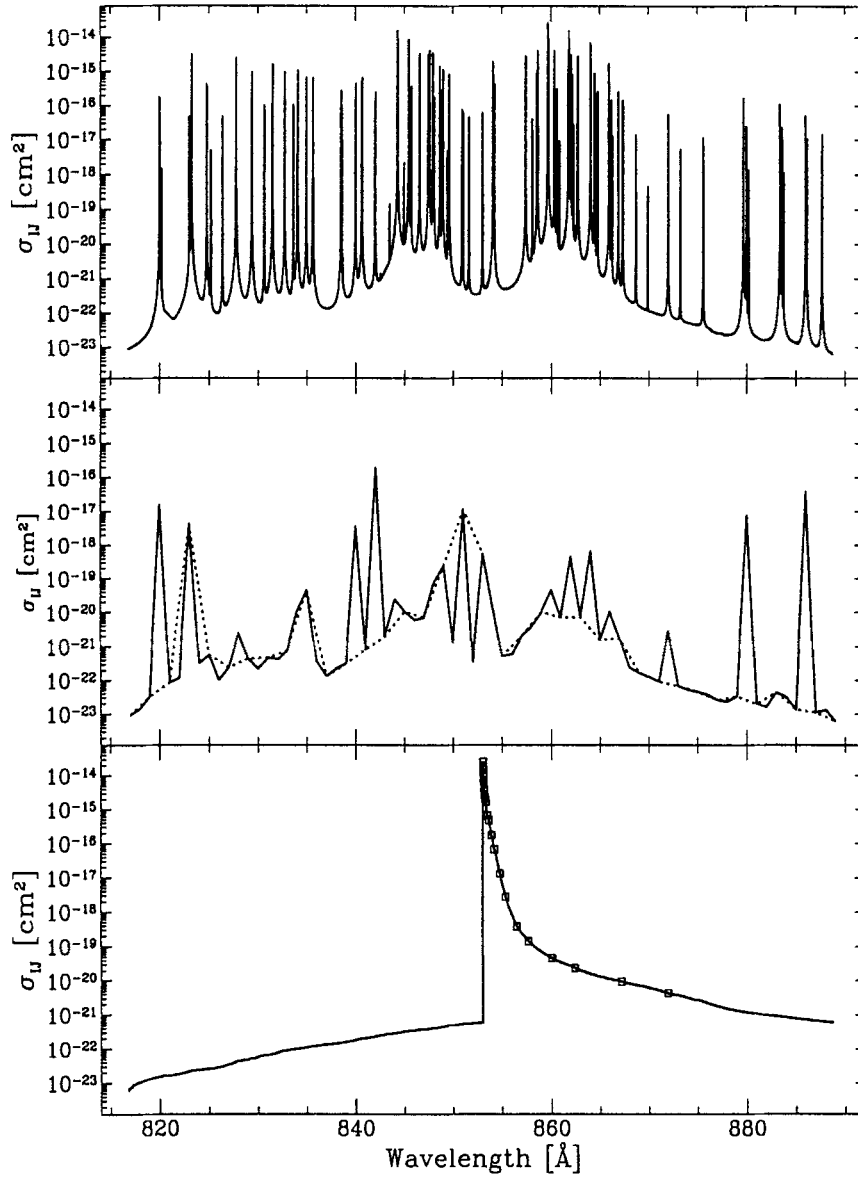


Fig. 5. An illustration of various numerical treatments of a typical superline. Upper panel: the detailed cross-section; Middle panel: the Opacity Sampling representation; Lower panel: the Opacity Distribution Function representation. Small squares indicate the points used to represent this ODF in model atmosphere calculations

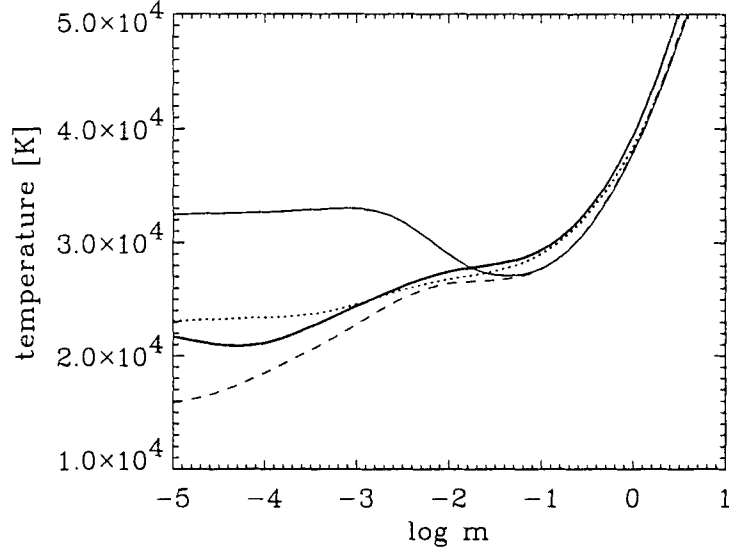


Fig. 6. Temperature structure for four model atmospheres with the same parameters: $T_{\text{eff}} = 35\,000\text{ K}$, $\log g = 4$. Thick line: fully blanketed NLTE H-He-C-N-O-Si-Fe-Ni model; dashed line: NLTE model with light elements (H-He-C-N-O-Si); thin line: NLTE H-He model; dotted line: LTE H-He model

Now, how it is possible that few lines (of H, He, or light elements) are able to cause a significant surface cooling, while a large number of lines is needed to get a significant backwarming? Again, this is explained by employing the two-step grey model considerations. Let us take equation (152). It shows that a strong opacity source completely dominates the radiative equilibrium integral, so that the other frequency regions become unimportant. The original two-step grey model considers the strong opacity source to extend from ν_0 to infinity; however, the essence remains the same if the strong opacity source is just one line, or few strong lines. In the case of one dominant line, the radiative equilibrium integral reduces to, in analogy to (152),

$$\bar{J} = S^L, \quad (155)$$

which follows from (137), (72), (73), and (78). In LTE, we get surface cooling due to the exactly same reasons as in the two-step grey model (LTE forces S to be equal to B , and B is forced to be equal to \bar{J} at the surface, which is low). In NLTE, the cooling effect may be even stronger, because the two-level

source function, (82), implies that $\bar{J} = S^L = B$, and we know from Sect. 3.1 that the two-level atom source function decreases significantly towards the surface.

On the other hand, the backwarming effect is primarily caused by blocking of the flux by additional opacity sources; the more extended (in the frequency space) the blocking is, the larger the backwarming (recall (154) and subsequent discussion). The actual strength of a line does not matter so much as soon as it is able to efficiently block the flux. Therefore, a single narrow and very strong line is quite efficient in the surface cooling, but relatively inefficient in the backwarming.

There is still one remaining puzzling feature: Why, in view of all what was said above, we obtain a large *surface heating* in the NLTE H-He models? This was indeed a big surprise when the effect was first discovered by Auer and Mihalas (1969), who have also provided its physical explanation. The effect is related, but not equivalent, to another, previously discovered NLTE surface temperature rise, called the Cayrel mechanism (Cayrel 1963).

The explanation of the Auer-Mihalas temperature rise goes as follows: It is true that lines always cause a surface cooling. However, in NLTE, a line radiation also influences the atomic level populations. From Sect. 3.1 we know that the main effect of line transfer is to overpopulate the lower level of a line transition. Considering Lyman and Balmer lines thus gives rise to an overpopulation of the hydrogen $n = 1$ and $n = 2$ states, and consequently to increasing the efficiency of the Lyman and Balmer continua. Since they are heating continua, this leads to an additional heating at the surface. There is a competition between this heating and traditional surface cooling caused by the Lyman and Balmer lines, but in the present case the indirect heating wins.

However, interesting as it may be from the theoretical point of view, the indirect heating due to the hydrogen (and to a lesser extent the He II) lines is in reality usually wiped out by the effect of metal lines (as it is in the case displayed in Fig. 6). Nevertheless, the Auer-Mihalas heating survives for metal-poor atmospheres, where it may give rise to observable effects in the hydrogen line profiles (e.g. for hot DA white dwarfs – see Lanz and Hubeny 1995 for a discussion and original references).

Finally, I stress that the behavior of temperature at the surface should not be overinterpreted. It only influences observed spectrum features which correspond to the strongest opacity sources, like the very cores of strongest lines (e.g. the C IV resonance lines in the present case). Yet, these features may in reality be more influenced by a stellar wind, which is neglected in the hydrostatic models anyway. Therefore, the most important effect of line blanketing is its influence on temperature in the deeper layers.

6 Using Model Atmospheres to Analyse Observed Spectra

So far, we have been mostly concerned with the question of how the model stellar atmospheres are constructed. In this chapter, we will discuss another, and equally important, question of how these models are used to address general astrophysical questions.

6.1 A Scheme of Spectroscopic Diagnostics

As was stated before, the observed spectrum is practically the only information about a star we have. The process of deducing stellar properties from its spectrum is therefore called *spectroscopic diagnostics*. This is a multi-step process with many interlinked steps. It is schematically displayed in Fig. 7.

The basic step is INPUT PHYSICS. By this term we mean a selection of the basic physical assumptions under which the medium is being described (i.e., which processes and phenomena are neglected; which equilibrium conditions are assumed to hold, etc.). The basic assumptions then determine the equations to be solved. They also tell us what are the basic input parameters of the model construction. For instance, when adopting the assumption of a plane-parallel atmosphere in the hydrostatic and radiative equilibrium, the input model parameters are the effective temperature, surface gravity, and chemical composition. These parameters are “basic” from the point of constructing model atmospheres, yet they are related to other parameters which may be viewed as more fundamental, like stellar mass, radius, and luminosity. The latter parameters are fundamental if one considers a certain instant of the stellar life. Yet, taking into account more extended input physics (i.e., adding the stellar evolution theory), we may then consider even more fundamental parameters like the initial stellar mass, initial composition, and the age.

Likewise, going to more complex models, like for instance the unified photosphere–wind models, we have different input parameters depending on the level of physical description we adopt. In a simple theory we have, in addition to the stellar mass, radius, and luminosity, two additional input parameters – the mass loss rate and the wind terminal velocity (see Lamers, this Volume). Yet, in a more involved physical picture we may come up with a relation between the wind parameters and other parameters.

Sometimes the additional input parameters make up for the lack of adequate physics. Typical examples are the so-called microturbulent velocity which is often used for describing short-scale non-thermal motions; or the mixing length parameter used in the mixing-length theory of convection. An example from a somewhat different yet related field is the α -parameter for describing a turbulent viscous dissipation in accretion disks. All such input parameters are convenient parameters which allow us to construct models even if we do not really know what is going on. Their values are constrained

by agreement between theoretical predictions and observations; it is generally believed that a more fundamental physics will either determine their values from other structural parameters, or will get rid of them completely. Nevertheless, there are cases where such parameters are very useful, for instance when a “better physics” would require an enormously complicated and time-consuming modeling.

The input physics, which tells us which equations are to be solved, thus influences profoundly the next step, **NUMERICS**. By this term we understand all the work necessary to develop a code for computing model stellar atmospheres. This involves adopting appropriate methods provided by numerical mathematics or, often, developing new methods suited to a particular modeling purpose (a good example being the ALI method). This also involves a lot of computer programming and, the most time-consuming part, code debugging and testing.

Having developed a stellar atmosphere code, one may proceed to the next step, **MODEL ATMOSPHERES**. It is depicted in Fig. 7 as a distinct step from numerics, despite the fact that it could have been a part of the Numerics box. Usually, a stellar atmosphere code contains a large number of various numerical options and tricks. One usually needs a lot of experience to cope successfully with various numerical problems (typically a slow convergence or divergence of iterations), and to find proper options to coax the code to work. Sometimes the author of the code builds a grid of models him or herself (typical example being Bob Kurucz), but it is still useful that a code itself is being available to the whole community. This is because the number of internal input parameters may be enormous to make it reasonable to construct a sufficiently dense, all-purpose grid. Many codes for stellar atmospheric modeling are indeed publicly available.¹

The last step of the “theoretical” branch of the spectroscopic diagnostic procedure is spectrum synthesis, which yields the main product, the **SYNTHETIC SPECTRUM**. It will be discussed in detail in the next section.

It should be realized that not all of the above steps have to be done in analyzing a particular object. One may work, for instance, with a pre-calculated grid of model atmospheres and construct only synthetic spectra. One may even work with an existing grid of synthetic spectra; one then avoids the theoretical part completely.

I will not discuss the other, “observational”, branch of diagnostics. The main steps are taking the rough data (by ground-based or space-based instruments) – the step **OBSERVATIONS** – and subsequent **DATA REDUCTIONS**. The final product is a well-calibrated **OBSERVED SPECTRUM**.

Now comes the crucial part of the spectroscopic diagnostics, the **COM-**

¹ The most extended collection of existing modeling codes is maintained on the CCP7 (Collaborative Computer Project No. 7 on the Analysis of Astronomical Spectra) library – Jeffery (1992). The library is also available via WWW on the address <http://star.arm.ac.uk/ccp7/>

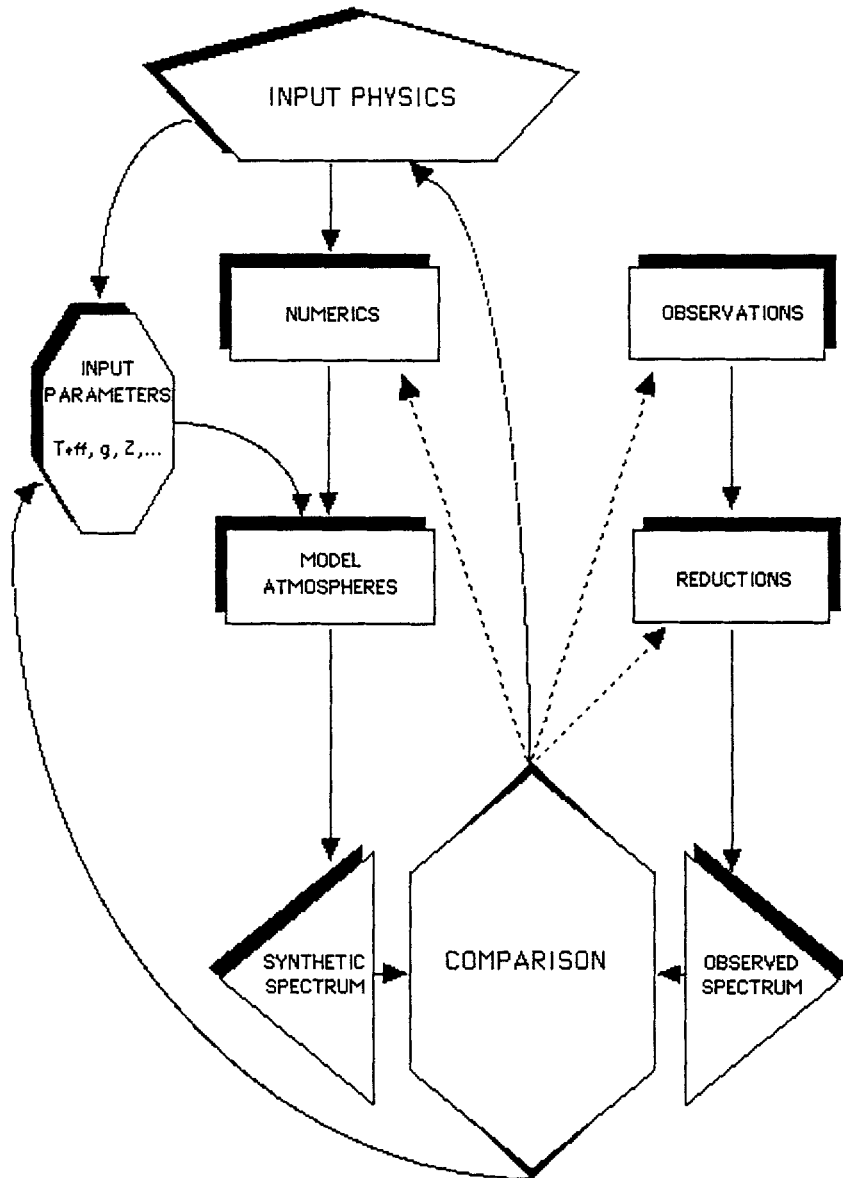


Fig. 7. A sketch of the individual steps of astrophysical spectroscopic diagnostics and their interconnections

PARISON of the observed and theoretical spectra. The actual procedure to be performed in this step is discussed in detail in Sect. 6.3. Here, I will only stress the significance of this step in the global context. Above all, the comparison determines the values of basic input parameters. One may proceed iteratively: after an initial guess of input parameters and constructing the first synthetic spectrum, the comparison step suggests new values of basic input parameters, which are then used for constructing a new model atmosphere and new synthetic spectrum, and the process is repeated. Alternatively, one may first construct a grid of synthetic spectra around the most probable values of basic parameters, and to determine their final values by some sort of χ^2 -fitting.

However, the most important point to realize is that the comparison step does not merely serve to determine values of model input parameters. It may happen that we are not able to match observations for any combination of input parameters. Then we have to go back to the input physics step, and revise the basic physical assumption under which the models were constructed. This may of course lead to a revision (or even to a rewriting) of the computer program and consequently to reconstructing the model grid. But by this connection we actually learn the most important part of all – the physics.

In Fig. 7, the dashed line drawn from the comparisons step to the numerics step is meant to indicate that lack of agreement between observations and theory does not have to be caused by an inadequacy of adopted physical description, but also by an inadequate numerical treatment of otherwise correct equations. The most trivial example of this phenomenon is a hidden bug in the program, which does not influence the results in some cases (usually those used for testing), but may have a dramatic effect in others. Also, this may indicate an insufficient accuracy or inadequacy of adopted numerical method(s) for solving a given set of equations, for inverting matrices, etc. Another example are various numerical approximations for atomic parameters. (e.g. polynomial expansions for transition cross-section or collisional rates, which are derived for a certain parameter range, but are not applicable for others, etc., etc.)

Finally, an unsuccessful match of observations and theory may reveal that the observations are at fault. For instance, an UV spectrum of a star may be contaminated by a contribution from a close object not seen in the optical region. Also, the data reduction step may be at fault – for instance a persistent mismatch of observations and models for various objects may lead to a discovery of an error in flatfield corrections, or an unexpected presence of scattered light in the spectrograph, etc.

6.2 Spectrum Synthesis

Ideally, there should be a one-to-one correspondence between a model atmosphere (the structure), and the synthetic spectrum. In other words, to every model atmosphere there should correspond a unique emergent spectrum. However, in the real life the model structure is always computed using

a simplified treatment of chemical species – some of them do not influence the atmospheric structure significantly and are therefore omitted (like, for instance, Li, etc.), or are treated in a simplified way when constructing the model.

However, one needs to include all the opacity sources available, lines and continua, when producing the synthetic spectrum. One can easily afford that. Since the temperature, electron density, and atomic level populations are specified by the model, the calculation of the synthetic spectrum consists of a simple wavelength-by-wavelength formal solution of the radiative transfer equation, with the absorption and emission coefficients given by (141) and (142). However, the summation over line transitions may actually include hundreds or even thousands of individual spectral lines contributing at a single wavelength point. This feature, and the very fact that we have to deal with literally millions of lines, make an efficient coding of this problem non-trivial. The most widely used general purpose codes of this kind are SYNTHE (Kurucz 1994), which is designed to produce spectra for Kurucz model atmospheres; and SYNSPEC (Hubeny et al. 1994), which calculates spectra for NLTE models created by TLUSTY, but works for Kurucz models as well.

Another important point: an input model atmosphere is constructed assuming certain abundances of chemical species. In order to be strictly consistent, one would have to consider the same abundances in the spectrum synthesis as well. However, due to the same reasons as put forward above, it is permissible to use different abundances in the spectrum synthesis step. It is clear that for “unimportant” species, one may change their abundance to any reasonable value. However, one should be careful with changing abundances of “important” species, like He, C, N, O, etc, significantly. If this is done, it is recommended to recalculate a full model atmosphere using these new values of abundances. This will not only show whether the previous approach was reasonably accurate, but also the new model may subsequently be used for a fine tuning of abundances.

It should be realized that the calculation of the final synthetic spectrum to be compared to observations involves two steps:

1. producing the net emergent spectrum (radiation flux at the stellar surface) as discussed above; and
2. performing a convolution with rotational and/or instrumental broadening.

Since a star generally rotates, one has to add contributions from all surface elements taking into account the Doppler shift due to the local projected rotational velocity. This procedure is described in detail for instance in Gray (1992). If one assumes a certain a priori given limb-darkening law (i.e. the dependence of specific intensity on μ), one may perform the rotational convolution with the radiation flux; otherwise, the rotational convolution needs a

specification of radiation intensities. The procedure is easy for well-behaving, spherically-symmetric stars. However, one may face complications either because of non-sphericity (for instance that implied by extremely fast rotation), or by departures from surface homogeneity (various starspots, etc.), or for a complicated pattern of velocity fields at the stellar surface (non-radial pulsations, macroturbulence, etc.).

Finally, to be able to compare the predicted spectrum to observations, one has to reproduce numerically a conversion of the incoming stellar spectrum by the spectrograph. In practice, this usually means accounting for a finite spectrum resolution of a spectrograph by convolving the net spectrum with a known instrumental broadening function (usually a Gaussian with a given FWHM). One can also include an instrumental spectrum sensitivity function at this stage. The final result of this step is a predicted spectrum which is directly comparable to the observed one.

6.3 Spectrum Fitting

The spectrum fitting is the procedure of finding the model spectrum that fits the observed spectrum best. It may be done by two different ways:

i) a “consecutive model construction” procedure, which consists of a) computing first a small number of initial models for some initial estimates of the basic parameters; b) finding the next estimate of basic model parameters (either by an educated guess, or by using more sophisticated mathematical techniques – for instance the Amoeba optimized search package – Press et al. 1986), and comparing the resulting spectra to observations. The process is repeated until the criteria for a successful match are satisfied. The basic characteristics of this approach is that one does not need any precalculated grid of models; instead, the models are calculated on the way of getting closer and closer to the final model. Obviously, this procedure is efficient only if an effort to generate a model spectrum from scratch is reasonably small.

ii) a “grid-fitting” procedure, which consists in having a precalculated grid of spectra, and finding a model which produces the best fit. One may either find the best-fit model (i.e. one of the models of the grid), or find the best-fit parameters by interpolating in the model grid, assuming that the synthetic spectra corresponding to model parameters in between the grid values may be approximated by an interpolation of tabulated model spectra. If the grid has a sufficiently small step in basic stellar parameters, this procedure is quite satisfactory.

Let us take an example of determining basic stellar parameters for OB stars from observed hydrogen and helium lines. Let us further assume that the mass loss rate is sufficiently low so that all the observed lines originate in the stellar photosphere, i.e. their profiles may be interpreted by means of hydrostatic model atmospheres. Finally, let us assume that we are fitting the observed spectra by means of simple H-He model atmospheres. This means that the grid of spectra depends on five input parameters: T_{eff} , $\log g$, Y (the

helium abundance), v_{tb} (microturbulent velocity), and $v \sin i$ (projected rotational velocity; i being the inclination of the rotation axis with respect to the direction to the observer). One may either determine all five of them by a χ^2 -fitting, or to determine some of them independently, and to fit only a subset of parameters. A typical case for OB main-sequence stars is to determine v_{tb} and $v \sin i$ from metal lines, and to determine the three remaining parameters by a line profile fitting. Sometimes, even Y may be determined independently (from profiles or equivalent widths of lines of the dominant ion of helium for which the profiles are not so sensitive to T_{eff} and $\log g$). One is then left with fitting the observed hydrogen and helium line profiles with only a 2-dimensional grid of spectra which depend only on T_{eff} and $\log g$.

There are two options to perform the actual fitting:

a) fitting both parameters simultaneously; or

b) using the *fit diagrams*. This consists in keeping one parameter fixed (typically $\log g$), and finding such a value of T_{eff} which fits the observed profile best. One then goes to the next grid value of $\log g$, and repeats the fitting. Every fitted spectral line then defines a curve in the $T_{\text{eff}}\text{--}\log g$ plane, on which the best-fit values of T_{eff} and $\log g$ are located. Ideally, all curves should intersect in one single point, which then determines the overall best fit values of T_{eff} and $\log g$. In reality, one usually does not get such a good fit, but at least one should obtain a relatively small region in the $T_{\text{eff}}\text{--}\log g$ plane where the curves intersect. If one single spectral line defines a significantly different fit curve, it is a strong indication that something on the theoretical or observational level was incorrect.

The fit diagram method is illustrated on the following example: I have constructed a grid of NLTE H-He model atmospheres with effective temperatures between 25000 and 45000 K, in steps of 2500 K, and for $\log g$ between 3.5 to 4.5, in steps of 0.25. All models have a solar abundance of helium. I will not fit an actual observed spectrum; instead, I will pretend that the “observed” spectrum is the synthetic spectrum computed for a fully metal line-blanketed NLTE model for $T_{\text{eff}} = 35\,000$ K, and $\log g = 4$.

This example will illustrate two features; namely i) what the fit diagrams look like, and ii) what error one makes if the spectrum is fitted by simple H-He model atmospheres instead of by line-blanketed models. The fit diagram for H, He I and He II lines is shown in Fig. 8. A very interesting result is that the H-He models would determine the best fit parameters $T_{\text{eff}} \approx 38\,000$ K, and $\log g \approx 4$. In other words, the H-He models will overestimate the deduced effective temperature, which is not surprising in view of the discussion presented in Sect. 5.5, namely that the local temperature in the H-He models in regions where H and He lines are formed is lower than in the line-blanketed models (no backwarming).

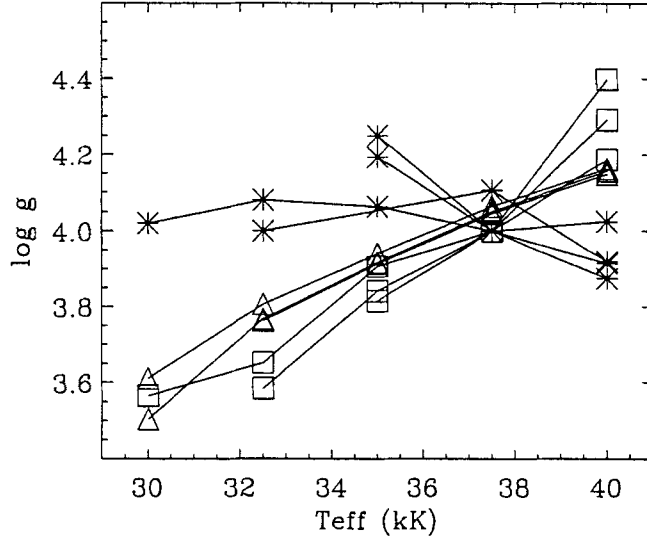


Fig. 8. A fit diagram for fitting the H, He I, He II line profiles by means of NLTE H-He model atmospheres. The “observed” spectrum is in fact a synthetic spectrum computed for a fully metal line-blanketed NLTE model for $T_{\text{eff}} = 35\,000$ K, and $\log g = 4$. Squares: hydrogen lines ($H\beta$ to $H\delta$); triangles: He I lines ($\lambda\lambda$ 4388, 4471, 4922 Å); stars: He II lines ($\lambda\lambda$ 4026, 4200, 4542, 4686 Å)

6.4 Determination of Fundamental Stellar Parameters

Here we will only be concerned with the question how the fundamental stellar parameters are determined from a photospheric analysis, i.e. by analyzing the observed stellar spectrum by means of hydrostatic model atmospheres. An important part of this procedure, which is nevertheless often forgotten, is to verify that the deduced stellar properties are indeed consistent with the assumption of hydrostatic equilibrium.

The fundamental stellar parameters to be determined are the stellar mass, M_* , radius, R_* , and luminosity, L_* . In general, we do not know the distance to the star, d , so we add this quantity to the list, even if it does not represent an intrinsic stellar property. (There are, obviously, other fundamental stellar parameters, like the chemical composition, rotational velocity, etc. For the purposes of this section, we assume that they are determined independently of the four fundamental parameters listed above.)

The parameters which we determine directly from observations are the effective temperature, T_{eff} , and surface gravity, g . In addition, we have the measured magnitude, m_{obs} that reflects the whole observationally accessible wavelength range. If the flux in the unobservable region is negligible, then this magnitude represent the total, *bolometric*, magnitude, m_{bol} . If not, one has to apply the bolometric correction, which follows from the model atmosphere.

In any case, we end up with three “measured” quantities, T_{eff} , g , and m_{bol} , but we have 4 unknown fundamental parameters, M_* , R_* , L_* , and d . The governing relations between them are

$$\sigma T_{\text{eff}}^4 = L_*/(4\pi R_*^2) , \quad (156)$$

$$g = GM_*/R_*^2 , \quad (157)$$

$$L_* = L_* [m_{\text{bol}} (m_{\text{obs}}, T_{\text{eff}}) , d] , \quad (158)$$

The last relation expresses the conversion of the observed magnitude to the stellar luminosity.

We thus have three relations for four unknowns. In fact, in some cases the stellar evolution theory may supply an independent additional relation between the fundamental parameters, for instance the mass–radius relation for white dwarfs (Hamada and Salpeter 1961), or the mass–luminosity relation for central stars of planetary nebulae (Paczynski 1971). However, in the general situation we do not have such a relation, and even if we do we may want to check the theoretically predicted relations observationally.

Therefore, from the photospheric analysis only, one cannot derive all four parameters simultaneously. This is easily understood from the physical point of view. A plane-parallel hydrostatic atmosphere is just a thin layer sitting on the top of a spherical star. The only information about a dimension of the underlying star is contained in the surface gravity g which depends also on the stellar mass. Since the atmosphere is thin, the emergent spectrum does not carry any independent information about the atmospheric extent.

To remove the radius–mass degeneracy, we need either independent geometrical information (knowing the radius or the distance), or an independent knowledge of the mass. The typical situation is that we know the distance d (the situation will be significantly improved when Hipparcos parallaxes are released); then the other parameters are determined as follows:

1. from known m_{obs} and d (and, possibly, T_{eff}), we determine the absolute bolometric magnitude, M_{bol} and, therefore, luminosity, L_* ;
2. from L_* and T_{eff} , we determine R_* ;
3. from R_* and g , we determine mass M_* .

As it turns out, if the mass of early-type O stars is determined in this way (which is called the spectroscopic mass), and if the mass is also determined by comparing the evolutionary tracks and the position of the star in the H-R diagram (the so-called evolutionary mass), one finds a significant discrepancy

(e.g. Herrero et al. 1992). The sense of discrepancy is that the spectroscopic masses are systematically lower than the evolutionary masses. The discrepancy arises either by inaccuracies of the stellar atmospheres theory, or the stellar evolution theory, or, most likely both. From the stellar atmospheres side, there has been a recent progress in understanding the reasons for the discrepancy (e.g. Lanz et al. 1996). However, the problem is not yet solved, and presents a challenge for future research.

Acknowledgements

It is a pleasure to thank the organizers of the 9th European Astrophysics Doctoral Network Summer School for the invitation to give these lectures. I would also like to thank my colleagues in the audience and my co-lecturers for stimulating discussions. I would like to thank Thierry Lanz, Alex de Koter, Steve Shore, Tom Brown and Mark Runacres for their careful reading of the manuscript and offering a number of useful suggestions.

References

- Allard, F., Hauschildt, P.H. (1995): *ApJ* **445**, 433
 Anderson, L. S. (1985): *ApJ* **298**, 848
 Anderson, L. S. (1987): in *Numerical Radiative Transfer*, ed. by W. Kalkofen, Cambridge Univ. Press, Cambridge, p. 163
 Anderson, L. S. (1989): *ApJ* **339**, 588
 Anderson, L. S. (1991): in *Stellar Atmospheres: Beyond Classical Models*, ed. by L. Crivellari, I. Hubeny, and D.G.Hummer, NATO ASI Series C 341, Kluwer, Dordrecht, p. 29
 Anderson, L. S., Grigsby, J.A. (1991): in *Stellar Atmospheres: Beyond Classical Models*, ed. by L. Crivellari, I. Hubeny, and D.G.Hummer, NATO ASI Series C 341, Kluwer, Dordrecht, p. 365
 Auer, L.H. (1987): in *Numerical Radiative Transfer*, ed. by W. Kalkofen, Cambridge Univ. Press, Cambridge, p. 101
 Auer, L.H. (1991): in *Stellar Atmospheres: Beyond Classical Models*, ed. by L. Crivellari, I. Hubeny, and D.G.Hummer, NATO ASI Series C 341, Kluwer, Dordrecht, p. 9
 Auer L.H., Mihalas D. (1969): *ApJ* **158**, 641
 Auer, L.H., Mihalas, D. (1970): *MNRAS* **149**, 60
 Avrett, E.H., Hummer, D.G. (1965): *MNRAS* **130**, 295
 Böhm-Vitense, E. (1989): *Introduction to Stellar Astrophysics II. Stellar Atmospheres*, Cambridge Univ. Press, Cambridge
 Butler, K., Giddings, J. (1985): in *Newsletter on Analysis of Astronomical Spectra* No. 9, Daresbury Laboratory, Daresbury, England
 Cannon, C.J. (1973): *J. Quant. Spectrosc. Radiat. Transfer* **13**, 627
 Carlsson, M. (1986): *A Computer program for Solving Multi-Level Non-LTE Radiative Transfer Problems in Moving or Static Atmospheres*, Report No. 33, Uppsala Astron. Obs.

- Castor, J. I., Abbott, D. C., Klein, R. I. (1975): ApJ **195**, 157
- Castor, J.I., Dykema, P.G., Klein R.I. (1991): in *Stellar Atmospheres: Beyond Classical Models*, ed. by L. Crivellari, I. Hubeny, and D.G.Hummer, NATO ASI Series C 341, Kluwer, Dordrecht, p. 49.
- Castor, J.I., Dykema, P.G., Klein, R.I. (1992): ApJ **387**, 561
- Cayrel, R. (1963): C. R. Acad. Sci. Paris **257**, 3309
- Chandrasekhar, S. (1960): *Radiative Transfer*, Dover, New York
- Crivellari, L., Hubeny, I., Hummer D. G. (Eds.) (1991): *Stellar Atmospheres: Beyond Classical Models*, NATO ASI Series C 152 (Dordrecht: Kluwer)
- De Koter, A., Schmutz, W., Lamers, H. J. G. L. M. (1993): A&A, **277**, 561
- Dreizler, S., Werner, K. (1993): A&A **278**, 199.
- Feautrier, P. (1964): C. R. Acad. Sci. Paris **258**, 3189
- Gabler, R., Gabler, A., Kudritzki, R. P., Puls, J., Pauldrach, A. (1989): A&A **226**, 162
- Garmany, C.D. (Ed.) (1990): *Properties of Hot Luminous Stars*, PASPC 7, Astron. Soc. Pacific, San Francisco
- Gray, D.F. (1992): *Observations and Analysis of Stellar Photospheres*, 2nd ed., Cambridge Univ. Press, Cambridge
- Griem, H.R. (1974): *Spectral Line Broadening by Plasmas*, Acad. Press, New York
- Gustafsson, R., Bell, R.A., Eriksson, K., Nordlund, A. (1975): A&A **42**, 407
- Hamada, T., Salpeter, E.E. (1961): ApJ **134**, 683
- Hamann, W.-R. (1985): A&A **148**, 364
- Heber, U., Jeffery, C.J. (Eds.) (1992): *The Atmospheres of Early-Type Stars*, Lecture Notes in Phys. 401, Springer, Berlin, p. 377
- Herrero, A., Kudritzki, R.P., Vilchez, J.M., Kunze, D., Butler, K., Haser, S. (1992): A&A **261**, 209
- Hillier, D.J. (1990): A&A **231**, 116
- Hubeny, I. (1985): in *Progress in Stellar Spectral Line Formation Theory*, ed. by J.E. Beckman and L. Crivellari, NATO ASI Series C 152, Reidel, Dordrecht
- Hubeny, I. (1987): A&A **185**, 332
- Hubeny, I. (1988): Comp. Phys. Comm. **52**, 103
- Hubeny, I. (1992): in *The Atmospheres of Early-Type Stars*, ed. by U. Heber and C.J. Jeffery, Lecture Notes in Phys. 401, Springer, Berlin, p. 377
- Hubeny, I., Lanz, T. (1992): A&A **262**, 501
- Hubeny, I., Lanz, T. (1995): ApJ **439**, 875
- Hubeny, I., Lanz, T., Jeffery, C. S. (1994): in *Newsletter on Analysis of Astronomical Spectra* No. 20, Ed. Jeffery C. S., St Andrews Univ., St Andrews, 30
- Hummer, D.G. (1981): J. Quant. Spectrosc. Radiat. Transfer **26**, 187
- Ivanov, V.V. (1973): *Transfer of Radiation in Spectral Lines*, English language translation of Radiative Transfer and the Spectra of Celestial Bodies, transl. by D.G. Hummer, NBS Special Publ. No. 385, National Bureau of Standards, Washington
- Jefferies, J. (1968): *Spectral Line Formation*, Blaisdel, Waltham
- Jeffery, C. S. (1992): in *Newsletter on Analysis of Astronomical Spectra* No. 17, Ed. Jeffery C. S., CCP7, (St Andrews: St Andrews Univ.), 33
- Jeffery, C.J., Heber, U. (Eds.) (1996): *Hydrogen-Deficient Stars*, PASPC 96, Astron. Soc. Pacific, San Francisco
- Johnson, H.R., Bernat, A.P., Krupp, B., Bell, R.A. (1977), ApJ **212**, 760

- Kalkofen, W. (Ed.) (1984): *Methods in Radiative Transfer*, Cambridge Univ. Press, Cambridge
- Kalkofen, W. (Ed.) (1987): *Numerical Radiative Transfer*, Cambridge Univ. Press, Cambridge
- Kudritzki, R.P. (1988): *The Atmospheres of Hot Stars: Modern Theory and Observation*, in *Radiation in Moving Gaseous Media*, ed. by Y. Chmielewski and T. Lanz, 18th Advanced Course, Swiss Soc. of Astron. and Astrophys., Geneva
- Kudritzki, R. P., Hummer D. G. (1990): ARA&A **28**, 303
- Kurucz, R. L. (1970): Smithsonian Astrophys. Obs. Spec. Rep. No. 309
- Kurucz, R. L. (1979): ApJS **40**, 1
- Kurucz, R. L. (1994): Kurucz CD-ROM No. 13, Smithsonian Astrophys. Obs.
- Lanz, T. , Hubeny, I. (1995): ApJ **439**, 905
- Lanz, T., de Koter, A., Hubeny, I., Heap, S. R. (1996): ApJ **465**, 359
- Mihalas, D. (1978): *Stellar Atmospheres*, Freeman, San Francisco
- Mihalas D., Heasley J.N., Auer L.H. (1975): *A Non-LTE model stellar atmospheres computer program*, NCAR-TN/STR-104, NCAR, Boulder
- Pauldrach, A.W.A, Puls, J., Kudritzki, R.P. (1986): A&A **164**, 86
- Paczynski, B.E. (1971): Acta Astr. **21**, 417
- Olson, G.L., Kunasz, P.B. (1987): J. Quant. Spectrosc. Radiat. Transfer **38**, 325
- Olson, G.L., Auer, L.H., Buchler, J.R. (1986): J. Quant. Spectrosc. Radiat. Transfer **35**, 431 (OAB)
- Oxenius, J. (1986): *Kinetic Theory of Particles and Photons*, Springer-Verlag, Berlin Heidelberg
- Press, W.H., Flannery, B.P., Teukolsky, S.A., Vetterling, W.T. (1986): *Numerical Recipes*, Cambridge Univ. Press, Cambridge
- Rutten, R.J. (1995): *Radiative Transfer in Stellar Atmospheres*, 2nd WWW edition, June 22, 1995, Robert J. Rutten, Utrecht, Netherlands
- Rybicki, G.B. (1971): J. Quant. Spectrosc. Radiat. Transfer **11**, 589
- Rybicki, G.B. (1984): in *Methods in Radiative Transfer*, ed. by W. Kalkofen, Cambridge Univ. Press, Cambridge, p. 21
- Rybicki, G.B., Hummer, D.G. (1991): A&A **245**, 171
- Rybicki, G.B., Hummer, D.G. (1992): A&A **262**, 209;
- Rybicki, G.B., Lightman, A.P. (1979): *Radiative Processes in Astrophysics*, Wiley-Interscience, New York
- Scharmer, G.B. (1981): ApJ **249**, 720
- Schaerer, D., Schmutz, W. (1994): A&A **228**, 231
- Sellmaier, F., Puls, J., Kudritzki, R.P., Gabler, A., Gabler, R., Voels, S.A. (1993): A&A **273**, 533
- Shu, F.H. (1991): *The Physics of Astrophysics I. Radiation*, University Science Books, Mill Valley
- Stenflo, J.O. (1994): *Solar Magnetic Fields, Polarized Radiation Diagnostics*, Kluwer, Dordrecht
- Tsuji, T. (1976): PASJ **28**, 543
- Werner, K. (1986): A&A **161**, 177
- Werner, K. (1987): in *Numerical Radiative Transfer*, ed. by W. Kalkofen, Cambridge Univ. Press, Cambridge, p. 67
- Werner, K. (1989): A&A **226**, 265
- Werner, K., Husfeld, D. (1985): A&A **148**, 417

Stellar Wind Theories

Henny J.G.L.M. Lamers

SRON Laboratory for Space Research and Astronomical Institute, Sorbonnelaan 2,
NL-3584 CA, Utrecht, The Netherlands
HENNYL@SRON.RUU.NL

Abstract. We describe the basic theory of stellar winds with momentum input due to a force or with energy input and we formulate the five laws of stellar winds.

Stellar winds can be driven by various mechanisms, specified by the main force that is responsible for the wind. These are:

- (1) Coronal winds, driven by gas pressure at high temperature
- (2) Line driven winds, due to radiation pressure in spectral lines
- (3) Dust driven winds, due to radiation pressure on dust
- (4) Pulsation driven winds, due to oscillating motions of the photosphere
- (5) Sound wave driven winds, due to wave pressure of acoustic waves
- (6) Alfvén wave driven winds, due to wave pressure by Alfvén waves
- (7) Magnetic rotating winds, due to magnetic corotation

We briefly review these mechanisms.

1 Introduction

Most stars are loosing mass in the form of a stellar wind. The mass loss rate of the sun is about $10^{-14} M_{\odot} \text{yr}^{-1}$. This is such a small amount that it does not affect the evolution. The mass loss by the solar wind is even smaller than the mass loss rate in the interior of the sun due to the nuclear fusion: $\dot{M}_{\text{nucl}} = L/c^2$. However in a later evolutionary phase low mass stars suffer much higher mass loss rates up to about $10^{-5} M_{\odot} \text{yr}^{-1}$ when they reach the Asymptotic Giant Branch. The late evolution of low mass stars is dominated by mass loss.

Massive stars with $M \gtrsim 30 M_{\odot}$ experience significant mass loss already on the main sequence. The typical mass loss rates of O stars during the main sequence is about 10^{-6} to $10^{-5} M_{\odot} \text{yr}^{-1}$. For those stars the whole evolution is seriously affected by mass loss.

Stellar winds can have very different forms:

- (1): cold ($T \approx T_{\star}$), slow ($v \ll v_{\text{esc}}$) and dense for late-type supergiant stars
- (2): cold ($T \approx T_{\star}$), fast ($v \gtrsim v_{\text{esc}}$) and dense for luminous hot stars
- (3): hot ($T \gg T_{\star}$), fast ($v \gtrsim v_{\text{esc}}$) and tenuous around cool dwarfs and giants.

This shows that there are different mechanisms which produce these winds. At least seven different mechanisms have been proposed to explain the observed properties of stellar winds in different types of stars. They are listed in the abstract.

The two most important theories for mass loss are the “dust driven wind theory” and the “line driven wind theory”. In both theories the wind is driven by radiation pressure. These theories are important because they are successful in explaining the gross properties of the observed winds in the two evolutionary phases with the highest mass loss rates: the cool luminous stars and the hot luminous stars. These two theories will be discussed in some detail in two chapters in this volume.

The main emphasis of this paper is on explaining the basic physical principles of stellar wind theories. We first discuss the theory of isothermal winds without extra forces other than the one due to the gas pressure gradient. We show that for a wind with a given density at its lower boundary, the velocity law and the mass loss rate are fixed by the condition that the wind should start subsonic at the photosphere and reach supersonic velocities further outwards. Then we describe the effects of momentum input (due to an extra outward force) and energy input (due to heating) on the structure of a stellar wind and on its mass loss rate. These principles hold for (almost) all wind theories. We show the results of forces acting at different distances in the wind. Based on these results we formulate the five laws of stellar wind theories. In the last section we briefly review the different wind theories.

An extensive discussion of the theories and observations of stellar winds will be published in *Introduction to Stellar Winds* by H.J.G.L.M. Lamers and J.P. Cassinelli (Cambridge University Press), in preparation.

2 Basic Concepts of Wind Theories

2.1 The Mass Continuity Equation

For a time-independent stellar wind with a constant mass loss rate, the amount of gas passing through any sphere of radius r is constant. This is expressed in the *equation of mass conservation*

$$\dot{M} = 4\pi r^2 \rho(r) v(r) . \quad (1)$$

Differentiation of this equation gives

$$\frac{1}{v} \frac{dv}{dr} = -\frac{1}{\rho} \frac{d\rho}{dr} - \frac{2}{r} . \quad (2)$$

2.2 The Momentum Equation

The motion of the gas in a stellar wind is described by Newton’s law $F = m.a$ or $F = \rho.dv/dt$ if F is the force per unit volume and $f = F/\rho$ is the force per unit mass. The velocity gradient in Newton’s law is

$$\frac{dv(r, t)}{dt} = \frac{\delta v(r, t)}{\delta t} + \frac{\delta v(r, t)}{\delta r} \frac{dr(t)}{dt} = v(r) \frac{dv}{dr} . \quad (3)$$

In a stationary wind $\delta v(r, t)/\delta t = 0$. The *equation of motion* or the *momentum equation* in a wind is

$$v \frac{dv}{dr} = -\frac{1}{\rho} \frac{dp}{dr} - \frac{GM_{\star}}{r^2} + f(r) . \quad (4)$$

The first term is the force due to the gradient of the gas pressure. This force is directed outwards (positive) because $dp/dr < 0$. The second term is the inward directed gravity and the third term describes any extra outward directed force.

2.3 The Energy Equation

The gas pressure gradient depends on the temperature structure of the wind, which depends on the heat input and cooling by expansion. The first law of thermodynamics states that

$$\frac{dQ}{dt} = \frac{du}{dt} + p \frac{d\rho^{-1}}{dt} \quad (5)$$

where Q is the heat energy per gram, and $u = (3/2)(\mathcal{R}T/\mu)$ is the internal energy for an ideal gas with mean particle weight μm_H . The gas pressure for an ideal gas is $p = \rho \mathcal{R}T/\mu$. For a stationary wind the time derivative is $d/dt = v d/dr$. Define $q(r) = dQ/dr$ as the heat input (positive) or heat loss (negative) per gram per cm in the wind, then the energy equation becomes

$$q = \frac{3}{2} \frac{\mathcal{R}}{\mu} \frac{dT}{dr} + p \frac{d\rho^{-1}}{dr} . \quad (6)$$

By substituting $p d(1/\rho) dr = d(p/\rho)/dr - (1/\rho) dp/dr$ with the ideal gas law we find

$$\frac{1}{\rho} \frac{dp}{dr} = \frac{5}{2} \frac{\mathcal{R}}{\mu} \frac{dT}{dr} - q(r) . \quad (7)$$

Combining (4) and (7) gives the *energy equation* of stellar winds

$$\frac{d}{dr} \left\{ \frac{v^2}{2} + \frac{5}{2} \frac{\mathcal{R}T}{\mu} - \frac{GM_{\star}}{r} \right\} = f(r) + q(r) . \quad (8)$$

This equation states that the change in energy of the gas as it moves 1 cm outwards is equal to the momentum input by the force and the heat input. The first left hand term is the kinetic energy of the flow, the second term is the enthalpy of the gas (the internal kinetic energy plus the capacity to do work) and the third term is the potential energy.

This energy equation can also be written in the integral form

$$e(r) \equiv \frac{v^2}{2} + \frac{5}{2} \frac{\mathcal{R}T}{\mu} - \frac{GM_{\star}}{r} = e(r_0) + \int_{r_0}^r f(r) dr + \int_{r_0}^r q(r) dr \quad (9)$$

where r_0 is some arbitrarily chosen lower limit.

Compare the energy of the wind just above the photosphere and at ∞ . In or just above the photosphere the potential energy is much larger than the enthalpy and the kinetic energy because for a normal star $v_{\text{esc}} \gg \mathcal{R}T_*/\mu$ and $v(R_*) \ll v_{\text{esc}}$ so the total energy is $e(r_0) \approx -GM_*/r_0$, which is negative. At large distance $r \rightarrow \infty$ the potential energy and the enthalpy both go to 0, so the total energy is the kinetic energy. This means that

$$\frac{v_\infty^2}{2} \approx -\frac{GM_*}{R_*} + \int_{R_*}^{\infty} f(r)dr + \int_{R_*}^{\infty} q(r)dr . \quad (10)$$

We see that *a stellar wind can only escape if there is an outward force that provides sufficient momentum input or an energy source that provides sufficient heat input for the wind to escape the potential well.*

3 Isothermal Winds Driven by Gas Pressure

Let us first consider an isothermal stellar wind. Such a wind obviously requires energy input, otherwise the gas would cool as it expands adiabatically. If the wind is isothermal, we do not have to worry about the energy equation and we can concentrate on the momentum equation and the resulting flow velocity. If there is no extra force, the wind is *driven by gas pressure only*. This is the case for the solar wind from the hot corona. Winds driven by gas pressure produce only small mass loss rates and are not important for stellar evolution. However, their theory gives insight into some of the basic physical principles of stellar wind theories.

3.1 The Critical Point of the Momentum Equation

The momentum equation of an isothermal wind with gas pressure only is

$$v \frac{dv}{dr} = -\frac{1}{\rho} \frac{dp}{dr} - \frac{GM_*}{r^2} . \quad (11)$$

In an isothermal wind consisting of an ideal gas of temperature T the force due to the pressure gradient can be written as

$$\frac{1}{\rho} \frac{dp}{dr} = \frac{\mathcal{R}}{\mu} \frac{dT}{dr} + \frac{\mathcal{R}T}{\mu\rho} \frac{d\rho}{dr} = \left(\frac{\mathcal{R}T}{\mu} \right) \frac{1}{\rho} \frac{d\rho}{dr} . \quad (12)$$

The density gradient can be expressed in a velocity gradient by (2). Substituting (2) and (12) into (11) yields

$$\frac{1}{v} \frac{dv}{dr} = \left\{ \frac{2a^2}{r} - \frac{GM_*}{r^2} \right\} / \{v^2 - a^2\} \quad (13)$$

with

$$a = (\mathcal{R}T/\mu)^{1/2} \quad (14)$$

is the isothermal speed of sound, which is constant in an isothermal wind. The lower boundary condition of (13) is the bottom of the isothermal region, located at r_0 where $v(r_0) = v_0$. In general r_0 is about the photospheric radius or a bit larger if the star is surrounded by an isothermal corona.

The momentum equation (13) has a singularity at the point where $v(r) = a$. We will show below that this singularity is extremely important, because it implies that the mass loss rate is fixed.

The numerator goes to 0 at a distance

$$r = r_c \equiv GM_*/2a^2. \quad (15)$$

This is the *critical distance*, or the distance of the *critical point*. The velocity gradient at the critical distance will be zero, because the numerator equals zero, unless $v(r_c) = a$. Similarly, the velocity gradient at the distance where $v = a$ will be $\pm\infty$, because the denominator = 0, unless $r = r_c$ when $v = a$. So the only solution which can have a positive velocity gradient at all distances is the one that goes through the critical point. This is the *critical solution* for which

$$v(r_c) = a \quad \text{at} \quad r_c = \frac{GM_*}{2a^2}. \quad (16)$$

So we find that at the critical point

$$v(r_c) = a = \frac{v_{\text{esc}}(r_c)}{2} \quad (17)$$

where $v_{\text{esc}}(r_c) = \sqrt{2GM_*/r_c}$ is the escape velocity at the critical point. The point in the wind where $v(r) = a$ is called the *sonic point*. In an isothermal wind the critical point coincides with the sonic point, but this is not necessarily true for other wind models. The critical solution is transonic, because it starts subsonic at small distances and reaches a supersonic velocity at large distances.

The topology of the solutions of (13) is shown in Fig. 1 for various initial velocities $v(r_0)$. Notice that only one solution (thick line) starts subsonic and ends supersonic.

The slope of the velocity law through the critical point can be derived by applying de l'Hopital's rule which states that the right hand side of a critical equation like (13) is equal to the quotient of the derivatives of the numerator and the denominator. (This can be proven by expressing both factors as a series around their zero point: $f(r) = f(r_c) + (r - r_c) \cdot (df/dr)_c$). De l'Hopital's rule results in

$$\frac{1}{v} \left(\frac{dv}{dr} \right)_{r_c} = \left\{ -\frac{2a^2}{r_c^2} + \frac{2GM_*}{r_c^3} \right\} / \left\{ \frac{2v}{dr} \frac{dv}{dr} \right\}_{r_c} = \frac{a^2}{r_c^2} \left(\frac{v}{dr} \frac{dv}{dr} \right)_{r_c}^{-1}. \quad (18)$$

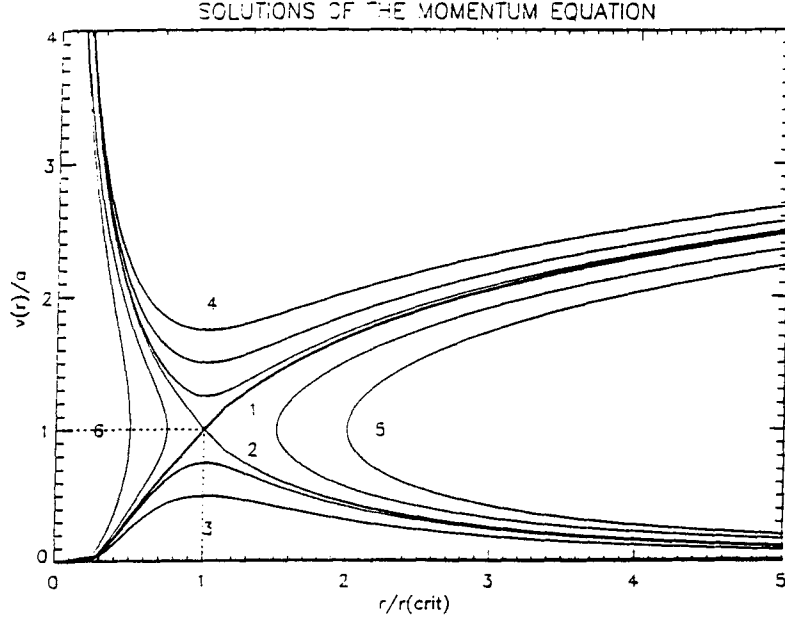


Fig. 1. Different types of solutions of the momentum equation for an isothermal wind with gas pressure only. For this particular case r_c is at $5 r_0$. The thick line passes through the critical point. It is the only transonic solution

This gives

$$\left(\frac{dv}{dr}\right)_{r_c} = \frac{\pm 2a^3}{GM_*} . \quad (19)$$

The positive or negative sign is a result of the fact that de l'Hopital's rule gives an expression for $(dv/dr)^2$. For a wind with an outward increasing velocity we obviously chose the positive gradient.

This discussion has shown that there is only one solution which starts subsonic and ends supersonic. This critical solution occurs for only one particular value of the velocity at the lower boundary: $v_0(\text{crit})$. This implies that an isothermal envelope with given density ρ_0 at its bottom can only produce a transonic wind if

$$\dot{M} = 4\pi r_0^2 \rho_0 v_0(\text{crit}) . \quad (20)$$

This is a very important result which shows that *an isothermal wind with a given lower boundary (ρ_0 , T_0 and gravity) can reach supersonic velocities for only one specific value of the mass loss rate!*

3.2 The Velocity Law of Isothermal Winds Driven by Gas Pressure

The momentum equation (13) has an analytic solution

$$\frac{v^2}{2} - a^2 \ln(v) = 2a^2 \ln(r) + \frac{GM_*}{r} + \text{constant} . \quad (21)$$

The constant is fixed by the condition $v(r_c) = a$ at the critical point. This gives an expression for the velocity law of an isothermal wind driven by gas pressure only

$$v \exp\left(-\frac{v^2}{2a^2}\right) = a \left(\frac{r_c}{r}\right)^2 \exp\left\{-\frac{2r_c}{r} + \frac{3}{2}\right\} \quad (22)$$

with $r_c = GM_*/2a^2$. This velocity law is shown in Fig. 2.

The initial velocity at the lower boundary of the isothermal region can be derived by applying (22) at r_0 . At the bottom of a gravitationally bound subsonic wind with $v_0 \ll a < v_{\text{esc}}$ one finds

$$\begin{aligned} v_0 &\approx a \left(\frac{r_c}{r_0}\right)^2 \exp\left\{-\frac{2r_c}{r_0} + \frac{3}{2}\right\} \\ &= a \left(\frac{v_{\text{esc}}(r_0)}{2a}\right)^2 \exp\left\{-\frac{v_{\text{esc}}^2(r_0)}{2a^2} + \frac{3}{2}\right\} . \end{aligned} \quad (23)$$

Equation (22) can also be written as

$$\frac{v}{v_0} \exp\left(-\frac{v^2}{2a^2}\right) = \left(\frac{r_0}{r}\right)^2 \exp\left\{\frac{GM_*}{a^2} \left(\frac{1}{r_0} - \frac{1}{r}\right)\right\} . \quad (24)$$

At large distances where $r \gg r_0$, the velocity law approaches

$$v(r \rightarrow \infty) \approx 2a\sqrt{\ln(r/r_0)} , \quad (25)$$

which increases infinitely. This is a consequence of the assumption that the wind is isothermal up to very large distances. It requires the continuous addition of energy and the resulting gas pressure then accelerates the wind indefinitely. Clearly this is an unrealistic situation. In reality the winds are approximately isothermal only up to a certain distance and the velocity does not increase beyond that distance.

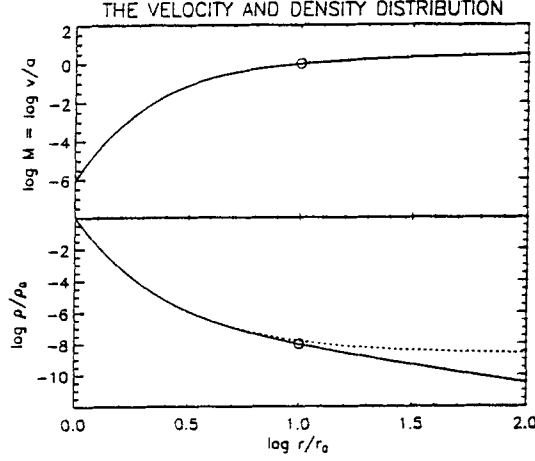


Fig. 2. The top part of the figure shows the velocity law, in terms of Mach-number ($M = v/a$) for an isothermal wind as a function of distance normalized to the lower boundary of the isothermal region r_0 . The location of the critical point is indicated by a dot. The lower part shows the logarithmic density distribution of the wind normalized to the density at r_0 (full line). The dashed line shows the density distribution of a hydrostatic atmosphere with the same temperature. The two density distributions are very similar in the subsonic part of the wind. The difference at the critical point is only a factor $e^{-0.5}$.

3.3 The Density Structure of Isothermal Winds Driven by Gas Pressure

The density structure is given by the mass continuity equation (1) and the velocity law (22) which yields

$$\frac{\rho}{\rho_0} \exp \left\{ + \frac{1}{2} \left(\frac{v_0 \rho_0 r_0^2}{a \rho r^2} \right)^2 \right\} = \exp \left\{ - \frac{GM_*}{a^2} \left(\frac{1}{r_0} - \frac{1}{r} \right) \right\} . \quad (26)$$

This equation can be solved numerically to give $\rho(r)/\rho_0$. The result is shown in Fig. 2 for a wind with a temperature such that $a^2 = 0.05 GM_*/r_0$, which implies a critical point at $r_c = 10r_0$. Let us now compare this with the density distribution of a hydrostatic atmosphere.

In a static atmosphere the density is given by the hydrostatic equation

$$\frac{1}{\rho} \frac{dp}{dr} + \frac{GM_*}{r^2} = 0 \quad (27)$$

which transforms, with (12), into

$$\frac{r^2}{\rho} \frac{d\rho}{dr} = - \frac{GM_*}{a^2} \quad (28)$$

if the atmosphere is isothermal. The solution is

$$\frac{\rho(r)}{\rho_0} = \exp \left\{ -\frac{GM_*}{a^2} \left(\frac{1}{r_0} - \frac{1}{r} \right) \right\} = \exp \left\{ -\frac{(r-r_0)}{\mathcal{H}_0} \frac{r_0}{r} \right\} \quad (29)$$

where

$$\mathcal{H}_0 = \mathcal{R}T/\mu g_0 \quad \text{with} \quad g_0 = GM_*/r_0^2 \quad (30)$$

is the density scale height at the bottom of the isothermal region.

The density structure (29) of the hydrostatic region is very similar to that of an isothermal wind. In fact, (29) is equal to (26) at the bottom of a wind if v_0 is highly subsonic. The difference at the critical or sonic point is exactly a factor $\exp(-0.5)$ because $v_0 \rho_0 r_0^2 = a \rho(r_c) r_c^2$.

The close agreement between the hydrostatic and wind density structure in the subsonic region where $v \lesssim 0.5a$ is due to the fact that the term vdv/dr in the momentum equation (4) is much smaller than the pressure gradient term. In other words: *the structure of the subsonic region is mainly determined by the hydrostatic density structure and not by the velocity law!*

3.4 The Mass Loss Rate of Isothermal Winds Driven by Gas Pressure

The mass loss rate of an isothermal wind driven by gas pressure follows from the equation of mass continuity at either the lower boundary or at the critical point.

$$\dot{M} = 4\pi r_0^2 \rho_0 v_0 = 4\pi r_c^2 \rho_c a \quad (31)$$

This gives

$$\begin{aligned} \dot{M} &= 4\pi \rho_0 a r_0^2 \left\{ \frac{v_{\text{esc}}(r_0)}{2a} \right\}^2 \exp \left\{ -\frac{(r_c - r_0)}{\mathcal{H}_0} \frac{r_0}{r_c} - \frac{1}{2} \right\} \\ &= 4\pi \rho_0 a r_0^2 \left\{ \frac{v_{\text{esc}}(r_0)}{2a} \right\}^2 \exp \left\{ -\frac{v_{\text{esc}}^2(r_0)}{2a^2} + \frac{3}{2} \right\} \quad (32) \end{aligned}$$

Estimates of the mass loss for a few characteristic stars are given in Table 1. Notice the extreme sensitivity of the mass loss rate to the height of the critical point in terms of the pressure scale height (column 8) because the density at the critical point decreases exponentially as $(r_c - r_0)/\mathcal{H}_0$. The predicted mass loss rate of a solar type star with a corona of 1×10^6 K and $\rho_0 = 10^{-14}$ g cm⁻³ is $1.6 \times 10^{-14} M_\odot \text{ yr}^{-1}$. This is in reasonable agreement with the observed rate of $2 \times 10^{-14} M_\odot \text{ yr}^{-1}$.

Table 1. Characteristics of isothermal winds with a density at the lower boundary of $\rho_0 = 10^{-14}$ g/cm³

M_* (M_\odot)	R_* (R_\odot)	v_{esc} (km/s)	T (K)	a (km/s)	\mathcal{H}_0 (R_*)	r_c (R_*)	$\frac{r_c - R_*}{\mathcal{H}_0}$	\dot{M} (M_\odot/yr)
1	1	617.5	1.10 ⁵	37.2	7.3 10 ⁻³	68.7	9.3 10 ³	1.2 10 ⁻⁶⁸
			3.10 ⁵	64.5	2.2 10 ⁻²	22.9	1.0 10 ³	1.5 10 ⁻²⁸
			1.10 ⁶	117.7	7.3 10 ⁻²	6.9	8.0 10 ¹	1.6 10 ⁻¹⁴
			3.10 ⁶	203.9	2.2 10 ⁻¹	2.3	5.9	8.2 10 ⁻¹¹
			5.10 ⁶	263.2	3.6 10 ⁻¹	1.4	1.1	4.0 10 ⁻¹⁰
1	100	61.7	3.10 ³	6.4	2.2 10 ⁻²	22.9	1.0 10 ³	1.5 10 ⁻²⁵
			1.10 ⁴	11.8	7.3 10 ⁻²	6.9	8.1 10 ¹	1.6 10 ⁻¹¹
			3.10 ⁴	20.4	2.2 10 ⁻¹	2.3	5.9	8.2 10 ⁻⁸
			5.10 ⁴	26.3	3.6 10 ⁻¹	1.4	1.1	4.0 10 ⁻⁷
10	10	617.5	1.10 ⁵	37.2	7.3 10 ⁻³	68.7	9.3 10 ³	1.2 10 ⁻⁶⁶
			3.10 ⁵	64.5	2.2 10 ⁻²	22.9	1.0 10 ³	1.5 10 ⁻²⁶
			1.10 ⁶	117.7	7.3 10 ⁻²	6.9	8.0 10 ¹	1.6 10 ⁻¹²
			3.10 ⁶	203.9	2.2 10 ⁻¹	2.3	5.9	8.2 10 ⁻⁹
			5.10 ⁶	263.2	3.6 10 ⁻¹	1.4	1.1	4.0 10 ⁻⁸
10	1000	61.7	3.10 ³	6.4	2.2 10 ⁻²	22.9	1.0 10 ³	1.5 10 ⁻²³
			1.10 ⁴	11.8	7.3 10 ⁻²	6.9	8.1 10 ¹	1.6 10 ⁻⁹
			3.10 ⁴	20.4	2.2 10 ⁻¹	2.3	5.9	8.2 10 ⁻⁶
			5.10 ⁴	26.3	3.6 10 ⁻¹	1.4	1.1	4.0 10 ⁻⁵

1 $M_\odot/\text{yr} = 6.303 \cdot 10^{25}$ g/s, $\mu = 0.60$

4 Isothermal Winds with an Outward Force

The momentum equation of an isothermal wind with an extra outward force f per unit mass can easily be derived from (4), (12) and (2)

$$\frac{1}{v} \frac{dv}{dr} = \frac{\frac{2a^2}{r} - \frac{GM_*}{r^2} + f(r)}{v^2 - a^2} . \quad (33)$$

We can immediately see from this equation that the effect of a force is very different for the subsonic and the supersonic regions.

(1). *Supersonic*: The denominator is positive so an extra force f results in an *increase* of the velocity gradient. The wind will reach a higher velocity.

(2). *Subsonic*: The denominator is negative so an extra force f results in a *decrease* of dv/dr . This may seem surprising, because it implies that if the wind is pushed outwards in the subsonic region it will accelerate slower, instead of faster. One can understand this by remembering the conclusion of the previous section, that the density structure of the subsonic region is mainly

determined by the hydrostatic equilibrium. So applying an outward force in the subsonic region has the same effect as reducing the gravity, which results in an increase in the pressure scaleheight. An increase in the pressure scaleheight gives a slower outward decrease of the density and, since the velocity has to follow the density structure (because of the mass continuity equation), a slower outward decrease in density means a slower outward increase of the velocity! (Note: this does not mean that the subsonic velocity is smaller if there is an outward force, but that the *subsonic velocity gradient* is smaller. We will argue below that the subsonic velocity is in fact larger).

What will be the result of the force on the mass loss rate? We have shown above that the mass loss rate is set by the condition that the solution of the momentum equation has to pass through the critical point. The conditions for the critical point are

$$r_c = \frac{GM_*}{2a^2} - \frac{f(r_c)r_c^2}{2a^2} \quad \text{and} \quad v_c = a . \quad (34)$$

We see that the critical velocity is again the isothermal sound speed, but the critical point is now closer to the star than for $f = 0$. Since the velocity at r_c is the same as for $f = 0$, but the velocity *gradient* in the subsonic region is smaller due to the force, the velocity below the critical point must be *higher* than without a force! This is also true at the lower boundary r_0 of the isothermal region. This means that the mass loss rate $\dot{M} = 4\pi r_0^2 v_0 \rho_0$ is higher!

This can also be understood in terms of the change in the density structure. Applying a force in the subsonic region results in a slower outward density decrease. Moreover, the critical point is closer to the star. Both effects imply that the density at the critical point, where $v = a$, will be higher than for $f = 0$. If the density at the critical point is higher and the velocity at the critical point is the same, the mass loss rate will be higher. We conclude that applying a force in the subsonic region results in a higher mass loss rate.

5 The Effect of Energy Input on a Stellar Wind

In Sect. 2.3 we have derived the energy equation (8) of a stellar wind with momentum and energy input. In this section we study the effect of energy input on the velocity law and the mass loss rate. The wind is no longer assumed to be isothermal.

The momentum equation (4) in a wind with energy and momentum deposition does not contain the thermal energy deposition $q(r)$. This does not mean, however, that the velocity in the wind is unaffected by heat deposition. Heat input changes the temperature structure of the wind and hence also the gas pressure. Since the momentum equation contains the force due to the gas pressure gradient, heat input affects the velocity law, density structure and the mass loss rate of a stellar wind. The effect of energy input on the

velocity can be derived from the momentum equation by taking into account its effects on the pressure gradient. This will be studied here.

The pressure term $\rho^{-1} dp/dr$ in the momentum equation can be expressed in terms of p/ρ

$$\frac{1}{\rho} \frac{dp}{dr} = \frac{d(p/\rho)}{dr} - p \frac{d\rho^{-1}}{dr} = \frac{d(p/\rho)}{dr} + \frac{p}{\rho} \frac{d \ln \rho}{dr} . \quad (35)$$

The density gradient can be eliminated by means of the mass continuity equation $d \ln \rho = -d \ln v - 2d \ln r$. Substitution of the isothermal sound speed $a(r)^2 = p/\rho = \mathcal{R}T/\mu$ for a perfect gas yields

$$\frac{1}{\rho} \frac{dp}{dr} = \frac{da^2}{dr} - \frac{2a^2}{r} - a^2 \frac{d \ln v}{dr} . \quad (36)$$

This results in the momentum equation in a general form that involves both the effects of a change in temperature and the external force

$$v \frac{dv}{dr} - \frac{a^2}{v} \frac{dv}{dr} + \frac{da^2}{dr} - \frac{2a^2}{r} + \frac{GM_*}{r^2} = f \quad (37)$$

or

$$\frac{1}{v} \frac{dv}{dr} = \left\{ \frac{2a^2}{r} - \frac{da^2}{dr} - \frac{GM_*}{r^2} + f \right\} / \{v^2 - a^2\} . \quad (38)$$

This equation contains the term $da^2/dr = (\mathcal{R}/\mu)dT/dr$. The energy equation (8) shows that in a wind with momentum and energy deposition

$$\frac{da^2}{dr} = \frac{\mathcal{R}}{\mu} \frac{dT}{dr} = \frac{\gamma - 1}{\gamma} \left\{ f + q - \frac{GM_*}{r^2} - v \frac{dv}{dr} \right\} . \quad (39)$$

With $\gamma = 5/3$ for an ideal gas. Substituting this expression for da^2/dr in the momentum equation one finds after multiplication of the result by γ

$$\frac{1}{v} \frac{dv}{dr} = \left\{ \frac{2c_s^2}{r} - \frac{GM_*}{r^2} + f - (\gamma - 1)q \right\} / \{v^2 - c_s^2\} . \quad (40)$$

In this expression $c_s = \sqrt{\gamma a^2}$ is the adiabatic speed of sound.

This is the most general form of the momentum equation of a spherically symmetric stellar wind with energy input and momentum input. Notice that *the energy input, $q > 0$, produces an inward directed force $(\gamma - 1)q$ which counteracts the outward force f .* This is because the energy input heats the gas which reduces the negative temperature gradient and thus the outward force of the pressure gradient.

The two forms of the momentum equation (38) and (40) show a curious difference. The first one suggests that the critical point occurs where $v = a$ whereas the second one suggests that the critical point occurs where $v = c_s$. The difference is due to the fact that (38) still contains the temperature gradient in the numerator through the term da^2/dr . This temperature gradient

depends on the velocity gradient as can easily be seen from (39). This extra $v dv/dr$ term means that the critical point is not at $v = a$ but at $v = c_s$.

Equation (40) seems to suggest that in the most general case of a wind with energy and momentum deposition the critical point is always the sonic point. This, however, is only true if both f and q do not depend on the velocity gradient dv/dr . If the momentum or energy deposition depends on dv/dr , it will produce additional terms of type dv/dr in the right hand side of (40) and move the critical point to another location. This is the case for line driven winds (see second contribution Lamers, this Volume).

For a wind with a given force $f(r)$ and given momentum input $q(r)$, the momentum equation (40) and the energy equation (8) can be solved simultaneously by standard numerical methods. This gives the velocity law and the temperature structure. The mass loss rate is set by the condition that the velocity law has to pass smoothly through the critical point.

6 A Wind with an $f \sim r^{-2}$ Force

Let us now consider the effect of an extra force on the mass loss rate and the velocity law. We take a simple $f \sim r^{-2}$ force that starts at different distances from the star. Such a force can be produced by radiation pressure due to optically thin lines or due to dust. This is because the radiative flux F varies as r^{-2} and thus the radiative acceleration is $g_{\text{rad}} = \kappa_F F(r)/c = \kappa_F F(R_*)(r/R_*)^{-2}/c \sim r^{-2}$ where κ_F is the flux-mean opacity. The last equality is only valid if κ_F is independent of distance.

The wind is again assumed to be isothermal. This simplifies the problems because the energy equation is reduced to $T(r) = T$ and it allows the isolation of the effects of the forces on the winds. The presence of a positive r^{-2} force which is smaller than the acceleration of gravity and which acts throughout the whole wind will obviously have the same effect as a reduction of the gravity or the mass of the star by a constant factor. In that case the mass loss rate and the velocity can simply be solutions of (24) and (32). However, if the force operates only in the lower part of the wind or only in the upper part, the solutions will be different.

The momentum equation of an isothermal wind with an additional positive force $f = Ar^{-2}$ is

$$v \frac{dv}{dr} = -\frac{1}{\rho} \frac{dp}{dr} - \frac{GM_*}{r^2} + \frac{A(r)}{r^2} \quad (41)$$

with

$$\begin{aligned} A(r) &= 0 & \text{for} & \quad r < r_d \\ A(r) &= A & \text{for} & \quad r \geq r_d \end{aligned} \quad (42)$$

In this equation A is a positive constant in the region $r > r_d$ where the force operates. The boundary is called r_d because of the similarity of this model to the dust driven wind, where the radiation pressure is switched on at the dust-formation radius. Expressing the pressure gradient in terms of the velocity gradient by means of the mass continuity equation (1), with (12) and (2) results in the momentum equation

$$\frac{r^2}{v} \frac{dv}{dr} = \frac{2a^2r - GM_* + A(r)}{v^2 - a^2} = \frac{2a^2r - GM_*(1 - \Gamma(r))}{v^2 - a^2} \quad (43)$$

with $\Gamma(r) = 0$ if $r < r_d$ and $\Gamma(r) = A/GM_*$ if $r > r_d$. The critical point occurs where

$$\frac{r_c}{1 - \Gamma(r_c)} = \frac{GM_*}{2a^2} \quad (44)$$

The models for different values of r_d are shown in Fig. 3 for $\Gamma(r) = 0.5$ at $r > r_d$. The temperature of the wind model is chosen such that $\mathcal{R}T/\mu = a^2 = (GM_*/r_0)/2\sqrt{10}$. As the location of the critical point depends on Γ , we will indicate it as $r_c(\Gamma)$. The dependence of \dot{M} in the five cases can be judged from the velocity laws by realizing that \dot{M} is proportional to $v(r_0)$ because $\rho(r_0)$ is a fixed boundary condition. The top figure shows the location of $r_c(0)$ in case of $\Gamma = 0$. The bottom figure shows the location of $r_c(\Gamma)$ in case of $\Gamma = 0.5$ throughout the wind. These are the two extreme cases.

If $r_d > r_c(0)$ the structure of the subsonic region nor the location of the critical point is affected by Γ . So the mass loss rate will be the same as in the case of $\Gamma = 0$. This shows a very important characteristic of stellar winds: *an outward force applied to the wind above the critical point does not affect the mass loss rate*. The velocity in the supersonic regions at $r > r_d$ will be larger however than in the case of $\Gamma = 0$, because the numerator of (43) is larger when $\Gamma > 0$ and the denominator of (43) is positive. So increasing Γ above the critical point will result in a steeper velocity law and larger velocities at $r > r_d$. In the supersonic region the value of Γ may exceed 1.

If $r_d < r_c(\Gamma)$ the critical point occurs at $r_c(\Gamma)$. This is due to the fact that the location of r_c is given by the *local* condition that the numerator of (43) is zero. The mass loss depends on the value of Γ through the whole subcritical region $r_0 < r < r_c(\Gamma)$ because the velocity law in this region is affected by $\Gamma(r)$ according to (43). A positive value of $\Gamma > 0$ implies a smaller velocity gradient and a smaller density gradient at $r_d < r < r_c(0)$ than in the case of $\Gamma = 0$. This smaller density gradient results in a higher value of ρ at $r_c(\Gamma)$ and thus a higher mass loss rate.

If the value of Γ becomes positive somewhere between $r_c(\Gamma)$ and $r_c(0)$ then the location of the critical point depends sensitively on the shape of the $\Gamma(r)$ function. If Γ jumps from 0 to a value larger than 1 at r_d , the critical point will occur at r_d . This resembles models with radiation pressure due to dust.

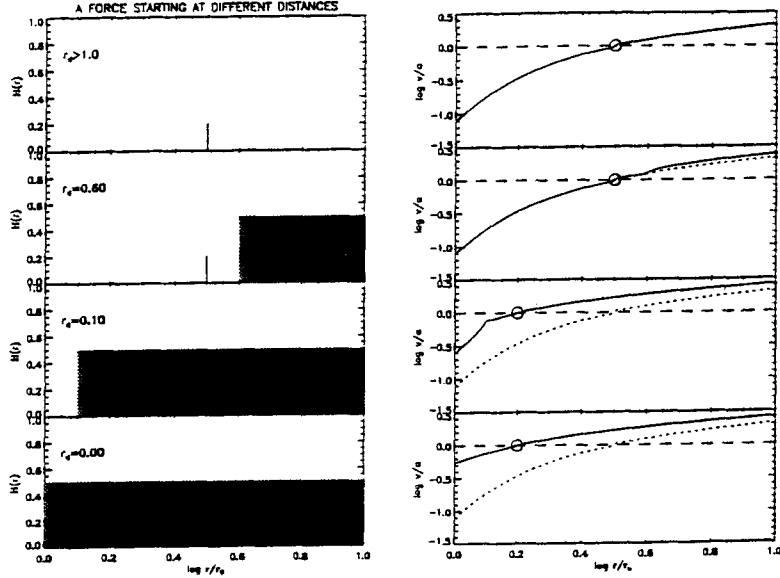


Fig. 3. The effect of an outward force $f(r) = \Gamma(r)GM_*/r^2$ on the velocity structure of an isothermal stellar wind. The left hand side shows the various distributions of $\Gamma(r)$ and the right hand side shows the resulting wind velocity. The wind velocity for $\Gamma(r) = 0$ is shown by a dotted line. The location of the critical point is indicated by a dot in the right hand figure and by a tickmark in the left figure. Notice the changes in the location of the critical point and in the mass loss rate $\dot{M} \sim v(r_0)$ if $\Gamma(r) > 0$ in the subsonic region

The mass loss rate can easily be predicted in the following way. Below the critical point, the density structure will be approximately as in hydrostatic equilibrium. This means that the density at r_d can simply be derived from the density at the lower boundary and the outward decrease with the pressure scale height. Since the sonic point is at r_d , the mass loss rate follows from the mass continuity equation.

7 The Five Laws of Stellar Wind Theory

Based on the arguments and the simple models described above, we can formulate five important laws for stellar winds.

1. *The first law of stellar winds:*

The mass loss rate is set by the condition that the velocity law should pass smoothly through the critical point.

2. *The second law of stellar winds:*

The mass loss rate is determined by the forces and the energy in the *subcritical* region of the wind.

3. *The third law of stellar winds:*

The input of energy (heat) or momentum (by an outward directed force) in the *subcritical* region results in a smaller velocity gradient but a higher velocity and a higher mass loss rate.

4. *The fourth law of stellar winds:*

The input of energy (heat) or momentum (by an outward directed force) in the *supercritical* region results in an increase in the terminal velocity of the wind, but does not affect the mass loss rate.

5. *The fifth law of stellar winds:*

In the subsonic part of the wind the density structure is very similar to that of a hydrostatic wind. The velocity law then follows from the mass continuity equation. In the supersonic part of the wind the forces determine the velocity structure. The density law then follows from the mass continuity equation.

8 Mass Loss Mechanisms

Several mechanisms have been suggested to explain the mass loss and stellar winds of different types of stars. We briefly summarize these, together with some references to the basic theory.

8.1 Coronal Winds

Coronal winds are driven by gas pressure due to the high temperature of stellar coronae. Stars with a sub-photospheric convection zone can be surrounded by a hot corona of a few 10^6 K. The theory of coronal winds is very similar to the basic theory of hot isothermal winds that was discussed in Sect. 3, apart from the fact that coronal winds are not really isothermal but have a slowly outward decreasing temperature. The temperature gradient is small and the wind remains hot up to a large distance because of thermal conduction. The mass loss rates of coronal winds is rather small (see Table 1) except for very low gravity stars. However, for these stars other mechanisms are more important.

References: Parker (1958), Brandt (1970)

8.2 Dust Driven Winds

The driving force of dust driven winds is the radiation pressure on dust. Dust can form in the envelopes of cool stars when the temperature has dropped to below $\sim 10^3$ K and the density is still sufficiently large. Since dust is a very good continuum absorber, the dust grains will be radiatively accelerated

outwards. Interactions with atoms provide the momentum-sharing needed to drag the gas component along. The wind theory is basically similar to that discussed in Sect. 5 for a wind with an $f \sim r^{-2}$ force from a certain distance onwards. The mass loss of the dust driven winds depends crucially on the location of the dust formation.

Reference: Sedlmayr (this Volume)

8.3 Line Driven Winds

The winds of hot stars are driven by radiation pressure on spectral lines due to ions of abundant elements that have very large numbers of absorption lines in the UV and the far-UV (below 912 Å). The radiation pressure depends strongly on the Doppler effect, because it allows the ions to intercept stellar radiation that was not absorbed in the lower layers of the wind. In this respect the line driven wind theory is very different from the dust driven wind theory and the basic theory described for gas-pressure driven winds because the force depends on the velocity *gradient*. The line driven wind theory is discussed in my other paper in this Volume.

References: Castor et al. (1975), Lamers (second contribution to this Volume).

8.4 Pulsation Driven Wind Theory

Cool supergiants such as the Mira stars and the AGB stars pulsate. During each expansion phase the atmosphere is tossed upward and it falls back during the contraction of the star. However, due to the low gravity, the layers in the outer atmosphere fall back so slowly that they are hit by the next expansion wave before they have reached their initial position. So the outer layers get a kick during every pulsation cycle. This results in a slow acceleration of outer layers of the atmosphere. This mass loss mechanism can be much more efficient if dust formation is taken into account because of the resulting radiation pressure on dust. The combination of pulsation and radiation pressure on dust provides a very efficient mass loss mechanism for luminous cool stars. Figure 4 shows the basic mechanism.

References: Bowen (1988).

8.5 Sound Wave Driven Winds

The convection zone below the photospheres of cool stars generates sound waves in the atmospheres. Sound waves generate a pressure very similar to the gas pressure by thermal motions. Outward travelling soundwaves produce a pressure gradient that results in an outward directed force. This force could in principle drive a stellar wind. The problem with the sound wave driven wind models is the same as for wind models driven by gas pressure (coronal

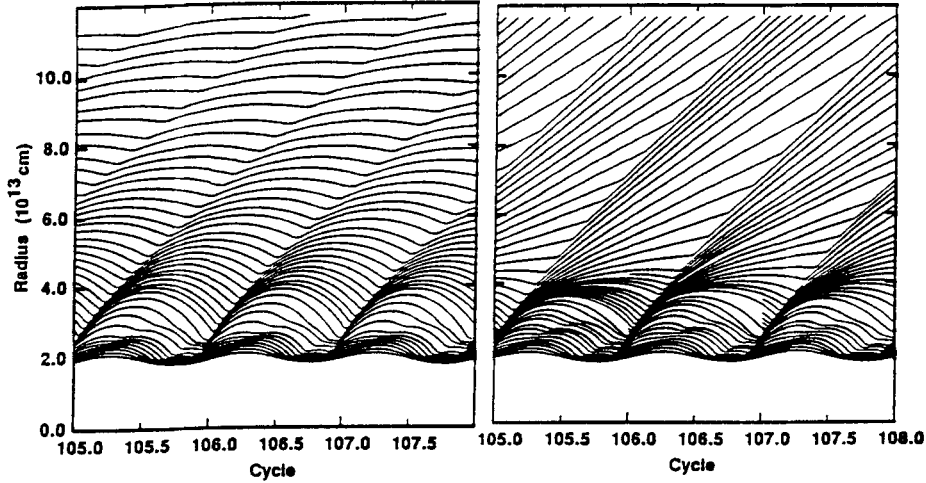


Fig. 4. The mass loss mechanism of pulsation. Left: pulsation only; right: pulsation and radiation pressure due to dust. The dust is formed at a distance of $4 \cdot 10^{13}$ cm. The figure shows the motions of the different layers during a pulsation cycle (from Bowen 1988)

winds): the mechanism produces only small mass loss rates. This is because the amplitude of the waves has to be small, otherwise dissipation would quickly decrease the wave pressure.

References: Pijpers and Hearn (1989), Pijpers and Habing (1989)

8.6 Alfvén Wave Driven Wind Models

Stars with magnetic fields can have a mass loss due to the wave pressure by Alfvén waves. This requires open magnetic field lines with their footpoints in the photosphere. When these footpoints are oscillating, a magnetic wave travels outwards with the Alfvén speed, $v_A = B/\sqrt{4\pi\rho}$. This mechanism is quite similar to that of the sound wave driven winds but it is more efficient because the Alfvén speed of magnetic waves is much larger than the sound speed. It can result in high mass loss rates and high wind speeds of several times the Alfvén speed. This mechanism is important for stars that are not luminous enough to have a strong radiation pressure, i.e. $L_* < 10^3 L_\odot$. It is the dominant mechanism for the fast wind from the coronal holes of the sun.

References: Hartmann and MacGregor (1980, 1982).

8.7 Magnetic Rotating Winds

In these models the wind is basically driven by the rotation. Since the plasma can only move along the magnetic field lines, material in the equatorial plane of the star will be “flung out” by the magnetic field lines that corotate with the star. (This is similar to the motion of a marble in a hollow flexible plastic-tube. When the tube is swayed around, the marble will be flung out of the tube). This process converts rotational energy into expansion from the outer atmosphere. The mass loss rate is mainly determined by the rotation, and the terminal velocity of the wind is determined by the strength of the magnetic field. This mechanism explains the fast deceleration of rapidly rotating pre-main sequence stars.

References: Weber and Davis (1967), Brandt (1970)

8.8 Summary of Wind Theories

Table 2 gives a summary of the characteristics of the mechanisms for mass loss not due to rotation.

Table 2. Mass loss mechanisms

Mechanism and Stars	Types	Characteristics
CORONAL WINDS		
Solar type	G,K	low \dot{M} , high v_∞
Giants ?		
LINE DRIVEN WINDS		
Hot stars	O,B,A CPN, WD WR?	high \dot{M} , high v_∞
DUST DRIVEN WINDS		
Cool supergiants	M, AGB	high \dot{M} , low v_∞
PULSATION DRIVEN WINDS		
Cool pulsating stars	Mira's, AGB?	high \dot{M} , low v_∞
ALFVEN WAVE DRIVEN WINDS		
Cool stars with magnetic fields	F,G,K,M,	low \dot{M} ?, high v_∞
MAGNETIC ROTATING WINDS		
Magnetic fast rotators	WR?	high \dot{M} , high v_∞
SOUND WAVE DRIVEN WINDS		
Stars with convective envelopes	??	low \dot{M} , low v_∞

References

- Bowen, G. H. (1988): ApJ **329**, 299
Brandt, J.C. (1970): *The Solar Wind*, Freeman, San Francisco
Castor, J.C., Abbott, D.C., Klein, R.I. (1975): ApJ **195**, 157
Hartmann, L., MacGregor, K.B. (1980): ApJ **242**, 260
Hartmann, L., MacGregor, K.B. (1982): ApJ **257**, 264
Parker, E.N. (1958): ApJ **128**, 664
Pijpers, F.P., Hearn, A.G. (1989): A&A **209**, 198
Pijpers, F.P., Habing, H.J. (1989): A&A **215**, 334
Weber, E.J., Davis, L. (1967): ApJ **148**, 217

Cool Star Winds and Mass Loss: Theory

Erwin Sedlmayr and Jan Martin Winters

Institut für Astronomie & Astrophysik, Technische Universität Berlin, Sekr. PN 8-1, Hardenbergstr. 36, D-10623 Berlin, Germany

e-mail: Sedlmayr@physik.TU-Berlin.DE; Winters@physik.TU-Berlin.DE

Abstract. We describe the ingredients necessary for the consistent theoretical description of dust forming circumstellar shells around Red Giants on the asymptotic giant branch. The complete set of equations required for the reliable modeling of stationary and pulsating situations is discussed and applied to a dust driven wind and to a typical carbon rich Mira atmosphere. Special emphasis is put on the theoretical description of the dust formation process and on the complex interaction among dust formation, chemistry, hydrodynamics, thermodynamics and radiative transfer. We present some fundamental implications of a consistent description of the dust forming system on its observable appearance.

1 General Overview

All stars, except perhaps the most compact objects like White Dwarfs or neutron stars, exhibit a more or less pronounced mass loss proved by clear observed signatures like circumstellar reddening, extended shells, P-Cygni line profiles, radial velocity fields, etc. The mass loss rates \dot{M} are strong functions of the object's position in the HR diagram and range from insignificant values ($\dot{M} < 10^{-12} M_{\odot} \text{yr}^{-1}$) characterizing objects at the lower main sequence up to huge values ($\dot{M} = 10^{-6} - 10^{-4} M_{\odot} \text{yr}^{-1}$) for objects in the upper region of the HR diagram, i.e. those objects having extremely high luminosities (see Fig. 1).

A detailed inspection of the stellar mass loss phenomenon reveals different modes of mass loss being connected with the various types of objects in the HR diagram (see Fig. 2):

i) *quasi stationary winds*: These are observed in hot O and B stars, in solar type objects and in K giants, where the mass loss phenomenon seems to be a long lasting process with typical time scales larger than 10^5yr .

ii) *periodic and semi regular mass loss*: In these cases, which are observed in the outflows of Miras and long-period variable stars (LPVs), the mass loss shows a distinct periodic variation which is believed to be connected with the intrinsic stellar pulsations and seems to be triggered by outwards traveling shock waves generated at the bottom of the stellar atmosphere.

iii) *episodic mass loss*: This mode is observed in RCrB-type stars, Wolf-Rayet stars and of course in explosive events like novae and supernovae.

Despite this rather complex observational situation there seems to be a rather systematic distinction between the various driving mechanisms for the

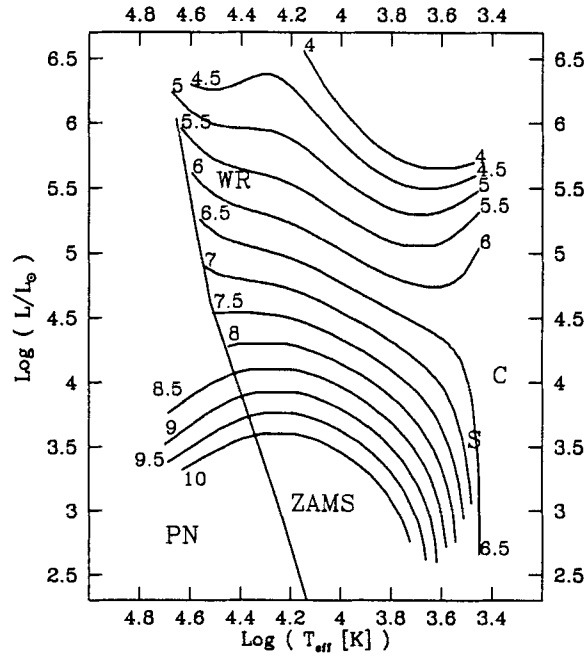


Fig. 1. Lines of constant mass loss rate in the HR diagram (after de Jager et al. 1988). Labels are $-\log_{10}(\dot{M})$

quasi-stationary	hot stars, K giants	ζ Pup, ζ Aur
(quasi)periodic	Miras, semi-regular Variables	α Cen, RScl
episodic	RCrB, Wolf-Rayet stars, SN, Novae	RCrB, WR140, SN1987a, V846Cen

Fig. 2. The different modes of mass loss, respective class of objects, and representative objects

mass loss as depicted in Fig. 3. There are only two basically different mechanisms: radiation induced (applicable to high luminosity objects) and wave induced winds (applicable to objects generating considerable wave energy near the surface of the star), respectively. As most giants and supergiants show a more or less pronounced variability, radiative acceleration of the wind might not be the only driving mechanism, but also momentum and energy input by waves should contribute to or even dominate the generation of the wind and consequently the radial structure of the velocity field. Therefore, a simultaneous treatment of radiative momentum transfer to the matter and momentum and energy dissipation in the wave field is required to model the mass loss phenomenon in these cases.

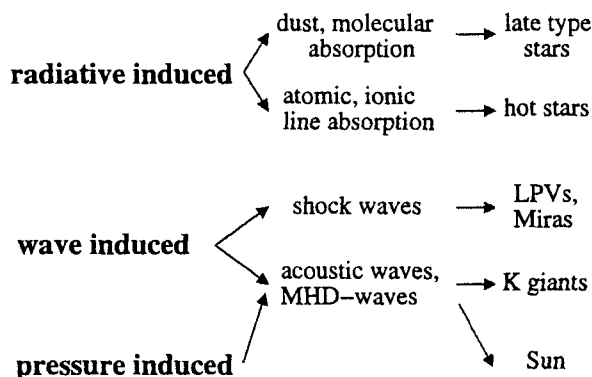


Fig. 3. Basic driving mechanisms

Since the lecture of H. Lamers (first contribution to this Volume) reviews the general aspects and the basic theoretical concepts of stellar winds throughout the HR diagram, in this lecture we will focus on the mass loss of late-type stars, in particular of AGB objects, where mass loss plays a central role not only for the understanding of their shell structure but also for the evolution of the object itself.

2 Basic Characteristics of Late-Type Stars

2.1 HR Diagram Characteristics

Red giants and supergiants are evolved objects occupying the upper right part of the HR diagram. These objects are characterized by rather cool (red!), extended (giant!) shells having low expansion velocities but rather large mass loss rates. A compilation of some important characteristic properties of these AGB objects is given in Table 1.

An important signature is the observation of significant dust formation causing pronounced reddening and, in extreme cases, complete obscuration of the central stars. Though most objects in this region of the HR diagram are due to their evolutionary state intrinsic variables like Miras and LPVs – which clearly can be found in the detailed temporal and spatial signatures of the wind – the stellar mass loss phenomenon itself in most cases seems to be a long-lasting process whose secular variations are finally controlled by the intrinsic evolutionary time scale of the star.

In all objects the occurrence of dust seems to have a decisive impact upon the detailed shell structure, the local dynamics, and finally upon the overall appearance of the object as manifested e.g. by a clear correlation between the observed stellar mass loss rate and the circumstellar dust abundance measured by the IRAS colors which is found for many late-type stars (cf.

Table 1. Characteristic quantities of dust forming late-type stars

stellar mass	M_*	$\sim 0.7 \dots 2.0 M_\odot$
stellar luminosity	L_*	$\sim 10^3 \dots 10^5 L_\odot$
stellar temperature	T_*	$\sim 2000 \dots 3000 \text{ K}$
mass loss rate	\dot{M}	$10^{-7} \dots 10^{-4} M_\odot \text{ yr}^{-1}$
wind velocity	v_∞	$\sim 10 \dots 30 \text{ km s}^{-1}$
mass of the shells	M_{CS}	$\sim 0.1 \dots 0.6 M_\odot$
pulsation period	P	$\sim 100 \dots 1000 \text{ d}$

Fig. 4). A second important fact is that the observed high mass loss rates are carried by rather low expansion velocities drawing a clear distinction to hot star winds where similar high mass loss rates always are connected with expansion velocities being at least a factor of 100 larger. The low expansion velocity and high mass loss rate, together with the fact, that the objects under consideration only have low surface gravity, places important constraints on the mass loss mechanism: Most of the energy transferred to the wind must be deposited in the sub-sonic (inner) region to account for the observed high mass loss rate. Only a small fraction of the driving energy can be supplied in the supersonic (outer) wind regime in order to accelerate the wind to its low terminal velocity. For a detailed discussion of the basic physical constraints imposed on the driving mechanism of the wind, we refer to the excellent review of Holzer and MacGregor (1985).

2.2 Shell Characteristics

For a typical Red Giant, Fig. 5 depicts both the observational side and the theoretical side of the problem by focusing various distinct features of the observational appearance as well as important processes constituting necessary ingredients of the theoretical description which are required for a reliable physical understanding of such objects.

Observational facts. The spectra of the objects show P Cygni line profiles, being a clear signature of the shell expansion caused by a stellar wind. Typical expansion velocities range from $10 \dots 30 \text{ km s}^{-1}$ thus being extremely supersonic. The P Cyg profiles are found in a variety of molecular lines (e.g. Keady and Ridgway 1993) demonstrating the radial evolution of both the complex chemistry and the increasing velocity. From a detailed modeling of these infrared molecular lines the radial density distribution and the mass loss rate can be inferred. In almost all AGB objects, also rotational emission lines of various molecules originating in the outer region of the shells are observed at radio wavelengths, from which usually the terminal wind velocity

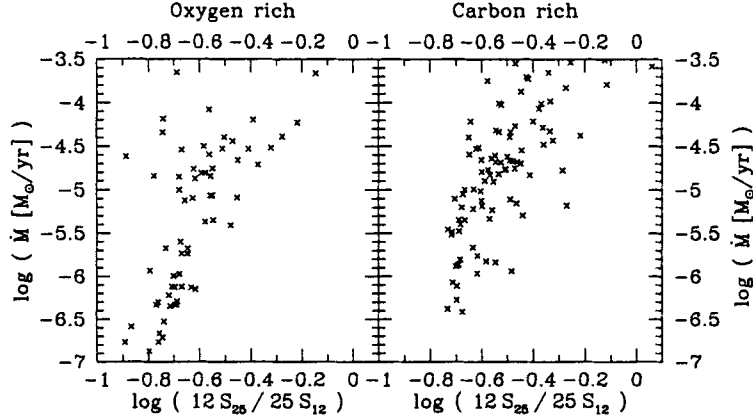


Fig. 4. Correlation between mass loss rate and IRAS colors (from Loup et al. 1993)

and the mass loss rates in the outer shell regions are derived (e.g. Knapp and Morris 1985).

A noticeable feature observed in nearly all objects in this region of the HR diagram is effective dust formation in the cooling outflow which manifests itself by a significant reddening of the continuum radiation field, large infrared (IR) excesses and specifically by pronounced dust absorption or emission bands. In some objects, in particular early M giants, also emission lines are observed in the UV and visual spectral region, indicating a non-monotonic temperature structure which usually is attributed to the existence of a chromosphere well inside the dust forming region.

High spatial resolution observations in different wavelength bands reveal a rather complex radial structure of the circumstellar dust shell (e.g. Ridgway and Keady 1988, Danchi et al. 1994). From such observations, the approximate location of the dust formation region can be inferred.

Physical processes. The basic feature of a red giant shell is the presence of a velocity field starting in the photosphere and showing a distinct subsonic-supersonic transition. This velocity field causes a cooling flow along which a more and more complex chemistry evolves providing beyond some radius (below 1300K) favorable conditions for cluster nucleation and grain growth. Due to its huge extinction coefficient, the dust grains very efficiently absorb radiation momentum and energy, which leads to an effective acceleration of the circumstellar material and to a pronounced infrared excess (see next section). Additional energy and momentum input to the material by wave dissipation causes a levitation of the atmosphere in the inner region and, in connection with the effects introduced by the dust, might lead to severe influences on the radial structure of the dust shell (see Sect. 4.4).

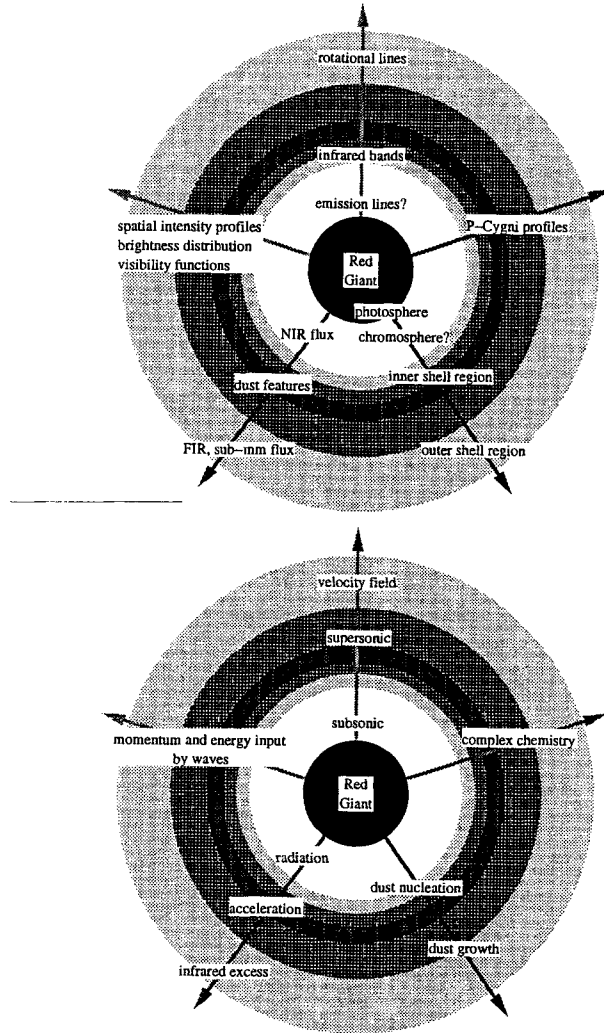


Fig. 5. Observed appearance and physical mechanisms in a typical circumstellar dust shell

3 Self-consistent Description of Dust Forming Circumstellar Shells

The presence of dust in general has three severe impacts upon the thermodynamic, hydrodynamic, and chemical structure of the dust forming system:

- i) Due to its specific absorption properties, dust grains – being macroscopic particles – dominantly absorb high energy photons and re-emit in the

infrared regime, thus transforming the trapped short wavelength photons into long wavelength photons, for which the systems usually are transparent. Therefore the dust grains act as an energy sink in the equation of energy by channeling the energy out of the system.

ii) Due to its large absorption and scattering cross sections, the momentum of the radiation field is very effectively taken up by the dust grains and subsequently is transferred to the ambient gas by frictional coupling, thus causing an efficient radiative acceleration of the matter.

iii) By formation of macroscopic dust particles the chemistry is affected with regard to two aspects:

- By the dust formation process itself, causing a significant depletion of the chemical species involved in the formation of grains.
- By the formation of grains, surfaces are introduced into the system, which now are available for a variety of chemical reactions (like H_2 formation from atomic hydrogen) to take place which usually would not occur in the gas phase.

Due to these significant impacts of the grains on any dust forming system, also for the consistent description of a dust forming AGB star shell these aspects are of particular importance providing a close coupling among the chemical, thermodynamic, and hydrodynamic structure of the dust forming circumstellar shell (see Fig. 6). In the numerical modeling, these different processes, which are described in the following, have to be treated simultaneously, taking into account their mutual interactions.

3.1 Chemistry of the Circumstellar Shell

Figure 7 shows that chemistry plays a central role with regard to three important aspects for the physical behavior of circumstellar shells which have to be considered in the quantitative modeling:

- a) The chemical structure of the atmosphere and the shell i.e. the knowledge of the local concentrations of the various ionic, atomic and molecular species, determines the transport coefficients of the gas, which are most important ingredients for the quantitative thermodynamic and hydrodynamic modeling. This concerns in particular the molecular opacity coefficients which in two ways influence the model structure: i) atomic and molecular absorption and emission determine the radiative transfer and hence determine via the energy equation the local temperature of the system, and ii) the extinction coefficient determines the absorption of radiative momentum in particular in the molecular lines which in the equation of motion might contribute significantly to the outward directed acceleration causing possibly a levitation of the atmosphere (e.g. Jørgensen et al. 1992). As this effect introduces a pronounced increase of the scale height of the system, this is of particular importance for hydrostatic models, which might become sufficiently extended for further effective molecule formation and even dust formation to take place.

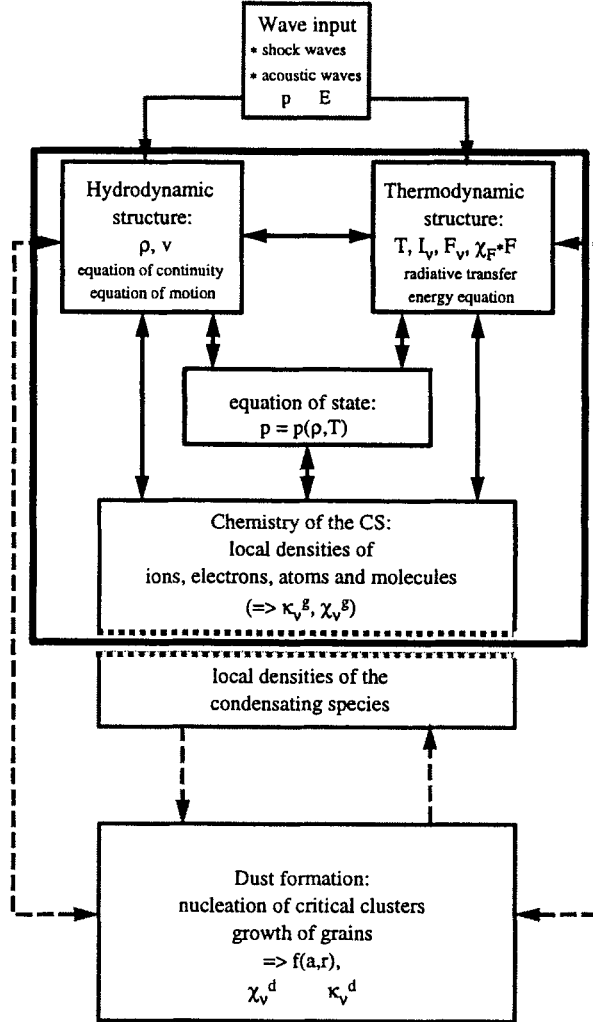


Fig. 6. Coupling among the different physical processes. The large box comprises the classical problem of a stellar atmosphere (after Sedlmayr and Winters 1991)

To get reliable molecular extinction, absorption and emission coefficients is by no means a simple problem since it requires both realistic local molecular concentrations (see Sect. 3.1.1) and reliable monochromatic molecular transport coefficients per particle where a huge number of transitions usually has to be taken into account. For this purpose, either direct methods are applied by taking into account millions of individual lines in the transfer calculations or statistical approaches like the use of opacity distribution functions (ODF)

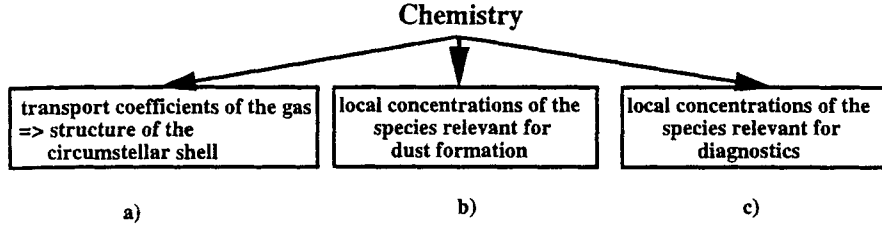


Fig. 7. General role of chemistry for a dust forming circumstellar shell

or opacity sampling methods (OS), where for each frequency interval suitable average values accounting for the total contribution of the corresponding transitions are constructed. For further reading see the excellent reviews of Tsuji (1986) and Gustafsson (1989) and the recent conference proceedings on molecules in the stellar environment (Jørgensen 1994).

b) A second important aspect of the chemistry is that it provides the concentrations of the species being able to condense and thus provides the prerequisites for primary dust nucleation and growth. As the species relevant for dust formation usually are different from those molecules determining the basic atmospheric structure (see a)) their determination requires particular arguments being provided by both the special nature of the observed circumstellar dust components and the individual chemical behavior of the molecules under consideration. This complex is discussed in Sect. 3.2.

c) Finally, chemistry plays a central role with regard to a reliable interpretation of actual observations of circumstellar shells aiming at a quantitative diagnostics for real objects. Any detailed quantitative analysis has to be based on the knowledge of the local concentrations of the various species and therefore involves the detailed investigation and modeling of the chemical shell structure. From Fig. 7 one infers that this structure is strongly coupled with the various other boxes, thus clearly demonstrating that any reliable quantitative diagnostics of circumstellar shells has to be based on self-consistent theoretical descriptions.

3.1.1 Level of Approach

In all model calculations the chemistry turns out to be a most time consuming part of the necessary numerics. For this reason, any qualified judgement which allows to reduce the complexity of the problem to a still realistic minimum level is very useful. The necessary level of approach can be inferred from comparing the different time scales describing the various processes in a chemical network. This network consists of a set of continuity equations

$$\frac{\partial n_i}{\partial t} + \text{div}(\mathbf{v} \cdot \mathbf{n}_i) = \sum_{j=1}^N (Q_{i,j}^{c,g} - Q_{i,j}^{c,l}) + \sum_{j=1}^N (Q_{i,j}^{p,g} - Q_{i,j}^{p,l}) \quad (1)$$

where c denotes kinetic reactions, p denotes photo reactions, g and l are the gain and loss terms, respectively, n_i is the number density of species i , and N is the number of species considered in the network. For spherical symmetry, the divergence term is given by

$$\text{div}(\mathbf{v} \cdot \mathbf{n}_i) = \frac{1}{r^2} \frac{\partial}{\partial r} (r^2 \mathbf{v} \cdot \mathbf{n}_i) = \mathbf{v} \frac{\partial \mathbf{n}_i}{\partial r} + \frac{2 \mathbf{v}}{r} \mathbf{n}_i + \frac{\partial \mathbf{v}}{\partial r} \mathbf{n}_i ,$$

and the time evolution of n_i in co-moving coordinates is

$$\dot{n}_i = \frac{dn_i}{dt} = \frac{\partial n_i}{\partial t} + v \frac{\partial n_i}{\partial r} .$$

Inserting these expressions into (1) and dividing by the density n_i provides the respective time scales defined in Table 2 where the different states of equilibrium – which in principle may be encountered in a circumstellar environment – are depicted.

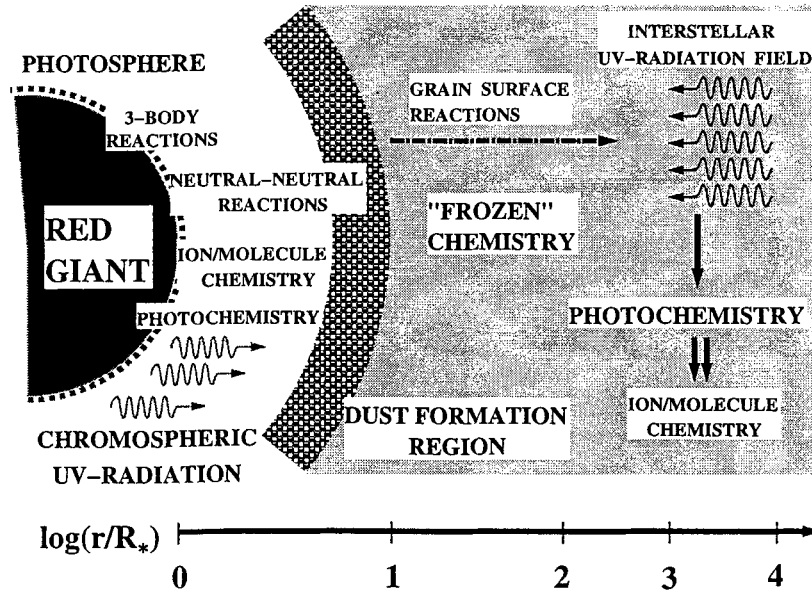


Fig. 8. Chemical processes in different regions of the circumstellar shells around red giants (adopted from Patzer et al. 1996a)

In a real circumstellar shell various chemical processes take place, which in their full complexity are depicted in Fig. 8. Though being impressively complicated, in many situations the description of the chemistry may be considerably simplified. Figure 9 shows various situations of circumstellar shells

Table 2. Definition of the different time scales and different states of equilibrium. Definition: $\underbrace{ab\dots}_{\text{min}} = \min\{a, b, \dots\} \gg |a + b + \dots|$. Terms marked by “<<” can be neglected against the terms inside the braces. CE: chemical equilibrium, KE kinetic equilibrium (adopted from Goeres et al. 1988)

hydrodynamics			source terms		
$\frac{\dot{n}_i}{n_i}$	$2 \frac{v}{r}$	$\frac{\partial v}{\partial r}$	$\frac{1}{n_i} \sum_j (Q_{i,j}^{c,g} - Q_{i,j}^{c,l})$	$\frac{1}{n_i} \sum_j (Q_{i,j}^{p,g} - Q_{i,j}^{p,l})$	
<<	<<	<<	$\underbrace{\hspace{2cm}}$	<<	<< CE (\rightarrow LTE)
$\underbrace{\hspace{2cm}}$			$\underbrace{\hspace{2cm}}$	<<	<< CE (\rightarrow LTE)
<<	<<	<<	$\underbrace{\hspace{4cm}}$		KE (\rightarrow non LTE)
$\underbrace{\hspace{2cm}}$			$\underbrace{\hspace{4cm}}$		KE (\rightarrow non LTE)
$\underbrace{\hspace{4cm}}$				<	<< non CE
$\underbrace{\hspace{4cm}}$					non KE
$\underbrace{\hspace{2cm}}$			<<	<<	frozen chemistry
τ_{dil}^{-1}	τ_{acc}^{-1}		τ_{ch}^{-1}	τ_{ph}^{-1}	time scales
			$\tau_{\text{source}}^{-1}$		

and the corresponding required approximations for the applied chemical network. As a general finding it may be stated that in the region beyond the sonic point, where the wind expands at a supersonic velocity, in any case a non-KE approach should be applied whereas for the inner region depending whether ionizing or dissociating photons are present or not, a CE or KE description might be appropriate. In situations, where shock waves are propagating through the system, always a non-KE approach has to be applied, even near

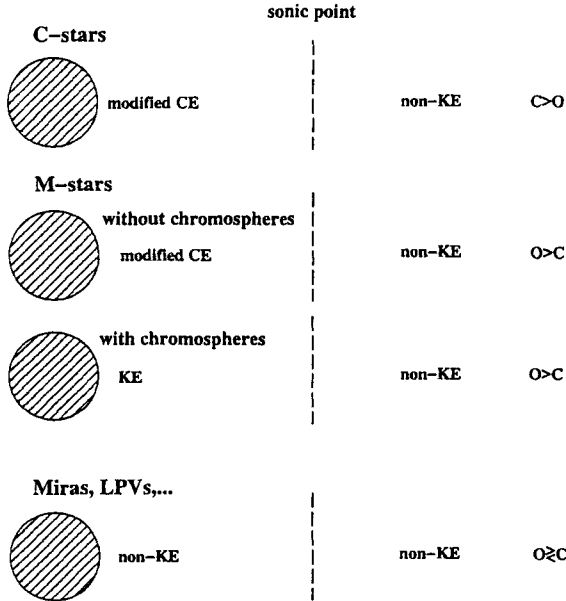


Fig. 9. Expected equilibrium situations with respect to the chemistry for different types of late-type stars

the stellar surface. The chemical network equations basically have the form of an equation of continuity i.e. the l.h.s. consists of a partial time derivative of the concentration of the considered species and a divergence term applied to the corresponding flux density. This system of rate equations usually is applied to a co-moving mass element where the rate equations simply reduce to a system of first order nonlinearly coupled ordinary differential equations. Due to the huge range in magnitude of the different time scales governing the various reactions contributing to the network, in most applications the rate network turns out to be a stiff system requiring especially designed codes for a stable and sufficiently accurate solution. Being of first order in time, any solution of the chemical network requires the prescription of a suitable initial condition for the species under consideration. For a stellar wind which due to its expansion can be considered as a basically monotonic situation usually an initial condition is chosen provided by the chemical composition at the base of the photosphere where the temperature is large enough for all molecules to be completely dissociated. In many cases it is also appropriate to start with the calculations at a layer being sufficiently dense for chemical equilibrium to hold.

In order to demonstrate the effects of a non-KE situation compared to a chemical equilibrium calculation, in Fig. 10 the radial course of important molecules is shown for the inner and outer region of a shell model for the

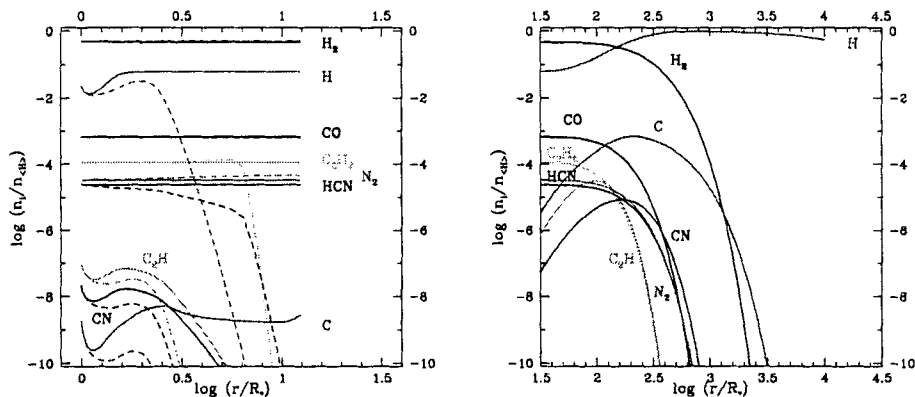


Fig. 10. Molecule concentrations in the inner region of a C-star shell (l.h.s. diagram, dashed lines are the equilibrium concentrations) and in the outer shell (r.h.s. diagram). From Patzer et al. (1996a)

prominent carbon-rich infrared object IRC +10216. One clearly sees that the non-LTE effect generally does not influence the key molecules (H_2 , CO , N_2) but obviously has a significant influence upon the reactive molecules (H , C_2H_2 , HCN , C_2H , C , CN). Thus, even in the inner region of this C-rich wind CE does not hold but, due to the rapid expansion in the acceleration region a frozen chemistry develops. The external regions of a shell are always affected by two important processes, both increasing a departure from CE: i) Because of the rapid dilution in the supersonic wind, most reactions freeze out at some non equilibrium value (i.e. the corresponding reaction rate becomes negligible) and ii) due to the strong, high energetic interstellar UV field dissociating and ionizing photo reactions begin to influence the circumstellar wind from outside causing a rapid drop of the molecule abundances and the corresponding atoms and ions to show up.

3.1.2 The Key Role of the CO Molecule

Due to its extremely high bond energy (11.09 eV), the CO molecule plays a most important role for the kind of chemistry to be expected in a circumstellar shell. Considering a mass element moving outwards along the expansion trajectory of the stellar wind, CO is the first molecule to be formed. As it can be dissociated only by very energetic photons, in the absence of dissociating UV fields, CO formation acts like an “absorber” removing C and O atoms from the surroundings until either all C atoms (for oxygen-rich situations) or all O atoms (for carbon-rich situations) are consumed (cf. Fig. 11). As the CO molecule is practically chemically inert, the chemistry of the system then is determined by the residual reactive specimens which in the case of oxygen-rich systems basically yields oxides whereas in the case of carbon-

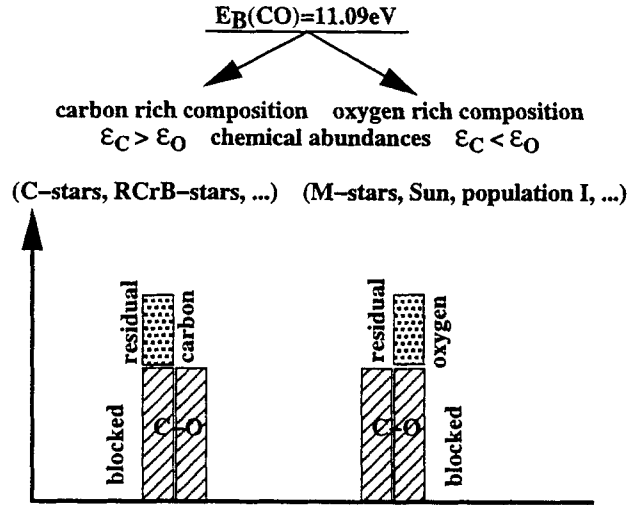


Fig. 11. Blockage by the CO molecule

rich systems predominantly carbon-hydrogen compounds, carbides and, if hydrogen is absent, other carbonaceous compounds are formed (cf. Table 3).

Detailed network calculations show that this key role of the CO molecule which is obvious for situations not too far from CE, generally also holds for most KE situations (Beck et al. 1992) yielding also for these systems a clear distinction of the character of the chemistry. Only for very pronounced UV fields e.g. in the late stages of a nova shell, also the CO molecule is ionized or dissociated by photo reactions, leading to a mixed oxygen-carbon chemistry in this case.

3.2 Dust Nucleation and Growth

3.2.1 Condensing Species

Astrophysical dust formation is a widespread phenomenon in particular observed in cool stellar outflows which are characteristic for red giants and supergiants. The detailed findings of corresponding observations demonstrate that circumstellar dust is a rather massive phenomenon being connected with substantial reddening of the stellar radiation field and hence indicating large optical depth produced by dust absorption and dust extinction. This clearly shows that the dust component is a major constituent of the circumstellar shells, the formation of which can not be explained by rare elements alone but in any case requires the contribution of the *abundant elements*.

Table 3. Molecules observed in the circumstellar shells of dust forming late type stars by microwave emission (e.g. Olofsson 1988)

Shells of M-stars	Shells of C-stars
H ₂ , CO	H ₂ , CO
OH, H ₂ O, SiO	hydrocarbons
CS, SiS, SO, SO ₂ , H ₂ S, OCS	CN, CS, SiC, SiC ₂ , SiS, HCO ⁺
HCO ⁺ , HCN, HNC, NH ₃	HCN, HNC, CH ₃ CN, HC ₃ N, HC ₅ N, HC ₇ N
	HC ₉ N, HC ₁₁ N, C ₂ H, C ₃ H, C ₄ H, C ₅ H, C ₆ H
	C ₃ H ₂ , C ₃ N, NH ₃ , C ₂ S, C ₃ S, HSiC ₂ , NaCl
	AlCl, KCl, AlF

Circumstellar dust often is observed at temperatures around 1000 K or even higher. In order for the dust grains to survive such hostile conditions, the dust material itself must form a so-called *high temperature condensate*, i.e. it has to consist of a substance which is able to form a macroscopic particle in this temperature range.

These two criteria which are a natural outcome of the observations, have to be supplemented by an additional argument concluded from the process of grain formation, which essentially proceeds via a sequence of chemical reactions. For this being efficiently possible, the molecules involved in the various steps have not to be blocked by exceptionally high bond energies making them inert. Applying these criteria (abundant species, high temperature condensates, not too high bond energies) to the hierarchy of element abundances observed in an astronomical system yields the results for the condensing species and the primary condensates shown in Fig. 12.

3.2.2 Grain Formation

Basically two philosophies of description are in use for describing the formation of macroscopic grains out of the gaseous phase having both its shortcomings and its individual strengths.

The first method is a thermodynamic point of view, conceiving the solid formation as kind of a phase transition taking place if the system trajectory crosses a borderline defined by specific critical conditions for the nucleation process, usually given by a suitably defined supersaturation ratio $S = 1$. A well-known example for this are the lines separating the various aggregation states in a phase diagram e.g. for water where a gaseous, liquid and solid phase may occur, which in a natural way explains the occurrence of mist, rain, and snowflakes.

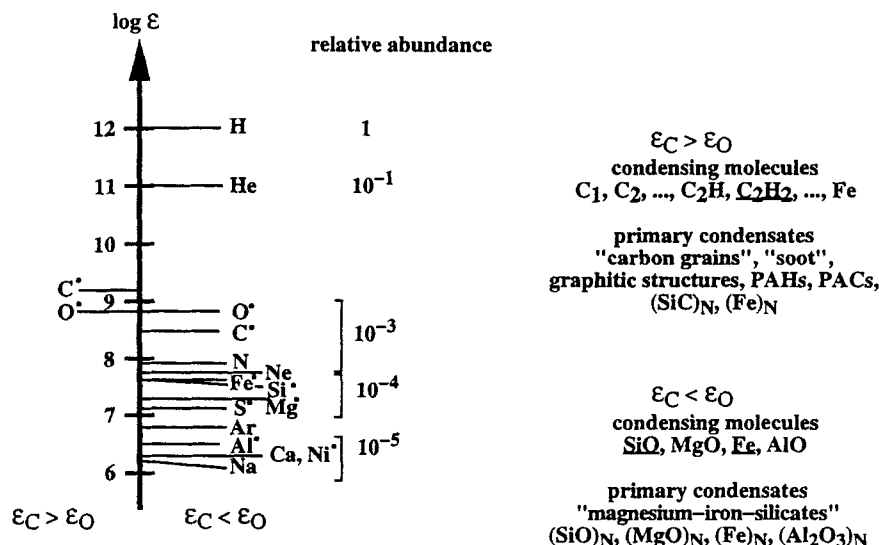


Fig. 12. Abundance hierarchy of the elements. * means, that this element is a constituent of high-temperature condensates. The leading molecules in the grain formation sequence are underlined

In all these situations for efficient dust formation to take place, a pronounced supersaturation ratio $S = p_i/p_{cl}$ (where p_i is the (gas) partial pressure of the condensing species i , and p_{cl} the corresponding vapor pressure of the considered cluster) considerably larger than unity has to be reached.

Applying this concept to circumstellar grain formation shows that effective grain condensation usually only occurs at temperatures far below the corresponding equilibrium lines thus indicating dust condensation to be a process which efficiently proceeds generally far from thermodynamical equilibrium, a finding being in total accordance with the general behavior of structure formation in nature.

The second method is a chemical point of view, conceiving cluster formation as the result of a sequence of chemical reactions, starting in a molecular domain and resulting finally at macroscopic specimens. From this microscopic point of view grain formation could be conceived naively as a complex network of *chemical reactions* leading under favorable conditions to more and more complex aggregates which finally grow to macroscopic particles. A realization of this method is however illusory not only due to the huge number of reactions involved ($10^6 - 10^{10}$) but also due to the lack of important input data (reaction efficiency, sticking coefficients), not to mention the unrealistic computing time required for such an approach. For this reason, any successful chemical approach is restricted to the construction of some suitable chemical pathway being determined by the most efficient chain of reactions leading

from molecules to macroscopic clusters. This approach requires of course

- the individual selection of the relevant molecules,
- a detailed determination of their thermodynamic functions and
- for each molecule the detailed discussion of its chemical reactions.

In order to select a certain pathway, it is essential that it contains all relevant reactions, i.e. that reactions along the pathway are much more important than reactions with other molecules. In this case the pathway is well isolated and the concentrations of the chain molecules are determined by chain processes only. For a detailed application of the chemical pathway method to the formation of polyaromatic hydrocarbons (PAHs) in C-star winds, see Fig. 14.

Irrespective of the specific treatment, the molecule–solid transition can be considered as a two step process which consists i) of the formation of small meta-stable clusters from gaseous molecules and ii) the growth of these clusters to macroscopic grains. This separation immediately follows from the thermodynamic properties of small clusters showing in the size–temperature space a critical limit line separating the regimes of dominant cluster evaporation and growth, respectively. This critical limit line defines the critical cluster by the equilibrium between evaporation and growth for given temperature. Any grain formation has to surmount the critical cluster size in order to arrive at thermodynamically stable macroscopic grains (see Fig. 13).

The regime with cluster sizes smaller than the critical cluster (i.e. where evaporation exceeds growth) is called the nucleation regime. In this regime, the properties of the clusters can not be described by simply applying bulk phase values but have to be determined by taking into account the individual structure of the clusters either from suitable calculations or from laboratory measurements (cf. Köhler et al. 1996, Patzer et al. 1995).

Detailed comparison of the time scales involved in the nucleation regime indicates that even in situations where moderate velocity fields are present usually the formation of the critical cluster i.e. the calculation of the nucleation rate, can be treated as a stationary problem (cf. Gail and Sedlmayr 1988, Gauger et al. 1990).

From (modified) classical nucleation theory in case of thermal and chemical equilibrium, the homogeneous nucleation rate J_* is given by

$$J_*(t) = \frac{f(1,t)}{\tau_{\text{gr}}(N_*,t)} Z(N_*) \exp \left[(N_* - 1) \ln S - \frac{\Delta G(N_*)}{RT} \right] \quad (2)$$

where $f(1,t)$ is the monomer density of the condensing species (e.g. the density of C_1 in the case of soot formation), $(\tau_{\text{gr}})^{-1}$ the growth time scale of the critical cluster, N_* the size of the critical cluster, Z the Zeldovich-factor (of order 1), S the supersaturation ratio and ΔG is in this notation the surface contribution to the Gibbs free energy change associated with the formation of the critical cluster from the vapor.

For homogeneous nucleation of monomers, $(\tau_{\text{gr}})^{-1}$ is simply given by the product of the monomer density and the rate coefficient for the reaction

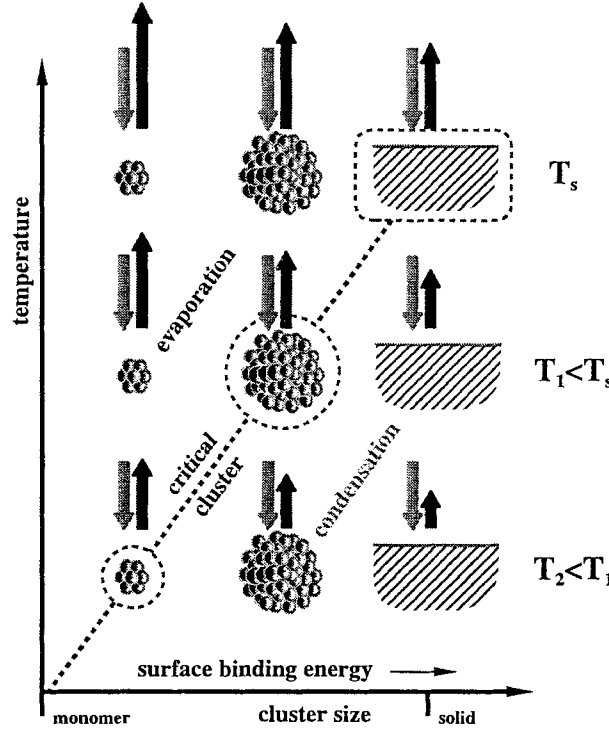


Fig. 13. Temperature dependence of the critical cluster size. T_s : sublimation temperature of the solid (adopted from Goeres et al. 1996)

between clusters of size N_* and the monomers. Gail and Sedlmayr (1988) generalized this approach to account for arbitrary chemical reactions. The influence of thermal and chemical non-equilibrium in the gas phase on the nucleation rate is discussed by Patzer et al. (1996b).

In the case of a chemical pathway approach the nucleation rate simply can be calculated by determining the rate of the slowest step on the most efficient pathway

$$J_* = \frac{f(N_*)}{\tau} \quad (3)$$

where $f(N_*)$ is the particle density of the critical cluster and τ is the characteristic formation time of clusters of size N_* from clusters of size $N_* - 1$.

Like in classical nucleation theory also in the pathway description the critical cluster determines a “bottleneck” separating the nucleation regime and the growth regime. This bottleneck has to be surmounted for effective grain growth to occur.

As an example of a chemical pathway, in Fig. 14 the formation of polyaromatic hydrocarbons (PAHs) is shown (Goeres 1993).

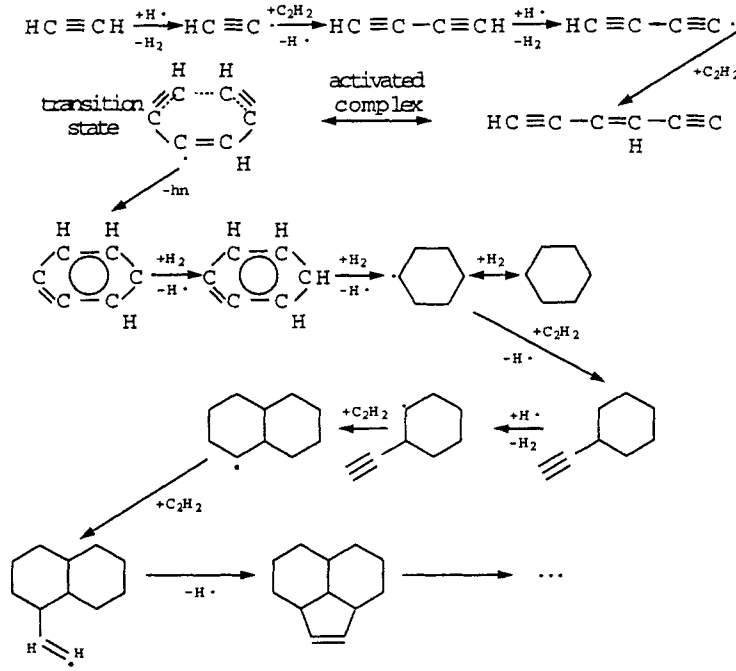


Fig. 14. Chemical pathway to PAH formation (adopted from Goeres 1993)

3.2.3 Grain Growth

Well beyond the critical cluster in all cases under consideration grain growth can reliably be treated by a thermodynamic approach. In this context the number densities of grains of size N are conceived as “level populations” which are changed by gain and loss processes:

$$\frac{df(x, N, t)}{dt} = R_{\uparrow} - R_{\downarrow} + R^{\downarrow} - R^{\uparrow} . \quad (4)$$

Figure 15 gives a schematic representation of the level diagram indicating gain and loss processes by transitions caused by the addition and the evaporation of molecules, respectively. Due to these processes, the actual local occupation density $f(x, N, t)$ of level N obeys an equation of continuity

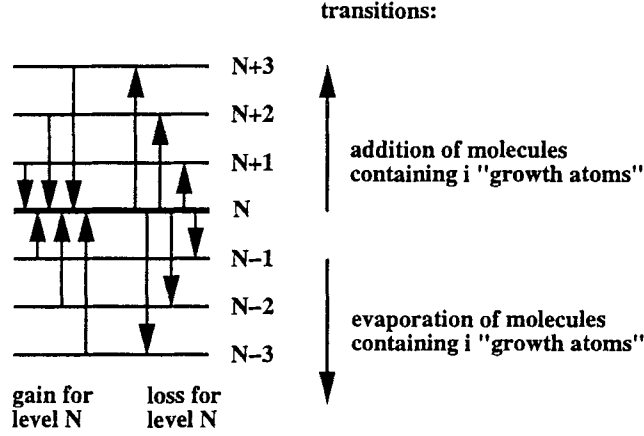


Fig. 15. Level representation of the cluster size space, possible transitions between the levels, and effective rates with respect to level N

$$\frac{df(x, N, t)}{dt} = \frac{\partial f(x, N, t)}{\partial t} + \text{div}(v f(x, N, t)) = \sum_{i=1}^I J_{N,i}(x, t) - \sum_{i=1}^I J_{N+i,i}(x, t) \quad (5)$$

with $\sum_{i=1}^I J_{N,i}$ being the net gain rate of level N from the levels below and I is the maximum i -mer changing the cluster size. The time derivative $d(\cdot)/dt = \partial(\cdot)/\partial t + \text{div}(v \cdot)$ on the l.h.s. comprises both the explicit change with time and the net gain due to surface fluxes via the mass flow of velocity v .

The rates $J_{N,i}$ are given by

$$J_{N,i}(x, t) = f(i) v_{N-i,i} A_{N-i} \alpha_{N-i,i} \left(f(N-i) - \frac{\overset{\circ}{f}(N-i)}{\overset{\circ}{f}(N)} f(N) \right) \quad (6)$$

where $f(i)$ is the density of the growth species, $v_{N-i,i}$ is the relative velocity between growth species i and a cluster of size $N-1$, A_{N-i} is the surface of a cluster with size $N-i$, $\alpha_{N-i,i}$ is the respective sticking efficiency, and $\overset{\circ}{f}(\cdot)$ denotes the respective distribution function in thermal equilibrium. In (6) LTE is assumed. More general expressions are discussed in Gail and Sedlmayr (1988), Gauger et al. (1990), and Patzer et al. (1996b).

In most astrophysical applications it is not necessary to solve the full network of rate equations (5) but it is sufficient to define suitable moments by summation over the cluster size space according to

$$K_j(x, t) = \sum_{N=N_\ell}^{N_{max}} N^{j/d} f(x, N, t) \quad (j = 0, 1, 2, \dots) \quad (7)$$

with d being the dimension of the considered clusters ($d = 3$ for 3-dimensional particles, $d = 2$ for 2-dimensional, e.g. flat particles) and N_ℓ is a lower limit size for the dust grains to be considered as macroscopic particles (usually $N_\ell \approx 1000$). Introducing these moments into (5) yields the system of moment equations describing grain growth in arbitrary moving media

$$\frac{dK_j}{dt} = \frac{j}{d} \frac{K_j}{\tau_{gr}} + N_\ell^{j/d} J_{N_\ell} \quad , \quad (8)$$

where the time scale for particle growth is given by

$$\frac{1}{\tau_{gr}} = \sum_{i=1}^I A_1 v_i \alpha_i i f(i) \quad . \quad (9)$$

A good approximation for this system, applicable to most astrophysical situations is given by

$$\frac{dK_j}{dt} = \begin{cases} J_* \quad , & j = 0, \\ \frac{j}{\tau_{gr} d} K_{j-1} \quad , & j > 0 \quad . \end{cases} \quad (10)$$

The first four moments have simple physical interpretations:

$$\begin{aligned} K_0 &= n_d = \text{dust number density} \\ \frac{K_1}{K_0} &= \langle N^{1/d} \rangle \propto \langle \text{size} \rangle \\ \frac{K_2}{K_0} &= \langle N^{2/d} \rangle \propto \langle \text{surface} \rangle \\ \frac{K_3}{K_0} &= \langle N^{3/d} \rangle \stackrel{d=3}{\propto} \langle \text{volume} \rangle \propto \text{extinction coefficient} \quad . \end{aligned}$$

3.2.4 Cluster Size Spectrum

In the case that grain evaporation can be neglected (e.g. in a stationary wind) the moment equation for $j = 0$

$$\frac{dK_0}{dt} = J_* \quad (11)$$

allows a straight-forward calculation of the grain size spectrum $f(N)$ (a complete treatment including the effects of grain evaporation is given in Gauger et al. 1990):

The growth of an individual grain of size N simply is given by:

$$\frac{dN}{dt} = \frac{1}{\tau_{\text{gr}}} N^{\frac{d-1}{d}} \quad (12)$$

from which we get

$$\frac{d(N^{1/d})}{dt} = \frac{1}{d \tau_{\text{gr}}} . \quad (13)$$

Defining the grain radius by $a = a_0 N^{1/d}$, where a_0 is the hypothetical radius of a monomer, we obtain for the time evolution of the particle size

$$\frac{da}{dt} = \frac{1}{\tau_{\text{gr}}} \frac{a_0}{d} . \quad (14)$$

Now assume that a cluster is created at time t_0 with size N_* . With this initial condition, (13) immediately can be integrated:

$$N(t, t_0) = \left\{ \frac{1}{d} \int_{t_0}^t dt' \frac{1}{\tau_{\text{gr}}(t')} + N_*^{1/d} \right\}^d . \quad (15)$$

$N(t, t_0)$ denotes the size of the particle at time t , which has formed with size N_* at time t_0 . Due to our assumption of monotonic growth, all particles smaller than $N(t, t_0)$ at time t must have been created later than t_0 . Thus, for the number of particles with sizes between N_* and $N(t, t_0)$ we obtain

$$\Delta K_0(N_*, N(t, t_0)) = \int_{t_0}^t dK_0 = \int_{N_*}^{N(t, t_0)} f(N, t) dN = \int_{t_0}^t J_*(t') dt' . \quad (16)$$

Differentiating (16) with respect to t_0 yields

$$J_*(t_0) = - \frac{d(N(t, t_0))}{dt_0} f(N(t, t_0), t) . \quad (17)$$

Solving this for the distribution function $f(t, N)$ yields

$$f(N(t, t_0), t) = \left(- \frac{d(N(t, t_0))}{dt_0} \right)^{-1} J_*(t_0) = \tau_{\text{gr}}(t_0) N(t, t_0)^{\frac{1-d}{d}} J_*(t_0) , \quad (18)$$

where the second equality follows from (15).

Thus, in an actual model calculation, one just has to integrate (12) along the flow trajectory (i.e. in each fixed volume element) and to store the current values of J_* and τ_{gr} in order to obtain the current size distribution in each gas element. As an example, Fig. 16 depicts the size distribution function resulting from a model calculation for a stationary dust driven wind (see Sect. 4.3).

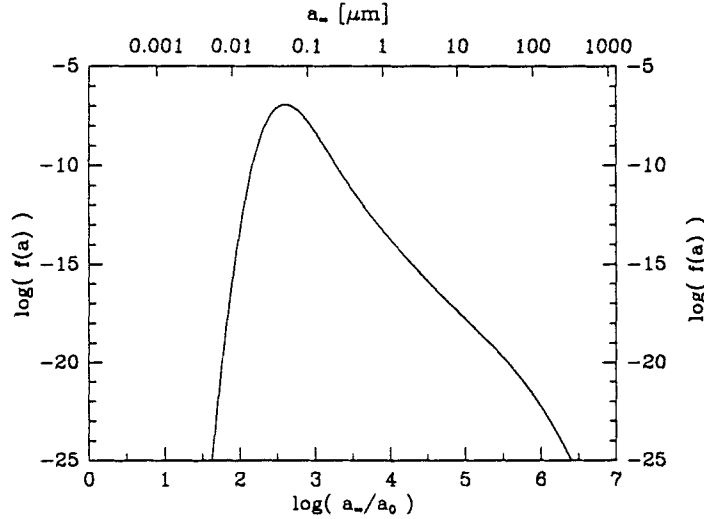


Fig. 16. Grain size distribution function in the outer region of a stationary dust driven wind model. a_∞ is the final particle size reached in an outer volume element, where grain nucleation and growth have ceased

For this calculation, the grains are assumed to consist of amorphous carbon and classical nucleation theory (cf. Sect. 3.2.2) has been applied to calculate the grain formation rate. The resulting size distribution function can well be approximated by a power law $f(a) \propto a^{-5}$ in the size range $0.05\mu\text{m} < a < 100\mu\text{m}$, a typical result for a stationary dust driven wind (see Dominik et al. 1989). Although most particles have radii of about $0.05\mu\text{m}$, there exists a considerable number of particles having much larger radii. These large particles are formed in the innermost region of the circumstellar dust shell (inside the sonic point), where the outflow velocity is still small and, therefore, the particles remain for a rather long time in a region of favorable growth conditions (for a detailed discussion see Dominik et al. 1989 and Winters et al. 1994a).

4 Modeling of Dust Shells Around Late-Type Giants

In this section we present the self-consistent description of cool, extended dust forming circumstellar shells, including a detailed treatment of

- hydrodynamics
- thermodynamics
- radiative transfer
- chemistry
- dust nucleation and growth.

The complete problem to be treated is sketched in Fig. 6. In the following we give the mathematical formulation of this problem and present typical numerical results for stationary dust driven winds and pulsating atmospheres around long-period variable stars. In both cases, spherical symmetry of the central star and its surrounding shell is assumed.

4.1 Basic Equations

4.1.1 Hydrodynamic Equations

From the law of mass conservation, the equation of continuity is given, which in spherical symmetry reads

$$\frac{\partial \rho}{\partial t} + \frac{1}{r^2} \frac{\partial}{\partial r} (r^2 \rho v) = 0 . \quad (19)$$

Here, t is the time, r is the radial coordinate, $\rho(r, t)$ is the mass density and $v(r, t)$ is the outflow velocity. In a **stationary situation** (i.e. $\partial/\partial t = 0$), (19) can be integrated to yield

$$\int_0^r dr' 4\pi r'^2 \left(\frac{1}{r'^2} \frac{\partial}{\partial r'} (r'^2 \rho v) \right) = 4\pi r^2 \rho v = \text{const} = \dot{M} , \quad (20)$$

where \dot{M} is the integration constant, describing the total mass transport through the surface of radius r . Thus, \dot{M} is the mass loss rate of the star. In general, the value of the mass loss rate depends on the fundamental stellar parameters: stellar mass M_* , stellar luminosity L_* , stellar temperature T_* , and the element abundances $\{\epsilon_i\}$.

Momentum conservation provides us with the equation of motion:

$$\frac{\partial v}{\partial t} + v \frac{\partial v}{\partial r} = -\frac{1}{\rho} \frac{\partial p}{\partial r} + a \quad (21)$$

with $p(r, t)$: thermal pressure and $a(r, t)$: acceleration due to *external* forces.

For the conditions typical of a circumstellar shell, the equation of state, relating thermal pressure, mass density, and gas temperature, is given by the ideal gas law

$$p = \frac{\rho}{\bar{\mu} m_{\text{H}}} kT \quad (22)$$

with $\bar{\mu}(r, t)$: mean molecular weight, $T(r, t)$: gas kinetic temperature, and m_{H} : mass of a hydrogen atom.

The acceleration $a(r, t)$ usually consists of the contribution of two different external forces

$$a = -g + a_{\text{rad}} \quad (23)$$

with the local (inwards directed) gravitational acceleration

$$g = G \frac{M_* + M_s(r, t)}{r^2} \quad (24)$$

caused by the stellar mass M_* and the mass contained in the circumstellar shell inside the radial surface at r

$$M_s(r, t) = \int_{R_*}^r dr' 4\pi r'^2 \rho(r', t) \quad (25)$$

and the (outward directed) radiative acceleration $a_{\text{rad}}(r, t)$ of the matter due to photon momentum extinction. In practice, (23) is usually written as

$$a = -g(1 - \alpha) \quad (26)$$

with

$$\alpha(r, t) = \frac{a_{\text{rad}}}{g} = \frac{4\pi}{cGM_*} \frac{\chi_H}{\rho} r^2 H \quad (27)$$

being the radiative acceleration measured in units of the local gravitational acceleration. The quantity H is the frequency integrated Eddington flux

$$H = \int_0^\infty d\nu H_\nu \quad (28)$$

and χ_H the flux-mean extinction coefficient

$$\chi_H = \frac{1}{H} \int_0^\infty d\nu \chi_\nu H_\nu . \quad (29)$$

The extinction coefficient

$$\chi_\nu = \kappa_\nu + s_\nu \quad (30)$$

is the sum of the absorption coefficient κ_ν and the scattering coefficient s_ν . Both, κ_ν and s_ν consist of all respective contributions from the gaseous species and the various dust components.

The absorption and scattering cross sections of a dust grain is huge compared to those of an atom or molecule. Therefore, if a noticeable amount of dust is present in a stellar atmosphere, it completely dominates the transport coefficients.

The transport coefficients of the dust components depend on the local size distribution of the grains:

$$\chi_\nu^{\text{d}} = \int_{a_{\text{t}}}^\infty da f(a) \sigma_{\text{ext}}^{\text{d}}(\nu, a) \quad (31)$$

$$s_\nu^{\text{d}} = \int_{a_{\text{t}}}^\infty da f(a) \sigma_{\text{sca}}^{\text{d}}(\nu, a) \quad (32)$$

$$\kappa_\nu^{\text{d}} = \chi_\nu^{\text{d}} - s_\nu^{\text{d}} = \int_{a_{\text{t}}}^\infty da f(a) \sigma_{\text{abs}}^{\text{d}}(\nu, a) . \quad (33)$$

The cross sections σ_{ν}^d usually are expressed as the product of the geometric cross section πa^2 of the particle (assumed here to be spherical with radius a) and an efficiency Q describing the interaction with the radiation field. These efficiency factors follow from Mie theory (see e.g. Bohren and Huffman 1983) and the size distribution function $f(a)$ is calculated according to the method given in Sect. 3.2.4.

For grains small compared to the wavelength of the radiation field (i.e. $a \ll \lambda/2\pi$) the *small particle limit* of Mie theory applies and the transport coefficients can be written as

$$\chi_{\nu}^d = A(\nu) \int da a^3 f(a) = A(\nu) \hat{K}_3 \quad (34)$$

$$s_{\nu}^d = B(\nu) \int da a^6 f(a) = B(\nu) \hat{K}_6 \quad (35)$$

while in the opposite case of the *large particle limit* of Mie theory (i.e. $a \gg \lambda/2\pi$)

$$\kappa_{\nu}^d = s_{\nu}^d = \int da \pi a^2 f(a) = \pi \hat{K}_2 = \frac{1}{2} \chi_{\nu}^d \quad (36)$$

holds. The “radius” moments

$$\hat{K}_j = \int da a^j f(a) \quad (37)$$

are related to the moments K_j defined in Sect. 3.2.3 via

$$\hat{K}_j = a_0^j K_j \quad j=0, 1, 2, \dots \quad (38)$$

where a_0 is the hypothetical radius of a monomer contained in a grain.

In a stationary situation, it is convenient to transform the equation of motion (21) into the so-called *wind equation*. This is accomplished by introducing the isothermal sound speed

$$c_T^2 = \frac{p}{\rho} \quad (39)$$

and making use of the equation of continuity (19) (where of course $\partial\rho/\partial t = 0$!). The result is

$$(v^2 - c_T^2) \frac{1}{v} \frac{\partial v}{\partial r} = \frac{2}{r} c_T^2 - \frac{\partial c_T^2}{\partial r} - g(1 - \alpha) \quad (40)$$

with the *critical point* r_c defined by the (implicit) conditions

$$v(r_c) = c_T(r_c) \quad (41)$$

and

$$\frac{2}{r_c} c_T^2(r_c) - \frac{\partial c_T^2}{\partial r} \Big|_{r_c} - g(r_c)(1 - \alpha(r_c)) = \phi(r_c) = 0 \quad (42)$$

(see also the lecture of H. Lamers, this Volume). If we neglect the temperature variation in (42), r_c is determined by the implicit equation

$$\alpha(r_c) = 1 - 4 \frac{r_c}{R_*} \left(\frac{c_T(r_c)}{v_e(R_*)} \right)^2 \quad (43)$$

with the escape velocity at the stellar surface

$$v_e = [2R_*g(R_*)]^{1/2} . \quad (44)$$

Self-consistent model calculations indicate, that for a dust driven wind the second term in (43) is always small compared to unity (thermally stable atmosphere!), i.e.

$$\alpha(r_c) \approx 1 \quad (45)$$

is a necessary condition for a dust driven wind to exist.

4.1.2 Thermodynamic Equations

The law of energy conservation provides us with an equation for the temperature of the gas and the dust. The balance equation for the *thermal* energy is given by

$$\frac{\partial(\rho e)}{\partial t} + \frac{1}{r^2} \frac{\partial}{\partial r} (r^2 \rho v h) - v \frac{\partial p}{\partial r} = Q_e , \quad (46)$$

where e is the specific energy and $h = e + p/\rho$ the specific enthalpy with $h = c_p T$ for an ideal gas. c_p is the specific heat for constant pressure and Q_e the local net energy input rate per unit volume due to external energy sources.

In the stationary case, (46) can be written as

$$v \left(\rho c_p \frac{\partial T}{\partial r} - \frac{\partial p}{\partial r} \right) = Q_e \quad (47)$$

where (20) has been used.

In a stationary dust driven wind radiative equilibrium holds (i.e. $Q_e = 0$), and the source term in (47) can be written as

$$Q_e = \Gamma_e - \Lambda_e = 0 = \int_0^\infty d\nu (\kappa_\nu^g + \kappa_\nu^d) J_\nu - \int_0^\infty d\nu (\epsilon_\nu^g + \epsilon_\nu^d) \quad (48)$$

where the gain and loss rates (Γ_e and Λ_e) are given by the absorption and emission of radiation energy. In writing (48), elastic scattering of the photons is assumed. J_ν is the monochromatic mean intensity of the radiation field (cf. (51)) and ϵ_ν is the emission coefficient (g and d refer to the gas and the

dust component, respectively). In many cases the dust component decouples thermally from the gas and the energy balance for the dust alone is given by

$$\int_0^\infty d\nu \kappa_\nu^d J_\nu = \int_0^\infty d\nu \epsilon_\nu^d = \int_0^\infty d\nu \kappa_\nu^d B_\nu(T^d) \quad (49)$$

where $B_\nu(T^d)$ is the Kirchhoff–Planck function at the internal dust temperature T^d . Equations (48) and (49) are an implicit system for the “gas temperature” $T(r)$ and the “dust temperature” $T^d(r)$.

4.1.3 Radiative Transfer

For the situations considered here, it is sufficient to consider the stationary radiative transfer equation (i.e. $\partial I_\nu / \partial t = 0$), since the transport coefficients vary on a time scale which is longer than the time needed for the photons to travel through the region where these changes occur. In the case of isotropic absorption, scattering and emission, the stationary radiative transfer equation in spherical symmetry is given by

$$\mu \frac{\partial I_\nu(r, \mu)}{\partial r} + \frac{1 - \mu^2}{r} \frac{\partial I_\nu(r, \mu)}{\partial \mu} = -(\kappa_\nu + s_\nu) I_\nu(r, \mu) + \epsilon_\nu + s_\nu J_\nu(r) \quad (50)$$

with the angle variable $\mu = \cos \theta$, where θ is the angle between the radial vector and the direction of light propagation, and the monochromatic mean intensity defined by

$$J_\nu(r) = \frac{1}{2} \int_{-1}^{+1} d\mu I_\nu(r, \mu) . \quad (51)$$

For given transport coefficients, the partial integro–differential equation (50) has to be solved numerically for the specific monochromatic intensity $I_\nu(r, \mu)$. This can be accomplished e.g. by the Feautrier method, which involves an iteration between the solution of (50) along the characteristic paths and the equations for the moments of $I_\nu(r, \mu)$ defined by

$$M_\nu^n(r) = \frac{1}{2} \int_{-1}^{+1} d\mu \mu^n I_\nu(r, \mu) \quad (52)$$

(for details see the standard textbook by Mihalas 1978).

4.1.4 Chemistry

In general, the number densities of the molecules are given by the solution of the chemical rate network (1) (see Sect. 3.1). In the special situation of chemical equilibrium, the rate network is replaced by the law of mass action which, if completed by the conservation of the elements reads

$$n_{<i>} - \sum_{j=1}^N \nu_i \nu_j n_i n_j K_{\text{eq}}(i, j) = 0 , \quad (53)$$

where ν_k are the stoichiometry coefficients and K_{eq} is the equilibrium constant.

4.1.5 Dust Formation and Growth

As discussed in Sect. 3.2, formation and growth of dust grains is described by the set of moment equations

$$\begin{aligned}\frac{dK_0}{dt} &= J_* \\ \frac{dK_j}{dt} &= \frac{j}{d\tau_{\text{gr}}} K_{j-1}\end{aligned}\quad (54)$$

which by consumption of the dust forming elements is coupled to the chemistry. In the simple case of homomolecular, homogeneous condensation of carbon, the consumption equation is given by

$$\frac{dn_{<C>}}{dt} = -\frac{dK_3}{dt} . \quad (55)$$

The chemistry and dust complex are solved considering a fixed mass element, i.e. in a co-moving frame (remember: $d \cdot / dt = \partial \cdot / \partial t + \text{div}(\cdot v)$)

The fundamental equations given in this section form the complete set necessary for the modeling of dust forming circumstellar shells. Of course, this set has to be solved by applying suitable boundary conditions, and in the case of a time-dependent description, also suitable initial conditions.

4.2 External Parameters

The self-consistent solution of this set of equations (i.e. the shell model) is completely determined by the prescription of 4 fundamental stellar parameters, e.g. the sets given in Table 4.

Table 4. Examples for different combinations of parameters describing a dust driven wind

M_*	or	M_*	or	M_*	or	\dot{M}	etc.
T_*		M		R_*		T_*	
L_*		L_*		L_*		L_*	
$\{\dots, \epsilon_i \dots\}$		$\{\dots, \epsilon_i \dots\}$		$\{\dots, \epsilon_i \dots\}$		$\{\dots, \epsilon_i \dots\}$	

Depending on the specific problem a suitable set of basic parameters is chosen. Besides these 4 prescribed parameters all other quantities are determined by the solution of the set of fundamental equations. Results of this

approach applied to stationary dust driven winds are given in Sect. 4.3. For the time-dependent modeling of circumstellar dust shells around pulsating long-period variable stars, assumed to exhibit a sinusoidal temporal variation inside the photosphere, two additional parameters have to be prescribed in order to simulate the pulsation of the star. This is necessary, since the current models only describe the circumstellar dust shell (CDS) but not the region well inside the photosphere, where the pulsation of the star is generated. Results of these time-dependent model calculations are presented in Sect. 4.4.

4.3 Stationary Dust Driven Winds

4.3.1 The Minimum Mass Loss Rate

In a dust driven wind, the only driving mechanism of the outflow is radiation pressure on the dust grains which is transferred to the ambient gas by momentum coupling between dust and gas. Other effects, like momentum and energy input to the atmosphere by wave dissipation are neglected. Therefore, we can derive a minimum luminosity or, equivalently, a minimum mass loss rate which has to be surmounted in order for a dust driven wind to exist (cf. Gail and Sedlmayr 1987, Dominik et al. 1990). From the definition of the radiative acceleration (27) we get

$$\begin{aligned}\alpha &= \frac{4\pi}{cGM_*} \frac{\chi_H}{\rho} r^2 H \\ &= \frac{4\pi}{cGM_*} \frac{\chi_H}{\rho} R_*^2 H_* \\ &= \frac{\chi_H}{4\pi cG\rho M_*} L_*\end{aligned}\tag{56}$$

where the condition of radiative equilibrium

$$r^2 H(r) = \text{const} = R_*^2 H_*\tag{57}$$

and the definition of the stellar luminosity

$$L_* = 16\pi^2 R_*^2 H_*\tag{58}$$

have been used. If dust is present, the extinction coefficient χ_H is essentially given by the dust component (i.e. $\chi_H \approx \chi_H^d$) which is proportional to the local amount of dust, i.e. the degree of condensation f_c :

$$f_c = \frac{K_3}{K_3^{\max}} = \frac{\chi_H}{\chi_H^{\max}}.\tag{59}$$

Inserting (59) into (56) yields

$$\alpha = f_c \frac{\chi_H^{\max}}{4\pi c G \rho M_*} L_* \quad (60)$$

$$= f_c \frac{L_*}{L_{\text{edd}}} \quad (61)$$

where we have defined the so-called Eddington luminosity

$$L_{\text{edd}} = \frac{4\pi c G \rho M_*}{\chi_H^{\max}} \quad (62)$$

which is the maximum luminosity for an atmosphere stable against radiation induced expansion (cf. (26): $\alpha = 1 \leftrightarrow a = 0$!).

According to (45) a dust driven wind requires

$$\alpha(r_c) = f_c(r_c) \frac{L_*}{L_{\text{edd}}} \geq 1 . \quad (63)$$

Thus, for a given value of f_c we get the desired minimum luminosity required to drive the wind solely by radiation pressure:

$$L_*^{\min} = \frac{L_{\text{edd}}}{f_c(r_c)} . \quad (64)$$

The r.h.s. of (64) is essentially determined by M_* and \dot{M} . Since \dot{M} is a function of the stellar parameters ($\dot{M} = f(L_*, T_*, M_*, \{\dots, \epsilon_i, \dots\})$), for given stellar mass M_* and element abundances $\{\dots, \epsilon_i, \dots\}$ a contour line

$$\dot{M}^{\min} = f(L_*^{\min}, T_*) \quad (65)$$

of minimum mass loss rate exists in the HRD, which confines objects producing dust driven winds to the region above this limiting line, i.e. to the region of high luminosities. This minimum mass loss rate typically is of the order of $10^{-7} \dots 10^{-6} M_{\odot} \text{yr}^{-1}$.

4.3.2 Typical Shell Structure of a Dust Driven Wind

Figure 17 shows the radial structure of a dust driven wind model designed to describe the observational data of the prototype of extreme carbon stars IRC +10216 (Winters et al. 1994a).

The formation of dust grains starts around $1.4R_0$ ($R_0 = 9.25 \cdot 10^{13} \text{cm}$), which leads to a steep increase of the dust extinction χ_H and, therefore, of the radiative force accelerating the dust grains. By momentum coupling of the grains to the surrounding gas, the momentum gained by the dust particles is transferred to the gas. This process results in an outward directed net acceleration ($\alpha > 1$ for $r > 2.25R_0$) of the grain-gas mixture leading to an increasing outflow velocity v of the material. The transition from sub-sonic to supersonic motion occurs at $r = r_c = 2.2R_0$ where α reaches a value of

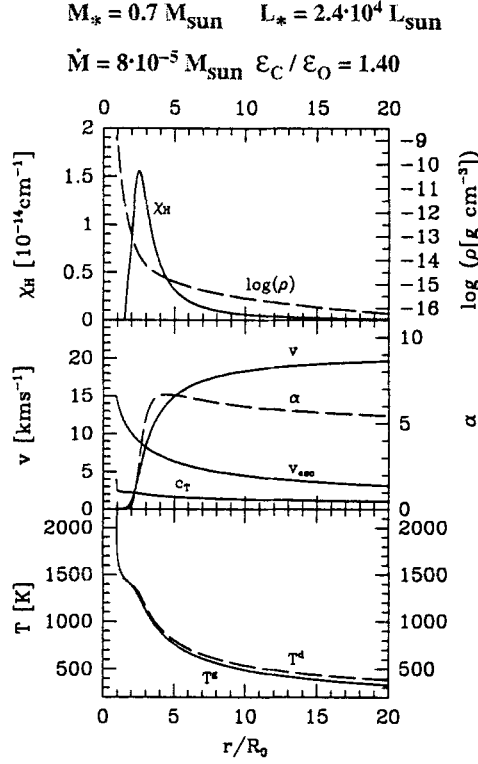


Fig. 17. Radial structure of a stationary dust driven wind model for IRC +10216. **Upper diagram:** flux-mean extinction coefficient χ_H of the dust component (solid line, l.h.s. ordinate) and logarithm of the density ρ (dashed line, r.h.s. ordinate); **middle diagram:** hydrodynamic velocity v and velocity of sound c_T (solid line, l.h.s. ordinate) and radiative acceleration in units of the local gravitational deceleration α (dashed line, r.h.s. ordinate); **lower diagram:** temperature of the gas (solid line) and the dust component (dashed line) (adopted from Winters et al. 1994a)

0.75. Around $3R_0$ the wind velocity exceeds the local escape velocity v_{esc} . The atmospheric material, therefore, is lifted out of the stellar gravitational field within the first two stellar radii above the photosphere. The final outflow velocity of 20.7 km s^{-1} is nearly reached at $20R_0$.

The essential acceleration of the material occurs in the region between $2R_0$ and $5R_0$. In the region of effective dust formation and growth (around $r = 2.5R_0$) the gas temperature is $T^g \approx 1300 \text{ K}$, while the mass density in this region is about $10^{-14} \text{ g cm}^{-3}$. Thermal dust emission from the inner edge of the circumstellar shell heats the gas inside the dust formation zone. The dust opacity, thus, leads to a substantial backwarming which results in an al-

most constant temperature throughout the region of effective dust formation. The size-independent dust temperature T^d (cf. (49)) exceeds the (grey) gas temperature. The temperature difference produced by this greenhouse effect increases with increasing distance from the photosphere. The temperature difference between gas and dust reaches a maximum value of about 50K in this model.

IRC +10216

$$M_* = 0.7 M_{\text{sun}} \quad L_* = 2.4 \cdot 10^4 L_{\text{sun}}$$

$$\dot{M} = 8 \cdot 10^{-5} M_{\text{sun}} \quad \epsilon_C / \epsilon_O = 1.40$$

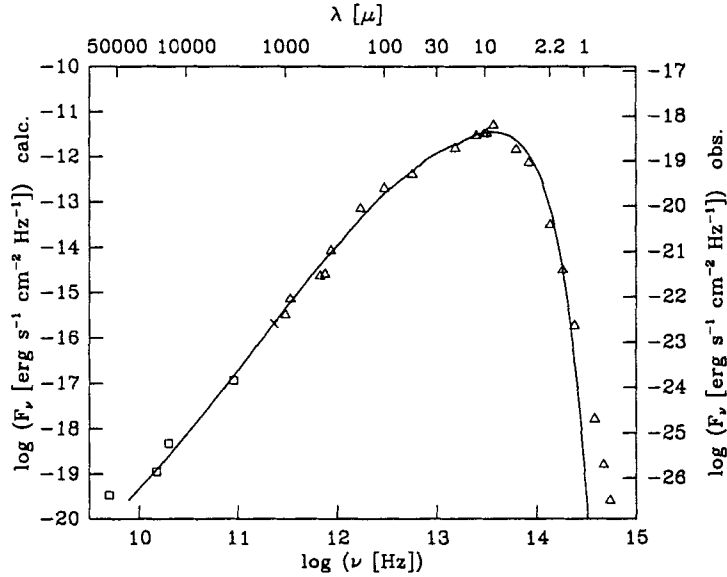


Fig. 18. Emergent spectrum of the dust shell model described in the text (solid line). The observed data for IRC +10216 are taken from Le Bertre 1987 and references therein (Δ), Sahai et al. 1989 (\square) and Walmsley et al. 1991 (\times)

In Fig. 18 the spectral energy distribution produced by the dust shell model is shown together with observed photometric data of IRC +10216. This source is known to be variable with a period of ~ 640 d (Witteborn et al. 1980; Ridgway and Keady 1988). The symbols shown in Figs. 18 represent fluxes measured near the maximum of the $2.2\mu\text{m}$ light curve. The calculated spectrum results from assuming amorphous carbon described by

the complex refractive index tabulated in Maron (1990). The outer boundary of the dust shell model is located at $2 \cdot 10^3 R_0$ which corresponds to a distance from the center of the star of $1.85 \cdot 10^{17} \text{cm}$. The synthetic spectrum of this model is in close agreement with the observed spectrum of IRC +10216 in the wavelength region between $2\mu\text{m}$ and 5cm . In the near infrared region short-ward of $\lambda \approx 2\mu\text{m}$ the calculated spectrum decreases much too steeply as compared to the observed fluxes. This behavior may be due to the existence of rather large dust particles in the inner part of the dust shell model, which is a result of the assumption of stationarity. A second, probably more important reason could be our assumption of spherical geometry, which cannot account for possible ‘holes’ in the dust shell, which would produce smaller optical depths along certain lines of sight in direction to the central object. In consequence, short wavelength radiation originating from the photosphere could escape through such holes and thus could lead to an emergent short wavelength flux which is possibly considerably enhanced compared to the flux resulting from a spherically symmetric model. From the absolute values of the calculated and observed fluxes we derive a distance to IRC +10216 of $d = 170\text{pc}$.

4.3.3 Dependence of the Models on the Stellar Parameters

Generally, the stationary dust driven wind represents the solution of a fully coupled non-linear problem which results in a rather intricate dependence of the models on the individual stellar parameters. In the following, we describe the qualitative dependence of important shell characteristics on the parameters chosen (M_* , L_* , \dot{M} , ϵ_C/ϵ_O , the other elements (including oxygen) are assumed to have solar abundances). In the following, \uparrow means increasing, \downarrow means decreasing. (An explicit description of these dependences is given in Winters et al. 1994a.)

stellar mass M_* :

For realistic values, M_* has only a minor influence on the model structure and the shell spectrum. However, for each given luminosity L_* , there exists a maximum mass $M_{*,\text{max}}$ above which no dust driven wind exists.

$M_* \uparrow \rightarrow v_\infty \downarrow \rightarrow \text{grain growth} \uparrow \rightarrow f_c \uparrow \rightarrow \chi_H^{\text{max}} \uparrow \rightarrow (\text{absorption} \uparrow \text{ and } T_* \downarrow) \rightarrow$
“cooling” of the spectrum

$M_* \uparrow \rightarrow (\alpha \propto 1/M_*) \downarrow$ (almost linear, cf. (27))

stellar luminosity L_* :

$L_* \uparrow \rightarrow \alpha \uparrow$ (cf. (56)) $\rightarrow v \uparrow$ (inside the sonic point) $\rightarrow \text{dilution} \uparrow \rightarrow \text{collision rate} \downarrow \rightarrow \text{effective growth} \downarrow \rightarrow (\text{grain size, } f_c) \downarrow \rightarrow \chi_H \downarrow \rightarrow \alpha_\infty \propto L_*(\chi_H/\rho)$
nearly unchanged and v_∞ nearly unchanged

$L_* \uparrow \rightarrow \dots \rightarrow \chi_H \downarrow (\kappa_H \downarrow) \rightarrow \tau \downarrow \rightarrow \text{shell more transparent}$

$L_* \uparrow \rightarrow T_* \uparrow$, together with the above \rightarrow “hotter” spectrum

Mass loss rate \dot{M} :

$\dot{M} \uparrow \rightarrow \rho \uparrow \rightarrow \text{collision rate} \uparrow \rightarrow \text{growth} \uparrow \rightarrow \text{grain size} \uparrow \rightarrow f_c \uparrow \rightarrow \chi_H, \kappa_H \uparrow \rightarrow \alpha(r > \text{sonic point}) \uparrow \rightarrow v_\infty \uparrow$
 $\dot{M} \uparrow \rightarrow \dots \rightarrow \chi_H, \kappa_H \uparrow \rightarrow \text{shell spectrum becomes "cooler"}$

Carbon abundance ϵ_C .

$\epsilon_C \uparrow \rightarrow (\epsilon_C - \epsilon_O) \uparrow \rightarrow (n_C = K_3^{\max} = (\epsilon_C - \epsilon_O)n_{<H>}) \uparrow \text{ and } J_*^{\max} \uparrow$
 $\rightarrow f_c \uparrow \rightarrow \chi_H \uparrow \rightarrow \alpha \uparrow \rightarrow v \uparrow \rightarrow \text{dilution} \uparrow \rightarrow \text{collision rate in co-moving element} \downarrow \rightarrow \text{growth} \downarrow \rightarrow \text{grain size} \downarrow$
¹result: $v_\infty = A(T_*, L_*) \frac{\epsilon_C - \epsilon_O}{\epsilon_O}$
hence: $\epsilon_C \uparrow \rightarrow \kappa_{\lambda \text{short}}^d \uparrow \rightarrow (\text{NIR and visible light}) \downarrow \text{ and simultaneously } \epsilon_{\lambda \text{long}}^d \uparrow \rightarrow (\text{FIR emission}) \uparrow$.

In the preceding section, we have chosen the quadruple $M_*, L_*, \dot{M}, \{\dots \epsilon_i, \dots\}$ as the set of parameters. Choosing the set $M_*, L_*, T_*, \{\dots \epsilon_i, \dots\}$ allows a direct investigation of the dependence of the mass loss rate on the classical stellar parameters. The result is, that the mass loss rate of a dust driven wind increases with increasing stellar luminosity, decreasing stellar temperature and decreasing stellar mass. Since the AGB evolution leads to increasing luminosities and (slightly) decreasing temperature, the mass loss rate strongly increases along the AGB evolution of a star. The mass loss process is self-accelerating: due to mass loss, the mass of the star decreases which leads to a further increase of the mass loss rate! The model calculations allow to derive a theoretical mass loss formula for dust driven winds:

$$\dot{M}[M_\odot \text{yr}^{-1}] = 10^{-3.7-0.93M_*/M_\odot} \cdot \left(\log\left(\frac{L_*}{L_\odot}\right) - \frac{T_*}{600\text{K}} \right)^{2.59M_*/M_\odot + 1.71} \quad (66)$$

(see Dominik et al. 1990). For more details about dust driven winds we refer to the review by Sedlmayr and Dominik (1995).

4.4 Dynamical Models for Dust Forming Shells Around Long-Period Variables

Although the stationary models are very successful for explaining the overall structure and appearance of dust forming AGB star shells and also clearly demonstrate that dust driving alone is capable of explaining the observed high mass loss rates and low outflow velocities of these objects, they of course neglect the effects introduced by the pulsation of the central stars. That these effects might be important can be inferred from several facts: i) We have seen that a purely dust driven wind is only possible for objects having luminosities higher than the Eddington luminosity defined by (62). Observations indicate that AGB stars with lower luminosities also produce massive, low velocity outflows. ii) Due to their evolutionary state, stars evolving along the AGB are unstable against pulsation, i.e. most objects on the AGB generally are

long-period variable stars. iii) There exists a clear correlation between the infrared excess (measuring the amount of dust) and the variability of the object (Jura 1986, see Fig. 19).

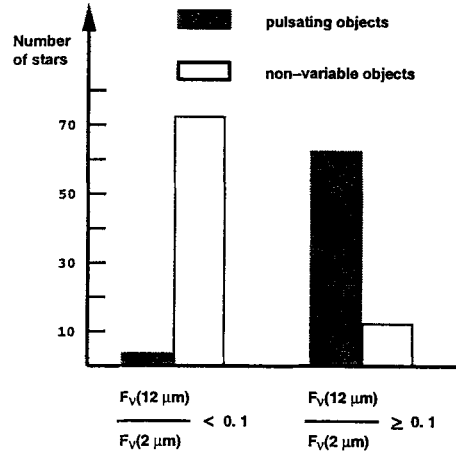


Fig. 19. Observed correlation between infrared excess and variability (after Jura 1986)

The momentum and energy input to the atmosphere by dissipation of shock waves (generated by the pulsation of the star) alone is not able to drive an outflow with the observed properties (e.g. Wood 1979). Therefore, a two step mechanism has been proposed as being responsible for the mass loss of LPVs (Jones et al. 1981): i) levitation of the atmosphere by dissipation of shock waves and ii) subsequent acceleration of the material by radiation pressure on dust. The first consistent models for dust forming shells around LPVs have been presented by Fleischer et al. (1992). These models include a consistent, simultaneous treatment of time-dependent hydrodynamics, (equilibrium) chemistry, dust formation, growth and evaporation and of the (grey) radiative transfer problem. Since in these models only the outer regions of the star (starting inside the photosphere) are modeled, the pulsation of the star itself has to be simulated by a suitable (inner) boundary condition. This boundary condition is provided by a so-called piston approximation: The velocity at the innermost grid point is assumed to vary sinusoidally with prescribed period P and velocity amplitude Δu . Therefore, these models are described by a set of six parameters, comprising the four fundamental stellar parameters M_* , L_* , T_* , $\{\dots, \epsilon_i, \dots\}$ and the parameters describing the stellar pulsation P , Δu . The equations are written in Lagrangian coordinates and the calculation is started with an initially hydrostatic dust free atmosphere as initial condition (details are given in Fleischer et al. 1992).

4.4.1 Radial Shell Structure of a Time-dependent Model

Figure 20 shows the radial shell structure for a model calculation with the parameters $M_* = 1M_\odot$, $L_* = 10^4 L_\odot$, $T_* = 2600$ K, $\epsilon_C = 1.80\epsilon_\odot$ (solar abundances for the other elements), $P = 650$ d, $\Delta u = 2 \text{ km s}^{-1}$ at a fixed instant of time. (This model is henceforth called Model A).

The following quantities are plotted: **upper diagram:** the velocity v (solid line), velocity of sound c_T (dotted line) and the temperature T (dashed line), **middle diagram:** the logarithm of the density ρ (solid line) and the degree of condensation f_c , i.e. the fraction of condensible material actually condensed into grains (dashed line) (cf. (59)), **lower diagram:** the logarithm of the nucleation rate per H-atom J_*/n_{H} , i.e. the number of dust grains formed per second and H-atom (solid line) and the logarithm of the number of dust grains per H-atom n_d/n_{H} (dashed line). Radii are always given in units of the stellar radius R_0 of the initial hydrostatic model.

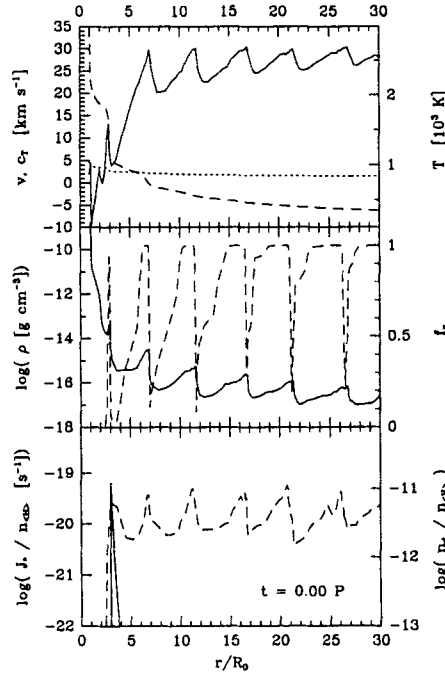


Fig. 20. Radial structure of consistent model for a pulsating, dust forming circumstellar shell

The consistent calculation of dust formation, grain growth and evaporation shows up to have significant influence on the resulting dynamic structure of the CDS.

As the degree of condensation and the number of dust grains per H-atom in Fig. 20 show, the dust is distributed inhomogeneously across the shell. The dust grains are concentrated in distinct layers and exhibit a shell or onion-like structure which is closely related to the hydrodynamic structure, e.g. the velocity profile of the CDS.

Figure 20 also shows the determining influence of the dust on the thermodynamic structure of the CDS. There are several steps in the course of the temperature which coincide with spikes in the degree of condensation.

The discrete structure of the atmosphere is not produced solely by the shock waves caused by the interior pulsation of the star, but is a very product of the process of dust formation. In a first step the interior pulsation defines the onset of dust *formation* by providing appropriate low temperatures in the region between 3 and $4R_0$. In a second step pulsation triggers grain *growth* by a compression of the material in this radius interval and, thus, provides the high densities favorable for the growth process. In a short time interval values of f_c as high as 1 are reached, i.e. all of the condensible material is actually condensed into grains. The radiative acceleration α is directly proportional to the degree of condensation f_c (cf. (60)). Since the grains are closely momentum coupled to the gas, the sudden increase of the radiative acceleration causes a perturbation in the velocity field which steepens to become a shock wave, thereby compresses the material and, in turn, accelerates dust growth. Thus, the prominent shock waves which propagate through the atmosphere (cf. upper diagram of Fig. 20) are produced by a self-accelerating mechanism caused by the interaction between dust formation and hydrodynamics.

Furthermore, the newly formed dust in the inner shells, due to its opacity, effectively blocks the outgoing radiation and heats the material located closer to the star. This backwarming, seen as steps in the temperature structure in the upper diagram of Fig. 20, also influences the formation of new dust particles. Caused by the enhanced temperature inside the innermost dust layer, the formation of new particles is confined to a rather narrow spatial region as can be seen from the course of the nucleation rate J_* (lower diagram of Fig. 20).

Due to pulsation and backwarming, dust formation and growth is only possible in a small radius range and during a limited time interval. This results in the discrete structure of the CDS. The complex interplay among the processes of dust formation and growth, hydrodynamics and thermodynamics shows that the dust particles play the key role in determining the atmospheric structure of LPVs and Miras.

4.4.2 Temporal Behavior of the Models

The model described in the preceding section (Model A) forms a new dust layer every piston period P . There are, however, also models, which produce new dust layers on a longer time scale, depending on the values chosen for the model parameters. This time scale is in particular sensitive to the amount

of dust formed, i.e. to the carbon abundance ϵ_C : the lower the carbon abundance, the longer the time interval between the formation of two successive dust layers becomes. Therefore, the formation of a new dust shell can take place *every* hydrodynamic period (as in Model A), but also every second, third ... pulsational period, i.e. the radial structure of the CDS at a certain instant of time $t = \beta P$ equals the structure at $t = (\beta + n_P)P$, where β is an arbitrary dimensionless time parameter and $n_P = 1, 2, \dots$ is the *multi-periodicity* number. (In general, n_P is not an integer number!) The formation of dust layers on time scales different from the pulsation period of the star leads to observable consequences e.g. for the light curves of these objects. As an example, Fig. 21 shows the light curves for Model A and a model calculated for the parameters $M_* = 1M_\odot$, $L_* = 3 \cdot 10^4 L_\odot$, $T_* = 2450$ K, $\epsilon_C = 1.25\epsilon_\odot$ (solar abundances for the other elements), $P = 621$ d, $\Delta u = 3 \text{ km s}^{-1}$ (Model B).

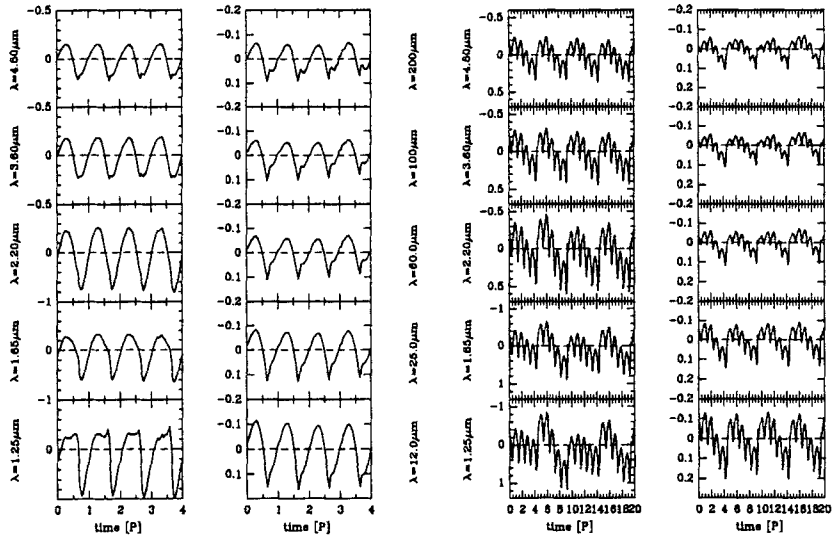


Fig. 21. Theoretical light curves (in magnitudes, relative to the mean magnitude) of Model A (l.h.s. diagrams) and Model B (r.h.s. diagrams) at different wavelengths. Note the different scaling of the ordinate at different wavelengths

From the periodic occurrence of the different intermediate structures in Model A (l.h.s. diagram) at short wavelengths $\lambda < 2.2\mu\text{m}$ and at long wavelengths $\lambda > 2.2\mu\text{m}$ it can be inferred that the formation of a new dust layer periodically takes place during every second half of each hydrodynamic cycle. The light curves at wavelengths $\lambda > 2.2\mu\text{m}$ show a slightly asymmetric shape and exhibit an internal structure on the rising branch which regularly oc-

curs and is even more pronounced towards longer wavelengths. All curves are characterized by a periodic re-occurrence of all features at the same phase during the sequence of hydrodynamic pulsation cycles.

In contrast to Model A, Model B exhibits a different behavior. Model B shows a quasi-sinusoidal variation on the time scale of one pulsational period which is superposed by a long-scale oscillation on a time scale of 5 pulsation periods. In principle, the process of the formation of a new dust layer is the same in Models A and B. The difference is the time scale: The formation of a fully evolved new dust layer takes a time interval of five pulsational cycles in Model B, compared to one pulsational cycle for Model A.

A behavior similar to that produced by Models A and B has also been found in the observed light curves of real objects, e.g. for the carbon-rich objects AFGL 1085 and R For (Le Bertre 1992).

The characteristic feature of the AFGL 1085 light curves is the occurrence of intermediate extrema, already noted by Le Bertre (1992). With respect to the model calculations, these intermediate structures could be caused by the sudden formation of a new dust layer similar to Model A.

The light curves of R For show a systematic drift in magnitude very similar to the multiperiodic Model B. Secondary variations with periods multiple times longer than the main period have also been found in the light curves of several other objects by Alksnis (1990). In terms of the model calculations, this behavior could be explained by the interplay of two distinct processes with different time scales: The regular pulsation of the star, which provides the "short" hydrodynamic time scale, and the process of dust formation and growth, which, under the conditions of Model B, has a time scale five times longer. Thus, the CDS can be conceived as a dynamic system under the influence of an external excitation mechanism, or, to use a simple analogy from classical mechanics, the CDS behaves similar to a pendulum, which is subject to a periodic external force.

Irrespective of the different long-term behavior of the light curves resulting from both individual models and also independent of the different shape-variations with wavelength of the light curves of each individual model, the light amplitude decreases with increasing wavelength (cf. Fig. 21). This behavior also seems to be a general property of the real LPVs and has been noticed for many objects (see e.g. Le Bertre 1992). In the synthetic light curves this wavelength dependence of the amplitude is largely due to the redistribution of radiative energy from short wavelengths to long wavelengths caused by the dust grains: The energy absorbed in the accessible rather narrow short wavelength portion of the stellar radiation field is redistributed by thermal dust emission over the broad infrared spectral range.

The presence of discrete dust layers in the models also causes rippled or even step-like structures in the radial brightness profiles as well as in the theoretical visibilities, which result from these calculations (see Winters et al. 1995). Similar structures have been observed e.g. for IRC +10216 by Ridgway

and Keady (1988). Therefore, the discrete structure of the dust shell may provide an explanation for both the occurrence of intermediate structures in the light curves as well as the pronounced structures in observed brightness distributions. A more detailed discussion of the observable consequences of the time-dependent model calculations can be found in Winters et al. (1994b, 1995, 1996).

5 Conclusions

We have presented the ingredients required to describe consistently the circumstellar dust shells of Red Giant stars evolving along the AGB in the HRD. An application of these considerations to the self consistent description of stationary dust driven wind situations shows that radiation pressure on dust grains alone is capable of driving a massive, low velocity outflow with the characteristic properties observed for these objects. However, this stationary wind mechanism is restricted to those objects having very high luminosities. The theoretical spectra produced by the dust shell models are in good agreement with the observations of cool carbon-rich AGB objects.

The assumption of stationarity results in the formation of rather large dust grains in the circumstellar shell. As the real dust forming objects are mostly pulsating variables, the formation of very large grains is prevented by the limitation of the time available for grain growth due to significant periodic changes of the hydrodynamic and thermodynamic conditions in the dust forming region.

Therefore, we also have presented respective consistent time-dependent model calculations, which reveal a complex interplay among the processes of dust formation and growth, hydrodynamics and thermodynamics leading to a discrete shell-like distribution of dust across the circumstellar shell. The periodic formation of these dust layers decisively influences the short-scale behavior as well as the long-term course of the light curves. The dust component plays the key role in producing features, such as intermediate extrema and secondary periods, which similarly occur in observed light curves. The layered dust distribution also causes significant time-dependent structures in the surface brightness distributions and in the synthetic visibility functions, which also are in agreement with the respective observations.

This behavior is only revealed by a consistent treatment of the complete coupled system consisting of chemistry, dust formation, hydrodynamics, thermodynamics, and radiative transfer.

Acknowledgments

We thank Dr. Cécile Loup for providing us with her tables of the CO/HCN observations in computer readable form. This work was supported by the BMBF (grant 05 3BT13A 6).

References

- Alksnis, A. (1990): in *From Miras to Planetary Nebulae: Which Path for Stellar Evolution?*, p.279–285, eds. Mennessier M., Omont A. Editions Frontières, Gif sur Yvette Cedex
- Beck, H. K. B., Gail, H.-P., Henkel, R., Sedlmayr, E. (1992): *A&A* **265**, 626–642
- Bohren, C. F., Huffman, D. R. (1983): *Absorption and Scattering of Light by Small Particles*, John Wiley & Sons, New York
- Danchi, W. C., Bester, M., Degiacomi, C. G., Greenhill, L. J., Townes, C. H. (1994): *AJ* **107**, 1469–1513
- De Jager, C., Nieuwenhuijzen, H., Van der Hucht, K. A. (1988): *A&AS* **72**, 259–289
- Dominik, C., Gail, H.-P., Sedlmayr, E. (1989): *A&A* **223**, 227–236
- Dominik, C., Gail, H.-P., Sedlmayr, E., Winters, J. M. (1990): *A&A* **240**, 365–375
- Fleischer, A. J., Gauger, A., Sedlmayr, E. (1992): *A&A* **266**, 321–339
- Gail, H.-P., Sedlmayr, E. (1987): *A&A* **177**, 186–192
- Gail, H.-P., Sedlmayr, E. (1988): *A&A* **206**, 153–168
- Gauger, A., Gail, H.-P., Sedlmayr, E. (1990): *A&A* **235**, 345–361
- Goeres, A. (1993): *Rev. Mod. Astron.* **6**, 165–177
- Goeres, A., Henkel, R., Sedlmayr, E., Gail, H.-P. (1988): *Rev. Mod. Astron.* **1**, 231–248
- Goeres, A., Keller, R., Sedlmayr, E., Gail, H.-P. (1996): *Polycyclic Aromatic Compounds* **8**, 129–165
- Gustafsson, B. (1989): *ARA&A* **27**, 701–756
- Holzer, T. E., MacGregor, K. B. (1985): in *Mass Loss from red giants*, p.229–255, eds. Morris M., Zuckerman B. D. Reidel Pub. Com.
- Jones, T. W., Ney, E. P., Stein, W. A. (1981): *ApJ* **250**, 324–326
- Jørgensen, U. G. (1994): *IAU Colloquium 146: Molecules in the Stellar Environment*, Springer Verlag, Berlin
- Jørgensen, U. G., Johnson, H. R. (1992): *A&A* **265**, 168–176
- Jura, M. (1986): *Ir. Astron. J.* **17**, 322–330
- Keady, J. J., Ridgway, S. T. (1993): *ApJ* **406**, 199–214
- Knapp, G. R., Morris, M. (1985): *ApJ* **292**, 640–669
- Köhler, T. M., Gail, H.-P., Sedlmayr, E. (1996): *A&A*, in press
- Le Bertre, T. (1987): *A&A* **176**, 107–113
- Le Bertre, T. (1992): *A&AS* **94**, 377–398
- Loup, C., Forveille, T., Omont, A., Paul, J. F. (1993): *A&AS* **99**, 291–377
- Maron, N. (1990): *Ap&SS* **172**, 21–28
- Mihalas, D. (1978): *Stellar Atmospheres*, W. H. Freeman and Company, San Francisco, 2nd edition
- Olofsson, H. (1988): *Space Sci. Rev.* **47**, 145–174
- Patzner, A. B. C., Köhler, T., Sedlmayr, E. (1995): *Planet. & Sp. Sci.* **43**, 1233–1239
- Patzner, A. B. C., Winters, J. M., Sedlmayr, E. (1996a): in *IAU Symp. 177: The Carbon Star Phenomenon*, ed. Wing R. F. Kluwer Academic Publishers, Dordrecht
- Patzner, A. B. C., Gauger, A., Sedlmayr, E. (1996b): *A&A*, submitted
- Ridgway, S. T., Keady, J. J. (1988): *ApJ* **326**, 843–858
- Sahai, R., Claussen, M. J., Masson, C. R. (1989): *A&A* **220**, 92–98
- Sedlmayr, E., Dominik, C. (1995): *Space Sci. Rev.* **73**, 211–272

- Sedlmayr, E., Winters, J. M. (1991): in *Stellar Atmospheres: Beyond Classical Models*, p.397–408, eds. Crivellari L., Hubeny I., Hummer D. G. Kluwer Academic Publishers, Dordrecht
- Tsuji, T. (1986): ARA&A **24**, 89–125
- Walmsley, C. M., Chini, R., Kreysa, E., et al. (1991): A&A **248**, 555–562
- Winters, J. M., Dominik, C., Sedlmayr, E. (1994a): A&A **288**, 255–272
- Winters, J. M., Fleischer, A. J., Gauger, A., Sedlmayr, E. (1994b): A&A **290**, 623–633
- Winters, J. M., Fleischer, A. J., Gauger, A., Sedlmayr, E. (1995): A&A **302**, 483–496
- Winters, J. M., Fleischer, A. J., Le Bertre, T., Sedlmayr, E. (1996): A&A, submitted
- Witteborn, F. C., Strecker, D. W., Erickson, E. F., et al. (1980): ApJ **238**, 577–584
- Wood, P. R. (1979): ApJ **227**, 220–231

Cool Stars Winds and Mass Loss: Observations

Thibaut Le Bertre

DEMIRM, Observatoire de Paris, 61 av. de l'Observatoire,
F-75014 Paris, France
e-mail: LEBERTRE@mesioa.obspm.fr

Abstract. Observational evidences for mass loss from cool stars are reviewed. The emphasis is put on Asymptotic Giant Branch stars which contribute to $\sim 50\%$ of the replenishment of the Interstellar Medium. The aim is to illustrate the richness of the informations provided by the observations obtained in the various wavelength ranges from the optical to the radio. A selection of on-going developments which are potentially important for this theme is presented.

1 Introduction

Cool stars are sometimes surrounded by an expanding circumstellar shell of gas and dust. Most of these mass-losing objects are on the Asymptotic Giant Branch (AGB) of the HR diagram, but some are red supergiants.

Mass loss is important for stellar evolution. For instance, stars of initial mass larger than $1.4 M_{\odot}$, and up to $6-8 M_{\odot}$, will avoid becoming supernovae by losing up to 80% of their initial mass. When nuclear burning stops, and after a spectacular Planetary Nebula phase, their remnants will simply cool down and evolve as white dwarfs of typically $0.6-0.8 M_{\odot}$.

Furthermore, through mass loss, AGB stars contribute to the replenishment of the interstellar medium. Most of the carbon in the Universe is produced in their interiors and a large fraction of the interstellar dust originates in their atmospheres. Mass loss from AGB stars is thus an important factor of the galactic evolution.

For many fields of Astrophysics, it is a necessity to understand the processes of mass loss in these stars and the physics in their circumstellar envelopes. The aim of this lecture is to provide an introduction to the observational study of winds from late-type stars with emphasis on those from AGB stars. Interested readers will find more informations in reviews and conference proceedings. A recent review on "Circumstellar envelopes and AGB stars" can be found in Habing (1996); it is mainly dedicated to oxygen-rich stars. A review on carbon stars was presented by Jura (1992). Conference proceedings are useful to get specific informations on the most recent developments and on works in progress; see for instance Mennessier and Omont (1990). An I.A.U. symposium on "The carbon star phenomenon" (n° 177) was held this year (1996) in Antalya. Other valuable references can be found in Habing (1996, Sect. 1.9).

2 Presentation of AGB Stars

2.1 The Evolution Towards the AGB

Thanks to elaborate codes, the evolution of a star can be numerically simulated in function of its initial mass (or mass on the Zero Age Main Sequence, ZAMS) and of its composition in helium and heavier elements. The physics is complex and sometimes has to be treated with phenomenological parameters (see the lecture by De Greve, this Volume). Depending on the values given to these parameters, the results may differ. However, the general lines of stellar evolution can be reproduced and are now basically understood (Iben and Renzini 1983; see also the pedagogical review of Iben 1985).

On the Main Sequence (MS), stars burn quietly hydrogen in their cores. When hydrogen begins to lack in the core, the star adapts its structure to allow for hydrogen burning around the core. It leaves the MS and, in an HR diagram, moves to the right and reaches the Red Giant Branch (RGB). For stars with a low mass ($\leq 2 M_{\odot}$), the electron gas is degenerated in the hydrogen-exhausted core so that the energy transport is very effective. For these stars the mass of the core on the RGB will increase up to $\sim 0.4 M_{\odot}$ and the luminosity, up to $\sim 2000 L_{\odot}$. At this stage, helium is ignited suddenly at the center (He core flash) and the electron-degeneracy is subsequently lifted. The luminosity drops ($L \leq 50 L_{\odot}$) and, thereafter, helium burns quiescently: the star sets on the Horizontal Branch (HB) of the HR diagram.

More massive stars follow the same kind of evolution after the MS, except that, as their central temperature is higher, they do not develop an electron-degenerate helium-core. They generally reach a lower luminosity on the RGB. However, after helium ignition they set on the HB at a higher luminosity ($L \geq 50 L_{\odot}$).

At this stage (HB), all stars burn helium quietly through the triple- α reaction which produces ^{12}C : $3\ ^4\text{He} \rightarrow\ ^{12}\text{C}$ (^8Be is not stable), and eventually ^{16}O by the capture of another ^4He nucleus. When helium is exhausted in the central parts, the star adapts again its structure so that now a shell where helium is burning surrounds a core containing carbon, oxygen and heavier elements.

For stars with low and intermediate mass ($M \leq 6\text{--}8 M_{\odot}$), the electron gas in this CO core is degenerated. The luminosity increases and the star arrives on the Asymptotic Giant Branch (AGB). The name Asymptotic Giant Branch comes from the fact that, in HR diagrams of globular clusters, the 2 Giant Branches are merging asymptotically.

Stars more massive than $6\text{--}8 M_{\odot}$ do not develop an electron-degenerate CO core. Nuclear fusion proceeds in the core with the synthesis of silicon and heavier elements. They evolve to the right of the HR diagram at almost constant luminosity and pass through a red supergiant (RSG) stage (at least those with a ZAMS mass less than $\sim 40 M_{\odot}$). Their luminosities range from $\sim 2 \cdot 10^4 L_{\odot}$ to $\sim 2 \cdot 10^5 L_{\odot}$. When they are in the RSG stage, they may occupy

a region which overlaps with the region of the HR diagram occupied by AGB stars and can be mistaken. These stars differentiate from AGB stars only by their internal structure.

Finally, objects of $\sim 60 M_{\odot}$ or more evolve in Luminous Blue Variables (LBVs) and probably never reach the region of stars with cool surfaces. They are supposed to be progenitors of Wolf-Rayets (WRs).

The following section will concern only low and intermediate mass stars ($M \leq 6-8 M_{\odot}$).

2.2 The Life on the AGB and Beyond

The AGB is divided into 2 parts: the Early AGB (E-AGB) and the Thermally Pulsing AGB (TP-AGB). On the E-AGB, stars are burning helium quiescently around a CO-core which increases in size with the products of helium combustion (^{12}C and ^{16}O).

When helium is exhausted the star enters a new phase of the AGB (TP-AGB). The combustion of hydrogen starts again in a shell around the core. A new helium layer is formed. Then, He is re-ignited and its rate of combustion increases until the occurrence of a thermonuclear runaway (He shell flash or He thermal pulse). The hydrogen burning layer is pushed outwards and cools; hydrogen combustion stops. The helium burning layer expands and cools also. A new phase of quiet helium burning develops that will last until helium-exhaustion. Then a new cycle starts again. A few tens of such cycles are expected to occur during the TP-AGB phase. For $\sim 10\%$ of the time, He-burning dominates and for the remaining 90%, H-burning. Within a cycle, the typical timescales are 10^4 years for the He-burning phase and 10^5 years for the H-burning phase; the exact durations depend on many parameters (core mass, number of the cycle, abundances, etc.). A thermal pulse lasts for ~ 100 years. During the thermal pulses, many neutrons are produced through reactions like $^{13}\text{C}(\alpha, n)^{16}\text{O}$ or $^{22}\text{Ne}(\alpha, n)^{25}\text{Mg}$. These are used in the production of neutron-rich isotopes such as zirconium (Zr). These isotopes are called s-elements (for slow process elements, by opposition to r-elements, or rapid process elements, which are formed in Nova or Supernova explosions). The elements are building up through neutron capture by nuclei heavier than Fe. For the formation of s-elements, the flux of neutrons is such that the seed nuclei are stable with respect to β -decay.

Therefore, the structure of a star on the AGB is that of a core where hydrogen and helium are exhausted, surrounded by a layer where these 2 elements are burning alternately. The size of the CO core is typically $\sim 10^8$ cm and the temperature, $2-4 \cdot 10^8$ K. Above the nuclear burning shell, there is a convective envelope of several 10^{13} cm radius (Fig. 1).

During the periods of hydrogen burning, the average luminosity of an AGB star is given by an empirical relation due to Paczynski:

$$L \approx 6 \times 10^4 L_{\odot} \times (M_{\text{core}}/M_{\odot} - 0.5).$$

On the AGB, the mass of the CO-core grows typically from $\sim 0.6 M_{\odot}$ to

$\sim 0.8 M_{\odot}$. The expected average luminosity of a star on the TP-AGB is thus in the range $5 \cdot 10^3$ – $2 \cdot 10^4 L_{\odot}$. Whatsoever, the CO core does not grow beyond the Chandrasekhar limit ($1.4 M_{\odot}$), so that, in any cases, the average luminosity of an AGB star is always expected to be below $\sim 5 \cdot 10^4 L_{\odot}$.

An important feature of the AGB is the phenomenon of dredge-up. After a He thermal-pulse, the base of the convective stellar envelope moves inward and reaches the zone where, during the pulse, carbon was synthesized. This element, together with other recently processed elements (e.g. the neutron-rich isotopes), can be brought to the surface. In such case, the photosphere exhibits overabundances of these elements. In that respect the C/O abundance ratio is of great importance. For RGB stars and stars on the E-AGB, it is expected to be ~ 0.5 . The photospheres of these stars have an effective temperature in the range 2000–3000 K. Their spectra are characterized by the presence of CO and oxygen-rich molecules such as TiO, VO or H₂O. They are said to be of M type. As long as the C/O ratio is smaller than 1, the star is said to be oxygen-rich. But with the arrival of s-elements at the surface new metal oxides, such as ZrO or YO, are formed; the stars in which the corresponding bands are detected are classified as of S type. The spectra of S stars are also characterized by lines of Technetium (Tc), an unstable s-element with half-lifetime $\leq 2 \cdot 10^5$ years. If the dredge-up is efficient enough, or after several thermal pulses, the C/O ratio may become larger than 1. The spectra of these carbon-rich stars (C type) are dominated by CO and carbon-rich molecules such as C₂, CN, HCN, C₂H₂, etc. Carbon stars show also the presence of s-elements in their spectra (Little et al. 1987).

It is worth noting that RSG stars do not experience dredge-up of carbon. Except in the case of mass-transfer across a binary star, the enhancement of carbon and of s-elements at the surface of a star is an unambiguous evidence that it is on (or has gone through) the TP-AGB.

Another important feature is the instability of the stellar atmosphere due to hydrogen opacity effects (κ mechanism, cf. De Greve, this Volume). AGB stars are generally variable and may pulsate as long-period variables ($P \geq 100$ days). The pulsations are not always periodic. The lightcurves are of various kinds. The classification which is commonly used is based on visual observations obtained through the last ~ 100 years (Kholopov et al. 1985).

- The **Mira** variables have a relatively well-defined period, although their lightcurves are not reproducible from cycle to cycle. The periods are found in the range 100–1000 days and the amplitudes in the visual are larger than 2.5 mag. The prototype and eponymous representative of this class is *o*Ceti (Mira Ceti).

- The **Semi-Regular** variables (SR type) are periodic but sometimes without a well-defined period. The amplitudes of the lightcurves are smaller than 2.5 mag. One makes the distinction between SRa and SRb. For the first subclass, SRa, the period is well-defined, but the shape of the lightcurve shows strong variations. For the second one, SRb, the periodicity is very poorly

defined, with strong variations on the duration of each cycle.

- The **irregular** variables (Lb type) are those for which there is no evidence of periodicity.

This classification is somewhat artificial, but has proven to be of some use. The distinction between Miras and SRa variables is probably unjustified, the SRa differing from the Miras only by the smaller amplitude of their lightcurves. Similarly, the separation between SRb and Lb variables is somewhat arbitrary and often dependent on the sampling of the observations.

The stellar atmosphere instability seems to be the cause of a third important feature (which is the topic of this lecture): mass loss. In the upper part of the atmosphere which is extended by its instability, refractory elements such as C or Si condense into dust particles. Once formed these particles are submitted to radiation pressure and are accelerated outwards, dragging the gas with them. It is by this mechanism (which is treated in detail by Sedlmayr and Winters, this Volume) that AGB stars surround themselves with an expanding circumstellar shell of dust and gas (Fig. 1).

Mass loss rates of typically 10^{-8} – $10^{-7} M_{\odot} \text{ yr}^{-1}$ are commonly observed, but they may reach values of several $10^{-5} M_{\odot} \text{ yr}^{-1}$. The mass loss phenomenon will culminate with the ejection of almost the complete atmosphere. The remaining atmosphere contracts and the star moves rapidly to the left of the HR diagram at almost constant luminosity. The surface temperature grows to several 10^5 K. For a short time (a few 10^4 years), the remnant will ionize the surrounding expanding shell (which at this stage is called a Planetary Nebula, PN) and then, after dispersion of the PN, cools to become a white dwarf on a timescale of a few 10^9 years.

An important effect of mass loss for the stellar evolution of AGB stars is to limit the growth of the CO core. It will never reach the Chandrasekhar limit for a stable nuclear-fuel-exhausted core ($1.4 M_{\odot}$). It is because of mass loss that intermediate mass stars evolve into white dwarfs through the PN phase instead of terminating their life in a Supernova explosion.

3 Evidence for Mass Loss in the Optical Range

3.1 Spectroscopy

By observing the companion of a mass-losing star in a binary system, one may detect absorption lines which reveal the presence of the wind. In fact, the first detection of a large-scale circumstellar wind around a late-type star was done in this way by Deutsch (1956). He observed stationary absorption lines (NaI, CaI, CaII, FeI) in the spectrum of the spectroscopic binary α^2 Her (G5III + A3V?) due to the envelope of α^1 Her (M5Ib-II)¹. He evaluated the mass loss rate to $\sim 3 \cdot 10^{-8} M_{\odot} \text{ yr}^{-1}$. As the distance on the sky of the 2 stars is

¹ Although, it has been classified spectroscopically as a supergiant, its luminosity places it on the AGB (Reimers 1977)

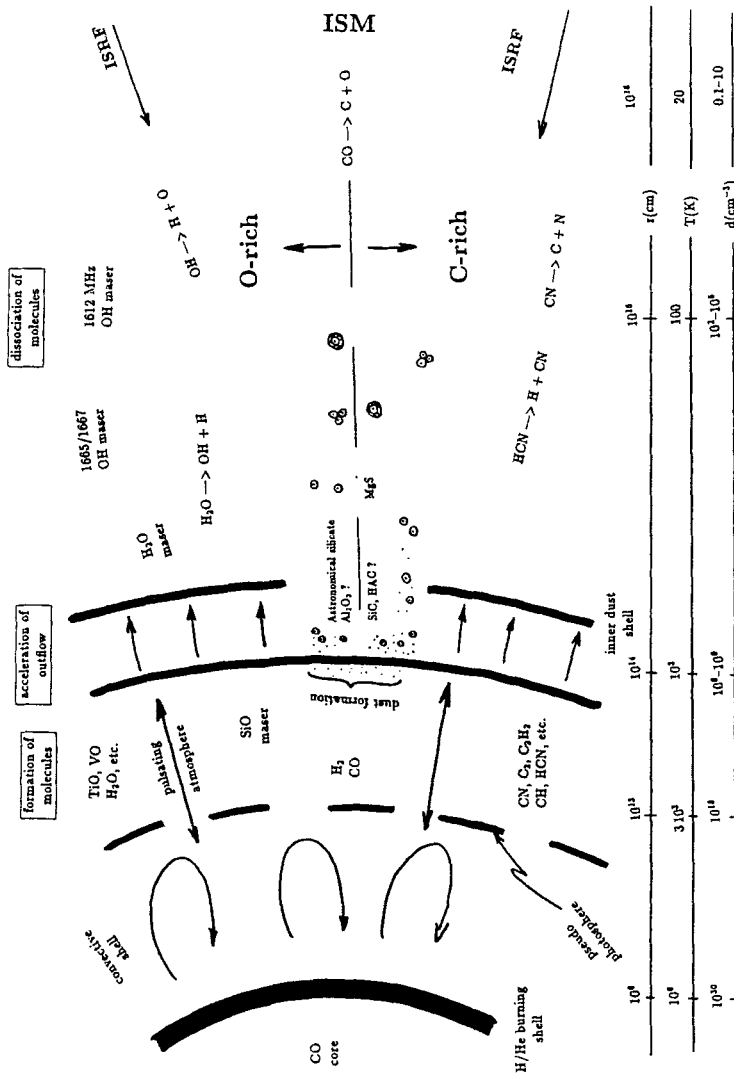


Fig. 1. A schematic view of a mass-losing AGB star. The numbers are only indications on the orders of magnitude. ISM stands for interstellar medium, ISRF for interstellar radiation field, and HAC for hydrogenated amorphous carbon. For comparison, the solar radius, R_{\odot} , is $\sim 7 \cdot 10^{10}$ cm, the astronomical unit, $\sim 1.5 \cdot 10^{13}$ cm, and the parsec, $\sim 3 \cdot 10^{18}$ cm

~ 5 arcsec, he could conclude that the wind extends to at least 1000 a.u. and lasted at least 500 years so that the quantity of matter in the α^1 Her shell is $\geq 10^{-5} M_{\odot}$. The agents responsible of such absorptions in companion spectra may be atoms, molecules or more complex carriers. For instance, Le Bertre and Lequeux (1993) could show that some carriers of the Diffuse Interstellar Bands are present in the winds of carbon stars.

Furthermore, the wind of the mass-losing giant modifies its spectrum by scattering. Two cases have to be considered: scattering by dust and resonant scattering by atoms. In the first case, outflowing grains are scattering the stellar light redshifted by an amount corresponding to the **dust** expansion velocity, V_d . If the Circumstellar Dust Shell (CDS) is optically thin and spherically symmetric, the resulting scattered spectrum is simply redshifted by $\Delta\lambda/\lambda = V_d/c$. In such conditions, it should be possible to measure the dust expansion velocity. The application is not easy. In the data, the scattered spectrum is combined with the stellar spectrum. The CDS may not be spherically symmetric, etc. Furthermore, the stellar atmosphere is pulsating with radial velocity amplitude of same order of magnitude (a few km s^{-1}). The observations are difficult to interpret (Dougados et al. 1992) and, up to now, the results have been disappointing (V_d smaller than V_{gas} !).

For resonant scattering, the absorption is shifted to the blue by an amount corresponding to the **gas** expansion velocity, V_g . Again in the case of an optically thin medium and of a spherical Circumstellar Shell (CS), the photons are re-emitted on average at the stellar velocity. On the stellar spectrum, the absorption lines (e.g. NaI, KI) are skewed to the blue (Bernat and Lambert 1975). On the other hand, if the envelope can be separated from the central star, one observes the lines in emission (Guilain and Maunon 1996 and ref. therein). In the case of an optically thin CS, the lines are centered at the stellar velocity. (However, note that in general the sodium lines at 5890 and 5896 Å are of comparable intensity so that the optically thin hypothesis does not hold.) This kind of observation allows to derive the flux of the corresponding resonant element (assuming that it is not depleted on the grains). It gives also constraints on the photoionization rates, electronic densities, gas-to-dust ratios, etc. (Maunon and Caux 1992). Observations of the KI emission from CSs around carbon stars and their exploitation are discussed in details by Gustafsson et al. (1996).

Spatially resolved spectroscopy in the optical range is a very sensitive technique to detect winds with low mass-loss rate around nearby late-type stars. For instance Maunon and Guilain (1995) have detected the resonant emission of NaI around β Peg, a nearby (~ 60 pc) giant of type M2III which is very likely on the RGB and for which the mass loss rate is evaluated to be $\sim 10^{-9} M_{\odot} \text{ yr}^{-1}$. It is worth noting that this result is one of the few direct observational evidences for mass loss during the first ascent of the giant branch.

3.2 Imagery

Direct imaging of CS is difficult and has emerged only recently. The extreme mass-losing carbon star CW Leo (IRC +10216) is seen diffuse and elongated on the Schmidt plate obtained at Palomar. CCD images obtained at the CFH telescope by Crabtree et al. (1987) show an envelope of radius ~ 40 arcsec. It appears to be clumpy with a structure composed of several discrete shells evoking a non-uniform mass loss. To the difference of the central peak which is due to dust-scattered stellar light, the external shells are due to scattered galactic light (ISRF). These shells are at the limit of detectability from the ground because their brightness is near or below the sky level. Similar structures might also be detectable around other AGB stars. Their studies would give insights on the geometry of the mass loss phenomenon and on its time variability.

Mapping in resonant-scattered emission-line should be extremely rewarding because, with resonant-scattering, one benefits of a contrast advantage as compared to dust scattering. An image in the NaI 5890 Å line of the envelope of μ Cep (actually a red supergiant) shows evidence of asymmetry in the wind and of multiple shells (Mauron et al. 1986). Plez and Lambert (1994) have obtained maps of the KI (7699 Å) emission around several AGB stars and found evidences of large asymmetries in their winds.

Spectacular images have been obtained from space with the Hubble Space Telescope. Images of the post-AGB source, CRL 2688, reveal a multi-shell structure as for IRC +10216. Images of the Planetary Nebula, NGC 7293 (Helix Nebula), show the existence of many small globules (~ 100 a.u.) of dense material ($\sim 10^{-5} M_{\odot}$) which are illuminated by the central star (O'Dell and Handron 1996). These globules may originate in condensations of matter inside the circumstellar envelope during the AGB phase. It has even been speculated that they could be the remnants of concentrations in the AGB stellar atmosphere like those which are revealed by the SiO maser phenomenon (see Sect. 5.3).

3.3 Polarimetry

Polarization is induced by scattering on dust. The radiation is linearly polarized in the direction perpendicular to the plane of scattering. Polarimetry is a difficult technique because of the instrumental and observational effects. For instance, polarization of the light can be induced by the optics of the telescope itself if circular symmetry is broken like in Coudé or Nasmyth foci. Also the sky background can be polarized by Moon light (and Sun light, outside the strict "astronomical" night). Usually, one defines the position angle on the sky in which the radiation is polarized, and the degree of polarization, p , which is the percentage of polarized light (see the lecture by Bjorkman, this Volume). The wavelength dependence of p gives an indication on the size of the scattering grains.

At low spatial resolution, with a diaphragm, one measures the light integrated from the star and the whole shell. In the case of a spherically symmetric dust shell with randomly oriented grains, there should be no net effect. Unless grains in the CDS are elongated and oriented in a preferential direction (which, in AGB stars, seems unlikely), the positive detection of polarization indicates that the geometry of the shell is non-spherical. Polarization degrees of a few percent are generally found (e.g. Kruszewski and Coyne 1976). In some cases, polarization degrees of $\sim 10\%$ have been detected, for instance in IRC +10216 (Shawl and Zellner 1970). Apart from pointing to asymmetries, these results are difficult to interpret.

More rewarding are the spatially resolved polarimetric observations. As the polarization degree and orientation change with position around the central star, observational and instrumental effects are more easy to control (McMillan and Tapia 1978). The results give indications on the real morphology of the dust shell. These observations are especially interesting when they can be complemented with emission-line maps. For instance, the polarization map around μ Cep (Le Borgne and Mauron 1989) shows a large envelope (~ 1 arcmin in diameter) with a structure composed of 2 dust shells which agrees with the structure seen in NaI emission (see previous section).

4 The Infrared Range

Circumstellar Shells (CS) are made of gas and dust. The dust is absorbing the stellar radiation and re-emitting it at longer wavelengths in the infrared (IR) range. Dust grains have spectral signatures that will appear in this range. Although only a small fraction of the matter is in dust ($\sim 0.5 - 1\%$), the CS may be so dense that the central star is completely hidden and the source shows up only at infrared wavelengths. Many mass-losing AGB stars have only been revealed in the course of IR surveys and they can hardly be studied in the optical range. For these reasons, the IR range is extremely important for the study of all mass-losing AGB sources.

4.1 Ground-Based Observations

Astronomical observations in the IR are hampered by two kinds of difficulties. First, the molecules in the Earth atmosphere (H_2O , CO_2 , etc.) are absorbing most of the light and the observations are possible only in a few spectral windows. Second, the telescope, the instrument and the atmosphere are radiating thermally at $\lambda \geq 2 \mu\text{m}$. This emission produces a background which has to be subtracted from the data in order to extract the astronomical signal. Even if this subtraction could be done perfectly, the noise in the background limits the detectability of the sources.

Photometric bands have been defined so that they fit into the atmospheric windows: J ($1.25 \mu\text{m}$), H ($1.65 \mu\text{m}$), K ($2.2 \mu\text{m}$) or K' ($2.1 \mu\text{m}$), L ($3.6 \mu\text{m}$)

or L' (3.8 μm), M (4.6 μm), N (10 μm) and Q (20 μm). The exact values of the effective wavelengths and bandwidths have not been standardized for practical reasons and depend on the instruments so that any comparison must be done with a lot of care.

Photometry of AGB sources through these bands has been done extensively allowing the determination of the energy distributions from 1 to 20 μm for many objects. All mass-losing source spectra exhibit an infrared continuum, in excess of the stellar spectrum, which is due to thermal emission by dust. Two kinds of spectra differentiate clearly. Those of carbon-rich sources are like blackbodies whereas those of oxygen-rich sources present spectral features at 10 and 20 μm either in emission or in absorption depending on the optical depth of the CS (Jones and Merrill 1976). Carbon-rich sources show a weak emission feature at 11 μm . As compared to the C-rich sources, the O-rich ones exhibit a larger excess of radiation at mid-infrared (10–20 μm) wavelengths relatively to the near-infrared (1–5 μm).

The spectral features have been studied at low spectral resolution ($\lambda/\Delta\lambda \approx 50$ to 100) since ~ 25 years (e.g. Merrill and Stein 1976). They are broad ($\Delta\lambda \approx 1 \mu\text{m}$) and smooth, without sub-structures. The 10 and 20- μm features seen in O-rich source spectra have been ascribed to silicate grains with an amorphous mineralogical structure (Day 1976). However, the continuum opacity, in particular at $\lambda \leq 8 \mu\text{m}$, is higher than expected and not well explained. As the match between the observations and the laboratory data is not entirely satisfactory, the concepts of "dirty" silicate or astronomical silicate have been introduced. The 11- μm feature in C-rich source spectra has been ascribed to silicon carbide (SiC, Treffers and Cohen 1974). Cohen (1984) distinguishes 2 types of SiC features that he relates to different grain mineralogical structures. In some extreme cases, the SiC feature can be seen in absorption (Justtanont et al. 1996). The continuum opacity is generally attributed to some kinds of hydrogenated amorphous carbon (HAC). In addition, a feature centered at $\sim 30 \mu\text{m}$ has been observed in several C-rich sources and ascribed to magnesium sulfide (MgS, Goebel and Moseley 1985). These identifications are consistent with the C/O abundance ratio of the central star. For an M star ($\text{C/O} < 1$) all carbon should be locked into the CO molecule because it is very stable (the dissociation energy of CO is 11 eV)². Carbon and/or carbonaceous molecules cannot contribute to the dust composition. For a C star ($\text{C/O} > 1$) the reverse applies; oxygen cannot enter into the composition of the dust.

In conclusion, M and C stars differentiate clearly in the IR range by the emission of dust. The differences are seen in the gross shapes of the broad-band energy distributions and in the spectral features and denote different properties of the dust in their CS. The IRAS photometric data (Sect. 4.2)

² Here some caution should be exercised as the presence of a hot companion or of a chromosphere may be a source of UV radiation photodissociating a part of the CO molecules.

complete profitably ground-based spectra up to $100\ \mu\text{m}$. From the resulting broad-band energy distributions and with the help of numerical models, it is possible to estimate the dust mass outflow. Values in the range 10^{-9} – $10^{-6}\ \text{M}_{\odot}\ \text{yr}^{-1}$ are commonly found (e.g. Le Sidaner and Le Bertre 1996). For the 2 kinds of CDS, the optical depth is well correlated to the infrared colors. Therefore, the colors can be used as indicators of the dust mass loss rate.

Some sources have been monitored in the infrared range. The amplitudes are generally decreasing with wavelength. The lightcurves show irregularities, but less pronounced than in the optical. Sometimes, intermediate extrema are seen on the lightcurve rising-branches. There is also a modulation of the mean infrared brightness on a timescale of a few stellar periods. The hydrodynamical models of dust formation developed by the Berlin's group (see the lecture by Sedlmayr and Winters, this Volume) provide a natural explanation to these lightcurve features.

With the development of IR and radio techniques, new sources have been discovered. Among them, several long-period variables were found. They have properties which connect them to the Miras. The periods of the sources detected only in the IR are generally longer than those of optical Miras. Some extreme sources (OH/IR, see Sect. 5.2) have periods up to 2000 days.

For each kind of source (C-rich and O-rich), one finds a loose correlation between the periods and the IR colors or the amplitudes of the lightcurves. This tends to show that mass loss depends on stellar variability. Also, the IR colors are well correlated with the amplitudes. However, this is only an effect of the shape of the spectrum; for Miras, the bolometric amplitude is always $\sim 1\ \text{mag}$.

Finally, for Miras, there is a correlation between the period and the luminosity. The relation may depend slightly on the type (M or C; Feast et al. 1989) and on the metallicity, but the latter has been challenged (Whitelock et al. 1994). There are also correlations between the period and the magnitudes, but because of the circumstellar extinction, they have to be handled with care for mass-losing Miras. However, the K magnitude seems reliable for this purpose since it should be affected only in the most extreme cases (Groenewegen and Whitelock 1996).

4.2 IRAS

The exploration from the ground of the IR sky is difficult, especially at $\lambda \geq 10\ \mu\text{m}$, because of the large thermal background and because of the poor atmospheric transmission. The Infrared Astronomical Satellite (IRAS) mission has been developed to conduct a survey of the sky in 4 IR bands with a cooled telescope (Neugebauer et al. 1984). The bands are centered at 12, 25, 60 and $100\ \mu\text{m}$ and have a width, $\Delta\lambda/\lambda \approx 0.5$ – 1.0 . The beams are $\sim 2\ \text{arcmin}$ wide, but the positional accuracy is generally much better ($\sim 10\ \text{arcsec}$). A catalogue of 2×10^5 sources (Point Sources Catalog, PSC) with positions and fluxes has been produced (IRAS Science Team 1988). In

addition, a low resolution spectrometer (LRS) provided good quality spectra, at a resolution ~ 50 , for about 6000 sources (IRAS Science Team 1986, Volk and Cohen 1989, Volk et al. 1991).

Several classification schemes of the LRS spectra have been developed, but the most commonly used is the original IRAS Science Team one. It is a two-digit system where spectra with a $10\text{-}\mu\text{m}$ feature in emission are registered as 2n, with a $10\text{-}\mu\text{m}$ feature in absorption as 3n and with an $11\text{-}\mu\text{m}$ feature in emission as 4n (n being an index of the feature strength). More than half of the LRS spectra were obtained on AGB stars and most pertain to one of these classes: O-rich sources are normally found in classes 2n and 3n, and C-rich ones, in classes 4n. However, the LRS classes should be handled with care as some O-rich sources, with a self-absorbed $10\text{-}\mu\text{m}$ feature mimicking the $11\text{-}\mu\text{m}$ emission feature, appear in a 4n class. In these cases the $20\text{-}\mu\text{m}$ feature is clearly seen in emission and a visual inspection is generally sufficient to correct the classification. Furthermore, many AGB sources with extreme properties are found in other classes. For instance, Omont et al. (1993a) find sources with very cold C-rich shells in classes 2n (especially 21 and 22) and also in other less populated classes. In addition to the silicate feature at $10\text{ }\mu\text{m}$, there is evidence in the LRS spectra of some oxygen-rich sources for an emission feature at $12\text{ }\mu\text{m}$ which has been ascribed to Al_2O_3 (Onaka et al. 1989). Finally, Little-Marenin and Little (1988) have found that the spectra of S-type stars show usually an emission feature peaking around $10.8\text{ }\mu\text{m}$.

The IRAS photometric data have been used to build IRAS color-color diagrams. For stellar sources the most useful one is the $[12\text{ }\mu\text{m}]\text{--}[25\text{ }\mu\text{m}]$ versus $[25\text{ }\mu\text{m}]\text{--}[60\text{ }\mu\text{m}]$ diagram which has been studied in details by van der Veen and Habing (1988, VH). They have divided this color diagram in 10 regions and have evaluated the composition of the population contributing to each region on the basis of the LRS spectra of identified sources. The region I, corresponding to blackbody colors $T_{\text{BB}} \geq 2000\text{ K}$, contains mainly stars without circumstellar emission. Regions II, III (a and b), and IV contain a majority of O-rich sources, and VII, C-rich sources, but without clear separation. For instance, Epchtein et al. (1990) found many carbon stars in regions II and III. Conversely, Guglielmo et al. (1993) found a majority of O-rich sources in region VII in contradiction with VH (they suspect selection biases in their own sample and in the VH one). Region V contains mainly Planetary Nebulae (PN) and proto-PN whereas regions VI (a and b) contain sources with cold dust at large distances from the central star which can be indifferently C-rich or O-rich. The salient presence of cold dust radiating at $60\text{ }\mu\text{m}$ can be explained as due to an interruption in the mass loss rate for $\sim 10^3\text{--}10^4$ years (or at least a significant reduction). Chan and Kwok (1988) have shown that such a process can explain the positions of the sources in region VI.

The IRAS colors diagram is therefore of some, but limited, use to discriminate O-rich sources from C-rich sources. As O-rich sources present a larger excess in the $10\text{--}20\text{ }\mu\text{m}$ range relatively to the $1\text{--}5\text{ }\mu\text{m}$ range than the

C-rich sources (Sect. 4.1), a better approach is to combine an IRAS color with a near-IR one. Epchtein et al. (1987) have shown that, in a K-L' versus $[12\ \mu\text{m}]-[25\ \mu\text{m}]$, the two populations are clearly separated. They describe a classification scheme of AGB sources based on these two colors.

Although it is difficult to characterize the sources from the IRAS colors, for sources of known type the IRAS colors are indicators of the mass loss rate. On this basis, Jura (1986) evaluates the mass loss rates of AGB sources and finds a correlation between the mass loss rates and the periods of the central stars suggesting again a dependency of mass loss on stellar variability.

In spite of the large IRAS beams, some sources have been resolved at 60 and 100 μm (Young et al. 1993). Indeed, for an AGB source of $2\ 10^4\ L_{\odot}$, dust emission at 60 μm is expected up to a distance where dust is at $\leq 50\ \text{K}$, i.e. $\sim 0.1\ \text{pc}$. Therefore, if at a distance from the Sun $\leq 500\ \text{pc}$, such an object should be resolved at 60 μm . However, this emission is difficult to recognize as it appears in the wings of the central core image. On the other hand, in the case of interrupted mass loss, the shell of cold dust can in principle be resolved more easily. Using an elaborate image reconstruction technique, Waters et al. (1994) have resolved at 60 μm the shell of U Hya. The shell is clearly detached from the central star. Waters et al. show that the formation of such a shell required a mass loss rate of $0.5\ 10^{-6}\ M_{\odot}\ \text{yr}^{-1}$, a factor 25 higher than the present-day rate.

5 The Radio Range

Most of the outflowing material from AGB stars consists of atomic and molecular gas (dust accounts for $\leq 1\%$). Therefore, important information should be expected from the molecular emission in the radio range. Unfortunately, the most abundant molecule, H_2 , is hard to detect. After H_2 , CO is the dominant molecular species in circumstellar envelopes. Depending on the C/O abundance ratio, other molecules are expected: H_2O , HCN, etc. Indeed lines of CO, HCN, OH and SiO have been detected in many sources (see for instance the catalogues of observations by Benson et al. 1990 for H_2O , SiO and OH, and by Loup et al. 1993 for CO and HCN). With the improvements in receiver sensitivity, more and more molecules have been detected, such as the cyanopolyynes HC_{2n+1}N with n up to 5, illustrating the richness of the circumstellar chemistry (see e.g. Olofsson 1994).

An immediate contribution of these observations is the determination of stellar radial velocities and circumstellar expansion velocities with a great accuracy ($\sim 1\ \text{km s}^{-1}$). Gas expansion velocities are found in the range $5\text{--}35\ \text{km s}^{-1}$, with the majority in the range $10\text{--}20\ \text{km s}^{-1}$. The mass loss rates can also be estimated, mainly from CO data, and are found in the range $10^{-8}\text{--}10^{-4}\ M_{\odot}\ \text{yr}^{-1}$. Furthermore, due to the numerous chemical reactions which are at work and to the presence of the Interstellar Radiation Field (ISRF) which is more or less attenuated by dust, the composition of the CS presents

a stratified structure. For instance, OH is formed by the photodissociation of H_2O ($\text{H}_2\text{O} + h\nu \rightarrow \text{OH} + \text{H}$) and destroyed, also by photodissociation, but further away from the central star (Fig. 1). The studies of the molecular emission lines can serve to determine this structure and to probe the physical conditions in the different layers. Also, the history of mass loss can be studied. Finally, the radio lines offer the possibility of determining isotopic abundance ratios.

The molecular emission may be thermal or non-thermal (maser). We first examine the CO emission which is a good example of thermal emission and then the OH maser emission at 1612 MHz.

5.1 CO Emission

CO is the most abundant molecule after H_2 ; the latter, being symmetric (as N_2 , C_2H_2 , etc.), has no rotational transition. It is expected in both kinds of sources, O-rich and C-rich. The rotation lines J(1-0) at 115 GHz (2.6 mm) and J(2-1) at 230 GHz (1.3 mm) have been detected in many nearby galactic objects (the catalogue of Loup et al. 1993 lists about 400 sources). Higher-J transitions have been observed in only a few sources, not so much because they would be less intense (in fact they may be more intense) but rather because of the atmospheric extinction in the sub-millimeter range.

The line profiles depend on the CO-shell optical depth and on the relative angular sizes of the telescope beam and of the shell. The lines are not found to be variable which can be understood as CO is excited mainly by collisions with H_2 . In general, the ^{12}CO lines are optically thick and the ^{13}CO lines, optically thin. Mass loss rates can be derived from the CO profiles assuming a CO/H abundance ratio (Knapp and Morris 1985, Loup et al. 1993). A detailed modelling taking into account the beam profile is necessary to interpret consistently the different lines. In such case, the physical conditions through the shell and the mass loss history can be derived (Truong-Bach et al. 1991).

The CO molecule is photodissociated by UV lines rather than by the continuum as most other molecules. Therefore, CO is self-shielded efficiently and is expected at much larger radii than the other species. Indeed, mapping has shown that CO may be found at distances up to $\sim 10^{18}$ cm from the central star. In some cases, the CO emission has been shown to arise in an expanding detached shell (Olofsson et al. 1990). The sources which show such a pattern are also known to have an excess at $60 \mu\text{m}$. This is another evidence for strong variation of mass loss on a scale of a few 10^3 years. For instance, a CO shell of $\sim 5 \cdot 10^{17}$ cm radius and $\sim 10^{17}$ cm thickness has been found around the carbon star S Scuti (Olofsson et al. 1992). The present mass loss rate would be $\sim 3 \cdot 10^{-8} M_{\odot} \text{ yr}^{-1}$ as compared to $\sim 4 \cdot 10^{-5} M_{\odot} \text{ yr}^{-1}$ during the shell formation, 10^4 years ago.

5.2 OH Maser Emission

In the non-excited states (fundamental state, $v=0$), the rotational levels of OH are split into 4 components. The selection rules allow 4 transitions at 18 cm between these components. For the ground level, they are referred to as the 1665 and 1667 MHz main lines (no change in the angular momentum, $\Delta F=0$), and as the 1612 and 1720 MHz satellite lines ($\Delta F=1$). The emission lines are so intense that explanations based on maser amplification have to be invoked. The line at 1720 MHz is observed only in early-type pre-main sequence stars whereas the 3 other lines are found in evolved stellar sources.

The maser emission associated to late-type stars is said to be of type I if one of the main lines dominates, and of type II if it is the satellite line. The emission is generally variable with the same period as the central source. This is an indication of a radiative excitation. For the type II masers, Elitzur et al. (1976) have developed a model of excitation by IR photons at $35\ \mu\text{m}$ which produce a strong inversion of the populations in the ground state levels connected by the 1612 MHz line. The maser emission arises in a shell of a few 10^{16} cm radius where the gas is at a temperature, $T_{\text{gas}} \approx 100\text{--}200\text{ K}$, and the density, $n_{\text{H}_2} \approx 10^5\text{ cm}^{-3}$ (Bujarrabal et al. 1980). The line has a two-peak profile with the peaks of emission emanating from the far and near sides of the expanding shell. This model has been widely confirmed by the observations. For instance, monitorings have shown that there is a delay of $\sim 10\text{--}30$ days between the variations of the two peaks which translates to an OH-shell radius $\sim 1\text{--}5\ 10^{16}$ cm (Herman and Habing 1985).

Radio surveys of the Galactic Plane at 1612 MHz have led to the discovery of many maser sources with unidentified counterparts. With subsequent searches, IR sources which radiate most of their energy in the mid-infrared have been found. They are variable with periods in the range 500–2000 days. Their properties connect them to the Miras or the red supergiants. These objects, without counterpart in the optical/NIR range, are called (type II) OH/IR sources.

High resolution maps (≤ 1 arcsec) have been obtained with radio interferometers, the Multi Element Radio Linked Interferometer Network (MERLIN) and the Very Large Array (VLA). The velocity resolved maps show spherical shells which sometimes break into individual components (Booth et al. 1981, Herman et al. 1985). The combination of these maps with the measurements of the phase lags between the two peaks of the line profile should, in principle, allow a direct determination of the source distances (van Langevelde et al. 1990).

The OH emission has also been probed with Very Long Baseline Interferometry (VLBI) techniques which give access to scales ~ 0.01 arcsec. It is resolved in emission spots of size $\sim 10^{15}$ cm with brightness temperature in the range $10^8\text{--}10^9$ K (Reid et al. 1977).

5.3 Other Molecules

In oxygen-rich sources, H_2O is expected to be the second most abundant molecule with microwave transition (after CO, because O_2 and N_2 have no such transition), up to the point where it is photodissociated. Unfortunately (?), it is abundant in the Earth atmosphere which makes its detection difficult. Nevertheless, maser lines have been discovered at 22 GHz (1.35 cm). This emission is present in O-rich sources. The intensities and the line profiles are strongly, and erratically, variable. High-resolution imaging (VLA/VLBI) has shown that the emission arises in spots of a few 10^{13} cm spread in a shell of $\sim 10^{15}$ – 10^{16} cm diameter.

Similarly, in carbon-rich sources, HCN is the second most abundant molecule with microwave transition (C_2H_2 is symmetric like N_2), up to the point where it is photodissociated. Thermal emission ($J = 1-0$, 88.6 GHz) has been detected in many carbon-rich sources and, surprisingly, also in some oxygen-rich sources (Lindqvist et al. 1988). Unfortunately, it is radiatively excited, which makes difficult the evaluation of its column density. A maser emission has also been found in one C-rich source (Guilloteau et al. 1987).

Another important molecule, in O-rich sources, is SiO. It is expected to be abundant in the region below the dust condensation layer ($\leq 10^{14}$ cm, Fig. 1) and depleted above ($\geq 10^{15}$ cm). Thermal emission has been detected in the $v = 0$ level ($J = 1-0$, 43 GHz, up to $J = 5-4$). The lines are weak indicating depletion by a factor ≥ 10 . In fact, the emission is confined in a region of a few 10^{15} cm in which SiO is partly condensed (Lucas et al. 1992). Maser emission has been detected in the excited states ($v = 1, 2, 3$, with J up to 5). Lines corresponding to transitions between higher rotational states are theoretically expected, but difficult to detect (Gray et al. 1995). The maser lines are narrower than the thermal lines suggesting that they form in a more interior region. Indeed, VLBI measurements show that the emission arises in spots of $\sim 10^{13}$ cm located in a ring of diameter of a few 10^{14} cm (Diamond et al. 1994, Greenhill et al. 1995). In conclusion, to the difference of the thermal emission, the maser emission is more related to the extended atmosphere of evolved stars than to their winds; therefore, they can be used to study the region at the base of the dust-flow (Doel et al. 1995).

Many other lines have been found in CSs around evolved stars, for instance those of S-bearing molecules: SiS, H_2S , SO_2 , SO, CS, OCS (Nguyen-Q-Rieu et al. 1984, Morris et al. 1987, Omont et al. 1993b). Also, organic molecules have been detected (mainly in the prototypical carbon star: IRC +10216), HC_{2n+1}N and C_nH (with n up to 6), and molecular rings, C_3H_2 and SiC_2 . Recently, C_8H has been discovered by Cernicharo and Guélin (1996).

For all the molecular lines, high-resolution imaging is important because the radial structures of the CSs can be studied for each of the corresponding chemical species. This gives important constraints on the physical and chemical processes leading to the observed molecules (Bieging and Nguyen-Q-Rieu 1988). Also one may discover deviations from spherical symmetry and inves-

tigate the circumstellar gas clumpiness (Guélin et al. 1996). Finally, with a velocity resolution of $\sim 1 \text{ km s}^{-1}$, departures from the constant outflow velocity can be revealed and quantified. In particular, imaging in the thermal SiO lines will be especially useful to study the condensation of SiO in dust and the acceleration of the gas in the dust-formation zone (Lucas et al. 1992).

6 Present Developments

6.1 High Spatial Resolution in the Optical and IR Range

Ground-based observations in the optical and infrared ranges are limited by the effects of the atmosphere on the image quality. At a wavelength λ , a telescope of diameter D should give a resolution $\theta \sim \lambda/D$ which corresponds to the diffraction limit (e.g. if $D = 1 \text{ m}$ and $\lambda = 0.5 \mu\text{m}$, $\theta \sim 0.1 \text{ arcsec}$). However, in a good astronomical site, the atmospheric turbulence limits the resolution to a value called the seeing, typically $\phi \approx 1 \text{ arcsec}$. This limit depends on wavelength as $\phi \propto \lambda^{-1/5}$, so that in principle better images can be obtained in the IR range. Several techniques have been developed to improve the spatial resolution up to the diffraction limit, for instance speckle interferometry and more recently adaptive optics. Also, there have been attempts to go beyond the diffraction limit of a single telescope by building arrays of telescopes coherently phased (interferometers).

Improving the spatial resolution in the optical range and up to $\sim 2 \mu\text{m}$ should give access to features at the surfaces of stars which may be correlated to structures in the circumstellar envelopes. As dust is scattering preferentially in the optical range, it would give access also to the structures in the inner dust shells. On the other hand, infrared wavelengths from $3 \mu\text{m}$ to $20 \mu\text{m}$ trace the grains thermal emission from the region of dust formation to the region where dust has cooled to $\sim 100 \text{ K}$ and has reached its terminal velocity.

The expected radius of a typical AGB star is $\sim 1 \text{ a.u.}$, of its inner dust shell $\sim 10 \text{ a.u.}$, and of the region where dust is at $100 \text{ K} \sim 1000 \text{ a.u.}$ (Fig. 1). For an object at a distance of 1 kpc , the diameter of the inner shell would be $\sim 0.02 \text{ arcsec}$, and of the region with dust at $100 \text{ K} \sim 2 \text{ arcsec}$. A hampering difficulty is the contrast between the emission from these regions and the emission from the central source. It is generally so large that the shell is simply lost in the wings of the central source profile.

Speckle interferometry has been applied in the near-infrared range ($1\text{--}5 \mu\text{m}$) to bright AGB sources such as IRC +10216 or OH/IR 26.5+0.6. Sub-arcsecond diameters have been estimated. The data are generally difficult to interpret because the observations give the Fourier transform of the spatial energy distribution of the source (visibility function) instead of a direct image. They require the use of an a-priori model that is fitted numerically to the data (e.g. Lopez et al. 1993). Evidence of non-sphericity of the dust shells and of variability correlated with the light-curve have been found (Dyck et al. 1991). The shells appear larger at the maxima of the lightcurves and smaller

at the minima. Recently, the technique of Adaptive Optics (AO) has been applied to AGB sources in the near-infrared range with success. In the mid-infrared ($8\text{--}20\ \mu\text{m}$), presently the largest conventional telescopes ($D \approx 4\text{ m}$) are most of the time limited by diffraction. This will be no more the case with the 8-m class telescopes which are entering into activity and AO will be also a necessity to reach the diffraction limit.

Although the principles of interferometry are well known and applied at radio-wavelengths since a long time, the applications in the optical and IR ranges are recent. Very promising results have been obtained with the Mount Wilson Infrared Spatial Interferometer, ISI, a system of 2 movable 1.65-m telescopes operated at $11\ \mu\text{m}$. The carbon source IRC+10216 has been resolved and shown to vary in size as a function of its luminosity (Danchi et al. 1990). The same team has studied the distribution of dust around 12 other AGB stars (Danchi et al. 1994). They find evidence for time-variations of the dust mass loss rates.

6.2 Laboratory Studies

The dream of any astrophysicist is to hold a sample of celestial matter for analysing it in the laboratory. The chemical abundances and the physical state of the matter could thus be determined directly instead of being inferred through hypothetical models. In this respect, it seems that investigators of AGB stars are favored. There are meteorites in the museum collections which probably contain samples of interstellar dust. Furthermore, good analogues of circumstellar grains are starting to be produced artificially.

It has been shown that some inclusions in the meteorites are of pre-solar origin, i.e. they are samples of interstellar matter. The carbonaceous chondrites appear to be the most primitive meteorites. Their formation temperature is relatively low ($\leq 500\text{ K}$) so that they incorporate interstellar material that has not been processed in the solar-system parent-bodies (comets or asteroids?). Some inclusions exhibit an abundance pattern, in carbon and s-elements, which is characteristic of TP-AGB stars. They must have formed in their winds. The analysis of these inclusions give informations on the composition of grains around AGB stars and on the nucleosynthesis processes which have been at work in the heart of the parent stars. They give also insights on the physics of their formation. For instance, Bernatowicz et al. (1991) found inclusions which have a structure with concentric layers of carbon. In addition, one of these inclusions contains crystals of TiC and SiC which have been included in the grain during its formation. Assuming equilibrium condensation, TiC should condense after carbon well below 1500 K . Therefore, this discovery points to an inhibited nucleation and growth of carbon grains.

The first attempt to produce in the laboratory a material matching the properties of interstellar dust was made by Day (1976, and ref. therein) who obtained amorphous silicate materials. These products had absorption properties in the mid-infrared range which are in fair agreement with the obser-

vations (cf. Sect. 4.1). More recently, Jäger et al. (1994) and Dorschner et al. (1995) have undertaken a systematic programme to produce and study analogues of interstellar grains. They produced two series of glasses with pyroxene ($\text{Mg}_x\text{Fe}_{1-x}\text{SiO}_3$) and olivine ($\text{Mg}_x\text{Fe}_{1-x}\text{SiO}_4$) stoichiometry and studied their properties on the basis of laboratory measurements. With this approach they can evaluate the influence of various parameters on Ultra-Violet/ Visual/ IR absorption (up to $500\text{ }\mu\text{m}$). They compare their experimental results with the IRAS observations of O-rich CDS and conclude that amorphous silicates with olivine stoichiometry can give a good fit to the astronomical spectra.

6.3 Space Projects

The wavelength range from 20 to $800\text{ }\mu\text{m}$ is extremely useful for the studies of circumstellar shells. Apart from the emission by cool dust, many important atomic and molecular lines are found in this range. Unfortunately, it is not accessible from the ground and requires observatories in orbit around the Earth. Another limitation of ground-based telescopes is the thermal background. Space-borne telescopes can be cooled (without risk of water condensation!). However, even when the telescope is cooled to less than 10 K (e.g. IRAS), the observations at long wavelengths are limited by the thermal emission from dust in the solar system (zodiacal light, $T_{\text{BB}} \approx 250\text{ K}$) or from dust in the interstellar medium (interstellar cirrus, $T_{\text{BB}} \approx 30\text{ K}$). The background emission received by a detector is proportional to the pass-band and to the solid angle illuminating the detector. There are 2 ways to minimize it and hence to increase the sensitivity: to increase the spectral resolution, i.e. to go towards emission line studies, or to increase the spatial resolution which implies to increase the telescope diameter.

ISO: The Infrared Space Observatory has been launched in November 1995 and is presently operated successfully. The telescope has a 0.6-m diameter, like for the IRAS mission. ISO is providing photometry and spectroscopy up to $200\text{ }\mu\text{m}$. It will be especially useful for the study of molecules which are abundant in the terrestrial atmosphere such as H_2O and CO_2 and which, for this reason, cannot be observed from the ground. Many lines of other important molecules such as OH and SiO fall in the range of ISO. Also there are fine structure lines of abundant elements which in CSs are expected to result from the dissociation of these molecules by the Interstellar Radiation Field (Fig. 1), e.g. OI ($63\text{ }\mu\text{m}$), CII ($158\text{ }\mu\text{m}$) or SiI ($68\text{ }\mu\text{m}$). ISO has also imaging capabilities that will allow to map the extended shells which have been suspected at 60 and $100\text{ }\mu\text{m}$ on the basis of the IRAS data (Young et al. 1993; Sect. 4.2). Finally, new dust features could be discovered in the wavelength range which has not been explored from the ground or with the IRAS LRS³.

³ The first ISO results (A&A, ISO Special Issue, Vol. 315 No. II) illustrate much better by themselves, and way beyond all expectations, the richness of the information contained in the 20– $200\text{ }\mu\text{m}$ range (e.g. Barlow et al., Waters et al., in that Issue).

FIRST: The Far Infra-Red and Submillimeter Space Telescope, to be launched in 10 years from now (~ 2005), will provide imaging photometry and spectroscopy in the domain $100\text{--}900\ \mu\text{m}$. It will thus cover the wavelength range longward of ISO and shortward of the ground-based radio-telescopes. The telescope is foreseen to have a 3-m diameter. High-resolution spectroscopy in the sub-millimeter range will give access to high- J rotational lines of molecules already observed in the millimeter range. This will be a natural follow-up for the studies described in Sect. 5. Also, a number of new chemical species should be discovered.

6.4 Near-Infrared Surveys

The near-infrared range ($1\text{--}2.5\ \mu\text{m}$) corresponds to the peak of emission of most AGB stars. Thirty years ago, the Two Micron Sky Survey (TMSS) was undertaken by Neugebauer and Leighton (1969). About 6000 sources, mostly RGB and AGB stars, were detected. Although limited in sensitivity ($K \approx 3$), the TMSS had a strong impact on the studies of AGB stars. Many mass-losing sources, extremely reddened by dust such as IRC +10216, were revealed for the first time. The TMSS contributed to the recognition that heavy mass loss is an important factor in the evolution of AGB stars. Since this pioneering work, there has been no attempt to survey the entire sky in the near-infrared. An extension of the TMSS to the southern Galactic Plane was done by Epchtein et al. (1987).

The recent availability of sensitive near-infrared arrays such as the 256×256 NICMOS detector has stimulated the development of 2 programmes aiming at surveying the near-infrared sky:

- (i) the Two Micron All Sky Survey (2MASS, Kleinmann et al. 1994),
- (ii) the DEep Near-Infrared Survey of the southern sky (DENIS, Epchtein et al. 1994, Le Bertre et al. 1995).

Although the exact specifications of these 2 programmes are somewhat different, they share many common features. In both cases, it is aimed to cover the sky with a spatial resolution ~ 1 arcsec down to a limiting magnitude $K \approx 14$. With such a sensitivity, all AGB stars in the Galaxy should be detectable. Except in the densest parts of the Galactic Plane, all objects should be well separated. By contrast, due to its wide beam (~ 1 arcmin at $10\ \mu\text{m}$), IRAS was limited by confusion in large areas around the Galactic Plane. With a limiting magnitude $K \approx 14$, most AGB stars should be detected in the Magellanic Clouds. Even very reddened sources like IRC +10216 might be discovered in the LMC.

As discussed previously (Sect. 4.2), IRAS has detected thousands of mass-losing AGB stars. Unfortunately, the IRAS photometric data alone are not sufficient to characterize these sources. However, the combination of these data with near-infrared ones coming from 2MASS and DENIS will allow such a characterization. For instance, in a $J\text{--}K$ versus $[12\ \mu\text{m}]\text{--}[25\ \mu\text{m}]$ diagram,

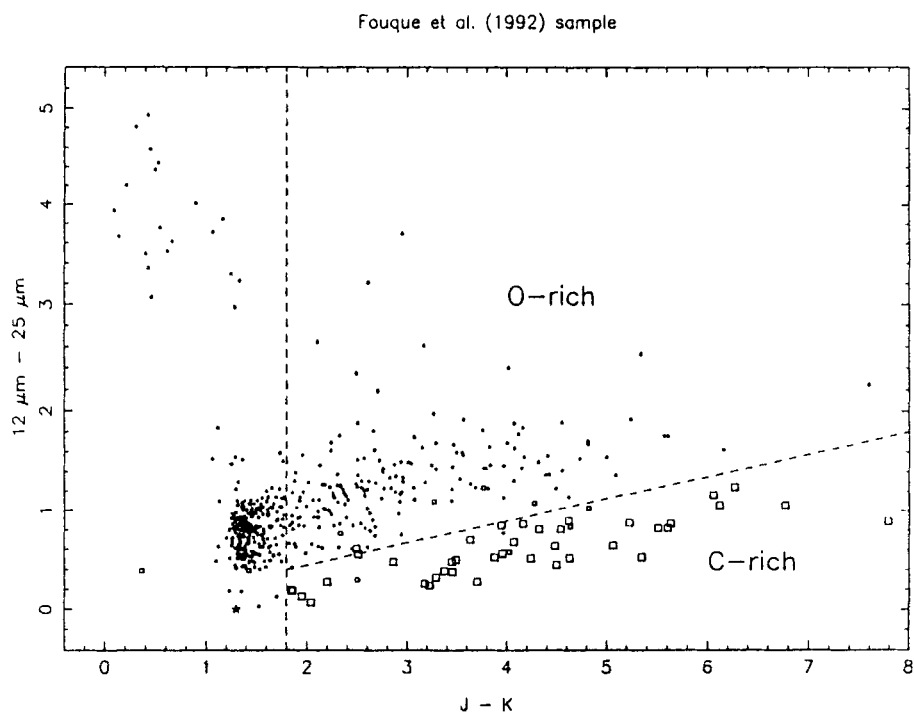


Fig. 2. J-K versus $[12\ \mu\text{m}]-[25\ \mu\text{m}]$ diagram for a sample of stars with Circumstellar Dust Shell (CDS). The data are taken from Fouqué et al. (1992). (large \square): sources with a confirmed Carbon-rich CDS. (small \square): sources with a suspected Carbon-rich CDS. (\bullet): sources with a confirmed or suspected Oxygen-rich CDS. The (\star) marks the position of an M6 giant without CDS. For $J-K > 1.8$, O-rich sources are clearly separated from C-rich ones. For $J-K < 1.8$, the sources may have a detached shell and the two types are mixed

the O-rich mass-losing AGB stars separate well from the C-rich ones (Le Bertre et al. 1994; Fig. 2).

7 Final Comments

We have seen that there are many observational tools that are useful to study the winds around cool stars. In the next years, new facilities will enter into operation completing the existing ones. These new facilities together with the improvements in detector (including radio receivers) sensitivity and the developments of new techniques will certainly bring new lights on circumstellar shells (CS). One should note especially the observations in the optical and IR range that will benefit considerably from the improved image quality and sensitivity. In the next years, direct imaging and spectroscopy of the CSs in the optical range will most probably bring a wealth of informations. An essential issue for the description of AGB stellar winds and a real observational challenge is the measurement of the **dust** expansion velocity.

One must mention also as extremely promising the progress obtained with interferometry at millimeter and sub-mm wavelengths which now provides resolution of a fraction of an arcsec. In addition, space will give access to the wavelength range which is not accessible from the ground. Especially promising are the observations of molecules such as OH, H₂O, CO, CO₂, but one should also stay open to unpredictable discoveries. The detections of new chemical species will be important for the understanding of the physical and chemical processes in CSs.

Furthermore, laboratory studies of interstellar grains as well as of their analogues should have a strong impact on our knowledges about circumstellar dust and about the formation and evolution of grains.

Finally, the increased capacities of computers will drive the applications of statistics to Astronomy. The exploitation of the huge amounts of data produced by large scale surveys such as 2MASS and DENIS will provide a new approach to the understanding of AGB stars and of their CSs in different environments.

Acknowledgements

I am grateful to J. Lequeux, B. Lopez, N. Maunon and Nguyen-Q-Rieu for many helpful discussions and for reading carefully an original version of these notes. Many thanks also to J.-P. De Greve for inviting me to the IXth EADN Summer School.

References

- Benson, P. J., Little-Marenin, I. R., Woods, T. C., et al. (1990): *ApJS* **74**, 911
- Bernat, A. P., Lambert, D. L. (1975): *ApJ* **201**, L153
- Bernatowicz, T. J., Amari, S., Zinner, E. K., Lewis, R. S. (1991): *ApJ* **373**, L73
- Bieging, J. H., Nguyen-Q-Rieu (1988): *ApJ* **329**, L107
- Bujarrabal, V., Guibert, J., Nguyen-Q-Rieu, Omont, A. (1980): *A&A* **84**, 311
- Booth, R. S., Kus, A. J., Norris, R. P., Porter, N. D. (1981): *Nat* **290**, 382
- Cernicharo, J., Guélin, M. (1996): *A&A* **309**, L27
- Chan, S. J., Kwok, S. (1988): *ApJ* **334**, 362
- Cohen, M. (1984): *MNRAS* **206**, 137
- Crabtree, D. R., McLaren, R. A., Christian, C. A. (1987): in *Late Stages of Stellar Evolution*, S. Kwok & S. R. Pottasch (eds.), Reidel, Dordrecht, p145
- Danchi, W. C., Bester, M., Degiacomi, C. G., McCullough, P. R., Townes, C. H. (1990): *ApJ* **359**, L59
- Danchi, W. C., Bester, M., Degiacomi, C. G., Greenhill, L. J., Townes, C. H. (1994): *AJ* **107**, 1469
- Day, K. L. (1976): *ApJ* **210**, 614
- Deutsch, A. J. (1956): *ApJ* **123**, 210
- Diamond, P. J., Kemball, A. J., Junor, W., et al. (1994): *ApJ* **430**, L61
- Doel, R. C., Gray, M. D., Humphreys, E. M. L., Braithwaite, M. F., Field, D. (1995): *A&A* **302**, 797
- Dorschner, J., Begemann, B., Henning, T., Jäger, C., Mutschke, H. (1995): *A&A* **300**, 503
- Dougados, C., Rouan, D., Léna, P. (1992): *A&A* **253**, 464
- Dyck, H. M., Benson, J. A., Howell, R. R., Joyce, R. R., Leinert, Ch. (1991): *AJ* **102**, 200
- Elitzur, M., Goldreich, P., Scoville, N. (1976): *ApJ* **205**, 384
- Epchtein, N., Le Bertre, T., Lépine, J. R. D., et al. (1987): *A&AS* **71**, 39
- Epchtein, N., Le Bertre, T., Lépine, J. R. D. (1990): *A&A* **227**, 82
- Epchtein, N., de Batz, B., Copet, E., et al. (1994): *Ap&SS* **217**, 3
- Feast, M. W., Glass, I. S., Whitelock, P. A., Catchpole, R. M. (1989): *MNRAS* **241**, 375
- Fouqué, P., Le Bertre, T., Epchtein, N., Guglielmo, F., Kerschbaum, F. (1992): *A&AS* **93**, 151
- Goebel, J. H., Moseley, S. H. (1985): *ApJ* **290**, L35
- Gray, M. D., Ivison, R. J., Yates, J. A., et al. (1995): *MNRAS* **277**, L67
- Greenhill, L. J., Colomer, F., Moran, J. M., et al. (1995): *ApJ* **449**, 365
- Groenewegen, M. A. T., Whitelock, P. A. (1996): *MNRAS* **281**, 1347
- Guélin, M., Lucas, R., Neri, R. (1996): *IAU Symposium n° 170, Twenty-five years of millimeter-wave spectroscopy*
- Guglielmo, F., Epchtein, N., Le Bertre, T., et al. (1993): *A&AS* **99**, 31
- Guilain, C., Maunon, N. (1996): *A&A*, in press
- Guilloteau, S., Omont, A., Lucas, R. (1987): *A&A* **176**, L24
- Gustafsson, B., Eriksson, K., Kiskelman, D., Olander, N., Olofsson, H. (1996): *A&A*, in press
- Habing, H.J. (1996): *A&AR* **7**, 97
- Herman, J., Habing, H. J. (1985): *A&AS* **59**, 523

- Herman, J., Baud, B., Habing, H. J., Winnberg, A. (1985): A&A **14** 3, 122
- Iben, I. (1985): QJRAS **26**, 1
- Iben, I., Renzini, A. (1983): ARA&A **21**, 271
- IRAS Science Team (1986): A&AS **65**, 607
- IRAS Science Team (1988): *IRAS Catalogs and Atlases*, NASA RP-1190
- Jäger, C., Mutschke, H., Begemann, B., Dorschner, J., Henning, T. (1994): A&A **292**, 641
- Jones, T. W., Merrill, K. M. (1976): ApJ **209**, 509
- Jura, M. (1986): ApJ **303**, 327
- Jura, M. (1992): A&AR **2**, 227
- Justtanont, K., Barlow, M. J., Skinner, C. J., et al. (1996): A&A **309**, 612
- Kholopov, P. N., Samus, N. N., Frolov, M. S., et al. (1985): *General Catalogue of Variable Stars*, fourth edition, "Nauka" Publishing House, Moscow
- Kleinmann, S. G., Lysaght, M. G., Pughe, W. L., et al. (1994): Ap&SS **217**, 11
- Knapp, G. R., Morris, M. (1985): ApJ **292**, 640
- Kruszewski, A., Coyne, G. V. (1976): AJ **81**, 641
- Le Bertre, T., Lequeux, J. (1993): A&A **274**, 909
- Le Bertre, T., Epchtein, N., Guglielmo, F., Le Sidaner, P. (1994): Ap&SS **217**, 105
- Le Bertre, T., Epchtein, N., de Batz, B., et al. (1995): in *Calibrating and Understanding HST and ESO instruments*, P. Benvenuti (ed.), ESO Conference and Workshop Proceedings No. 53, p195
- Le Borgne, J. F., Maun, N. (1989): A&A **210**, 198
- Le Sidaner, P., Le Bertre, T. (1996): A&A, in press
- Lindqvist, M., Nyman, L.-Å., Olofsson, H., Winnberg, A. (1988): A&A **205**, L15
- Little, S. J., Little-Marein, I. R., Bauer, W. H. (1987): AJ **94**, 981
- Little-Marein, I. R., Little, S. J. (1988): ApJ **333**, 305
- Lopez, B., Perrier, C., Mékarnia, D., Lefèvre, J., Gay, J. (1993): A&A **270**, 462
- Loup, C., Forveille, T., Omont, A., Paul, J. F. (1993): A&AS **99**, 291
- Lucas, R., Bujarrabal, V., Guilloteau, S., et al. (1992) A&A **262**, 491
- Maun, N., Caux, E. (1992): A&A **265**, 711
- Maun, N., Guilain, C. (1995): A&A **298**, 869
- Maun, N., Cailloux, M., Tilloles, P., Le fèvre, O. (1986) A&A **165**, L9
- McMillan, R. S., Tapia, S. (1978): ApJ **226**, L87
- Mennessier, M.-O., Omont, A. (eds.) (1990): *From Miras to Planetary Nebulae: Which path for stellar evolution?*, Editions Frontières
- Merrill, K. M., Stein, W. A. (1976): PASP **88**, 285 & 294 & 874
- Morris, M., Guilloteau, S., Lucas, R., Omont, A. (1987): ApJ **321**, 888
- Neugebauer, G., Leighton, R. B. (1969): *The Two Micron Sky Survey*, NASA SP-3047
- Neugebauer, G., Habing, G., Van Duinen, R., et al. (1984): ApJ **278**, L1
- Nguyen-Q-Rieu, Bujarrabal, V., Olofsson, H., Johansson, L. E. B., Turner, B. E. (1984): ApJ **286**, 276
- O'Dell, C. R., Handron, K. D. (1996): AJ **111**, 1630
- Olofsson, H. 1994 in *Molecules in the Stellar Environment*, Proceedings of I.A.U. Colloquium n° 146, U. G. Jørgensen (ed.), Lecture Notes in Physics, Springer-Verlag, p113
- Olofsson, H., Carlström, U., Eriksson, K., Gustafsson, B., Willson, L. A. (1990): A&A **230**, L13

- Olofsson, H., Carlström, U., Eriksson, K., Gustafsson, B. (1992): A&A **253**, L17
Omont, A., Loup, C., Forveille, T., et al. (1993a): A&A **267**, 515
Omont, A., Lucas, R., Morris, M., Guilloteau, S. (1993b): A&A **267**, 490
Onaka, T., de Jong, T., Willems, F. J. (1989): A&A **218**, 169
Plez, B., Lambert, D. L. (1994): ApJ **425**, L101
Reid, M.J., Muhleman, D. O., Moran, J. M., Johnston, K. J., Schwartz, P. R.
(1977): ApJ **214**, 60
Reimers, D. (1977): A&A **61**, 217
Shaw, S. J., Zellner, B. (1970): ApJ **162**, L19
Treffers, R., Cohen, M. (1974): ApJ **188**, 545
Truong-Bach, Morris, D., Nguyen-Q-Rieu (1991): A&A **249**, 435
Van der Veen, W. E. C. J., Habing, H. J. (1988): A&A **194**, 125
Van Langevelde, H. J., Van der Heiden, R., Van Schooneveld, C. (1990): A&A **239**,
193
Volk, K., Cohen, M. (1989): AJ **98**, 931
Volk, K., Kwok, S., Stencel, R. E., Brugel, E. (1991): ApJS **77**, 607
Waters, L. B. F. M., Loup, C., Kester, D. J. M., Bontekoe, Tj. R., de Jong, T.
(1994): A&A **281**, L1
Whitelock, P., Menzies, J., Feast, M., et al. (1994): MNRAS **267**, 711
Young, K., Phillips, T. G., Knapp, G. R. (1993): ApJS **86**, 517

Cool Stars Winds and Mass Loss: Observations

Thibaut Le Bertre

DEMIRM, Observatoire de Paris, 61 av. de l'Observatoire,
F-75014 Paris, France
e-mail: LEBERTRE@mesioa.obspm.fr

Abstract. Observational evidences for mass loss from cool stars are reviewed. The emphasis is put on Asymptotic Giant Branch stars which contribute to $\sim 50\%$ of the replenishment of the Interstellar Medium. The aim is to illustrate the richness of the informations provided by the observations obtained in the various wavelength ranges from the optical to the radio. A selection of on-going developments which are potentially important for this theme is presented.

1 Introduction

Cool stars are sometimes surrounded by an expanding circumstellar shell of gas and dust. Most of these mass-losing objects are on the Asymptotic Giant Branch (AGB) of the HR diagram, but some are red supergiants.

Mass loss is important for stellar evolution. For instance, stars of initial mass larger than $1.4 M_{\odot}$, and up to $6-8 M_{\odot}$, will avoid becoming supernovae by losing up to 80% of their initial mass. When nuclear burning stops, and after a spectacular Planetary Nebula phase, their remnants will simply cool down and evolve as white dwarfs of typically $0.6-0.8 M_{\odot}$.

Furthermore, through mass loss, AGB stars contribute to the replenishment of the interstellar medium. Most of the carbon in the Universe is produced in their interiors and a large fraction of the interstellar dust originates in their atmospheres. Mass loss from AGB stars is thus an important factor of the galactic evolution.

For many fields of Astrophysics, it is a necessity to understand the processes of mass loss in these stars and the physics in their circumstellar envelopes. The aim of this lecture is to provide an introduction to the observational study of winds from late-type stars with emphasis on those from AGB stars. Interested readers will find more informations in reviews and conference proceedings. A recent review on "Circumstellar envelopes and AGB stars" can be found in Habing (1996); it is mainly dedicated to oxygen-rich stars. A review on carbon stars was presented by Jura (1992). Conference proceedings are useful to get specific informations on the most recent developments and on works in progress; see for instance Mennessier and Omont (1990). An I.A.U. symposium on "The carbon star phenomenon" (n° 177) was held this year (1996) in Antalya. Other valuable references can be found in Habing (1996, Sect. 1.9).

2 Presentation of AGB Stars

2.1 The Evolution Towards the AGB

Thanks to elaborate codes, the evolution of a star can be numerically simulated in function of its initial mass (or mass on the Zero Age Main Sequence, ZAMS) and of its composition in helium and heavier elements. The physics is complex and sometimes has to be treated with phenomenological parameters (see the lecture by De Greve, this Volume). Depending on the values given to these parameters, the results may differ. However, the general lines of stellar evolution can be reproduced and are now basically understood (Iben and Renzini 1983; see also the pedagogical review of Iben 1985).

On the Main Sequence (MS), stars burn quietly hydrogen in their cores. When hydrogen begins to lack in the core, the star adapts its structure to allow for hydrogen burning around the core. It leaves the MS and, in an HR diagram, moves to the right and reaches the Red Giant Branch (RGB). For stars with a low mass ($\leq 2 M_{\odot}$), the electron gas is degenerated in the hydrogen-exhausted core so that the energy transport is very effective. For these stars the mass of the core on the RGB will increase up to $\sim 0.4 M_{\odot}$ and the luminosity, up to $\sim 2000 L_{\odot}$. At this stage, helium is ignited suddenly at the center (He core flash) and the electron-degeneracy is subsequently lifted. The luminosity drops ($L \leq 50 L_{\odot}$) and, thereafter, helium burns quiescently: the star sets on the Horizontal Branch (HB) of the HR diagram.

More massive stars follow the same kind of evolution after the MS, except that, as their central temperature is higher, they do not develop an electron-degenerate helium-core. They generally reach a lower luminosity on the RGB. However, after helium ignition they set on the HB at a higher luminosity ($L \geq 50 L_{\odot}$).

At this stage (HB), all stars burn helium quietly through the triple- α reaction which produces ^{12}C : $3\ ^4\text{He} \rightarrow\ ^{12}\text{C}$ (^8Be is not stable), and eventually ^{16}O by the capture of another ^4He nucleus. When helium is exhausted in the central parts, the star adapts again its structure so that now a shell where helium is burning surrounds a core containing carbon, oxygen and heavier elements.

For stars with low and intermediate mass ($M \leq 6\text{--}8 M_{\odot}$), the electron gas in this CO core is degenerated. The luminosity increases and the star arrives on the Asymptotic Giant Branch (AGB). The name Asymptotic Giant Branch comes from the fact that, in HR diagrams of globular clusters, the 2 Giant Branches are merging asymptotically.

Stars more massive than $6\text{--}8 M_{\odot}$ do not develop an electron-degenerate CO core. Nuclear fusion proceeds in the core with the synthesis of silicon and heavier elements. They evolve to the right of the HR diagram at almost constant luminosity and pass through a red supergiant (RSG) stage (at least those with a ZAMS mass less than $\sim 40 M_{\odot}$). Their luminosities range from $\sim 2 \cdot 10^4 L_{\odot}$ to $\sim 2 \cdot 10^5 L_{\odot}$. When they are in the RSG stage, they may occupy

a region which overlaps with the region of the HR diagram occupied by AGB stars and can be mistaken. These stars differentiate from AGB stars only by their internal structure.

Finally, objects of $\sim 60 M_{\odot}$ or more evolve in Luminous Blue Variables (LBVs) and probably never reach the region of stars with cool surfaces. They are supposed to be progenitors of Wolf-Rayets (WRs).

The following section will concern only low and intermediate mass stars ($M \leq 6-8 M_{\odot}$).

2.2 The Life on the AGB and Beyond

The AGB is divided into 2 parts: the Early AGB (E-AGB) and the Thermally Pulsing AGB (TP-AGB). On the E-AGB, stars are burning helium quiescently around a CO-core which increases in size with the products of helium combustion (^{12}C and ^{16}O).

When helium is exhausted the star enters a new phase of the AGB (TP-AGB). The combustion of hydrogen starts again in a shell around the core. A new helium layer is formed. Then, He is re-ignited and its rate of combustion increases until the occurrence of a thermonuclear runaway (He shell flash or He thermal pulse). The hydrogen burning layer is pushed outwards and cools; hydrogen combustion stops. The helium burning layer expands and cools also. A new phase of quiet helium burning develops that will last until helium-exhaustion. Then a new cycle starts again. A few tens of such cycles are expected to occur during the TP-AGB phase. For $\sim 10\%$ of the time, He-burning dominates and for the remaining 90%, H-burning. Within a cycle, the typical timescales are 10^4 years for the He-burning phase and 10^5 years for the H-burning phase; the exact durations depend on many parameters (core mass, number of the cycle, abundances, etc.). A thermal pulse lasts for ~ 100 years. During the thermal pulses, many neutrons are produced through reactions like $^{13}\text{C}(\alpha, n)^{16}\text{O}$ or $^{22}\text{Ne}(\alpha, n)^{25}\text{Mg}$. These are used in the production of neutron-rich isotopes such as zirconium (Zr). These isotopes are called s-elements (for slow process elements, by opposition to r-elements, or rapid process elements, which are formed in Nova or Supernova explosions). The elements are building up through neutron capture by nuclei heavier than Fe. For the formation of s-elements, the flux of neutrons is such that the seed nuclei are stable with respect to β -decay.

Therefore, the structure of a star on the AGB is that of a core where hydrogen and helium are exhausted, surrounded by a layer where these 2 elements are burning alternately. The size of the CO core is typically $\sim 10^8$ cm and the temperature, $2-4 \cdot 10^8$ K. Above the nuclear burning shell, there is a convective envelope of several 10^{13} cm radius (Fig. 1).

During the periods of hydrogen burning, the average luminosity of an AGB star is given by an empirical relation due to Paczynski:

$$L \approx 6 \times 10^4 L_{\odot} \times (M_{\text{core}}/M_{\odot} - 0.5).$$

On the AGB, the mass of the CO-core grows typically from $\sim 0.6 M_{\odot}$ to

$\sim 0.8 M_{\odot}$. The expected average luminosity of a star on the TP-AGB is thus in the range $5 \cdot 10^3$ – $2 \cdot 10^4 L_{\odot}$. Whatsoever, the CO core does not grow beyond the Chandrasekhar limit ($1.4 M_{\odot}$), so that, in any cases, the average luminosity of an AGB star is always expected to be below $\sim 5 \cdot 10^4 L_{\odot}$.

An important feature of the AGB is the phenomenon of dredge-up. After a He thermal-pulse, the base of the convective stellar envelope moves inward and reaches the zone where, during the pulse, carbon was synthesized. This element, together with other recently processed elements (e.g. the neutron-rich isotopes), can be brought to the surface. In such case, the photosphere exhibits overabundances of these elements. In that respect the C/O abundance ratio is of great importance. For RGB stars and stars on the E-AGB, it is expected to be ~ 0.5 . The photospheres of these stars have an effective temperature in the range 2000–3000 K. Their spectra are characterized by the presence of CO and oxygen-rich molecules such as TiO, VO or H₂O. They are said to be of M type. As long as the C/O ratio is smaller than 1, the star is said to be oxygen-rich. But with the arrival of s-elements at the surface new metal oxides, such as ZrO or YO, are formed; the stars in which the corresponding bands are detected are classified as of S type. The spectra of S stars are also characterized by lines of Technetium (Tc), an unstable s-element with half-lifetime $\leq 2 \cdot 10^5$ years. If the dredge-up is efficient enough, or after several thermal pulses, the C/O ratio may become larger than 1. The spectra of these carbon-rich stars (C type) are dominated by CO and carbon-rich molecules such as C₂, CN, HCN, C₂H₂, etc. Carbon stars show also the presence of s-elements in their spectra (Little et al. 1987).

It is worth noting that RSG stars do not experience dredge-up of carbon. Except in the case of mass-transfer across a binary star, the enhancement of carbon and of s-elements at the surface of a star is an unambiguous evidence that it is on (or has gone through) the TP-AGB.

Another important feature is the instability of the stellar atmosphere due to hydrogen opacity effects (κ mechanism, cf. De Greve, this Volume). AGB stars are generally variable and may pulsate as long-period variables ($P \geq 100$ days). The pulsations are not always periodic. The lightcurves are of various kinds. The classification which is commonly used is based on visual observations obtained through the last ~ 100 years (Kholopov et al. 1985).

- The **Mira** variables have a relatively well-defined period, although their lightcurves are not reproducible from cycle to cycle. The periods are found in the range 100–1000 days and the amplitudes in the visual are larger than 2.5 mag. The prototype and eponymous representative of this class is *o*Ceti (Mira Ceti).
- The **Semi-Regular** variables (SR type) are periodic but sometimes without a well-defined period. The amplitudes of the lightcurves are smaller than 2.5 mag. One makes the distinction between SRa and SRb. For the first subclass, SRa, the period is well-defined, but the shape of the lightcurve shows strong variations. For the second one, SRb, the periodicity is very poorly

defined, with strong variations on the duration of each cycle.

- The **irregular** variables (Lb type) are those for which there is no evidence of periodicity.

This classification is somewhat artificial, but has proven to be of some use. The distinction between Miras and SRa variables is probably unjustified, the SRa differing from the Miras only by the smaller amplitude of their lightcurves. Similarly, the separation between SRb and Lb variables is somewhat arbitrary and often dependent on the sampling of the observations.

The stellar atmosphere instability seems to be the cause of a third important feature (which is the topic of this lecture): mass loss. In the upper part of the atmosphere which is extended by its instability, refractory elements such as C or Si condense into dust particles. Once formed these particles are submitted to radiation pressure and are accelerated outwards, dragging the gas with them. It is by this mechanism (which is treated in detail by Sedlmayr and Winters, this Volume) that AGB stars surround themselves with an expanding circumstellar shell of dust and gas (Fig. 1).

Mass loss rates of typically 10^{-8} – $10^{-7} M_{\odot} \text{ yr}^{-1}$ are commonly observed, but they may reach values of several $10^{-5} M_{\odot} \text{ yr}^{-1}$. The mass loss phenomenon will culminate with the ejection of almost the complete atmosphere. The remaining atmosphere contracts and the star moves rapidly to the left of the HR diagram at almost constant luminosity. The surface temperature grows to several 10^5 K. For a short time (a few 10^4 years), the remnant will ionize the surrounding expanding shell (which at this stage is called a Planetary Nebula, PN) and then, after dispersion of the PN, cools to become a white dwarf on a timescale of a few 10^9 years.

An important effect of mass loss for the stellar evolution of AGB stars is to limit the growth of the CO core. It will never reach the Chandrasekhar limit for a stable nuclear-fuel-exhausted core ($1.4 M_{\odot}$). It is because of mass loss that intermediate mass stars evolve into white dwarfs through the PN phase instead of terminating their life in a Supernova explosion.

3 Evidence for Mass Loss in the Optical Range

3.1 Spectroscopy

By observing the companion of a mass-losing star in a binary system, one may detect absorption lines which reveal the presence of the wind. In fact, the first detection of a large-scale circumstellar wind around a late-type star was done in this way by Deutsch (1956). He observed stationary absorption lines (NaI, CaI, CaII, FeI) in the spectrum of the spectroscopic binary α^2 Her (G5III + A3V?) due to the envelope of α^1 Her (M5Ib-II)¹. He evaluated the mass loss rate to $\sim 3 \cdot 10^{-8} M_{\odot} \text{ yr}^{-1}$. As the distance on the sky of the 2 stars is

¹ Although, it has been classified spectroscopically as a supergiant, its luminosity places it on the AGB (Reimers 1977)

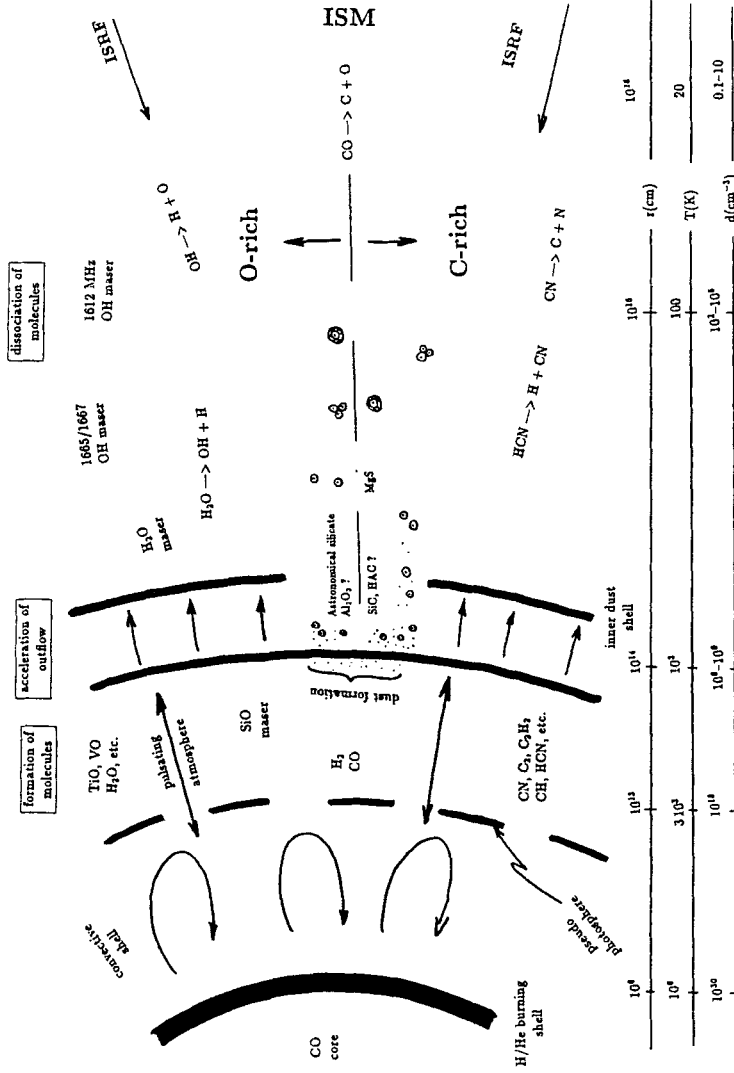


Fig. 1. A schematic view of a mass-losing AGB star. The numbers are only indications on the orders of magnitude. ISM stands for interstellar medium, ISRF for interstellar radiation field, and HAC for hydrogenated amorphous carbon. For comparison, the solar radius, R_{\odot} , is $\sim 7 \cdot 10^{10}$ cm, the astronomical unit, $\sim 1.5 \cdot 10^{13}$ cm, and the parsec, $\sim 3 \cdot 10^{18}$ cm

~ 5 arcsec, he could conclude that the wind extends to at least 1000 a.u. and lasted at least 500 years so that the quantity of matter in the α^1 Her shell is $\geq 10^{-5} M_{\odot}$. The agents responsible of such absorptions in companion spectra may be atoms, molecules or more complex carriers. For instance, Le Bertre and Lequeux (1993) could show that some carriers of the Diffuse Interstellar Bands are present in the winds of carbon stars.

Furthermore, the wind of the mass-losing giant modifies its spectrum by scattering. Two cases have to be considered: scattering by dust and resonant scattering by atoms. In the first case, outflowing grains are scattering the stellar light redshifted by an amount corresponding to the **dust** expansion velocity, V_d . If the Circumstellar Dust Shell (CDS) is optically thin and spherically symmetric, the resulting scattered spectrum is simply redshifted by $\Delta\lambda/\lambda = V_d/c$. In such conditions, it should be possible to measure the dust expansion velocity. The application is not easy. In the data, the scattered spectrum is combined with the stellar spectrum. The CDS may not be spherically symmetric, etc. Furthermore, the stellar atmosphere is pulsating with radial velocity amplitude of same order of magnitude (a few km s^{-1}). The observations are difficult to interpret (Dougados et al. 1992) and, up to now, the results have been disappointing (V_d smaller than V_{gas} !).

For resonant scattering, the absorption is shifted to the blue by an amount corresponding to the **gas** expansion velocity, V_g . Again in the case of an optically thin medium and of a spherical Circumstellar Shell (CS), the photons are re-emitted on average at the stellar velocity. On the stellar spectrum, the absorption lines (e.g. NaI, KI) are skewed to the blue (Bernat and Lambert 1975). On the other hand, if the envelope can be separated from the central star, one observes the lines in emission (Guilain and Maunon 1996 and ref. therein). In the case of an optically thin CS, the lines are centered at the stellar velocity. (However, note that in general the sodium lines at 5890 and 5896 Å are of comparable intensity so that the optically thin hypothesis does not hold.) This kind of observation allows to derive the flux of the corresponding resonant element (assuming that it is not depleted on the grains). It gives also constraints on the photoionization rates, electronic densities, gas-to-dust ratios, etc. (Maunon and Caux 1992). Observations of the KI emission from CSs around carbon stars and their exploitation are discussed in details by Gustafsson et al. (1996).

Spatially resolved spectroscopy in the optical range is a very sensitive technique to detect winds with low mass-loss rate around nearby late-type stars. For instance Maunon and Guilain (1995) have detected the resonant emission of NaI around β Peg, a nearby (~ 60 pc) giant of type M2III which is very likely on the RGB and for which the mass loss rate is evaluated to be $\sim 10^{-9} M_{\odot} \text{ yr}^{-1}$. It is worth noting that this result is one of the few direct observational evidences for mass loss during the first ascent of the giant branch.

3.2 Imagery

Direct imaging of CS is difficult and has emerged only recently. The extreme mass-losing carbon star CW Leo (IRC +10216) is seen diffuse and elongated on the Schmidt plate obtained at Palomar. CCD images obtained at the CFH telescope by Crabtree et al. (1987) show an envelope of radius ~ 40 arcsec. It appears to be clumpy with a structure composed of several discrete shells evoking a non-uniform mass loss. To the difference of the central peak which is due to dust-scattered stellar light, the external shells are due to scattered galactic light (ISRF). These shells are at the limit of detectability from the ground because their brightness is near or below the sky level. Similar structures might also be detectable around other AGB stars. Their studies would give insights on the geometry of the mass loss phenomenon and on its time variability.

Mapping in resonant-scattered emission-line should be extremely rewarding because, with resonant-scattering, one benefits of a contrast advantage as compared to dust scattering. An image in the NaI 5890 Å line of the envelope of μ Cep (actually a red supergiant) shows evidence of asymmetry in the wind and of multiple shells (Mauron et al. 1986). Plez and Lambert (1994) have obtained maps of the KI (7699 Å) emission around several AGB stars and found evidences of large asymmetries in their winds.

Spectacular images have been obtained from space with the Hubble Space Telescope. Images of the post-AGB source, CRL 2688, reveal a multi-shell structure as for IRC +10216. Images of the Planetary Nebula, NGC 7293 (Helix Nebula), show the existence of many small globules (~ 100 a.u.) of dense material ($\sim 10^{-5} M_{\odot}$) which are illuminated by the central star (O'Dell and Handron 1996). These globules may originate in condensations of matter inside the circumstellar envelope during the AGB phase. It has even been speculated that they could be the remnants of concentrations in the AGB stellar atmosphere like those which are revealed by the SiO maser phenomenon (see Sect. 5.3).

3.3 Polarimetry

Polarization is induced by scattering on dust. The radiation is linearly polarized in the direction perpendicular to the plane of scattering. Polarimetry is a difficult technique because of the instrumental and observational effects. For instance, polarization of the light can be induced by the optics of the telescope itself if circular symmetry is broken like in Coudé or Nasmyth foci. Also the sky background can be polarized by Moon light (and Sun light, outside the strict "astronomical" night). Usually, one defines the position angle on the sky in which the radiation is polarized, and the degree of polarization, p , which is the percentage of polarized light (see the lecture by Bjorkman, this Volume). The wavelength dependence of p gives an indication on the size of the scattering grains.

At low spatial resolution, with a diaphragm, one measures the light integrated from the star and the whole shell. In the case of a spherically symmetric dust shell with randomly oriented grains, there should be no net effect. Unless grains in the CDS are elongated and oriented in a preferential direction (which, in AGB stars, seems unlikely), the positive detection of polarization indicates that the geometry of the shell is non-spherical. Polarization degrees of a few percent are generally found (e.g. Kruszewski and Coyne 1976). In some cases, polarization degrees of $\sim 10\%$ have been detected, for instance in IRC +10216 (Shawl and Zellner 1970). Apart from pointing to asymmetries, these results are difficult to interpret.

More rewarding are the spatially resolved polarimetric observations. As the polarization degree and orientation change with position around the central star, observational and instrumental effects are more easy to control (McMillan and Tapia 1978). The results give indications on the real morphology of the dust shell. These observations are especially interesting when they can be complemented with emission-line maps. For instance, the polarization map around μ Cep (Le Borgne and Mauron 1989) shows a large envelope (~ 1 arcmin in diameter) with a structure composed of 2 dust shells which agrees with the structure seen in NaI emission (see previous section).

4 The Infrared Range

Circumstellar Shells (CS) are made of gas and dust. The dust is absorbing the stellar radiation and re-emitting it at longer wavelengths in the infrared (IR) range. Dust grains have spectral signatures that will appear in this range. Although only a small fraction of the matter is in dust ($\sim 0.5 - 1\%$), the CS may be so dense that the central star is completely hidden and the source shows up only at infrared wavelengths. Many mass-losing AGB stars have only been revealed in the course of IR surveys and they can hardly be studied in the optical range. For these reasons, the IR range is extremely important for the study of all mass-losing AGB sources.

4.1 Ground-Based Observations

Astronomical observations in the IR are hampered by two kinds of difficulties. First, the molecules in the Earth atmosphere (H_2O , CO_2 , etc.) are absorbing most of the light and the observations are possible only in a few spectral windows. Second, the telescope, the instrument and the atmosphere are radiating thermally at $\lambda \geq 2\ \mu\text{m}$. This emission produces a background which has to be subtracted from the data in order to extract the astronomical signal. Even if this subtraction could be done perfectly, the noise in the background limits the detectability of the sources.

Photometric bands have been defined so that they fit into the atmospheric windows: J ($1.25\ \mu\text{m}$), H ($1.65\ \mu\text{m}$), K ($2.2\ \mu\text{m}$) or K' ($2.1\ \mu\text{m}$), L ($3.6\ \mu\text{m}$)

or L' (3.8 μm), M (4.6 μm), N (10 μm) and Q (20 μm). The exact values of the effective wavelengths and bandwidths have not been standardized for practical reasons and depend on the instruments so that any comparison must be done with a lot of care.

Photometry of AGB sources through these bands has been done extensively allowing the determination of the energy distributions from 1 to 20 μm for many objects. All mass-losing source spectra exhibit an infrared continuum, in excess of the stellar spectrum, which is due to thermal emission by dust. Two kinds of spectra differentiate clearly. Those of carbon-rich sources are like blackbodies whereas those of oxygen-rich sources present spectral features at 10 and 20 μm either in emission or in absorption depending on the optical depth of the CS (Jones and Merrill 1976). Carbon-rich sources show a weak emission feature at 11 μm . As compared to the C-rich sources, the O-rich ones exhibit a larger excess of radiation at mid-infrared (10–20 μm) wavelengths relatively to the near-infrared (1–5 μm).

The spectral features have been studied at low spectral resolution ($\lambda/\Delta\lambda \approx 50$ to 100) since ~ 25 years (e.g. Merrill and Stein 1976). They are broad ($\Delta\lambda \approx 1 \mu\text{m}$) and smooth, without sub-structures. The 10 and 20- μm features seen in O-rich source spectra have been ascribed to silicate grains with an amorphous mineralogical structure (Day 1976). However, the continuum opacity, in particular at $\lambda \leq 8 \mu\text{m}$, is higher than expected and not well explained. As the match between the observations and the laboratory data is not entirely satisfactory, the concepts of "dirty" silicate or astronomical silicate have been introduced. The 11- μm feature in C-rich source spectra has been ascribed to silicon carbide (SiC, Treffers and Cohen 1974). Cohen (1984) distinguishes 2 types of SiC features that he relates to different grain mineralogical structures. In some extreme cases, the SiC feature can be seen in absorption (Justtanont et al. 1996). The continuum opacity is generally attributed to some kinds of hydrogenated amorphous carbon (HAC). In addition, a feature centered at $\sim 30 \mu\text{m}$ has been observed in several C-rich sources and ascribed to magnesium sulfide (MgS, Goebel and Moseley 1985). These identifications are consistent with the C/O abundance ratio of the central star. For an M star ($\text{C/O} < 1$) all carbon should be locked into the CO molecule because it is very stable (the dissociation energy of CO is 11 eV)². Carbon and/or carbonaceous molecules cannot contribute to the dust composition. For a C star ($\text{C/O} > 1$) the reverse applies; oxygen cannot enter into the composition of the dust.

In conclusion, M and C stars differentiate clearly in the IR range by the emission of dust. The differences are seen in the gross shapes of the broad-band energy distributions and in the spectral features and denote different properties of the dust in their CS. The IRAS photometric data (Sect. 4.2)

² Here some caution should be exercised as the presence of a hot companion or of a chromosphere may be a source of UV radiation photodissociating a part of the CO molecules.

complete profitably ground-based spectra up to $100\ \mu\text{m}$. From the resulting broad-band energy distributions and with the help of numerical models, it is possible to estimate the dust mass outflow. Values in the range 10^{-9} – $10^{-6}\ \text{M}_{\odot}\ \text{yr}^{-1}$ are commonly found (e.g. Le Sidaner and Le Bertre 1996). For the 2 kinds of CDS, the optical depth is well correlated to the infrared colors. Therefore, the colors can be used as indicators of the dust mass loss rate.

Some sources have been monitored in the infrared range. The amplitudes are generally decreasing with wavelength. The lightcurves show irregularities, but less pronounced than in the optical. Sometimes, intermediate extrema are seen on the lightcurve rising-branches. There is also a modulation of the mean infrared brightness on a timescale of a few stellar periods. The hydrodynamical models of dust formation developed by the Berlin's group (see the lecture by Sedlmayr and Winters, this Volume) provide a natural explanation to these lightcurve features.

With the development of IR and radio techniques, new sources have been discovered. Among them, several long-period variables were found. They have properties which connect them to the Miras. The periods of the sources detected only in the IR are generally longer than those of optical Miras. Some extreme sources (OH/IR, see Sect. 5.2) have periods up to 2000 days.

For each kind of source (C-rich and O-rich), one finds a loose correlation between the periods and the IR colors or the amplitudes of the lightcurves. This tends to show that mass loss depends on stellar variability. Also, the IR colors are well correlated with the amplitudes. However, this is only an effect of the shape of the spectrum; for Miras, the bolometric amplitude is always $\sim 1\ \text{mag}$.

Finally, for Miras, there is a correlation between the period and the luminosity. The relation may depend slightly on the type (M or C; Feast et al. 1989) and on the metallicity, but the latter has been challenged (Whitelock et al. 1994). There are also correlations between the period and the magnitudes, but because of the circumstellar extinction, they have to be handled with care for mass-losing Miras. However, the K magnitude seems reliable for this purpose since it should be affected only in the most extreme cases (Groenewegen and Whitelock 1996).

4.2 IRAS

The exploration from the ground of the IR sky is difficult, especially at $\lambda \geq 10\ \mu\text{m}$, because of the large thermal background and because of the poor atmospheric transmission. The Infrared Astronomical Satellite (IRAS) mission has been developed to conduct a survey of the sky in 4 IR bands with a cooled telescope (Neugebauer et al. 1984). The bands are centered at 12, 25, 60 and $100\ \mu\text{m}$ and have a width, $\Delta\lambda/\lambda \approx 0.5$ – 1.0 . The beams are $\sim 2\ \text{arcmin}$ wide, but the positional accuracy is generally much better ($\sim 10\ \text{arcsec}$). A catalogue of 2×10^5 sources (Point Sources Catalog, PSC) with positions and fluxes has been produced (IRAS Science Team 1988). In

addition, a low resolution spectrometer (LRS) provided good quality spectra, at a resolution ~ 50 , for about 6000 sources (IRAS Science Team 1986, Volk and Cohen 1989, Volk et al. 1991).

Several classification schemes of the LRS spectra have been developed, but the most commonly used is the original IRAS Science Team one. It is a two-digit system where spectra with a $10\text{-}\mu\text{m}$ feature in emission are registered as 2n, with a $10\text{-}\mu\text{m}$ feature in absorption as 3n and with an $11\text{-}\mu\text{m}$ feature in emission as 4n (n being an index of the feature strength). More than half of the LRS spectra were obtained on AGB stars and most pertain to one of these classes: O-rich sources are normally found in classes 2n and 3n, and C-rich ones, in classes 4n. However, the LRS classes should be handled with care as some O-rich sources, with a self-absorbed $10\text{-}\mu\text{m}$ feature mimicking the $11\text{-}\mu\text{m}$ emission feature, appear in a 4n class. In these cases the $20\text{-}\mu\text{m}$ feature is clearly seen in emission and a visual inspection is generally sufficient to correct the classification. Furthermore, many AGB sources with extreme properties are found in other classes. For instance, Omont et al. (1993a) find sources with very cold C-rich shells in classes 2n (especially 21 and 22) and also in other less populated classes. In addition to the silicate feature at $10\text{ }\mu\text{m}$, there is evidence in the LRS spectra of some oxygen-rich sources for an emission feature at $12\text{ }\mu\text{m}$ which has been ascribed to Al_2O_3 (Onaka et al. 1989). Finally, Little-Marenin and Little (1988) have found that the spectra of S-type stars show usually an emission feature peaking around $10.8\text{ }\mu\text{m}$.

The IRAS photometric data have been used to build IRAS color-color diagrams. For stellar sources the most useful one is the $[12\text{ }\mu\text{m}]\text{--}[25\text{ }\mu\text{m}]$ versus $[25\text{ }\mu\text{m}]\text{--}[60\text{ }\mu\text{m}]$ diagram which has been studied in details by van der Veen and Habing (1988, VH). They have divided this color diagram in 10 regions and have evaluated the composition of the population contributing to each region on the basis of the LRS spectra of identified sources. The region I, corresponding to blackbody colors $T_{\text{BB}} \geq 2000\text{ K}$, contains mainly stars without circumstellar emission. Regions II, III (a and b), and IV contain a majority of O-rich sources, and VII, C-rich sources, but without clear separation. For instance, Epchtein et al. (1990) found many carbon stars in regions II and III. Conversely, Guglielmo et al. (1993) found a majority of O-rich sources in region VII in contradiction with VH (they suspect selection biases in their own sample and in the VH one). Region V contains mainly Planetary Nebulae (PN) and proto-PN whereas regions VI (a and b) contain sources with cold dust at large distances from the central star which can be indifferently C-rich or O-rich. The salient presence of cold dust radiating at $60\text{ }\mu\text{m}$ can be explained as due to an interruption in the mass loss rate for $\sim 10^3\text{--}10^4$ years (or at least a significant reduction). Chan and Kwok (1988) have shown that such a process can explain the positions of the sources in region VI.

The IRAS colors diagram is therefore of some, but limited, use to discriminate O-rich sources from C-rich sources. As O-rich sources present a larger excess in the $10\text{--}20\text{ }\mu\text{m}$ range relatively to the $1\text{--}5\text{ }\mu\text{m}$ range than the

C-rich sources (Sect. 4.1), a better approach is to combine an IRAS color with a near-IR one. Epchtein et al. (1987) have shown that, in a K-L' versus $[12\ \mu\text{m}]-[25\ \mu\text{m}]$, the two populations are clearly separated. They describe a classification scheme of AGB sources based on these two colors.

Although it is difficult to characterize the sources from the IRAS colors, for sources of known type the IRAS colors are indicators of the mass loss rate. On this basis, Jura (1986) evaluates the mass loss rates of AGB sources and finds a correlation between the mass loss rates and the periods of the central stars suggesting again a dependency of mass loss on stellar variability.

In spite of the large IRAS beams, some sources have been resolved at 60 and 100 μm (Young et al. 1993). Indeed, for an AGB source of $2\ 10^4\ L_{\odot}$, dust emission at 60 μm is expected up to a distance where dust is at $\leq 50\ \text{K}$, i.e. $\sim 0.1\ \text{pc}$. Therefore, if at a distance from the Sun $\leq 500\ \text{pc}$, such an object should be resolved at 60 μm . However, this emission is difficult to recognize as it appears in the wings of the central core image. On the other hand, in the case of interrupted mass loss, the shell of cold dust can in principle be resolved more easily. Using an elaborate image reconstruction technique, Waters et al. (1994) have resolved at 60 μm the shell of U Hya. The shell is clearly detached from the central star. Waters et al. show that the formation of such a shell required a mass loss rate of $0.5\ 10^{-6}\ M_{\odot}\ \text{yr}^{-1}$, a factor 25 higher than the present-day rate.

5 The Radio Range

Most of the outflowing material from AGB stars consists of atomic and molecular gas (dust accounts for $\leq 1\%$). Therefore, important information should be expected from the molecular emission in the radio range. Unfortunately, the most abundant molecule, H_2 , is hard to detect. After H_2 , CO is the dominant molecular species in circumstellar envelopes. Depending on the C/O abundance ratio, other molecules are expected: H_2O , HCN, etc. Indeed lines of CO, HCN, OH and SiO have been detected in many sources (see for instance the catalogues of observations by Benson et al. 1990 for H_2O , SiO and OH, and by Loup et al. 1993 for CO and HCN). With the improvements in receiver sensitivity, more and more molecules have been detected, such as the cyanopolyynes HC_{2n+1}N with n up to 5, illustrating the richness of the circumstellar chemistry (see e.g. Olofsson 1994).

An immediate contribution of these observations is the determination of stellar radial velocities and circumstellar expansion velocities with a great accuracy ($\sim 1\ \text{km s}^{-1}$). Gas expansion velocities are found in the range $5\text{--}35\ \text{km s}^{-1}$, with the majority in the range $10\text{--}20\ \text{km s}^{-1}$. The mass loss rates can also be estimated, mainly from CO data, and are found in the range $10^{-8}\text{--}10^{-4}\ M_{\odot}\ \text{yr}^{-1}$. Furthermore, due to the numerous chemical reactions which are at work and to the presence of the Interstellar Radiation Field (ISRF) which is more or less attenuated by dust, the composition of the CS presents

a stratified structure. For instance, OH is formed by the photodissociation of H_2O ($\text{H}_2\text{O} + h\nu \rightarrow \text{OH} + \text{H}$) and destroyed, also by photodissociation, but further away from the central star (Fig. 1). The studies of the molecular emission lines can serve to determine this structure and to probe the physical conditions in the different layers. Also, the history of mass loss can be studied. Finally, the radio lines offer the possibility of determining isotopic abundance ratios.

The molecular emission may be thermal or non-thermal (maser). We first examine the CO emission which is a good example of thermal emission and then the OH maser emission at 1612 MHz.

5.1 CO Emission

CO is the most abundant molecule after H_2 ; the latter, being symmetric (as N_2 , C_2H_2 , etc.), has no rotational transition. It is expected in both kinds of sources, O-rich and C-rich. The rotation lines J(1-0) at 115 GHz (2.6 mm) and J(2-1) at 230 GHz (1.3 mm) have been detected in many nearby galactic objects (the catalogue of Loup et al. 1993 lists about 400 sources). Higher-J transitions have been observed in only a few sources, not so much because they would be less intense (in fact they may be more intense) but rather because of the atmospheric extinction in the sub-millimeter range.

The line profiles depend on the CO-shell optical depth and on the relative angular sizes of the telescope beam and of the shell. The lines are not found to be variable which can be understood as CO is excited mainly by collisions with H_2 . In general, the ^{12}CO lines are optically thick and the ^{13}CO lines, optically thin. Mass loss rates can be derived from the CO profiles assuming a CO/H abundance ratio (Knapp and Morris 1985, Loup et al. 1993). A detailed modelling taking into account the beam profile is necessary to interpret consistently the different lines. In such case, the physical conditions through the shell and the mass loss history can be derived (Truong-Bach et al. 1991).

The CO molecule is photodissociated by UV lines rather than by the continuum as most other molecules. Therefore, CO is self-shielded efficiently and is expected at much larger radii than the other species. Indeed, mapping has shown that CO may be found at distances up to $\sim 10^{18}$ cm from the central star. In some cases, the CO emission has been shown to arise in an expanding detached shell (Olofsson et al. 1990). The sources which show such a pattern are also known to have an excess at $60 \mu\text{m}$. This is another evidence for strong variation of mass loss on a scale of a few 10^3 years. For instance, a CO shell of $\sim 5 \cdot 10^{17}$ cm radius and $\sim 10^{17}$ cm thickness has been found around the carbon star S Scuti (Olofsson et al. 1992). The present mass loss rate would be $\sim 3 \cdot 10^{-8} M_{\odot} \text{ yr}^{-1}$ as compared to $\sim 4 \cdot 10^{-5} M_{\odot} \text{ yr}^{-1}$ during the shell formation, 10^4 years ago.

5.2 OH Maser Emission

In the non-excited states (fundamental state, $v=0$), the rotational levels of OH are split into 4 components. The selection rules allow 4 transitions at 18 cm between these components. For the ground level, they are referred to as the 1665 and 1667 MHz main lines (no change in the angular momentum, $\Delta F=0$), and as the 1612 and 1720 MHz satellite lines ($\Delta F=1$). The emission lines are so intense that explanations based on maser amplification have to be invoked. The line at 1720 MHz is observed only in early-type pre-main sequence stars whereas the 3 other lines are found in evolved stellar sources.

The maser emission associated to late-type stars is said to be of type I if one of the main lines dominates, and of type II if it is the satellite line. The emission is generally variable with the same period as the central source. This is an indication of a radiative excitation. For the type II masers, Elitzur et al. (1976) have developed a model of excitation by IR photons at $35\ \mu\text{m}$ which produce a strong inversion of the populations in the ground state levels connected by the 1612 MHz line. The maser emission arises in a shell of a few 10^{16} cm radius where the gas is at a temperature, $T_{\text{gas}} \approx 100\text{--}200$ K, and the density, $n_{\text{H}_2} \approx 10^5\text{ cm}^{-3}$ (Bujarrabal et al. 1980). The line has a two-peak profile with the peaks of emission emanating from the far and near sides of the expanding shell. This model has been widely confirmed by the observations. For instance, monitorings have shown that there is a delay of $\sim 10\text{--}30$ days between the variations of the two peaks which translates to an OH-shell radius $\sim 1\text{--}5\ 10^{16}$ cm (Herman and Habing 1985).

Radio surveys of the Galactic Plane at 1612 MHz have led to the discovery of many maser sources with unidentified counterparts. With subsequent searches, IR sources which radiate most of their energy in the mid-infrared have been found. They are variable with periods in the range 500–2000 days. Their properties connect them to the Miras or the red supergiants. These objects, without counterpart in the optical/NIR range, are called (type II) OH/IR sources.

High resolution maps (≤ 1 arcsec) have been obtained with radio interferometers, the Multi Element Radio Linked Interferometer Network (MERLIN) and the Very Large Array (VLA). The velocity resolved maps show spherical shells which sometimes break into individual components (Booth et al. 1981, Herman et al. 1985). The combination of these maps with the measurements of the phase lags between the two peaks of the line profile should, in principle, allow a direct determination of the source distances (van Langevelde et al. 1990).

The OH emission has also been probed with Very Long Baseline Interferometry (VLBI) techniques which give access to scales ~ 0.01 arcsec. It is resolved in emission spots of size $\sim 10^{15}$ cm with brightness temperature in the range $10^8\text{--}10^9$ K (Reid et al. 1977).

5.3 Other Molecules

In oxygen-rich sources, H_2O is expected to be the second most abundant molecule with microwave transition (after CO, because O_2 and N_2 have no such transition), up to the point where it is photodissociated. Unfortunately (?), it is abundant in the Earth atmosphere which makes its detection difficult. Nevertheless, maser lines have been discovered at 22 GHz (1.35 cm). This emission is present in O-rich sources. The intensities and the line profiles are strongly, and erratically, variable. High-resolution imaging (VLA/VLBI) has shown that the emission arises in spots of a few 10^{13} cm spread in a shell of $\sim 10^{15}$ – 10^{16} cm diameter.

Similarly, in carbon-rich sources, HCN is the second most abundant molecule with microwave transition (C_2H_2 is symmetric like N_2), up to the point where it is photodissociated. Thermal emission ($J = 1-0$, 88.6 GHz) has been detected in many carbon-rich sources and, surprisingly, also in some oxygen-rich sources (Lindqvist et al. 1988). Unfortunately, it is radiatively excited, which makes difficult the evaluation of its column density. A maser emission has also been found in one C-rich source (Guilloteau et al. 1987).

Another important molecule, in O-rich sources, is SiO. It is expected to be abundant in the region below the dust condensation layer ($\leq 10^{14}$ cm, Fig. 1) and depleted above ($\geq 10^{15}$ cm). Thermal emission has been detected in the $v = 0$ level ($J = 1-0$, 43 GHz, up to $J = 5-4$). The lines are weak indicating depletion by a factor ≥ 10 . In fact, the emission is confined in a region of a few 10^{15} cm in which SiO is partly condensed (Lucas et al. 1992). Maser emission has been detected in the excited states ($v = 1, 2, 3$, with J up to 5). Lines corresponding to transitions between higher rotational states are theoretically expected, but difficult to detect (Gray et al. 1995). The maser lines are narrower than the thermal lines suggesting that they form in a more interior region. Indeed, VLBI measurements show that the emission arises in spots of $\sim 10^{13}$ cm located in a ring of diameter of a few 10^{14} cm (Diamond et al. 1994, Greenhill et al. 1995). In conclusion, to the difference of the thermal emission, the maser emission is more related to the extended atmosphere of evolved stars than to their winds; therefore, they can be used to study the region at the base of the dust-flow (Doel et al. 1995).

Many other lines have been found in CSs around evolved stars, for instance those of S-bearing molecules: SiS, H_2S , SO_2 , SO, CS, OCS (Nguyen-Q-Rieu et al. 1984, Morris et al. 1987, Omont et al. 1993b). Also, organic molecules have been detected (mainly in the prototypical carbon star: IRC +10216), HC_{2n+1}N and C_nH (with n up to 6), and molecular rings, C_3H_2 and SiC_2 . Recently, C_8H has been discovered by Cernicharo and Guélin (1996).

For all the molecular lines, high-resolution imaging is important because the radial structures of the CSs can be studied for each of the corresponding chemical species. This gives important constraints on the physical and chemical processes leading to the observed molecules (Bieging and Nguyen-Q-Rieu 1988). Also one may discover deviations from spherical symmetry and inves-

tigate the circumstellar gas clumpiness (Guélin et al. 1996). Finally, with a velocity resolution of $\sim 1 \text{ km s}^{-1}$, departures from the constant outflow velocity can be revealed and quantified. In particular, imaging in the thermal SiO lines will be especially useful to study the condensation of SiO in dust and the acceleration of the gas in the dust-formation zone (Lucas et al. 1992).

6 Present Developments

6.1 High Spatial Resolution in the Optical and IR Range

Ground-based observations in the optical and infrared ranges are limited by the effects of the atmosphere on the image quality. At a wavelength λ , a telescope of diameter D should give a resolution $\theta \sim \lambda/D$ which corresponds to the diffraction limit (e.g. if $D = 1 \text{ m}$ and $\lambda = 0.5 \mu\text{m}$, $\theta \sim 0.1 \text{ arcsec}$). However, in a good astronomical site, the atmospheric turbulence limits the resolution to a value called the seeing, typically $\phi \approx 1 \text{ arcsec}$. This limit depends on wavelength as $\phi \propto \lambda^{-1/5}$, so that in principle better images can be obtained in the IR range. Several techniques have been developed to improve the spatial resolution up to the diffraction limit, for instance speckle interferometry and more recently adaptive optics. Also, there have been attempts to go beyond the diffraction limit of a single telescope by building arrays of telescopes coherently phased (interferometers).

Improving the spatial resolution in the optical range and up to $\sim 2 \mu\text{m}$ should give access to features at the surfaces of stars which may be correlated to structures in the circumstellar envelopes. As dust is scattering preferentially in the optical range, it would give access also to the structures in the inner dust shells. On the other hand, infrared wavelengths from $3 \mu\text{m}$ to $20 \mu\text{m}$ trace the grains thermal emission from the region of dust formation to the region where dust has cooled to $\sim 100 \text{ K}$ and has reached its terminal velocity.

The expected radius of a typical AGB star is $\sim 1 \text{ a.u.}$, of its inner dust shell $\sim 10 \text{ a.u.}$, and of the region where dust is at $100 \text{ K} \sim 1000 \text{ a.u.}$ (Fig. 1). For an object at a distance of 1 kpc , the diameter of the inner shell would be $\sim 0.02 \text{ arcsec}$, and of the region with dust at $100 \text{ K} \sim 2 \text{ arcsec}$. A hampering difficulty is the contrast between the emission from these regions and the emission from the central source. It is generally so large that the shell is simply lost in the wings of the central source profile.

Speckle interferometry has been applied in the near-infrared range ($1\text{--}5 \mu\text{m}$) to bright AGB sources such as IRC +10216 or OH/IR 26.5+0.6. Sub-arcsecond diameters have been estimated. The data are generally difficult to interpret because the observations give the Fourier transform of the spatial energy distribution of the source (visibility function) instead of a direct image. They require the use of an a-priori model that is fitted numerically to the data (e.g. Lopez et al. 1993). Evidence of non-sphericity of the dust shells and of variability correlated with the light-curve have been found (Dyck et al. 1991). The shells appear larger at the maxima of the lightcurves and smaller

at the minima. Recently, the technique of Adaptive Optics (AO) has been applied to AGB sources in the near-infrared range with success. In the mid-infrared ($8\text{--}20\ \mu\text{m}$), presently the largest conventional telescopes ($D \approx 4\text{ m}$) are most of the time limited by diffraction. This will be no more the case with the 8-m class telescopes which are entering into activity and AO will be also a necessity to reach the diffraction limit.

Although the principles of interferometry are well known and applied at radio-wavelengths since a long time, the applications in the optical and IR ranges are recent. Very promising results have been obtained with the Mount Wilson Infrared Spatial Interferometer, ISI, a system of 2 movable 1.65-m telescopes operated at $11\ \mu\text{m}$. The carbon source IRC+10216 has been resolved and shown to vary in size as a function of its luminosity (Danchi et al. 1990). The same team has studied the distribution of dust around 12 other AGB stars (Danchi et al. 1994). They find evidence for time-variations of the dust mass loss rates.

6.2 Laboratory Studies

The dream of any astrophysicist is to hold a sample of celestial matter for analysing it in the laboratory. The chemical abundances and the physical state of the matter could thus be determined directly instead of being inferred through hypothetical models. In this respect, it seems that investigators of AGB stars are favored. There are meteorites in the museum collections which probably contain samples of interstellar dust. Furthermore, good analogues of circumstellar grains are starting to be produced artificially.

It has been shown that some inclusions in the meteorites are of pre-solar origin, i.e. they are samples of interstellar matter. The carbonaceous chondrites appear to be the most primitive meteorites. Their formation temperature is relatively low ($\leq 500\text{ K}$) so that they incorporate interstellar material that has not been processed in the solar-system parent-bodies (comets or asteroids?). Some inclusions exhibit an abundance pattern, in carbon and s-elements, which is characteristic of TP-AGB stars. They must have formed in their winds. The analysis of these inclusions give informations on the composition of grains around AGB stars and on the nucleosynthesis processes which have been at work in the heart of the parent stars. They give also insights on the physics of their formation. For instance, Bernatowicz et al. (1991) found inclusions which have a structure with concentric layers of carbon. In addition, one of these inclusions contains crystals of TiC and SiC which have been included in the grain during its formation. Assuming equilibrium condensation, TiC should condense after carbon well below 1500 K . Therefore, this discovery points to an inhibited nucleation and growth of carbon grains.

The first attempt to produce in the laboratory a material matching the properties of interstellar dust was made by Day (1976, and ref. therein) who obtained amorphous silicate materials. These products had absorption properties in the mid-infrared range which are in fair agreement with the obser-

vations (cf. Sect. 4.1). More recently, Jäger et al. (1994) and Dorschner et al. (1995) have undertaken a systematic programme to produce and study analogues of interstellar grains. They produced two series of glasses with pyroxene ($\text{Mg}_x\text{Fe}_{1-x}\text{SiO}_3$) and olivine ($\text{Mg}_x\text{Fe}_{1-x}\text{SiO}_4$) stoichiometry and studied their properties on the basis of laboratory measurements. With this approach they can evaluate the influence of various parameters on Ultra-Violet/ Visual/ IR absorption (up to $500\text{ }\mu\text{m}$). They compare their experimental results with the IRAS observations of O-rich CDS and conclude that amorphous silicates with olivine stoichiometry can give a good fit to the astronomical spectra.

6.3 Space Projects

The wavelength range from 20 to $800\text{ }\mu\text{m}$ is extremely useful for the studies of circumstellar shells. Apart from the emission by cool dust, many important atomic and molecular lines are found in this range. Unfortunately, it is not accessible from the ground and requires observatories in orbit around the Earth. Another limitation of ground-based telescopes is the thermal background. Space-borne telescopes can be cooled (without risk of water condensation!). However, even when the telescope is cooled to less than 10 K (e.g. IRAS), the observations at long wavelengths are limited by the thermal emission from dust in the solar system (zodiacal light, $T_{\text{BB}} \approx 250\text{ K}$) or from dust in the interstellar medium (interstellar cirrus, $T_{\text{BB}} \approx 30\text{ K}$). The background emission received by a detector is proportional to the pass-band and to the solid angle illuminating the detector. There are 2 ways to minimize it and hence to increase the sensitivity: to increase the spectral resolution, i.e. to go towards emission line studies, or to increase the spatial resolution which implies to increase the telescope diameter.

ISO: The Infrared Space Observatory has been launched in November 1995 and is presently operated successfully. The telescope has a 0.6-m diameter, like for the IRAS mission. ISO is providing photometry and spectroscopy up to $200\text{ }\mu\text{m}$. It will be especially useful for the study of molecules which are abundant in the terrestrial atmosphere such as H_2O and CO_2 and which, for this reason, cannot be observed from the ground. Many lines of other important molecules such as OH and SiO fall in the range of ISO. Also there are fine structure lines of abundant elements which in CSs are expected to result from the dissociation of these molecules by the Interstellar Radiation Field (Fig. 1), e.g. OI ($63\text{ }\mu\text{m}$), CII ($158\text{ }\mu\text{m}$) or SiI ($68\text{ }\mu\text{m}$). ISO has also imaging capabilities that will allow to map the extended shells which have been suspected at 60 and $100\text{ }\mu\text{m}$ on the basis of the IRAS data (Young et al. 1993; Sect. 4.2). Finally, new dust features could be discovered in the wavelength range which has not been explored from the ground or with the IRAS LRS³.

³ The first ISO results (A&A, ISO Special Issue, Vol. 315 No. II) illustrate much better by themselves, and way beyond all expectations, the richness of the information contained in the 20– $200\text{ }\mu\text{m}$ range (e.g. Barlow et al., Waters et al., in that Issue).

FIRST: The Far Infra-Red and Submillimeter Space Telescope, to be launched in 10 years from now (~ 2005), will provide imaging photometry and spectroscopy in the domain $100\text{--}900\ \mu\text{m}$. It will thus cover the wavelength range longward of ISO and shortward of the ground-based radio-telescopes. The telescope is foreseen to have a 3-m diameter. High-resolution spectroscopy in the sub-millimeter range will give access to high- J rotational lines of molecules already observed in the millimeter range. This will be a natural follow-up for the studies described in Sect. 5. Also, a number of new chemical species should be discovered.

6.4 Near-Infrared Surveys

The near-infrared range ($1\text{--}2.5\ \mu\text{m}$) corresponds to the peak of emission of most AGB stars. Thirty years ago, the Two Micron Sky Survey (TMSS) was undertaken by Neugebauer and Leighton (1969). About 6000 sources, mostly RGB and AGB stars, were detected. Although limited in sensitivity ($K \approx 3$), the TMSS had a strong impact on the studies of AGB stars. Many mass-losing sources, extremely reddened by dust such as IRC +10216, were revealed for the first time. The TMSS contributed to the recognition that heavy mass loss is an important factor in the evolution of AGB stars. Since this pioneering work, there has been no attempt to survey the entire sky in the near-infrared. An extension of the TMSS to the southern Galactic Plane was done by Epchtein et al. (1987).

The recent availability of sensitive near-infrared arrays such as the 256×256 NICMOS detector has stimulated the development of 2 programmes aiming at surveying the near-infrared sky:

- (i) the Two Micron All Sky Survey (2MASS, Kleinmann et al. 1994),
- (ii) the DEep Near-Infrared Survey of the southern sky (DENIS, Epchtein et al. 1994, Le Bertre et al. 1995).

Although the exact specifications of these 2 programmes are somewhat different, they share many common features. In both cases, it is aimed to cover the sky with a spatial resolution ~ 1 arcsec down to a limiting magnitude $K \approx 14$. With such a sensitivity, all AGB stars in the Galaxy should be detectable. Except in the densest parts of the Galactic Plane, all objects should be well separated. By contrast, due to its wide beam (~ 1 arcmin at $10\ \mu\text{m}$), IRAS was limited by confusion in large areas around the Galactic Plane. With a limiting magnitude $K \approx 14$, most AGB stars should be detected in the Magellanic Clouds. Even very reddened sources like IRC +10216 might be discovered in the LMC.

As discussed previously (Sect. 4.2), IRAS has detected thousands of mass-losing AGB stars. Unfortunately, the IRAS photometric data alone are not sufficient to characterize these sources. However, the combination of these data with near-infrared ones coming from 2MASS and DENIS will allow such a characterization. For instance, in a $J\text{--}K$ versus $[12\ \mu\text{m}]\text{--}[25\ \mu\text{m}]$ diagram,

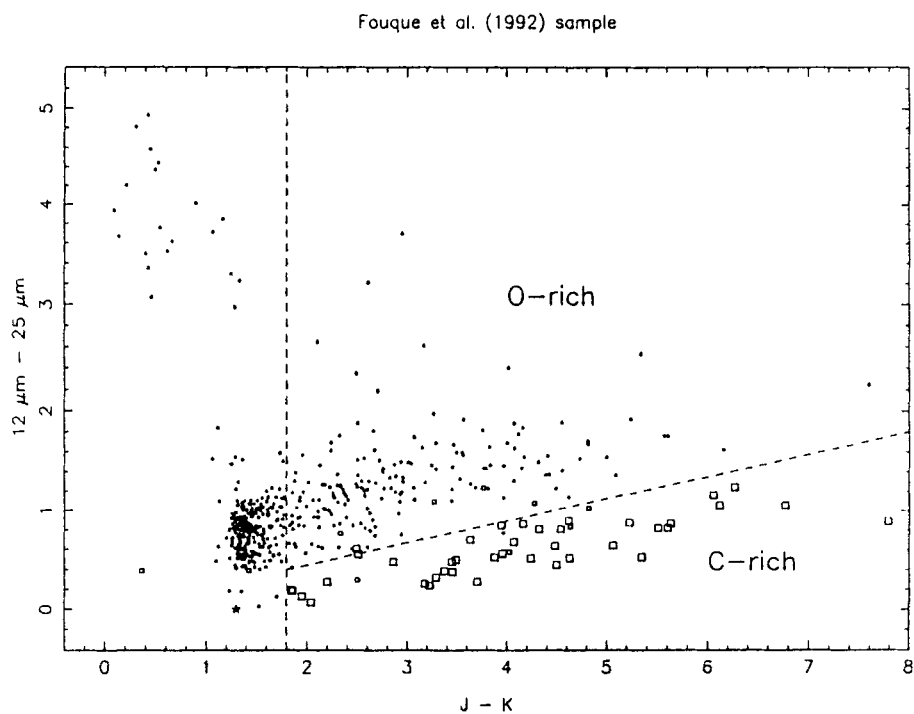


Fig. 2. $J-K$ versus $[12\ \mu\text{m}]-[25\ \mu\text{m}]$ diagram for a sample of stars with Circumstellar Dust Shell (CDS). The data are taken from Fouqué et al. (1992). (large \square): sources with a confirmed Carbon-rich CDS. (small \square): sources with a suspected Carbon-rich CDS. (\bullet): sources with a confirmed or suspected Oxygen-rich CDS. The (\star) marks the position of an M6 giant without CDS. For $J-K > 1.8$, O-rich sources are clearly separated from C-rich ones. For $J-K < 1.8$, the sources may have a detached shell and the two types are mixed

the O-rich mass-losing AGB stars separate well from the C-rich ones (Le Bertre et al. 1994; Fig. 2).

7 Final Comments

We have seen that there are many observational tools that are useful to study the winds around cool stars. In the next years, new facilities will enter into operation completing the existing ones. These new facilities together with the improvements in detector (including radio receivers) sensitivity and the developments of new techniques will certainly bring new lights on circumstellar shells (CS). One should note especially the observations in the optical and IR range that will benefit considerably from the improved image quality and sensitivity. In the next years, direct imaging and spectroscopy of the CSs in the optical range will most probably bring a wealth of informations. An essential issue for the description of AGB stellar winds and a real observational challenge is the measurement of the **dust** expansion velocity.

One must mention also as extremely promising the progress obtained with interferometry at millimeter and sub-mm wavelengths which now provides resolution of a fraction of an arcsec. In addition, space will give access to the wavelength range which is not accessible from the ground. Especially promising are the observations of molecules such as OH, H₂O, CO, CO₂, but one should also stay open to unpredictable discoveries. The detections of new chemical species will be important for the understanding of the physical and chemical processes in CSs.

Furthermore, laboratory studies of interstellar grains as well as of their analogues should have a strong impact on our knowledges about circumstellar dust and about the formation and evolution of grains.

Finally, the increased capacities of computers will drive the applications of statistics to Astronomy. The exploitation of the huge amounts of data produced by large scale surveys such as 2MASS and DENIS will provide a new approach to the understanding of AGB stars and of their CSs in different environments.

Acknowledgements

I am grateful to J. Lequeux, B. Lopez, N. Maunon and Nguyen-Q-Rieu for many helpful discussions and for reading carefully an original version of these notes. Many thanks also to J.-P. De Greve for inviting me to the IXth EADN Summer School.

References

- Benson, P. J., Little-Marenin, I. R., Woods, T. C., et al. (1990): *ApJS* **74**, 911
- Bernat, A. P., Lambert, D. L. (1975): *ApJ* **201**, L153
- Bernatowicz, T. J., Amari, S., Zinner, E. K., Lewis, R. S. (1991): *ApJ* **373**, L73
- Bieging, J. H., Nguyen-Q-Rieu (1988): *ApJ* **329**, L107
- Bujarrabal, V., Guibert, J., Nguyen-Q-Rieu, Omont, A. (1980): *A&A* **84**, 311
- Booth, R. S., Kus, A. J., Norris, R. P., Porter, N. D. (1981): *Nat* **290**, 382
- Cernicharo, J., Guélin, M. (1996): *A&A* **309**, L27
- Chan, S. J., Kwok, S. (1988): *ApJ* **334**, 362
- Cohen, M. (1984): *MNRAS* **206**, 137
- Crabtree, D. R., McLaren, R. A., Christian, C. A. (1987): in *Late Stages of Stellar Evolution*, S. Kwok & S. R. Pottasch (eds.), Reidel, Dordrecht, p145
- Danchi, W. C., Bester, M., Degiacomi, C. G., McCullough, P. R., Townes, C. H. (1990): *ApJ* **359**, L59
- Danchi, W. C., Bester, M., Degiacomi, C. G., Greenhill, L. J., Townes, C. H. (1994): *AJ* **107**, 1469
- Day, K. L. (1976): *ApJ* **210**, 614
- Deutsch, A. J. (1956): *ApJ* **123**, 210
- Diamond, P. J., Kembell, A. J., Junor, W., et al. (1994): *ApJ* **430**, L61
- Doel, R. C., Gray, M. D., Humphreys, E. M. L., Braithwaite, M. F., Field, D. (1995): *A&A* **302**, 797
- Dorschner, J., Begemann, B., Henning, T., Jäger, C., Mutschke, H. (1995): *A&A* **300**, 503
- Dougados, C., Rouan, D., Léna, P. (1992): *A&A* **253**, 464
- Dyck, H. M., Benson, J. A., Howell, R. R., Joyce, R. R., Leinert, Ch. (1991): *AJ* **102**, 200
- Elitzur, M., Goldreich, P., Scoville, N. (1976): *ApJ* **205**, 384
- Epchtein, N., Le Bertre, T., Lépine, J. R. D., et al. (1987): *A&AS* **71**, 39
- Epchtein, N., Le Bertre, T., Lépine, J. R. D. (1990): *A&A* **227**, 82
- Epchtein, N., de Batz, B., Copet, E., et al. (1994): *Ap&SS* **217**, 3
- Feast, M. W., Glass, I. S., Whitelock, P. A., Catchpole, R. M. (1989): *MNRAS* **241**, 375
- Fouqué, P., Le Bertre, T., Epchtein, N., Guglielmo, F., Kerschbaum, F. (1992): *A&AS* **93**, 151
- Goebel, J. H., Moseley, S. H. (1985): *ApJ* **290**, L35
- Gray, M. D., Ivison, R. J., Yates, J. A., et al. (1995): *MNRAS* **277**, L67
- Greenhill, L. J., Colomer, F., Moran, J. M., et al. (1995): *ApJ* **449**, 365
- Groenewegen, M. A. T., Whitelock, P. A. (1996): *MNRAS* **281**, 1347
- Guélin, M., Lucas, R., Neri, R. (1996): *IAU Symposium n° 170, Twenty-five years of millimeter-wave spectroscopy*
- Guglielmo, F., Epchtein, N., Le Bertre, T., et al. (1993): *A&AS* **99**, 31
- Guilain, C., Maunon, N. (1996): *A&A*, in press
- Guilloteau, S., Omont, A., Lucas, R. (1987): *A&A* **176**, L24
- Gustafsson, B., Eriksson, K., Kiskelman, D., Olander, N., Olofsson, H. (1996): *A&A*, in press
- Habing, H.J. (1996): *A&AR* **7**, 97
- Herman, J., Habing, H. J. (1985): *A&AS* **59**, 523

- Herman, J., Baud, B., Habing, H. J., Winnberg, A. (1985): A&A **14** 3, 122
- Iben, I. (1985): QJRAS **26**, 1
- Iben, I., Renzini, A. (1983): ARA&A **21**, 271
- IRAS Science Team (1986): A&AS **65**, 607
- IRAS Science Team (1988): *IRAS Catalogs and Atlases*, NASA RP-1190
- Jäger, C., Mutschke, H., Begemann, B., Dorschner, J., Henning, T. (1994): A&A **292**, 641
- Jones, T. W., Merrill, K. M. (1976): ApJ **209**, 509
- Jura, M. (1986): ApJ **303**, 327
- Jura, M. (1992): A&AR **2**, 227
- Justtanont, K., Barlow, M. J., Skinner, C. J., et al. (1996): A&A **309**, 612
- Kholopov, P. N., Samus, N. N., Frolov, M. S., et al. (1985): *General Catalogue of Variable Stars*, fourth edition, "Nauka" Publishing House, Moscow
- Kleinmann, S. G., Lysaght, M. G., Pughe, W. L., et al. (1994): Ap&SS **217**, 11
- Knapp, G. R., Morris, M. (1985): ApJ **292**, 640
- Kruszewski, A., Coyne, G. V. (1976): AJ **81**, 641
- Le Bertre, T., Lequeux, J. (1993): A&A **274**, 909
- Le Bertre, T., Epchtein, N., Guglielmo, F., Le Sidaner, P. (1994): Ap&SS **217**, 105
- Le Bertre, T., Epchtein, N., de Batz, B., et al. (1995): in *Calibrating and Understanding HST and ESO instruments*, P. Benvenuti (ed.), ESO Conference and Workshop Proceedings No. 53, p195
- Le Borgne, J. F., Maun, N. (1989): A&A **210**, 198
- Le Sidaner, P., Le Bertre, T. (1996): A&A, in press
- Lindqvist, M., Nyman, L.-Å., Olofsson, H., Winnberg, A. (1988): A&A **205**, L15
- Little, S. J., Little-Marenin, I. R., Bauer, W. H. (1987): AJ **94**, 981
- Little-Marenin, I. R., Little, S. J. (1988): ApJ **333**, 305
- Lopez, B., Perrier, C., Mékarnia, D., Lefèvre, J., Gay, J. (1993): A&A **270**, 462
- Loup, C., Forveille, T., Omont, A., Paul, J. F. (1993): A&AS **99**, 291
- Lucas, R., Bujarrabal, V., Guilloteau, S., et al. (1992) A&A **262**, 491
- Maun, N., Caux, E. (1992): A&A **265**, 711
- Maun, N., Guilain, C. (1995): A&A **298**, 869
- Maun, N., Cailloux, M., Tilloles, P., Le fèvre, O. (1986) A&A **165**, L9
- McMillan, R. S., Tapia, S. (1978): ApJ **226**, L87
- Mennessier, M.-O., Omont, A. (eds.) (1990): *From Miras to Planetary Nebulae: Which path for stellar evolution?*, Editions Frontières
- Merrill, K. M., Stein, W. A. (1976): PASP **88**, 285 & 294 & 874
- Morris, M., Guilloteau, S., Lucas, R., Omont, A. (1987): ApJ **321**, 888
- Neugebauer, G., Leighton, R. B. (1969): *The Two Micron Sky Survey*, NASA SP-3047
- Neugebauer, G., Habing, G., Van Duinen, R., et al. (1984): ApJ **278**, L1
- Nguyen-Q-Rieu, Bujarrabal, V., Olofsson, H., Johansson, L. E. B., Turner, B. E. (1984): ApJ **286**, 276
- O'Dell, C. R., Handron, K. D. (1996): AJ **111**, 1630
- Olofsson, H. 1994 in *Molecules in the Stellar Environment*, Proceedings of I.A.U. Colloquium n° 146, U. G. Jørgensen (ed.), Lecture Notes in Physics, Springer-Verlag, p113
- Olofsson, H., Carlström, U., Eriksson, K., Gustafsson, B., Willson, L. A. (1990): A&A **230**, L13

- Olofsson, H., Carlström, U., Eriksson, K., Gustafsson, B. (1992): A&A **253**, L17
Omont, A., Loup, C., Forveille, T., et al. (1993a): A&A **267**, 515
Omont, A., Lucas, R., Morris, M., Guilloteau, S. (1993b): A&A **267**, 490
Onaka, T., de Jong, T., Willems, F. J. (1989): A&A **218**, 169
Plez, B., Lambert, D. L. (1994): ApJ **425**, L101
Reid, M.J., Muhleman, D. O., Moran, J. M., Johnston, K. J., Schwartz, P. R.
(1977): ApJ **214**, 60
Reimers, D. (1977): A&A **61**, 217
Shaw, S. J., Zellner, B. (1970): ApJ **162**, L19
Treffers, R., Cohen, M. (1974): ApJ **188**, 545
Truong-Bach, Morris, D., Nguyen-Q-Rieu (1991): A&A **249**, 435
Van der Veen, W. E. C. J., Habing, H. J. (1988): A&A **194**, 125
Van Langevelde, H. J., Van der Heiden, R., Van Schooneveld, C. (1990): A&A **239**,
193
Volk, K., Cohen, M. (1989): AJ **98**, 931
Volk, K., Kwok, S., Stencel, R. E., Brugel, E. (1991): ApJS **77**, 607
Waters, L. B. F. M., Loup, C., Kester, D. J. M., Bontekoe, Tj. R., de Jong, T.
(1994): A&A **281**, L1
Whitelock, P., Menzies, J., Feast, M., et al. (1994): MNRAS **267**, 711
Young, K., Phillips, T. G., Knapp, G. R. (1993): ApJS **86**, 517

The Theory of Line Driven Stellar Winds

Henny J.G.L.M. Lamers

SRON Laboratory for Space Research and Astronomical Institute, Sorbonnelaan 2,
NL-3584 CA, Utrecht, The Netherlands
HENNYL@SRON.RUU.NL

Abstract. We describe the theory of line driven winds. First we explain the concept and give some simple estimates. Next we derive expressions for the radiative acceleration due to lines. The equation of motion for a line driven wind from a star in the point source limit is solved. This gives simple analytical expressions for the predicted mass loss rates and the terminal velocities. The equations show that $\dot{M} \sim L_*^{1.6}$ and $v_\infty \sim v_{\text{esc}}$, in agreement with the observations. The theory is refined by a correction for the finite size of the star. We also discuss the stability of line driven wind and show that these winds are intrinsically unstable. This explains the observed super-ionization and the X-rays from line driven winds. We compare the predictions with observations and show that the theory is very successful in explaining the overall features of the winds of hot stars.

1 Introduction

Luminous hot stars have stellar winds with high terminal velocities of typically about 2 to 3 times v_{esc} . The mass loss rates depend very strongly on the luminosity of the star. Observations show that \dot{M} scales approximately as $L_*^{1.6}$. Both arguments suggest very strongly that these winds are driven by line radiation pressure. This was first suggested by Lucy and Solomon (1967), immediately after the first rocket UV observations showed that the very luminous hot stars in the Belt of Orion have stellar winds with typical velocities of about 2000 km s^{-1} , and mass loss rates of a few times $10^{-6} M_\odot \text{ yr}^{-1}$.

The radiation driven theory as we know it now was originally developed by Castor et al. (1975), (called: CAK-theory) and improved by Abbott (1982), Friend and Abbott (1986), Pauldrach et al. (1986) and Kudritzki et al. (1989). It is based on the fact that stellar photons can be very efficiently absorbed or scattered in the winds of hot stars, by very large numbers of absorption lines. The photons which are scattered in the wind transfer their outward directed momentum to the gas. The Coulomb interactions of the absorbing (and thus accelerated) ions with electrons and protons then results in a sharing of the momentum with the whole plasma. So the winds of hot stars are driven by momentum transfer from the photons to the gas. The theory has also been applied to explain the mass loss from the cooler yellow supergiants (Achmad and Lamers, 1997).

In this paper I discuss the basics of the line driven wind theory. Section 2 gives some basic estimates for the momentum transfer and the mass loss of radiation driven winds. Section 3 deals with the radiation pressure and the radiative force (the gradient of the radiation pressure) due to spectral lines. We will see that the radiative acceleration can be expressed in terms of a very simple function of density and velocity gradient, by means of the concept of a *force multiplier*. In Sect. 4 I describe a very simple way to solve the momentum equation of a line driven wind in case the star can be considered as a point source. This leads to expressions for the predicted mass loss rates and terminal velocities. In Sect. 5 the simple theory is improved by taking into account the finite size of the star. In Sect. 6 the stability of radiation driven winds is discussed and in Sect. 7 I discuss the observed values of the mass loss rate and terminal velocities for comparison with the theory.

An extensive description of the theories and observations of stellar winds will be published in *Introduction to Stellar Winds* by H.J.G.L.M. Lamers and J.P. Cassinelli (Cambridge University Press), in preparation.

2 Basic Concepts and Some Estimates

Hot stars emit the bulk of their radiation in the ultraviolet where the outer atmospheres of these stars have many absorption lines. The opacity in absorption lines is much larger than the opacity in the continuum. The dominant UV continuum opacity in the atmospheres of hot stars is due to scattering on free electrons (Thomson scattering). The opacity of one strong line, say the C IV resonance line at 1550\AA , can easily be a factor of 10^6 larger than the opacity for electron scattering.

The large radiation force on ions because of their spectral lines would not be efficient in driving a stellar wind if it were not for the Doppler effect. In a static atmosphere with strong line-absorption, the radiation from the photosphere of the star will be absorbed or scattered in the lower layers of the atmosphere. The outer layers will not receive direct radiation from the photosphere at the wavelength of the line, and so the radiative acceleration in the outer layers of a static atmosphere due to the spectral lines is strongly diminished. However, if the outer atmosphere is moving outward, there is a velocity gradient in the atmosphere allowing the atoms in the atmosphere see the radiation from the photosphere as red shifted. This is because in the frame comoving with the gas the photosphere is receding. The Doppler shift thus allows the atoms to absorb undiminished continuum photons in their line transitions. This makes the radiative acceleration due to spectral lines in the atmospheres of hot luminous stars very efficient for driving a stellar wind.

Suppose that the ions which provide the dominant radiative acceleration in the winds of hot stars constitute about 10^{-5} of all ions by number and 10^{-4} by mass. This is a reasonable assumption because the majority of the

ions, H and He, contribute very little to the radiative acceleration because they are fully ionized (H^+ , He^{++}) or they have their strongest absorption lines in the far UV where the stellar flux is small (He^+). So the driving is mainly done by the ions of C, N, O, Ne, Si, S and the metals, as we will see later.

An absorption of an UV photon increases the momentum of the absorbing ion by $h\nu/c$, which typically corresponds to a velocity increase by about 20 cm s^{-1} for $\lambda = 1000 \text{ \AA}$ and the mass of the ion is $m_i = 20m_H$. If the ion would not interact with its surrounding plasma, its velocity would reach about the speed of light after $1.5 \cdot 10^9$ absorptions which could occur in about 10^3 seconds for a typical hot luminous star. However, Coulomb interactions with other charged ions and electrons result in a redistribution of the momentum over all the gas. So the momentum gained by the absorbing ions has to be shared by the rest of the gas and hence the effective velocity increase per absorption is only $2 \times 10^{-3} \text{ cm s}^{-1}$. To accelerate the wind to $v_\infty = 2000 \text{ km s}^{-1}$ requires 10^{11} absorptions per absorbing ion. The terminal velocity of a wind is reached within a few stellar radii, so the time it takes to accelerate the gas to v_∞ is on the order of $3R_*/v_\infty \approx 10^4 \text{ s}$ if $R_* = 10R_\odot$. Therefore the ions that provide the radiative acceleration have to absorb about 10^7 photons s^{-1} . This implies that only transitions to levels with short lifetimes ($\tau \lesssim 10^{-7} \text{ sec}$), i.e. transitions with oscillator strengths $f \gtrsim 0.01$, will contribute effectively to the radiative acceleration. Lines with smaller oscillator strengths will only contribute to the radiative acceleration if their number is very large. We will see later in Sect. 3.3 that this is indeed the case in the winds of hot stars.

Photons transfer not only momentum to the wind but also energy. The radiation provides the kinetic energy of the wind, the potential energy to lift the gas out of the potential well of the star and the thermal energy of the wind. For typical O-stars, all these forms of energy are less than 10^{-2} of the luminosity of the star. We conclude that the luminosity of the star decreases very little by the radiative acceleration of the wind.

2.1 How Many Lines Are Needed to Drive a Wind?

Consider a line driven wind with a terminal velocity of v_∞ . We calculate how many lines are needed at least to drive the wind. See Fig. 1.

Suppose that the star emits a black body spectrum. The peak of L_λ is at λ_{max} . Suppose there is one strong line of rest wavelength $\lambda_0 \approx \lambda_{\text{max}}$ near the maximum of the radiation curve. That line can absorb all the flux from the star in the wavelength range between λ_0 and $\lambda_0(1 - v_\infty/c)$. So the total amount of energy absorbed in the wind per second by the one line is

$$E_l = \frac{L_{\lambda_{\text{max}}} \lambda_{\text{max}} v_\infty}{c} \quad (1)$$

and the radiative momentum, transferred from the radiation to the wind due to this one line dP_{rad}/dt , is

THE FLUX ABSORBED IN THE WIND BY ONE STRONG LINE

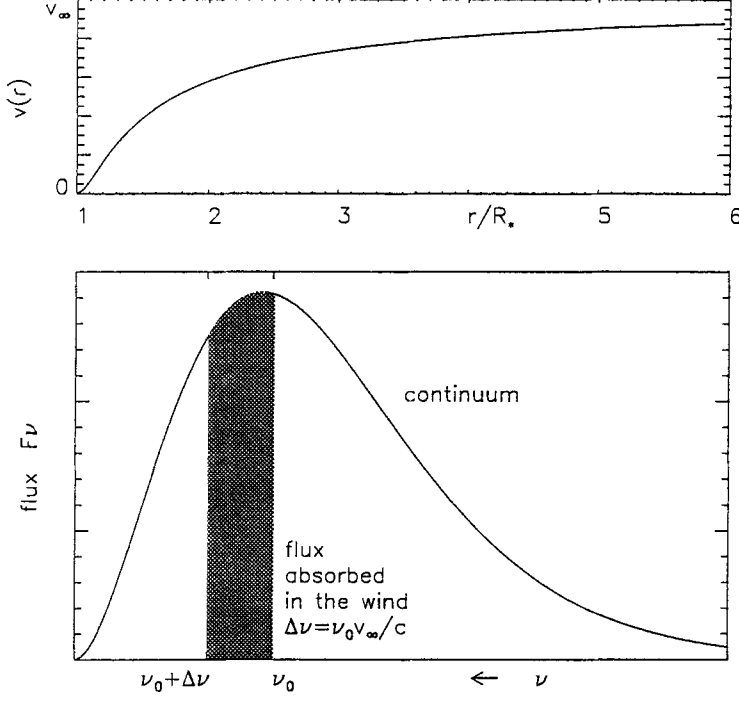


Fig. 1. Schematic picture of the luminosity absorbed by one strong absorption line near the maximum of the energy distribution

$$\frac{dP_{\text{rad}}}{dt} = \frac{E_l}{c} = \frac{L_{\lambda_{\text{max}}} \lambda_{\text{max}} v_{\infty}}{c^2} . \quad (2)$$

The momentum of the wind lost per second, dP_{wind}/dt , is the product of the mass loss rate per second and the terminal velocity

$$\frac{dP_{\text{wind}}}{dt} = \dot{M} v_{\infty} . \quad (3)$$

If the wind is driven by radiation pressure, which means that the momentum of the wind is due the momentum of the photons transferred to the gas, then $P_{\text{wind}} = P_{\text{rad}}$, so

$$\dot{M}(\text{one strong line}) \approx \frac{L_{\text{max}} \lambda_{\text{max}}}{c^2} \approx \frac{L_{*}}{c^2} \quad (4)$$

where we have used the property of the Planck function that $L_{\max}\lambda_{\max} \approx L_*$. So we see that one optically thick line near the maximum of the radiation curve produces a mass loss rate of the order of L_*/c^2 . If there are N_{eff} strong lines near the peak of the stellar energy distribution, then we expect

$$\dot{M} \approx N_{\text{eff}} \frac{L_*}{c^2} . \quad (5)$$

Table 1. The wind of ζ Pup (O4 If)

L_*	$= 8 \cdot 10^5 L_{\odot}$	$N_{\text{eff}} = \dot{M} c^2 / L_* = 80$
T_{eff}	$= 42000 \text{ K}$	$dP_{\text{rad}}/dt = L_*/c = 1 \cdot 10^{29} \text{ g cm}^{-1}\text{s}^{-2}$
v_{∞}	$= 2200 \text{ km s}^{-1}$	$dP_{\text{wind}}/dt = \dot{M} v_{\infty} = 7 \cdot 10^{28} \text{ g cm}^{-1}\text{s}^{-2}$
\dot{M}	$= 5 \cdot 10^{-6} M_{\odot} \text{ yr}^{-1}$	$\eta \equiv \dot{M} v_{\infty} / (L_*/c) = 0.70$
L_*/c^2	$= 6 \cdot 10^{-8} M_{\odot} \text{ yr}^{-1}$	

Table 1 shows the data for a typical O-star, ζ Pup. We see that the wind of ζ Pup can be driven by about 80 strong lines. In reality the wind is driven by a mixture of optically thick lines and a very large number of optically thin lines, as we will see below.

We can also derive an upper limit for the mass loss rate of line driven winds. If *all* the photons from the star were absorbed or scattered once in the wind, the wind momentum loss would be equal to the total momentum of the radiation. The resulting maximum mass loss is

$$\frac{L_*}{c} = \dot{M}_{\text{max}} v_{\infty} \rightarrow \dot{M}_{\text{max}} = \frac{L_*}{c v_{\infty}} . \quad (6)$$

This maximum is called the “single scattering limit” because it is calculated under the assumption that all the photons from the star are scattered once. (After the first scattering the photons have a more or less random distribution in direction, so the second and later scatterings are much less effective in driving the wind).

The resulting ratio $\dot{M}/\dot{M}_{\text{max}} = \eta$ is the “momentum transfer efficiency factor” (sometimes called the “wind performance number”). For most O-stars the mass loss rate corresponds to $\eta \approx 0.5$ to 1.0, indicating that the momentum of the radiation is efficiently transferred to the wind.

Wolf-Rayet stars have a much higher momentum transfer efficiency factor $10 < \eta < 10^2$. So *if* the winds of Wolf-Rayet stars are driven by radiation pressure, there must be a much more efficient way to transfer momentum to the wind. This might be reached by photon-diffusion in the wind if there are so many absorption lines that the wind opacity is large and the lines do

not leave gaps in the frequency space through which the photons can escape (Gayley et al. 1995).

3 Radiation Pressure Due to Lines

3.1 The Radiation Pressure Due to One Line

First we derive expressions for the radiation pressure provided by one line in a moving atmosphere. Figure 2 gives a schematic picture.

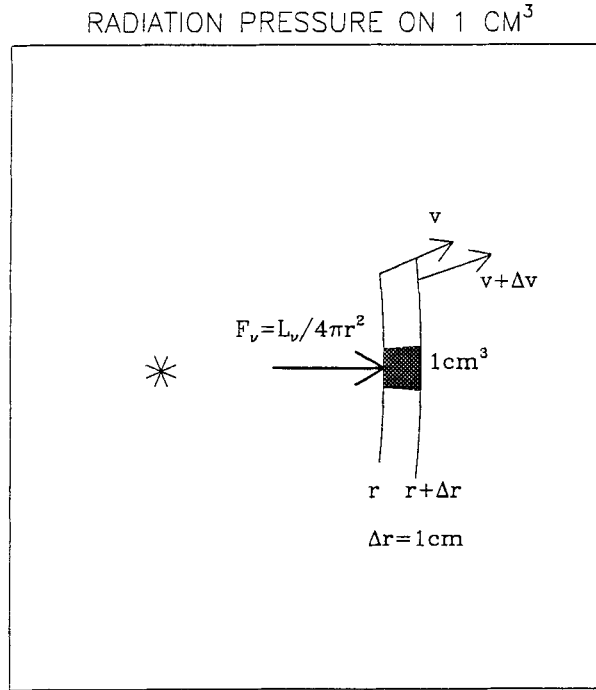


Fig. 2. Schematic figure of the radiation pressure due to one line in a moving atmosphere

The absorption coefficient of a line per cm³ gas is

$$\kappa_\nu = \frac{\pi e^2}{m_e c} \cdot f \cdot n_i \cdot \phi(\nu) \quad (7)$$

where the first factor $\pi e^2 / m_e c = 0.02654 \text{ cm}^2$ is the cross-section of the classical oscillator, f is the oscillator strength which depends on the line, n_i

is the number of atoms of ion i that can absorb the line. The profile of the absorption coefficient $\phi(\nu)$ is a Gaussian centered at the rest frequency ν_0 of the transition, normalized to $\int \phi(\nu) d\nu = 1$. The profile function is a Doppler profile with a typical width of the thermal velocity of the atoms, i.e. typically a few km s^{-1} , if there is no turbulence in the wind. If the thermal velocity is much smaller than the flow velocity in the wind, we can ignore the width of the profile function and approximate it with a δ -function. This is called the *Sobolev* approximation.

The radiation force due to a line is equal to the amount of radiative momentum absorbed by 1 cm^3 per second: $f = dp_{\text{rad}}/dt = c^{-1}(dE_{\text{rad}}/dt)$, where E_{rad} is the radiative energy absorbed per second per gram by the line. The radiation force due to one line on a cm^3 of the gas depends on the optical thickness of the gas for that line.

(1) *Optically thin lines*

If the gas is optically thin to the line, the amount of energy absorbed by the line is simply proportional to the stellar flux F_ν at distance r and the number of absorbing ions per cm^3 . So radiative acceleration due to one line, which is the radiative force divided by ρ , is

$$g_\ell = \frac{F_\nu}{c} \left(\frac{n_i}{\rho} \right) \left(\frac{\pi e^2}{m_e c} \cdot f \right) \sim \frac{L_\nu}{r^2} \left(\frac{n_i}{\rho} \right) \quad (8)$$

where L_ν is the monochromatic luminosity of the star. Notice that the radiative acceleration is proportional to n_i/ρ . If the ionization and excitation in the wind does not change with distance, this ratio is constant and $g_\ell \sim L_\nu/r^2$.

(2) *Optically thick lines*

If the gas is optically thick for the line transition, a cm^3 of gas will absorb all the flux within the frequency range of $\nu_1 = \nu_0(1 + v_1/c)$ and $\nu_2 = \nu_0(1 + v_2/c)$ because the outward moving gas will see the stellar flux red-shifted. Here v_1 and v_2 are the radial outflow velocities at the bottom and the top of the cm^3 , and $v_2 - v_1$ is the velocity difference over a distance of 1 cm^3 , which is dv/dr . The frequency width is $\Delta\nu = \nu_0(v_2 - v_1)/c = \nu_0(dv/dr)/c$. So the radiative acceleration is

$$g_\ell = \frac{F_\nu}{c} \frac{\nu_0}{c} \frac{1}{\rho} \frac{dv}{dr} \sim \frac{L_\nu}{r^2} \frac{1}{\rho} \frac{dv}{dr} \quad (9)$$

We see that the radiative acceleration by optically thick lines is proportional to $\rho^{-1} dv/dr$, whereas that by optically thin lines is independent of $\rho^{-1} dv/dr$.

3.2 Radiation Pressure by an Ensemble of Lines

The radiation pressure due to an ensemble of lines is the sum of g_ℓ of all the lines, optically thick as well as optically thin lines and those in between. Castor et al. (1975) have shown that the radiative acceleration, g_L , due to a realistic ensemble of lines of different optical depths will be proportional to

$$g_L \sim (\rho^{-1} dv/dr)^\alpha \sim \{(vr^2/\dot{M}) dv/dr\}^\alpha \sim \{(r^2 v dv/dr)/\dot{M}\}^\alpha \quad (10)$$

with α between the value for the optically thin ($\alpha = 0$) and optically thick lines ($\alpha = 1$). Here we have used the mass continuity equation

$$\dot{M} = 4\pi r^2 \rho(r) v(r) . \quad (11)$$

Therefore they proposed the following expression for g_L in terms of the radiative acceleration due to electron scattering times a multiplication factor $M(t)$ for the contribution by the lines

$$g_L = g_e M(t) . \quad (12)$$

The radiative acceleration due to electron scattering is

$$g_L(e) = \frac{\kappa_e}{c} \frac{L_*}{4\pi r^2} = \Gamma_e \frac{GM_*}{r^2} \quad (13)$$

with

$$\Gamma_e = \frac{\kappa_e}{4\pi c G} \frac{L_*}{M_*} . \quad (14)$$

The *force multiplier* $M(t)$ can be written as

$$M(t) \equiv kt^{-\alpha} s^\delta \quad (15)$$

where k , α and δ are the so-called *force multiplier parameters* and t is the *optical depth parameter*

$$t \equiv \kappa_e v_{th} \rho \frac{dr}{dv} \equiv \kappa_e \sqrt{\frac{2kT_{\text{eff}}}{m_H}} \rho \frac{dr}{dv} \sim \rho \frac{dr}{dv} \quad (16)$$

(CAK adopted a constant value of $\kappa_e = 0.325 \text{ cm}^2 \text{ g}^{-1}$).

The parameter s describes the ratio between the characteristic particle density in the wind and some normalization value and is defined as

$$s \equiv \frac{10^{-11} \rho}{m_H W} . \quad (17)$$

The factor s^δ in (15) describes the dependence of the radiation pressure on the ionization of the wind. The degree of ionization is expected to depend on the ratio ρ/W , where ρ is the density and W is the geometrical dilution factor for the mean intensity of the stellar radiation at distance r

$$W(r) = 0.5 \left\{ 1 - \sqrt{1 - (R_*/r)^2} \right\} \sim \left\{ \frac{R_*}{2r} \right\}^2 . \quad (18)$$

Combining these equation we find an expression for g_L

$$g_L = \frac{\kappa_e}{c} \frac{L_*}{4\pi r^2} k t^{-\alpha} s^\delta. \quad (19)$$

The force multiplier contains the sum of all the contributions of all the spectral lines, distributed over the spectral energy distribution, that can contribute to the radiation pressure. Therefore it depends on the energy distribution of the stellar spectrum as well as on the chemical composition and on the ionization and excitation stage. The force multipliers have been calculated for a grid of wind models by Abbott (1982), by the Munich group (e.g. Pauldrach 1987) and by Shimada et al. (1994). Table 2 gives the list from Abbott (A), Pauldrach et al. (P) and Shimada et al. (S). Notice that the value of α is about 0.52 for early-B and O stars.

Table 2. The force multiplier parameters

T_{eff} (K)	k	α	δ	Ref	k	α	δ	Ref
6000	0.029	0.465	0.160	A				
8000	0.105	0.542	0.020	A				
10000	0.866	0.454	0.058	S				
15000	0.922	0.446	0.134	S				
20000	0.709	0.470	0.089	S	0.320	0.565	0.020	P
30000	0.385	0.522	0.099	S	0.170	0.590	0.090	P
40000	0.483	0.526	0.061	S	0.124	0.640	0.070	P
50000	0.917	0.510	0.040	S	0.124	0.640	0.070	P

A = Abbott (1982) modified to our definition of $M(t)$

S = Shimada et al. (1994)

P = Pauldrach et al. (1986)

Computations of the radiative acceleration for other abundances suggests that the force multiplier depends on the metallicity Z (i.e. the mass fraction of all species other than H and He) as $g_L \sim Z^{1.0}$, thus

$$M_n(t_n) = M_n(t_n)_\odot (Z/Z_\odot) \quad (20)$$

with $Z_\odot = 0.020$ (Abbott 1982; Shimada 1994). So the radiation pressure for stars in the Small Magellanic Cloud, which has a ten times lower metallicity than our Galaxy, is ten times smaller than for Galactic stars of the same mass, radius and temperature.

3.3 The Lines That Drive the Winds

Figure 3 shows the amount of stellar flux used by the lines in the wind for the radiative acceleration. First of all, notice that a considerable fraction of

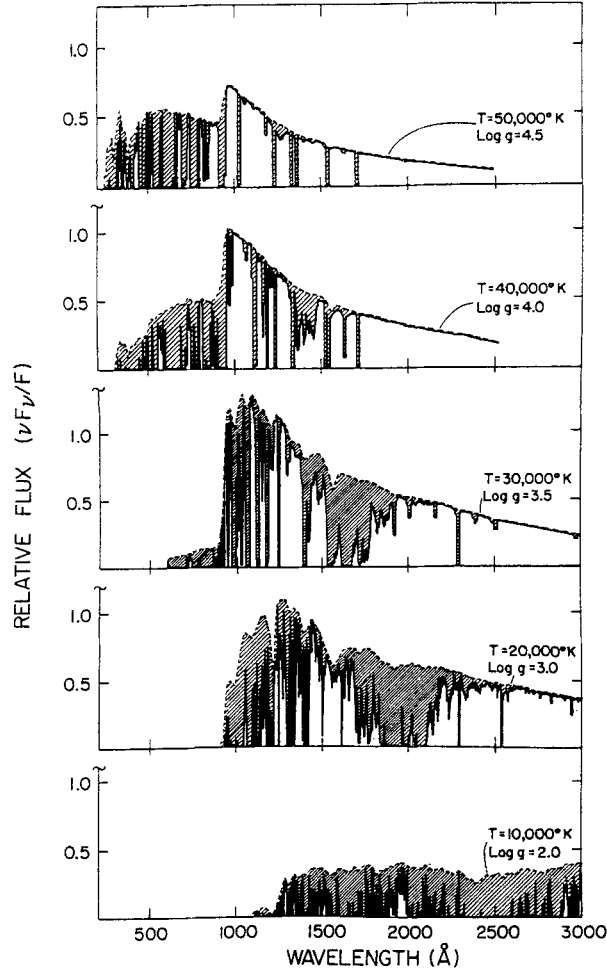


Fig. 3. The fraction of the stellar radiation that is scattered or absorbed in the winds of stars of different T_{eff} . For the hottest stars most of the lines that drive the wind are in the Lyman continuum. For stars with $20\,000 \leq T_{\text{eff}} \leq 30\,000 \text{ K}$ most of the lines that drive the wind are in the Balmer continuum due to doubly ionized metals. For stars with $T_{\text{eff}} \leq 10\,000 \text{ K}$ the singly ionized metals with thousands of lines in the Balmer continuum drive the winds (from Abbott 1982)

the flux is used for the radiative acceleration. This explains why the values of η , which is the efficiency for transferring radiative momentum into wind momentum, is 0.7 for the star ζ Pup in Table 1. Secondly, notice that the wavelength bands where most of the radiative acceleration occurs gradually shifts to longer wavelengths as T_{eff} decreases. There are two reasons for this effect: (i) as T_{eff} decreases the wavelength where most of the energy is emitted by the star moves to longer wavelength, (ii) as T_{eff} decreases the degree of ionization in the wind decreases and the wavelengths of the strong lines move to longer wavelengths.

Figure 4 shows the contribution to the radiative acceleration by lines from different groups of ions. At the highest temperature, $T_{\text{eff}} = 50\,000$ K, the largest contribution comes from the lines of Ne to Ca, i.e. mainly Si, S, P. At temperatures in the range of $25\,000 \leq T_{\text{eff}} \leq 40\,000$ K the dominant contribution is by C, N and O, i.e. mainly N IV and O IV. However, more recent calculations with largely extended line lists indicate that the contribution by Fe-group elements is larger than in Abbott's calculations (Pauldrach et al. 1989). Between 6000 K and 25 000 K the Fe-group elements provide the dominant contribution, mainly in the form of doubly ionized metals near 20 000 K and as singly ionized metals at 10 000 K or cooler. Hydrogen and helium contribute very little to g_L except for winds of stars with $T_{\text{eff}} \leq 6000$ K, where the Balmer lines of H become important.

4 The Theory of Line Driven Winds

In this section we will derive radiation driven wind models based on expression (19) for g_L and under the assumption that the photosphere can be treated as a point-source. This last assumption implies that the stellar radiation is assumed to emerge only in the radial direction. (In the next section we will describe the corrections due to the finite extent of the photosphere).

The equation of motion for a steady state spherically symmetric wind is

$$\frac{v dv}{dr} = -\frac{GM_*}{r^2} - \frac{1}{\rho} \frac{dp}{dr} + g_c + g_L \quad (21)$$

where g_c and g_L are the radiative accelerations due to continuum and lines.

For the line radiative acceleration we take the simplest possible expression

$$g_L = g_e k t^{-\alpha} s^\delta . \quad (22)$$

We also assume that the wind is isothermal so that the term with the pressure gradient in (21) can be expressed in a velocity gradient using $p = \rho a^2$ with $a^2 = \mathcal{R}T/\mu$ and the mass continuity equation, which gives $(1/\rho)dp/dr = (a^2/\rho)d\rho/dr = -(a^2/v)dv/dr - 2a^2/r$. This gives a momentum equation

$$\frac{v dv}{dr} = -\frac{GM_*}{r^2} + \frac{2a^2}{r} + \frac{a^2}{v} \frac{dv}{dr} + \frac{GM_*}{r^2} \Gamma_e + \frac{\kappa_e L_*}{4\pi c} \frac{k}{r^2} \cdot t^{-\alpha} s^\delta \quad (23)$$

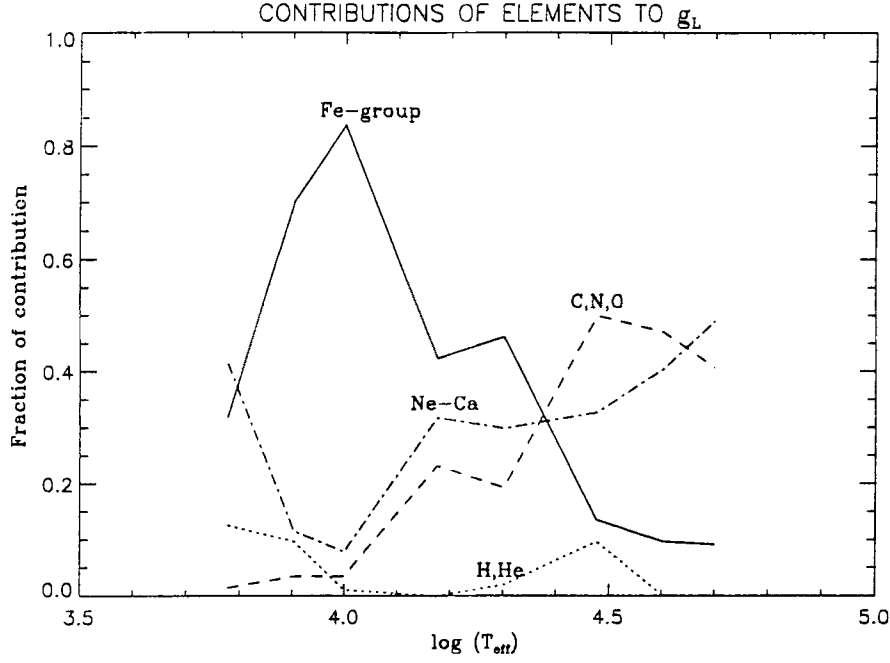


Fig. 4. The contribution to the radiative acceleration by lines of different ions as a function of temperature. For $T_{\text{eff}} \geq 25\,000\text{ K}$ the lines of C, N, O and Ne-Ca dominate the radiative acceleration. For cooler stars the Fe-group elements produce the largest contribution to the line acceleration. H and He hardly contribute (from Abbott 1982)

with

$$t = C_T \rho (dv/dr)^{-1} = \frac{C_T \dot{M}}{4\pi} (r^2 v dv/dr)^{-1} \quad (24)$$

with

$$C_T = \kappa_e \sqrt{\frac{2kT_{\text{eff}}}{m_H}}. \quad (25)$$

After multiplying (23) by r^2 , and rearranging the terms, we obtain the momentum equation for a line driven wind

$$\left(1 - \frac{a^2}{v^2}\right) r^2 \frac{v dv}{dr} = -GM_*(1 - \Gamma_e) + 2a^2 r + C(r^2 v dv/dr)^\alpha. \quad (26)$$

with

$$C = \frac{\kappa_e L_*}{4\pi c} \cdot k \cdot \left\{ \frac{C_T \dot{M}}{4\pi} \right\}^{-\alpha} \left\{ \frac{10^{-11} \rho}{m_H W} \right\}^\delta. \quad (27)$$

The factor ρ/W is not really constant in the wind because $\rho \sim r^{-2}v^{-1}$. However, since δ is very small we can adopt it to be constant.

This momentum equation has the character of a critical equation that we have encountered in the Chapter on the general theories of stellar winds (Lamers, first contribution to this Volume). In this case, the solution is more difficult because of its nonlinear character due to the $(r^2 v dv/dr)^\alpha$ term. However, if we ignore the forces due to the gas pressure the solution becomes very simple, as was first shown by Kudritzki et al. (1989). (CAK have derived the full solution with the gas pressure taken into account and found almost the same expressions for the mass loss and the velocity law). We are looking for a solution with a monotonically increasing velocity law, so the right-hand side of this equation should be 0 at the sonic point where $v = a$ and the left-hand side vanishes.

If we ignore the gradient of the gas pressure in (21) the two terms containing a^2 disappear from (26) and the momentum equation reads

$$r^2 \frac{v dv}{dr} - C \left(r^2 \frac{v dv}{dr} \right)^\alpha = -GM_*(1 - \Gamma_e) = \text{constant} . \quad (28)$$

This condition can only be fulfilled at every distance r if

$$r^2 \frac{v dv}{dr} \equiv D = \text{constant} , \quad (29)$$

thus (28) reduces to

$$CD^\alpha = D + GM_*(1 - \Gamma_e) . \quad (30)$$

The left-hand side and the right-hand side of this equation are plotted in Figure 5. The figure shows that there are either no, or one or two solutions, depending on the value of C . Since the value of C depends on the mass loss rate, (27), and we want the mass loss rate uniquely determined by the momentum equation we can only accept the value of C for which there is only one solution of (30). This is the case if the straight line of the right-hand side of (30) grazes the curved line of the left-hand side. In that case the mass loss rate and the velocity law are uniquely defined and they are self-consistent. If we bring the left-hand side of (30) to the right-hand side, the resulting equation

$$CD^\alpha - D - GM_*(1 - \Gamma_e) = 0 \quad (31)$$

has a single solution at its minimum (see Fig. 5). This minimum is found by differentiating the equation and by finding its zero point. This gives

$$C = \frac{D^{1-\alpha}}{\alpha} . \quad (32)$$

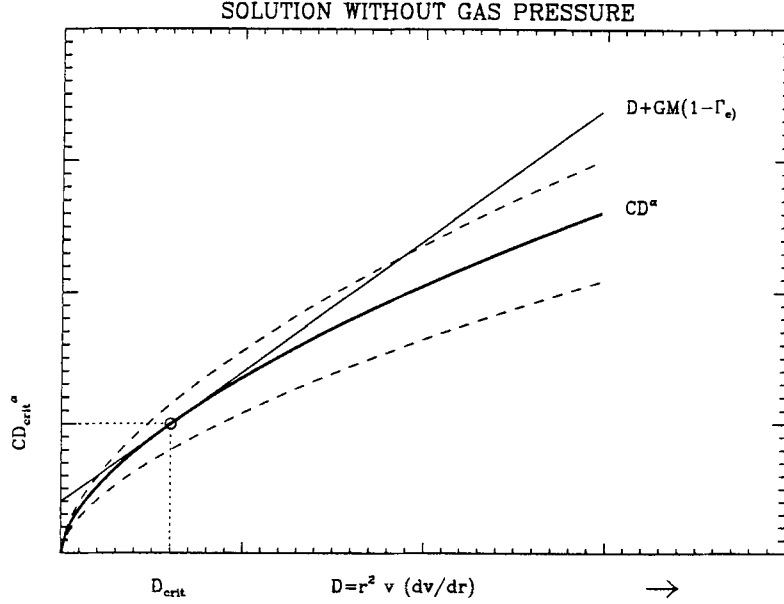


Fig. 5. The simple solution of the momentum equation for line driven winds derived by ignoring the gas pressure. The figure shows the functions $D + GM_*(1 - \Gamma_e)$ (thin straight line), and the functions CD^α for different values of C (dashed and thick curved lines). Depending on the value of C the momentum equation has 2, 1 or 0 solutions. The unique solution (thick line) gives a consistent model for a line driven wind (after Kudritzki et al. 1989)

Substituting this into (30) gives an expression for the velocity law

$$r^2 \frac{v dv}{dr} = D = \frac{\alpha}{1 - \alpha} GM_*(1 - \Gamma_e) . \quad (33)$$

Realizing that the left-hand side of this equation is $-0.5 d(v^2)/d(1/r)$ we can easily integrate this expression from the photosphere, where $v(R_*)$ is negligible, outward. We find

$$v(r) = \left\{ \frac{\alpha}{1 - \alpha} 2GM_*(1 - \Gamma_e) \left(\frac{1}{R_*} - \frac{1}{r} \right) \right\}^{1/2} = v_\infty \sqrt{1 - \frac{R_*}{r}} . \quad (34)$$

Notice that this is a β -type velocity law, $v(r) \sim (1 - R_*/r)^\beta$, with $\beta = 1/2$.

The terminal velocity is

$$v_{\infty} = \sqrt{\frac{\alpha}{1-\alpha} \frac{2GM_*(1-\Gamma_e)}{R_*}} = \sqrt{\frac{\alpha}{1-\alpha}} v_{esc} . \quad (35)$$

So we see that the terminal velocity of a radiation driven wind scales with the escape velocity at the photosphere and with $\sqrt{\alpha/(1-\alpha)}$. Notice that v_{∞} depends only on α and not on k . For $\alpha \approx 0.52$ we predict $v_{\infty} \approx 1.04v_{esc}$. This ratio is smaller than observed, but we will see in the next section that the finite disk correction improves the predictions considerably.

The mass loss rate for this simple model follows from the substitution of C (32) into (27). This gives

$$\dot{M} = \frac{4\pi}{C} \left(\frac{\kappa_e}{4\pi}\right)^{\frac{1}{\alpha}} \left(\frac{1-\alpha}{\alpha}\right)^{\frac{1-\alpha}{\alpha}} (k\alpha)^{\frac{1}{\alpha}} s^{\frac{1}{\alpha}} \left(\frac{L_*}{c}\right)^{\frac{1}{\alpha}} \{GM_*(1-\Gamma_e)\}^{\frac{\alpha-1}{\alpha}} . \quad (36)$$

Notice that the predicted mass loss rate is proportional to $\dot{M} \sim L_*^{1/\alpha} M_*^{(\alpha-1)/\alpha} \sim L_*^{1.9} M_*^{-0.96}$. Since $L_* \sim M_*^{2.5}$ for massive stars, we expect $\dot{M} \sim L_*^{1.5}$ if $\alpha = 0.52$. This agrees reasonably well with the observations.

In this simple derivation we completely ignored the gas pressure. The full solution, derived by CAK with the gas pressure taken into account, results in exactly the same expressions for \dot{M} and v_{∞} .

5 The Correction for the Finite Size of the Star

In the previous section we have described the models of line driven winds with the assumption that the radiation from the wind is only in the radial direction, i.e. the star is considered to be a point source. This is a good approximation far from the star, but it is inaccurate close to the star where the radiation has a significant amount of non-radial momentum. Therefore the line radiation force in the point source model is overestimated close to the star. We will show below that this results in an overestimate of the mass loss rate and an underestimate of the terminal velocity. We will describe a correction factor for the radiation pressure that takes into account the finite size of the star. This is called the *finite disk correction factor*.

Pauldrach et al. (1986) have shown that if the finite disk is taken into account, g_L becomes

$$g_L = \frac{\kappa_e}{c} \frac{L_*}{4\pi r^2} . k . t^{-\alpha} s^{\delta} D_f \quad (37)$$

which differs from (19) by the *finite disk correction factor*, D_f ,

$$D_f = \frac{(1+\sigma)^{\alpha+1} - (1+\sigma\mu_*^2)^{\alpha+1}}{(1-\mu_*^2)(\alpha+1)\sigma(1+\sigma)^{\alpha}} \quad (38)$$

with

$$\sigma \equiv \frac{r}{v} \frac{dv}{dr} - 1 \quad (39)$$

and

$$\mu_* = \sqrt{1 - R_*/r} . \quad (40)$$

Figure 6 shows the finite disk correction factor D_f as a function of distance from the star for β -type velocity laws

$$v(r) = v_\infty \left\{ 1 - \frac{R_*}{r} \right\}^\beta \quad (41)$$

with $\beta = 0.5, 0.7, 1.0, 2.0$, and 10 and a force multiplier $\alpha = 0.60$. The value of D_f increases from $D_f = 1/(1 + \alpha)$ at $r = R_*$, to a value larger than unity and converges to 1 at $r = \infty$. The small value of D_f near $r \approx R_*$ is due to the fact that the radiation close to the star reaches r from a wide angle so the radiative acceleration is smaller than in the case of a radial photon flux. The increase to $D_f > 1$ is due to the fact that the Sobolev optical depth of the lines in the transverse direction is smaller than in the radial direction at large distances. A decrease in the optical depth results in an increase in the radiative acceleration. At $r = \infty$ the radiation comes out radially, so the point source approximation is valid there and $D_f = 1$.

5.1 The Effect of the Finite Disk on the Mass Loss Rate and Velocity

If the finite disk is taken into account, the *momentum equation* (26) for line driven winds becomes

$$\left(1 - \frac{a^2}{v^2} \right) r^2 v \frac{dv}{dr} = -GM_*(1 - \Gamma_e) + 2a^2 r + C D_f \left\{ \frac{10^{-11} \rho}{m_H W} \right\}^\delta \left(r^2 v \frac{dv}{dr} \right)^\alpha . \quad (42)$$

The momentum equation (42) for a finite disk is more complicated, due to the factor D_f , than (26) for a point source. There is no analytic solution to it, which implies that the momentum equation has to be solved numerically. Kudritzki et al. (1989) have described a simple program for calculating the mass loss rate and terminal velocity of any star as a function of the force multiplier parameters.

The results of the finite disk models differ from the models in the point source limit in three ways:

- (i): The mass loss rate is smaller by about a factor of 0.5 . This is because the radiative acceleration close to the star is reduced. We have seen in the Chapter about the general theories of stellar winds (in this Volume) that a reduction of the acceleration in the subcritical region always leads to a decrease in \dot{M} , because the density scale height in the subcritical

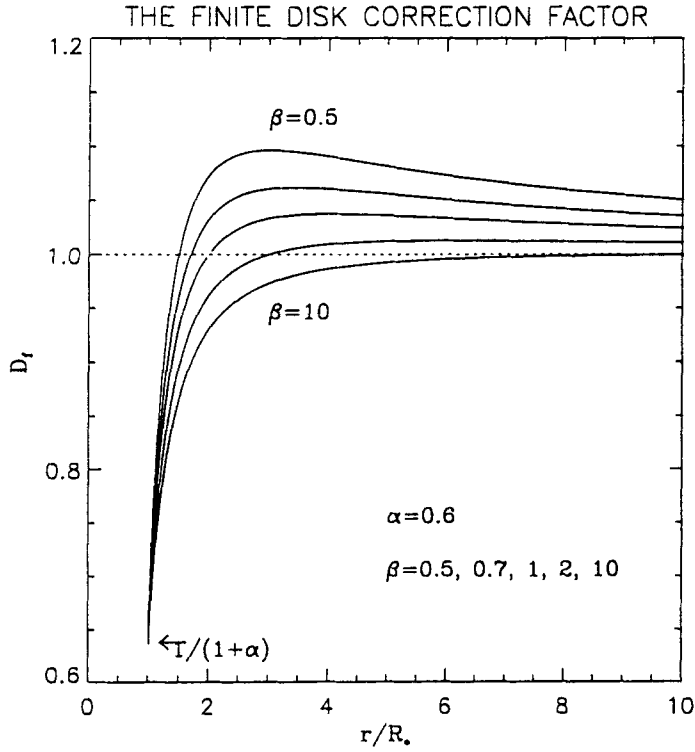


Fig. 6. The finite disk correction factor, D_f , in the case of a force multiplier $\alpha = 0.6$ and a β -type velocity law with several values of β

region becomes smaller which results in a lower density at the critical point. Figure 7 shows the mass loss rates of a number of early-type stars calculated with and without the finite disk correction.

- (ii): The terminal velocity of the wind is larger by about a factor of 2. This arises from two effects.
 - a) Since the mass loss rate is smaller, the density in the wind is smaller and the Sobolev optical depth of the lines is smaller. A larger radiative acceleration then occurs because $g_L \sim t^{-\alpha}$, and this results in a higher terminal velocity. This effect explains an increase in v_∞ by about a factor 1.5.
 - b) The correction factor D_f is larger than unity beyond the critical point. This produces an additional increase in v_∞ . Figure 8 shows the values of v_∞ for a number of early-type stars calculated with and without the finite disk correction factor.

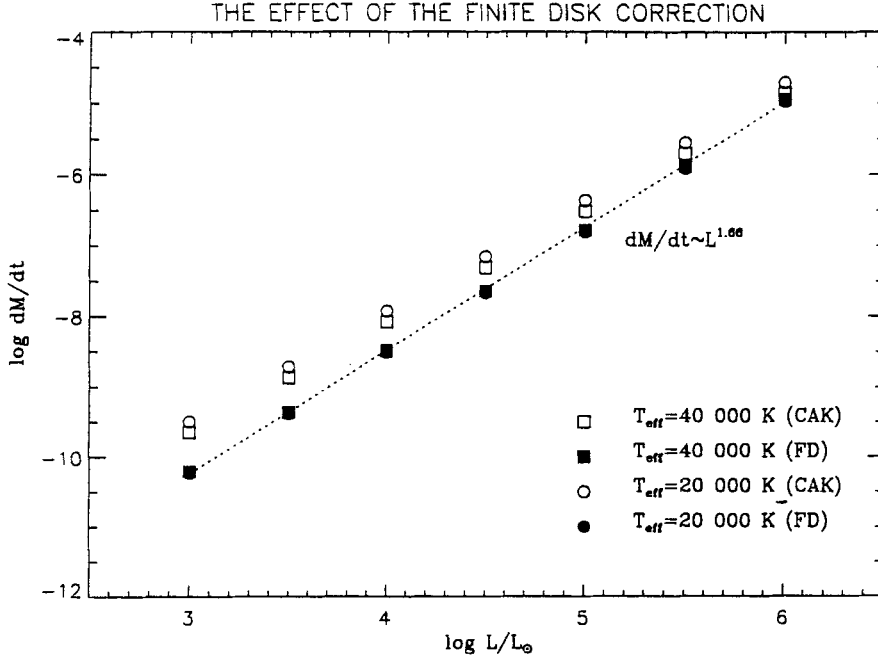


Fig. 7. The effect of the finite disk correction on the mass loss rates of line driven wind models. Filled and open symbols refer to models with and without the finite disk correction respectively for stars of $T_{\text{eff}} = 20000$ K and 40000 K. The mass loss rates are calculated with force multipliers $k = 0.40$, $\alpha = 0.52$ and $\delta = 0.10$. The models with the finite disk correction have mass loss rates lower than for point source models by 0.2 dex at $10^6 L_{\odot}$ to 0.8 dex at $10^3 L_{\odot}$. The mass loss rate scales as $L_*^{1.66}$.

- (iii): The velocity law is slightly “softer” as it rises more gradually. It is approximately a β -law with $\beta \approx 0.8$ rather than $\beta = 0.5$ in the point source limit. Figure 9 shows the calculated velocity law in a wind of an O4-star. Notice the drastic difference of the velocity laws calculated in the Sobolev approximation with or without the finite disk correction factor. The velocity law, calculated with the finite disk correction factor, can be very well represented by a β -law of

$$v(r) = v_{\infty} \left\{ 1 - \frac{0.9983 R_*}{r} \right\}^{0.83}. \quad (43)$$

The figure also shows the results of a stellar wind calculation in which the Sobolev approximation is not applied, but the radiative acceleration

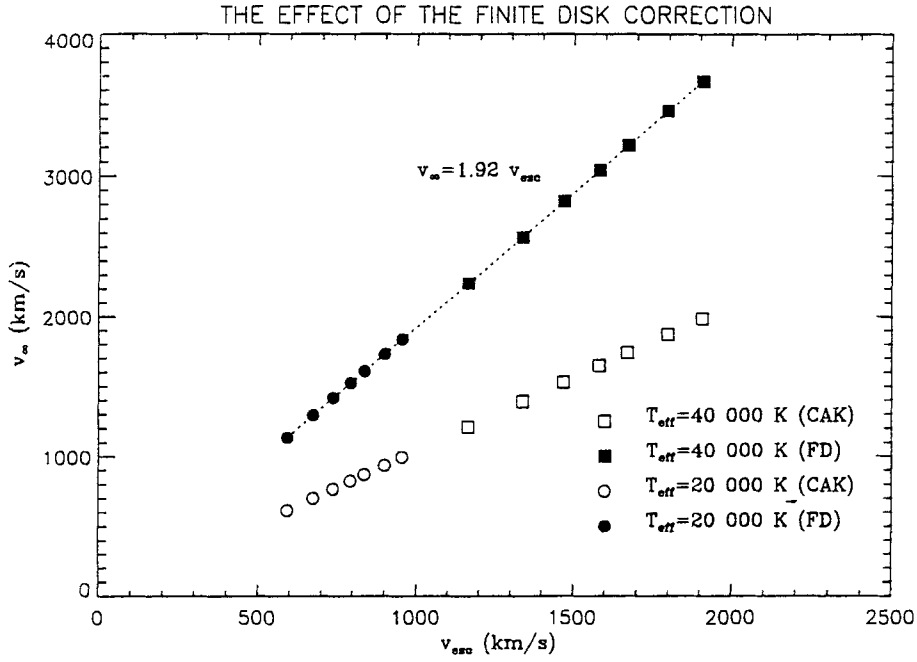


Fig. 8. The effect of the finite disk correction on the terminal velocities of line driven winds. The calculations are for the same models as in the previous figure. The models with the finite disk correction (filled symbols) have almost twice as large terminal velocities as the point source models. The predicted terminal velocities scale with the photospheric escape velocity as $v_\infty \approx 1.92 v_{esc}$ if $\alpha = 0.52$

is calculated exactly with the “comoving frame method”. Notice the very good agreement between the results of the comoving frame method and the Sobolev method with the finite disk correction.

6 The Instability of Line Driven Winds

Up to now we have assumed that the line driven winds are homogeneous and stationary. The results of line driven wind models in terms of mass loss rates, terminal velocities and velocity laws agree very well with the observations. This implies that the stationary models are adequate for describing the global structure of the line driven winds. However, they fail to explain some of the important details of the observations of the winds of hot stars. In particular: the X-rays from the winds of hot stars; superionization of the

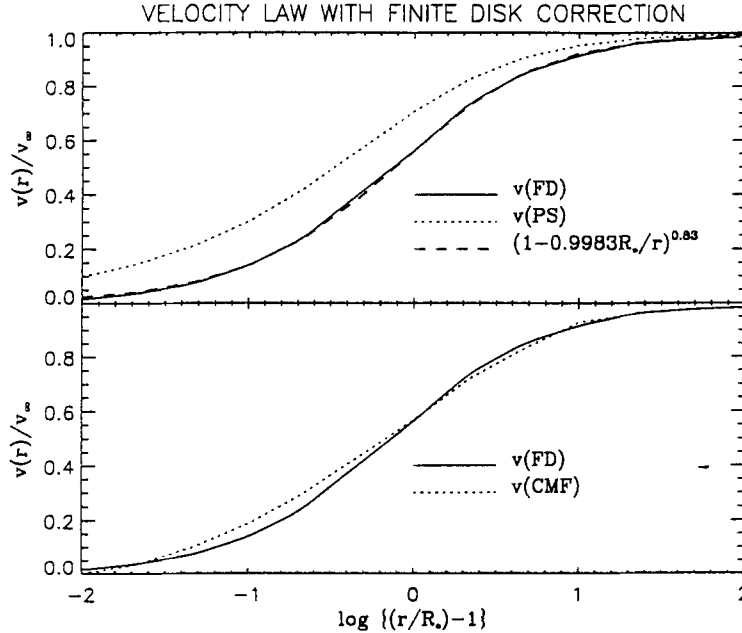


Fig. 9. Upper figure: Comparison between the velocity law of a line driven wind calculated in the point source limit (PS, dotted line) and with the finite disk correction (FD, full line). Notice the large difference. The velocity can very well be fitted to a simple β -law (dashed line) Lower figure: Comparison between the model calculated with the Sobolev approximation (FD, dashed line) and with the more accurate Comoving Frame Method (CMF, full line). This difference is small (from Kudritzki et al. 1989)

winds to ions such as O VI which clearly require an extra source of high energy photons; and the presence and variability of the discrete absorption components in the P Cygni profiles formed in the winds of hot stars. These observations suggest that the radiation-driven winds of O-stars are unstable. We will show by a simple argument why the line driven winds are unstable to small perturbations, e.g. due to small amplitude stellar pulsations.

Suppose a hot star has a stationary line driven wind with a smooth distribution of velocity, density and temperature. Assume that at a certain moment the velocity distribution is slightly perturbed and that this perturbation has the shape of a sine-wave, between r_1 and r_4 , as shown in Fig. 10.

Due to this sine-wave the velocity gradient in the layers where the perturbation occurs changes. Define r_2 and r_3 as the points where the perturbed velocity has the same gradient as the unperturbed velocity law. In the layers $r_1 < r < r_2$ and $r_3 < r < r_4$ the velocity gradient is larger than in the

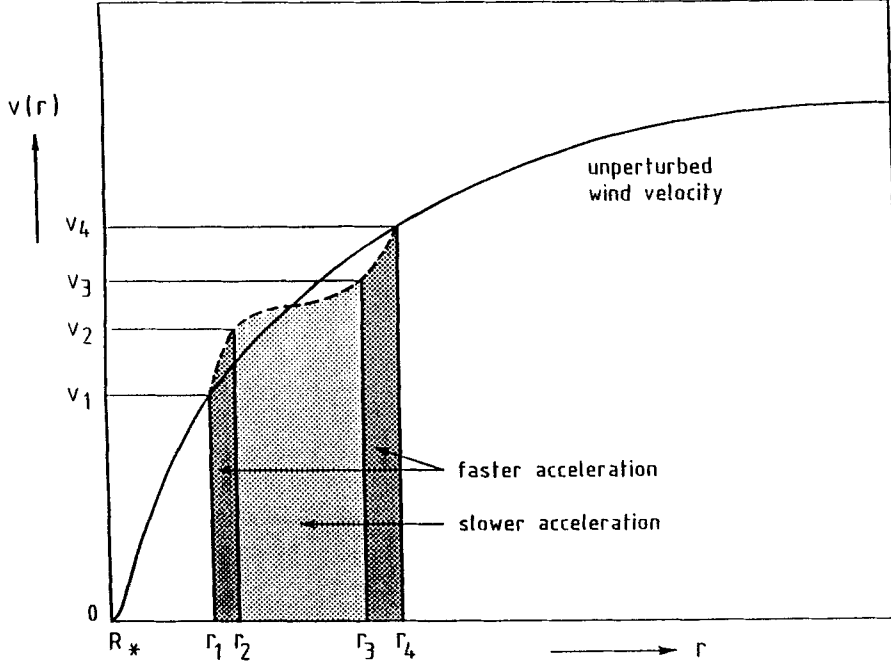


Fig. 10. The effect of a sinusoidal velocity perturbation in a line driven wind. The radiative acceleration is proportional to $(dv/dr)^\alpha$ with $\alpha \approx 0.6$. The velocity gradient between r_1 and r_2 and between r_3 and r_4 is larger than in the unperturbed wind so these layers will be accelerated faster. The layer between r_2 and r_3 has a smaller velocity gradient than in the unperturbed wind, so this layer will be accelerated slower. The difference in acceleration between the layer $r_1 < r < r_2$ and the layer $r_2 < r < r_3$ will produce a shock

unperturbed wind, and in the layer $r_2 < r < r_3$ it is smaller.

The radiative acceleration depends on the velocity gradient and on the density as

$$g_L \sim kt^{-\alpha} \sim \rho^{-\alpha} \left(\frac{dr}{dv} \right)^{-\alpha} \sim \rho^{-\alpha} \left(\frac{dv}{dr} \right)^\alpha. \quad (44)$$

Therefore the layers with a higher velocity gradient, $r_1 < r < r_2$ and $r_3 < r < r_4$, will be accelerated faster than the unperturbed wind at that distance and in the layer $r_2 < r < r_3$ the acceleration will be smaller. (This effect is modified if the change in density is also taken into account). A layer which has a higher value of $\rho^{-1} dv/dr$ than normal will be accelerated with respect to the layers where this value is lower than normal, and the reverse is true for a layer with a lower velocity gradient. In addition there is an effect of a

decreased “shadowing” of the stellar flux by the lower layers of the wind if the gas has a higher velocity than its surroundings. (This effect depends on the velocity increase, rather than on the velocity gradient). It also results in an increase of the radiation pressure on velocity perturbations.

This implies that velocity perturbations will grow in the wind. This will give rise to shocks in the winds because the gas in the layers with higher velocity gradient or lower density will catch up with the slowly moving layer above until they run into each other and shock.

The effects of instabilities in radiation-driven winds have been studied by various groups and have been reviewed by Owocki (1994). Figure 11 shows the results of the time dependent calculations.

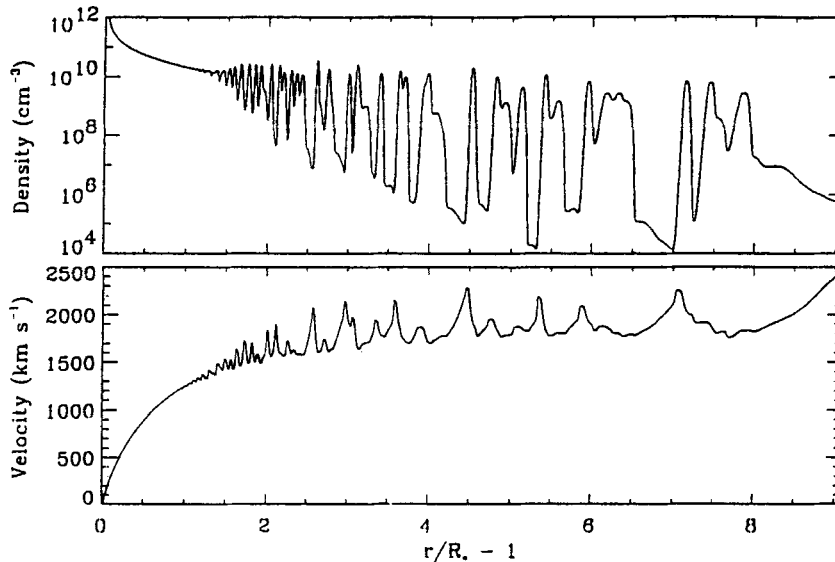


Fig. 11. A snapshot picture of time dependent calculations of a radiation driven stellar wind. Notice the variations in v and ρ due to the occurrence of shocks. The “mean wind” has about the same mass loss rate and the same velocity structure as the shocked wind (from Owocki 1994)

These effects are

- (i): The mean, i.e. time-averaged, mass loss rate of unstable line driven winds is the same as found in the stationary solutions. The time-averaged terminal velocity of the wind and the time-averaged velocity law are also very similar to the stationary case.

- (ii): Velocity and density perturbations can grow on a timescale which is short compared to the characteristic flow time $3R_*/v_\infty$, of the wind. Thus a considerable fraction of the wind, i.e. more than about 10 per cent of its mass, will have gone through shocks. The velocity perturbations in the shocks can easily be about 30 percent of the normal values in a stationary wind. This results in a broadening of the absorption and emission parts of the P Cygni profiles formed in the winds.
- (iii): The shocks can reach temperatures of about 10^7 K. This explains the observed X-ray flux from the winds of hot stars. The high temperature regions correspond to high density regions.
- (iv): The X-rays created in the shocks can superionize part of the wind to high stages of ionization. In particular, ions such as O VI and N V can be created by Auger ionization in which the absorption of a soft X-ray photon results in the ejection of two electrons, e.g. $\text{O IV} + h\nu \rightarrow \text{O VI} + 2e^-$.

7 Comparison Between Observations and Predictions for O and B Stars

7.1 Comparison Between Observed and Predicted v_∞

Lamers et al. (1995) have studied the terminal velocities of winds of O, B and A stars derived from the profiles of UV resonance lines. Their result is shown in Figs. 12 and 13. Figure 12 shows that v_∞ roughly scales with the effective escape velocity, (i.e. corrected for the radiation pressure by electron scattering) as predicted by the line driven wind theory with $v_\infty \approx 1.0$ to $3.0 v_{\text{esc}}$. However, there is a significant scatter in this diagram. This turns out to be due to the fact that the ratio v_∞/v_{esc} is temperature dependent. This is shown in Fig. 13.

The line driven wind theory predicts that

$$v_\infty = X_{FD} \sqrt{\frac{\alpha}{1-\alpha}} v_{\text{esc}} \quad (45)$$

where X_{FD} depends on the finite disk correction and α is temperature dependent.

The jump near 21 000 K is due to the “bi-stability jump” of line-driven winds: the winds of stars with $T_{\text{eff}} > 21\,000$ K are driven by lines in the Lyman continuum, whereas the winds of the cooler stars are driven by lines in the Balmer continuum. The many lines in the Balmer continuum are less optically thick than those in the Lyman continuum, which implies a decrease in the force multiplier α and hence in v_∞/v_{esc} for the cooler stars (Pauldrach and Puls 1990; Lamers et al. 1995). The data also suggest a second bi-stability jump near $T_{\text{eff}}=10\,000$ K.

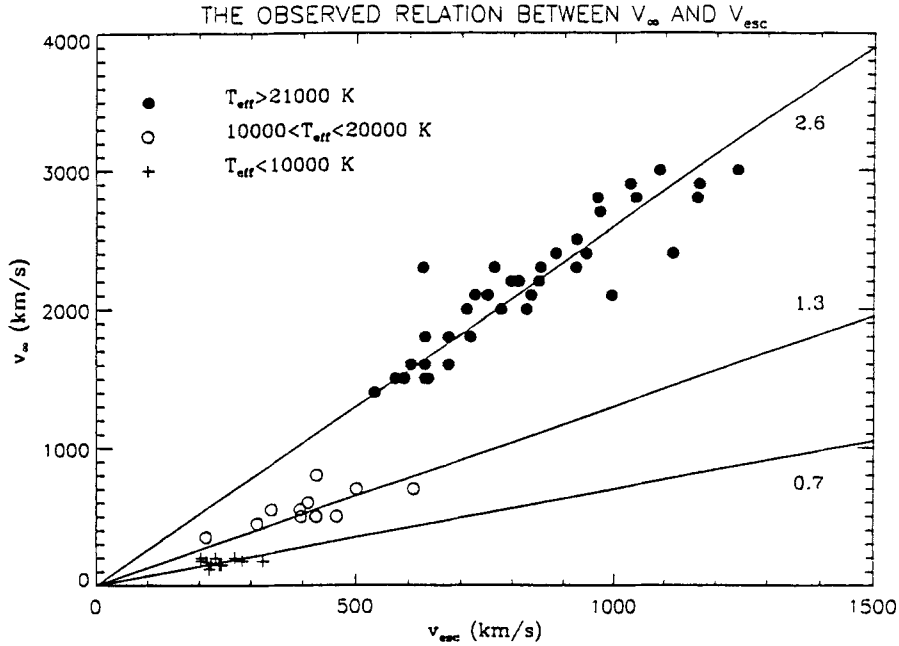


Fig. 12. The terminal velocities, v_∞ of O, B, A supergiants derived from UV lines are plotted versus the effective escape velocities, v_{esc} . The figure clearly shows four branches: Stars with $T_{eff} > 21000$ K (black dots) have a mean ratio of 2.7. Stars with $10000 < T_{eff} < 20000$ K (open circles) have a mean ratio of 1.3. Stars with $20000 < T_{eff} < 21000$ (crosses) have ratios in between 2.7 and 1.3. Stars with $T_{eff} < 10000$ K have a mean ratio of 0.7 (after Lamers et al. 1995)

7.2 Comparison Between Observed and Predicted \dot{M}

The line driven wind theory assumes that the momentum of the wind $\dot{M}v_\infty$ is due to the transfer of radiative momentum L_*/c from the photons to the gas. Therefore the best way to confront the theory with the observations is the comparison between the observed and predicted *momentum* of the wind. This was done for a number of hot stars with well known mass loss rates by Lamers and Leitherer (1993) and by Puls et al. (1996). The result is shown in Fig. 14. The upper part of this figure shows the observed wind momentum as a function of L_*/c and the lower part shows the predicted wind momentum. This figure shows that the observed momentum of the O-stars is approximately in agreement with the predictions (but slightly too high). However, the observed momentum of the Wolf-Rayet stars of types WNL is considerably higher than predicted.

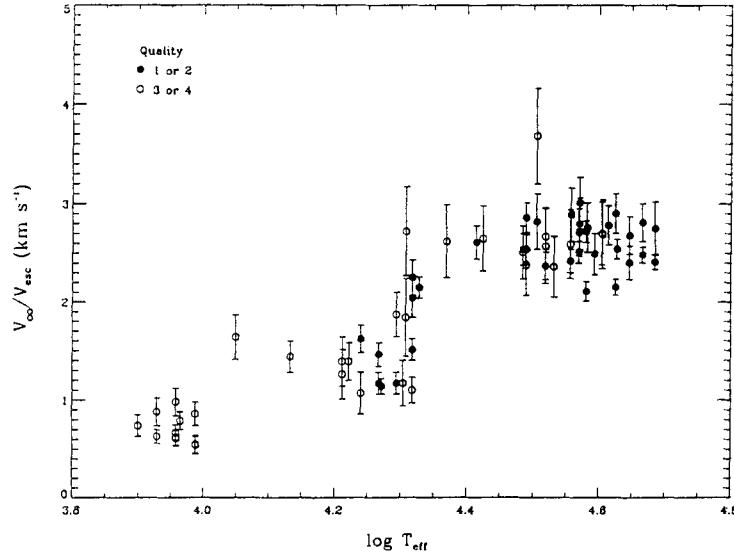


Fig. 13. The ratio $v_{\infty}/v_{\text{esc}}$ as a function of T_{eff} . The same data as in the previous figure. This figure clearly shows that the ratio $v_{\infty}/v_{\text{esc}}$ depends on T_{eff} . There are three regions: $T_{\text{eff}} < 10000$ K, $10000 < T_{\text{eff}} < 20000$ K, $T_{\text{eff}} > 21000$ K. Stars with $20000 < T_{\text{eff}} < 21000$ K show a very large range, which is much larger than the observational uncertainty (from Lamers et al. 1995)

8 Conclusion

The radiation driven wind theory is very successful in explaining the gross properties of the winds of O, B and A stars. The theory is simple and the predicted mass loss rates and terminal velocities depend on the three force multiplier parameters k , α and δ . The difficulties of calculating the radiation pressure due to millions of spectral lines is hidden in these three parameters. The calculations of these three parameters is an enormous task, that has been undertaken by only a few groups.

Although the simple theory can explain the gross properties of the winds, there are several observational indications that real stellar winds are much more complicated: they emit X-rays, they are super-ionized, and they show fast variations in the line profiles. All these effects can in principle be explained by shocks in instable winds. There are however also effects that are not understood: the most prominent one is the large mass loss rate of Wolf-Rayet stars. Another significant unexplained feature is the observed variation of line profiles over periods of days, which seem to be due to some rotation

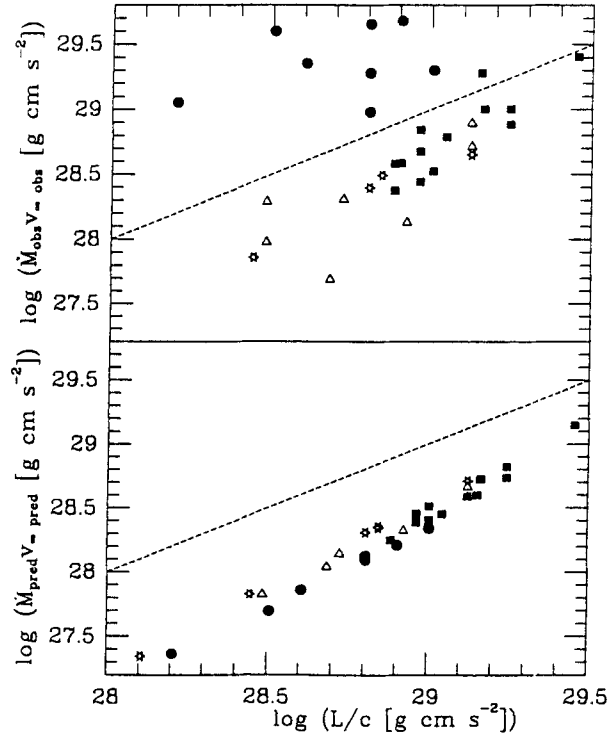


Fig. 14. The observed (upper figure) and predicted (lower figure) wind momentum of O-stars and Wolf-Rayet stars of type WNL versus the photon momentum L_*/c . Dots are WNL stars, other symbols are O stars. The dotted line shows the unity-relation for $\dot{M}v_\infty = L_*/c$. Notice that the observed momentum of the O-stars is slightly higher than predicted, but it is an order of magnitude too high for the WNL stars (from Lamers and Leitherer 1993)

modulated (corotating?) structure in the wind (Kaper and Henrichs, 1994).

We can conclude that the theory is sufficiently accurate to predict and explain the mass loss rates of O, B and A stars, but it still fails on the level of understanding the inhomogeneities and variations in their winds.

References

- Abbott, D.C. (1982): ApJ **259**, 282
 Achmad, L., Lamers, H.J.G.L.M. (1997): A&A in press
 Castor, J., Abbott, D.C., Klein, R.I. (1975): ApJ **195**, 157
 Friend, D., Abbott, D.C. (1986): ApJ **311**, 701
 Gayley, K.G. (1995): ApJ **442**, 296

- Kaper, L., Henrichs, H.F. (1994): Ap&SS **221**, 115
 Kudritzki, R.P., Pauldrach, A., Puls, J., Abbott, D.C. (1989): A&A **219**, 205
 Lamers, H.J.G.L.M., Leitherer, C. (1993): ApJ **412**, 771
 Lamers, H.J.G.L.M., Snow, T.P., Lindholm, D.M. (1995): ApJ **455**, 269
 Owocki, S.P. (1994): Ap&SS **221**, 3
 Pauldrach, A. (1987): A&A **183**, 295
 Pauldrach, A., Puls, J. (1990): A&A **237**, 409
 Pauldrach, A., Puls, J., Kudritzki, R.P. (1986): A&A **164**, 86
 Puls, J., Kudritzki, R. P., Herrero, A. (1996): A&A **305**, 171
 Shimada, M.R., Ito, M., Hirata, R., Horaguchi, T. (1994): in *Pulsation, Rotation and Mass Loss in Early Type Stars*, eds. L.A. Balona et al. (Kluwer Acad. Publ.), p487

Observations of Hot-Star Winds

A.W. Fullerton

Universitäts-Sternwarte München, Scheinerstraße 1, D-81679 München, Germany
e-mail: alex@usm.uni-muenchen.de

1 Introduction

Stellar winds from early-type stars have been studied observationally for more than 120 years, beginning with the detection of peculiar bright lines in visual spectra of a few hot objects by Wolf and Rayet (1867). Beals (1930) first recognized that the emission features of these “Wolf-Rayet stars” (WR stars) were signatures of mass loss, since the observational material available to him showed that some of the line profiles were of the “P Cygni type”. This distinctive shape, named because of its prevalence in the spectrum of the famous B2pe hypergiant P Cygni, is also found in the spectra of novae shortly after outburst, i.e., during a time when they are manifestly experiencing explosive mass ejection. On this basis, Beals inferred that WR stars were also losing mass, and concluded that “practically all of the characteristic features of Wolf-Rayet spectra may be explained on the hypothesis that gaseous material from a Wolf-Rayet star is being continually ejected in a radial direction and with high velocity into space”.

Thus, more than 60 years ago the modern basis for interpreting spectroscopic emission features in terms of dense, extended, and expanding outflows had already been established. What was not initially clear was that the WR stars and the few objects like P Cygni (which we now call luminous blue variables, or LBVs) are just the tip of the iceberg: they are extreme examples of a phenomenon that is ubiquitous among the early-type stars. Important observations by Wilson (1958) and Underhill (1958) provided hints that mass loss occurs commonly by showing that the emission features of a selection of O-type supergiants and giants could be traced to velocities of 500–1000 km s^{-1} , which are comparable to or in excess of the escape velocity. Nevertheless, during the early and mid-1960s the emphasis in hot-star research was on static atmospheric modelling without the assumption of local thermodynamic equilibrium (LTE), while the field of stellar winds lay fallow.

This situation changed abruptly as a result of technological advances that opened the vacuum ultraviolet region of the spectrum to astronomical observations. The modern era of hot-star wind research began on 1965 October 13 when an Aerobee rocket launched from the White Sands Missile Range in New Mexico briefly carried an ultraviolet spectrograph aloft and returned the first ultraviolet spectra of six early-type stars in Orion (Morton 1967a).

As always, a bit of good luck was required to push open a new observational window: Morton (1967a) writes that during the descent,

the cameras, platform, and gyro had broken free of their mounts and pieces of grating, mirror, and film cassette went flying out of the open end of the rocket skin. Both the calcium fluoride spectrograph camera and a 35-mm camera for photographing the star field were lost, and a 2-day search of the impact area yielded nothing. Fortunately, however, the lithium fluoride film cassette was still attached and was recovered

Morton's analysis (1967a, 1967b) of these hard-earned data showed that the resonance lines of highly ionized species like Si IV, C IV, and N V exhibited P Cygni profiles. In contrast to the P Cygni profiles that were typically observed in optical spectra of hot stars, velocities well in excess of the escape velocity were directly measured in these ultraviolet data. For the three stars that make up the belt of Orion (from east to west, these are δ , ϵ , and ζ Orionis, with spectral types of O9.5 II, B0 Ia, and O9.7 Ib, respectively), Morton (1967b) estimated mass-loss rates of $\sim 1 \times 10^{-6} M_{\odot} \text{ yr}^{-1}$ and concluded that these stars would lose a few per cent of their initial mass during their lifetimes. It at once became clear that garden-variety OB supergiants lose mass continuously at rates that are sufficiently high to affect the course of their evolution.

This result came as a complete surprise at the time. Over the past generation, observational and theoretical efforts to understand the nature and origin of these stellar winds have been a dominant theme of hot-star research. It is a tribute to the success of these efforts that the mass loss carried by these outflows is now recognized to be a fundamental astrophysical process that not only causes individual stars to "evaporate" significantly over their short lifetimes (thereby altering their trajectory through the H-R diagram) but also dumps substantial amounts of energy, momentum, and chemically enriched material into their local galactic environment (thereby influencing the dynamics of the interstellar medium and subsequent formation of stars). Excellent introductions to hot stars and their winds include Kudritzki (1988), Kudritzki and Hummer (1990), and Owocki (1990), while Maeder and Conti (1994) provide an overview of the role these objects play in the evolution of galaxies.

The aim of these lectures is to provide an introduction to the most useful observational signatures of the stellar winds of early-type stars. The goal is to provide an appreciation of the physical ingredients and assumptions that are required to obtain estimates of the physical parameters of the winds from these diagnostics, in particular the mass-loss rate, \dot{M} , and the asymptotic (terminal) velocity of the wind at large distances from the star, v_{∞} . The problems associated with each type of diagnostic are also discussed, in order to assess the reliability of the parameters determined from them. The emphasis is on Population I objects, especially O stars and BA supergiants,

though many of the same diagnostics can be applied to related (but more complicated) objects like WR stars and LBVs, and hot Population II objects like the central stars of planetary nebulae.

2 Tracers of Stellar Winds

The observable manifestations of stellar winds are all attributable to the fact that rapidly expanding material surrounds that star, and this material constitutes an excess with respect to an otherwise identical star whose photosphere manages to maintain strict hydrostatic equilibrium. The fundamental equation that connects the hydrodynamic variables of the outflow is the equation of mass continuity. For a homogeneous, steady, spherically symmetric wind, it reduces to a formula for the mass-loss rate:

$$\dot{M} = 4 \pi r^2 v(r) \rho(r) . \quad (1)$$

Rearrangement of (1) shows that at large distances in the wind, where $v(r) \approx v_\infty$, the density decreases only as r^{-2} , which is much slower than the exponential decrease characteristic of the hydrostatic layers of the photosphere. It is the presence and motion of this excess circumstellar material that ultimately permit the outflow to be observed.

Even though they represent large density excesses with respect to hydrostatic atmospheres, the stellar winds of early-type stars consist of very rarefied gas. For example, if we insert parameters typical of an O supergiant into (1), we find that at a height of $1 R_\star$, the density of the wind is approximately $5 \times 10^{-15} \text{ g cm}^{-3}$, which is more than three orders of magnitude smaller than photospheric densities. Thus, stellar winds are environments where radiative processes dominate over collisional processes in determining level populations; i.e., they are very far from being in LTE.

The tracers of this material can be grouped into two main categories: spectroscopic or line diagnostics; and photometric or continuum diagnostics. Signatures can be found in all wavelength regions, from the radio and infrared (IR) through the optical and ultraviolet (UV) to X-rays and possibly even γ -rays (see, e.g., Chen et al. 1996). The emission of these extremely energetic photons is believed to result from time-dependent processes in the wind and not from the steady-state outflow itself, and will not be discussed in detail here.

3 Spectroscopic Diagnostics

Quite generally, spectroscopic observations of absorption or emission lines formed in the atmospheres of stars can be characterized by their positions (i.e., their radial velocities), their strength (i.e., their equivalent widths), and their overall morphology (i.e., the shape of their flux profiles). Each of these

measurable quantities can be used to obtain information about the presence of stellar winds.

For example, systematic trends showing decreasing blue shifts for lines formed at increasing photospheric depth – the so-called Balmer progressions or velocity-excitation relations – are frequently used as stellar wind indicators, because they imply the presence of a deep-seated velocity field that increases outwards and presumably drives mass loss (Hutchings 1979; Kaufer et al. 1997). Systematic trends in the strength of photospheric lines as a function of luminosity may also provide evidence for an outward accelerating velocity field, particularly if they are accompanied by asymmetric line profiles with extended blue wings. The velocity gradient is the essential physical ingredient here, because it systematically shifts the absorption profile of the particular ion to smaller wavelengths at greater atmospheric heights, with the result that more atoms can participate in the formation of the flux profile (hence the increase in the equivalent width of the line) and the flux profile has an extended blue wing (since some of the profile is actually formed at blue-shifted velocities). Mihalas (1979) and Kudritzki (1992) provide useful discussions of this phenomenon, which is nicely illustrated for a sequence of B1 supergiants by Massa et al. (1992).

However, the dominant spectroscopic signatures of stellar winds are the profiles associated with lines that are formed in the rapidly expanding part of the wind. Many profile morphologies are recognized as being formed in out-flowing material. These shapes were classified qualitatively by Beals (1950), and although his scheme is not much used these days, it still provides a useful introduction to the phenomenology associated with stellar wind profiles. Beals recognized eight classes of wind profiles.

- Type I:** This is the classic P Cygni profile, which consists of a blue-shifted absorption “trough” and a red-shifted emission “lobe”. The origin of this shape is discussed in Sect. 3.2.
- Type II:** These profiles are composed of a Type I profile superimposed on a broad, shallow absorption line, typically one from the Balmer series of hydrogen.
- Type III:** This morphology consists of red- and blue-shifted emission peaks and a central reversal. It occurs rarely in OB stars, and then only in some lines of rapid rotators. Although its origin is not completely understood, this shape is due to a combination of the velocity fields associated with radial outflow and rapid stellar rotation; see, e.g., the profiles calculated by Petrenz and Puls (1996), in particular their Figs. 12 and 14.
- Type IV:** These profiles are similar to those of Type I, except they also have one or more extra absorption components in the absorption trough or near the center of the emission lobe.
- Type V:** These “pure emission” profiles are approximately symmetric about the systemic velocity of the star and do not exhibit the absorption trough characteristic of P Cygni profiles. The spectra of WR stars are dominated

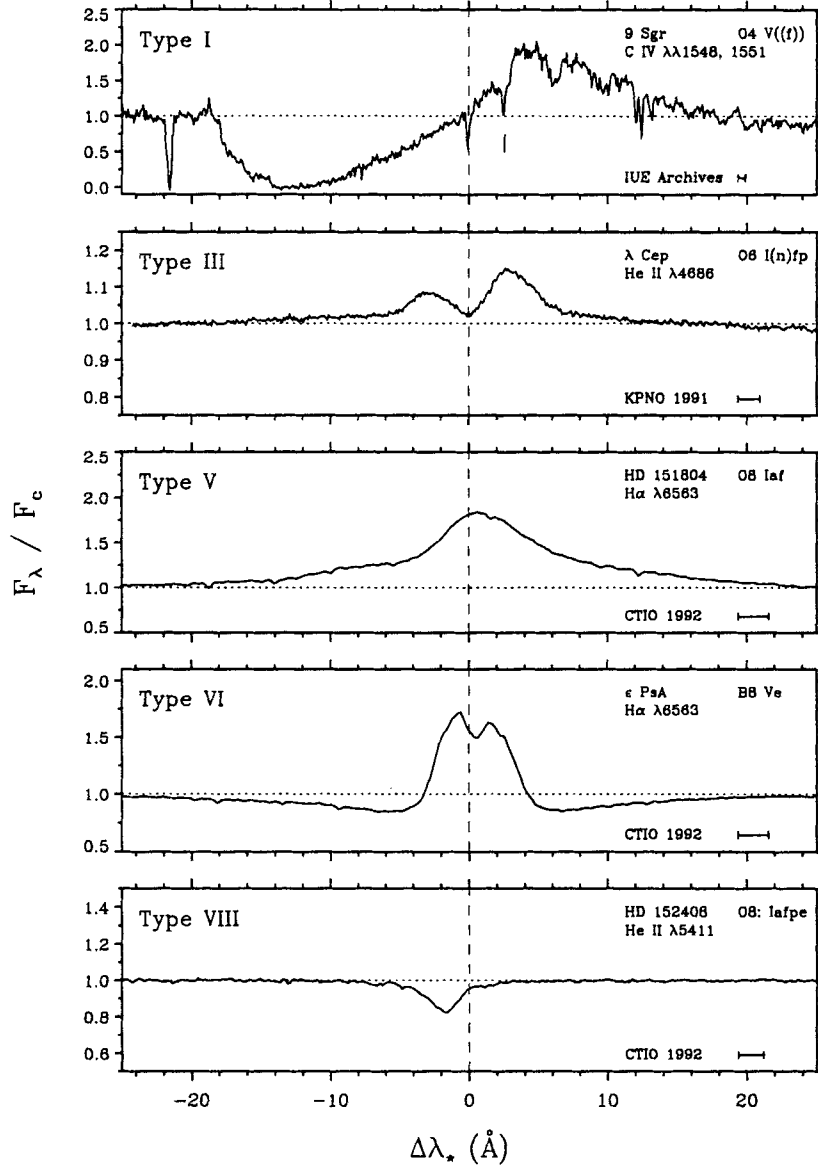


Fig. 1. A selection of line profile morphologies attributed to stellar winds, with classifications according to the scheme of Beals (1950). The wavelength interval corresponding to a velocity of 100 km s^{-1} is indicated by a horizontal bar in the lower right-hand corner, and the position of the red component of the C IV doublet is marked by a vertical line (and the sharp interstellar component)

Table 1. Selected atlases of stellar wind profiles

Reference	Wavelength	Source	Objects
Walborn et al. (1985)	1200–1900 Å	IUE/SWP	O stars
Snow et al. (1994)	1200–3000 Å	IUE	O3–F8 stars
Walborn et al. (1995)	1200–1900 Å	IUE/SWP	B stars
Walborn and Bohlin (1996)	1000–1200 Å	Copernicus	OB stars
Stahl et al. (1993)	4050–9050 Å	FLASH	P Cygni
Hanson et al. (1996)	K band (2 μ)	various	OB stars

by such emission lines, which can also be found in spectra of OB supergiants.

Type VI: This strange morphology consists of a central emission feature that is superimposed on a broad underlying absorption line. The emission is frequently double peaked. These profiles are most commonly associated with Be stars, and consequently a complicated structure of a rotating, expanding stellar wind is implicated in their formation.

Type VII: Beals (1950) describes this morphology as “simply an ordinary undisplaced absorption line such as may appear in any normal star . . .”, and as such it perhaps best serves as a reminder that not all the lines in the spectrum of an early-type star are formed in the moving envelope.

Type VIII: Lines of this type are blue-shifted absorption features, which Beals (1950) thought of as Type I profiles without the emission lobe. The displaced absorption is frequently asymmetric, with a shallower blue wing that is presumably due to the velocity gradient through its region of formation.

Part of this classification scheme is illustrated in Fig. 1, which shows normalized flux profiles as a function of wavelength offset from the rest velocity (corrected for the systemic velocity of the star). Examples of stellar wind profiles can be found throughout the observable regions of the spectrum, from the UV through the optical to the IR. Table 1 lists several atlases that illustrate the rich variety of wind profile morphologies implied by the Beals classification scheme.

3.1 Scattering Versus ρ^2 Formation Processes

The resonance lines of singly or multiply ionized species that are typically found in the UV region of the spectra of early-type stars are superb tracers of the rarefied material found in stellar winds. By definition, resonance lines

are the lowest energy transitions that arise from the ground state. Consequently, these transitions have very short lifetimes, which in turn means that they occur frequently and are intrinsically strong. In particular, the lifetime of a resonance transition is usually much shorter than the time required for radiative excitations or collisions, especially in environments characterized by dilute radiation fields and low particle densities. Thus, when an electron is promoted from the ground state to the first permitted level by absorption of a stellar continuum photon of the appropriate frequency, it will de-excite very rapidly and a resonance line photon will be emitted. The net result of such an interaction is that the incoming, almost radially directed, stellar photon will be scattered into some different direction, thereby imparting radial momentum to the ion without changing the population of the ground state. Consequently, in low-density gases the degree of excitation of an ionic species tends to be very low and there is always a large pool of electrons sitting in the ground state that are capable of scattering radiation.

These factors make resonance lines strong and easily detectable throughout the entire volume of the wind where the ion exists. Since these lines are formed by scattering of continuum photons, their strength depends linearly on ρ , the density of matter, and also on the mean intensity of the dilute radiation field from the star. The resonance lines that are important depend on the ionization balance of the wind, which is largely determined by the radiation field. For O- and early B-type stars, they include multiply ionized species like C IV, N V, and Si IV; for mid- to late B- and early A-type supergiants the resonance lines of singly ionized C, Mg, Al, Si, and Fe are important.

However, as Fig. 1 indicates, wind profiles can also be found in the excited (i.e., non-resonance) transitions that are typically located in the optical and infrared regions of early-type spectra, especially those arising from H, He I and He II. They are usually the result of recombinations from a higher ionization stage, which are followed by radiative de-excitations that create photons. These transitions are intrinsically weaker than resonance lines; furthermore, since the process of recombination requires the interaction of an electron and an ion, they are sensitive to ρ^2 . Consequently, and in contrast to resonance lines, excited transitions are only sensitive diagnostics of the densest regions of the wind, which are usually the parts closest to the star. An important exception occurs if a large population accrues in the lower level of an optical transition for some reason (e.g., the level is metastable or susceptible to non-LTE/dilution effects), in which case the transitions arising from it behave a bit like resonance lines. The He I $\lambda 5876$ triplet in the “yellow” region of the visible spectrum is an example of such a transition.

3.2 Dissecting the P Cygni Profile

Before we can determine what information about the stellar wind is contained in line profiles like those shown in Fig. 1, we need to understand how these

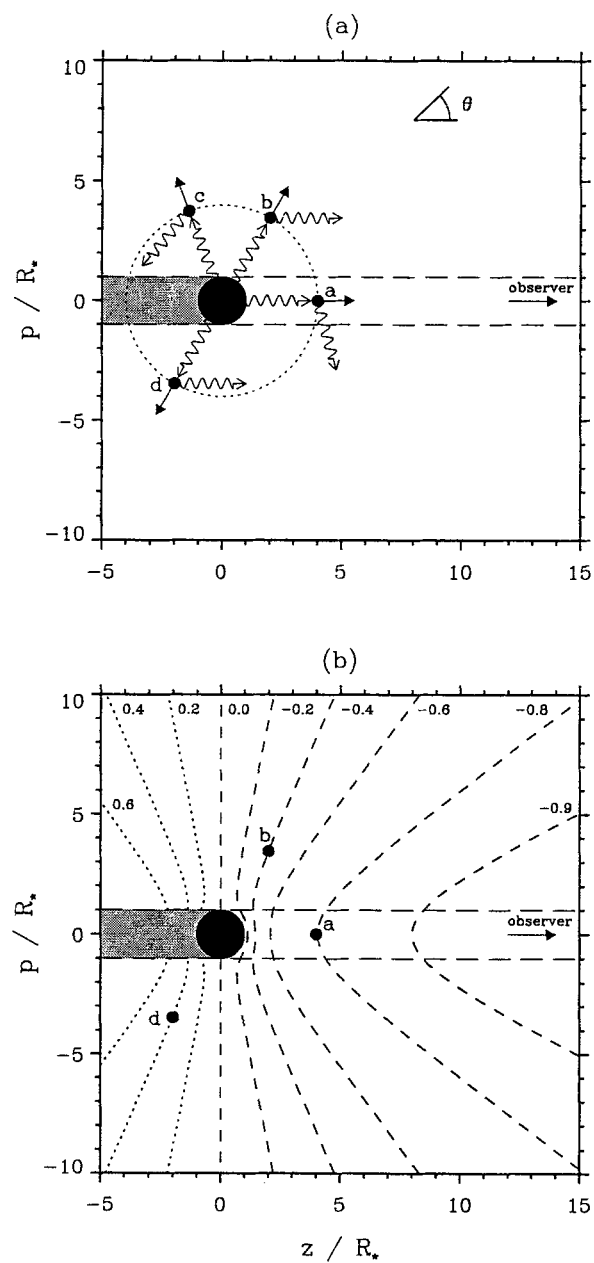


Fig. 2. (a) Schematic diagram of the scattering process. (b) The isovelocity contours associated with the velocity field of a smooth, spherically symmetric stellar wind

profiles are formed. The P Cygni profiles (Beals Type 1) of resonance lines provide the key to understanding these morphologies.

The basic picture is illustrated schematically in Fig. 2(a), which shows a plane through a smooth, spherically symmetric stellar wind. Four ions (labelled a–d) are shown, all of which are located at the same radial distance from the star and therefore experience the same expansion velocity (which is indicated by short, radially directed vectors). Ions at larger (smaller) radii than those illustrated will be moving faster (slower), since the velocity field of a smooth wind increases monotonically outwards. Stellar continuum photons are injected continuously into the wind from the star along paths that are nearly radial. If their wavelength matches the Doppler-shifted wavelength of the resonance line transition associated with ions a–d, then the photon can interact radiatively; since the wind material is moving away from the star, this means that the wavelength of the continuum photons must be blueward of the rest wavelength of the resonance line. An important consequence of this “tuning” is that if a continuum photon can interact with the resonance transitions at some particular radius, it cannot interact with ions at larger or smaller radii, because their Doppler shifts will be greater or smaller, respectively. Consequently, at larger or smaller radii the wind is *transparent* to the photons that can be scattered in the resonance lines of the ions indicated in Fig. 2.

As described above, the net result of this interaction for a resonance line is that the incoming photon is scattered into some different direction. These scatterings have two consequences for a distant observer (who is arbitrarily situated in the z -direction in Fig. 2): (1) photons that were destined to be recorded by the observer can be removed from the line of sight, as in the case of the scattering illustrated for ion “a”; and (2) photons that were not originally heading in his/her direction can be redirected into his/her telescope, as illustrated for ions “b” (where the photon is forward-scattered into the direction of the observer from an ion in the hemisphere approaching the observer) and “d” (where the photon is back-scattered from an ion in the receding hemisphere). Since the observer’s direction subtends a very small fraction of the 4π steradians surrounding the star, there is a good chance that an originally unobservable photon will be scattered into a new direction that is also unobservable, as illustrated for ion “c”. Some photons will even be back-scattered directly to the stellar surface where they will be reabsorbed by the photosphere.

We can be more specific about the distribution of the scattered photons as a function of position in the flux profile seen by the distant observer. This position may be given in terms of wavelength, frequency, or “radial velocity”; we will usually use the velocity coordinate, but will refer to it as “line-of-sight” velocity, (V_{los}), in order to avoid confusion with the radial component of the velocity field associated with the stellar wind. The V_{los} of a scattered photon depends on the Doppler shift due to wind expansion of

the ion that it interacted with and the projection of this displacement onto the observer's line of sight, i.e., the cosine of the angle θ between the velocity vectors and the z-axis indicated in Fig. 2(a). Contours of equal V_{Los} for the velocity field of a typical expanding stellar wind are shown in Fig. 2(b), where they are labelled in units of v_∞ with positive velocities denoting recession. Of course, these contours in the equatorial plane are actually surfaces in 3D space; they are sometimes called "common direction" (CD) surfaces since they require the specification of the direction of an observer (see, e.g., Rybicki and Hummer 1978).

The isovelocity contours permit the redistribution of continuum photons to be mapped to positions in the observed line profile, which can be conveniently divided into an absorption part and an emission part. This mapping is illustrated in Fig. 3 for a line of moderate strength (panel a) and a strong line (panel b). Three regions of the wind contribute to the profile:

1. Material in the column projected against the disk of the star removes continuum photons from the line of sight at blue-shifted velocities that range from 0 to the maximum expansion velocity where the ion still exists (which is frequently v_∞), thereby producing the blue-shifted absorption trough. Ion "a" provides an example of the removal of a photon at $V_{\text{Los}} = -0.8 v_\infty$.
2. Material at other places in the approaching hemisphere adds photons at blue-shifted velocities (e.g., ion "b": $V_{\text{Los}} = -0.4 v_\infty$) by forward-scattering, which collectively produce the blue-shifted emission shown in the middle panels of Fig. 3. In contrast to the absorption trough, the emission at a particular V_{Los} includes contributions from many different radii that will in general sample a wide range of densities, temperatures, and ionization equilibria.
3. Material in the receding hemisphere adds back-scattered photons at red-shifted velocities (e.g., ion "d": $V_{\text{Los}} = +0.4 v_\infty$) to the emission profile. The emission profile is not symmetric about $V_{\text{Los}} = 0$ because back-scattered photons originating in the shaded "occultation region" are re-absorbed by the stellar core before they can reach the observer. The differences between the blue- and red-shifted emission are especially pronounced for winds that expand more slowly, since in these cases the star subtends a larger solid angle at radii where the density is still high enough for many scattering interactions to occur.

The bottom panel shows how a P Cygni profile results from adding the absorption and emission contributions from these regions to produce the characteristic morphology of a blue-shifted absorption trough and a red-shifted emission lobe.

The comparison between moderate and strong scattering lines in Fig. 3 is also instructive. The upper panels show that for a line of sufficient intrinsic strength, all the continuum photons can be scattered from the observer's line

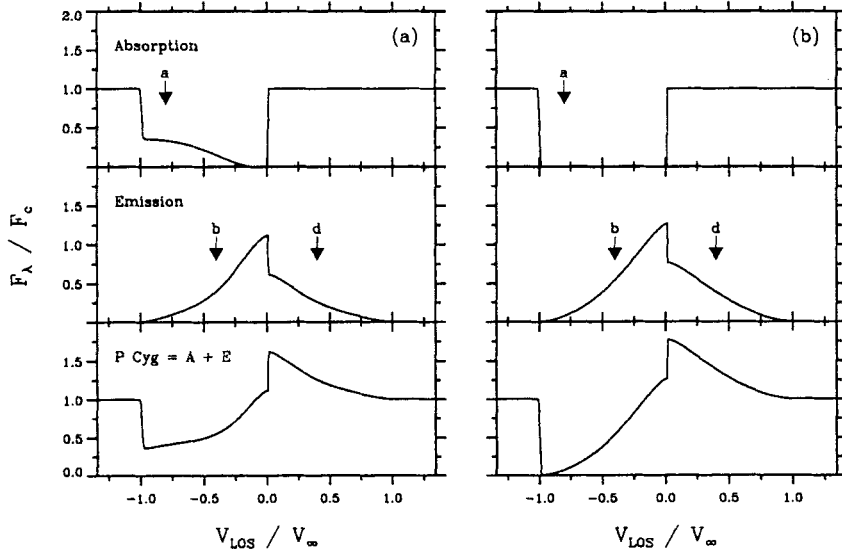


Fig. 3. Schematic diagram showing the formation of a P Cygni profile of a UV resonance line for the case of (a) a moderately strong line; and (b) a strong line

of sight, whereas a weak line in the same wind (i.e., same ionization and density structure) will not completely extinguish the continuum light directed toward the observer. By the same token, the strong line will scatter more photons towards the observer, so that its emission component (middle panel) is stronger at all velocities. This is a reflection of the fact that scattering is a conservative process: since photons are not created or destroyed in the wind (though some are lost through back-scattering to the photosphere), and since the absorption component of a strong line removes more photons from the observer's line of sight compared to a weak line, more photons must be forward- and back-scattered towards the observer.¹ Thus, despite the total extinction of the continuum source by the cylinder of material projected against the disk of the star, the P Cygni absorption trough of a strong line formed in a smooth, spherically symmetric wind never exhibits extended regions of zero flux. If the ion responsible for the strong resonance line exists throughout the wind, then the only place where its absorption trough will have zero flux is at $V_{\text{LOS}} = v_{\infty}$, since forward-scattering from material anywhere else in the approaching hemisphere will necessarily be seen at smaller line-of-sight

¹ This argument breaks down after all photons have been removed from the absorption trough, at which point the strength of the emission lobe also saturates.

velocities. Put another way, the isovelocity contours collapse to a point for $V_{\text{LOS}} = \pm v_{\infty}$, and the positive case is not observable due to occultation by the star. Hence, for monotonically expanding winds, the maximum velocity seen at the blue-edge of the absorption trough of a strong line is a good diagnostic of v_{∞} .

P Cygni profiles are formed when scattering dominates the transfer of radiation through the wind. If instead photons are created in the wind through radiative or collisional (“ ρ^2 ”) processes, the absorption component tends to be filled in by locally produced photons. Similarly, the emission component can become very strong, since the number of photons that emerge from the wind is not simply a reflection of the number of stellar continuum photons initially injected. Unless there is some additional factor associated with the physics of the transition in question (e.g., the lower level is overpopulated for some reason), “pure emission” profiles are formed in these cases. Although the atomic processes responsible for these spectral features are more complicated than resonance line scattering, the mapping between isovelocity contours and position in the profile remains the same. Of course, more complicated velocity fields (e.g., coupling between rotation and expansion) or geometries (e.g., disks) will change the shape of the contours, and the interplay between the velocity field, density distribution, and ionization balance in the wind are ultimately responsible for the variety of wind profile morphologies catalogued by Beals.

Although P Cygni profiles are unambiguous signatures of outflow, the same is not true of pure emission features. For example, there are a number of narrow emission lines in the spectra of O stars (see, e.g., Morrell et al. 1991 or Underhill 1995a,b for recent discussions), most of which are formed by two-electron processes (“dielectronic recombinations”) in deep layers of the atmosphere. The most famous of these are the N III $\lambda\lambda 4634, 4640, 4641$ lines, whose formation in static, plane parallel atmospheres was first explained by Mihalas and Hummer (1973). Although the strength of these features often suggests that they are partially formed in the low-velocity region of the stellar wind, they should be distinguished from the very broad stellar wind profiles typical of Beals Type III or V.

3.3 Calculation of Line Profiles Formed in Stellar Winds

The preceding discussion of the P Cygni profile also illuminates many aspects of the problem of computing line profiles formed in a stellar wind. In general, this is a formidable task; but, as Castor 1970 realized, it can be handled very effectively by combining the formalism of escape probabilities (see, e.g., Sect. 3.2 of Hubeny, this Volume) with the Sobolev approximation. What follows is a sketch of this approach as it applies to smooth, spherically symmetric, monotonically expanding winds. For rigorous discussions of this elegant technique, see Castor 1970, Rybicki and Hummer (1978), Rybicki

(1984), or Mihalas (1978; Chapter 14). Although the escape-probability formalism is at present the most widely used, alternative approaches exist: see, e.g., Lucy (1971).

The equation of radiative transfer in the observer's frame for spherically symmetric geometry is given, e.g., by (27) in Hubeny's lectures.² It can be reformulated in the Cartesian "p-z" geometry illustrated in Fig. 2 as an ordinary differential equation for rays specified by their impact parameter p :

$$\frac{dI_\nu(z; p)}{dz} = k_\nu(z; p) [S_\nu(z; p) - I_\nu(z; p)] \quad (2)$$

where $r, z = r\mu$ and $p = r\sqrt{1 - \mu^2}$ are measured in units of R_\star and $\mu \equiv \cos \theta$ is the cosine of the angle between a point in the wind and the direction to the observer, as indicated in Fig. 2(a); k_ν is the absorption coefficient; and where "complete redistribution" has been assumed (see Sect. 3.1 of Hubeny, this Volume). This reformulation is a great simplification, and allows the "formal solution" to be written down immediately. If I_ν^* is the continuum intensity of the star at frequency ν and $z_\star = \sqrt{1 - p^2}$ denotes the z-coordinate associated with the stellar surface for $p \leq 1$, then the formal solution is:

$$I_\nu(p) = \begin{cases} \int_{z'=-\infty}^{\infty} S_\nu(z') e^{-\tau_\nu(z')} d\tau_\nu(z') & \text{for } p \geq 1 \\ \int_{z'=z_\star}^{\infty} S_\nu(z') e^{-\tau_\nu(z')} d\tau_\nu(z') + I_\nu^* e^{-\tau_\nu(\infty)} & \text{for } p < 1 \end{cases} \quad (3)$$

where the optical depth variable is

$$\tau_\nu(z; p) = \int_{z_{\min}}^z k_\nu(z'; p) dz' \quad (4)$$

with $z_{\min} = -\infty$ for $p \geq 1$ and $z_{\min} = z_\star$ for $p < 1$. Once $I_\nu(p)$ is known, the flux profile can be calculated directly:

$$F_\nu/F_c = \int_0^\infty [I_\nu(p)/I_\nu^*] 2p dp \quad (5)$$

In the case of line radiation, (3) can be viewed as the mathematical equivalent of Fig. 3. It says that for rays projected against the stellar disk (i.e., $p < 1$) the flux received by a distant observer is made up of a "direct" component that is extinguished by material in front of it (i.e., the absorption trough) and a "diffuse" component (i.e., sources of emission due to forward-scattering). For rays not projected against the stellar disk ($p \geq 1$), only diffuse light is sent to a distant observer. In the case of UV resonance lines, the diffuse light is entirely due to scattering.

Since (3) is a formal solution, the source function and the optical depth for the line of interest need to be known before it can be applied. The level

² For convenience, results presented by Hubeny (this Volume) will be referred to by their equation numbers in his lectures preceded by "H": e.g., (H27).

populations for resonance lines are controlled by radiative transitions between only two levels, and so the source function for the two-level atom given by (H82) for the case of “pure scattering” ($\epsilon = 0$) is directly applicable. Hence, $S_\nu = \bar{J}$, where \bar{J} is the frequency-averaged mean intensity of line radiation defined by (H81). Schematically, the mean intensity can be viewed as a competition between the number of continuum photons that arrive at location r versus the number of line photons that escape from the same location, so that

$$\bar{J}(r) = \frac{\text{probability that a stellar continuum photon penetrates to } r}{\text{probability that a line photon escapes from } r} . \quad (6)$$

These quantities are related to the angle- and frequency-averaged escape probabilities defined by (H88), which in turn depend fundamentally on the optical depth variable for different directions μ at location r in the wind. Consequently, the computation of a line profile pivots on the computation of τ_ν , after which the calculation can be charted as $\tau_\nu \rightarrow$ escape probabilities $\rightarrow \bar{J} \rightarrow S_\nu \rightarrow I_\nu(p) \rightarrow F_\nu$.

Unfortunately, the calculation of τ_ν for arbitrarily moving media is complicated by the frequency dependence of the absorption coefficient, k_ν . In static atmospheres, k_ν is often written as the product of a spatial part and a normalized absorption profile that accounts for the frequency dependence (and is generally assumed to be constant);

$$k_\nu = k_0(r) \times \varphi(\Delta\nu) , \quad (7)$$

where $\int_{-\infty}^{+\infty} \varphi(\Delta\nu) d\nu = 1$ and $\Delta\nu = \nu - \nu_0$ for a line with rest frequency ν_0 . This separation is not strictly valid in a moving atmosphere, because ν is itself a function of r owing to the bulk motion of the fluid, but the functional form can be recovered by allowing explicitly for the Doppler shift in frequency, which can be accomplished by redefining $\Delta\nu = \nu - \nu_0 + [\nu_0 \cos \psi v(r)]/c$, where ψ is the angle between the radial direction and the direction of scattering, so that $\cos \psi v(r)$ is the projection of the expansion velocity onto the new direction of flight. Although this simple redefinition allows us to retain the form of (7), it also shows that in a moving medium, $k_\nu \equiv k_\nu(r, v, \psi)$, i.e., that frequency and spatial variables are intertwined, so that many different combinations of positions and frequency contribute to a particular frequency in the observer’s frame; recall, e.g., the isovelocity contours illustrated in Fig. 2(b).

However, in the presence of sufficiently large velocity gradients, the “tuning” required for a photon to excite a line transition localizes the material that is capable of absorbing it, and this breaks the coupling between frequency and spatial variables. This localization is the essence of the Sobolev approximation, which is sometimes called the “large velocity gradient” or “supersonic” approximation. Fig. 4(a) illustrates the Sobolev approximation in a schematic way for the frame of reference that is moving with the mean

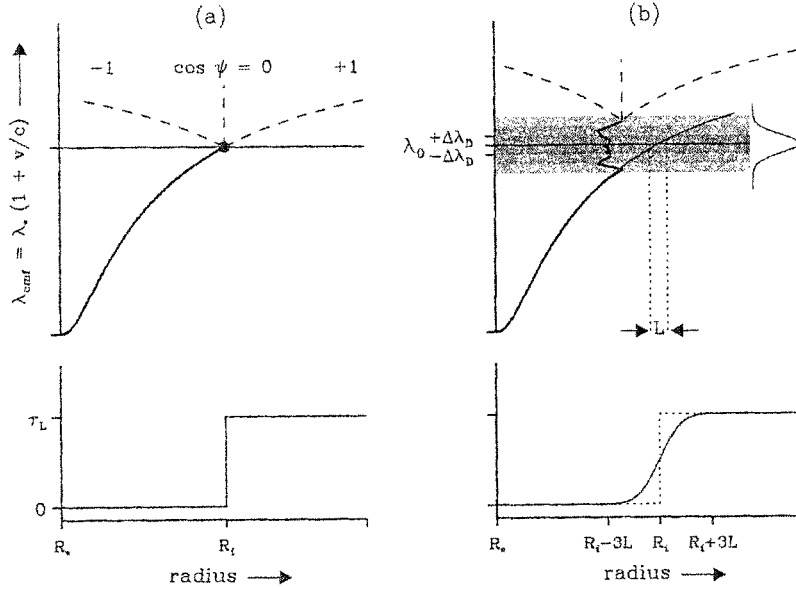


Fig. 4. Schematic illustration of the Sobolev approximation (after Owocki 1990) and the distribution of Sobolev optical depth for (a) an infinitely thin transition centered on λ_0 ; (b) a transition with a Gaussian profile characterized by a 1-sigma dispersion of $\Delta\lambda_D$

flow of the expanding wind. The star is receding with respect to this “co-moving frame”, and the thick solid line shows the systematic redshift of a photon emitted with wavelength λ_* at the stellar surface as a function of radius. Consider a bound-bound transition with rest wavelength λ_0 in the spectrum of an ion, and suppose for the moment that the absorption profile $\varphi(\Delta\lambda)$ of this transition is a delta function. The photon λ_* travels *unimpeded* through the material of the stellar wind until its wavelength in the comoving frame matches λ_0 , whereupon it may be absorbed by the line transition and re-emitted in some other direction. Three possible scatterings are indicated in the upper panel of Fig. 4(a), which correspond to forward-scattering ($\cos \psi = 1$; i.e., the photon continues along its original course); sideways-scattering ($\cos \psi = 0$); and back-scattering towards the star ($\cos \psi = -1$).

The key point is that since the wind is an expanding medium, the material in *any* direction is receding from the scattering site, just as all galaxies recede from one another in the case of the expanding universe. Thus, irrespective of the scattering angle, the wavelength of the redirected photon in the comoving frame must be redshifted, which means it cannot interact again with

a transition of wavelength λ_0 and is free to travel through the wind along its new trajectory. As a result, the processing of stellar continuum photons through a bound-bound transition is localized to a single radius, R_i , which is determined by λ_* , and the variation of optical depth with radius is the step-function shown in the lower panel of Fig. 4(a). For this simplified case, the solution of the equation of radiation transfer reduces to determining the fraction of incident photons that are scattered into the different directions ψ .

In practice, the absorption profile of a transition is never a delta function, but has a finite width $\Delta\lambda$ associated with it; e.g., the absorption profile is dominated by thermal Doppler broadening in the low-density environments typical of hot-star winds, so that φ is a Gaussian characterized by a root-mean-square dispersion parameter (sigma) of $\Delta\lambda = \Delta\lambda_D = v_{th}\lambda_0/c$, where v_{th} is the thermal velocity of the parent ion. This case is illustrated in Fig. 4(b), which shows that after travelling freely through lower regions of the wind (as before) the stellar photon first impinges on the blue wing of the line. The scattered photon will in general be redirected and redistributed in wavelength (frequency), so that it will perform a random walk in space and wavelength that takes it from the weak absorption typical of the blue wing to the strong absorption of the line core. The step size associated with this random walk gets quite small as the photon makes its way towards the line core, but its eventual emergence at the red wing – possibly after many scatterings – is assured because of the overall expansion of the wind.

However, even though the number of scatterings may be very much larger than in the case of the infinitely narrow line, the net result is that a photon is absorbed at the blue wing of the line, emerges after a final scattering in the red wing, and continues its travel in a different direction but without further interactions, exactly as before except that the interaction occurs over a larger range of radii. As shown in the lower panel of Fig. 4(b), the finite width of the line softens the step-function character of the radial distribution of optical depth, but does not affect the essential localization of the interaction region *provided that the velocity gradient is sufficiently steep*. The relevant figure of merit to describe “sufficient steepness” is the Sobolev length, L , which is the distance over which the mean flow speed of the wind increases by v_{th} , and can be thought of as the local optical depth scale height. From Fig. 4(b), $dv/dr \approx v_{th}/L$ or $L = v_{th}(dv/dr)^{-1}$. The Sobolev approximation is valid when L is much smaller than the distance over which other hydrodynamical variables (e.g., density) change. The local density scale height, L_ρ , may be estimated from (1):

$$L_\rho \equiv \frac{\rho}{|d\rho/dr|} \approx \frac{v}{|dv/dr|} \gg \frac{v_{th}}{|dv/dr|} = L, \quad (8)$$

since $v_{th} \approx 10 \text{ km s}^{-1}$ while $v \approx 1000 \text{ km s}^{-1}$ for hot-star winds. Thus, the Sobolev approximation is generally excellent, except at small velocities, where $v \approx v_{th}$.

This localization of the radiative transfer enormously simplifies the calculations of τ_ν . Since the radiative transfer occurs over spatial scales that are much smaller than other hydrodynamical scale lengths, the spatial part of absorption coefficient (7) can be taken outside the optical depth integral (4):

$$\tau_\nu(z; p) \stackrel{\text{SA}}{\approx} k_0(r) \int_{z_{\min}}^z \varphi(\nu - \nu_0 + [\nu_0 \mu v(z; p)]/c) dz', \quad (9)$$

which can then be transformed in a straightforward way to an integral over frequency in the comoving frame (i.e., spatial variables can be exchanged for frequency variables). For Gaussian absorption profiles, the integral can be done analytically, which represents a tremendous simplification even compared to static atmospheres. An important result to emerge from these manipulations is the expression for the Sobolev optical depth in the radial direction at a particular radius (or, equivalently, velocity) in the wind. For a transition between a lower level l and an upper level u of an ion, this is

$$\pi_\nu(r) = \left(\frac{\pi e^2}{m_e c} \right) f_{lu} g_l \lambda_{lu} \left(\frac{n_l}{g_l} - \frac{n_u}{g_u} \right) \left(\frac{dv}{dr} \right)^{-1}, \quad (10)$$

where the first terms on the right-hand side denote the strength of the transition in terms of its classical oscillator strength (where all symbols have their usual meanings), λ_{lu} is the rest wavelength of the transition, g_l (n_l) and g_u (n_u) are the statistical weight (number density) of the lower and upper levels, respectively, and dv/dr is the local radial gradient of the velocity field.

Once $\tau_\nu(z)$ is known, the calculation of a line profile formed in the stellar wind can proceed according to the plan outlined before. Several computer programs are available for this purpose, the most widely used of which is the efficient ‘‘Sobolev with Exact Integration’’ (SEI) program described by Lamers et al. (1987)³. The idea of using the Sobolev approximation to compute the source function, but doing the flux integration ‘‘exactly’’, is due to Hamann 1981 and is in contrast to the previous approach of relying on the step-function behaviour in $\tau_\nu(r)$ inherent to the Sobolev approximation to simplify the integrations as well (e.g., Castor and Lamers 1979). With the SEI approach, it is straightforward to allow for the radiative coupling of the source functions of closely spaced doublets (Olson 1982; see also Lamers et al. 1987), which is of practical importance since most of the UV resonance lines are blended doublets. The SEI formalism is also sufficiently flexible that generalizations to allow for deviations from spherical symmetry (e.g., Bjorkman et al. 1994; Cranmer 1996) or monotonic expansions (e.g., Puls et al. 1993) can be implemented in a simple way. More complicated situations like these can also be treated by using a Monte Carlo approach to radiative transfer: see, e.g., Caroff et al. (1972), Lucy (1983), or Puls et al. (1994).

³ A FORTRAN version of this program can be downloaded from the homepage of Collaborative Computer Project No. 7 (CCP7) on the Analysis of Astronomical Spectra. Its URL is currently <http://star.arm.ac.uk/ccp7/>.

3.4 UV Resonance Lines

Equation (1) shows that the mass-loss rate for a spherically symmetric wind can be calculated once the radial distribution of velocity and mass density are known. Although quite a lot of information about the “velocity law”, $v(r)$, is encoded in the shape of the P Cygni profile, it is not possible to measure the density distribution directly because the winds of hot stars cannot be spatially resolved at UV wavelengths. On the other hand, the strength of the absorption and emission components constrain the total number of ions of the species responsible for the resonance line that are present in the wind. Consequently, the general strategy for extracting information from the P Cygni profiles of UV resonance lines is to use the integrated line strength from *unsaturated* profiles to constrain the left-hand side of (1), and to rely on the velocity law (which is best determined from strong or saturated lines) for information concerning the radial distribution of the material. The line strength and shape of the velocity law are determined by fitting synthetic profiles computed from parameterized models of the stellar wind to observed line profiles.

Consider the resonance line of ion j of the element with atomic number k . Let the mass of a particle of element k be m_k and its abundance by weight be X_k ; then, if $n_{jk}(r)$ and $n_k(r)$ represent the number densities of the ion and its parent element, respectively, it follows that

$$n_{jk}(r) = \frac{n_{jk}(r)}{n_k(r)} n_k(r) = q_{jk}(r) \frac{X_k}{m_k} \rho(r) = \frac{\dot{M}}{4\pi} \frac{X_k}{m_k} \frac{q_{jk}(r)}{v(r) r^2}, \quad (11)$$

where $q_{jk}(r) \equiv n_{jk}(r)/n_k(r)$ is the fraction of element k that exists in the ground state of ion j , and where the expression for ρ from (1) has been substituted. We have previously argued that the degree of excitation will be low for ions in a rarefied medium, so that to a good approximation all of the ions k will be in their ground state, which implies that the local Sobolev optical depth in the radial direction given by (10) can be simplified:

$$\tau_{uv}(v(r)) = \left(\frac{\pi e^2}{m_e c} \right) f_{lu} \lambda_0 n_{jk} \left(\frac{dv}{dr} \right)^{-1}. \quad (12)$$

The usual approach is to parameterize $\tau_{uv}(v)$ as the product of the integrated optical depth (for ion j of element k), \mathcal{T}_{jk} , and a normalized function of velocity, $\mathcal{F}(v; \alpha)$ that is defined by adjustable parameters $\alpha = (\alpha_1, \alpha_2, \dots)$, so that

$$\tau_{uv}(v) = \mathcal{T}_{jk} \mathcal{F}(v; \alpha). \quad (13)$$

Lamers et al. (1987) discuss the motivation for some of the more popular functional forms of $\mathcal{F}(v; \alpha)$. It is not strictly necessary to assume a functional form for the radial distribution of optical depth, since the absorption trough of unsaturated P Cygni profiles contains sufficient information to determine this empirically (see, e.g., Haser 1995 or Haser et al. 1995 for an alternate,

and probably preferable, approach). Nevertheless, with this ansatz, the direct integration of (12) can proceed in terms of known parameters:

$$\begin{aligned}
 \int_{v_0}^{v_\infty} \tau_{uv} \, dv &= \int_{v_0}^{v_\infty} \mathcal{T}_{jk} \mathcal{F}(v; \alpha) \, dv \\
 &= \mathcal{T}_{jk} \\
 &= \left(\frac{\pi e^2}{m_e c} \right) f_{lu} \lambda_0 \int_{R_*}^{\infty} n_{jk} \, dr \\
 &= \left(\frac{\pi e^2}{m_e c} \right) f_{lu} \lambda_0 \mathcal{N}_{jk} \, , \tag{14}
 \end{aligned}$$

where \mathcal{N}_{jk} is the column density of ion j of element k between the surface of the star and the observer. The parameters α and \mathcal{T}_{jk} are determined from the fit to the profile, and hence \mathcal{N}_{jk} is also known.

However, in order to fit the profile, the velocity law that describes the distribution of velocity as a function of radius must also be determined. The key parameter (which is traditionally called “ β ”) defines the steepness of the spatial velocity gradient associated with the expansion. There are several versions of the “beta-velocity law” that are distinguished by their treatment of the velocity field near the photosphere, but the conventional form is

$$v(r; v_0, \beta) = v_0 + (v_\infty - v_0) \left(1 - \frac{R_*}{r} \right)^\beta \, , \tag{15}$$

where v_0 is the outflow velocity deep in the wind⁴. Fig. 5 shows the shape of the beta-velocity law for several values of β , and emphasizes that small values of β signify steeper (“faster”) gradients. This functional form reflects the necessity of lifting the material out of the gravitational potential well of the star, though the exact value of β depends on details of the mechanism responsible for driving the wind; see, e.g., the lectures by Lamers (second contribution to this Volume) on the theory of line-driven stellar winds. The theory of radiatively driven stellar winds predicts that β should be near 0.8 for O-type stars (Pauldrach et al. 1986).

For a spherically symmetric wind that is smooth and steady, we have already seen that the position of the blue edge of the absorption trough of a strong P Cygni profile is a diagnostic of v_∞ . The emission lobe of P Cygni profiles provides information about β ; see, e.g., Fig. 6, which shows that both the shape and strength of the emission lobe are sensitive to the velocity gradient for the case of a strong line. Physically, this sensitivity arises from the inverse proportionality between density and velocity implied by (1): for

⁴ Formally, v_0 is the wind velocity at $r = R_*$, though it is preferable to think of it as the velocity at the sonic point (i.e., the sonic velocity for the ion) since this is where deviations from the hydrostatic density stratification start to become significant.

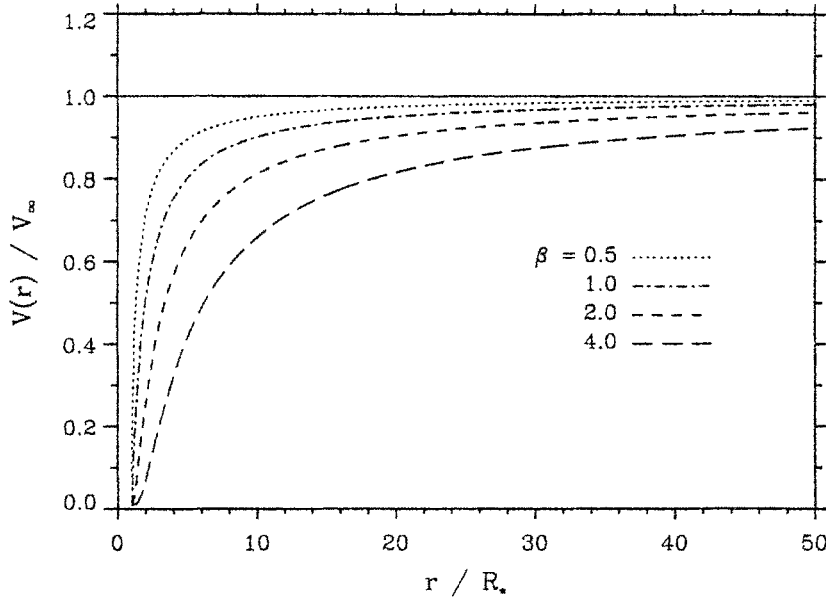


Fig. 5. The beta-velocity law given by (15) as a function of radius for $v_0 = 0.01 v_\infty$ and several values of β

a fixed \dot{M} , a “slower” velocity law (larger β) results in higher densities of material at small radii, which enhances the number of photons scattered towards the observer at small values of V_{Los} , all other things being equal. Weaker lines also respond in a similar way to changes in β , but in practice the parameters associated with the velocity field are more difficult to disentangle from the other factors (e.g., $q_{jk}(r)$, \mathcal{T}_{jk}) that affect their shapes. Thus, the main parameters associated with the velocity field of the wind, v_∞ and β , can both be determined from the P Cygni profiles of strong UV resonance lines.

Suppose that we have used our favourite computer program to achieve an acceptable fit of the P Cygni profile of an unsaturated UV resonance line. In order to do this, we have had to overcome the usual sort of practical problems, like rectifying the observed data (which can be difficult in the UV due to heavy line blanketing) and allowing for the underlying photospheric line (either by using an observed, purely photospheric template spectrum or by computing the profile in some way). At the end of this process, we’ve determined:

- the parameters v_0 , v_∞ , and β that define the velocity law.
- the total optical depth of the resonance transition, \mathcal{T}_{jk} , and hence its column depth, \mathcal{N}_{jk} , via (14).

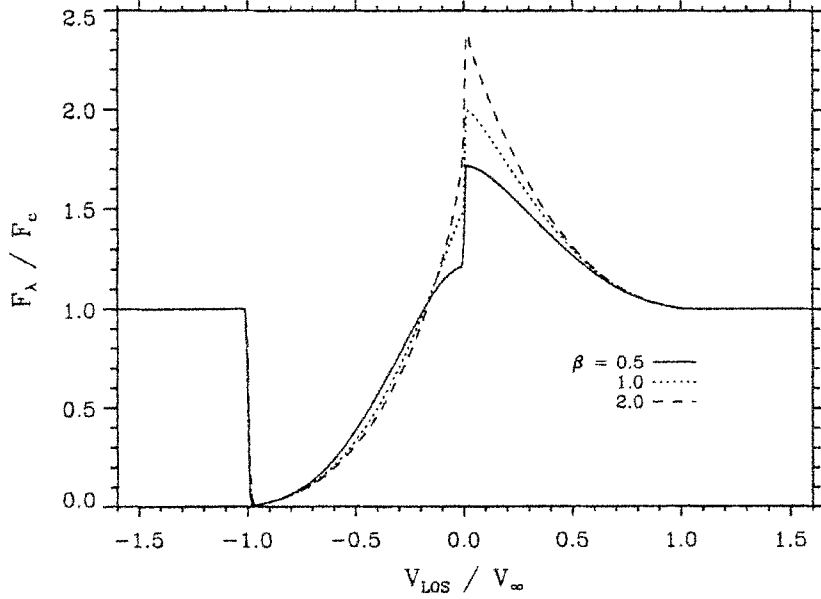


Fig. 6. P Cygni profiles of a strong resonance singlet line calculated for several values of the velocity-law parameter β . More emission results from “slower” velocity laws

- the parameters α describing the distribution of optical depth as a function of velocity (or radius).

How close does this information get us to \dot{M} ? The column depth can also be determined by direct integration of (11), which, after some rearranging becomes

$$\dot{M} \int_{R_*}^{\infty} \frac{q_{jk}(r)}{r^2 v(r)} dr = 4\pi \frac{m_k}{X_k} \int_{R_*}^{\infty} n_{jk}(r) dr = 4\pi \frac{m_k}{X_k} \mathcal{N}_{jk} . \quad (16)$$

Following Howarth and Prinja (1989), the mean value of $q_{jk}(r)$ can in addition be defined by

$$\bar{q}_{jk} \equiv \frac{\int_{R_*}^{\infty} q_{jk}(r) / [r^2 v(r)] dr}{\int_{R_*}^{\infty} 1 / [r^2 v(r)] dr} = \frac{\int_{R_*}^{\infty} q_{jk}(r) / [r^2 v(r)] dr}{\mathcal{I}(v_0, v_{\infty}, \beta)} , \quad (17)$$

and so

$$\dot{M} \bar{q}_{jk} = 4\pi \frac{m_k}{X_k} \frac{\mathcal{N}_{jk}}{\mathcal{I}(v_0, v_{\infty}, \beta)} . \quad (18)$$

Everything on the right-hand side has been measured or is otherwise known, with the possible exception of X_k , which has to be determined from photospheric analysis of the star or simply assumed.

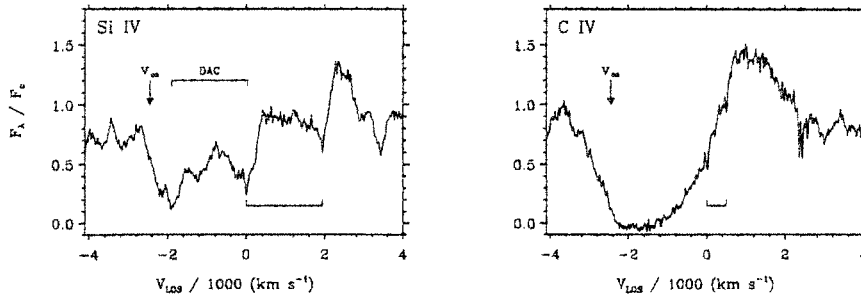


Fig. 7. An IUE spectrum of ξ Per (SWP 34559) showing the P Cygni profiles of two UV resonance lines. Left: the unsaturated Si IV doublet, with a soft blue edge and DACs in the absorption trough. Right: the saturated C IV doublet, with a soft blue edge and an extended black trough. The rest positions of the blue and red components of the doublets are marked; the velocity scale refers to the blue component

However, we ultimately fail to determine \dot{M} because we don't know \bar{q}_{jk} : it is simply not possible to measure the ionization fraction of an element on the basis of a single line. Usually, the ionization balance can be constrained by examining the strength of lines from the adjacent stages. Unfortunately, the resonance lines of stages adjacent to those responsible for the observed P Cygni profiles usually fall in the extreme UV region of the spectrum, where the flux of early-type stars is small owing to absorption in the Lyman continuum of interstellar hydrogen. To make matters worse, theoretical predictions are not especially helpful: if the prediction is that the ion is the dominant stage, then the P Cygni profile is invariably saturated, and only provides a lower limit on \mathcal{N}_{jk} . Alternately, if the ion is a trace stage, theoretically predicted values of its q_{jk} are uncertain since they depend sensitively on the details of the calculation (e.g., inclusion of X-rays from shocks, inclusion of line blanketing in the extreme UV region of the spectrum; see Pauldrach et al. 1994) that are not yet considered to be completely reliable (Groenewegen and Lamers 1991). The only option at present is to try to estimate \bar{q}_{jk} by comparing the values of $\dot{M}\bar{q}_{jk}$ obtained from UV resonance lines with mass-loss rates determined from other diagnostics that are not sensitive to ionization (e.g., radio continuum measurements; see Howarth and Prinja 1989). So, for the moment, we are left in the unsatisfying situation that the best qualitative tracers of the diffuse gas in stellar winds are not the best estimators of the mass-loss rate.

To compound these difficulties, there are also complications with the determination of the velocity law from the P Cygni profiles of UV resonance lines. The problem is that the blue edges of the absorption trough of strong lines are rarely observed to be as steep and well defined as illustrated in

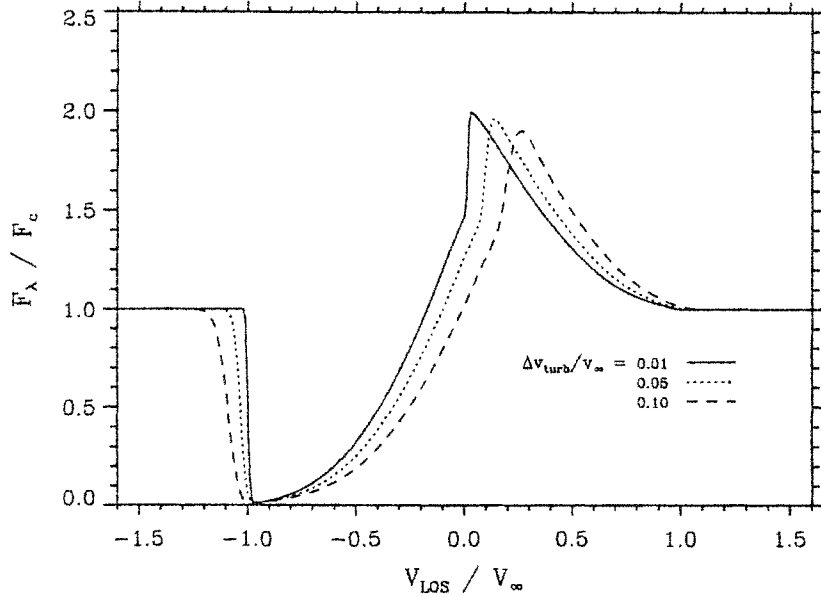


Fig. 8. P Cygni profiles of a strong resonance singlet line calculated for several values of the velocity dispersion parameter Δv_{turb} . These calculations assume that the dispersion is constant throughout the wind, and show that increasing the size of Δv_{turb} softens the blue edge, extends the region of saturation in the absorption trough, and shifts the emission peak redward

Figs. 4 and 5, but approach the continuum more gradually. Consequently, the interpretation of the position of the blue edge as a “clear-cut” diagnostic of v_{∞} is compromised. This deviation from the classical P Cygni shape is illustrated in Fig. 7 for the Si IV and C IV resonance doublets of the O7.5 giant ξ Persei; see also the C IV profile of 9 Sge in the top panel of Fig. 1.

The “softening” of the blue edge of the absorption trough is generally interpreted as an indicator that another, more chaotic velocity field is superimposed upon the mean expansion of the wind (Sect. 3.6). This extra velocity field is usually referred to as “turbulence”, though it is preferable to think of it as a velocity dispersion that acts as an extra broadening agent for the material in the wind rather than turbulence in a strict hydrodynamical sense. Purely for convenience, it is assumed to have a Gaussian distribution that is characterized by its root-mean-square dispersion parameter, Δv_{turb} , which can be added in quadrature to the v_{th} to produce a net broadening that does not require substantial changes to the SEI approach to calculating line profiles. The dispersion parameter Δv_{turb} may be taken to be constant throughout the wind (as in Groenewegen and Lamers 1989) or as an increas-

ing function of radius (as in Haser 1995 or Haser et al. 1995; this tends to suppress the redshift of the emission lobe, which is overestimated for some of the fits presented by Groenewegen and Lamers 1989). Figure 8 illustrates the effect of a constant broadening on the P Cygni profile of a strong singlet, and shows in particular the “softening” of the blue edge of the absorption trough by the extra broadening, which shifts the maximum blue-shifted velocity in the absorption trough to $v_{\infty} + n \Delta v_{\text{turb}}$ (where $n \lesssim 3$ depends on the total optical depth of the line). Thus, in practice, v_{∞} is *overestimated* if it is assumed to correspond to the blue edge of the trough. Since the determination of β depends on the shape of the emission lobe, it will also be affected by the inclusion of turbulent broadening. In practice, this complication just means that Δv_{turb} must also be determined simultaneously with v_{∞} and β by a detailed fit to the observed profile.

However, Fig. 7 also shows that there are several additional peculiarities associated with the UV P Cygni profiles of ξ Per. First, the absorption trough of the strong C IV doublet exhibits an extended interval of blackness (a “black trough”), something that we previously noted is impossible for a smooth wind. Second, the absorption trough of the unsaturated Si IV line is disrupted by the presence of narrow optical depth enhancements, which are called “discrete absorption components” (DACs). These three peculiarities – a soft blue edge, black troughs, and DACs – occur very commonly among OB stars; as discussed in Sect. 3.6, they are all evidence for the presence of time-dependent structure in the stellar wind of most or all early-type stars. As such, they tend to undermine the picture of the stellar wind as a smooth, spherically symmetric, steady outflow that currently serves as the basis for quantitative modelling.

3.5 Optical Emission Lines

The main diagnostics of hot-star winds at optical wavelengths are the broad emission features that are found in transitions of H, He I, and He II. $H\alpha$ is typically the strongest of these features, though lines like He I $\lambda 5876$ and He II $\lambda 4686$ are also important, particularly in spectra of O-type supergiants. A wide range of morphologies can be observed in these profiles (see Fig. 1), including partially filled photospheric absorption lines in the case of weak winds. The information about the structure of the stellar wind contained in them is comparable to the information contained in UV resonance lines: for a spherically symmetric wind, the overall strength of the emission indicates the amount of material, while the shape of the line profile depends on how the material is distributed.

However, there are also significant differences compared to resonance lines. From a practical point of view, the ρ^2 dependence of recombination lines means that they are not sensitive diagnostics of rarefied gas. Consequently, they are not well suited to determining v_{∞} , and in practice this parameter

must be obtained from UV resonance lines. At the same time, their comparative weakness is partially offset by the relative ease with which high resolution, high signal-to-noise ratio (S/N) spectroscopic observations can be obtained from ground-based observatories. Since the shape of the line profile can be defined quite precisely from such high-quality data, very weak, high velocity emission wings can be used to determine M , providing that emission above the continuum is present. Similarly, the height and width of the central part of the line profile can be used to constrain the β -exponent of the velocity law, since slower velocity laws produce stronger and narrower central emission peaks. Although ground-based observations of $H\alpha$ (and $\text{He I } \lambda 5876$) are frequently contaminated by blending with dense concentrations of telluric lines (mostly due to water vapour) and sometimes by nebular emission, effective techniques exist to remove these features from the observed spectrum or otherwise limit their impact on the quantitative analysis of the spectra.

Unfortunately, the optical emission lines are a much more complicated case to analyze quantitatively. On the positive side, we know from the outset that H and He are completely ionized until spectral types near A (for H) or early B (for He), so that the main stumbling block encountered for resonance lines is entirely avoided for optical emission features. However, on the negative side (and in contrast to the resonance lines), the excitation balance governing the transition of interest is not known a priori, and detailed non-LTE calculations of the statistical equilibrium in the accelerating atmosphere are required to determine the relevant level populations. The non-LTE population of level i in ion j of element k , n_{ijk} , is often expressed in terms of its LTE value, n_{ijk}^* , and its "departure coefficient", $b_{ijk} \equiv n_{ijk}/n_{ijk}^*$, so that

$$n_{ijk} = b_{ijk} n_{ijk}^* = b_{ijk} n_{0(j+1)k} n_e \Phi_{ijk}(T_e) \quad , \quad (19)$$

where $n_{0(j+1)k}$ and n_e are the number densities of the ground state of the next higher ionization stage and electrons, respectively, and $\Phi_{ijk}(T_e)$ is the Saha-Boltzmann factor defined by Mihalas (1978; equation 5-14), which depends on the electron temperature (T_e) and the difference in energy between state i and the continuum of ion j . Analogous expressions for the populations of the lower and upper levels of a line transition can be substituted into (10) to obtain the Sobolev optical depth in the supersonic part of the wind. For the important case of $H\alpha$, $(l, u) = (2, 3)$ and we obtain

$$\begin{aligned} \tau_{23}(r) &= \left(\frac{\pi e^2}{m_e c} \right) f_{23} g_2 \lambda_{23} \left(\frac{n_2}{g_2} - \frac{n_3}{g_3} \right) \left(\frac{dv}{dr} \right)^{-1} \\ &\propto n_H n_e [b_2 \Phi_2(T_e) - b_3 \Phi_3(T_e)] \left(\frac{dv}{dr} \right)^{-1} \\ &\propto \left(\frac{\rho}{m_H} \right)^2 \left(\frac{4X^2 + I_{\text{He}}XY}{4} \right) [b_2 \Phi_2(T_e) - b_3 \Phi_3(T_e)] \left(\frac{dv}{dr} \right)^{-1} \quad (20) \end{aligned}$$

where the subscripts $j = 0$ and $k = 1$ have been suppressed; we have noted that n_{011} is the number density of protons in the wind, which in turn is given

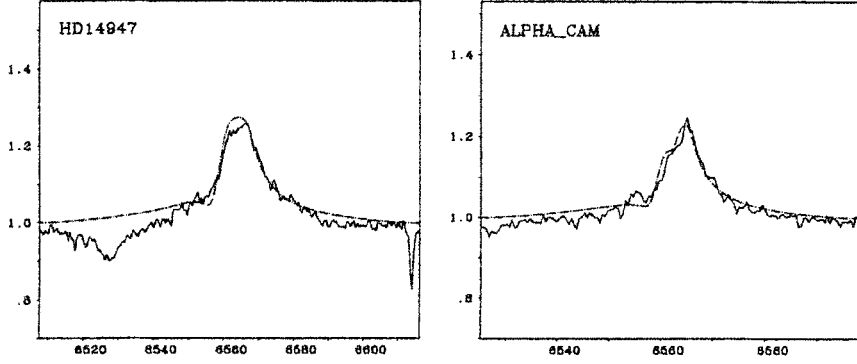


Fig. 9. Fits to observed $H\alpha$ profiles by Puls et al. (1996). Left: HD 14947 (O5 If⁺; $\dot{M} = 7.5 \times 10^{-6} M_{\odot} \text{ yr}^{-1}$; $\beta = 1.0$). Right: α Cam (O9.5 Ia; $\dot{M} = 5.2 \times 10^{-6} M_{\odot} \text{ yr}^{-1}$; $\beta = 1.1$)

by the number density of hydrogen, n_H ; and we have made the approximation $n_e \approx n_H + I_{He} n_{He} = (\rho/m_H)(X + I_{He}Y/4)$, where $(X, Y) \equiv (X_1, X_2)$ are the abundances of hydrogen and helium by mass fraction, and I_{He} is the number of electrons released per helium ion ($I_{He} = 2$ for O and early B-type stars). Equation (20) emphasizes the ρ^2 dependence of the optical depth in $H\alpha$, and shows the explicit dependence of recombination processes on T_e through the Saha-Boltzmann functions.

The observed profile of an optical emission line typically includes significant contributions from the quasi-static photospheric layers, the zone that spans the sonic point of the wind, and the supersonic region of the wind, and the necessity of calculating non-LTE departure coefficients over such a large line-forming region represents an imposing computational challenge. In particular, the Sobolev approximation is not applicable in the deepest of these layers, where the velocity gradient of the expansion is small; and the artifice of dividing the line formation regions into a hydrostatic photosphere and a supersonically expanding wind (the “core-halo” approach) does not treat the density and velocity structure of the transition zone properly. Moreover, radiative couplings with other bound-bound transitions (e.g., the blending of He II $\lambda 6560$ with $H\alpha$) or the complex effects of line blocking in the far UV (in the case of He II $\lambda 4686$) must also be incorporated. Puls et al. (1996) provide a comprehensive discussion of all these problems, with special emphasis on the formation of $H\alpha$ profiles in the winds of early-type stars.

These complications can be treated rigorously only in the framework of “unified model atmospheres”, which perform complete non-LTE treatments

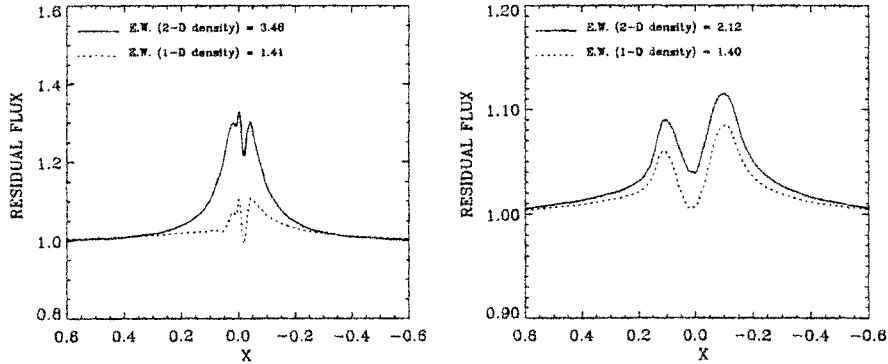


Fig. 10. $H\alpha$ profile strength and morphology as a function of inclination angle for 1D (dotted) and 2D (solid) density distributions, a fixed $\dot{M} = 6 \times 10^{-6} M_{\odot} \text{ yr}^{-1}$, and $v_{\text{rot}} = 250 \text{ km s}^{-1}$. Left: $i = 0^{\circ}$. Right: $i = 90^{\circ}$. The abscissa is $V_{\text{Los}}/v_{\infty}$ in the reference frame centered on the star (opposite to previous figures); note the difference in ordinate scales. In both cases, the 2D distributions produce more emission from the same amount of wind material; the difference is particularly dramatic for the “pole-on” orientation. See Petrenz and Puls (1996) for details

of moving atmospheres without introducing artificial distinctions between the photosphere and the wind (Gabler et al. 1989). Although the initial calculations of such models were quite cumbersome, more efficient algorithms (that still use a variety of approximations) have been developed in the past few years, and several programs are now capable of performing interactive (or nearly interactive) modelling of optical emission lines: see, e.g., de Koter et al. (1993), Schaerer and Schmutz (1994), and Santolaya-Rey et al. (1997). Alternately, Puls et al. (1996) describe a very efficient hybrid approach that can be used to model line profiles of a particular wind feature for objects that span a limited range of spectral types by using parameterized fits to the radial distribution of the relevant departure coefficients, which are obtained from a grid of unified model atmospheres. Puls et al. (1996) applied this approach to the determination of \dot{M} from $H\alpha$ profiles of a large sample of O stars, for which the other fundamental stellar parameters (T_{eff} , $\log g$, R_{\star} , Y , $v \sin i$, and v_{∞}) had previously been determined by the methods of “quantitative spectroscopy”. Figure 9 shows that very good fits to observed spectra can be obtained, which result in precise determinations of \dot{M} and β .

However, the *accuracy* of these determinations depends rather strongly on the correctness of the assumptions of spherical symmetry and homogeneity, i.e., on whether the assumed distribution of material in the wind is a good approximation for the real distribution. Consider, e.g., two equal volumes of a uniform, spherically symmetric wind that are located at the same radial distance from the star. Let the density in one volume be half the density in

a corresponding volume of a uniform wind (i.e., $\Delta m_1 = 0.5 \rho_0 \Delta V$, where ρ_0 is the density of the smooth wind) and the density in the other be 50% more ($\Delta m_2 = 1.5 \rho_0 \Delta V$). The total mass in these two “clumps” is the same as in the corresponding volumes of the smooth wind, but since the number of recombinations scales with ρ^2 , the emission that arises from them is proportional to $(0.5^2 + 1.5^2) \rho_0^2 = 2.5 \rho_0^2$, which is 1.25 times that from the smooth wind. If we attempted to model the emission from the “clumped” volumes by assuming a smooth density distribution, we would mistakenly attribute this “excess” emission to a higher density. In this case, we would overestimate the amount of material they contain by $\sim 12\%$.

Similarly, the mass-loss rates of winds that are structured or aspherical will be *systematically overestimated* if their optical emission lines are interpreted in terms of a density distribution that is smooth and spherically symmetric. Both these complications are expected to occur in the winds of early-type stars: clumping because the line-driving mechanism is unstable (see, e.g., Owocki 1990), and asphericity because sufficiently rapid rotation concentrates the material of the wind towards a preferred plane (e.g., the equatorial plane in the “wind-compressed disk” [WCD] or “wind-compressed zone” [WCZ] model discussed by Bjorkman in his lectures (this Volume). Figure 10 compares the H α line profiles computed from a smooth, 1D density distribution with those from the 2D density distribution appropriate to a WCZ. The total amount of material in the wind is the same in both cases, but is concentrated towards the equatorial plane in the WCZ models, with the result that more emission is produced by the 2D models. The two panels of Fig. 10 also show that there is a further dependence on the angle at which the WCZ is viewed, with much stronger emission occurring when the star is seen “pole on” ($i = 0^\circ$) because the area the equatorial concentration presents to the observer is maximized in this configuration.

Petrenz and Puls (1996) have considered the impact that aspherical density distributions have on the determination of stellar wind parameters by fitting synthetic profiles computed from 1D (spherically symmetric) wind models and 2D (WCZ) models to observed H α profiles. Figure 11 shows that both models provide fits of comparable quality to the H α profile of O4 supergiant ζ Puppis, which is a rapid rotator ($v \sin i = 210 \text{ km s}^{-1}$) for its luminosity class. However, the wind parameters inferred from the fits are substantially different: the 1D model gives $(\dot{M}, \beta) = (5.9 \times 10^{-6} \text{ M}_\odot \text{ yr}^{-1}, 1.15)$, while the 2D model gives $(\dot{M}, \beta) = (3.4 \times 10^{-6} \text{ M}_\odot \text{ yr}^{-1}, 2.00)$ and an inclination of 53 degrees. Thus, in this case, the assumption of spherical symmetry implies that \dot{M} is overestimated by $\sim 70\%$, and that the velocity law is faster than the values obtained from 2D models. Since early-type stars tend to be rapid rotators, WCZs are expected to occur commonly (Bjorkman and Cassinelli 1993; Ignace et al. 1996): failure to account for them (or other structures) when modelling recombination lines will result in mass-loss determinations that are systematically overestimated.

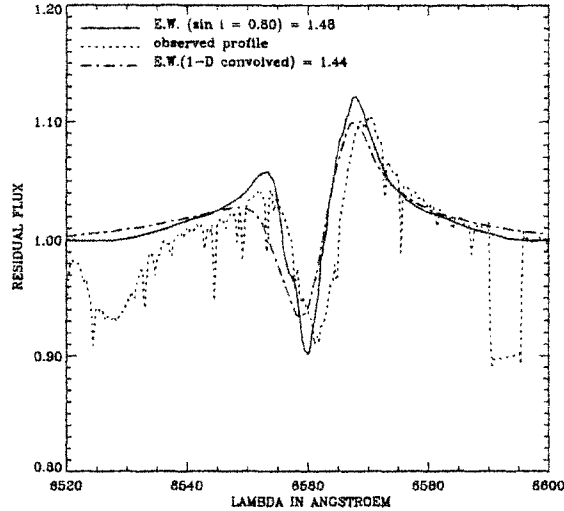


Fig. 11. Fits of 1D (dot-dash) and 2D (solid) density distributions to the $H\alpha$ profile of the O4 supergiant ζ Puppis (dotted). Figure courtesy of P. Petrenz

3.6 Time-Dependent Structure in Hot-Star Winds

In Sect. 3.4, we noted three common peculiarities in the absorption troughs of the P Cygni profiles of the UV resonance lines: soft blue edges, extended regions of blackness, and DACs. Although these deviations from the expected morphology are present in some of the earliest observations from the Copernicus satellite observatory (e.g., Morton 1976), they did not initially attract much attention. Lamers et al. (1982) noticed that DACs occurred quite commonly in “snapshot” observations of a sample of OB stars obtained with Copernicus, a result that was soon confirmed with the International Ultraviolet Explorer (IUE) satellite observatory (Prinja and Howarth 1986). However, it was not until IUE began to provide routine monitoring capability that the DACs were recognized to be fundamentally a time-dependent phenomenon. Subsequent work has shown that the shape and strength of the blue edge of the absorption trough are also variable.

The characteristic behaviour of DACs is illustrated in Fig. 12, which shows a series of 24 spectra of the Si IV resonance doublet of ξ Per obtained with IUE by H. F. Henrichs and collaborators over ~ 2.6 days in 1988 October. The spectra are presented in the form of a grey-scale image where darker shades represent less flux (excess absorption) and lighter shades represent more flux with respect to the mean spectrum, which is plotted below the image. This format, which is often called a “dynamic spectrum” (a term borrowed from radio astronomers who monitor pulsars), is an ideal way to show the progressive evolution of weak features through a large number of spectra. A given

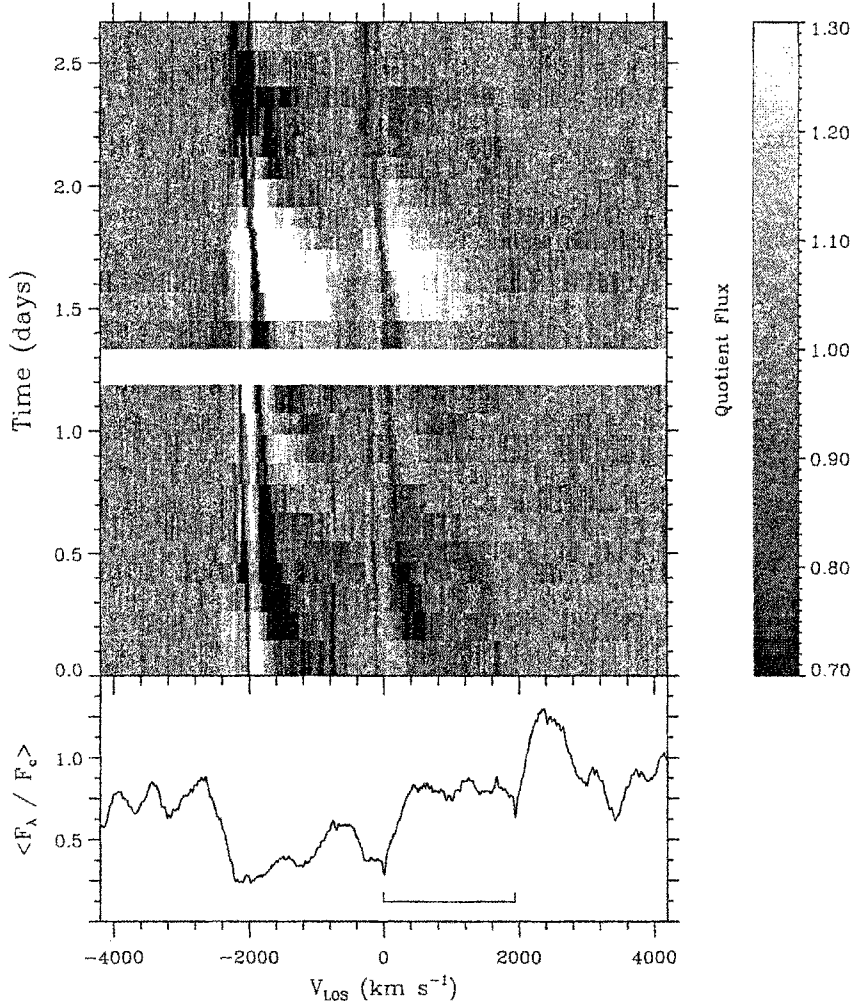


Fig. 12. Dynamic spectrum of the Si IV resonance doublet of ξ Per showing the blueward acceleration of two DACs. Individual spectra in the time series have been divided by the mean in order to enhance the contrast of the variations. The rest positions of the components of the doublet are indicated; the behaviour of the DACs is the same in both components. The white strip near the middle of the time series denotes a significant gap in the time sampling

DAC first becomes visible in both components of the doublet as a broad optical depth enhancement at an intermediate velocity, but is not accompanied by significant variations in the emission lobe. It accelerates blueward through the trough and becomes narrower as it reaches its asymptotic velocity, which is approximately equal to v_∞ . The time scale for the acceleration is ~ 1 day in the case of ξ Per, which is quite slow compared with the characteristic flow time of its wind: $t_{\text{flow}} \gtrsim R_*/v_\infty \approx 1$ hour. For ξ Per, the recurrence time between the appearance of strong DACs is ~ 2 days; in the time series illustrated in Fig. 12, a weaker component may be present in between the stronger ones.

Although ξ Per is one of the most intensively studied objects (Prinja et al. 1987; Henrichs et al. 1994), its behaviour is certainly not unique. Howarth and Prinja (1989) reported the detection of DACs in 80% of the objects in their thorough study of the IUE “snapshot” spectra of 203 O stars; detailed monitoring of a subset of these objects has subsequently shown behavioural patterns that are qualitatively similar to the DACs of ξ Per (Kaper et al. 1996). DACs have also been tracked in the UV spectra of B-type supergiants (e.g., Massa et al. 1995b), a WR star (Prinja and Smith 1992), and optical P Cygni profiles of O supergiants (e.g., Fullerton et al. 1992; Prinja and Fullerton 1994) and B hypergiants (Rivinius et al. 1997).

The widespread occurrence of DACs implies that at least one of the assumptions of the “standard model” of hot-star winds – stationarity – is not valid. From (11) and (12), we see that a DAC could be produced at a particular position in the absorption trough by enhancing τ_{UV} in one of three ways:

- locally *increasing* the ionization fraction, $q_{jk}(r)$.
- locally *increasing* the density, $\rho(r)$, either as a spherically symmetric shell or as a “clump” of arbitrary shape.
- *decreasing* the velocity gradient (dv/dr) over some range of radii, thereby producing a “plateau” in the radial velocity law.

When DACs can be observed in unsaturated lines with very different ionization energies (e.g., Si IV and N V), they usually occur at the same velocity and evolve in the same way; consequently, changes in the ionization fraction are generally not thought to be responsible for the absorption excess (but see Prinja et al. 1997 for an important exception). Since variations in the emission lobe are rarely observed, dense shells are more or less ruled out, though big clumps that cover most of the stellar disk do seem to be required to explain the depth of some DACs (and possibly also the [presumably related] phenomenon of “moving bumps” in the emission lines of WR stars; see Moffat et al. 1988). In any case, each of these methods of producing a DAC implies that there is some extra “structure” in the wind, and consequently the validity of the remaining assumptions of the “standard model” (homogeneity and spherical symmetry) are also dubious. A crucial issue is to assess

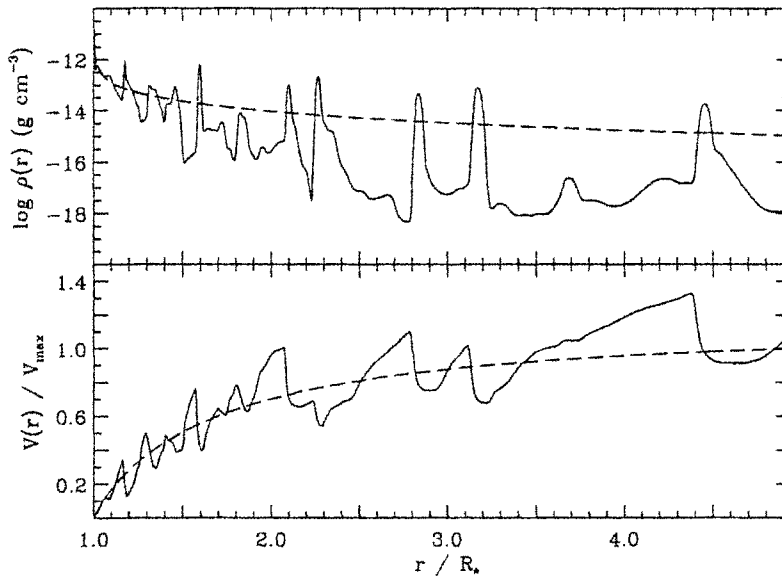


Fig. 13. The density and velocity distributions obtained from time-dependent simulations of a hot-star wind that is disrupted by the line-driven instability. The dashed line indicates the distribution of density and velocity from a comparable stationary model. From Puls et al. (1993)

the impact that these time-dependent wind structures have on the determination of mass-loss rates, which first requires that the origin and nature of the wind structures be clarified.

Much of this structure is believed to be the result of a potent instability that is intrinsic to the line-driving mechanism; i.e., the winds of early-type stars are variable by virtue of the way they accelerated. The origin of this instability is described in very clear, graphical fashion by Owocki (1992). Although this instability has been recognized for a long time (e.g., Lucy and Solomon 1970; MacGregor et al. 1979; Carlberg 1980; Owocki and Rybicki 1984), it has only recently become possible to study its impact on the structure of a stellar wind by following its nonlinear growth in radiation hydrodynamics simulations (Owocki et al. 1988, Feldmeier 1995). These computations are technically very challenging, because the line-driven instability grows most strongly on small spatial scales, and consequently the Sobolev approximation cannot be used to simplify the radiative transfer. The current generation of simulations are limited to one spatial dimension, which means that the structures that result from them consist of spherically symmetric shells.

Figure 13 shows a typical “snapshot” of $v(r)$ and $\rho(r)$ in a model of a hot-star wind at a time approximately 15 hours after basal perturbations in the form of a coherent photospheric sound wave were introduced. The deep-seated perturbations are amplified by the instability, which results in small amounts of gas being driven to very high velocities. This high-velocity, rarefied gas ultimately crashes into the more slowly moving material in front of it (i.e., at larger radii), and the resulting compression concentrates the wind into a series of dense clumps (i.e., shells in these 1D simulations). Thus, instead of the smooth, monotonic distributions expected from the stationary model, the material of the wind is inhomogeneously redistributed into a series of dense shells that are separated by regions where there is very little gas. The velocity of the rarefied gas can exceed v_∞ , while the dense shells move at about the speed of the gas at the same radii in an unstructured wind.

The nonmonotonic density and velocity distributions in Fig. 13 introduce some interesting complications to the picture of line formation that was outlined in Sect. 3.2 and 3.3. Since the velocity law is no longer a smoothly increasing function of radius, a photon will not necessarily be free to travel unimpeded through the wind after it works its way through the first scattering zone (as was the case, e.g., in the discussion of Fig. 4). Instead, it might encounter other clumps of material, possibly at very different positions in the wind but nonetheless moving with velocities “tuned” to the resonance line transition, which therefore permits further scattering interactions to occur. The possibility for multiple interactions can be easily seen from Fig. 13, since a horizontal line at a fixed velocity (which represents a fixed photon frequency in the observer’s frame) intersects the computed velocity distribution at several widely separated radii: e.g., a line at $v(r)/v_{\max}$ (where $v_{\max} \equiv v_\infty$) of 0.8 intersects the velocity law at values of r/R_\star near 2, 2.5, 3.0, and 3.4, instead of the single value (~ 2.3) in the case of a smooth, monotonically expanding wind.

As Lucy (1982) first realized, the net effect of these multiple interactions is to increase the amount of back-scattering. Consider again a horizontal line drawn across the velocity distribution in Fig. 13, and suppose for simplicity that scatterings only occur in the radial direction (i.e., $\cos\psi = \pm 1$ in the notation of Fig. 4). Further suppose that at each scattering surface there is roughly a 50% chance that a photon will be forward-scattered and a 50% chance that it will be back-scattered. Consequently, after n such scatterings, the fraction of the original beam of continuum photons that is still travelling in the forward direction is $(0.5)^n$, while the remainder have been back-scattered towards the star. In fact, the situation is a bit more complicated, because photons that are back-scattered at scattering surface i can be back-scattered another time when they encounter scattering surface $i - 1$ on their inward journey, and so rejoin the outward propagating beam. Nevertheless, the basic point is that essentially all the outward propagating photons will end up being back-scattered towards the star if there are a sufficiently large number of interaction surfaces.

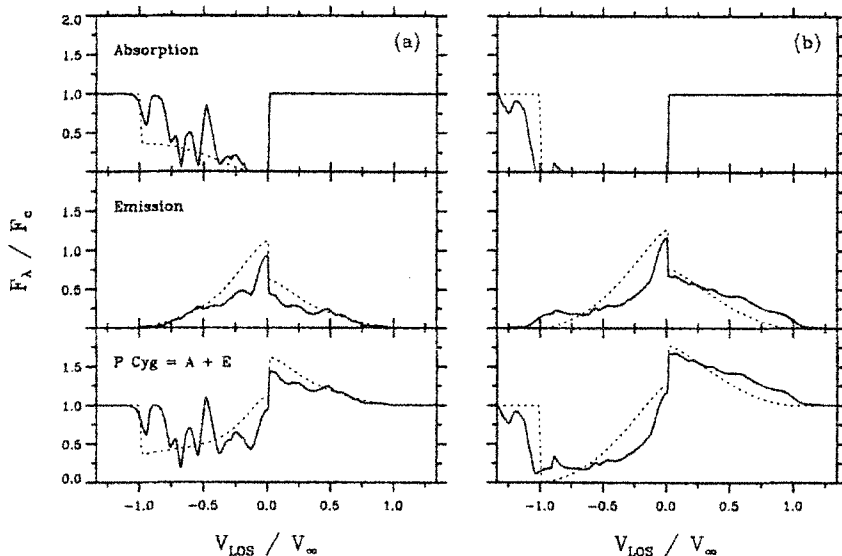


Fig. 14. P Cygni profiles of UV resonance singlets from the structured stellar wind model illustrated in Fig. 13, computed for the case of (a) a moderately strong line and (b) a strong line. The dashed lines indicate the various components of the profiles for the case of the smooth wind illustrated in Fig. 3. DACs are visible in the absorption trough of (a); the soft blue edge extending beyond v_∞ is clearly seen in (b). Changes in the shape of the blue- and red-shifted emission due to increased back-scattering from the multiple interactions in the nonmonotonic velocity law are also evident

The effects of these multiple and nonlocal interactions can be incorporated into the Sobolev formalism in a straightforward way; see, e.g., Rybicki and Hummer (1978) and Puls et al. (1993). Figure 14 illustrates the changes in the structure of the absorption and emission components of the P Cygni profiles of resonance singlets that result from the nonmonotonic (but spherically symmetric) distributions shown in Fig. 13. The clumpy distribution of material is directly visible in the absorption component of an unsaturated line, which shows both excesses and deficits of optical depth (with respect to the absorption trough of a comparable smooth wind) that are due to the dense clumps and the rarefied regions, respectively. Since all the photons are removed from the absorption trough of an intrinsically strong line, these clumpy structures are not visible in its absorption component. However, for a strong line, the small amounts of rarefied gas that have been driven to velocities in excess of v_∞ have sufficient optical depth to produce a shallow, extended, and time-

dependent blue edge. The forward-scattered emission components of both moderate and strong lines are generally weaker than the components of a comparable smooth wind at low V_{Los} , which is a direct consequence of the tendency for multiple interactions to preferentially back-scatter photons. Of course, an excess of back-scattering in the *receding* hemisphere tends to produce more photons in the redshifted part of the emission component: this effect is most clearly seen for the strong line, where the detailed distribution of emission depends on the exact location and density contrast of the clumps. The net result is that the unsaturated lines exhibit absorption components in their absorption troughs and weaker emission lobes, while the strong lines exhibit shallow blue edges that extend beyond v_{∞} , broad absorption troughs, and stronger emission lobes (which are at least partially due to spherically symmetric geometry implied by Fig. 13).

Evidently, the wind structures that arise in a natural way due to the action of the line-driven instability go a long way towards explaining the time-dependent peculiarities seen in P Cygni profiles:

- DACs can be attributed to the slowly moving dense clumps.
- soft blue edges and blue-edge variability of strong lines can be attributed to the presence of variable amounts of rarefied gas at velocities in excess of the time-averaged value of v_{∞} . Although the Gaussian velocity dispersion parameter Δv_{turb} discussed in Sect. 3.4 mimics this effect, it does not incorporate the essential physical ingredients (i.e., strongly driven gas, multiple couplings due to the nonmonotonic velocity field) in a meaningful way, and is therefore of limited diagnostic value. Moreover, the redshift of the emission lobe with increasing values of Δv_{turb} (Fig. 8) seems to be an artifact of the ad hoc way in which the velocity dispersion is introduced to the calculation of line profiles: no such shifts occur for the profiles in Fig. 14.
- black troughs occur in strong lines when there are enough structures in the forward hemisphere of the wind to produce complete back-scattering over a range of V_{Los} . The profile in Fig. 14(b) does not exhibit a black trough only because the wind model used to compute it (Fig. 13) does not have enough structure near v_{∞} ; see, e.g., Lucy (1983) and Puls et al. (1994).

These successes are emphasized qualitatively in Fig. 15, which shows synthetic dynamic spectra computed for the full run of a radiation hydrodynamics simulation (Owocki et al. 1994). These synthetic time series show weak variability in the emission lobe, which is largely because the structures are assumed to be spherically symmetric; there are also some very narrow, rapidly evolving features that do not correspond to observed variations. Nevertheless, the general characteristics of DACs in unsaturated lines that accelerate over the course of ~ 1 day (e.g., in the second half of the time series shown in the left-hand panel) and extensive blue-edge variability (e.g., in the first half of the time series in the right-hand panel) have many points of correspondence with the observed variations of ξ Per (Fig. 12).

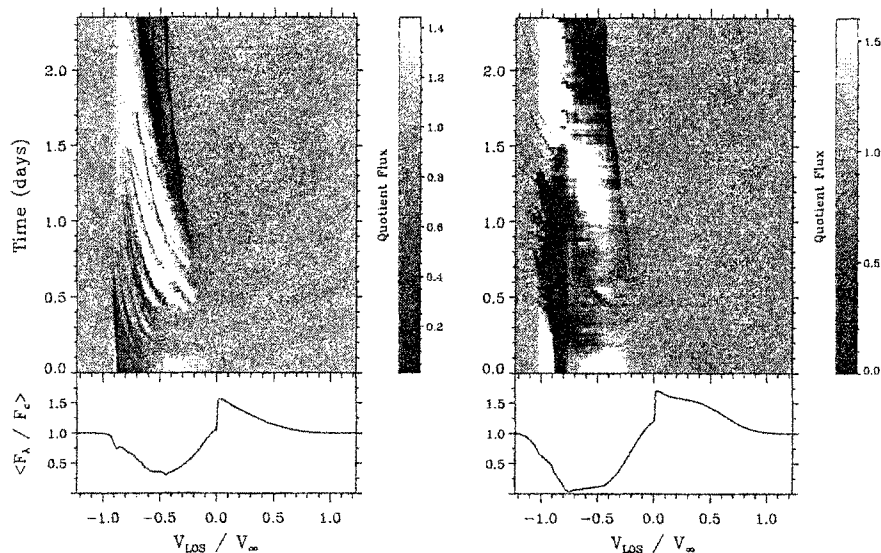


Fig. 15. Dynamic spectra generated from radiation hydrodynamics simulations of the growth of the line-driven instability by Owocki et al. (1994). Left: DAC variability in a line of modest strength. Right: blue-edge variability in a strong line; DAC is also visible since this line is not saturated. Individual spectra in the time series have been divided by the mean in order to enhance the contrast

However, despite these promising developments, the origin and nature of the DACs is still mysterious. Monitoring campaigns (e.g., Prinja 1988; Kaper et al. 1996) of many objects have linked the acceleration and recurrence of DACs to the projected rotational velocity of the underlying star, which suggests that the wind structures responsible for these spectroscopic features might ultimately be controlled by the stellar rotation rate. The recent IUE “MEGA Campaign” (Massa et al. 1995a) tested the strength of this connection directly by monitoring the UV resonance lines of three early-type stars continuously for an unprecedented interval of ~ 16 days. In all three cases – most directly for ζ Puppis (Howarth et al. 1995) and the B0.5 supergiant HD 64760 (Prinja et al. 1995) – the time scales for at least some of the wind variability could be tied directly to the estimated rotational period of the star. It is very difficult to understand how structures generated by dynamical processes in the wind (like the line-driven instability) can be tightly coupled to the stellar rotation rate, and the focus of recent work has been on finding alternative ways of generating structures that can rotationally modulate

the wind. The corotating interaction regions (CIRs) originally suggested by Mullan (1984) are among the most promising of these alternatives. Hydrodynamical simulations by Cranmer and Owocki (1996) confirm that CIRs can produce DACs that evolve over time scales determined by the stellar rotation rate. Interestingly, they find that the velocity gradient term in τ_{UV} is responsible for these optical depth enhancements, not the density term. Much more work remains to be done in order to understand the origin of DACs, whether the mechanism responsible for them can also explain soft blue edges and black troughs independent of the line-driven instability, and what impact these time-dependent structures in the wind have on the determination of mass-loss rates from spectroscopic (and continuum) diagnostics.

4 Continuum Diagnostics

At first glance, continuum measurements may not seem like a very promising method of determining \dot{M} , since they contain little information about the velocity law and would thus appear to provide insufficient data to satisfy (1). In fact, flux measurements at single wavelengths in the far infrared and radio region can provide quite reliable estimates of \dot{M} , provided that the distance to the star and v_∞ are known. The velocity law can also be determined by measuring the flux distribution at several widely spaced wavelengths. Consequently, the overall usefulness of continuum measurements is limited not so much by the physics of their formation as by the spatial resolution and instrumental sensitivity required to detect intrinsically weak flux levels (typically $\ll 1$ jansky [Jy]) from distant objects at these wavelengths.

4.1 Free-Free Emission

The contribution of the wind to the flux at infrared and radio wavelengths usually comes from free-free emission (bremsstrahlung) that arises when a free electron moves in the Coulomb field of another charged particle – usually a proton or alpha particle – but does not become bound to it. The electron is accelerated during this interaction, which alters its hyperbolic orbit and results in the absorption or emission of a photon, depending on whether the new orbit has more or less energy than the original. The energy of such interactions is not quantized, and so the photons from many such interactions will be emitted with a continuous spectrum: since the radiation field results from a collisional coupling between particles that define the thermal energy reservoir of the material in the wind, the relevant distributions are driven towards their LTE values. In particular, the source function for the emitted spectrum is the Planck function, $B_\nu(T_e)$, and the free-free emission coefficient is just

$$j_\nu^{\text{ff}} = \alpha_\nu^{\text{ff}} B_\nu(T_e) . \quad (21)$$

Derivations of the free-free absorption coefficient, α_ν^{ff} , can be found in standard texts (e.g., Rybicki and Lightman 1979, Chapter 5); in cgs units, it is given by

$$\alpha_\nu^{\text{ff}} = 3.7 \times 10^8 T^{-1/2} Z^2 n_e n_i \nu^{-3} \left(1 - e^{-h\nu/kT}\right) g(\nu, T) \text{ [cm}^{-1}\text{]} , \quad (22)$$

where Z is the mean charge per ion; n_e and n_i are the number densities of electrons and ions, respectively; $g(\nu, T)$ is the Gaunt factor (i.e., the correction factor needed to bring the free-free absorption cross-sections derived semi-classically into agreement with their quantum mechanical values); and all other symbols have their conventional meanings. For infrared and radio frequencies, $h\nu \ll kT$, and the correction for stimulated emission simplifies to $(1 - e^{-h\nu/kT}) \approx (h\nu/kT)$, whence

$$\alpha_\nu^{\text{ff}} = 1.8 \times 10^{-3} T^{-3/2} Z^2 n_e n_i \nu^{-2} g(\nu, T) \text{ [cm}^{-1}\text{]} . \quad (23)$$

Consequently, at these frequencies $d\tau_\nu^{\text{ff}} = \alpha_\nu^{\text{ff}} dr \propto \nu^{-2}$ if the weak functional dependence of the Gaunt factor on frequency is neglected ($g \propto \ln[T^{1.5}/\nu]$); alternately, $\tau_\lambda^{\text{ff}} \propto \lambda^2$.

This strong dependence of optical depth on wavelength provides the key to understanding the power of continuum methods, since – leaving aside the practical issues of detectability, correction for interstellar extinction, absolute calibration, etc. – it implies that for any M it is possible to find a wavelength where $\tau_\lambda^{\text{ff}} \approx 1$, i.e., where free-free emission in the wind creates an observable excess of flux over that expected from the stellar photosphere alone. Alternately, observations tuned to progressively longer wavelengths reach $\tau_\lambda^{\text{ff}} \approx 1$ at successively larger radial distances from the star. The fast, low-density winds typical of O stars become optically thick at radio wavelengths (2–6 cm), which originate at radii of $\sim 100 R_\star$ or more, at which point $v(r) \approx v_\infty$. Consequently, uncertainties in the shape of the velocity law do not enter directly into the interpretation of the observed flux, which is sensitive only to the amount of material in the wind. By the same argument, though, the winds of O stars are still optically thin to free-free emission at IR wavelengths, and flux measurements in the IR only provide a measure of the total volume emission; i.e., there is no information about the radial stratification of density (Abbott et al. 1984). Slower, denser winds become optically thick in the continuum at IR (e.g., for LBVs) or even optical wavelengths (e.g., WR stars).

The observed IR and radio fluxes of ζ Puppis are compared with the flux levels expected from the stellar photosphere in Fig. 16. The excess emission due to the wind is evident for wavelengths longer than the M-band ($\sim 5\mu$), and amounts to ~ 2 orders of magnitude or more in the radio region. Notice, however, that even though ζ Pup is the nearest O star ($D \approx 430$ pc) and has a strong stellar wind, the radio fluxes are only a few millijanskies.

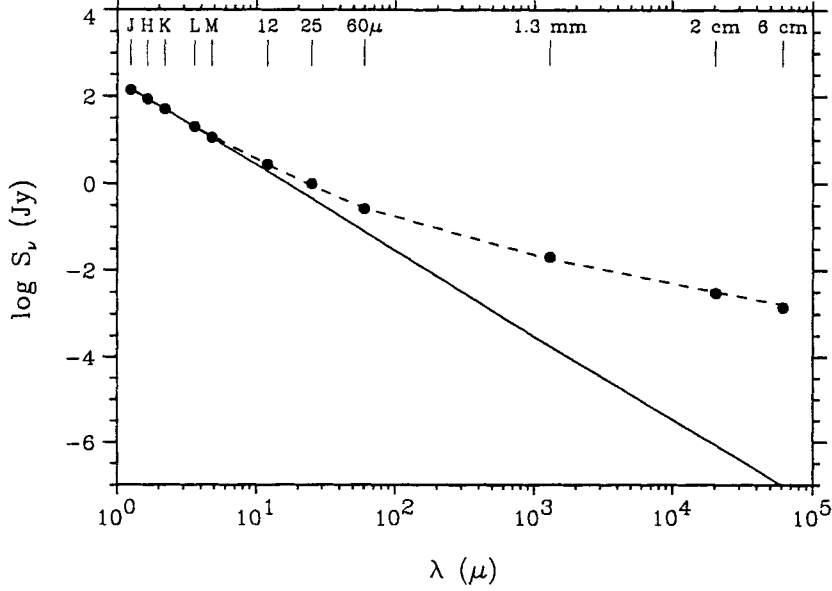


Fig. 16. Observed and predicted continuum flux excesses for ζ Puppis as a function of wavelength, with data from Abbott et al. (1984), Lamers et al. (1984), Leitherer and Robert (1991), and Bieging et al. (1989). The solid line indicates the photospheric flux from a unified model atmosphere, while the dashed line is a fit to the flux distribution by (24). Figure courtesy of F. Najarro

4.2 Spectrum of Free-Free Emission from a Stellar Wind

The continuum flux expected from a homogeneous, spherically symmetric, isothermal wind expanding with constant velocity can be obtained by directly integrating (3), the formal solution to the equation of radiative transfer. The analysis is simpler than that required to compute line profiles, since the source function is known from the outset to be the Planck function for a particular electron temperature (which is usually assumed to be constant through the wind) and there is no need to invoke the Sobolev approximation. Wright and Barlow (1975) and Panagia and Felli (1975) were the first to perform the integrations (which can be done analytically; see also Abbott et al. 1981 and Lamers and Waters 1984) to obtain the following expression for the flux from free-free emission in the wind:

$$S_\nu = 23.2 \left(\frac{\dot{M}Z}{\mu_i v_\infty} \right)^{4/3} \left(\frac{\gamma g}{D^3} \right)^{2/3} \nu^{2/3} \text{ [Jy]} , \quad (24)$$

where \dot{M} is in $M_\odot \text{ yr}^{-1}$, v_∞ is in km s^{-1} , D is the distance in kpc, and ν is in Hz; and where μ_i , Z , and γ are the mean ionic weight, the root-mean square charge per ion, and the number of electrons per ion, respectively. Lamers and Leitherer (1993) provide a useful table (their Table 4) of values of these parameters for several assumed chemical compositions; for typical Pop. I abundances with complete ionization of H and He, $\mu_i = 1.339$, $Z = 1.149$, and $\gamma = 1.149$.

Equation (24) shows that the flux from free-free emission in a stellar wind $S_\nu \propto \nu^{2/3}$; if the weak frequency dependence of the Gaunt factor is included, the dependence becomes a bit flatter, $S_\nu \propto \nu^{0.6}$. This is intermediate between the spectral distributions expected for homogeneous plasma that is optically thin ($\propto \nu^{-0.1}$) and thick ($\propto \nu^2$), since both extremes and the complete range of intermediate values contribute to the observed flux at any given frequency. The spectral index is positive since higher frequencies have smaller optical depths ($\tau_\nu^{\text{ff}} \propto \nu^{-2}$) and therefore probe systematically deeper layers of the wind, where higher densities produce comparatively more free-free emission.

Equation (24) can be rearranged to obtain a simple expression for the mass-loss rate,

$$\dot{M} = 0.095 \mu_i v_\infty (Z^2 \gamma \nu g(\nu, T))^{-1/2} D^{3/2} S_\nu^{3/4} [M_\odot \text{ yr}^{-1}] , \quad (25)$$

which emphasizes that both v_∞ and D must be known by some other means in order to convert S_ν to \dot{M} . Otherwise, the expression appears to be quite model independent and straightforward to evaluate. This apparent simplicity is slightly misleading, since the abundances and ionization state of the wind need to be known in order to calculate Z and γ , which implies that the temperature structure must be known. The assumptions of isothermality, Pop. I abundances, and complete ionization are entirely adequate for O-type stars, but may require modifications for objects with denser winds or weaker radiation fields, particularly when recombinations occur for a dominant species, or in the winds of evolved objects with different chemical compositions.

Figure 16 shows that the spectral distribution predicted by (24) fits the observed excesses at IR and radio wavelengths very well, which in turn confirms that it originates from free-free emission in the wind. In principle, the flux excess at any wavelength where the wind is opaque is sufficient to determine \dot{M} via (25). When measurements at several widely spaced wavelengths are available, the density stratification (or, equivalently, the velocity law) can be probed; see, e.g., Runacres and Blomme (1996). For a distance of 435 pc and $v_\infty = 2200 \text{ km s}^{-1}$, the fit to the flux distribution of ζ Pup in Fig. 16 gives $\dot{M} = 3.1 \times 10^{-6} M_\odot \text{ yr}^{-1}$, which is in good agreement with the value derived by fitting the 2D density distribution to the H α profile shown in Fig. 11. The value of β derived from wavelength dependence of the excess is 1.4, somewhat “faster” than the velocity law determined by the fit of the 2D model.

Table 2. Selected radio continuum studies

Reference	λ (cm)	Telescope ^a	Objects	Yield ^b
Abbott et al. (1980)	6.1	VLA	OBA	6/10
Abbott et al. (1981)	6.1	VLA	OB	6/10
Bieging et al. (1982)	6.1	VLA	WR	8/13
Vallée and Moffat (1985)	2.8	ARO, VLA	O, WR	0/19
Abbott et al. (1986)	2.0, 6.1	VLA	WR	14/23
Bieging et al. (1989)	2.0, 6.1, 20	VLA	OBA	18/88
Leitherer and Robert (1991)	0.13	SEST	OB, WR	7/ 7
Altenhoff et al. (1994)	0.12	IRAM	OB, WR	18/45
Leitherer et al. (1995)	3.4, 6.2	ATCA	OB, WR	10/11
Contreras et al. (1996)	0.7, 3.5, 6	VLA	OB, WR	8/ 8

^a VLA – Very Large Array; ARO – Algonquin Radio Observatory; SEST – Swedish-ESO Submillimeter Telescope; IRAM – Instituto de Radioastronomia Millimetrica, Spain; ATCA – Australia Telescope Compact Array.

^b N(detected) / N(observed)

4.3 Mass-Loss Rates from Continuum Observations

Starting with the pioneering work of Barlow and Cohen (1977), much effort has been devoted to using continuum observations of the IR and radio excesses of hot stars to infer mass-loss rates and the radial structure of the stellar wind. Unfortunately, the winds of OB stars are typically optically thin at the near-IR wavelengths accessible from the ground, and consequently the IR excesses are small (see, e.g., Figs. 16 and 17) and subject to uncertainties from corrections for interstellar extinction and the absolute flux calibration. Even when they exist, the excesses at wavelengths where the wind is optically thin are determined by \dot{M} , $v(r)$, and the temperature stratification of the wind, $T(r)$, and it is impossible to disentangle the contributions of each of these parameters uniquely; see, e.g., Abbott et al. (1984) for a clear discussion of these problems. The situation is better for objects with larger values of \dot{M} like LBVs or WR stars, since the wind is opaque at infrared wavelengths. It also improves for far-IR wavelengths accessible to satellite observatories like the Infrared Astronomical Satellite (IRAS) mission of the early 1980s or, more recently, the Infrared Space Observatory (ISO).

Since hot-star winds are opaque at radio wavelengths, measurements of the free-free continuum between ~ 1 mm and ~ 20 cm provide more useful information about \dot{M} . Table 2 lists a selection of continuum studies of hot stars

at radio wavelengths. These observations are difficult to make, since high angular resolution is required to isolate the flux from the wind (which is usually a point source; but see White and Becker 1982 for an important exception) and since the expected flux levels are small, both because of the intrinsic weakness of the emission and the large distances typical of early-type stars. Indeed, from a practical point of view, sensitivity is the biggest drawback to radio continuum observations. This is suggested by the low “yields” typical of the studies listed in Table 2, except for samples that are strongly biased towards extreme objects. Bieging et al. (1989) have completed the largest survey of OB stars to date, and it is interesting to note that while they detected 15 of the 23 sources (65%) they observed in a distance-limited sample ($D < 2.5$ kpc; $\delta \geq -40^\circ$), they only detected 3 more sources in their total sample of 88 targets, with sensitive upper limits on nondetections of $\lesssim 0.5$ mJy. Thus, it is unlikely that significantly more stars will be detected in the northern hemisphere, though the advent of the Australia Telescope Compact Array will help to enlarge the sample by providing access to the early-type stars in the rich star fields of the southern skies; see, e.g., Leitherer et al. (1995).

The continuum flux excesses at radio wavelengths are generally thought to provide the most reliable estimates of \dot{M} for hot, luminous OB stars, because (1) when it is detectable, the observed free-free emission originates at great distances from the star and is unaffected by uncertainties in the shape of the velocity law; and (2) the emission does not depend on the detailed ionization or excitation equilibrium in the wind, which, in the case of O stars, can be assumed to be completely ionized. Thus, the main difficulties associated with UV resonance lines and optical emission lines are circumvented. Unfortunately, the assumption of complete ionization cannot be justified for stars with $T_{\text{eff}} \lesssim 17,000$ K owing to the recombination of helium, and in practice a detailed model of the temperature structure of the wind must be used to interpret the radio continuum flux for supergiants later than $\sim B2$. Moreover, since free-free emission is a ρ^2 process, values of \dot{M} determined from (25) are also sensitive to clumping; as in the case of optical emission lines, the presence of structures in a density distribution that is assumed to be smooth will cause \dot{M} to be systematically overestimated.

The most forceful argument *against* clumping being an important source of bias is that when determinations of \dot{M} from $H\alpha$ profile fitting and radio continuum measurements are both available, they agree reasonably well with each other on average (Lamers and Leitherer 1993; Puls et al. 1993). These diagnostics probe very different radial distances in the wind: $H\alpha$ is formed predominantly in the first few stellar radii, while the “radio photosphere” is at tens or hundreds of stellar radii, depending on the wavelength of observation and the amount of material in the wind. Since $H\alpha$ and free-free emission are sensitive to clumping in exactly the same way, their approximate equality implies that either the degree of clumping (i.e., volume filling factor, density

ratio) must be preserved over a enormous range of radii, despite the expansion of the wind, or significant clumping is not in fact present. The first alternative is thought to be unlikely (though not proven to be impossible), which implies that significant clumping is not present at any radius in the wind.

However, this line of reasoning is not completely convincing, since the behaviour of clumped material will depend on the mechanism responsible for introducing the inhomogeneity in the first place. In the case of ζ Puppis, e.g., we have already seen how structures like WCZs may be able to resolve the long-standing “factor of 2” discrepancy between the values of \dot{M} determined from $H\alpha$ (where the equatorial concentration of material is important) and the radio measurements (where the density distribution is more nearly symmetric); yet this is one of the stars that defines the “on average” equality of \dot{M} determined from these two diagnostics. On a more fundamental level, the widespread variability of hot-star winds strongly suggests that they are inhomogeneous on large spatial scales (Sect. 3.6). Until the nature of these inhomogeneities are established more firmly, the impact of wind structures on specific diagnostics of \dot{M} cannot be assessed.

4.4 Nonthermal Radio Emission

An unanticipated difficulty with determining accurate mass-loss rates from radio flux measurements appeared shortly after observations with the Very Large Array began in earnest, when Abbott et al. (1984) recognized that for a minority of targets (initially just 2 stars: 9 Sagittarii [O4: V((f))] and Cyg OB2 No. 9 [O5 If]) the inferred values of \dot{M} were an order of magnitude larger than the values estimated by other methods. Subsequent multi-wavelength observations showed that the flux distribution for these targets was substantially different from that predicted by (24), with spectral indices $\alpha \leq 0$ (where $S_\nu \propto \nu^\alpha$) rather than the value of +0.6 expected for free-free emission. Both the monochromatic flux levels and the spectral indices were found to be highly variable over intervals of months. These characteristics are illustrated for Cyg OB2 No. 9 in Fig. 17, which shows that – in complete contrast to the case of ζ Pup illustrated in Fig. 16 – the IR and radio flux distributions cannot be fit simultaneously by (24), because there is too much radio emission. Figure 17 also emphasizes the flatness of the observed radio continuum and the extreme variability, which amounts to more than an order of magnitude at 6 cm.

Abbott et al. (1984) recognized that this behaviour is characteristic of nonthermal radio emission, which contaminates (and in fact dominates) the free-free emission and invalidates the use of (25) to determine \dot{M} . Although nonthermal emitters comprise only 24% of the distance-limited sample surveyed by Bieging et al. (1989), they are systematically the most bolometrically luminous stars. They are also systematically stronger radio sources than thermal (free-free) emitters and will therefore tend to be seen to greater distances. Fortunately, they can be distinguished from thermal sources by

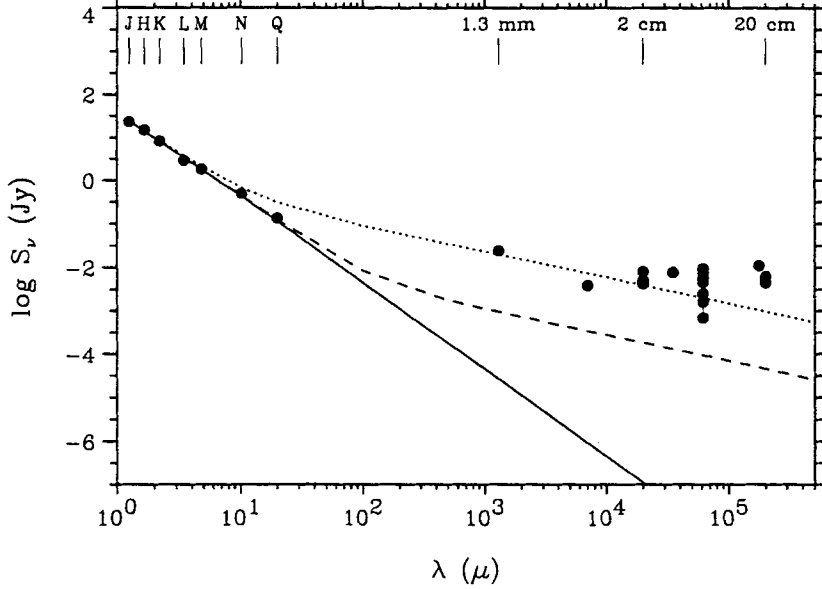


Fig. 17. Observed and predicted continuum flux excesses for Cyg OB2 No. 9 (spectral type O5 If) as a function wavelength, with data from Abbott et al. (1984), Altenhoff et al. (1994), Contreras et al. (1996), Bieging et al. (1989), White and Becker (1983), and Phillips and Titus (1990). The solid line indicates the photospheric flux, while the dashed and dotted lines indicate the predicted flux for mass-loss rates of $4 \times 10^{-6} M_{\odot} \text{ yr}^{-1}$ (which does not fit the radio observations) and $4 \times 10^{-5} M_{\odot} \text{ yr}^{-1}$ (which does not fit the IR observation), respectively. Variability and strong deviations from the flux distribution expected for free-free emission are evident at longer wavelengths. Figure courtesy of F. Najarro

multiwavelength observations to determine the spectral index α , or by their large variations. Consequently, the complication posed by the existence of nonthermal sources is mostly practical, in that more observing time is required to observe a source at several wavelengths or at several epochs in order to ensure that it is thermal before applying (25) to determine \dot{M} .

The origin of the nonthermal emission is unknown, but is probably due to synchrotron emission from electrons that are accelerated to mildly relativistic energies by multiple interactions with strong shocks in the presence of a weak stellar magnetic field (White 1985). The nonthermal source in Cyg OB2 No. 9 has recently been resolved via very-long baseline interferometry (Phillips and Titus 1990), which confirms that the nonthermal component originates at or beyond the radius where the 20 cm free-free continuum is formed and that

the emitting volume is large. At the same time, however, Bieging et al. (1989) point out that the nonthermal fluxes at different wavelengths vary in concert, which is difficult to understand in terms of the chaotic, embedded shock model since the “free-free” photospheres at different wavelengths sample very different radii ($\tau_{\lambda}^{\text{ff}} \propto \lambda^2$). On at least one occasion, the nonthermal component of Cyg OB2 No. 9 faded altogether, revealing an underlying spectrum with a spectral index of ~ 0.6 that permitted Abbott et al. (1984) to derive $\dot{M} = 1.9 \times 10^{-5} M_{\odot} \text{ yr}^{-1}$. Clearly, there is still work to be done to understand the origin of nonthermal radio emission and the implications that its presence has for the structure of hot-star winds.

4.5 The New Frontier: Spectroscopy in the Near and Far IR

The steady improvement in IR detector technology has recently produced an explosion of interest in studying early-type stars spectroscopically in the J, H, and K bands, which have central wavelengths of ~ 1.25 , 1.65 , and 2.20μ , respectively. These wavelengths have many advantages for studying hot stars in environments that are highly obscured by dust, like young star clusters (e.g., Hanson et al. 1993) or the Galactic Center (e.g., Najarro et al. 1994). These wavebands contain important lines of H (e.g., the Paschen and Brackett series), He I, and He II, most of which are partially formed in the stellar wind. They generally have a ρ^2 character and resemble optical emission lines, except that they tend to be weaker because they are due to transitions between higher energy levels in their parent atoms. Figure 18 illustrates the quality of spectroscopic material that can now be obtained at near IR wavelengths by showing the hydrogen lines of $P\beta$ and $B\gamma$ (which fall in the J and K bands, respectively) of the LBV HD 160529. Both lines exhibit P Cygni profiles, the detailed shape and strength of which reflect the different emitting volumes appropriate to these transitions.

At still longer wavelengths, IR lines have an important advantage that is not shared by optical emission features, which once again stems from the fact that *continuum* optical depths scale with λ^2 . As a result, the “effective photosphere” is a strong function of radius for IR wavelengths beyond the limit where the wind first becomes opaque. Line profiles are only formed at radii that are *larger* than the effective photosphere, and (as we have seen) they can be used to determine the velocity law and density structure starting from that point. Since the (optically thick) continua associated with progressively longer wavelengths form at systematically greater distances from the star, the wind lines at longer wavelengths are formed at larger velocities (i.e., more blue-shifted V_{los}). Consequently, the information provided by IR wind lines in different wavelength intervals is not redundant, and can be used to piece together the velocity and density structure of the wind – providing that the underlying continuum is optically thick.

Figure 18 shows that the $P\beta$ and $B\gamma$ lines of HD 160529 are not systematically offset from each other: despite its enormous mass-loss rate (1.3×10^{-5}

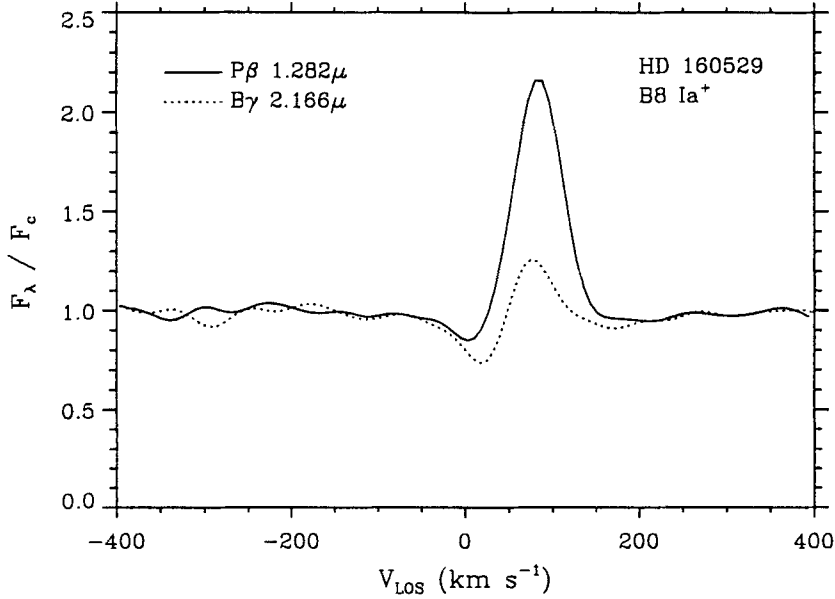


Fig. 18. Infrared P Cygni profiles of $P\beta$ (in the J band) and $B\gamma$ (in the K band) for HD 160529. These high-resolution spectra were obtained with the Fourier Transform Spectrometer of the Canada-France-Hawaii Telescope; the small undulations in the continuum are artifacts (“ringing”) typical of FTS spectra

$M_\odot \text{ yr}^{-1}$, according to Leitherer et al. 1995), its J and K band continua are not optically thick. Instead, observations at wavelengths in the satellite IR are required to achieve this “infrared advantage”, which even then can only be applied to the stars with the densest winds. Despite these caveats, this method promises to become an important new probe of the structure of the outflows from these stars. Indeed, observations of the H and He I lines in the $2.4\text{--}45\mu$ region obtained with the short-wavelength spectrometer on board ISO have already provided detailed insights into the wind of the famous LBV P Cygni (Lamers et al. 1996).

5 Summary and Outlook

It should be clear from the preceding discussion that no single diagnostic provides a completely reliable measurement of the mass-loss rate of an early-type star. The UV resonance lines are by far the best indicators of v_∞ , and the shape of the profile also provides good constraints on the gradient of the radial velocity field of the wind. Unfortunately, the strength of UV resonance

lines cannot be converted to \dot{M} easily because of the large uncertainties in the ionization balance of hot-star winds, uncertainties that are in part due to the presence of time-dependent processes in the wind. However, once v_∞ is known, continuum methods come to the fore, and measurements in the radio range between 1 mm and 20 cm are generally believed to provide the most reliable estimates of \dot{M} . In practice, though, the weakness of the flux levels due to free-free emission in hot-star winds limits the applicability of these techniques to the nearest objects, which nevertheless play a key role by acting as calibrators for other techniques.

In contrast, H α emission profiles can now be observed with good spectral resolution for stars as far away as the Local Group of galaxies. Sufficiently strong emission permits estimates of the velocity gradient and \dot{M} , and sometimes also v_∞ (e.g., for late B and early A supergiants). The caveat applicable to these (and other) ρ^2 diagnostics is that they are very susceptible to the distribution of wind material assumed by the model used to interpret them. In particular, \dot{M} will be systematically overestimated if a smooth, spherically symmetric model is used to interpret recombination line profiles from a wind that is in fact asymmetric or otherwise structured. More detailed physical information concerning the effect of rotation on the distribution of material in hot-star winds and the nature of the structures responsible for their ubiquitous variability is required in order to quantify this effect. There may still be uncertainties as large as a factor of two lurking in the determinations of the mass-loss rates of early-type stars.

Even so, the stationary properties of hot-star winds can be explained acceptably well by the theory of line-driven winds; see, e.g., the lectures by Lamers (second contribution to this Volume). Consequently, it seems likely that in the coming years stellar wind research will begin to emphasize the role these outflows can play as tools to investigate astrophysical problems. For example, Kudritzki and his colleagues are currently developing the “Wind-Momentum-Luminosity Relationship”, by which the stellar wind profiles observed in the luminous stars of external galaxies can be used as “standard candles” to determine distances out to the Fornax and Virgo Clusters; see Kudritzki (1997) for details of this exciting application of stellar wind theory. More generally, stellar winds can be used to probe astronomical situations that range from the formation of bow shocks, bubbles, and chimneys in the interstellar medium to measuring the abundance gradients in external galaxies and determining the chemical composition of early generations of massive stars in high redshift galaxies. Observations of these phenomena represent the frontiers of stellar wind research; together with ongoing investigations into the nonstationary behaviour of hot-star winds, they are expected to provide further surprising insights into the physics of hot stars and their environments.

Acknowledgements

It is a pleasure to thank the organizers and participants of this summer school for many stimulating discussions concerning stellar atmospheres and astrophysics, and for the opportunity to sample a wide variety of Belgian beer – which is very compelling, despite the “impurities” that my Bavarian colleagues warned me about! I am indebted to Joachim Puls, Achim Feldmeier, Paco Najarro, Peter Petrenz, and Anne Fullerton for their contributions to this manuscript, and would like to express my thanks to the many colleagues around the world who have taught me about hot-star winds over the years, most particularly Stan Owocki and Joachim Puls. I would also like to thank Prof. R.-P. Kudritzki for the opportunity to deliver these lectures. Financial support from the Deutsche Forschungsgemeinschaft (grant Pu 117/3-1) during the preparation of the written version of these lectures is gratefully acknowledged.

References

- Abbott, D. C., Biegging, J. H., Churchwell, E., Cassinelli, J. P. (1980): *ApJ* **238**, 196
- Abbott, D. C., Biegging, J. H., Churchwell, E. (1981): *ApJ* **250**, 645
- Abbott, D. C., Biegging, J. H., Churchwell, E. (1984): *ApJ* **280**, 671
- Abbott, D. C., Telesco, C. M., Wolff, S. C. (1984): *ApJ* **279**, 225
- Abbott, D. C., Biegging, J. H., Churchwell, E., Torres, A. V. (1986): *ApJ* **303**, 239
- Altenhoff, W. J., Thum, C., Wendker, H. J. (1994): *A&A* **281**, 161
- Barlow, M. J., Cohen, M. (1977): *ApJ* **213**, 737
- Beals, C. S. (1930): *Publ. DAO* **4**, 271
- Beals, C. S. (1950): *Publ. DAO* **9**, 1
- Biegging, J. H., Abbott, D. C., Churchwell, E. (1982): *ApJ* **263**, 207
- Biegging, J. H., Abbott, D. C., Churchwell, E. (1989): *ApJ* **340**, 518
- Bjorkman, J. E., Cassinelli, J. P. (1993): *ApJ* **409**, 429
- Bjorkman, J. E., Ignace, R., Tripp, T. M., Cassinelli, J. P. (1994): *ApJ* **435**, 416
- Carlberg, R. G. (1980): *ApJ* **241**, 1131
- Caroff, L. J., Noerdlinger, P. D., Scargle, J. D. (1972): *ApJ* **176**, 439
- Castor, J. I. (1970): *MNRAS* **149**, 111
- Castor, J. I., Lamers, H. J. G. L. M. (1979): *ApJS* **39**, 481
- Chen, W., White, R. L., Bertsch, D. (1996): *A&AS* **120**, 423
- Contreras, M. E., Rodríguez, L. F., Gómez, Y., Velázquez, A. (1996): *ApJ* **469**, 329
- Cranmer, S. R. (1996): Ph.D. thesis, Univ. of Delaware
- Cranmer, S. R., Owocki, S. P. (1996): *ApJ* **462**, 469
- De Koter, A., Schmutz, W., Lamers, H. J. G. L. M. (1993): *A&A* **277**, 561
- Feldmeier, A. (1995): *A&A* **299**, 523
- Fullerton, A. W., Gies, D. R., Bolton, C. T. (1992): *ApJ* **390**, 650
- Gabler, R., Gabler, A., Kudritzki, R. P., Puls, J., Pauldrach, A. W. A. (1989): *A&A* **226**, 162
- Groenewegen, M. A. T., Lamers, H. J. G. L. M. (1989): *A&AS* **79**, 359

- Groenewegen, M. A. T., Lamers, H. J. G. L. M. (1991): A&A **243**, 429
- Hamann, W.-R. (1981): A&A **93**, 353
- Hanson, M. M., Geballe, T. R., Conti, P. S., Block, D. L. (1993): A&A **273**, L44
- Hanson, M. M., Conti, P. S., Rieke, M. J. (1996): ApJS **107**, 281
- Haser, S. M. (1995): Ph.D. thesis, Ludwig-Maximilians-Universität München
- Haser, S. M., Lennon, D. J., Kudritzki, R.-P., et al. (1995): A&A **295**, 136
- Henrichs, H. F., Kaper, L., Nichols, J. S. (1994): A&A **285**, 565
- Howarth, I. D., Prinja, R. K. (1989): ApJS **69**, 527
- Howarth, I. D., Prinja, R. K., Massa, D. (1995): ApJ **452**, L65
- Hutchings, J. B. (1979): *The O Stars: Optical Review*, in: Mass Loss and Evolution of O-Type Stars (proceedings of IAU Symp. 83), ed. P. S. Conti and C. W. H. de Loore (Reidel, Dordrecht), p.3
- Ignace, R., Cassinelli, J. P., Bjorkman, J. E. (1996): ApJ **459**, 671
- Kaper, L., Henrichs, H. F., Nichols, J. S., et al. (1996): A&AS **116**, 257
- Kaufer, A., Stahl, O., Wolf, B., et al. (1997): A&A **320**, 273
- Kudritzki, R. P. (1988): *The Atmospheres of Hot Stars: Modern Theory and Observation*, in: Radiation in Moving Gaseous Media (18th Advanced Course of the Swiss Society of Astronomy & Astrophysics), ed. Y. Chmielewski and T. Lanz (Geneva: Geneva Observatory), p.1
- Kudritzki, R. P. (1992): A&A **266**, 395
- Kudritzki, R.-P. (1997): *Quantitative Spectroscopy of the Brightest Blue Supergiant Stars in Galaxies*, in: Stellar Astrophysics for the Local Group (Proceedings of VIII Canary Islands Winter School of Astrophysics), ed. A. Aparicio, A. Herrero, F. Sánchez (Cambridge: CUP), in press
- Kudritzki, R. P., Hummer, D. G. (1990): ARA&A **28**, 303
- Lamers, H. J. G. L. M., Leitherer, C. (1993): ApJ **412**, 771
- Lamers, H. J. G. L. M., Waters, L. B. F. M. (1984): A&A **136**, 37
- Lamers, H. J. G. L. M., Gathier, R., Snow, T. P. (1982): ApJ **258**, 186
- Lamers, H. J. G. L. M., Waters, L. B. F. M., Wesselius, P. R. (1984): A&A **134**, L17
- Lamers, H. J. G. L. M., Cerruti-Sola, M., Perinotto, M. (1987): ApJ **314**, 726
- Lamers, H. J. G. L. M., Najarro, F., Kudritzki, R. P., et al. (1996): A&A **315**, 229
- Leitherer, C., Robert, C. (1991): ApJ **377**, 629
- Leitherer, C., Chapman, J. M., Koribalski, B. (1995): ApJ **450**, 289
- Lucy, L. B. (1971): ApJ **163**, 95
- Lucy, L. B. (1982): ApJ **255**, 278
- Lucy, L. B. (1983): ApJ **274**, 372
- Lucy, L. B., Solomon, P. M. (1970): ApJ **159**, 879
- MacGregor, K. B., Hartmann, L., Raymond, J. C. (1979): ApJ **231**, 514
- Maeder, A., Conti, P. S. (1994): ARA&A **32**, 227
- Massa, D., Shore, S. N., Wynne, D. (1992): A&A **264**, 169
- Massa, D., Fullerton, A. W., Nichols, J. S., et al. (1995a): ApJ **452**, L53
- Massa, D., Prinja, R. K., Fullerton, A. W. (1995b): ApJ **452**, 842
- Mihalas, D. (1978): *Stellar Atmospheres* (Freeman, San Francisco)
- Mihalas, D. (1979): MNRAS **189**, 671
- Mihalas, D., Hummer, D. G. (1973): ApJ **179**, 827
- Moffat, A. F. J., Drissen, L., Lamontagne, R., Robert, C. (1988): ApJ **334**, 1038
- Morrell, N. I., Walborn, N. R., Fitzpatrick, E. L. (1991): PASP **103**, 341

- Morton, D. C. (1967a): ApJ **147**, 1017
Morton, D. C. (1967b): ApJ **150**, 535
Morton, D. C. (1976): ApJ **203**, 386
Mullan, D. J. (1984): ApJ **283**, 303
Najarro, F., Hillier, D. J., Kudritzki, R. P., et al. (1994): A&A **285**, 573
Olson, G. L. (1982): ApJ **255**, 267
Owocki, S. P. (1990): Reviews of Modern Astronomy **3** (Springer, Berlin), 98
Owocki, S. P. (1992): *Instabilities in Hot-Star Winds: Basic Physics and Recent Developments*, in: Atmospheres of Early-Type Stars, ed. U. Heber and S. Jeffery (Springer, Berlin), p.393
Owocki, S. P., Rybicki, G. B. (1984): ApJ **284**, 337
Owocki, S. P., Castor, J. I., Rybicki, G. B. (1988): ApJ **335**, 914
Owocki, S. P., Fullerton, A. W., Puls, J. (1994): Ap&SS **221**, 437
Panagia, N., Felli, M. (1975): A&A **39**, 1
Pauldrach, A. W. A., Puls, J., Kudritzki, R. P. (1986): A&A **164**, 86
Pauldrach, A. W. A., Kudritzki, R. P., Puls, J., Butler, K., Hunsinger, J. (1994): A&A **283**, 525
Petrenz, P., Puls, J. (1996): A&A **312**, 195
Phillips, R. B., Titus, M. A. (1990): ApJ **359**, L15
Prinja, R. K. (1988): MNRAS **231**, 21P
Prinja, R. K., Fullerton, A. W. (1994): ApJ **426**, 345
Prinja, R. K., Howarth, I. D. (1986): ApJS **61**, 357
Prinja, R. K., Smith, L. J. (1992): A&A **266**, 377
Prinja, R. K., Howarth, I. D., Henrichs, H. F. (1987): ApJ **317**, 389
Prinja, R. K., Massa, D., Fullerton, A. W. (1995): ApJ **452**, L61
Prinja, R. K., Massa, D., Fullerton, A. W., Howarth, I. D., Pontefract, M. (1997): A&A **318**, 157
Puls, J., Owocki, S. P., Fullerton, A. W. (1993): A&A **279**, 457
Puls, J., Feldmeier, A., Springmann, U. W. E., Owocki, S. P., Fullerton, A. W. (1994): Ap&SS **221**, 409
Puls, J., Kudritzki, R. P., Herrero, A., et al. (1996): A&A **305**, 171
Rivinius, Th., Stahl, O., Wolf, B., et al. (1997): A&A **318**, 819
Runacres, M. C., Blomme, R. (1996): A&A **309**, 544
Rybicki, G. B. (1984): *Escape Probability Methods*, in: Methods of Radiative Transfer, ed. W. Kalkofen (Cambridge: CUP), p.21
Rybicki, G. B., Hummer, D. G. (1978): ApJ **219**, 654
Rybicki, G. B., Lightman, A. P. (1979): *Radiative Processes in Astrophysics* (Wiley, New York)
Santolaya-Rey, A. E., Puls, J., Herrero, A. (1997): A&A, in press
Schaerer, D., Schmutz, W. (1994): A&A **288**, 231
Snow, T. P., Lamers, H. J. G. L. M., Lindholm, D. M., Odell, A. P. (1994): ApJS **95**, 163
Stahl, O., Mandel, H., Wolf, B., et al. (1993): A&AS **99**, 167
Underhill, A. B. (1958): Mem. R. Soc. Liège **20**, 91
Underhill, A. B. (1995a): ApJS **100**, 433
Underhill, A. B. (1995b): ApJS **100**, 461
Vallée, J. P., Moffat, A. F. J. (1985): AJ **90**, 315
Walborn, N. R., Bohlin, R. C. (1996): PASP **108**, 477

- Walborn, N. R., Nichols-Bohlin, J. S., Panek, R. J. (1985): *International Ultraviolet Explorer Atlas of O-Type Spectra from 1200 to 1900 Å* (NASA RP-1155)
- Walborn, N. R., Parker, J. W., Nichols, J. S. (1995): *International Ultraviolet Explorer Atlas of B-Type Spectra from 1200 to 1900 Å* (NASA RP-1363)
- White, R. L. (1985): ApJ **289**, 698
- White, R. L., Becker, R. H. (1982): ApJ **262**, 657
- White, R. L., Becker, R. H. (1983): ApJ **272**, L19
- Wilson, R. (1958): Mem. R. Soc. Liège **20**, 85
- Wolf, C. J. E., Rayet, G. (1867): Observatoire de Paris Comptes Rendus **65**, 292
- Wright, A. E., Barlow, M. J. (1975): MNRAS **170**, 41

Observations of Hot-Star Winds

A.W. Fullerton

Universitäts-Sternwarte München, Scheinerstraße 1, D-81679 München, Germany
e-mail: alex@usm.uni-muenchen.de

1 Introduction

Stellar winds from early-type stars have been studied observationally for more than 120 years, beginning with the detection of peculiar bright lines in visual spectra of a few hot objects by Wolf and Rayet (1867). Beals (1930) first recognized that the emission features of these “Wolf-Rayet stars” (WR stars) were signatures of mass loss, since the observational material available to him showed that some of the line profiles were of the “P Cygni type”. This distinctive shape, named because of its prevalence in the spectrum of the famous B2pe hypergiant P Cygni, is also found in the spectra of novae shortly after outburst, i.e., during a time when they are manifestly experiencing explosive mass ejection. On this basis, Beals inferred that WR stars were also losing mass, and concluded that “practically all of the characteristic features of Wolf-Rayet spectra may be explained on the hypothesis that gaseous material from a Wolf-Rayet star is being continually ejected in a radial direction and with high velocity into space”.

Thus, more than 60 years ago the modern basis for interpreting spectroscopic emission features in terms of dense, extended, and expanding outflows had already been established. What was not initially clear was that the WR stars and the few objects like P Cygni (which we now call luminous blue variables, or LBVs) are just the tip of the iceberg: they are extreme examples of a phenomenon that is ubiquitous among the early-type stars. Important observations by Wilson (1958) and Underhill (1958) provided hints that mass loss occurs commonly by showing that the emission features of a selection of O-type supergiants and giants could be traced to velocities of 500–1000 km s^{-1} , which are comparable to or in excess of the escape velocity. Nevertheless, during the early and mid-1960s the emphasis in hot-star research was on static atmospheric modelling without the assumption of local thermodynamic equilibrium (LTE), while the field of stellar winds lay fallow.

This situation changed abruptly as a result of technological advances that opened the vacuum ultraviolet region of the spectrum to astronomical observations. The modern era of hot-star wind research began on 1965 October 13 when an Aerobee rocket launched from the White Sands Missile Range in New Mexico briefly carried an ultraviolet spectrograph aloft and returned the first ultraviolet spectra of six early-type stars in Orion (Morton 1967a).

As always, a bit of good luck was required to push open a new observational window: Morton (1967a) writes that during the descent,

the cameras, platform, and gyro had broken free of their mounts and pieces of grating, mirror, and film cassette went flying out of the open end of the rocket skin. Both the calcium fluoride spectrograph camera and a 35-mm camera for photographing the star field were lost, and a 2-day search of the impact area yielded nothing. Fortunately, however, the lithium fluoride film cassette was still attached and was recovered

Morton's analysis (1967a, 1967b) of these hard-earned data showed that the resonance lines of highly ionized species like Si IV, C IV, and N V exhibited P Cygni profiles. In contrast to the P Cygni profiles that were typically observed in optical spectra of hot stars, velocities well in excess of the escape velocity were directly measured in these ultraviolet data. For the three stars that make up the belt of Orion (from east to west, these are δ , ϵ , and ζ Orionis, with spectral types of O9.5 II, B0 Ia, and O9.7 Ib, respectively), Morton (1967b) estimated mass-loss rates of $\sim 1 \times 10^{-6} M_{\odot} \text{ yr}^{-1}$ and concluded that these stars would lose a few per cent of their initial mass during their lifetimes. It at once became clear that garden-variety OB supergiants lose mass continuously at rates that are sufficiently high to affect the course of their evolution.

This result came as a complete surprise at the time. Over the past generation, observational and theoretical efforts to understand the nature and origin of these stellar winds have been a dominant theme of hot-star research. It is a tribute to the success of these efforts that the mass loss carried by these outflows is now recognized to be a fundamental astrophysical process that not only causes individual stars to "evaporate" significantly over their short lifetimes (thereby altering their trajectory through the H-R diagram) but also dumps substantial amounts of energy, momentum, and chemically enriched material into their local galactic environment (thereby influencing the dynamics of the interstellar medium and subsequent formation of stars). Excellent introductions to hot stars and their winds include Kudritzki (1988), Kudritzki and Hummer (1990), and Owocki (1990), while Maeder and Conti (1994) provide an overview of the role these objects play in the evolution of galaxies.

The aim of these lectures is to provide an introduction to the most useful observational signatures of the stellar winds of early-type stars. The goal is to provide an appreciation of the physical ingredients and assumptions that are required to obtain estimates of the physical parameters of the winds from these diagnostics, in particular the mass-loss rate, \dot{M} , and the asymptotic (terminal) velocity of the wind at large distances from the star, v_{∞} . The problems associated with each type of diagnostic are also discussed, in order to assess the reliability of the parameters determined from them. The emphasis is on Population I objects, especially O stars and BA supergiants,

though many of the same diagnostics can be applied to related (but more complicated) objects like WR stars and LBVs, and hot Population II objects like the central stars of planetary nebulae.

2 Tracers of Stellar Winds

The observable manifestations of stellar winds are all attributable to the fact that rapidly expanding material surrounds that star, and this material constitutes an excess with respect to an otherwise identical star whose photosphere manages to maintain strict hydrostatic equilibrium. The fundamental equation that connects the hydrodynamic variables of the outflow is the equation of mass continuity. For a homogeneous, steady, spherically symmetric wind, it reduces to a formula for the mass-loss rate:

$$\dot{M} = 4 \pi r^2 v(r) \rho(r) . \quad (1)$$

Rearrangement of (1) shows that at large distances in the wind, where $v(r) \approx v_\infty$, the density decreases only as r^{-2} , which is much slower than the exponential decrease characteristic of the hydrostatic layers of the photosphere. It is the presence and motion of this excess circumstellar material that ultimately permit the outflow to be observed.

Even though they represent large density excesses with respect to hydrostatic atmospheres, the stellar winds of early-type stars consist of very rarefied gas. For example, if we insert parameters typical of an O supergiant into (1), we find that at a height of $1 R_\star$, the density of the wind is approximately $5 \times 10^{-15} \text{ g cm}^{-3}$, which is more than three orders of magnitude smaller than photospheric densities. Thus, stellar winds are environments where radiative processes dominate over collisional processes in determining level populations; i.e., they are very far from being in LTE.

The tracers of this material can be grouped into two main categories: spectroscopic or line diagnostics; and photometric or continuum diagnostics. Signatures can be found in all wavelength regions, from the radio and infrared (IR) through the optical and ultraviolet (UV) to X-rays and possibly even γ -rays (see, e.g., Chen et al. 1996). The emission of these extremely energetic photons is believed to result from time-dependent processes in the wind and not from the steady-state outflow itself, and will not be discussed in detail here.

3 Spectroscopic Diagnostics

Quite generally, spectroscopic observations of absorption or emission lines formed in the atmospheres of stars can be characterized by their positions (i.e., their radial velocities), their strength (i.e., their equivalent widths), and their overall morphology (i.e., the shape of their flux profiles). Each of these

measurable quantities can be used to obtain information about the presence of stellar winds.

For example, systematic trends showing decreasing blue shifts for lines formed at increasing photospheric depth – the so-called Balmer progressions or velocity-excitation relations – are frequently used as stellar wind indicators, because they imply the presence of a deep-seated velocity field that increases outwards and presumably drives mass loss (Hutchings 1979; Kaufer et al. 1997). Systematic trends in the strength of photospheric lines as a function of luminosity may also provide evidence for an outward accelerating velocity field, particularly if they are accompanied by asymmetric line profiles with extended blue wings. The velocity gradient is the essential physical ingredient here, because it systematically shifts the absorption profile of the particular ion to smaller wavelengths at greater atmospheric heights, with the result that more atoms can participate in the formation of the flux profile (hence the increase in the equivalent width of the line) and the flux profile has an extended blue wing (since some of the profile is actually formed at blue-shifted velocities). Mihalas (1979) and Kudritzki (1992) provide useful discussions of this phenomenon, which is nicely illustrated for a sequence of B1 supergiants by Massa et al. (1992).

However, the dominant spectroscopic signatures of stellar winds are the profiles associated with lines that are formed in the rapidly expanding part of the wind. Many profile morphologies are recognized as being formed in out-flowing material. These shapes were classified qualitatively by Beals (1950), and although his scheme is not much used these days, it still provides a useful introduction to the phenomenology associated with stellar wind profiles. Beals recognized eight classes of wind profiles.

- Type I:** This is the classic P Cygni profile, which consists of a blue-shifted absorption “trough” and a red-shifted emission “lobe”. The origin of this shape is discussed in Sect. 3.2.
- Type II:** These profiles are composed of a Type I profile superimposed on a broad, shallow absorption line, typically one from the Balmer series of hydrogen.
- Type III:** This morphology consists of red- and blue-shifted emission peaks and a central reversal. It occurs rarely in OB stars, and then only in some lines of rapid rotators. Although its origin is not completely understood, this shape is due to a combination of the velocity fields associated with radial outflow and rapid stellar rotation; see, e.g., the profiles calculated by Petrenz and Puls (1996), in particular their Figs. 12 and 14.
- Type IV:** These profiles are similar to those of Type I, except they also have one or more extra absorption components in the absorption trough or near the center of the emission lobe.
- Type V:** These “pure emission” profiles are approximately symmetric about the systemic velocity of the star and do not exhibit the absorption trough characteristic of P Cygni profiles. The spectra of WR stars are dominated

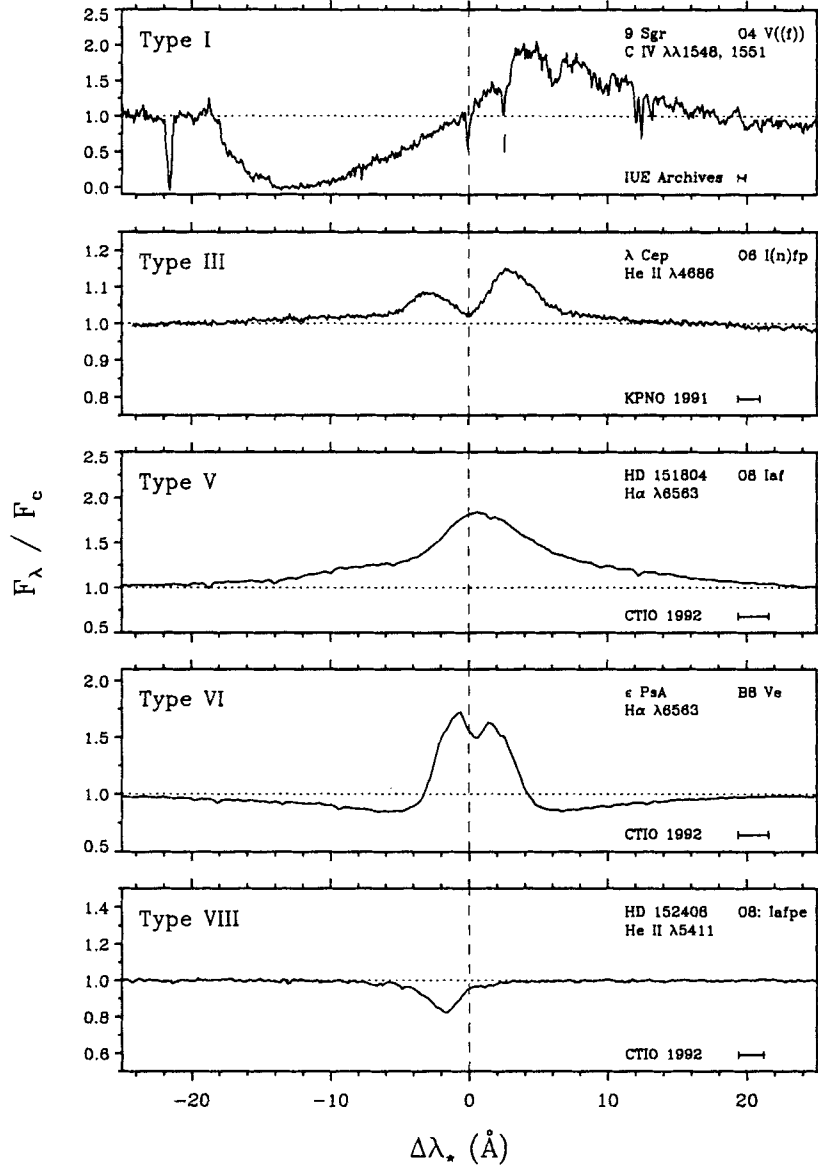


Fig. 1. A selection of line profile morphologies attributed to stellar winds, with classifications according to the scheme of Beals (1950). The wavelength interval corresponding to a velocity of 100 km s^{-1} is indicated by a horizontal bar in the lower right-hand corner, and the position of the red component of the C IV doublet is marked by a vertical line (and the sharp interstellar component)

Table 1. Selected atlases of stellar wind profiles

Reference	Wavelength	Source	Objects
Walborn et al. (1985)	1200–1900 Å	IUE/SWP	O stars
Snow et al. (1994)	1200–3000 Å	IUE	O3–F8 stars
Walborn et al. (1995)	1200–1900 Å	IUE/SWP	B stars
Walborn and Bohlin (1996)	1000–1200 Å	Copernicus	OB stars
Stahl et al. (1993)	4050–9050 Å	FLASH	P Cygni
Hanson et al. (1996)	K band (2 μ)	various	OB stars

by such emission lines, which can also be found in spectra of OB supergiants.

Type VI: This strange morphology consists of a central emission feature that is superimposed on a broad underlying absorption line. The emission is frequently double peaked. These profiles are most commonly associated with Be stars, and consequently a complicated structure of a rotating, expanding stellar wind is implicated in their formation.

Type VII: Beals (1950) describes this morphology as “simply an ordinary undisplaced absorption line such as may appear in any normal star . . .”, and as such it perhaps best serves as a reminder that not all the lines in the spectrum of an early-type star are formed in the moving envelope.

Type VIII: Lines of this type are blue-shifted absorption features, which Beals (1950) thought of as Type I profiles without the emission lobe. The displaced absorption is frequently asymmetric, with a shallower blue wing that is presumably due to the velocity gradient through its region of formation.

Part of this classification scheme is illustrated in Fig. 1, which shows normalized flux profiles as a function of wavelength offset from the rest velocity (corrected for the systemic velocity of the star). Examples of stellar wind profiles can be found throughout the observable regions of the spectrum, from the UV through the optical to the IR. Table 1 lists several atlases that illustrate the rich variety of wind profile morphologies implied by the Beals classification scheme.

3.1 Scattering Versus ρ^2 Formation Processes

The resonance lines of singly or multiply ionized species that are typically found in the UV region of the spectra of early-type stars are superb tracers of the rarefied material found in stellar winds. By definition, resonance lines

are the lowest energy transitions that arise from the ground state. Consequently, these transitions have very short lifetimes, which in turn means that they occur frequently and are intrinsically strong. In particular, the lifetime of a resonance transition is usually much shorter than the time required for radiative excitations or collisions, especially in environments characterized by dilute radiation fields and low particle densities. Thus, when an electron is promoted from the ground state to the first permitted level by absorption of a stellar continuum photon of the appropriate frequency, it will de-excite very rapidly and a resonance line photon will be emitted. The net result of such an interaction is that the incoming, almost radially directed, stellar photon will be scattered into some different direction, thereby imparting radial momentum to the ion without changing the population of the ground state. Consequently, in low-density gases the degree of excitation of an ionic species tends to be very low and there is always a large pool of electrons sitting in the ground state that are capable of scattering radiation.

These factors make resonance lines strong and easily detectable throughout the entire volume of the wind where the ion exists. Since these lines are formed by scattering of continuum photons, their strength depends linearly on ρ , the density of matter, and also on the mean intensity of the dilute radiation field from the star. The resonance lines that are important depend on the ionization balance of the wind, which is largely determined by the radiation field. For O- and early B-type stars, they include multiply ionized species like C IV, N V, and Si IV; for mid- to late B- and early A-type supergiants the resonance lines of singly ionized C, Mg, Al, Si, and Fe are important.

However, as Fig. 1 indicates, wind profiles can also be found in the excited (i.e., non-resonance) transitions that are typically located in the optical and infrared regions of early-type spectra, especially those arising from H, He I and He II. They are usually the result of recombinations from a higher ionization stage, which are followed by radiative de-excitations that create photons. These transitions are intrinsically weaker than resonance lines; furthermore, since the process of recombination requires the interaction of an electron and an ion, they are sensitive to ρ^2 . Consequently, and in contrast to resonance lines, excited transitions are only sensitive diagnostics of the densest regions of the wind, which are usually the parts closest to the star. An important exception occurs if a large population accrues in the lower level of an optical transition for some reason (e.g., the level is metastable or susceptible to non-LTE/dilution effects), in which case the transitions arising from it behave a bit like resonance lines. The He I $\lambda 5876$ triplet in the “yellow” region of the visible spectrum is an example of such a transition.

3.2 Dissecting the P Cygni Profile

Before we can determine what information about the stellar wind is contained in line profiles like those shown in Fig. 1, we need to understand how these

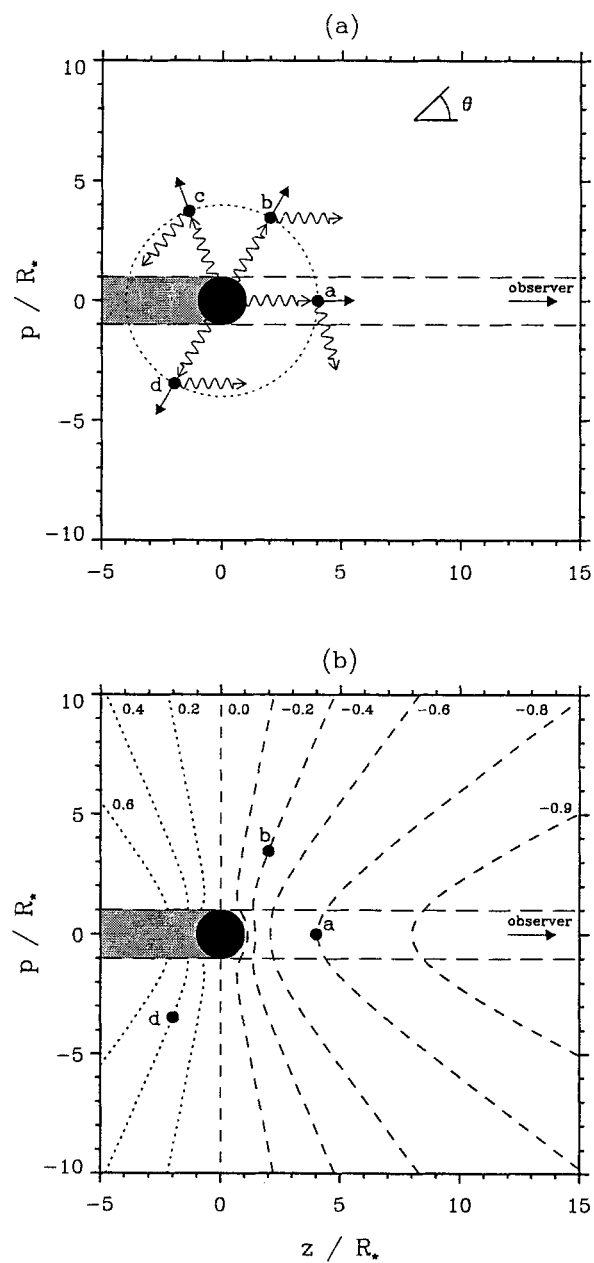


Fig. 2. (a) Schematic diagram of the scattering process. (b) The isovelocity contours associated with the velocity field of a smooth, spherically symmetric stellar wind

profiles are formed. The P Cygni profiles (Beals Type 1) of resonance lines provide the key to understanding these morphologies.

The basic picture is illustrated schematically in Fig. 2(a), which shows a plane through a smooth, spherically symmetric stellar wind. Four ions (labelled a–d) are shown, all of which are located at the same radial distance from the star and therefore experience the same expansion velocity (which is indicated by short, radially directed vectors). Ions at larger (smaller) radii than those illustrated will be moving faster (slower), since the velocity field of a smooth wind increases monotonically outwards. Stellar continuum photons are injected continuously into the wind from the star along paths that are nearly radial. If their wavelength matches the Doppler-shifted wavelength of the resonance line transition associated with ions a–d, then the photon can interact radiatively; since the wind material is moving away from the star, this means that the wavelength of the continuum photons must be blueward of the rest wavelength of the resonance line. An important consequence of this “tuning” is that if a continuum photon can interact with the resonance transitions at some particular radius, it cannot interact with ions at larger or smaller radii, because their Doppler shifts will be greater or smaller, respectively. Consequently, at larger or smaller radii the wind is *transparent* to the photons that can be scattered in the resonance lines of the ions indicated in Fig. 2.

As described above, the net result of this interaction for a resonance line is that the incoming photon is scattered into some different direction. These scatterings have two consequences for a distant observer (who is arbitrarily situated in the z -direction in Fig. 2): (1) photons that were destined to be recorded by the observer can be removed from the line of sight, as in the case of the scattering illustrated for ion “a”; and (2) photons that were not originally heading in his/her direction can be redirected into his/her telescope, as illustrated for ions “b” (where the photon is forward-scattered into the direction of the observer from an ion in the hemisphere approaching the observer) and “d” (where the photon is back-scattered from an ion in the receding hemisphere). Since the observer’s direction subtends a very small fraction of the 4π steradians surrounding the star, there is a good chance that an originally unobservable photon will be scattered into a new direction that is also unobservable, as illustrated for ion “c”. Some photons will even be back-scattered directly to the stellar surface where they will be reabsorbed by the photosphere.

We can be more specific about the distribution of the scattered photons as a function of position in the flux profile seen by the distant observer. This position may be given in terms of wavelength, frequency, or “radial velocity”; we will usually use the velocity coordinate, but will refer to it as “line-of-sight” velocity, (V_{los}), in order to avoid confusion with the radial component of the velocity field associated with the stellar wind. The V_{los} of a scattered photon depends on the Doppler shift due to wind expansion of

the ion that it interacted with and the projection of this displacement onto the observer's line of sight, i.e., the cosine of the angle θ between the velocity vectors and the z-axis indicated in Fig. 2(a). Contours of equal V_{Los} for the velocity field of a typical expanding stellar wind are shown in Fig. 2(b), where they are labelled in units of v_∞ with positive velocities denoting recession. Of course, these contours in the equatorial plane are actually surfaces in 3D space; they are sometimes called "common direction" (CD) surfaces since they require the specification of the direction of an observer (see, e.g., Rybicki and Hummer 1978).

The isovelocity contours permit the redistribution of continuum photons to be mapped to positions in the observed line profile, which can be conveniently divided into an absorption part and an emission part. This mapping is illustrated in Fig. 3 for a line of moderate strength (panel a) and a strong line (panel b). Three regions of the wind contribute to the profile:

1. Material in the column projected against the disk of the star removes continuum photons from the line of sight at blue-shifted velocities that range from 0 to the maximum expansion velocity where the ion still exists (which is frequently v_∞), thereby producing the blue-shifted absorption trough. Ion "a" provides an example of the removal of a photon at $V_{\text{Los}} = -0.8 v_\infty$.
2. Material at other places in the approaching hemisphere adds photons at blue-shifted velocities (e.g., ion "b": $V_{\text{Los}} = -0.4 v_\infty$) by forward-scattering, which collectively produce the blue-shifted emission shown in the middle panels of Fig. 3. In contrast to the absorption trough, the emission at a particular V_{Los} includes contributions from many different radii that will in general sample a wide range of densities, temperatures, and ionization equilibria.
3. Material in the receding hemisphere adds back-scattered photons at red-shifted velocities (e.g., ion "d": $V_{\text{Los}} = +0.4 v_\infty$) to the emission profile. The emission profile is not symmetric about $V_{\text{Los}} = 0$ because back-scattered photons originating in the shaded "occultation region" are re-absorbed by the stellar core before they can reach the observer. The differences between the blue- and red-shifted emission are especially pronounced for winds that expand more slowly, since in these cases the star subtends a larger solid angle at radii where the density is still high enough for many scattering interactions to occur.

The bottom panel shows how a P Cygni profile results from adding the absorption and emission contributions from these regions to produce the characteristic morphology of a blue-shifted absorption trough and a red-shifted emission lobe.

The comparison between moderate and strong scattering lines in Fig. 3 is also instructive. The upper panels show that for a line of sufficient intrinsic strength, all the continuum photons can be scattered from the observer's line

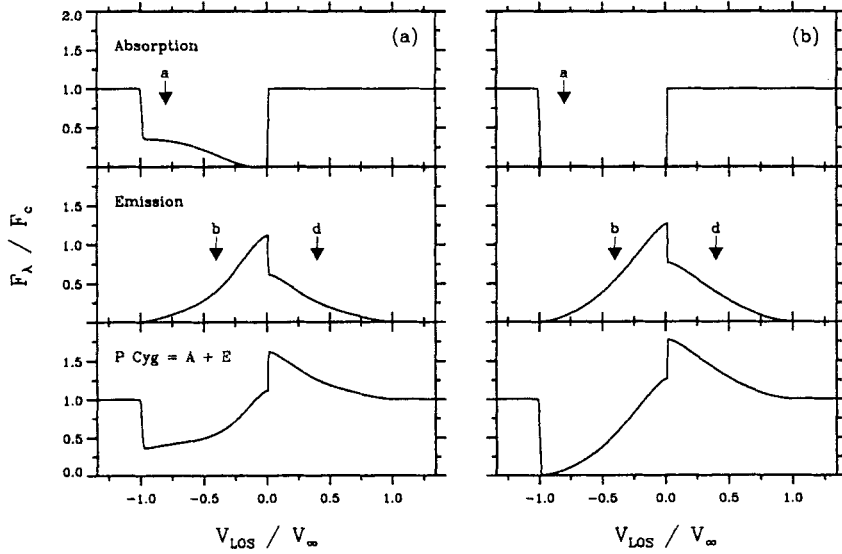


Fig. 3. Schematic diagram showing the formation of a P Cygni profile of a UV resonance line for the case of (a) a moderately strong line; and (b) a strong line

of sight, whereas a weak line in the same wind (i.e., same ionization and density structure) will not completely extinguish the continuum light directed toward the observer. By the same token, the strong line will scatter more photons towards the observer, so that its emission component (middle panel) is stronger at all velocities. This is a reflection of the fact that scattering is a conservative process: since photons are not created or destroyed in the wind (though some are lost through back-scattering to the photosphere), and since the absorption component of a strong line removes more photons from the observer's line of sight compared to a weak line, more photons must be forward- and back-scattered towards the observer.¹ Thus, despite the total extinction of the continuum source by the cylinder of material projected against the disk of the star, the P Cygni absorption trough of a strong line formed in a smooth, spherically symmetric wind never exhibits extended regions of zero flux. If the ion responsible for the strong resonance line exists throughout the wind, then the only place where its absorption trough will have zero flux is at $V_{\text{LOS}} = v_{\infty}$, since forward-scattering from material anywhere else in the approaching hemisphere will necessarily be seen at smaller line-of-sight

¹ This argument breaks down after all photons have been removed from the absorption trough, at which point the strength of the emission lobe also saturates.

velocities. Put another way, the isovelocity contours collapse to a point for $V_{\text{LOS}} = \pm v_{\infty}$, and the positive case is not observable due to occultation by the star. Hence, for monotonically expanding winds, the maximum velocity seen at the blue-edge of the absorption trough of a strong line is a good diagnostic of v_{∞} .

P Cygni profiles are formed when scattering dominates the transfer of radiation through the wind. If instead photons are created in the wind through radiative or collisional (“ ρ^2 ”) processes, the absorption component tends to be filled in by locally produced photons. Similarly, the emission component can become very strong, since the number of photons that emerge from the wind is not simply a reflection of the number of stellar continuum photons initially injected. Unless there is some additional factor associated with the physics of the transition in question (e.g., the lower level is overpopulated for some reason), “pure emission” profiles are formed in these cases. Although the atomic processes responsible for these spectral features are more complicated than resonance line scattering, the mapping between isovelocity contours and position in the profile remains the same. Of course, more complicated velocity fields (e.g., coupling between rotation and expansion) or geometries (e.g., disks) will change the shape of the contours, and the interplay between the velocity field, density distribution, and ionization balance in the wind are ultimately responsible for the variety of wind profile morphologies catalogued by Beals.

Although P Cygni profiles are unambiguous signatures of outflow, the same is not true of pure emission features. For example, there are a number of narrow emission lines in the spectra of O stars (see, e.g., Morrell et al. 1991 or Underhill 1995a,b for recent discussions), most of which are formed by two-electron processes (“dielectronic recombinations”) in deep layers of the atmosphere. The most famous of these are the N III $\lambda\lambda 4634, 4640, 4641$ lines, whose formation in static, plane parallel atmospheres was first explained by Mihalas and Hummer (1973). Although the strength of these features often suggests that they are partially formed in the low-velocity region of the stellar wind, they should be distinguished from the very broad stellar wind profiles typical of Beals Type III or V.

3.3 Calculation of Line Profiles Formed in Stellar Winds

The preceding discussion of the P Cygni profile also illuminates many aspects of the problem of computing line profiles formed in a stellar wind. In general, this is a formidable task; but, as Castor 1970 realized, it can be handled very effectively by combining the formalism of escape probabilities (see, e.g., Sect. 3.2 of Hubeny, this Volume) with the Sobolev approximation. What follows is a sketch of this approach as it applies to smooth, spherically symmetric, monotonically expanding winds. For rigorous discussions of this elegant technique, see Castor 1970, Rybicki and Hummer (1978), Rybicki

(1984), or Mihalas (1978; Chapter 14). Although the escape-probability formalism is at present the most widely used, alternative approaches exist: see, e.g., Lucy (1971).

The equation of radiative transfer in the observer's frame for spherically symmetric geometry is given, e.g., by (27) in Hubeny's lectures.² It can be reformulated in the Cartesian "p-z" geometry illustrated in Fig. 2 as an ordinary differential equation for rays specified by their impact parameter p :

$$\frac{dI_\nu(z; p)}{dz} = k_\nu(z; p) [S_\nu(z; p) - I_\nu(z; p)] \quad (2)$$

where $r, z = r\mu$ and $p = r\sqrt{1 - \mu^2}$ are measured in units of R_\star and $\mu \equiv \cos \theta$ is the cosine of the angle between a point in the wind and the direction to the observer, as indicated in Fig. 2(a); k_ν is the absorption coefficient; and where "complete redistribution" has been assumed (see Sect. 3.1 of Hubeny, this Volume). This reformulation is a great simplification, and allows the "formal solution" to be written down immediately. If I_ν^* is the continuum intensity of the star at frequency ν and $z_\star = \sqrt{1 - p^2}$ denotes the z-coordinate associated with the stellar surface for $p \leq 1$, then the formal solution is:

$$I_\nu(p) = \begin{cases} \int_{z'=-\infty}^{\infty} S_\nu(z') e^{-\tau_\nu(z')} d\tau_\nu(z') & \text{for } p \geq 1 \\ \int_{z'=z_\star}^{\infty} S_\nu(z') e^{-\tau_\nu(z')} d\tau_\nu(z') + I_\nu^* e^{-\tau_\nu(\infty)} & \text{for } p < 1 \end{cases} \quad (3)$$

where the optical depth variable is

$$\tau_\nu(z; p) = \int_{z_{\min}}^z k_\nu(z'; p) dz' \quad (4)$$

with $z_{\min} = -\infty$ for $p \geq 1$ and $z_{\min} = z_\star$ for $p < 1$. Once $I_\nu(p)$ is known, the flux profile can be calculated directly:

$$F_\nu/F_c = \int_0^\infty [I_\nu(p)/I_\nu^*] 2p dp \quad (5)$$

In the case of line radiation, (3) can be viewed as the mathematical equivalent of Fig. 3. It says that for rays projected against the stellar disk (i.e., $p < 1$) the flux received by a distant observer is made up of a "direct" component that is extinguished by material in front of it (i.e., the absorption trough) and a "diffuse" component (i.e., sources of emission due to forward-scattering). For rays not projected against the stellar disk ($p \geq 1$), only diffuse light is sent to a distant observer. In the case of UV resonance lines, the diffuse light is entirely due to scattering.

Since (3) is a formal solution, the source function and the optical depth for the line of interest need to be known before it can be applied. The level

² For convenience, results presented by Hubeny (this Volume) will be referred to by their equation numbers in his lectures preceded by "H": e.g., (H27).

populations for resonance lines are controlled by radiative transitions between only two levels, and so the source function for the two-level atom given by (H82) for the case of “pure scattering” ($\epsilon = 0$) is directly applicable. Hence, $S_\nu = \bar{J}$, where \bar{J} is the frequency-averaged mean intensity of line radiation defined by (H81). Schematically, the mean intensity can be viewed as a competition between the number of continuum photons that arrive at location r versus the number of line photons that escape from the same location, so that

$$\bar{J}(r) = \frac{\text{probability that a stellar continuum photon penetrates to } r}{\text{probability that a line photon escapes from } r} . \quad (6)$$

These quantities are related to the angle- and frequency-averaged escape probabilities defined by (H88), which in turn depend fundamentally on the optical depth variable for different directions μ at location r in the wind. Consequently, the computation of a line profile pivots on the computation of τ_ν , after which the calculation can be charted as $\tau_\nu \rightarrow$ escape probabilities $\rightarrow \bar{J} \rightarrow S_\nu \rightarrow I_\nu(p) \rightarrow F_\nu$.

Unfortunately, the calculation of τ_ν for arbitrarily moving media is complicated by the frequency dependence of the absorption coefficient, k_ν . In static atmospheres, k_ν is often written as the product of a spatial part and a normalized absorption profile that accounts for the frequency dependence (and is generally assumed to be constant);

$$k_\nu = k_0(r) \times \varphi(\Delta\nu) , \quad (7)$$

where $\int_{-\infty}^{+\infty} \varphi(\Delta\nu) d\nu = 1$ and $\Delta\nu = \nu - \nu_0$ for a line with rest frequency ν_0 . This separation is not strictly valid in a moving atmosphere, because ν is itself a function of r owing to the bulk motion of the fluid, but the functional form can be recovered by allowing explicitly for the Doppler shift in frequency, which can be accomplished by redefining $\Delta\nu = \nu - \nu_0 + [\nu_0 \cos \psi v(r)]/c$, where ψ is the angle between the radial direction and the direction of scattering, so that $\cos \psi v(r)$ is the projection of the expansion velocity onto the new direction of flight. Although this simple redefinition allows us to retain the form of (7), it also shows that in a moving medium, $k_\nu \equiv k_\nu(r, v, \psi)$, i.e., that frequency and spatial variables are intertwined, so that many different combinations of positions and frequency contribute to a particular frequency in the observer’s frame; recall, e.g., the isovelocity contours illustrated in Fig. 2(b).

However, in the presence of sufficiently large velocity gradients, the “tuning” required for a photon to excite a line transition localizes the material that is capable of absorbing it, and this breaks the coupling between frequency and spatial variables. This localization is the essence of the Sobolev approximation, which is sometimes called the “large velocity gradient” or “supersonic” approximation. Fig. 4(a) illustrates the Sobolev approximation in a schematic way for the frame of reference that is moving with the mean

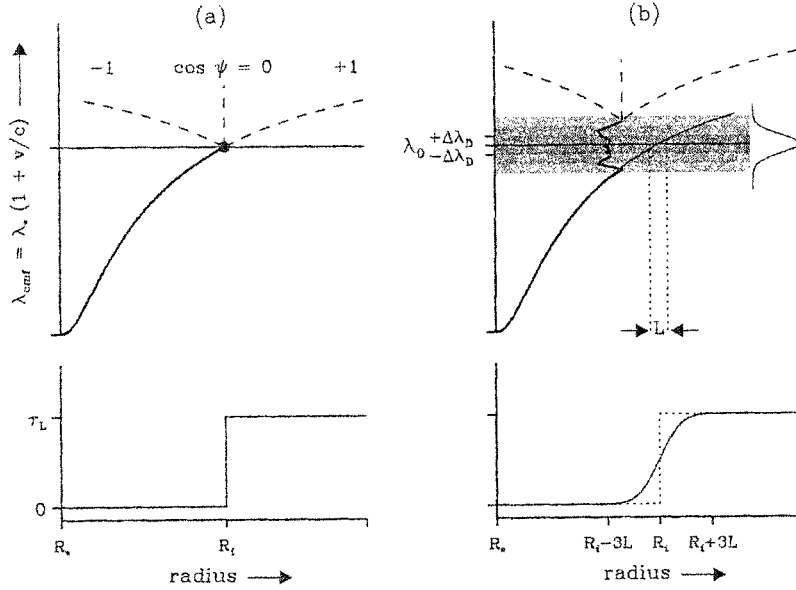


Fig. 4. Schematic illustration of the Sobolev approximation (after Owocki 1990) and the distribution of Sobolev optical depth for (a) an infinitely thin transition centered on λ_0 ; (b) a transition with a Gaussian profile characterized by a 1-sigma dispersion of $\Delta\lambda_D$

flow of the expanding wind. The star is receding with respect to this “co-moving frame”, and the thick solid line shows the systematic redshift of a photon emitted with wavelength λ_* at the stellar surface as a function of radius. Consider a bound-bound transition with rest wavelength λ_0 in the spectrum of an ion, and suppose for the moment that the absorption profile $\varphi(\Delta\lambda)$ of this transition is a delta function. The photon λ_* travels *unimpeded* through the material of the stellar wind until its wavelength in the comoving frame matches λ_0 , whereupon it may be absorbed by the line transition and re-emitted in some other direction. Three possible scatterings are indicated in the upper panel of Fig. 4(a), which correspond to forward-scattering ($\cos \psi = 1$; i.e., the photon continues along its original course); sideways-scattering ($\cos \psi = 0$); and back-scattering towards the star ($\cos \psi = -1$).

The key point is that since the wind is an expanding medium, the material in *any* direction is receding from the scattering site, just as all galaxies recede from one another in the case of the expanding universe. Thus, irrespective of the scattering angle, the wavelength of the redirected photon in the comoving frame must be redshifted, which means it cannot interact again with

a transition of wavelength λ_0 and is free to travel through the wind along its new trajectory. As a result, the processing of stellar continuum photons through a bound-bound transition is localized to a single radius, R_i , which is determined by λ_* , and the variation of optical depth with radius is the step-function shown in the lower panel of Fig. 4(a). For this simplified case, the solution of the equation of radiation transfer reduces to determining the fraction of incident photons that are scattered into the different directions ψ .

In practice, the absorption profile of a transition is never a delta function, but has a finite width $\Delta\lambda$ associated with it; e.g., the absorption profile is dominated by thermal Doppler broadening in the low-density environments typical of hot-star winds, so that φ is a Gaussian characterized by a root-mean-square dispersion parameter (sigma) of $\Delta\lambda = \Delta\lambda_D = v_{th}\lambda_0/c$, where v_{th} is the thermal velocity of the parent ion. This case is illustrated in Fig. 4(b), which shows that after travelling freely through lower regions of the wind (as before) the stellar photon first impinges on the blue wing of the line. The scattered photon will in general be redirected and redistributed in wavelength (frequency), so that it will perform a random walk in space and wavelength that takes it from the weak absorption typical of the blue wing to the strong absorption of the line core. The step size associated with this random walk gets quite small as the photon makes its way towards the line core, but its eventual emergence at the red wing – possibly after many scatterings – is assured because of the overall expansion of the wind.

However, even though the number of scatterings may be very much larger than in the case of the infinitely narrow line, the net result is that a photon is absorbed at the blue wing of the line, emerges after a final scattering in the red wing, and continues its travel in a different direction but without further interactions, exactly as before except that the interaction occurs over a larger range of radii. As shown in the lower panel of Fig. 4(b), the finite width of the line softens the step-function character of the radial distribution of optical depth, but does not affect the essential localization of the interaction region *provided that the velocity gradient is sufficiently steep*. The relevant figure of merit to describe “sufficient steepness” is the Sobolev length, L , which is the distance over which the mean flow speed of the wind increases by v_{th} , and can be thought of as the local optical depth scale height. From Fig. 4(b), $dv/dr \approx v_{th}/L$ or $L = v_{th}(dv/dr)^{-1}$. The Sobolev approximation is valid when L is much smaller than the distance over which other hydrodynamical variables (e.g., density) change. The local density scale height, L_ρ , may be estimated from (1):

$$L_\rho \equiv \frac{\rho}{|d\rho/dr|} \approx \frac{v}{|dv/dr|} \gg \frac{v_{th}}{|dv/dr|} = L, \quad (8)$$

since $v_{th} \approx 10 \text{ km s}^{-1}$ while $v \approx 1000 \text{ km s}^{-1}$ for hot-star winds. Thus, the Sobolev approximation is generally excellent, except at small velocities, where $v \approx v_{th}$.

This localization of the radiative transfer enormously simplifies the calculations of τ_ν . Since the radiative transfer occurs over spatial scales that are much smaller than other hydrodynamical scale lengths, the spatial part of absorption coefficient (7) can be taken outside the optical depth integral (4):

$$\tau_\nu(z; p) \stackrel{\text{SA}}{\approx} k_0(r) \int_{z_{\min}}^z \varphi(\nu - \nu_0 + [\nu_0 \mu v(z; p)]/c) dz', \quad (9)$$

which can then be transformed in a straightforward way to an integral over frequency in the comoving frame (i.e., spatial variables can be exchanged for frequency variables). For Gaussian absorption profiles, the integral can be done analytically, which represents a tremendous simplification even compared to static atmospheres. An important result to emerge from these manipulations is the expression for the Sobolev optical depth in the radial direction at a particular radius (or, equivalently, velocity) in the wind. For a transition between a lower level l and an upper level u of an ion, this is

$$\pi_\nu(r) = \left(\frac{\pi e^2}{m_e c} \right) f_{lu} g_l \lambda_{lu} \left(\frac{n_l}{g_l} - \frac{n_u}{g_u} \right) \left(\frac{dv}{dr} \right)^{-1}, \quad (10)$$

where the first terms on the right-hand side denote the strength of the transition in terms of its classical oscillator strength (where all symbols have their usual meanings), λ_{lu} is the rest wavelength of the transition, g_l (n_l) and g_u (n_u) are the statistical weight (number density) of the lower and upper levels, respectively, and dv/dr is the local radial gradient of the velocity field.

Once $\tau_\nu(z)$ is known, the calculation of a line profile formed in the stellar wind can proceed according to the plan outlined before. Several computer programs are available for this purpose, the most widely used of which is the efficient ‘‘Sobolev with Exact Integration’’ (SEI) program described by Lamers et al. (1987)³. The idea of using the Sobolev approximation to compute the source function, but doing the flux integration ‘‘exactly’’, is due to Hamann 1981 and is in contrast to the previous approach of relying on the step-function behaviour in $\tau_\nu(r)$ inherent to the Sobolev approximation to simplify the integrations as well (e.g., Castor and Lamers 1979). With the SEI approach, it is straightforward to allow for the radiative coupling of the source functions of closely spaced doublets (Olson 1982; see also Lamers et al. 1987), which is of practical importance since most of the UV resonance lines are blended doublets. The SEI formalism is also sufficiently flexible that generalizations to allow for deviations from spherical symmetry (e.g., Bjorkman et al. 1994; Cranmer 1996) or monotonic expansions (e.g., Puls et al. 1993) can be implemented in a simple way. More complicated situations like these can also be treated by using a Monte Carlo approach to radiative transfer: see, e.g., Caroff et al. (1972), Lucy (1983), or Puls et al. (1994).

³ A FORTRAN version of this program can be downloaded from the homepage of Collaborative Computer Project No. 7 (CCP7) on the Analysis of Astronomical Spectra. Its URL is currently <http://star.arm.ac.uk/ccp7/>.

3.4 UV Resonance Lines

Equation (1) shows that the mass-loss rate for a spherically symmetric wind can be calculated once the radial distribution of velocity and mass density are known. Although quite a lot of information about the “velocity law”, $v(r)$, is encoded in the shape of the P Cygni profile, it is not possible to measure the density distribution directly because the winds of hot stars cannot be spatially resolved at UV wavelengths. On the other hand, the strength of the absorption and emission components constrain the total number of ions of the species responsible for the resonance line that are present in the wind. Consequently, the general strategy for extracting information from the P Cygni profiles of UV resonance lines is to use the integrated line strength from *unsaturated* profiles to constrain the left-hand side of (1), and to rely on the velocity law (which is best determined from strong or saturated lines) for information concerning the radial distribution of the material. The line strength and shape of the velocity law are determined by fitting synthetic profiles computed from parameterized models of the stellar wind to observed line profiles.

Consider the resonance line of ion j of the element with atomic number k . Let the mass of a particle of element k be m_k and its abundance by weight be X_k ; then, if $n_{jk}(r)$ and $n_k(r)$ represent the number densities of the ion and its parent element, respectively, it follows that

$$n_{jk}(r) = \frac{n_{jk}(r)}{n_k(r)} n_k(r) = q_{jk}(r) \frac{X_k}{m_k} \rho(r) = \frac{\dot{M}}{4\pi} \frac{X_k}{m_k} \frac{q_{jk}(r)}{v(r) r^2}, \quad (11)$$

where $q_{jk}(r) \equiv n_{jk}(r)/n_k(r)$ is the fraction of element k that exists in the ground state of ion j , and where the expression for ρ from (1) has been substituted. We have previously argued that the degree of excitation will be low for ions in a rarefied medium, so that to a good approximation all of the ions k will be in their ground state, which implies that the local Sobolev optical depth in the radial direction given by (10) can be simplified:

$$\tau_{uv}(v(r)) = \left(\frac{\pi e^2}{m_e c} \right) f_{lu} \lambda_0 n_{jk} \left(\frac{dv}{dr} \right)^{-1}. \quad (12)$$

The usual approach is to parameterize $\tau_{uv}(v)$ as the product of the integrated optical depth (for ion j of element k), \mathcal{T}_{jk} , and a normalized function of velocity, $\mathcal{F}(v; \alpha)$ that is defined by adjustable parameters $\alpha = (\alpha_1, \alpha_2, \dots)$, so that

$$\tau_{uv}(v) = \mathcal{T}_{jk} \mathcal{F}(v; \alpha). \quad (13)$$

Larners et al. (1987) discuss the motivation for some of the more popular functional forms of $\mathcal{F}(v; \alpha)$. It is not strictly necessary to assume a functional form for the radial distribution of optical depth, since the absorption trough of unsaturated P Cygni profiles contains sufficient information to determine this empirically (see, e.g., Haser 1995 or Haser et al. 1995 for an alternate,

and probably preferable, approach). Nevertheless, with this ansatz, the direct integration of (12) can proceed in terms of known parameters:

$$\begin{aligned}
 \int_{v_0}^{v_\infty} \tau_{uv} \, dv &= \int_{v_0}^{v_\infty} \mathcal{T}_{jk} \mathcal{F}(v; \alpha) \, dv \\
 &= \mathcal{T}_{jk} \\
 &= \left(\frac{\pi e^2}{m_e c} \right) f_{lu} \lambda_0 \int_{R_*}^{\infty} n_{jk} \, dr \\
 &= \left(\frac{\pi e^2}{m_e c} \right) f_{lu} \lambda_0 \mathcal{N}_{jk} \, ,
 \end{aligned} \tag{14}$$

where \mathcal{N}_{jk} is the column density of ion j of element k between the surface of the star and the observer. The parameters α and \mathcal{T}_{jk} are determined from the fit to the profile, and hence \mathcal{N}_{jk} is also known.

However, in order to fit the profile, the velocity law that describes the distribution of velocity as a function of radius must also be determined. The key parameter (which is traditionally called “ β ”) defines the steepness of the spatial velocity gradient associated with the expansion. There are several versions of the “beta-velocity law” that are distinguished by their treatment of the velocity field near the photosphere, but the conventional form is

$$v(r; v_0, \beta) = v_0 + (v_\infty - v_0) \left(1 - \frac{R_*}{r} \right)^\beta \, , \tag{15}$$

where v_0 is the outflow velocity deep in the wind⁴. Fig. 5 shows the shape of the beta-velocity law for several values of β , and emphasizes that small values of β signify steeper (“faster”) gradients. This functional form reflects the necessity of lifting the material out of the gravitational potential well of the star, though the exact value of β depends on details of the mechanism responsible for driving the wind; see, e.g., the lectures by Lamers (second contribution to this Volume) on the theory of line-driven stellar winds. The theory of radiatively driven stellar winds predicts that β should be near 0.8 for O-type stars (Pauldrach et al. 1986).

For a spherically symmetric wind that is smooth and steady, we have already seen that the position of the blue edge of the absorption trough of a strong P Cygni profile is a diagnostic of v_∞ . The emission lobe of P Cygni profiles provides information about β ; see, e.g., Fig. 6, which shows that both the shape and strength of the emission lobe are sensitive to the velocity gradient for the case of a strong line. Physically, this sensitivity arises from the inverse proportionality between density and velocity implied by (1): for

⁴ Formally, v_0 is the wind velocity at $r = R_*$, though it is preferable to think of it as the velocity at the sonic point (i.e., the sonic velocity for the ion) since this is where deviations from the hydrostatic density stratification start to become significant.

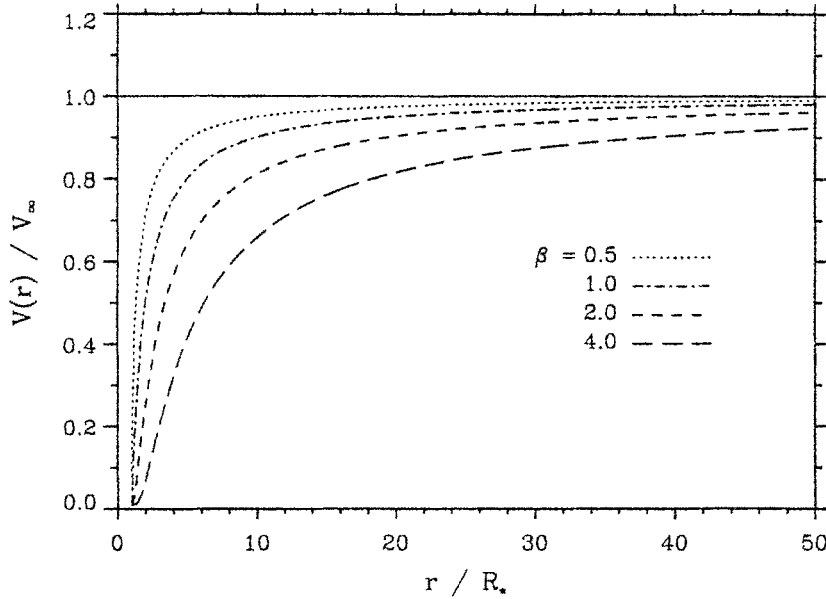


Fig. 5. The beta-velocity law given by (15) as a function of radius for $v_0 = 0.01 v_\infty$ and several values of β

a fixed \dot{M} , a “slower” velocity law (larger β) results in higher densities of material at small radii, which enhances the number of photons scattered towards the observer at small values of V_{Los} , all other things being equal. Weaker lines also respond in a similar way to changes in β , but in practice the parameters associated with the velocity field are more difficult to disentangle from the other factors (e.g., $q_{jk}(r)$, \mathcal{T}_{jk}) that affect their shapes. Thus, the main parameters associated with the velocity field of the wind, v_∞ and β , can both be determined from the P Cygni profiles of strong UV resonance lines.

Suppose that we have used our favourite computer program to achieve an acceptable fit of the P Cygni profile of an unsaturated UV resonance line. In order to do this, we have had to overcome the usual sort of practical problems, like rectifying the observed data (which can be difficult in the UV due to heavy line blanketing) and allowing for the underlying photospheric line (either by using an observed, purely photospheric template spectrum or by computing the profile in some way). At the end of this process, we’ve determined:

- the parameters v_0 , v_∞ , and β that define the velocity law.
- the total optical depth of the resonance transition, \mathcal{T}_{jk} , and hence its column depth, \mathcal{N}_{jk} , via (14).

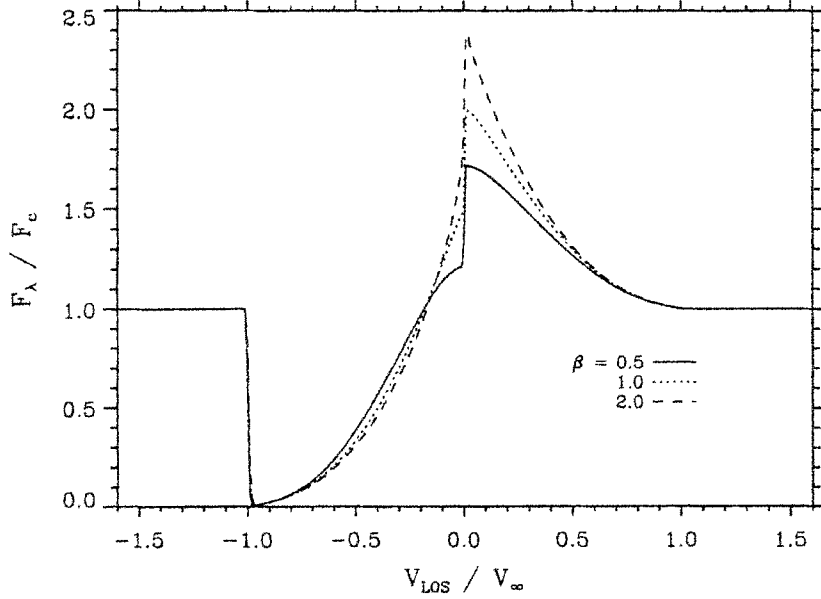


Fig. 6. P Cygni profiles of a strong resonance singlet line calculated for several values of the velocity-law parameter β . More emission results from “slower” velocity laws

- the parameters α describing the distribution of optical depth as a function of velocity (or radius).

How close does this information get us to \dot{M} ? The column depth can also be determined by direct integration of (11), which, after some rearranging becomes

$$\dot{M} \int_{R_*}^{\infty} \frac{q_{jk}(r)}{r^2 v(r)} dr = 4\pi \frac{m_k}{X_k} \int_{R_*}^{\infty} n_{jk}(r) dr = 4\pi \frac{m_k}{X_k} \mathcal{N}_{jk} . \quad (16)$$

Following Howarth and Prinja (1989), the mean value of $q_{jk}(r)$ can in addition be defined by

$$\bar{q}_{jk} \equiv \frac{\int_{R_*}^{\infty} q_{jk}(r) / [r^2 v(r)] dr}{\int_{R_*}^{\infty} 1 / [r^2 v(r)] dr} = \frac{\int_{R_*}^{\infty} q_{jk}(r) / [r^2 v(r)] dr}{\mathcal{I}(v_0, v_{\infty}, \beta)} , \quad (17)$$

and so

$$\dot{M} \bar{q}_{jk} = 4\pi \frac{m_k}{X_k} \frac{\mathcal{N}_{jk}}{\mathcal{I}(v_0, v_{\infty}, \beta)} . \quad (18)$$

Everything on the right-hand side has been measured or is otherwise known, with the possible exception of X_k , which has to be determined from photospheric analysis of the star or simply assumed.

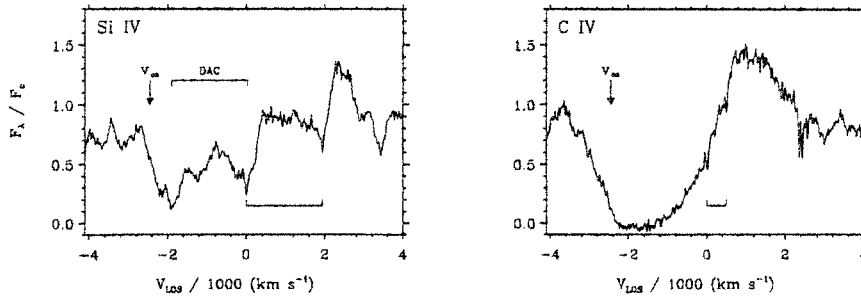


Fig. 7. An IUE spectrum of ξ Per (SWP 34559) showing the P Cygni profiles of two UV resonance lines. Left: the unsaturated Si IV doublet, with a soft blue edge and DACs in the absorption trough. Right: the saturated C IV doublet, with a soft blue edge and an extended black trough. The rest positions of the blue and red components of the doublets are marked; the velocity scale refers to the blue component

However, we ultimately fail to determine \dot{M} because we don't know \bar{q}_{jk} : it is simply not possible to measure the ionization fraction of an element on the basis of a single line. Usually, the ionization balance can be constrained by examining the strength of lines from the adjacent stages. Unfortunately, the resonance lines of stages adjacent to those responsible for the observed P Cygni profiles usually fall in the extreme UV region of the spectrum, where the flux of early-type stars is small owing to absorption in the Lyman continuum of interstellar hydrogen. To make matters worse, theoretical predictions are not especially helpful: if the prediction is that the ion is the dominant stage, then the P Cygni profile is invariably saturated, and only provides a lower limit on \mathcal{N}_{jk} . Alternately, if the ion is a trace stage, theoretically predicted values of its q_{jk} are uncertain since they depend sensitively on the details of the calculation (e.g., inclusion of X-rays from shocks, inclusion of line blanketing in the extreme UV region of the spectrum; see Pauldrach et al. 1994) that are not yet considered to be completely reliable (Groenewegen and Lamers 1991). The only option at present is to try to estimate \bar{q}_{jk} by comparing the values of $\dot{M}\bar{q}_{jk}$ obtained from UV resonance lines with mass-loss rates determined from other diagnostics that are not sensitive to ionization (e.g., radio continuum measurements; see Howarth and Prinja 1989). So, for the moment, we are left in the unsatisfying situation that the best qualitative tracers of the diffuse gas in stellar winds are not the best estimators of the mass-loss rate.

To compound these difficulties, there are also complications with the determination of the velocity law from the P Cygni profiles of UV resonance lines. The problem is that the blue edges of the absorption trough of strong lines are rarely observed to be as steep and well defined as illustrated in

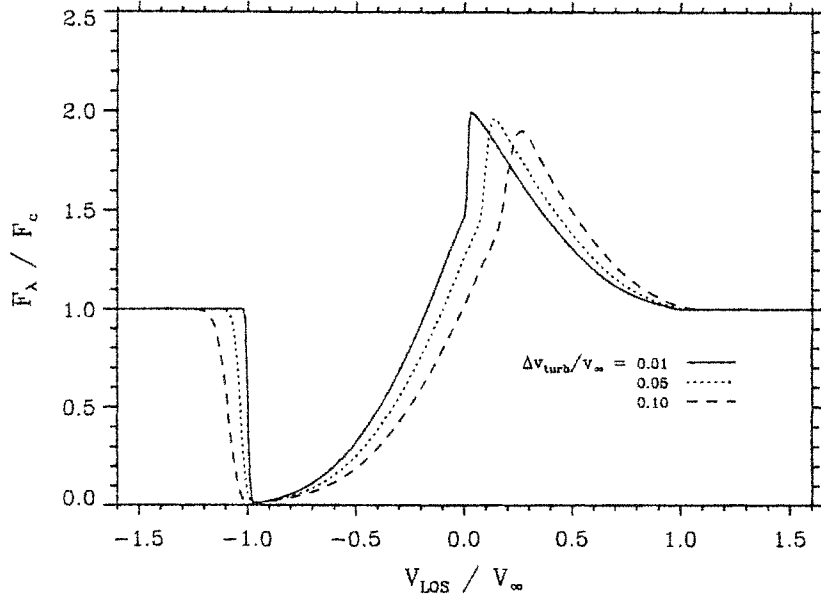


Fig. 8. P Cygni profiles of a strong resonance singlet line calculated for several values of the velocity dispersion parameter Δv_{turb} . These calculations assume that the dispersion is constant throughout the wind, and show that increasing the size of Δv_{turb} softens the blue edge, extends the region of saturation in the absorption trough, and shifts the emission peak redward

Figs. 4 and 5, but approach the continuum more gradually. Consequently, the interpretation of the position of the blue edge as a “clear-cut” diagnostic of v_{∞} is compromised. This deviation from the classical P Cygni shape is illustrated in Fig. 7 for the Si IV and C IV resonance doublets of the O7.5 giant ξ Persei; see also the C IV profile of 9 Sge in the top panel of Fig. 1.

The “softening” of the blue edge of the absorption trough is generally interpreted as an indicator that another, more chaotic velocity field is superimposed upon the mean expansion of the wind (Sect. 3.6). This extra velocity field is usually referred to as “turbulence”, though it is preferable to think of it as a velocity dispersion that acts as an extra broadening agent for the material in the wind rather than turbulence in a strict hydrodynamical sense. Purely for convenience, it is assumed to have a Gaussian distribution that is characterized by its root-mean-square dispersion parameter, Δv_{turb} , which can be added in quadrature to the v_{th} to produce a net broadening that does not require substantial changes to the SEI approach to calculating line profiles. The dispersion parameter Δv_{turb} may be taken to be constant throughout the wind (as in Groenewegen and Lamers 1989) or as an increas-

ing function of radius (as in Haser 1995 or Haser et al. 1995; this tends to suppress the redshift of the emission lobe, which is overestimated for some of the fits presented by Groenewegen and Lamers 1989). Figure 8 illustrates the effect of a constant broadening on the P Cygni profile of a strong singlet, and shows in particular the “softening” of the blue edge of the absorption trough by the extra broadening, which shifts the maximum blue-shifted velocity in the absorption trough to $v_\infty + n \Delta v_{\text{turb}}$ (where $n \lesssim 3$ depends on the total optical depth of the line). Thus, in practice, v_∞ is *overestimated* if it is assumed to correspond to the blue edge of the trough. Since the determination of β depends on the shape of the emission lobe, it will also be affected by the inclusion of turbulent broadening. In practice, this complication just means that Δv_{turb} must also be determined simultaneously with v_∞ and β by a detailed fit to the observed profile.

However, Fig. 7 also shows that there are several additional peculiarities associated with the UV P Cygni profiles of ξ Per. First, the absorption trough of the strong C IV doublet exhibits an extended interval of blackness (a “black trough”), something that we previously noted is impossible for a smooth wind. Second, the absorption trough of the unsaturated Si IV line is disrupted by the presence of narrow optical depth enhancements, which are called “discrete absorption components” (DACs). These three peculiarities – a soft blue edge, black troughs, and DACs – occur very commonly among OB stars; as discussed in Sect. 3.6, they are all evidence for the presence of time-dependent structure in the stellar wind of most or all early-type stars. As such, they tend to undermine the picture of the stellar wind as a smooth, spherically symmetric, steady outflow that currently serves as the basis for quantitative modelling.

3.5 Optical Emission Lines

The main diagnostics of hot-star winds at optical wavelengths are the broad emission features that are found in transitions of H, He I, and He II. $H\alpha$ is typically the strongest of these features, though lines like He I $\lambda 5876$ and He II $\lambda 4686$ are also important, particularly in spectra of O-type supergiants. A wide range of morphologies can be observed in these profiles (see Fig. 1), including partially filled photospheric absorption lines in the case of weak winds. The information about the structure of the stellar wind contained in them is comparable to the information contained in UV resonance lines: for a spherically symmetric wind, the overall strength of the emission indicates the amount of material, while the shape of the line profile depends on how the material is distributed.

However, there are also significant differences compared to resonance lines. From a practical point of view, the ρ^2 dependence of recombination lines means that they are not sensitive diagnostics of rarefied gas. Consequently, they are not well suited to determining v_∞ , and in practice this parameter

must be obtained from UV resonance lines. At the same time, their comparative weakness is partially offset by the relative ease with which high resolution, high signal-to-noise ratio (S/N) spectroscopic observations can be obtained from ground-based observatories. Since the shape of the line profile can be defined quite precisely from such high-quality data, very weak, high velocity emission wings can be used to determine M , providing that emission above the continuum is present. Similarly, the height and width of the central part of the line profile can be used to constrain the β -exponent of the velocity law, since slower velocity laws produce stronger and narrower central emission peaks. Although ground-based observations of $H\alpha$ (and $\text{He I } \lambda 5876$) are frequently contaminated by blending with dense concentrations of telluric lines (mostly due to water vapour) and sometimes by nebular emission, effective techniques exist to remove these features from the observed spectrum or otherwise limit their impact on the quantitative analysis of the spectra.

Unfortunately, the optical emission lines are a much more complicated case to analyze quantitatively. On the positive side, we know from the outset that H and He are completely ionized until spectral types near A (for H) or early B (for He), so that the main stumbling block encountered for resonance lines is entirely avoided for optical emission features. However, on the negative side (and in contrast to the resonance lines), the excitation balance governing the transition of interest is not known a priori, and detailed non-LTE calculations of the statistical equilibrium in the accelerating atmosphere are required to determine the relevant level populations. The non-LTE population of level i in ion j of element k , n_{ijk} , is often expressed in terms of its LTE value, n_{ijk}^* , and its "departure coefficient", $b_{ijk} \equiv n_{ijk}/n_{ijk}^*$, so that

$$n_{ijk} = b_{ijk} n_{ijk}^* = b_{ijk} n_{0(j+1)k} n_e \Phi_{ijk}(T_e) \quad , \quad (19)$$

where $n_{0(j+1)k}$ and n_e are the number densities of the ground state of the next higher ionization stage and electrons, respectively, and $\Phi_{ijk}(T_e)$ is the Saha-Boltzmann factor defined by Mihalas (1978; equation 5-14), which depends on the electron temperature (T_e) and the difference in energy between state i and the continuum of ion j . Analogous expressions for the populations of the lower and upper levels of a line transition can be substituted into (10) to obtain the Sobolev optical depth in the supersonic part of the wind. For the important case of $H\alpha$, $(l, u) = (2, 3)$ and we obtain

$$\begin{aligned} \tau_{23}(r) &= \left(\frac{\pi e^2}{m_e c} \right) f_{23} g_2 \lambda_{23} \left(\frac{n_2}{g_2} - \frac{n_3}{g_3} \right) \left(\frac{dv}{dr} \right)^{-1} \\ &\propto n_H n_e [b_2 \Phi_2(T_e) - b_3 \Phi_3(T_e)] \left(\frac{dv}{dr} \right)^{-1} \\ &\propto \left(\frac{\rho}{m_H} \right)^2 \left(\frac{4X^2 + I_{\text{He}}XY}{4} \right) [b_2 \Phi_2(T_e) - b_3 \Phi_3(T_e)] \left(\frac{dv}{dr} \right)^{-1} \quad (20) \end{aligned}$$

where the subscripts $j = 0$ and $k = 1$ have been suppressed; we have noted that n_{011} is the number density of protons in the wind, which in turn is given

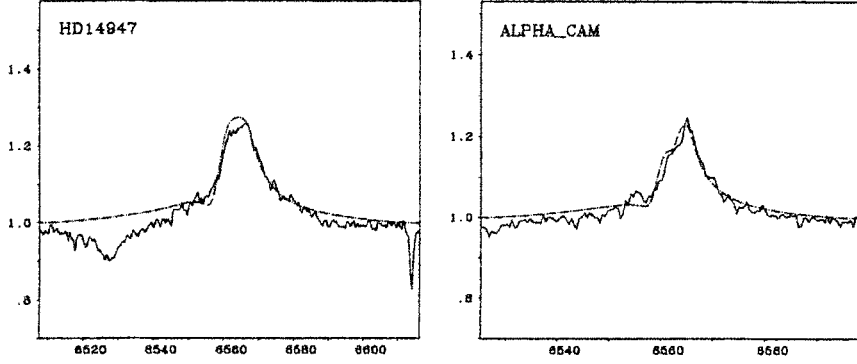


Fig. 9. Fits to observed $H\alpha$ profiles by Puls et al. (1996). Left: HD 14947 (O5 If⁺; $\dot{M} = 7.5 \times 10^{-6} M_{\odot} \text{ yr}^{-1}$; $\beta = 1.0$). Right: α Cam (O9.5 Ia; $\dot{M} = 5.2 \times 10^{-6} M_{\odot} \text{ yr}^{-1}$; $\beta = 1.1$)

by the number density of hydrogen, n_{H} ; and we have made the approximation $n_e \approx n_{\text{H}} + I_{\text{He}} n_{\text{He}} = (\rho/m_{\text{H}})(X + I_{\text{He}}Y/4)$, where $(X, Y) \equiv (X_1, X_2)$ are the abundances of hydrogen and helium by mass fraction, and I_{He} is the number of electrons released per helium ion ($I_{\text{He}} = 2$ for O and early B-type stars). Equation (20) emphasizes the ρ^2 dependence of the optical depth in $H\alpha$, and shows the explicit dependence of recombination processes on T_e through the Saha-Boltzmann functions.

The observed profile of an optical emission line typically includes significant contributions from the quasi-static photospheric layers, the zone that spans the sonic point of the wind, and the supersonic region of the wind, and the necessity of calculating non-LTE departure coefficients over such a large line-forming region represents an imposing computational challenge. In particular, the Sobolev approximation is not applicable in the deepest of these layers, where the velocity gradient of the expansion is small; and the artifice of dividing the line formation regions into a hydrostatic photosphere and a supersonically expanding wind (the “core-halo” approach) does not treat the density and velocity structure of the transition zone properly. Moreover, radiative couplings with other bound-bound transitions (e.g., the blending of He II $\lambda 6560$ with $H\alpha$) or the complex effects of line blocking in the far UV (in the case of He II $\lambda 4686$) must also be incorporated. Puls et al. (1996) provide a comprehensive discussion of all these problems, with special emphasis on the formation of $H\alpha$ profiles in the winds of early-type stars.

These complications can be treated rigorously only in the framework of “unified model atmospheres”, which perform complete non-LTE treatments

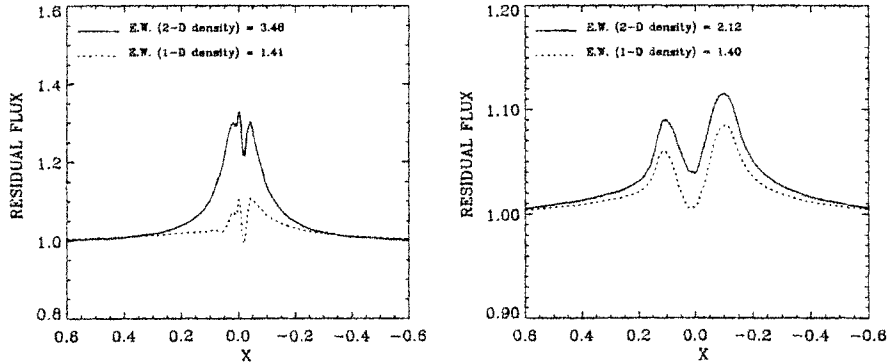


Fig. 10. $H\alpha$ profile strength and morphology as a function of inclination angle for 1D (dotted) and 2D (solid) density distributions, a fixed $\dot{M} = 6 \times 10^{-6} M_{\odot} \text{ yr}^{-1}$, and $v_{\text{rot}} = 250 \text{ km s}^{-1}$. Left: $i = 0^{\circ}$. Right: $i = 90^{\circ}$. The abscissa is $V_{\text{Los}}/v_{\infty}$ in the reference frame centered on the star (opposite to previous figures); note the difference in ordinate scales. In both cases, the 2D distributions produce more emission from the same amount of wind material; the difference is particularly dramatic for the “pole-on” orientation. See Petrenz and Puls (1996) for details

of moving atmospheres without introducing artificial distinctions between the photosphere and the wind (Gabler et al. 1989). Although the initial calculations of such models were quite cumbersome, more efficient algorithms (that still use a variety of approximations) have been developed in the past few years, and several programs are now capable of performing interactive (or nearly interactive) modelling of optical emission lines: see, e.g., de Koter et al. (1993), Schaerer and Schmutz (1994), and Santolaya-Rey et al. (1997). Alternately, Puls et al. (1996) describe a very efficient hybrid approach that can be used to model line profiles of a particular wind feature for objects that span a limited range of spectral types by using parameterized fits to the radial distribution of the relevant departure coefficients, which are obtained from a grid of unified model atmospheres. Puls et al. (1996) applied this approach to the determination of \dot{M} from $H\alpha$ profiles of a large sample of O stars, for which the other fundamental stellar parameters (T_{eff} , $\log g$, R_{\star} , Y , $v \sin i$, and v_{∞}) had previously been determined by the methods of “quantitative spectroscopy”. Figure 9 shows that very good fits to observed spectra can be obtained, which result in precise determinations of \dot{M} and β .

However, the *accuracy* of these determinations depends rather strongly on the correctness of the assumptions of spherical symmetry and homogeneity, i.e., on whether the assumed distribution of material in the wind is a good approximation for the real distribution. Consider, e.g., two equal volumes of a uniform, spherically symmetric wind that are located at the same radial distance from the star. Let the density in one volume be half the density in

a corresponding volume of a uniform wind (i.e., $\Delta m_1 = 0.5 \rho_0 \Delta V$, where ρ_0 is the density of the smooth wind) and the density in the other be 50% more ($\Delta m_2 = 1.5 \rho_0 \Delta V$). The total mass in these two “clumps” is the same as in the corresponding volumes of the smooth wind, but since the number of recombinations scales with ρ^2 , the emission that arises from them is proportional to $(0.5^2 + 1.5^2) \rho_0^2 = 2.5 \rho_0^2$, which is 1.25 times that from the smooth wind. If we attempted to model the emission from the “clumped” volumes by assuming a smooth density distribution, we would mistakenly attribute this “excess” emission to a higher density. In this case, we would overestimate the amount of material they contain by $\sim 12\%$.

Similarly, the mass-loss rates of winds that are structured or aspherical will be *systematically overestimated* if their optical emission lines are interpreted in terms of a density distribution that is smooth and spherically symmetric. Both these complications are expected to occur in the winds of early-type stars: clumping because the line-driving mechanism is unstable (see, e.g., Owocki 1990), and asphericity because sufficiently rapid rotation concentrates the material of the wind towards a preferred plane (e.g., the equatorial plane in the “wind-compressed disk” [WCD] or “wind-compressed zone” [WCZ] model discussed by Bjorkman in his lectures (this Volume). Figure 10 compares the H α line profiles computed from a smooth, 1D density distribution with those from the 2D density distribution appropriate to a WCZ. The total amount of material in the wind is the same in both cases, but is concentrated towards the equatorial plane in the WCZ models, with the result that more emission is produced by the 2D models. The two panels of Fig. 10 also show that there is a further dependence on the angle at which the WCZ is viewed, with much stronger emission occurring when the star is seen “pole on” ($i = 0^\circ$) because the area the equatorial concentration presents to the observer is maximized in this configuration.

Petrenz and Puls (1996) have considered the impact that aspherical density distributions have on the determination of stellar wind parameters by fitting synthetic profiles computed from 1D (spherically symmetric) wind models and 2D (WCZ) models to observed H α profiles. Figure 11 shows that both models provide fits of comparable quality to the H α profile of O4 supergiant ζ Puppis, which is a rapid rotator ($v \sin i = 210 \text{ km s}^{-1}$) for its luminosity class. However, the wind parameters inferred from the fits are substantially different: the 1D model gives $(\dot{M}, \beta) = (5.9 \times 10^{-6} \text{ M}_\odot \text{ yr}^{-1}, 1.15)$, while the 2D model gives $(\dot{M}, \beta) = (3.4 \times 10^{-6} \text{ M}_\odot \text{ yr}^{-1}, 2.00)$ and an inclination of 53 degrees. Thus, in this case, the assumption of spherical symmetry implies that \dot{M} is overestimated by $\sim 70\%$, and that the velocity law is faster than the values obtained from 2D models. Since early-type stars tend to be rapid rotators, WCZs are expected to occur commonly (Bjorkman and Cassinelli 1993; Ignace et al. 1996): failure to account for them (or other structures) when modelling recombination lines will result in mass-loss determinations that are systematically overestimated.

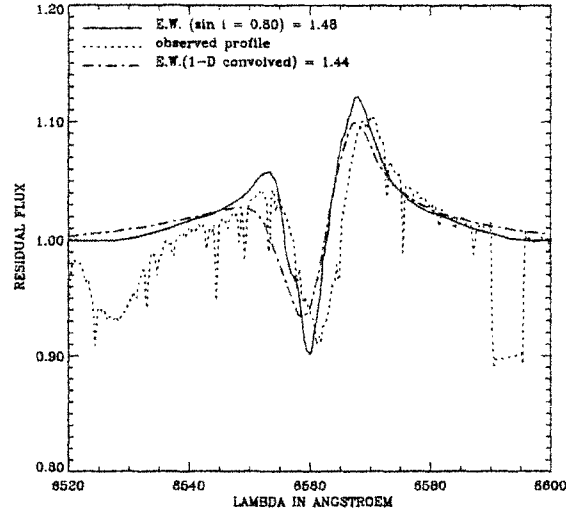


Fig. 11. Fits of 1D (dot-dash) and 2D (solid) density distributions to the $H\alpha$ profile of the O4 supergiant ζ Puppis (dotted). Figure courtesy of P. Petrenz

3.6 Time-Dependent Structure in Hot-Star Winds

In Sect. 3.4, we noted three common peculiarities in the absorption troughs of the P Cygni profiles of the UV resonance lines: soft blue edges, extended regions of blackness, and DACs. Although these deviations from the expected morphology are present in some of the earliest observations from the Copernicus satellite observatory (e.g., Morton 1976), they did not initially attract much attention. Lamers et al. (1982) noticed that DACs occurred quite commonly in “snapshot” observations of a sample of OB stars obtained with Copernicus, a result that was soon confirmed with the International Ultraviolet Explorer (IUE) satellite observatory (Prinja and Howarth 1986). However, it was not until IUE began to provide routine monitoring capability that the DACs were recognized to be fundamentally a time-dependent phenomenon. Subsequent work has shown that the shape and strength of the blue edge of the absorption trough are also variable.

The characteristic behaviour of DACs is illustrated in Fig. 12, which shows a series of 24 spectra of the Si IV resonance doublet of ξ Per obtained with IUE by H. F. Henrichs and collaborators over ~ 2.6 days in 1988 October. The spectra are presented in the form of a grey-scale image where darker shades represent less flux (excess absorption) and lighter shades represent more flux with respect to the mean spectrum, which is plotted below the image. This format, which is often called a “dynamic spectrum” (a term borrowed from radio astronomers who monitor pulsars), is an ideal way to show the progressive evolution of weak features through a large number of spectra. A given

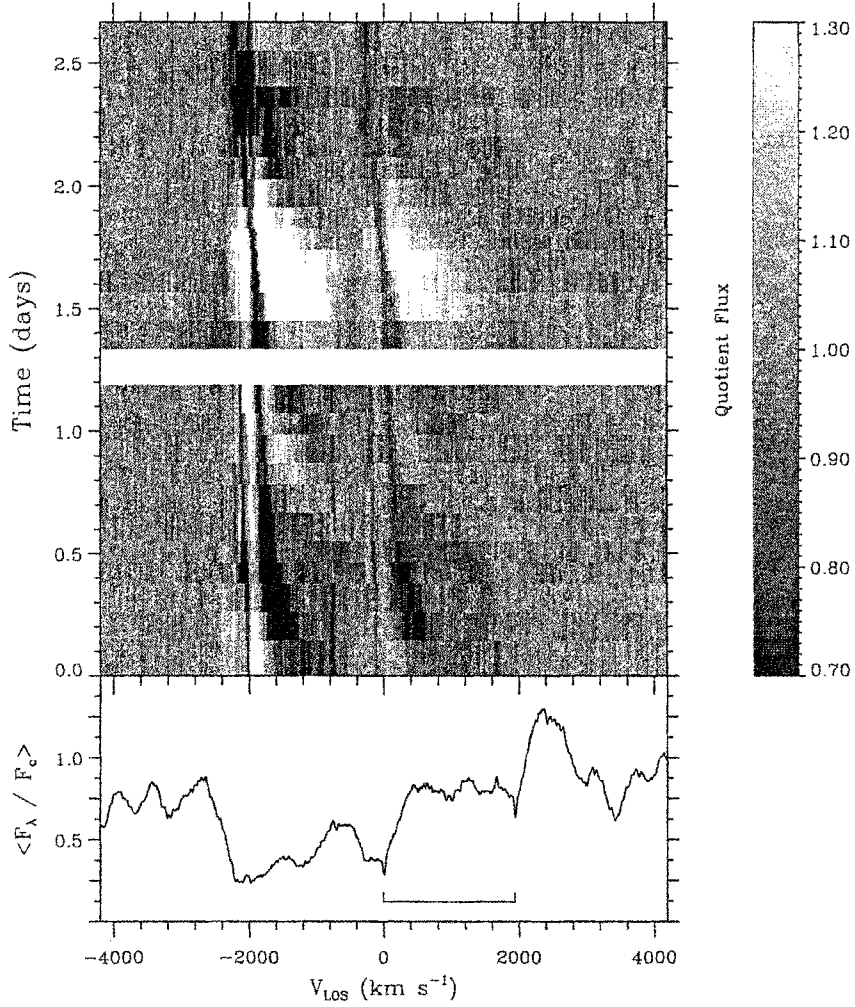


Fig. 12. Dynamic spectrum of the Si IV resonance doublet of ξ Per showing the blueward acceleration of two DACs. Individual spectra in the time series have been divided by the mean in order to enhance the contrast of the variations. The rest positions of the components of the doublet are indicated; the behaviour of the DACs is the same in both components. The white strip near the middle of the time series denotes a significant gap in the time sampling

DAC first becomes visible in both components of the doublet as a broad optical depth enhancement at an intermediate velocity, but is not accompanied by significant variations in the emission lobe. It accelerates blueward through the trough and becomes narrower as it reaches its asymptotic velocity, which is approximately equal to v_∞ . The time scale for the acceleration is ~ 1 day in the case of ξ Per, which is quite slow compared with the characteristic flow time of its wind: $t_{\text{flow}} \gtrsim R_*/v_\infty \approx 1$ hour. For ξ Per, the recurrence time between the appearance of strong DACs is ~ 2 days; in the time series illustrated in Fig. 12, a weaker component may be present in between the stronger ones.

Although ξ Per is one of the most intensively studied objects (Prinja et al. 1987; Henrichs et al. 1994), its behaviour is certainly not unique. Howarth and Prinja (1989) reported the detection of DACs in 80% of the objects in their thorough study of the IUE “snapshot” spectra of 203 O stars; detailed monitoring of a subset of these objects has subsequently shown behavioural patterns that are qualitatively similar to the DACs of ξ Per (Kaper et al. 1996). DACs have also been tracked in the UV spectra of B-type supergiants (e.g., Massa et al. 1995b), a WR star (Prinja and Smith 1992), and optical P Cygni profiles of O supergiants (e.g., Fullerton et al. 1992; Prinja and Fullerton 1994) and B hypergiants (Rivinius et al. 1997).

The widespread occurrence of DACs implies that at least one of the assumptions of the “standard model” of hot-star winds – stationarity – is not valid. From (11) and (12), we see that a DAC could be produced at a particular position in the absorption trough by enhancing τ_{UV} in one of three ways:

- locally *increasing* the ionization fraction, $q_{jk}(r)$.
- locally *increasing* the density, $\rho(r)$, either as a spherically symmetric shell or as a “clump” of arbitrary shape.
- *decreasing* the velocity gradient (dv/dr) over some range of radii, thereby producing a “plateau” in the radial velocity law.

When DACs can be observed in unsaturated lines with very different ionization energies (e.g., Si IV and N V), they usually occur at the same velocity and evolve in the same way; consequently, changes in the ionization fraction are generally not thought to be responsible for the absorption excess (but see Prinja et al. 1997 for an important exception). Since variations in the emission lobe are rarely observed, dense shells are more or less ruled out, though big clumps that cover most of the stellar disk do seem to be required to explain the depth of some DACs (and possibly also the [presumably related] phenomenon of “moving bumps” in the emission lines of WR stars; see Moffat et al. 1988). In any case, each of these methods of producing a DAC implies that there is some extra “structure” in the wind, and consequently the validity of the remaining assumptions of the “standard model” (homogeneity and spherical symmetry) are also dubious. A crucial issue is to assess

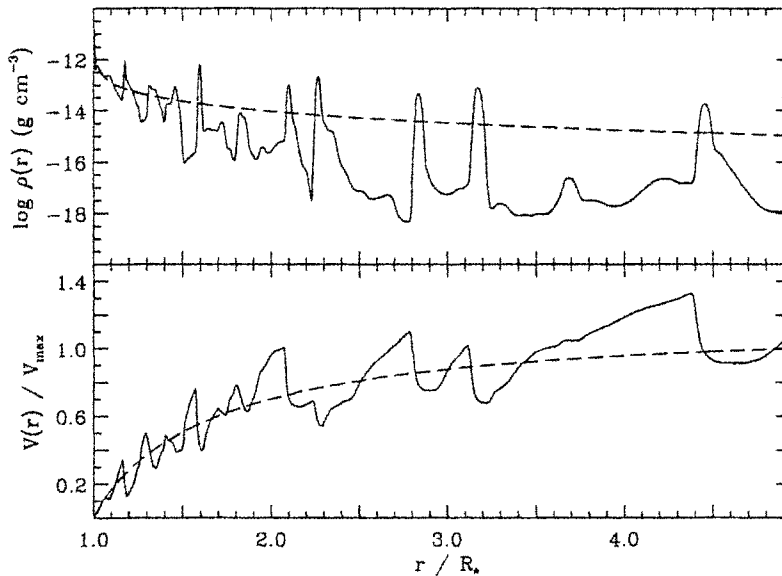


Fig. 13. The density and velocity distributions obtained from time-dependent simulations of a hot-star wind that is disrupted by the line-driven instability. The dashed line indicates the distribution of density and velocity from a comparable stationary model. From Puls et al. (1993)

the impact that these time-dependent wind structures have on the determination of mass-loss rates, which first requires that the origin and nature of the wind structures be clarified.

Much of this structure is believed to be the result of a potent instability that is intrinsic to the line-driving mechanism; i.e., the winds of early-type stars are variable by virtue of the way they accelerated. The origin of this instability is described in very clear, graphical fashion by Owocki (1992). Although this instability has been recognized for a long time (e.g., Lucy and Solomon 1970; MacGregor et al. 1979; Carlberg 1980; Owocki and Rybicki 1984), it has only recently become possible to study its impact on the structure of a stellar wind by following its nonlinear growth in radiation hydrodynamics simulations (Owocki et al. 1988, Feldmeier 1995). These computations are technically very challenging, because the line-driven instability grows most strongly on small spatial scales, and consequently the Sobolev approximation cannot be used to simplify the radiative transfer. The current generation of simulations are limited to one spatial dimension, which means that the structures that result from them consist of spherically symmetric shells.

Figure 13 shows a typical “snapshot” of $v(r)$ and $\rho(r)$ in a model of a hot-star wind at a time approximately 15 hours after basal perturbations in the form of a coherent photospheric sound wave were introduced. The deep-seated perturbations are amplified by the instability, which results in small amounts of gas being driven to very high velocities. This high-velocity, rarefied gas ultimately crashes into the more slowly moving material in front of it (i.e., at larger radii), and the resulting compression concentrates the wind into a series of dense clumps (i.e., shells in these 1D simulations). Thus, instead of the smooth, monotonic distributions expected from the stationary model, the material of the wind is inhomogeneously redistributed into a series of dense shells that are separated by regions where there is very little gas. The velocity of the rarefied gas can exceed v_∞ , while the dense shells move at about the speed of the gas at the same radii in an unstructured wind.

The nonmonotonic density and velocity distributions in Fig. 13 introduce some interesting complications to the picture of line formation that was outlined in Sect. 3.2 and 3.3. Since the velocity law is no longer a smoothly increasing function of radius, a photon will not necessarily be free to travel unimpeded through the wind after it works its way through the first scattering zone (as was the case, e.g., in the discussion of Fig. 4). Instead, it might encounter other clumps of material, possibly at very different positions in the wind but nonetheless moving with velocities “tuned” to the resonance line transition, which therefore permits further scattering interactions to occur. The possibility for multiple interactions can be easily seen from Fig. 13, since a horizontal line at a fixed velocity (which represents a fixed photon frequency in the observer’s frame) intersects the computed velocity distribution at several widely separated radii: e.g., a line at $v(r)/v_{\max}$ (where $v_{\max} \equiv v_\infty$) of 0.8 intersects the velocity law at values of r/R_\star near 2, 2.5, 3.0, and 3.4, instead of the single value (~ 2.3) in the case of a smooth, monotonically expanding wind.

As Lucy (1982) first realized, the net effect of these multiple interactions is to increase the amount of back-scattering. Consider again a horizontal line drawn across the velocity distribution in Fig. 13, and suppose for simplicity that scatterings only occur in the radial direction (i.e., $\cos\psi = \pm 1$ in the notation of Fig. 4). Further suppose that at each scattering surface there is roughly a 50% chance that a photon will be forward-scattered and a 50% chance that it will be back-scattered. Consequently, after n such scatterings, the fraction of the original beam of continuum photons that is still travelling in the forward direction is $(0.5)^n$, while the remainder have been back-scattered towards the star. In fact, the situation is a bit more complicated, because photons that are back-scattered at scattering surface i can be back-scattered another time when they encounter scattering surface $i - 1$ on their inward journey, and so rejoin the outward propagating beam. Nevertheless, the basic point is that essentially all the outward propagating photons will end up being back-scattered towards the star if there are a sufficiently large number of interaction surfaces.

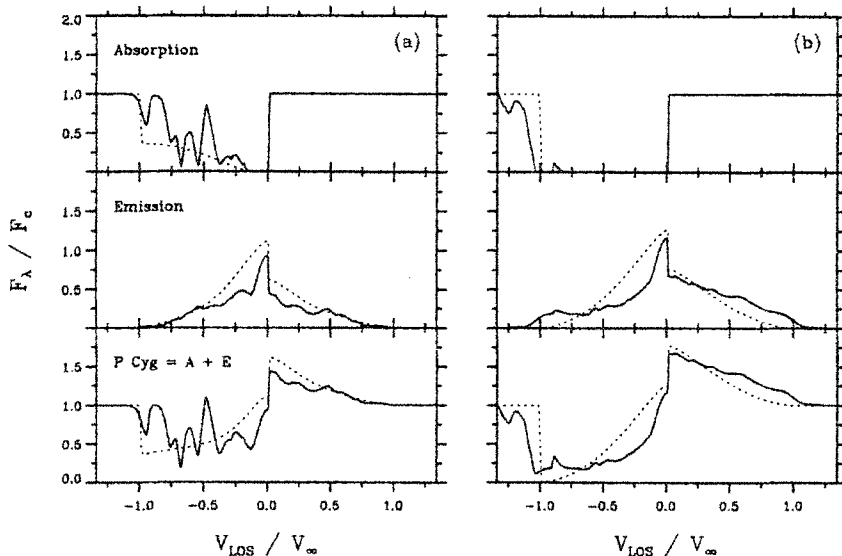


Fig. 14. P Cygni profiles of UV resonance singlets from the structured stellar wind model illustrated in Fig. 13, computed for the case of (a) a moderately strong line and (b) a strong line. The dashed lines indicate the various components of the profiles for the case of the smooth wind illustrated in Fig. 3. DACs are visible in the absorption trough of (a); the soft blue edge extending beyond v_∞ is clearly seen in (b). Changes in the shape of the blue- and red-shifted emission due to increased back-scattering from the multiple interactions in the nonmonotonic velocity law are also evident

The effects of these multiple and nonlocal interactions can be incorporated into the Sobolev formalism in a straightforward way; see, e.g., Rybicki and Hummer (1978) and Puls et al. (1993). Figure 14 illustrates the changes in the structure of the absorption and emission components of the P Cygni profiles of resonance singlets that result from the nonmonotonic (but spherically symmetric) distributions shown in Fig. 13. The clumpy distribution of material is directly visible in the absorption component of an unsaturated line, which shows both excesses and deficits of optical depth (with respect to the absorption trough of a comparable smooth wind) that are due to the dense clumps and the rarefied regions, respectively. Since all the photons are removed from the absorption trough of an intrinsically strong line, these clumpy structures are not visible in its absorption component. However, for a strong line, the small amounts of rarefied gas that have been driven to velocities in excess of v_∞ have sufficient optical depth to produce a shallow, extended, and time-

dependent blue edge. The forward-scattered emission components of both moderate and strong lines are generally weaker than the components of a comparable smooth wind at low V_{Los} , which is a direct consequence of the tendency for multiple interactions to preferentially back-scatter photons. Of course, an excess of back-scattering in the *receding* hemisphere tends to produce more photons in the redshifted part of the emission component: this effect is most clearly seen for the strong line, where the detailed distribution of emission depends on the exact location and density contrast of the clumps. The net result is that the unsaturated lines exhibit absorption components in their absorption troughs and weaker emission lobes, while the strong lines exhibit shallow blue edges that extend beyond v_{∞} , broad absorption troughs, and stronger emission lobes (which are at least partially due to spherically symmetric geometry implied by Fig. 13).

Evidently, the wind structures that arise in a natural way due to the action of the line-driven instability go a long way towards explaining the time-dependent peculiarities seen in P Cygni profiles:

- DACs can be attributed to the slowly moving dense clumps.
- soft blue edges and blue-edge variability of strong lines can be attributed to the presence of variable amounts of rarefied gas at velocities in excess of the time-averaged value of v_{∞} . Although the Gaussian velocity dispersion parameter Δv_{turb} discussed in Sect. 3.4 mimics this effect, it does not incorporate the essential physical ingredients (i.e., strongly driven gas, multiple couplings due to the nonmonotonic velocity field) in a meaningful way, and is therefore of limited diagnostic value. Moreover, the redshift of the emission lobe with increasing values of Δv_{turb} (Fig. 8) seems to be an artifact of the ad hoc way in which the velocity dispersion is introduced to the calculation of line profiles: no such shifts occur for the profiles in Fig. 14.
- black troughs occur in strong lines when there are enough structures in the forward hemisphere of the wind to produce complete back-scattering over a range of V_{Los} . The profile in Fig. 14(b) does not exhibit a black trough only because the wind model used to compute it (Fig. 13) does not have enough structure near v_{∞} ; see, e.g., Lucy (1983) and Puls et al. (1994).

These successes are emphasized qualitatively in Fig. 15, which shows synthetic dynamic spectra computed for the full run of a radiation hydrodynamics simulation (Owocki et al. 1994). These synthetic time series show weak variability in the emission lobe, which is largely because the structures are assumed to be spherically symmetric; there are also some very narrow, rapidly evolving features that do not correspond to observed variations. Nevertheless, the general characteristics of DACs in unsaturated lines that accelerate over the course of ~ 1 day (e.g., in the second half of the time series shown in the left-hand panel) and extensive blue-edge variability (e.g., in the first half of the time series in the right-hand panel) have many points of correspondence with the observed variations of ξ Per (Fig. 12).

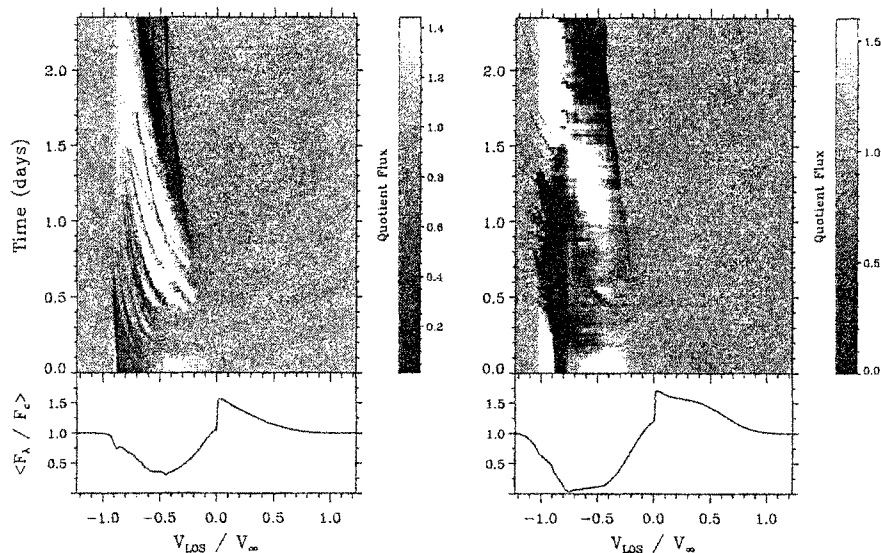


Fig. 15. Dynamic spectra generated from radiation hydrodynamics simulations of the growth of the line-driven instability by Owocki et al. (1994). Left: DAC variability in a line of modest strength. Right: blue-edge variability in a strong line; DAC is also visible since this line is not saturated. Individual spectra in the time series have been divided by the mean in order to enhance the contrast

However, despite these promising developments, the origin and nature of the DACs is still mysterious. Monitoring campaigns (e.g., Prinja 1988; Kaper et al. 1996) of many objects have linked the acceleration and recurrence of DACs to the projected rotational velocity of the underlying star, which suggests that the wind structures responsible for these spectroscopic features might ultimately be controlled by the stellar rotation rate. The recent IUE “MEGA Campaign” (Massa et al. 1995a) tested the strength of this connection directly by monitoring the UV resonance lines of three early-type stars continuously for an unprecedented interval of ~ 16 days. In all three cases – most directly for ζ Puppis (Howarth et al. 1995) and the B0.5 supergiant HD 64760 (Prinja et al. 1995) – the time scales for at least some of the wind variability could be tied directly to the estimated rotational period of the star. It is very difficult to understand how structures generated by dynamical processes in the wind (like the line-driven instability) can be tightly coupled to the stellar rotation rate, and the focus of recent work has been on finding alternative ways of generating structures that can rotationally modulate

the wind. The corotating interaction regions (CIRs) originally suggested by Mullan (1984) are among the most promising of these alternatives. Hydrodynamical simulations by Cranmer and Owocki (1996) confirm that CIRs can produce DACs that evolve over time scales determined by the stellar rotation rate. Interestingly, they find that the velocity gradient term in τ_{UV} is responsible for these optical depth enhancements, not the density term. Much more work remains to be done in order to understand the origin of DACs, whether the mechanism responsible for them can also explain soft blue edges and black troughs independent of the line-driven instability, and what impact these time-dependent structures in the wind have on the determination of mass-loss rates from spectroscopic (and continuum) diagnostics.

4 Continuum Diagnostics

At first glance, continuum measurements may not seem like a very promising method of determining \dot{M} , since they contain little information about the velocity law and would thus appear to provide insufficient data to satisfy (1). In fact, flux measurements at single wavelengths in the far infrared and radio region can provide quite reliable estimates of \dot{M} , provided that the distance to the star and v_∞ are known. The velocity law can also be determined by measuring the flux distribution at several widely spaced wavelengths. Consequently, the overall usefulness of continuum measurements is limited not so much by the physics of their formation as by the spatial resolution and instrumental sensitivity required to detect intrinsically weak flux levels (typically $\ll 1$ jansky [Jy]) from distant objects at these wavelengths.

4.1 Free-Free Emission

The contribution of the wind to the flux at infrared and radio wavelengths usually comes from free-free emission (bremsstrahlung) that arises when a free electron moves in the Coulomb field of another charged particle – usually a proton or alpha particle – but does not become bound to it. The electron is accelerated during this interaction, which alters its hyperbolic orbit and results in the absorption or emission of a photon, depending on whether the new orbit has more or less energy than the original. The energy of such interactions is not quantized, and so the photons from many such interactions will be emitted with a continuous spectrum: since the radiation field results from a collisional coupling between particles that define the thermal energy reservoir of the material in the wind, the relevant distributions are driven towards their LTE values. In particular, the source function for the emitted spectrum is the Planck function, $B_\nu(T_e)$, and the free-free emission coefficient is just

$$j_\nu^{\text{ff}} = \alpha_\nu^{\text{ff}} B_\nu(T_e) . \quad (21)$$

Derivations of the free-free absorption coefficient, α_ν^{ff} , can be found in standard texts (e.g., Rybicki and Lightman 1979, Chapter 5); in cgs units, it is given by

$$\alpha_\nu^{\text{ff}} = 3.7 \times 10^8 T^{-1/2} Z^2 n_e n_i \nu^{-3} \left(1 - e^{-h\nu/kT}\right) g(\nu, T) \text{ [cm}^{-1}\text{]} , \quad (22)$$

where Z is the mean charge per ion; n_e and n_i are the number densities of electrons and ions, respectively; $g(\nu, T)$ is the Gaunt factor (i.e., the correction factor needed to bring the free-free absorption cross-sections derived semi-classically into agreement with their quantum mechanical values); and all other symbols have their conventional meanings. For infrared and radio frequencies, $h\nu \ll kT$, and the correction for stimulated emission simplifies to $(1 - e^{-h\nu/kT}) \approx (h\nu/kT)$, whence

$$\alpha_\nu^{\text{ff}} = 1.8 \times 10^{-3} T^{-3/2} Z^2 n_e n_i \nu^{-2} g(\nu, T) \text{ [cm}^{-1}\text{]} . \quad (23)$$

Consequently, at these frequencies $d\tau_\nu^{\text{ff}} = \alpha_\nu^{\text{ff}} dr \propto \nu^{-2}$ if the weak functional dependence of the Gaunt factor on frequency is neglected ($g \propto \ln[T^{1.5}/\nu]$); alternately, $\tau_\lambda^{\text{ff}} \propto \lambda^2$.

This strong dependence of optical depth on wavelength provides the key to understanding the power of continuum methods, since – leaving aside the practical issues of detectability, correction for interstellar extinction, absolute calibration, etc. – it implies that for any M it is possible to find a wavelength where $\tau_\lambda^{\text{ff}} \approx 1$, i.e., where free-free emission in the wind creates an observable excess of flux over that expected from the stellar photosphere alone. Alternately, observations tuned to progressively longer wavelengths reach $\tau_\lambda^{\text{ff}} \approx 1$ at successively larger radial distances from the star. The fast, low-density winds typical of O stars become optically thick at radio wavelengths (2–6 cm), which originate at radii of $\sim 100 R_\star$ or more, at which point $v(r) \approx v_\infty$. Consequently, uncertainties in the shape of the velocity law do not enter directly into the interpretation of the observed flux, which is sensitive only to the amount of material in the wind. By the same argument, though, the winds of O stars are still optically thin to free-free emission at IR wavelengths, and flux measurements in the IR only provide a measure of the total volume emission; i.e., there is no information about the radial stratification of density (Abbott et al. 1984). Slower, denser winds become optically thick in the continuum at IR (e.g., for LBVs) or even optical wavelengths (e.g., WR stars).

The observed IR and radio fluxes of ζ Puppis are compared with the flux levels expected from the stellar photosphere in Fig. 16. The excess emission due to the wind is evident for wavelengths longer than the M-band ($\sim 5\mu$), and amounts to ~ 2 orders of magnitude or more in the radio region. Notice, however, that even though ζ Pup is the nearest O star ($D \approx 430$ pc) and has a strong stellar wind, the radio fluxes are only a few millijanskies.

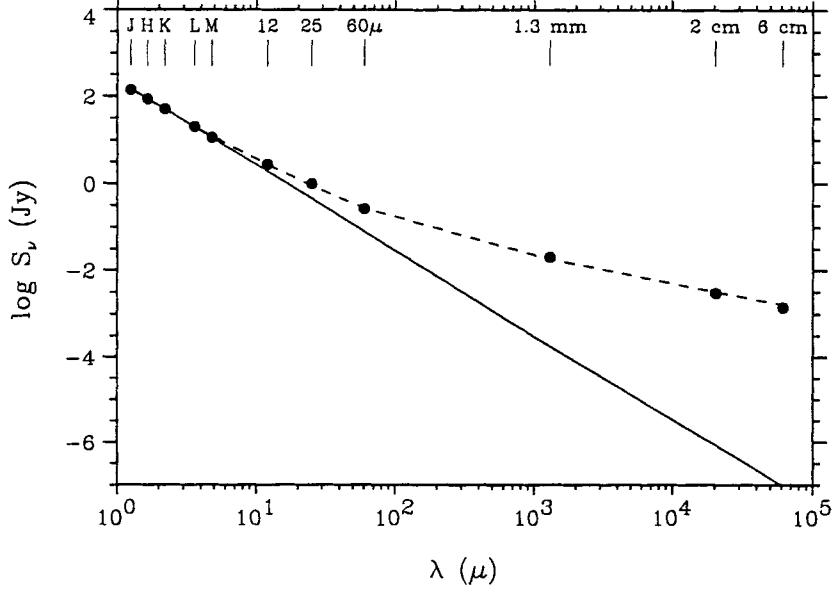


Fig. 16. Observed and predicted continuum flux excesses for ζ Puppis as a function of wavelength, with data from Abbott et al. (1984), Lamers et al. (1984), Leitherer and Robert (1991), and Bieging et al. (1989). The solid line indicates the photospheric flux from a unified model atmosphere, while the dashed line is a fit to the flux distribution by (24). Figure courtesy of F. Najarro

4.2 Spectrum of Free-Free Emission from a Stellar Wind

The continuum flux expected from a homogeneous, spherically symmetric, isothermal wind expanding with constant velocity can be obtained by directly integrating (3), the formal solution to the equation of radiative transfer. The analysis is simpler than that required to compute line profiles, since the source function is known from the outset to be the Planck function for a particular electron temperature (which is usually assumed to be constant through the wind) and there is no need to invoke the Sobolev approximation. Wright and Barlow (1975) and Panagia and Felli (1975) were the first to perform the integrations (which can be done analytically; see also Abbott et al. 1981 and Lamers and Waters 1984) to obtain the following expression for the flux from free-free emission in the wind:

$$S_\nu = 23.2 \left(\frac{\dot{M}Z}{\mu_i v_\infty} \right)^{4/3} \left(\frac{\gamma g}{D^3} \right)^{2/3} \nu^{2/3} \text{ [Jy]} , \quad (24)$$

where \dot{M} is in $M_\odot \text{ yr}^{-1}$, v_∞ is in km s^{-1} , D is the distance in kpc, and ν is in Hz; and where μ_i , Z , and γ are the mean ionic weight, the root-mean square charge per ion, and the number of electrons per ion, respectively. Lamers and Leitherer (1993) provide a useful table (their Table 4) of values of these parameters for several assumed chemical compositions; for typical Pop. I abundances with complete ionization of H and He, $\mu_i = 1.339$, $Z = 1.149$, and $\gamma = 1.149$.

Equation (24) shows that the flux from free-free emission in a stellar wind $S_\nu \propto \nu^{2/3}$; if the weak frequency dependence of the Gaunt factor is included, the dependence becomes a bit flatter, $S_\nu \propto \nu^{0.6}$. This is intermediate between the spectral distributions expected for homogeneous plasma that is optically thin ($\propto \nu^{-0.1}$) and thick ($\propto \nu^2$), since both extremes and the complete range of intermediate values contribute to the observed flux at any given frequency. The spectral index is positive since higher frequencies have smaller optical depths ($\tau_\nu^{\text{ff}} \propto \nu^{-2}$) and therefore probe systematically deeper layers of the wind, where higher densities produce comparatively more free-free emission.

Equation (24) can be rearranged to obtain a simple expression for the mass-loss rate,

$$\dot{M} = 0.095 \mu_i v_\infty (Z^2 \gamma \nu g(\nu, T))^{-1/2} D^{3/2} S_\nu^{3/4} [M_\odot \text{ yr}^{-1}] , \quad (25)$$

which emphasizes that both v_∞ and D must be known by some other means in order to convert S_ν to \dot{M} . Otherwise, the expression appears to be quite model independent and straightforward to evaluate. This apparent simplicity is slightly misleading, since the abundances and ionization state of the wind need to be known in order to calculate Z and γ , which implies that the temperature structure must be known. The assumptions of isothermality, Pop. I abundances, and complete ionization are entirely adequate for O-type stars, but may require modifications for objects with denser winds or weaker radiation fields, particularly when recombinations occur for a dominant species, or in the winds of evolved objects with different chemical compositions.

Figure 16 shows that the spectral distribution predicted by (24) fits the observed excesses at IR and radio wavelengths very well, which in turn confirms that it originates from free-free emission in the wind. In principle, the flux excess at any wavelength where the wind is opaque is sufficient to determine \dot{M} via (25). When measurements at several widely spaced wavelengths are available, the density stratification (or, equivalently, the velocity law) can be probed; see, e.g., Runacres and Blomme (1996). For a distance of 435 pc and $v_\infty = 2200 \text{ km s}^{-1}$, the fit to the flux distribution of ζ Pup in Fig. 16 gives $\dot{M} = 3.1 \times 10^{-6} M_\odot \text{ yr}^{-1}$, which is in good agreement with the value derived by fitting the 2D density distribution to the H α profile shown in Fig. 11. The value of β derived from wavelength dependence of the excess is 1.4, somewhat “faster” than the velocity law determined by the fit of the 2D model.

Table 2. Selected radio continuum studies

Reference	λ (cm)	Telescope ^a	Objects	Yield ^b
Abbott et al. (1980)	6.1	VLA	OBA	6/10
Abbott et al. (1981)	6.1	VLA	OB	6/10
Bieging et al. (1982)	6.1	VLA	WR	8/13
Vallée and Moffat (1985)	2.8	ARO, VLA	O, WR	0/19
Abbott et al. (1986)	2.0, 6.1	VLA	WR	14/23
Bieging et al. (1989)	2.0, 6.1, 20	VLA	OBA	18/88
Leitherer and Robert (1991)	0.13	SEST	OB, WR	7/ 7
Altenhoff et al. (1994)	0.12	IRAM	OB, WR	18/45
Leitherer et al. (1995)	3.4, 6.2	ATCA	OB, WR	10/11
Contreras et al. (1996)	0.7, 3.5, 6	VLA	OB, WR	8/ 8

^a VLA – Very Large Array; ARO – Algonquin Radio Observatory; SEST – Swedish-ESO Submillimeter Telescope; IRAM – Instituto de Radioastronomia Millimetrica, Spain; ATCA – Australia Telescope Compact Array.

^b N(detected) / N(observed)

4.3 Mass-Loss Rates from Continuum Observations

Starting with the pioneering work of Barlow and Cohen (1977), much effort has been devoted to using continuum observations of the IR and radio excesses of hot stars to infer mass-loss rates and the radial structure of the stellar wind. Unfortunately, the winds of OB stars are typically optically thin at the near-IR wavelengths accessible from the ground, and consequently the IR excesses are small (see, e.g., Figs. 16 and 17) and subject to uncertainties from corrections for interstellar extinction and the absolute flux calibration. Even when they exist, the excesses at wavelengths where the wind is optically thin are determined by \dot{M} , $v(r)$, and the temperature stratification of the wind, $T(r)$, and it is impossible to disentangle the contributions of each of these parameters uniquely; see, e.g., Abbott et al. (1984) for a clear discussion of these problems. The situation is better for objects with larger values of \dot{M} like LBVs or WR stars, since the wind is opaque at infrared wavelengths. It also improves for far-IR wavelengths accessible to satellite observatories like the Infrared Astronomical Satellite (IRAS) mission of the early 1980s or, more recently, the Infrared Space Observatory (ISO).

Since hot-star winds are opaque at radio wavelengths, measurements of the free-free continuum between ~ 1 mm and ~ 20 cm provide more useful information about \dot{M} . Table 2 lists a selection of continuum studies of hot stars

at radio wavelengths. These observations are difficult to make, since high angular resolution is required to isolate the flux from the wind (which is usually a point source; but see White and Becker 1982 for an important exception) and since the expected flux levels are small, both because of the intrinsic weakness of the emission and the large distances typical of early-type stars. Indeed, from a practical point of view, sensitivity is the biggest drawback to radio continuum observations. This is suggested by the low “yields” typical of the studies listed in Table 2, except for samples that are strongly biased towards extreme objects. Bieging et al. (1989) have completed the largest survey of OB stars to date, and it is interesting to note that while they detected 15 of the 23 sources (65%) they observed in a distance-limited sample ($D < 2.5$ kpc; $\delta \geq -40^\circ$), they only detected 3 more sources in their total sample of 88 targets, with sensitive upper limits on nondetections of $\lesssim 0.5$ mJy. Thus, it is unlikely that significantly more stars will be detected in the northern hemisphere, though the advent of the Australia Telescope Compact Array will help to enlarge the sample by providing access to the early-type stars in the rich star fields of the southern skies; see, e.g., Leitherer et al. (1995).

The continuum flux excesses at radio wavelengths are generally thought to provide the most reliable estimates of \dot{M} for hot, luminous OB stars, because (1) when it is detectable, the observed free-free emission originates at great distances from the star and is unaffected by uncertainties in the shape of the velocity law; and (2) the emission does not depend on the detailed ionization or excitation equilibrium in the wind, which, in the case of O stars, can be assumed to be completely ionized. Thus, the main difficulties associated with UV resonance lines and optical emission lines are circumvented. Unfortunately, the assumption of complete ionization cannot be justified for stars with $T_{\text{eff}} \lesssim 17,000$ K owing to the recombination of helium, and in practice a detailed model of the temperature structure of the wind must be used to interpret the radio continuum flux for supergiants later than $\sim B2$. Moreover, since free-free emission is a ρ^2 process, values of \dot{M} determined from (25) are also sensitive to clumping; as in the case of optical emission lines, the presence of structures in a density distribution that is assumed to be smooth will cause \dot{M} to be systematically overestimated.

The most forceful argument *against* clumping being an important source of bias is that when determinations of \dot{M} from $H\alpha$ profile fitting and radio continuum measurements are both available, they agree reasonably well with each other on average (Lamers and Leitherer 1993; Puls et al. 1993). These diagnostics probe very different radial distances in the wind: $H\alpha$ is formed predominantly in the first few stellar radii, while the “radio photosphere” is at tens or hundreds of stellar radii, depending on the wavelength of observation and the amount of material in the wind. Since $H\alpha$ and free-free emission are sensitive to clumping in exactly the same way, their approximate equality implies that either the degree of clumping (i.e., volume filling factor, density

ratio) must be preserved over a enormous range of radii, despite the expansion of the wind, or significant clumping is not in fact present. The first alternative is thought to be unlikely (though not proven to be impossible), which implies that significant clumping is not present at any radius in the wind.

However, this line of reasoning is not completely convincing, since the behaviour of clumped material will depend on the mechanism responsible for introducing the inhomogeneity in the first place. In the case of ζ Puppis, e.g., we have already seen how structures like WCZs may be able to resolve the long-standing “factor of 2” discrepancy between the values of \dot{M} determined from $H\alpha$ (where the equatorial concentration of material is important) and the radio measurements (where the density distribution is more nearly symmetric); yet this is one of the stars that defines the “on average” equality of \dot{M} determined from these two diagnostics. On a more fundamental level, the widespread variability of hot-star winds strongly suggests that they are inhomogeneous on large spatial scales (Sect. 3.6). Until the nature of these inhomogeneities are established more firmly, the impact of wind structures on specific diagnostics of \dot{M} cannot be assessed.

4.4 Nonthermal Radio Emission

An unanticipated difficulty with determining accurate mass-loss rates from radio flux measurements appeared shortly after observations with the Very Large Array began in earnest, when Abbott et al. (1984) recognized that for a minority of targets (initially just 2 stars: 9 Sagittarii [O4: V((f))] and Cyg OB2 No. 9 [O5 If]) the inferred values of \dot{M} were an order of magnitude larger than the values estimated by other methods. Subsequent multi-wavelength observations showed that the flux distribution for these targets was substantially different from that predicted by (24), with spectral indices $\alpha \leq 0$ (where $S_\nu \propto \nu^\alpha$) rather than the value of +0.6 expected for free-free emission. Both the monochromatic flux levels and the spectral indices were found to be highly variable over intervals of months. These characteristics are illustrated for Cyg OB2 No. 9 in Fig. 17, which shows that – in complete contrast to the case of ζ Pup illustrated in Fig. 16 – the IR and radio flux distributions cannot be fit simultaneously by (24), because there is too much radio emission. Figure 17 also emphasizes the flatness of the observed radio continuum and the extreme variability, which amounts to more than an order of magnitude at 6 cm.

Abbott et al. (1984) recognized that this behaviour is characteristic of nonthermal radio emission, which contaminates (and in fact dominates) the free-free emission and invalidates the use of (25) to determine \dot{M} . Although nonthermal emitters comprise only 24% of the distance-limited sample surveyed by Bieging et al. (1989), they are systematically the most bolometrically luminous stars. They are also systematically stronger radio sources than thermal (free-free) emitters and will therefore tend to be seen to greater distances. Fortunately, they can be distinguished from thermal sources by

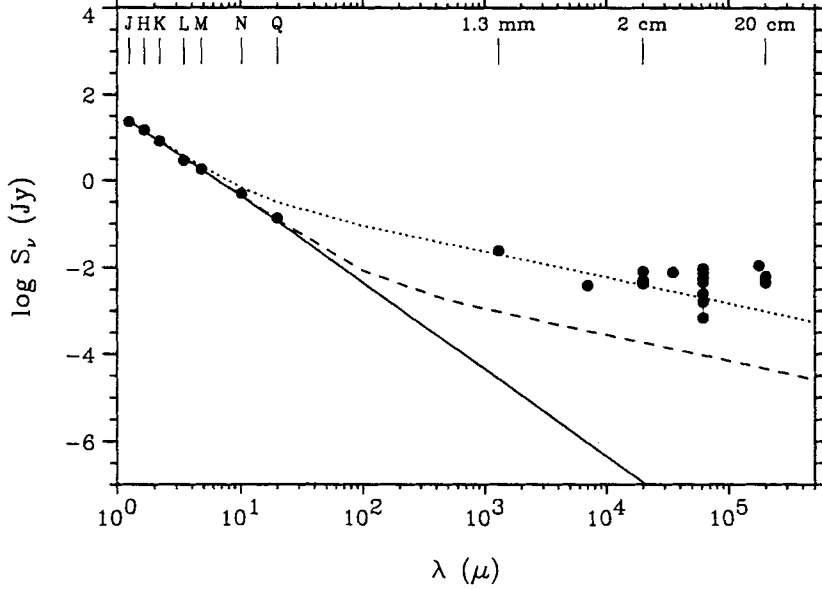


Fig. 17. Observed and predicted continuum flux excesses for Cyg OB2 No. 9 (spectral type O5 If) as a function wavelength, with data from Abbott et al. (1984), Altenhoff et al. (1994), Contreras et al. (1996), Bieging et al. (1989), White and Becker (1983), and Phillips and Titus (1990). The solid line indicates the photospheric flux, while the dashed and dotted lines indicate the predicted flux for mass-loss rates of $4 \times 10^{-6} M_{\odot} \text{ yr}^{-1}$ (which does not fit the radio observations) and $4 \times 10^{-5} M_{\odot} \text{ yr}^{-1}$ (which does not fit the IR observation), respectively. Variability and strong deviations from the flux distribution expected for free-free emission are evident at longer wavelengths. Figure courtesy of F. Najarro

multiwavelength observations to determine the spectral index α , or by their large variations. Consequently, the complication posed by the existence of nonthermal sources is mostly practical, in that more observing time is required to observe a source at several wavelengths or at several epochs in order to ensure that it is thermal before applying (25) to determine \dot{M} .

The origin of the nonthermal emission is unknown, but is probably due to synchrotron emission from electrons that are accelerated to mildly relativistic energies by multiple interactions with strong shocks in the presence of a weak stellar magnetic field (White 1985). The nonthermal source in Cyg OB2 No. 9 has recently been resolved via very-long baseline interferometry (Phillips and Titus 1990), which confirms that the nonthermal component originates at or beyond the radius where the 20 cm free-free continuum is formed and that

the emitting volume is large. At the same time, however, Bieging et al. (1989) point out that the nonthermal fluxes at different wavelengths vary in concert, which is difficult to understand in terms of the chaotic, embedded shock model since the “free-free” photospheres at different wavelengths sample very different radii ($\tau_{\lambda}^{\text{ff}} \propto \lambda^2$). On at least one occasion, the nonthermal component of Cyg OB2 No. 9 faded altogether, revealing an underlying spectrum with a spectral index of ~ 0.6 that permitted Abbott et al. (1984) to derive $\dot{M} = 1.9 \times 10^{-5} M_{\odot} \text{ yr}^{-1}$. Clearly, there is still work to be done to understand the origin of nonthermal radio emission and the implications that its presence has for the structure of hot-star winds.

4.5 The New Frontier: Spectroscopy in the Near and Far IR

The steady improvement in IR detector technology has recently produced an explosion of interest in studying early-type stars spectroscopically in the J, H, and K bands, which have central wavelengths of ~ 1.25 , 1.65 , and 2.20μ , respectively. These wavelengths have many advantages for studying hot stars in environments that are highly obscured by dust, like young star clusters (e.g., Hanson et al. 1993) or the Galactic Center (e.g., Najarro et al. 1994). These wavebands contain important lines of H (e.g., the Paschen and Brackett series), He I, and He II, most of which are partially formed in the stellar wind. They generally have a ρ^2 character and resemble optical emission lines, except that they tend to be weaker because they are due to transitions between higher energy levels in their parent atoms. Figure 18 illustrates the quality of spectroscopic material that can now be obtained at near IR wavelengths by showing the hydrogen lines of $P\beta$ and $B\gamma$ (which fall in the J and K bands, respectively) of the LBV HD 160529. Both lines exhibit P Cygni profiles, the detailed shape and strength of which reflect the different emitting volumes appropriate to these transitions.

At still longer wavelengths, IR lines have an important advantage that is not shared by optical emission features, which once again stems from the fact that *continuum* optical depths scale with λ^2 . As a result, the “effective photosphere” is a strong function of radius for IR wavelengths beyond the limit where the wind first becomes opaque. Line profiles are only formed at radii that are *larger* than the effective photosphere, and (as we have seen) they can be used to determine the velocity law and density structure starting from that point. Since the (optically thick) continua associated with progressively longer wavelengths form at systematically greater distances from the star, the wind lines at longer wavelengths are formed at larger velocities (i.e., more blue-shifted V_{los}). Consequently, the information provided by IR wind lines in different wavelength intervals is not redundant, and can be used to piece together the velocity and density structure of the wind – providing that the underlying continuum is optically thick.

Figure 18 shows that the $P\beta$ and $B\gamma$ lines of HD 160529 are not systematically offset from each other: despite its enormous mass-loss rate (1.3×10^{-5}

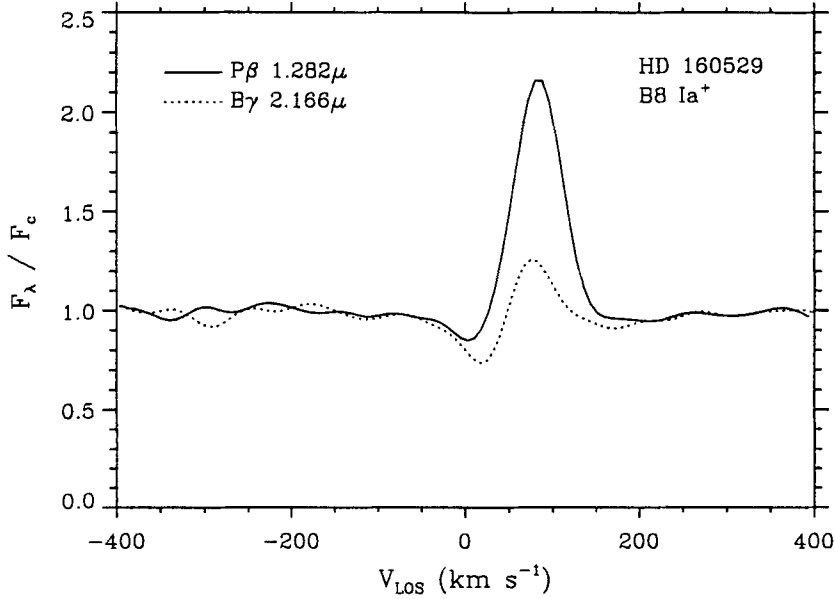


Fig. 18. Infrared P Cygni profiles of $P\beta$ (in the J band) and $B\gamma$ (in the K band) for HD 160529. These high-resolution spectra were obtained with the Fourier Transform Spectrometer of the Canada-France-Hawaii Telescope; the small undulations in the continuum are artifacts (“ringing”) typical of FTS spectra

$M_{\odot} \text{ yr}^{-1}$, according to Leitherer et al. 1995), its J and K band continua are not optically thick. Instead, observations at wavelengths in the satellite IR are required to achieve this “infrared advantage”, which even then can only be applied to the stars with the densest winds. Despite these caveats, this method promises to become an important new probe of the structure of the outflows from these stars. Indeed, observations of the H and He I lines in the $2.4\text{--}45\mu$ region obtained with the short-wavelength spectrometer on board ISO have already provided detailed insights into the wind of the famous LBV P Cygni (Lamers et al. 1996).

5 Summary and Outlook

It should be clear from the preceding discussion that no single diagnostic provides a completely reliable measurement of the mass-loss rate of an early-type star. The UV resonance lines are by far the best indicators of v_{∞} , and the shape of the profile also provides good constraints on the gradient of the radial velocity field of the wind. Unfortunately, the strength of UV resonance

lines cannot be converted to \dot{M} easily because of the large uncertainties in the ionization balance of hot-star winds, uncertainties that are in part due to the presence of time-dependent processes in the wind. However, once v_∞ is known, continuum methods come to the fore, and measurements in the radio range between 1 mm and 20 cm are generally believed to provide the most reliable estimates of \dot{M} . In practice, though, the weakness of the flux levels due to free-free emission in hot-star winds limits the applicability of these techniques to the nearest objects, which nevertheless play a key role by acting as calibrators for other techniques.

In contrast, H α emission profiles can now be observed with good spectral resolution for stars as far away as the Local Group of galaxies. Sufficiently strong emission permits estimates of the velocity gradient and \dot{M} , and sometimes also v_∞ (e.g., for late B and early A supergiants). The caveat applicable to these (and other) ρ^2 diagnostics is that they are very susceptible to the distribution of wind material assumed by the model used to interpret them. In particular, \dot{M} will be systematically overestimated if a smooth, spherically symmetric model is used to interpret recombination line profiles from a wind that is in fact asymmetric or otherwise structured. More detailed physical information concerning the effect of rotation on the distribution of material in hot-star winds and the nature of the structures responsible for their ubiquitous variability is required in order to quantify this effect. There may still be uncertainties as large as a factor of two lurking in the determinations of the mass-loss rates of early-type stars.

Even so, the stationary properties of hot-star winds can be explained acceptably well by the theory of line-driven winds; see, e.g., the lectures by Lamers (second contribution to this Volume). Consequently, it seems likely that in the coming years stellar wind research will begin to emphasize the role these outflows can play as tools to investigate astrophysical problems. For example, Kudritzki and his colleagues are currently developing the “Wind-Momentum-Luminosity Relationship”, by which the stellar wind profiles observed in the luminous stars of external galaxies can be used as “standard candles” to determine distances out to the Fornax and Virgo Clusters; see Kudritzki (1997) for details of this exciting application of stellar wind theory. More generally, stellar winds can be used to probe astronomical situations that range from the formation of bow shocks, bubbles, and chimneys in the interstellar medium to measuring the abundance gradients in external galaxies and determining the chemical composition of early generations of massive stars in high redshift galaxies. Observations of these phenomena represent the frontiers of stellar wind research; together with ongoing investigations into the nonstationary behaviour of hot-star winds, they are expected to provide further surprising insights into the physics of hot stars and their environments.

Acknowledgements

It is a pleasure to thank the organizers and participants of this summer school for many stimulating discussions concerning stellar atmospheres and astrophysics, and for the opportunity to sample a wide variety of Belgian beer – which is very compelling, despite the “impurities” that my Bavarian colleagues warned me about! I am indebted to Joachim Puls, Achim Feldmeier, Paco Najarro, Peter Petrenz, and Anne Fullerton for their contributions to this manuscript, and would like to express my thanks to the many colleagues around the world who have taught me about hot-star winds over the years, most particularly Stan Owocki and Joachim Puls. I would also like to thank Prof. R.-P. Kudritzki for the opportunity to deliver these lectures. Financial support from the Deutsche Forschungsgemeinschaft (grant Pu 117/3-1) during the preparation of the written version of these lectures is gratefully acknowledged.

References

- Abbott, D. C., Bieging, J. H., Churchwell, E., Cassinelli, J. P. (1980): *ApJ* **238**, 196
- Abbott, D. C., Bieging, J. H., Churchwell, E. (1981): *ApJ* **250**, 645
- Abbott, D. C., Bieging, J. H., Churchwell, E. (1984): *ApJ* **280**, 671
- Abbott, D. C., Telesco, C. M., Wolff, S. C. (1984): *ApJ* **279**, 225
- Abbott, D. C., Bieging, J. H., Churchwell, E., Torres, A. V. (1986): *ApJ* **303**, 239
- Altenhoff, W. J., Thum, C., Wendker, H. J. (1994): *A&A* **281**, 161
- Barlow, M. J., Cohen, M. (1977): *ApJ* **213**, 737
- Beals, C. S. (1930): *Publ. DAO* **4**, 271
- Beals, C. S. (1950): *Publ. DAO* **9**, 1
- Bieging, J. H., Abbott, D. C., Churchwell, E. (1982): *ApJ* **263**, 207
- Bieging, J. H., Abbott, D. C., Churchwell, E. (1989): *ApJ* **340**, 518
- Bjorkman, J. E., Cassinelli, J. P. (1993): *ApJ* **409**, 429
- Bjorkman, J. E., Ignace, R., Tripp, T. M., Cassinelli, J. P. (1994): *ApJ* **435**, 416
- Carlberg, R. G. (1980): *ApJ* **241**, 1131
- Caroff, L. J., Noerdlinger, P. D., Scargle, J. D. (1972): *ApJ* **176**, 439
- Castor, J. I. (1970): *MNRAS* **149**, 111
- Castor, J. I., Lamers, H. J. G. L. M. (1979): *ApJS* **39**, 481
- Chen, W., White, R. L., Bertsch, D. (1996): *A&AS* **120**, 423
- Contreras, M. E., Rodríguez, L. F., Gómez, Y., Velázquez, A. (1996): *ApJ* **469**, 329
- Cranmer, S. R. (1996): Ph.D. thesis, Univ. of Delaware
- Cranmer, S. R., Owocki, S. P. (1996): *ApJ* **462**, 469
- De Koter, A., Schmutz, W., Lamers, H. J. G. L. M. (1993): *A&A* **277**, 561
- Feldmeier, A. (1995): *A&A* **299**, 523
- Fullerton, A. W., Gies, D. R., Bolton, C. T. (1992): *ApJ* **390**, 650
- Gabler, R., Gabler, A., Kudritzki, R. P., Puls, J., Pauldrach, A. W. A. (1989): *A&A* **226**, 162
- Groenewegen, M. A. T., Lamers, H. J. G. L. M. (1989): *A&AS* **79**, 359

- Groenewegen, M. A. T., Lamers, H. J. G. L. M. (1991): A&A **243** 429
- Hamann, W.-R. (1981): A&A **93**, 353
- Hanson, M. M., Geballe, T. R., Conti, P. S., Block, D. L. (1993): A&A **273**, L44
- Hanson, M. M., Conti, P. S., Rieke, M. J. (1996): ApJS **107**, 281
- Haser, S. M. (1995): Ph.D. thesis, Ludwig-Maximilians-Universität München
- Haser, S. M., Lennon, D. J., Kudritzki, R.-P., et al. (1995): A&A **295**, 136
- Henrichs, H. F., Kaper, L., Nichols, J. S. (1994): A&A **285**, 565
- Howarth, I. D., Prinja, R. K. (1989): ApJS **69**, 527
- Howarth, I. D., Prinja, R. K., Massa, D. (1995): ApJ **452**, L65
- Hutchings, J. B. (1979): *The O Stars: Optical Review*, in: Mass Loss and Evolution of O-Type Stars (proceedings of IAU Symp. 83), ed. P. S. Conti and C. W. H. de Loore (Reidel, Dordrecht), p.3
- Ignace, R., Cassinelli, J. P., Bjorkman, J. E. (1996): ApJ **459**, 671
- Kaper, L., Henrichs, H. F., Nichols, J. S., et al. (1996): A&AS **116**, 257
- Kaufer, A., Stahl, O., Wolf, B., et al. (1997): A&A **320**, 273
- Kudritzki, R. P. (1988): *The Atmospheres of Hot Stars: Modern Theory and Observation*, in: Radiation in Moving Gaseous Media (18th Advanced Course of the Swiss Society of Astronomy & Astrophysics), ed. Y. Chmielewski and T. Lanz (Geneva: Geneva Observatory), p.1
- Kudritzki, R. P. (1992): A&A **266**, 395
- Kudritzki, R.-P. (1997): *Quantitative Spectroscopy of the Brightest Blue Supergiant Stars in Galaxies*, in: Stellar Astrophysics for the Local Group (Proceedings of VIII Canary Islands Winter School of Astrophysics), ed. A. Aparicio, A. Herrero, F. Sánchez (Cambridge: CUP), in press
- Kudritzki, R. P., Hummer, D. G. (1990): ARA&A **28**, 303
- Lamers, H. J. G. L. M., Leitherer, C. (1993): ApJ **412**, 771
- Lamers, H. J. G. L. M., Waters, L. B. F. M. (1984): A&A **136**, 37
- Lamers, H. J. G. L. M., Gathier, R., Snow, T. P. (1982): ApJ **258**, 186
- Lamers, H. J. G. L. M., Waters, L. B. F. M., Wesselius, P. R. (1984): A&A **134**, L17
- Lamers, H. J. G. L. M., Cerruti-Sola, M., Perinotto, M. (1987): ApJ **314**, 726
- Lamers, H. J. G. L. M., Najarro, F., Kudritzki, R. P., et al. (1996): A&A **315**, 229
- Leitherer, C., Robert, C. (1991): ApJ **377**, 629
- Leitherer, C., Chapman, J. M., Koribalski, B. (1995): ApJ **450**, 289
- Lucy, L. B. (1971): ApJ **163**, 95
- Lucy, L. B. (1982): ApJ **255**, 278
- Lucy, L. B. (1983): ApJ **274**, 372
- Lucy, L. B., Solomon, P. M. (1970): ApJ **159**, 879
- MacGregor, K. B., Hartmann, L., Raymond, J. C. (1979): ApJ **231**, 514
- Maeder, A., Conti, P. S. (1994): ARA&A **32**, 227
- Massa, D., Shore, S. N., Wynne, D. (1992): A&A **264**, 169
- Massa, D., Fullerton, A. W., Nichols, J. S., et al. (1995a): ApJ **452**, L53
- Massa, D., Prinja, R. K., Fullerton, A. W. (1995b): ApJ **452**, 842
- Mihalas, D. (1978): *Stellar Atmospheres* (Freeman, San Francisco)
- Mihalas, D. (1979): MNRAS **189**, 671
- Mihalas, D., Hummer, D. G. (1973): ApJ **179**, 827
- Moffat, A. F. J., Drissen, L., Lamontagne, R., Robert, C. (1988): ApJ **334**, 1038
- Morrell, N. I., Walborn, N. R., Fitzpatrick, E. L. (1991): PASP **103**, 341

- Morton, D. C. (1967a): ApJ **147**, 1017
Morton, D. C. (1967b): ApJ **150**, 535
Morton, D. C. (1976): ApJ **203**, 386
Mullan, D. J. (1984): ApJ **283**, 303
Najarro, F., Hillier, D. J., Kudritzki, R. P., et al. (1994): A&A **285**, 573
Olson, G. L. (1982): ApJ **255**, 267
Owocki, S. P. (1990): Reviews of Modern Astronomy **3** (Springer, Berlin), 98
Owocki, S. P. (1992): *Instabilities in Hot-Star Winds: Basic Physics and Recent Developments*, in: Atmospheres of Early-Type Stars, ed. U. Heber and S. Jeffery (Springer, Berlin), p.393
Owocki, S. P., Rybicki, G. B. (1984): ApJ **284**, 337
Owocki, S. P., Castor, J. I., Rybicki, G. B. (1988): ApJ **335**, 914
Owocki, S. P., Fullerton, A. W., Puls, J. (1994): Ap&SS **221**, 437
Panagia, N., Felli, M. (1975): A&A **39**, 1
Pauldrach, A. W. A., Puls, J., Kudritzki, R. P. (1986): A&A **164**, 86
Pauldrach, A. W. A., Kudritzki, R. P., Puls, J., Butler, K., Hunsinger, J. (1994): A&A **283**, 525
Petrenz, P., Puls, J. (1996): A&A **312**, 195
Phillips, R. B., Titus, M. A. (1990): ApJ **359**, L15
Prinja, R. K. (1988): MNRAS **231**, 21P
Prinja, R. K., Fullerton, A. W. (1994): ApJ **426**, 345
Prinja, R. K., Howarth, I. D. (1986): ApJS **61**, 357
Prinja, R. K., Smith, L. J. (1992): A&A **266**, 377
Prinja, R. K., Howarth, I. D., Henrichs, H. F. (1987): ApJ **317**, 389
Prinja, R. K., Massa, D., Fullerton, A. W. (1995): ApJ **452**, L61
Prinja, R. K., Massa, D., Fullerton, A. W., Howarth, I. D., Pontefract, M. (1997): A&A **318**, 157
Puls, J., Owocki, S. P., Fullerton, A. W. (1993): A&A **279**, 457
Puls, J., Feldmeier, A., Springmann, U. W. E., Owocki, S. P., Fullerton, A. W. (1994): Ap&SS **221**, 409
Puls, J., Kudritzki, R. P., Herrero, A., et al. (1996): A&A **305**, 171
Rivinius, Th., Stahl, O., Wolf, B., et al. (1997): A&A **318**, 819
Runacres, M. C., Blomme, R. (1996): A&A **309**, 544
Rybicki, G. B. (1984): *Escape Probability Methods*, in: Methods of Radiative Transfer, ed. W. Kalkofen (Cambridge: CUP), p.21
Rybicki, G. B., Hummer, D. G. (1978): ApJ **219**, 654
Rybicki, G. B., Lightman, A. P. (1979): *Radiative Processes in Astrophysics* (Wiley, New York)
Santolaya-Rey, A. E., Puls, J., Herrero, A. (1997): A&A, in press
Schaerer, D., Schmutz, W. (1994): A&A **288**, 231
Snow, T. P., Lamers, H. J. G. L. M., Lindholm, D. M., Odell, A. P. (1994): ApJS **95**, 163
Stahl, O., Mandel, H., Wolf, B., et al. (1993): A&AS **99**, 167
Underhill, A. B. (1958): Mem. R. Soc. Liège **20**, 91
Underhill, A. B. (1995a): ApJS **100**, 433
Underhill, A. B. (1995b): ApJS **100**, 461
Vallée, J. P., Moffat, A. F. J. (1985): AJ **90**, 315
Walborn, N. R., Bohlin, R. C. (1996): PASP **108**, 477

- Walborn, N. R., Nichols-Bohlin, J. S., Panek, R. J. (1985): *International Ultraviolet Explorer Atlas of O-Type Spectra from 1200 to 1900 Å* (NASA RP-1155)
- Walborn, N. R., Parker, J. W., Nichols, J. S. (1995): *International Ultraviolet Explorer Atlas of B-Type Spectra from 1200 to 1900 Å* (NASA RP-1363)
- White, R. L. (1985): ApJ **289**, 698
- White, R. L., Becker, R. H. (1982): ApJ **262**, 657
- White, R. L., Becker, R. H. (1983): ApJ **272**, L19
- Wilson, R. (1958): Mem. R. Soc. Liège **20**, 85
- Wolf, C. J. E., Rayet, G. (1867): Observatoire de Paris Comptes Rendus **65**, 292
- Wright, A. E., Barlow, M. J. (1975): MNRAS **170**, 41

Circumstellar Disks

J.E. Bjorkman

University of Toledo, Dept. of Physics and Astronomy, Toledo, OH 43606, USA
e-mail: jon@physics.utoledo.edu

Abstract. In these lectures, I discuss the theory of circumstellar disks. There appear to be two basic categories: Accretion disks, which are formed from infalling material, and outflow disks, which are formed in rotating stellar winds. Here I discuss the basic hydrodynamics of rotationally supported (nearly Keplerian) accretion disks, as well as how a rotating stellar wind naturally leads to the formation of a dense wind-compressed equatorial disk. To observationally determine the geometry, density, and velocity structure of these disks, we must be able to calculate their observable properties, so these lectures also cover radiation transport in axisymmetric geometries. Here I discuss the calculation of infrared excess emission, intrinsic linear polarization, and spectroscopic line profiles.

1 Introduction

Circumstellar disks occur around a variety of stars throughout the H-R diagram. New HST images vividly demonstrate the existence of accretion disks around young stellar objects (YSOs), while at the opposite evolutionary extreme, we see a disk in the ejecta of the luminous blue variable (LBV) η Carinae. There is also evidence for disks around post-asymptotic giant branch (AGB) stars that are making their transition to the planetary nebulae phase. These disks are largely responsible for shaping the ejected nebula into the intriguing bipolar bubbles that are so prevalent in HST images of highly evolved stars. Even some rapidly rotating near main sequence stars (Be stars) show evidence for circumstellar disks. As our primary example, I will focus on Be stars throughout these lectures, but we should keep in mind that similar observations exist for virtually all disk-like systems. The differences are mostly ones of detail (YSOs are dusty with *very* optically thick disks, while AGNs have high temperature disks, which changes the ionization state and corresponding disk emission processes).

So what is a Be star? Be stars are near main sequence B stars (luminosity classes III–IV) that have hydrogen (and sometimes Fe) emission lines in their optical spectra (at one time or another — they can be highly variable); for a review, see Underhill and Doazan (1982). As a class, they are rapidly rotating stars (about 70% of break-up) as compared to normal B stars. We are now certain that they have circumstellar disks because they are just now beginning to be resolved by optical H α interferometry (Thom et al. 1986, Mourard et al. 1989, Quirrenbach et al. 1993, 1994, 1997). Even so, it has been suspected

for quite some time that both Be stars and YSOs (such as T Tauri stars) are surrounded by circumstellar disks, *even though these systems were unresolved*.

2 Disk Diagnostics

How can we determine that unresolved stars are surrounded by rotating disks? Well, we have to use indirect evidence. This evidence comes principally from three kinds of observations: excess IR emission, intrinsic polarization data, and $H\alpha$ line profiles. The excess IR emission indicates the presence of circumstellar material (see Fullerton, this Volume). Intrinsic polarization implies that this material cannot be spherically distributed (as I discuss later). Finally for Be stars, the $H\alpha$ profiles are double-peaked. The simplest explanation for this morphology is a rotating ring (or disk) of material (Struve 1931). The material beside the star produces emission, but the disk is also rotating. So on the left side of the star, that emission is blueshifted, while on the right it is redshifted. In front of the star, the disk material rotates perpendicularly to the line of sight, so it produces unshifted absorption. Combining red- and blueshifted emission with unshifted absorption produces the classic double-peaked emission line profile so characteristic of Be stars. Incidentally, this shape also implies that the disk expansion velocity (if there is any) is much smaller than the rotation velocity. Waters (1986) has shown that the $H\alpha$ equivalent width is positively correlated with the IR excess, which implies that both the $H\alpha$ and IR excess come from the same region around the star. So evidently, a rotating circumstellar disk can simultaneously explain the IR excess, intrinsic polarization, and double-peaked $H\alpha$ emission lines.

In addition to the disk, Be stars also possess a stellar wind as evidenced by their (weak) asymmetric blueshifted UV absorption lines, principally Si IV and C IV (Snow 1981). Although these lines are not as strong as the classic P Cygni line profiles (they have virtually no emission and no sharp blue absorption edge) that indicate massive stellar winds in O stars (see Fullerton elsewhere in these lectures), they do indicate a substantial mass loss from the star; main sequence B stars are merely the much weaker siblings of the “live fast, die young” O stars. The terminal speed of these winds can be determined from the edge-velocity of the blueshifted absorption, and one finds terminal speeds of about 1000 km s^{-1} (c.f. O stars, which have $v_\infty = 2000\text{--}3000 \text{ km s}^{-1}$).

This high speed wind must simultaneously exist with a slowly expanding disk. The usual picture that one adopts to achieve this is to assume that the UV lines are formed in a stellar wind that fills the polar regions, while there is also a dense rapidly rotating disk in the equatorial regions (see Fig. 1). Of course the fundamental question is what is the origin of this disk?

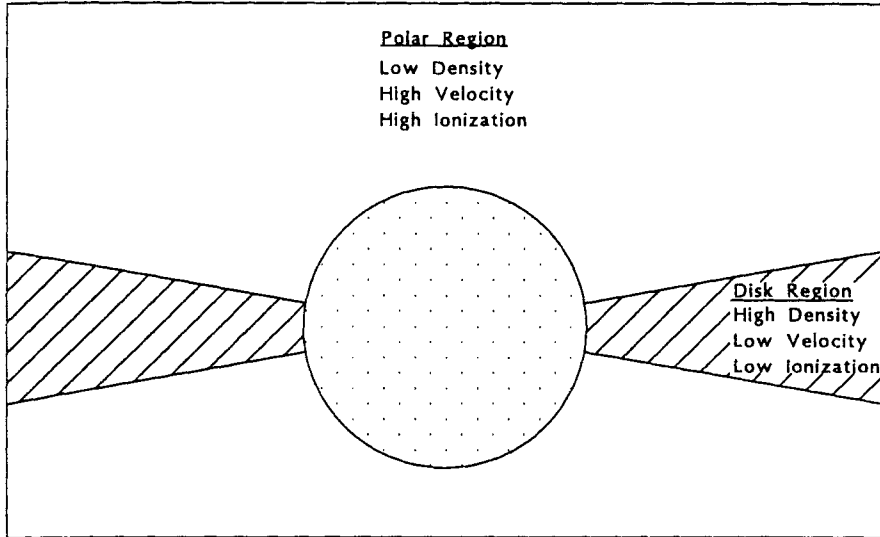


Fig. 1. Standard picture of the elements required for a model of a Be star disk

3 Theory of Circumstellar Disks

There are two primary situations where we have seen that circumstellar disks occur: Outflow from a rotating star, as in the Be stars, and infall (accretion), as in the T Tauri stars. The fundamental fluid dynamics of rotating disks is best illustrated by hydrostatic rotationally supported disks, so I will first discuss accretion disks and then proceed to outflow disks in rotating stellar winds.

3.1 Accretion Disks

There are two common situations that lead to the formation of an accretion disk: protostellar collapse, and Roche lobe overflow in a binary star system. In protostellar collapse, a gravitationally bound cloud contracts under the influence of its self gravity. However, this cloud has some initial angular momentum, so the fluid elements cannot fall directly onto the protostar. Instead, they tend to orbit around the protostar as they fall inward. This naturally leads to the formation of an equatorial disk. The new material that falls onto the disk first hits (after passing through shocks above or below the disk surface) at large radii where it mixes with the disk. This material is subsequently accreted onto the star, but only after it makes its way inward through the disk. Similarly, the material that overflows the Roche lobe in an evolved binary star produces an accretion stream that falls toward the companion star.

Again the initial angular momentum prevents the flow from falling directly onto the secondary star, so it instead orbits around the star and is added into an accretion disk. Thus we see that the primary character of an accretion disk is that it is material that has too much angular momentum to fall directly onto the star; it is composed of fluid packets that *orbit* the star. In other words, the disk velocity is nearly Keplerian. This means that centrifugal force supports the disk in the radial direction, while in the vertical direction, it is pressure supported.

Hydrostatic Structure. Let us now obtain the equations describing a Keplerian (hydrostatic) disk. The fluid equations are the continuity equation,

$$\frac{\partial \rho}{\partial t} + \nabla_i(\rho v_i) = 0 , \quad (1)$$

and the momentum equation,

$$\frac{\partial(\rho v_i)}{\partial t} + \nabla_j(\rho v_i v_j) = -\nabla_i P + \rho f_i , \quad (2)$$

where f_i is the force per unit mass (acceleration) acting on a fluid element with density ρ , pressure P , and velocity components v_i . In cylindrical coordinates (ϖ, ϕ, z) the fluid equations (1) and (2) are

$$\frac{\partial \rho}{\partial t} + \frac{1}{\varpi} \frac{\partial}{\partial \varpi}(\varpi \rho v_\varpi) + \frac{1}{\varpi} \frac{\partial}{\partial \phi}(\rho v_\phi) + \frac{\partial}{\partial z}(\rho v_z) = 0 , \quad (3)$$

$$\frac{\partial v_\varpi}{\partial t} + v_\varpi \frac{\partial v_\varpi}{\partial \varpi} + \frac{v_\phi}{\varpi} \frac{\partial v_\varpi}{\partial \phi} + v_z \frac{\partial v_\varpi}{\partial z} - \frac{v_\phi^2}{r} = -\frac{1}{\rho} \frac{\partial P}{\partial \varpi} + f_\varpi , \quad (4)$$

$$\frac{\partial v_\phi}{\partial t} + v_\varpi \frac{\partial v_\phi}{\partial \varpi} + \frac{v_\phi}{\varpi} \frac{\partial v_\phi}{\partial \phi} + v_z \frac{\partial v_\phi}{\partial z} + \frac{v_\varpi v_\phi}{r} = -\frac{1}{\rho \varpi} \frac{\partial P}{\partial \phi} + f_\phi , \quad (5)$$

$$\frac{\partial v_z}{\partial t} + v_\varpi \frac{\partial v_z}{\partial \varpi} + \frac{v_\phi}{\varpi} \frac{\partial v_z}{\partial \phi} + v_z \frac{\partial v_z}{\partial z} = -\frac{1}{\rho} \frac{\partial P}{\partial z} + f_z . \quad (6)$$

Fluid equations like these are generally too difficult to solve directly, so the trick always is to identify which terms determine the major flow characteristics and which terms may be ignored. The physical situation that we are trying to model is steady flow ($\partial/\partial t \rightarrow 0$), where the gas orbits the star. In other words, $v_\varpi = v_z = 0$. Let us assume that the star dominates gravity, which is the only external force; i.e., assume $M_{\text{disk}} \ll M_*$. Then the external force components are

$$f_\varpi = -\frac{GM_* \varpi}{(\varpi^2 + z^2)^{3/2}} , \quad (7)$$

$$f_z = -\frac{GM_* z}{(\varpi^2 + z^2)^{3/2}} . \quad (8)$$

Since gravity exerts no torques ($f_\phi = 0$), the model must be axisymmetric ($\partial/\partial\phi \rightarrow 0$). Using the above restrictions, the fluid equations (3)–(6) simplify enormously. The only non-trivial equations are

$$\frac{1}{\rho} \frac{\partial P}{\partial \varpi} = \frac{v_\phi^2}{\varpi} + f_\varpi, \quad (9)$$

$$\frac{1}{\rho} \frac{\partial P}{\partial z} = f_z, \quad (10)$$

the ϖ - and z -momentum equations, respectively. These are the equations we must solve to determine the structure of a Keplerian disk.

To specify the pressure we introduce the equation of state,

$$P = a^2 \rho, \quad (11)$$

where a is the isothermal sound speed. Note that this equation relates the pressure to a velocity scale. Similarly, gravity is related to a velocity scale, the escape speed, $V_{\text{esc}}^2 = 2GM_*/R$, or equivalently the break-up velocity, $V_{\text{crit}}^2 = V_{\text{esc}}^2/2$ (the break-up velocity is the maximum stellar rotation speed and occurs when the rotation speed equals the orbital speed at the equatorial radius, R). It is very useful to rewrite the fluid equations using such a velocity scale, because we can easily identify which terms dominate the equations. Eliminating P and GM_* in (9) and (10) in favor of a^2 and V_{crit}^2 , we find

$$\frac{v_\phi^2}{\varpi} = \frac{1}{\rho} \frac{\partial(a^2 \rho)}{\partial \varpi} + \frac{V_{\text{crit}}^2 R}{\varpi^2} \left[1 + \left(\frac{z}{\varpi} \right)^2 \right]^{-3/2}, \quad (12)$$

$$\frac{1}{a^2 \rho} \frac{\partial(a^2 \rho)}{\partial z} = -\frac{V_{\text{crit}}^2 R z}{a^2 \varpi^3} \left[1 + \left(\frac{z}{\varpi} \right)^2 \right]^{-3/2}. \quad (13)$$

The interesting thing about (12) is that typically a is a few kms^{-1} , while V_{crit} is a few hundred kms^{-1} . This implies that we may ignore the pressure gradient term in comparison to gravity. Thus we find that the disk rotational velocity is

$$v_\phi = V_{\text{crit}} \sqrt{R/\varpi} [1 + O(a/V_{\text{crit}})^2] \quad (z \ll \varpi). \quad (14)$$

This is Kepler's law, so the disk does indeed simply orbit the star like we initially anticipated; however, there are corrections of order the square of the ratio of the sound speed to critical speed, and these corrections depend on the height z above the equatorial plane (we will soon discover that z/ϖ is of order a/V_{crit}).

To determine the disk density, we must integrate the hydrostatic equilibrium equation (13). For simplicity, we assume the disk is isothermal in the z -direction; i.e., $a = a(\varpi)$. Then the disk density is

$$\begin{aligned} \rho &= \rho_0(\varpi) e^{-(V_{\text{crit}}/a)^2 (R/\varpi) [1 - 1/\sqrt{1 + (z/\varpi)^2}]} \\ &\approx \rho_0(\varpi) e^{-\frac{1}{2}(z/H)^2} \quad (z \ll \varpi), \end{aligned} \quad (15)$$

where ρ_0 is the disk density at the mid-plane ($z = 0$), and the disk scale height is given by

$$H = (a/v_\phi)\varpi . \quad (16)$$

Note that $H \ll \varpi$, which is why we can assume the disk is thin ($z \ll \varpi$). Interestingly, we find that the value of $\rho_0(\varpi)$ is completely undetermined. This is because we can choose to place an arbitrary amount of material in orbit at a given radius, ϖ ; however, once we place that material in orbit, then the vertical structure is exponential with scale height (16). For these reasons, a Keplerian disk can have an arbitrary mass with an arbitrary distribution of its surface density,

$$\Sigma = \int_{-\infty}^{\infty} \rho dz = \sqrt{2\pi} H \rho_0 . \quad (17)$$

Temperature Structure. The scale height is determined by the sound speed, a , which depends on the disk temperature, T_d . So to find the scale height, we must first determine the temperature. Up to this point we have ignored the hydrodynamic energy equation. However, our disk is hydrostatic, so the heating and cooling terms dominate the energy equation, and the disk temperature is determined purely by radiative equilibrium. Let us assume that the disk is optically thick — very much the case for protostellar disks. Consider a differential area element, dA , on top of the disk. The energy that it radiates is $F_{\text{emit}} = \sigma T_d^4$, while the absorbed flux is

$$\begin{aligned} F_{\text{abs}} &= \int_{\frac{1}{2}\Omega_*} I_\nu^* \cos \theta' d\Omega d\nu \\ &= \int_0^\infty d\nu \int_{-\pi/2}^{\pi/2} d\phi \int_0^{\theta_*} d\theta B_\nu \sin^2 \theta \cos \phi \\ &= B \left[\theta_* - \frac{1}{2} \sin(2\theta_*) \right] , \end{aligned} \quad (18)$$

where θ' is the angle between the unit normal to the disk and the line of sight direction (θ, ϕ) toward the star, and $\theta_* = \sin^{-1}(R/\varpi)$ is the angle subtended by the star. Note that we have assumed that the stellar intensity $I_\nu^* = B_\nu(T_*)$ and that we have only integrated over half the solid angle subtended by the star, $\Omega_*/2$, because the optically thick disk occults the light from below the disk; the only stellar radiation that can be absorbed by the disk surface comes from the stellar hemisphere above the disk. In radiative equilibrium, $F_{\text{emit}} = F_{\text{abs}}$, so the disk temperature is

$$\begin{aligned} T_d &= \left(\frac{1}{\pi}\right)^{1/4} T_* \left[\sin^{-1} \left(\frac{R}{\varpi} \right) - \left(\frac{R}{\varpi} \right) \sqrt{1 - \left(\frac{R}{\varpi} \right)^2} \right]^{1/4} \\ &= T_0 \left(\frac{\varpi}{R} \right)^{-3/4} \quad (\varpi \gg R), \end{aligned} \quad (19)$$

where $T_0 = (2/3\pi)^{1/4}T_*$. Substituting this power law dependence for the disk temperature into the scale height (16), we find that

$$H = H_0 \left(\frac{\varpi}{R} \right)^{9/8} . \quad (20)$$

where $H_0 = [a(R)/V_{\text{crit}}]R$. Thus we see that the latitudinal thickness of the disk increases slightly as we go to large radii. In principle this flaring changes the absorbed stellar flux (the unit normal is no longer in the z -direction), which effects both the disk temperature distribution and disk scale height; however, $9/8$ is the exponent often quoted for the disk scale height, so we will ignore this minor inconsistency.

Now that we know the disk temperature distribution, we may now determine the spectral energy distribution as well as the total energy emitted by the disk. For simplicity we assume that the disk is viewed pole-on. Then the observed flux is given by

$$F_\nu = \int_R^\infty B_\nu(\varpi) \frac{2\pi\varpi}{d^2} d\varpi . \quad (21)$$

Consider an IR frequency, ν , in the Rayleigh-Jeans tail of the stellar spectrum. At small radii, the disk is hot, so the disk is also emitting in the Rayleigh-Jeans limit; i.e., $\nu_{\text{max}}(\varpi) \gg \nu$, where $\nu_{\text{max}}(\varpi)$ is the frequency of the Wien peak of the local Planck function in the disk. However at large radii, the disk is cool, so the outer disk emits in the Wien limit. Since the Planck function decreases exponentially at large radii, the outer disk contributes essentially nothing to the flux integral (21). So we approximate $B_\nu(\varpi)$ by

$$B_\nu(\varpi) = \begin{cases} 2kT\nu^2/c^2 & (\varpi < r_{\text{eff}}, \nu_{\text{max}}(\varpi) \gg \nu), \\ (2h\nu^3/c^2)e^{-h\nu/kT} \rightarrow 0 & (\varpi > r_{\text{eff}}, \nu_{\text{max}}(\varpi) \ll \nu), \end{cases} \quad (22)$$

where r_{eff} is defined by $\nu_{\text{max}}(r_{\text{eff}}) = \nu$. Using this approximation, the flux is given by

$$\begin{aligned} F_\nu &= \frac{2\pi R^2}{d^2} \int_R^{r_{\text{eff}}} \frac{2kT\nu^2}{c^2} \frac{\varpi d\varpi}{R^2} \\ &= \frac{8\pi R^2}{5d^2} \left(\frac{2kT_0\nu^2}{c^2} \right) \left[\left(\frac{r_{\text{eff}}}{R} \right)^{5/4} - 1 \right] . \end{aligned} \quad (23)$$

The Wien peak, ν_{max} , is proportional to the disk temperature, so $T_d(r_{\text{eff}}) \propto \nu$. We also know that $T_d \propto \varpi^{-3/4}$, so $r_{\text{eff}} \propto \nu^{-4/3}$. Thus we see that the shape of the spectral energy distribution is given by the power law

$$\nu F_\nu \propto \nu^{4/3} . \quad (24)$$

To find the total energy radiated by the disk, we integrate the emitted flux, F_{emit} , over the disk surface, remembering that the disk emits from both its top and bottom sides. Thus the disk luminosity is

$$L_d = 2 \int_R^\infty (\sigma T_d^4) 2\pi\varpi d\varpi = \frac{1}{4} L_* . \quad (25)$$

Interestingly, the disk absorbs exactly one quarter of the stellar radiation and re-emits it in the IR with a power law SED whose slope is 4/3. For this reason, optically thick disks with no internal energy generation, such as these, are sometimes called reprocessing disks.

Effects of Viscosity. The disks that we have discussed so far are pure Keplerian disks. If the star is to actually accrete matter, then some mechanism must be responsible for removing the excess angular momentum of the disk material; otherwise, the disk fluid elements happily orbit the star forever. Probably the most popular method for generating accretion is to consider viscous effects.

In a Keplerian disk the orbital angular frequency $\Omega = v_\phi/\varpi \propto \varpi^{-3/2} \neq$ constant. Consider a test fluid element orbiting the star. In a reference frame co-rotating with the test element, fluid elements interior to the test element have shorter periods, while those exterior have longer periods. Thus, there is a velocity shear in the ϕ direction. Consequently viscosity exerts a torque on the flow, which transports angular momentum and dissipates energy via viscous heating. The result is that the test element loses energy and angular momentum and drops to a lower-radius-orbit. Therefore viscosity causes accretion.

The only problem is that molecular viscosity is much too small. Steady flow occurs in a viscous diffusion timescale $t_\nu = R^2/\nu$, where ν is the kinematic viscosity. For molecular viscosity, $t_\nu \approx 10^{14}$ yr, much longer than the Hubble time! Shakura and Sunyaev (1973) appealed instead to so-called eddy (or turbulent) viscosity, where $\nu \sim vl$. The turbulence is composed of eddies (vortices) and l is the size scale of the largest eddies, while v is the “turnover” velocity of the eddies. The largest eddies can be at most about the size of the disk scale height, so we set $l = H$. Unfortunately, we don’t really know the velocity, but it is reasonable to assume $v < a$; otherwise, the turbulence would be supersonic and the eddies would fragment into a series of shocks. Since we don’t know the actual velocity, Shakura and Sunyaev introduced a parameter, α , and supposed $v = \alpha a$, where $0 < \alpha < 1$. Thus the viscosity is

$$\nu = \alpha a H . \quad (26)$$

With this value of the viscosity, the viscous diffusion timescale is reduced to $t_\nu \approx 10^6$ yr, which is short enough to be dynamically interesting. Accretion disks that use this prescription for the viscosity are called α -disks.

How are the fluid equations modified by the viscosity? We can still assume that the disk is axisymmetric and that the vertical structure is hydrostatic ($v_z = 0$), but the presence of accretion implies that $v_\varpi \neq 0$. However, unless the accretion rates are unrealistically large, $v_\varpi \ll a$. In other words, the accretion is subsonic. To obtain 1-d fluid equations, we integrate (3)–(6) over ϕ and z . The ϖ - and z -momentum equations are the same as before, so v_ϕ

and ρ are the same as in the pure Keplerian case. The continuity equation (3) becomes

$$0 = \frac{\partial}{\partial \varpi} (2\pi \varpi \Sigma v_{\varpi}) , \quad (27)$$

but the accretion rate $\dot{M} = -2\pi \varpi \Sigma v_{\varpi}$. So the continuity equation implies that the accretion rate through the disk is constant ($d\dot{M}/d\varpi = 0$). Thus the radial velocity component is

$$v_{\varpi} = -\frac{\dot{M}}{2\pi \varpi \Sigma} . \quad (28)$$

The remaining fluid equation is the ϕ -momentum equation (5). This equation now is more complicated because viscosity exerts a torque, which is described by the viscous shear stress tensor, π_{ij} (the shear stress is the force per area perpendicular to $d\mathbf{A}$). Including this shear stress, the ϕ -momentum equation becomes

$$v_{\varpi} \frac{\partial v_{\phi}}{\partial \varpi} + \frac{v_{\varpi} v_{\phi}}{\varpi} = \frac{1}{\rho \varpi^2} \frac{\partial}{\partial \varpi} (\varpi^2 \pi_{\varpi \phi}) , \quad (29)$$

where

$$\pi_{\varpi \phi} = (\alpha a H) \rho \varpi \frac{\partial (v_{\phi}/\varpi)}{\partial \varpi} . \quad (30)$$

(recall that the kinematic viscosity $\nu = \alpha a H$). Multiplying (29) by $\rho \varpi^2$ and integrating over ϕ and z , we find

$$-\dot{M} \frac{\partial}{\partial \varpi} (\varpi v_{\phi}) = \frac{\partial \mathcal{T}}{\partial \varpi} \quad (31)$$

where

$$\mathcal{T} = \int_{-\infty}^{\infty} \varpi \pi_{\varpi \phi} 2\pi \varpi dz = -3\pi \alpha a^2 \varpi^2 \Sigma \quad (32)$$

is the viscous torque. Note that the angular momentum per unit mass $j = \varpi v_{\phi}$, so the ϕ -momentum equation (31) simply expresses that the change in the angular momentum flux is given by the gradient of the viscous torque. Since the continuity equation (27) implies that \dot{M} is constant, we integrate (31) over ϖ to obtain

$$\mathcal{T} = -\dot{M} V_{\text{crit}} \sqrt{\varpi R} + \text{constant} . \quad (33)$$

The actual value of the integration constant is a difficult question to answer — it depends on the details of how material is actually accreted onto the star, so I feel that the best approach is to let its value be arbitrary. Substituting (32) into (33), we solve for the surface density to find

$$\Sigma = \frac{\dot{M} V_{\text{crit}} R^{1/2}}{3\pi \alpha a^2 \varpi^{3/2}} \left(1 \pm \sqrt{R_0/\varpi} \right) , \quad (34)$$

where $\sqrt{R_0}$ is determined by the arbitrary integration constant in (33) and the sign of the integration constant determines whether the plus or minus sign is

used. Although I feel it is best to let R_0 be arbitrary, there is a commonly used value. Recall that as ϖ decreases, the disk rotation speed increases; however, the stellar rotation speed is less than V_{crit} , the Keplerian velocity at the stellar surface. Therefore, v_ϕ attains a maximum value before decreasing down to the stellar rotation speed (assuming a smooth transition in a viscous boundary layer). At the location where the orbital frequency v_ϕ/ϖ is maximum, the shear stress $\pi_{\varpi\phi}$ vanishes (see (30)), so $\mathcal{T} = 0$ near the stellar surface. This implies that $R_0 \approx R$ and the minus sign in (34) is employed. Note that $\Sigma \rightarrow 0$ and $v_\varpi \rightarrow \infty$ at $\varpi = R_0$, so the fundamental assumptions we used in deriving the fluid equations break down at this location. This is another reason why I think the value of R_0 is a tricky question to answer.

In principle the accretion rate, \dot{M} , is determined by the disk surface density, Σ , and the viscosity parameter, α . However, equation (34) tells us that the radial dependence of the surface density is not arbitrary; starting from an arbitrary distribution of material, the surface density will adopt the functional form (34) after a viscous diffusion timescale. We have now completed the hydrodynamic description of the accretion disk. In summary,

$$v_\phi = V_{\text{crit}} \sqrt{R/\varpi} , \quad (35)$$

$$v_\varpi = -\frac{3}{2} \left(\frac{\alpha a^2}{V_{\text{crit}}} \right) \frac{\sqrt{\varpi/R}}{1 \pm \sqrt{R_0/\varpi}} , \quad (36)$$

$$\Sigma = \frac{\dot{M} V_{\text{crit}} R^{1/2}}{3\pi\alpha a^2 \varpi^{3/2}} \left(1 \pm \sqrt{R_0/\varpi} \right) , \quad (37)$$

$$\rho = \frac{\Sigma}{\sqrt{2\pi}H} e^{-\frac{1}{2}(z/H)^2} , \quad (38)$$

$$H = (a/v_\phi)\varpi . \quad (39)$$

Spectral Energy Distribution. Although we have found the velocity and density of the disk, we must still determine the disk temperature, which will govern both the spectral energy distribution of the emitted flux, and the pressure scale height vs. radius. Again the disk temperature is determined by the condition of radiative equilibrium; however, owing to the viscous energy dissipation within the disk, viscosity produces an additional source of disk heating, which depends on the accretion rate. If the accretion rate is large, the viscous energy dissipation dominates the absorbed stellar flux. In this case the disk is no longer a reprocessing disk, but is now called an active accretion disk. The viscous energy generation per unit volume is given by

$$\frac{dE}{dV} = -\pi_{ik} \frac{\partial v_i}{\partial x_k} = \pi_{\varpi\phi} \varpi \frac{\partial(v_\phi/\varpi)}{\partial \varpi} . \quad (40)$$

Integrating over z , we find that the flux to be radiated by the surface of an active accretion disk is

$$\sigma T_d^4 = \frac{1}{2} \frac{dE}{dA} = \frac{1}{2} \int_{-\infty}^{\infty} \pi_{\varpi\phi} \varpi \frac{\partial(v_\phi/\varpi)}{\partial \varpi} dz$$

$$\begin{aligned}
&= \frac{\mathcal{T}}{4\pi\varpi} \frac{\partial(v_\phi/\varpi)}{\partial\varpi} \\
&= \frac{3}{8\pi} \frac{GM_*\dot{M}}{\varpi^3} \left(1 \pm \sqrt{R_0/\varpi}\right) \quad (41)
\end{aligned}$$

(the factor 1/2 multiplying dE/dA arises because the disk radiates from both sides). Interestingly, we find that $T_d \propto \varpi^{-3/4}$, which is the same as for reprocessing disks. Therefore the SEDs of active accretion disks have the same slope ($\nu F_\nu \propto \nu^{4/3}$) as reprocessing disks, so one cannot distinguish between them merely on the basis of their slope. However, if the disk is an active accretion disk, then its luminosity will exceed one quarter L_* , the reprocessing result. The total accretion luminosity is

$$L_{\text{acc}} = \int_R^\infty (2\sigma T_d^4) 2\pi\varpi d\varpi = \frac{1}{2} \frac{GM_*\dot{M}}{R} . \quad (42)$$

This is one half the potential energy change of the accreted matter. What happens to the other half? Recall that the kinetic energy of the orbiting fluid elements equals one half their potential energy change (virial theorem). However, if the star is not rotating at the Keplerian speed (T Tauri stars have rotation speeds much less than V_{crit}) then there will be a large velocity shear between the disk and the stellar surface. Thus the excess kinetic energy will be dissipated in a (turbulent) boundary layer between the star and the disk. Since the surface area of this region is small (compared to the stellar surface area) and the radiated energy is comparable to (or greater than) the stellar luminosity, the temperature of this boundary layer will be much larger than the stellar effective temperature. As a result, this hot boundary layer will produce a UV excess. Note that both the IR and UV excesses are correlated. Such UV excesses are observed in YSOs and they are indeed correlated with the IR excess.

I should also mention that there is an alternate scenario to the equatorial boundary layer that is becoming quite popular. If the star has a large dipolar magnetic field, then close to the stellar surface, the magnetic pressure can support the disk, halting the accretion and truncating the disk at some inner radius. However material cannot continue to build up at this truncation radius. Instead the material “climbs” upward onto the magnetic field lines. A portion of this material is ejected from the system, producing bipolar jets, while the remainder is accreted onto a high latitude ring around the magnetic poles. The accretion shock dissipates the kinetic energy of the accreted matter, so there is again a high temperature region that produces a UV excess that is correlated with the accretion rate and IR excess. One new feature of this model is that the magnetic field permits the disk to exert a torque on the star via the magnetic stresses. This torque forces the star to co-rotate with the material at the disk truncation radius (determined by the strength of the stellar magnetic field). In other words, the star rotates with the Keplerian frequency at the disk truncation radius, which can be significantly less than

V_{crit} . Thus this model naturally explains why T Tauri stars can be slowly rotating.

3.2 Outflow Disks

As I mentioned in the introduction, there is quite substantial evidence that disks (equatorial density enhancements) exist within stellar winds. Although binarity may certainly play a role, the frequency of disks is probably too large for all disks to be produced by binary stars, so it is desirable to explore the possible mechanisms for forming disks in the winds of single stars. One of the best known examples of stars that have both disks and winds are Be stars, which are rapidly rotating stars. Since rotation is such an obvious candidate, let us explore the effects that rotation can have on a stellar wind. As a starting point, we note that supergiants have stronger winds than dwarfs. Primarily this is because the surface gravity of supergiants is much smaller than that of dwarfs, so the mass flux is larger. Rotation also reduces the effective surface gravity, so we expect that rotation will increase the mass flux. To study the effects of rotation, let us investigate the mass loss through a streamtube; i.e., a one-dimensional model.

1-D Effects of Rotation. In spherical polar coordinates (r, θ, ϕ) , the fluid equations are

$$\begin{aligned} \frac{\partial \rho}{\partial t} + \frac{1}{r^2} \frac{\partial}{\partial r}(\rho r^2 v_r) + \frac{1}{r \sin \theta} \frac{\partial}{\partial \theta}(\rho \sin \theta v_\theta) \\ + \frac{1}{r \sin \theta} \frac{\partial}{\partial \phi}(\rho v_\phi) = 0 , \end{aligned} \quad (43)$$

$$\frac{\partial v_r}{\partial t} + v_r \frac{\partial v_r}{\partial r} + \frac{v_\theta}{r} \frac{\partial v_r}{\partial \theta} + \frac{v_\phi}{r \sin \theta} \frac{\partial v_r}{\partial \phi} - \frac{v_\theta^2 + v_\phi^2}{r} = -\frac{1}{\rho} \frac{\partial P}{\partial r} + f_r , \quad (44)$$

$$\begin{aligned} \frac{\partial v_\theta}{\partial t} + v_r \frac{\partial v_\theta}{\partial r} + \frac{v_\theta}{r} \frac{\partial v_\theta}{\partial \theta} + \frac{v_\phi}{r \sin \theta} \frac{\partial v_\theta}{\partial \phi} + \frac{v_r v_\theta}{r} \\ - \frac{\cot \theta v_\phi^2}{r} = -\frac{1}{\rho r} \frac{\partial P}{\partial \theta} + f_\theta , \end{aligned} \quad (45)$$

$$\begin{aligned} \frac{\partial v_\phi}{\partial t} + v_r \frac{\partial v_\phi}{\partial r} + \frac{v_\theta}{r} \frac{\partial v_\phi}{\partial \theta} + \frac{v_\phi}{r \sin \theta} \frac{\partial v_\phi}{\partial \phi} + \frac{v_r v_\phi}{r} \\ + \frac{\cot \theta v_\theta v_\phi}{r} = -\frac{1}{\rho r \sin \theta} \frac{\partial P}{\partial \phi} + f_\phi \end{aligned} \quad (46)$$

Gravity is radial ($f_\theta = f_\phi = 0$), so again we assume steady axisymmetric flow ($\partial/\partial t \rightarrow 0$, $\partial/\partial \phi \rightarrow 0$). Since we are interested in studying a simple 1-d model where the rotation has non-trivial effects, let us examine the flow in the equatorial plane, $\theta = \pi/2$. Under reflection about the equator, ρ , P , v_r , and v_ϕ are all even, while v_θ is odd, so

$$\frac{\partial v_r}{\partial \theta} = \frac{\partial v_\phi}{\partial \theta} = \frac{\partial \rho}{\partial \theta} = \frac{\partial P}{\partial \theta} = v_\theta = \frac{\partial v_\theta}{\partial r} = 0 . \quad (47)$$

In the equatorial plane, the θ -momentum equation (45) is trivial, and the continuity, r -, and ϕ -momentum equations (43), (44), and (46) become

$$\frac{1}{r^2} \frac{\partial}{\partial r} (\rho r^2 v_r) + \frac{\rho}{r} \frac{\partial v_\theta}{\partial \theta} = 0 , \quad (48)$$

$$v_r \frac{\partial v_r}{\partial r} - \frac{v_\phi^2}{r} = -\frac{1}{\rho} \frac{\partial P}{\partial r} + f_r , \quad (49)$$

$$v_r \frac{\partial v_\phi}{\partial r} + \frac{v_r v_\phi}{r} = 0 . \quad (50)$$

Near the equator v_θ is small, so assume $\partial v_\theta / \partial \theta \ll (1/r\rho) \partial(\rho r^2 v_r) / \partial r$ (however, note that this assumption is not always very good). In this case, the continuity equation (48) becomes $\partial(\rho r^2 v_r) / \partial r = 0$, which implies

$$\rho r^2 v_r = \text{constant} = \frac{\dot{M}}{4\pi} , \quad (51)$$

which is the same as a spherically symmetric wind. The ϕ -momentum equation (50) is also an exact differential, so

$$v_\phi = V_{\text{rot}} \left(\frac{R}{r} \right) . \quad (52)$$

In other words the specific angular momentum $j_z \equiv r v_\phi$ is constant (because there are no torques about the z -axis in an axisymmetric model). Substituting (51) and (52) into the radial momentum equation (49), we obtain the wind equation

$$v_r \frac{dv_r}{dr} - \frac{V_{\text{rot}}^2 R^2}{r^3} = -a^2 \frac{d \ln \rho}{dr} - \frac{GM_*}{r^2} + \frac{\sigma_e L}{4\pi r^2 c} \left\{ 1 + kf \left[\frac{(dv/dr)}{\sigma_e \rho v_{\text{th}}} \right]^\alpha \right\} . \quad (53)$$

We have assumed that the wind is isothermal ($P = a^2 \rho$) and that the external forces are gravity and the radiation force. For the radiation force, we use line absorption as parameterized by Castor et al. (1975, also see second contribution Lamers, this Volume). Friend and Abbott (1986) solved this equation (53) numerically and obtained the following fits to their solution:

$$v_\phi = V_{\text{rot}} \left(\frac{R}{r} \right) , \quad (54)$$

$$v_r = v_\infty \left(1 - \frac{R}{r} \right)^\beta \quad (r > r_s), \quad (55)$$

$$v_\infty = 2.2 \left(\frac{\alpha}{1 - \alpha} \right) \left(\frac{v_{\text{esc}}}{10^3 \text{ km s}^{-1}} \right)^{0.2} \left(1 - \frac{V_{\text{rot}}}{V_{\text{crit}}} \right)^{0.35} , \quad (56)$$

$$\dot{M} = \frac{1}{2} \dot{M}_{\text{CAK}} \left(\frac{v_{\text{esc}}}{10^3 \text{ km s}^{-1}} \right)^{-0.3} \left(1 - \frac{V_{\text{rot}}}{V_{\text{crit}}} \right)^{-0.43} , \quad (57)$$

where $\beta = 0.8$, and r_s is the sonic radius. Note that as the rotation rate increases, the terminal speed, v_∞ , decreases. This is because the terminal speed of the wind is set by the local value of the escape speed, which is decreased by rotation. Similarly in a radiatively driven wind, we expect the momentum transfer $L/c \approx Mv_\infty$. So as the terminal speed decreases, we expect a corresponding increase in the mass loss rate. Since at large radii

$$\rho(\theta) = \frac{\dot{M}(\theta)}{4\pi r^2 v_\infty(\theta)} \quad (58)$$

(in a 1-d model), the decrease in the escape speed as a function of latitude implies that both these effects combine to increase the equatorial density. Unfortunately to be large enough to produce the dense disks that are observed around Be stars, the rotation rate must be quite close to the critical velocity, but Be stars only rotate at about 75% the critical speed. We conclude that some other effect is required to increase the equatorial densities of the wind.

Recall that mass conservation tells us that the density of material flowing through a streamtube is inversely proportional to its area. The cross sectional area of the streamtube depends on the location of the adjacent streamlines, so in addition to the mass loss rate and terminal speed, the geometry of the streamlines also plays a role in determining the density.

What do the equatorial streamlines look like? We can obtain a differential equation for the position by dividing v_ϕ by v_r ,

$$\frac{d\phi}{dr} = \frac{\dot{\phi}}{\dot{r}} = \frac{v_\phi}{rv_r} \quad (59)$$

Integrating outward from the sonic radius,

$$\frac{r_s}{R} = \left[1 - \left(\frac{a}{v_\infty} \right)^{1/\beta} \right]^{-1}, \quad (60)$$

the differential equation (59) has the solution

$$\phi = \frac{V_{\text{rot}}}{(1-\beta)v_\infty} \left[\left(1 - \frac{R}{r} \right)^{1-\beta} - \left(\frac{a}{v_\infty} \right)^{(1-\beta)/\beta} \right]. \quad (61)$$

Initially the streamline is almost tangent to the stellar surface. As the fluid travels (initially sideways), it begins to be accelerated outward, so the streamline deflects outward in the radial direction (see Fig. 2). As $r \rightarrow \infty$, $\phi \rightarrow \phi_{\text{max}}$, where

$$\phi_{\text{max}} = \frac{V_{\text{rot}}}{(1-\beta)v_\infty} \left[1 - \left(\frac{a}{v_\infty} \right)^{(1-\beta)/\beta} \right]. \quad (62)$$

Thus the streamline eventually becomes purely radial with a maximum azimuthal deflection ϕ_{max} .

We have now determined the shape of the streamlines in a 1-d model in the equatorial plane, but up to this point we have ignored the 2-d (latitudinal) effects on the streamline locations.

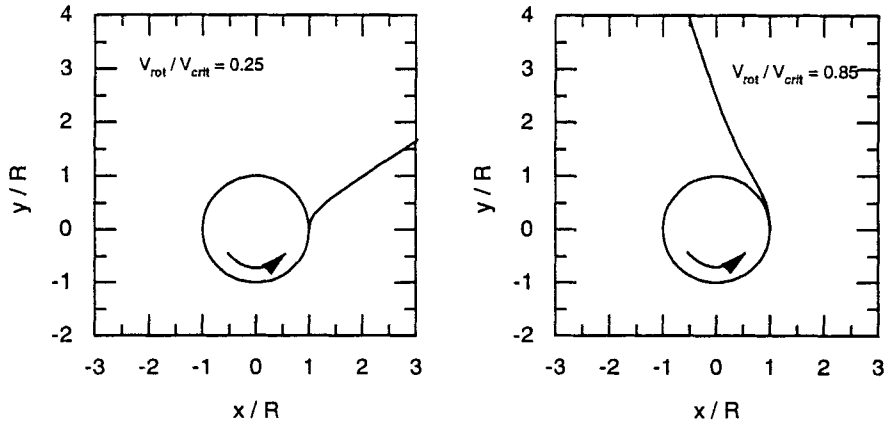


Fig. 2. Equatorial Streamlines. Shown are the streamlines from the Friend and Abbott (1986) model of the equatorial outflow for two different stellar rotation rates. Note that for slow rotation (left panel) the streamline is rapidly accelerated outward, while for rapid rotation rates (right panel) the streamline orbits farther around the star before being accelerated outward

2-D Effects of Rotation. In a rotating two-dimensional axisymmetric model, the streamlines do not spiral outward on surfaces (cones) of constant latitude, as is often assumed. Instead they bend toward the equator due to the centrifugal and Coriolis forces. To determine the structure of the wind, we must solve the fluid equations (1) and (2) and find the location of the resulting streamlines. These equations are quite difficult; however, an enormous simplification occurs in the supersonic portion of the flow.

Supersonic Limit. Consider the forces acting on the fluid. For an axisymmetric geometry, the pressure gradient only has r - and θ -components. Although the θ -component is large at the stellar surface (to enforce hydrostatic equilibrium), it drops rapidly beyond the sonic radius, r_s . The other forces are gravity and radiation, which are central forces. Thus, beyond the sonic point, there are no external torques, so both the θ - and ϕ -components of the velocity are determined by angular momentum conservation. This implies that v_θ and v_ϕ are $O(V_{\text{rot}}R/r)$. Typically for an early-type star, the rotation speed, V_{rot} , is highly supersonic. So, as long as $r \gg r_s$ and $r \gg R$, all three velocity components are highly supersonic.

Note that the left hand side of the momentum equation (2) is $O(v^2)$, but the pressure gradient on the right hand side is $O(a^2)$. As long as all three velocity components $v_r, v_\theta, v_\phi \gg a$, we may completely ignore the pressure gradient. If there are no pressure forces, there are no interactions between the individual fluid elements. This implies that the streamlines are free particle trajectories corresponding to the external forces.

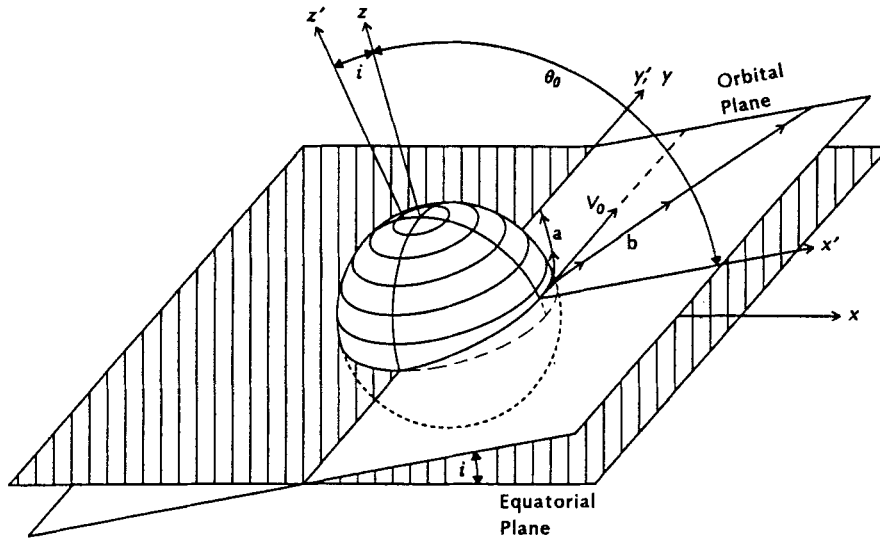


Fig. 3. Orientation of the orbital plane for a streamline originating at a polar angle θ_0 . The streamline labeled (a) is a case with a high rotation rate and the streamline labeled (b) denotes a low rotation rate. (Figure from Bjorkman and Cassinelli 1993)

Orbital Plane. Much can be learned about the location of the streamline by recalling that gravity and radiation are central forces. Therefore, the *total* angular momentum is constant along a streamline. So just like a Keplerian orbit, the streamline lies in an orbital plane, containing the center of the star, the initial location, and velocity vector, V_0 (see Fig. 3). To find the streamline trajectories, we simply rotate the 1-d solution in the equatorial plane (Fig. 2) up to the initial latitude of the streamline and adjust the rotation velocity by $V_{\text{rot}} \rightarrow V_{\text{rot}} \sin \theta_0$.

Figure 3 shows two trajectories labeled (a) and (b), that correspond to different initial conditions. Trajectory (a) has a slow initial acceleration and occurs when there is a large rotation rate. Trajectory (b) has a fast initial acceleration and occurs when there is a slow rotation rate. Note that as trajectory (a) orbits around the star, it has a decreasing altitude, z , and eventually crosses the equator. Conversely, trajectory (b) deflects outward and has an increasing altitude.

The curvature of the streamline depends on the forces and is most easily understood in the non-rotating reference frame. In this frame, there are only two forces, and each is in the radial direction; gravity points inward, and the radiation force points outward. To produce a net force with a negative z -component, we must have $F_{\text{grav}} > F_{\text{rad}}$. Thus, the equator-crossing trajectory (a) corresponds to initial conditions where the force of gravity exceeds the

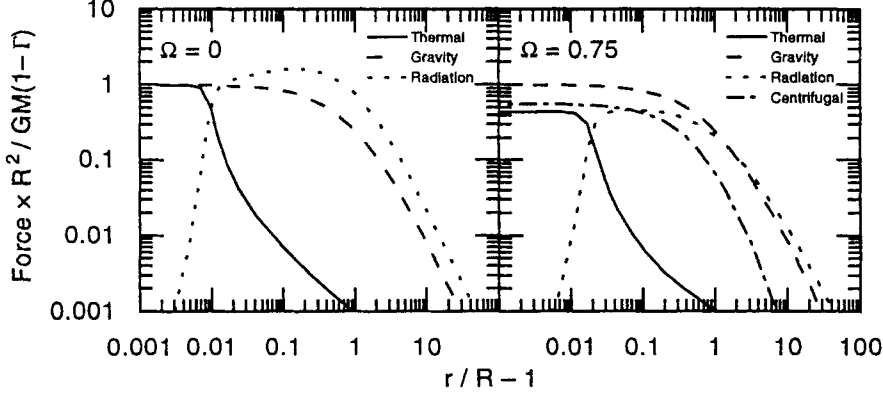


Fig. 4. Forces vs. radius in a Friend and Abbott (1986) 1-d equatorial rotating wind model that has $v_\infty/v_{\text{esc}} = 1.4$. Shown are a non-rotating case, $\Omega \equiv V_{\text{rot}}/V_{\text{crit}} = 0$, and a rapidly rotating case with $\Omega = 0.75$. (Figure from Bjorkman and Cassinelli 1993)

radiation force, and trajectory (b) occurs when the radiation force is larger than gravity.

Forces in Rotating Winds. The location where the radiation force exceeds gravity depends on the subtle interaction of the radiation force with the velocity gradient, dv_r/dr . In the orbital plane, the r -component of the momentum equation is

$$v_r \frac{dv_r}{dr} = -\frac{a^2}{\rho} \frac{d\rho}{dr} + F_{\text{rad}} - F_{\text{grav}} + \frac{v_\phi^2 + v_\theta^2}{r}. \quad (63)$$

The last term on the right hand side is the centrifugal force, so the velocity gradient, dv_r/dr , is determined in the *rotating* reference frame. To maintain an outward flow, a line-driven wind must constantly accelerate to higher velocities, so that there is always a supply of unattenuated stellar photons. Since the radiation force depends on dv_r/dr (see (53)), the velocity adjusts until the radiation force maintains a positive dv_r/dr .

Figure 4 compares the forces for rotating and non-rotating winds. In the non-rotating case, $\Omega \equiv V_{\text{rot}}/V_{\text{crit}} = 0$, thermal pressure supports the flow out to the sonic radius, $r_s \approx 1.01R$. Beyond the sonic point, the thermal pressure support is negligible; therefore, the radiation force must increase until it is larger than gravity (so that dv_r/dr is positive). Note that the radiation force exceeds gravity at all locations beyond the sonic point. In the rapidly rotating case, $\Omega = 0.75$, most of the support is instead from the centrifugal force. When the thermal pressure support is lost at the sonic point, the radiation force again increases to supply the missing force, but

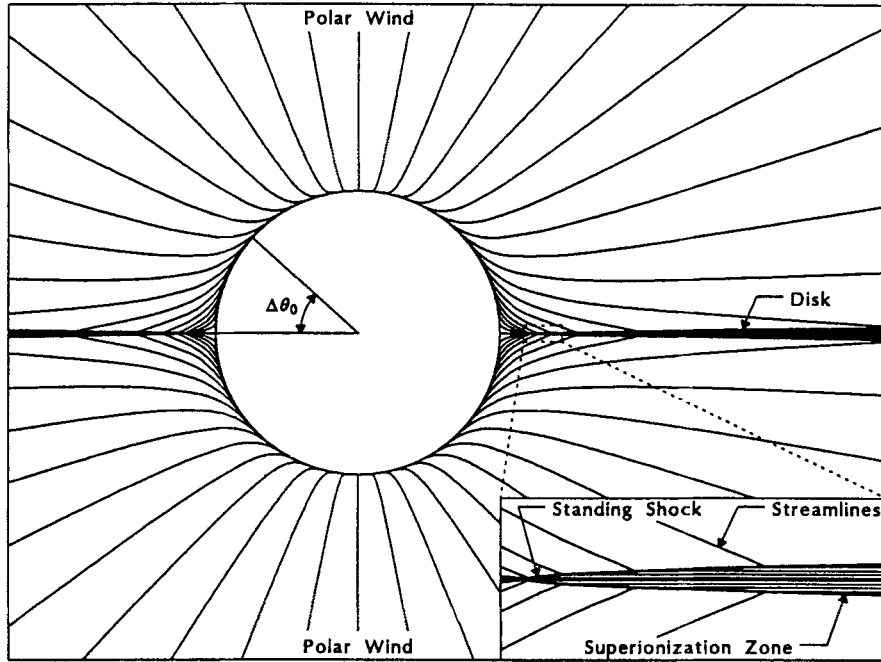


Fig. 5. Diagram of the stellar wind and wind-compressed disk. Shown are the wind streamlines, which fall toward the equator. The expanded view shows the standing shocks that form above and below the disk. (Figure from Bjorkman and Cassinelli 1993)

because of the large centrifugal support, the required amount is smaller than gravity. The centrifugal support falls as $1/r^3$ (much slower than the thermal pressure) and it is not until the centrifugal support is lost that the radiation force finally exceeds gravity at about $3R$. Thus there is a region between the sonic point and about $3R$ where gravity is larger than the radiation force. Within this region, the streamlines fall toward the equator, and if this region is large enough, the streamlines attempt to cross the equator.

Streamlines. To build a model for the entire two-dimensional structure of the wind, we calculate the shape of the streamlines as a function of initial latitude on the surface of the star. If the star is not rotating, then the streamlines are entirely in the radial direction. On the other hand, if the star is rotating, then the streamlines fall toward the equator between the sonic point and the location where the radiation force exceeds gravity (see Fig. 5). Near the pole, the rotation velocity is small, so the streamlines are radial. But for streamlines closer to the equator, the rotation velocity is higher, the region where gravity exceeds the radiation force is larger, and the streamlines

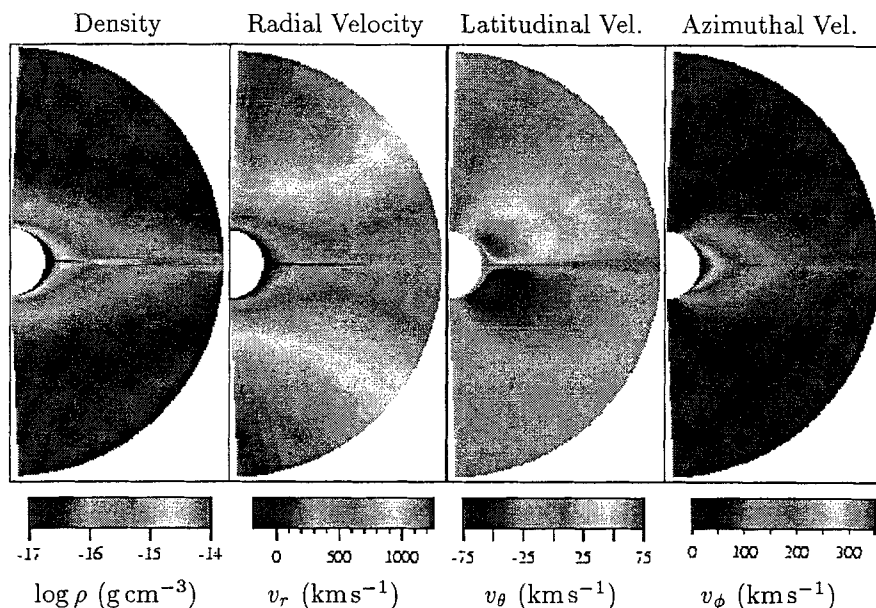


Fig. 6. Time-dependent numerical simulation of the wind-compressed disk for a B2.5 V star with $V_{\text{rot}} = 350 \text{ km s}^{-1}$. Shown (from left to right) are the density and the r -, θ -, and ϕ -velocity components. (Figure from Owocki et al. 1994)

fall farther before turning in the radial direction. If the equatorial rotation rate of the star, V_{rot} , is above a threshold value, V_{th} , then for latitudes less than $\Delta\theta_0$, the streamlines attempt to cross the equator (see Fig. 5).

When the streamlines cross the equator, they collide with the streamlines from the opposite hemisphere of the star. Streamlines cannot cross because the density diverges. Instead, the increase in density causes a large pressure gradient, and since the flow velocity (perpendicular to the equator) is supersonic, a pair of shocks form above and below the equator. The pressure at the equator must balance the ram pressure of the wind, so between the shocks there is a dense equatorial wind-compressed disk.

3.3 Time-Dependent Hydrodynamics

This Wind-Compressed Disk (WCD) model, which was developed by Bjorkman and Cassinelli (1993, hereafter BC), is only valid in the supersonic region of the flow, and thus requires initial conditions at the sonic point. To obtain these initial conditions, BC assumed that the subsonic expansion is in the radial direction; i.e., θ is constant and $v_\theta = 0$ for $r < r_s$. Another approximation BC employed was to assume a shape for the WCD shock surface, because the actual shape depends on the detailed dynamics of the disk.

To assess the validity of the WCD approximations and to examine in detail the dynamics of the disk, Owocki et al. (1994, hereafter OCB) developed a 2-d time-dependent numerical simulation of the wind from a rotating star. Aside from properly including shocks and gas pressure, OCB also included an oblate lower boundary condition that accounts for the rotational distortion of the star. Starting with a wind that is initially spherically symmetric, OCB find that, after about 50000 sec, the time-dependent solution relaxes to a steady-state solution with a thin equatorial disk (see Fig. 6).

The qualitative appearance of the disk agrees quite well with that predicted by BC. The thickness of the disk is about 3° in latitude (BC predicted $0^\circ5$), and the disk density is about two orders of magnitude higher than the density at the pole, which is somewhat lower than predicted by BC. Interestingly, a weak disk persists even at rotation rates below the rotation threshold predicted by BC.

There are two fundamental differences between OCB's results and the predictions by BC. First, the disk is not detached from the stellar surface (compare Figs. 5 and 6). Second, there is a stagnation point in the disk. Exterior to the stagnation point, the disk material flows outward. Interior to the stagnation point, the material falls back onto the stellar surface. Thus there is simultaneous outflow and infall in the disk.

Rotation Threshold. The disk forms only when the star is rotating faster than the equator-crossing threshold, V_{th} . This disk formation threshold depends on the ratio of the terminal speed of the wind to escape speed of the star, v_∞/v_{esc} . This is because a faster wind implies a larger radiative acceleration, which decreases the size of the region where the streamlines fall toward the equator. To compensate, the stellar rotation rate must be increased. Thus the disk formation threshold increases with increasing v_∞/v_{esc} .

Figure 7 shows both the observed and theoretical values of the wind terminal speed ratio, v_∞/v_{esc} , as a function of main-sequence spectral type. The observed and theoretical values mostly agree for O stars; however, for late B stars, the observed terminal speeds are significantly lower than the theoretical terminal speeds. The observed terminal speeds of B stars are estimated from the edge-velocities of the C IV and Si IV line profiles (K.S. Bjorkman 1989). Typically these profiles are quite weak, so it is quite likely that the observed B star terminal speeds are systematically underestimated. On the other hand, there are many uncertainties in the theoretical calculations. At this time, it is unclear which terminal speeds are more reliable for B stars.

Using the terminal speeds shown in Fig. 7, we find the disk formation threshold, shown in Fig. 8, as a function of spectral type. Assuming that the winds of B stars are radiatively-driven, Fig. 8 indicates that any B star that rotates faster than the rotation threshold will have a thin equatorial disk, which could be responsible for the Be phenomena. Note that the rotation threshold has a minimum at B2, if one uses the theoretical terminal speeds.

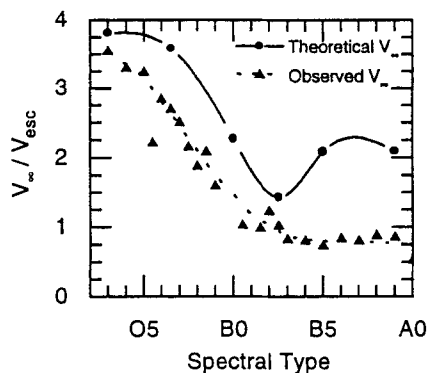


Fig. 7. Ratio of wind terminal speed to stellar escape speed vs. spectral type. The solid curve is obtained from theoretical calculations of the terminal speed, and the dashed curve is from observations. (Figure from Bjorkman and Cassinelli 1993)

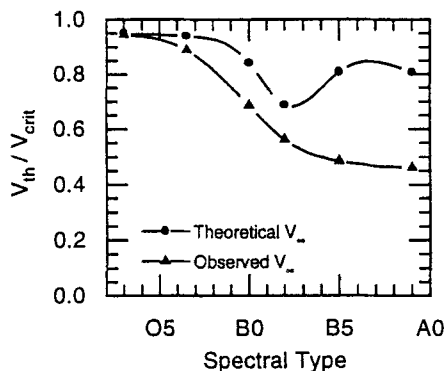


Fig. 8. Disk formation threshold vs. spectral type. The curve with filled circles is the threshold obtained using the theoretical values of the terminal speed, and the curve with triangles employs the observed terminal speeds.

This minimum may qualitatively explain the frequency distribution of Be stars; i.e., why Be stars are most common at a spectral type of B2.

Shock Temperature and Disk Density. To investigate more quantitatively whether or not the WCD model can explain the Be phenomena, we must determine the properties of the disk. For a concrete example, we consider a B2 V star with a mass-loss rate of $10^{-9} M_{\odot} \text{ yr}^{-1}$ and a terminal speed ratio $v_{\infty}/v_{esc} = 1$. The WCD shock temperature is determined by the shock velocity, which is approximately the θ -component of the velocity of the wind when it enters the disk. The shock temperature, shown in Fig. 9, is typically a few 10^5 K, which is large enough to produce C IV and Si IV by collisional ionization. Thus the disk is bounded above and below by a thin superionization layer. In addition to the shocks that produce the disk, there is also an accretion shock (due to the disk inflow) in the equator at the stellar surface. The disk infall velocities are typically a few hundred km s^{-1} , so the accretion shock can have temperatures of order 10^6 K and may produce soft X-rays. Note that the temperature due to the accretion shock is not shown in Fig. 9. Since all of these shocks can produce superionization, they may be responsible for the excess superionization of Be stars compared to normal B stars (Grady et al. 1987, 1989).

The disk density may be estimated by equating the gas pressure in the disk with the ram pressure of the wind entering the disk. Assuming that the shocked material that enters the disk cools to the same radiative equilibrium temperature as the stellar wind (the shock cooling length is thinner than the disk), we find $\rho_{\text{disk}} \approx \rho_{\text{wind}}[1 + (v_{\theta}/a)^2]$, where the right hand side is

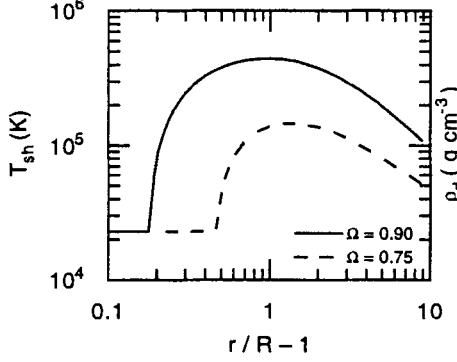


Fig. 9. Shock temperature as a function of radius for two values of the rotation rate, Ω . Note the increase in the maximum shock temperature as the rotation rate increases.

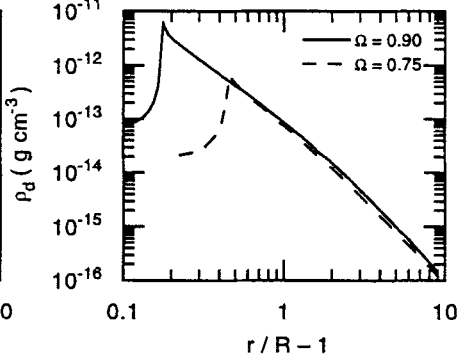


Fig. 10. Disk density as a function of radius for two values of the rotation rate, Ω . Note that the slope of the curve indicates that the density falls as $(r/R - 1)^{-3}$.

evaluated in the wind just prior to the shock that forms the disk. The disk density is shown in Fig. 10. Note that the disk density is $\rho \approx \rho_0 (r/R - 1)^{-n}$, where $\rho_0 \approx 10^{-13} \text{ g cm}^{-3}$ and $n \approx 3$.

4 Radiation Transfer in Axisymmetric Systems

Now that we have developed a theory of circumstellar disk formation, we would like to be able to test that theory against observations. To do so, we must be able to calculate observational properties of our models. Unfortunately our models are not spherically symmetric, so we are faced with the task of performing radiation transfer in an axisymmetric geometry. True radiation transfer models (those that include scattering, line transfer, and non-LTE opacities) in two and three dimensions are still in their infancy, and most employ several practical approximations to make the problem computationally tractable. However, before discussing some of these methods, let me suppose that one already knows the value of the source function. In this situation, one can directly integrate the transfer equation to find the specific intensity, I_ν . Then to determine the observed flux, we integrate the emergent intensity, I_ν^{emerg} , over the surface area of the sky; i.e.,

$$\begin{aligned} F_\nu &= \int I_\nu^{\text{emerg}} d\Omega = \int I_\nu^{\text{emerg}} \frac{dA}{d^2} \\ &= \left(\frac{R}{d}\right)^2 \int I_\nu^{\text{emerg}} q dq d\alpha, \end{aligned} \quad (64)$$

where q and α are the impact parameter and position angle of the line of sight (note that q is measured in stellar radii), and d is the distance to

the star. The rotation axis is inclined by an angle i with respect to the observer's line of sight, so the coordinate transformations from the line of sight cylindrical coordinates (q, α, z) to the observer's Cartesian coordinates (x, y, z) and stellar Cartesian coordinates (x_*, y_*, z_*) are given by

$$x = q \cos \alpha , \quad (65)$$

$$y = q \sin \alpha , \quad (66)$$

$$x_* = -q \sin \alpha \cos i + z \sin i , \quad (67)$$

$$y_* = q \cos \alpha , \quad (68)$$

$$z_* = q \sin \alpha \sin i + z \cos i . \quad (69)$$

Again we are using dimensionless coordinates (in units of stellar radii) with the observer at $z = \infty$, and we have oriented the observer's y -axis along the projected stellar rotation axis.

We must integrate the transfer equation along the line of sight to evaluate the emergent intensity. Recall the formal solution to the transfer equation, which implies

$$I_\nu^{\text{emerg}} = \int_0^{\tau_\nu^{\text{max}}} e^{-\tau_\nu} S_\nu d\tau_\nu + \begin{cases} e^{-\tau_\nu^{\text{max}}} I_\nu^* & (q < 1), \\ 0 & (q > 1), \end{cases} \quad (70)$$

$$\tau_\nu(z) = - \int_\infty^z \kappa_\nu dz' . \quad (71)$$

Computationally it is very inefficient to re-evaluate (71) for every point in the integrand of (70), so it is much more efficient to solve the transfer equation by recasting (70) and (71) as the following pair of simultaneous first order differential equations:

$$\frac{d\tau_\nu}{dz} = -\kappa_\nu , \quad (72)$$

$$\frac{dI_\nu}{dz} = -e^{-\tau_\nu} \kappa_\nu S_\nu , \quad (73)$$

with the boundary conditions $\tau_\nu = I_\nu = 0$ at $z = \infty$. Note that $I_\nu(z)$ is not the value of the specific intensity at z ; it is the contribution to the emergent intensity between z and ∞ . We can avoid evaluating the exponential in (73) if we define an attenuation factor $t_\nu \equiv e^{-\tau_\nu}$, then (72) and (73) become

$$\frac{dt_\nu}{dz} = \kappa_\nu t_\nu , \quad (74)$$

$$\frac{dI_\nu}{dz} = - \left(\frac{dt_\nu}{dz} \right) S_\nu , \quad (75)$$

with boundary conditions $t_\nu = 1$ and $I_\nu = 0$ at $z = \infty$. Some lines of sight intersect the star while others do not, so (74) and (75) are to be integrated from $z = \infty$ to $z = z_{\text{min}}$, where

$$z_{\text{min}} = \begin{cases} \sqrt{1 - q^2} & (q < 1), \\ -\infty & (q > 1). \end{cases} \quad (76)$$

The emergent intensity is then given by

$$I_{\nu}^{\text{emerg}} = I_{\nu}(z_{\min}) + \begin{cases} t_{\nu}(z_{\min})I_{\nu}^* & (q < 1), \\ 0 & (q > 1). \end{cases} \quad (77)$$

Note that the differential equations (74) and (75) are in the form of an initial value problem, so we can use a simultaneous first order ODE numerical integrator to solve them. I highly recommend the Bulirsch-Stoer integrator in *Numerical Recipes* (Press et al. 1986). Their algorithm uses an adaptive step size, where the step size is automatically adjusted to maintain a given error tolerance. A problem that one frequently encounters when integrating the transfer equation in disk geometries is that the opacity varies over several orders of magnitude and can be highly peaked in the vicinity of the disk. This is the primary reason I prefer to use an adaptive step size differential equation integrator instead of the more usual Feautrier method. The Feautrier method solves the transfer equation using a two point boundary value (2nd order) ODE. Consequently, the solution algorithm usually uses a finite difference scheme to solve the transfer equation. One problem with such finite difference methods is how to set the grid size to achieve a given error tolerance. In practice one usually just doubles the number of points until the answer converges. However, unless one has some physical guidance for how to set the *relative* sizes of the grid cells (such as choosing the cell size to obtain constant optical depth spacing — a difficult problem in multiple dimensions), often times some grid cells have very small errors (i.e., the grid is oversampled in these regions) while the errors are dominated by just a few badly behaved undersampled grid cells. In contrast, adaptive mesh integrators automatically adjust the step size *locally* and automatically avoid oversampling while not undersampling the highly peaked opacity in the disk.

4.1 IR Excess Emission

An application where we know the source function a priori is calculating the IR flux. The IR flux is dominated by free-free emission from the disk. Free-free emission is produced by free electrons that have a Maxwellian velocity distribution, so it is an LTE process; i.e., $S_{\nu} = B_{\nu}^w$, where B_{ν}^w is the local value of the Planck function in the wind. In the IR (Rayleigh-Jeans limit), the free-free opacity

$$\kappa_{\nu} \propto \nu^{-2} \rho^2. \quad (78)$$

We can gain much insight into the behavior of the IR excess by studying a simple isothermal model, $B_{\nu}^w = \text{constant} = B_{\nu}^*$. For a simple axisymmetric disk-like density distribution, we adopt the parameterization

$$\rho = \rho_0 \sin^m \theta \left(\frac{R}{r} \right)^n. \quad (79)$$

The exponent n determines the radial distribution of material, m controls the latitudinal thickness of the disk, $\Delta\theta = \cos^{-1}(1/2)^{1/m}$, and ρ_0 sets the density scale or equivalently the optical depth of the envelope.

Since the envelope is isothermal, the solution to the transfer equation (70) is

$$I_\nu^{\text{emerg}} = \begin{cases} B_\nu & (q < 1), \\ B_\nu [1 - e^{-\tau_\nu^{\text{max}}(q, \alpha)}] & (q > 1), \end{cases} \approx \begin{cases} B_\nu & (q < q_{\text{eff}}), \\ 0 & (q > q_{\text{eff}}), \end{cases} \quad (80)$$

where $\tau_\nu^{\text{max}} = \tau_\nu(z_{\text{min}})$. Interior to the effective impact parameter, q_{eff} , the wind is optically thick (so the intensity equals the source function), while exterior to the effective impact parameter, the wind is optically thin and $I_\nu \approx \tau_\nu^{\text{max}} B_\nu \rightarrow 0$. For a density $\rho \propto r^{-n} \sin^m \theta$, the value of q_{eff} is determined by the condition (Bjorkman 1992)

$$\tau_\nu^{\text{max}}(q_{\text{eff}}, \alpha) = \left[\Gamma \left(\frac{2n-3}{2n-1} \right) \right]^{-\left(\frac{2n-1}{2} \right)} = \begin{cases} 0.23 & (n=2), \\ 0.37 & (n=3). \end{cases} \quad (81)$$

Note that the effective impact parameter is a function of position angle, α . This contour is a line of constant column density through the envelope and is the effective transition radius between optically thick and thin, so it also defines the projected area of the effective photosphere. Since the optical depth is constant on this line, it is also an intensity isophot. Substituting (80) into (64), the observed flux is

$$F_\nu = \left(\frac{R}{d} \right)^2 B_\nu \int_0^{2\pi} \frac{1}{2} q_{\text{eff}}^2 d\alpha = B_\nu A_{\text{eff}}/d^2, \quad (82)$$

which is the product of the source function and the effective area, A_{eff} . As a function of wavelength, the opacity increases ($\kappa_\nu \propto \lambda^2$), so the effective impact parameter increases ($q_{\text{eff}} \propto \nu^{-2/(2n-1)}$) as does the effective area. We now see why there is an IR excess; in the IR the effective photospheric area is larger than the star. Since the flux is determined by the apparent solid angle, A_{eff}/d^2 , which is much larger in the IR, there is a flux excess. Using the frequency dependence of q_{eff} , we find that the slope of the spectral energy distribution is given by

$$F_\nu \propto B_\nu q_{\text{eff}}^2 \propto \nu^{\left(\frac{4n-6}{2n-1} \right)}. \quad (83)$$

Thus we see that the slope of the free-free continuum determines the radial density exponent, n . Using IRAS data, Waters et al. (1987) measured the slope of the IR free-free continuum for a large sample of Be stars. They found that n usually lies in the range 2–3.5.

In principle the amplitude of the IR excess provides information about the density of the envelope, ρ_0 , because $q_{\text{eff}} \propto \rho_0^{2/(2n-1)}$. Unfortunately the

amplitude of the IR flux is also geometry-dependent. If we increase the opening angle of the disk, $\Delta\theta$ (i.e., m), the column density through the disk also increases, which implies that q_{eff} will increase. Therefore increasing the disk opening angle will increase the IR flux. Similarly if we change the stellar inclination angle, the effective area changes. The smallest effective area occurs edge-on, while the largest occurs pole-on. Therefore the IR flux decreases as the inclination angle increases. Combining all these effects, the IR flux is given by

$$F_{\nu}^{\text{IR}} = C(i, m) \rho_0^{\left(\frac{4}{2n-1}\right)} \nu^{\left(\frac{4n-6}{2n-1}\right)}, \quad (84)$$

where C is a geometry-dependent constant (it also depends on the disk temperature, unless $n = 2$).

In summary, the slope of the free-free continuum determines the radial exponent, n , but the amplitude of the IR excess only determines the density, ρ_0 , if the geometry (i, m) and temperature are known. Consequently we need another observational quantity that will help us determine the geometry. Polarization is dependent on the scattering geometry, so polarization measurements can help determine the geometry of the circumstellar envelope.

4.2 Intrinsic Polarization

Since photons are massless spin-one particles, they are polarized with two helicity states. However, an ensemble of photons (uncorrelated sum) is only partially polarized. The polarization state is described by a Stokes vector $S = (I, Q, U, V)$, which is equivalent to a density matrix description in quantum mechanics (see Landau and Lifshitz 1975, §50, and Berestetskii et al. 1971, §8). To qualitatively understand the degree of polarization, consider the classic observation of linearly polarized light through a Polaroid filter. If we rotate the filter to find the direction of maximum light transmission, then the degree of polarization is given by

$$P = \frac{I_{\text{max}} - I_{\text{min}}}{I_{\text{max}} + I_{\text{min}}}, \quad (85)$$

where I_{min} is the transmitted intensity in the direction perpendicular to the direction of maximum transmission. Qualitatively, the degree of polarization is the difference between the intensity parallel and perpendicular to some reference direction.

There are several polarizing mechanisms that have astrophysical importance, such as synchrotron emission, dichroic absorption, and electron or dust scattering. Synchrotron emission occurs when electrons spiral around magnetic field lines, so they radiate light that is polarized perpendicular to the B field. Dichroic absorption occurs when spinning cylindrical dust grains are aligned by the magnetic field in the interstellar medium. The spin axis is parallel to the magnetic field, but perpendicular to the long axis of the grain (so the cylindrical grain sweeps out a disk-shaped region as it spins around

the magnetic field). The attenuation cross section for light polarized parallel to the long axis is larger than for light polarized perpendicular to the long axis, so as the light is extinguished during its passage through the interstellar medium, it is more extinguished parallel to the grain's long axis than perpendicular. Therefore, the light becomes polarized perpendicular to the spinning grain and parallel to the magnetic field. Finally for circumstellar envelopes, the polarizing mechanism is scattering by dust (YSOs) or electrons (hot stars).

When light scatters, it becomes linearly polarized perpendicular to the scattering plane. The degree of polarization depends on the scattering angle (and scattering mechanism) — 90° Rayleigh scattering is 100% polarized while forward and backward scattering is unpolarized. If we consider integrating along a line of sight passing by the star, the orientation of the scattering plane is constant for all points on that line of sight. Therefore the partial polarization contributions may be summed and the emergent light is partially polarized perpendicular to the radius vector of the line of sight (projected on the sky). If the envelope is spherically symmetric, for every line of sight there is another line of sight (at the same impact parameter) at a position angle 90° away that is polarized perpendicular to the original line of sight. So when you integrate over the envelope, the total polarization sums to zero. Therefore, unresolved spherical sources must be unpolarized. If any intrinsic polarization is observed (after removing any interstellar polarization due to dichroic absorption), then the source cannot be a spherically symmetric wind. On the other hand, if a circumstellar disk is present, more light is scattered by the disk, so the net polarization will be perpendicular to the plane of the disk. Similarly, the scattering from bi-polar jets will be polarized perpendicular to the jet axis.

Optically Thin. To determine the geometry dependence of the polarization produced by circumstellar disks, it is useful to first calculate the polarization in the optically thin limit where one can obtain analytic expressions for the polarization. In the optically thin limit, the polarization is produced by singly scattered stellar photons, so the fundamental scaling of the polarization is given by

$$P \sim \frac{F_{\perp}^{\text{scat}} - F_{\parallel}^{\text{scat}}}{F_{\star}} \sim \frac{\int dV \int I_{\nu} n_e \left[\left(\frac{d\sigma}{d\Omega'} \right)_{\perp} - \left(\frac{d\sigma}{d\Omega'} \right)_{\parallel} \right] d\Omega'}{\pi B_{\nu} R^2}, \quad (86)$$

where F_{\perp}^{scat} and $F_{\parallel}^{\text{scat}}$ are the scattered fluxes with polarization perpendicular and parallel to the disk, respectively, n_e is the electron number density and $(d\sigma/d\Omega)$ is the differential cross section for electron scattering. Note that the scattered (polarized) flux is proportional to a volume integral of the electron density times a geometric factor that accounts for the scattering angles. Fundamentally the polarization depends on the total number of scatterers

as well as a geometry-dependent factor. If we increase the envelope density, the polarization increases linearly with the mass of the envelope. Including all the scattering geometry-dependent factors (see Bjorkman and Bjorkman 1994, or Cassinelli et al. 1987 for details), the polarization of an axisymmetric electron distribution is given by

$$P = \frac{3\sigma_T}{16\pi B_\nu R^2} \left\{ \int dV n_e (3K - J)(1 - 3\mu^2) \right\} \sin^2 i \\ \sim \tau_{es} \gamma \sin^2 i, \quad (87)$$

where J and K are the usual intensity moments, $\mu = \cos \theta$, $\tau_{es} = \int_R^\infty n_e \sigma_T dr$ is the radial electron scattering optical depth, σ_T is the Thomson cross section, and γ is a factor that depends on the shape of the envelope (see Brown and McLean 1977).

We see that the polarization depends on three factors. First, it increases linearly with the electron scattering optical depth (or envelope mass). Second, it depends on the inclination (or viewing) angle. Pole-on there is no polarization because the envelope is circularly symmetric on the sky (so the net polarization sums to zero). It then increases monotonically to its maximum when viewed edge-on. Third, it also depends on the overall shape of the envelope (whether it is very flattened or almost spherical). Holding the density (or τ_{es}) constant, if we start with a thin disk and increase the opening angle of the disk, the polarization initially rises (because the volume of the disk increases, the total number of scatterers increases, and all the scatterers produce polarization perpendicular to the disk). The polarization attains a maximum value when the opening angle is about 30° and decreases back to zero as the envelope becomes spherically symmetric and the opening angle approaches 90° (because the scattering in the polar region produces polarization perpendicular to the scattering in the disk, it cancels the equatorial polarization and drives the net polarization back to zero). Owing to this non-monotonic behavior of the polarization versus opening angle, for any given polarization level, there will be two possible disk opening angles that could produce the observed polarization.

Optically Thick. Unfortunately, the circumstellar disks around Be stars are optically thick, so the previous discussion about how the polarization depends on the disk geometry is only a qualitative guide. When the disk is optically thick, multiple scattering becomes important, so one must begin to perform true radiation transfer (because the source functions depend on both the stellar and the scattered radiation field). Various methods have been developed for radiation transfer in multiple dimensions, such as the diffusion approximation, the method of discrete ordinates, and Monte Carlo simulation. The diffusion approximation is only valid at very large optical depth, so it is really a stellar interiors approximation. However, it can be extended moderately easily to three dimensions, and it has been successfully

employed in modeling the very optically thick envelopes of YSOs. The method of discrete ordinates treats the transfer equation as a PDE in six dimensional space (three spatial coordinates, two angular coordinates, and potentially a frequency coordinate). This method has some numerical difficulties that can make it difficult to implement. For example the specific intensity can become negative and it can also become quite highly peaked in the radial direction once the envelope becomes optically thin at large radii. This forward peaking of the radiation field can require a large number of angular grid cells. The last method is Monte Carlo simulation, which tracks the paths of individual photon packets as they travel through the envelope.

Historically, the Monte Carlo method has not been a very popular technique in stellar atmospheres. Most likely this is because Monte Carlo simulation generally has poor convergence properties. Since it is a statistical sampling method, the errors decrease only as $1/\sqrt{N}$, where N is the number of photon packets employed in the simulation. In addition the method will fail miserably if the optical depths become enormous, because each photon performs a random walk, so the total number of scatterings is much larger than the optical depth. Once the optical depth exceeds about 10–100 along all escape paths, Monte Carlo simulation becomes difficult. In one dimension, very sophisticated numerical methods, such as ALI (see Hubeny, this Volume), have been developed and are much faster; however, in three dimensions, I suspect that Monte Carlo simulation may begin to be competitive, especially in very complicated geometries. Despite the apparent problems with the Monte Carlo technique, there are two compelling reasons why I employ Monte Carlo simulation for disk geometries. The first is that one may incorporate polarization calculations with no penalty in the execution speed and it is almost trivially easy to include the polarization transfer. The second is the flexibility and adaptability of the technique. Monte Carlo simulation is inherently a 3-d technique, so it is relatively easy to adapt the model to a variety of geometries. It is also quite easy to extend the model to include more physics (such as scattering by a non-thermal distribution of electrons). For example, the time required to change the model from an electron scattering Be star disk to a dusty pre-main sequence disk with bipolar jets requires about a day of work. In contrast, more traditional methods, such as the method of discrete ordinates solve a differential equation. In these models the geometry is determined by the boundary conditions. Often times to adapt the model from one geometry to another (or from one physical mechanism to another) requires a major rewrite of the code to incorporate a different grid structure or complex geometrical boundary. Although Monte Carlo may not be the fastest numerical technique, I have found it to be a *highly productive* technique that I have been able to quickly use for a wide variety of astrophysical problems.

Monte Carlo Radiation Transport. We simulate the transport of energy in the circumstellar envelope by following individual packets of energy as they

are scattered and absorbed along a randomly sampled set of paths (it is the random nature of this game that gives rise to the Monte Carlo appellation). To make measurements, we construct an antenna and count the number of packets that pass through the antenna (the antenna might be a grid cell or a direction-of-observation solid angle bin). In general we perform the following tasks:

1. Divide the total luminosity, $L = L_* + L_{\text{env}}$, into N “photon” packets, each containing an equal amount of energy, L/N . Thus,

$$N_* = (L_*/L)N , \quad (88)$$

$$N_{\text{env}} = (L_{\text{env}}/L)N , \quad (89)$$

where N_* and N_{env} are the number of stellar and envelope photon packets, respectively. Note that a photon packet may be partially polarized, so the packet energy is described by a Stokes vector, $S = (I, Q, U, V)$.

2. Transport the photon packets through the envelope. Scatter, Doppler shift, and absorb energy as appropriate until the packet emerges.
3. Bin the emergent energy into direction-of-observation bins and frequency bins. The amount of energy in each bin provides the flux (and polarization) as a function of direction and frequency.
4. To determine position-dependent quantities such as the mean intensity, J_ν , or flux, H_ν , count the number of photons passing through a given grid cell, or across a cell wall, respectively.

Algorithm. We want to calculate an emergent spectrum as a function of frequency and the direction of observation. Let me now outline in more detail the individual steps that are taken for each photon.

1. Pick a random point on the stellar surface. The energy per area emitted from the star is given by the flux, H , so the probability per area

$$\frac{dP}{dA} \propto T_{\text{eff}}^4 . \quad (90)$$

2. Pick a random direction and frequency for the photon packet. The probability distribution is given by

$$\frac{dP}{d\Omega d\nu} \propto \mu I_\nu^*(\mu) , \quad (91)$$

where $\mu = \hat{\mathbf{r}} \cdot \hat{\mathbf{n}}$; i.e., the cosine of the angle between the radial direction, $\hat{\mathbf{r}}$ (unit normal to the stellar surface), and the photon direction, $\hat{\mathbf{n}}$. The factor μ is required because the stellar specific intensity, I_ν^* , is the energy per area perpendicular to the beam, but we are emitting photons from the stellar surface, which is not perpendicular to the beam. To convert from intensity to surface flux, we must multiply by μ .

3. Calculate a random optical depth. Photon scattering and absorption is a Poisson process (equal probability per optical depth), so at a given cumulative optical depth, τ , the number of photons that scatter and absorb is given by the number that travel optical depths greater than τ , $e^{-\tau}$, times the probability of interaction, $d\tau$. Therefore,

$$\frac{dP}{d\tau} = e^{-\tau} , \quad (92)$$

and the cumulative probability $P(\tau) = 1 - e^{-\tau}$, which implies $\tau = -\ln \xi_i$, where ξ_i is a (new) random number uniformly distributed between 0 and 1.

4. Find the scattering location, s , given by

$$\tau = \int_0^s (\kappa + \sigma) \rho ds , \quad (93)$$

where κ is the absorptive opacity and σ is the scattering opacity (if the photon passes through the star, re-emit it at step 2). Finding the value of s is where most Monte Carlo codes spend 99% of their time, so efficiency is of the utmost concern for this subroutine.

5. Determine if the photon is absorbed or scattered. The probability of absorption is

$$P_{\text{abs}} = \frac{\kappa}{\kappa + \sigma} . \quad (94)$$

If $\xi_i < P_{\text{abs}}$ destroy the photon and go to step 9.

6. Doppler shift the photon into the fluid rest frame, scatter it into a new direction, and Doppler shift back to the stellar frame. The probability distribution is given by the normalized differential cross section (also known as the phase function),

$$\frac{dP}{d\Omega} = \frac{1}{\sigma} \frac{d\sigma}{d\Omega} . \quad (95)$$

7. Repeat steps 3–6 until the photon emerges from the circumstellar envelope.
8. Bin the emergent photon into direction-of-observation and frequency bins.
9. Repeat steps 1–8 for each stellar photon. The statistical sampling errors are determined by the number of photons observed in each bin, so set the total number of photons and bin sizes accordingly.
10. Once all the stellar photons have been emitted, repeat for the envelope photons. Choose their initial locations and directions with a probability

$$\frac{dP}{dV d\Omega} = j_\nu , \quad (96)$$

where j_ν is the emissivity per volume per solid angle.

Using this Monte Carlo technique, Wood et al. (1996) investigated the effects of multiple scattering on the polarization produced by axisymmetric circumstellar envelopes. There are two fundamental differences in the results for optically thin and optically thick disks. For optically thin disks, the polarization rises linearly with the electron scattering optical depth. However as the envelope becomes optically thick, the polarization stops increasing, attains a maximum value (typically a few percent) and then begins to decrease as the optical depth becomes very large. If the envelope is not extremely oblate, the polarization will actually decrease to zero, whereupon the position angle “flips” by 90° and the polarization level begins to rise again. This is because, for very opaque envelopes, one can only observe the scattering from the polar regions (the disk is essentially black), so the polarization position angle is now orthogonal to the optically thin results. The second difference is in the behavior of the polarization versus inclination angle. For optically thin disks, the polarization increases monotonically with inclination angle ($P \propto \sin^2 i$). For optically thick disks, the polarization initially rises as the inclination angle increases. However the polarization attains a maximum value at $i \approx 70^\circ$ and then decreases as the disk becomes more edge-on. Again this is because the optically thick disk attenuates the polarized light that was scattered in its interior, thereby decreasing the polarized flux.

4.3 Spectral Line Profiles

The radiation transfer methods that we have been discussing until now have been used for continuum problems. Line transfer is more difficult because the lines can be very optically thick and the opacity is highly peaked in frequency (or velocity) space, which implies that for an expanding envelope, the opacity is highly peaked in position space as well. Since the lines are so optically thick, one cannot use a Monte Carlo simulation to directly track the photons in detail as they traverse the line formation regions. However, Monte Carlo simulation has been employed successfully for pure scattering resonance lines. For pure scattering lines, photons are conserved, which means that any photon that is scattered in a line formation zone will eventually escape in some random direction. Using the Sobolev approximation, one can determine the escape probability as a function of direction and use this escape probability for the scattering phase function. In this way, resonance line scattering has been successfully modeled using the Monte Carlo technique (see Knigge et al. 1995).

One can also use the Sobolev approximation to directly calculate line profiles by integrating the transfer equation. In expanding atmospheres, Hamann (1981) noted that most of the short-comings of the Sobolev approximation were its application to the integration of the transfer equation. In contrast, the Sobolev approximation produces quite good estimates of the source function. Lamers et al. (1987) applied this observation and developed the Sobolev with Exact Integration (SEI) method for spherically symmetric winds. In

their method they use the Sobolev approximation to calculate the source function. Knowing the source function, they then perform an exact numerical integration of the transfer equation using a line profile function, ϕ_ν , with a finite Doppler or turbulent width, v_{turb} (in contrast, the Sobolev approximation integrates the transfer equation by assuming that the line profile is very narrow — essentially a Dirac delta function). This SEI method is quite fast and its accuracy is quite good compared with the more accurate co-moving frame methods.

2-D SEI Method. In principle it is relatively straight-forward to extend the SEI method to 2-d axisymmetric geometries. One uses the generalized Sobolev method (Rybicki and Hummer 1978) to obtain the source function, and then one solves the transfer equation. The formal solution is

$$\tau_\nu = - \int_{-\infty}^z \kappa_L \phi_\nu [\nu - \nu_0(1 + v_z/c)] dz' , \quad (97)$$

$$I_\nu = \int e^{-\tau_\nu(z)} S \kappa_L \phi_\nu [\nu - \nu_0(1 + v_z/c)] dz' + \begin{cases} e^{-\tau_\nu^{\text{max}}} I_\nu^* & (q < 1), \\ 0 & (q > 1). \end{cases} \quad (98)$$

Again we transform this pair into the simultaneous differential equations,

$$\frac{dt_\nu}{dz} = t_\nu \kappa_L \phi_\nu [\nu - \nu_0(1 + v_z/c)] , \quad (99)$$

$$\frac{dI_\nu}{dz} = - \left(\frac{dt_\nu}{dz} \right) S . \quad (100)$$

Of course there are some technical difficulties in solving these equations. The first is that the line profile function is highly peaked, so the only contributions occur where $v_z = v_{\text{obs}}$, where $v_{\text{obs}}/c = (\nu - \nu_0)/\nu_0$. These regions are surfaces of constant v_z , called common velocity surfaces. In spherically symmetric winds with monotonically increasing velocity laws, there is only one common velocity surface for a given frequency of observation, and the original SEI code uses a velocity root finder to locate this surface for each line of sight. However, for axisymmetric geometries, there is no longer a single common velocity surface. The velocity can be quite complicated, so it is difficult to determine a priori the number of common velocity surfaces and even more difficult to find their locations. There is, however, a trick that one can employ to avoid altogether the task of finding the common velocity surfaces. The problem with trying to use an adaptive mesh integrator to solve (99) and (100) is that the line is so narrow that it is quite likely that the integrator will step over the common velocity surface without ever seeing any contribution from the line. One way to avoid this problem is to find the location of the common velocity surface and force the integrator to use points in this vicinity, which requires a velocity root finder. However if we extend the pair of differential equations (99) and (100) to include all frequencies simultaneously (i.e., the

number of simultaneous differential equations that the integrator solves is twice the total number of frequencies, $2n_f$, in the line profile) then there is always a contribution at some frequency (as long as the spacing of the frequency grid is less than the turbulent width of the line profile function). This means that the integrator will never miss (step over) any of the common velocity surfaces. Using this method, we can completely avoid the need for a general velocity root finder. The only penalty is that the total number of frequency points is set by the turbulent width, so $n_f \approx v_\infty/v_{\text{turb}}$. If the line is very narrow (say the thermal width) then the number of frequencies begins to be prohibitive. Fortunately the turbulent width is usually a large fraction of the terminal speed (Groenewegen and Lamers 1989).

Generalized Sobolev Approximation. Now we need to obtain values for the line source function, S , as a function of position. For this calculation we employ the generalized Sobolev method as developed by Rybicki and Hummer (1978). For resonance lines we make the usual assumption that a reasonable approximation is a two level atom. For a two-level atom, the source function is

$$S = (1 - \epsilon)\bar{J} + \epsilon B_\nu , \quad (101)$$

$$\bar{J} = \frac{1}{4\pi} \int d\Omega \int I_\nu \phi_\nu [\nu - \nu_0(1 + \hat{\mathbf{n}} \cdot \mathbf{v}/c)] d\nu , \quad (102)$$

where \bar{J} is the frequency-integrated mean intensity and ϵ is determined by the ratio of collisional to radiative rates. The specific intensity can be split into three contributions: the local emission (within the local Sobolev surface), the stellar emission, and the diffuse envelope emission from other points in the envelope. A 2-d axisymmetric envelope does not necessarily have all points expanding away from each other as does a spherically symmetric expanding envelope, so the contribution to the diffuse envelope emission comes from all points that have zero Doppler shift with respect to the point of interest. These surfaces are called common point surfaces. For example, a disk in pure (but differential) rotation has common point surfaces that are rings of constant radii. Combining all three contributions to the specific intensity, we write the mean intensity as

$$\bar{J} = \bar{J}_{\text{local}} + \bar{J}_* + \bar{J}_{\text{env}} . \quad (103)$$

Using the Sobolev approximation, the local contribution to the mean intensity is

$$\bar{J}_{\text{local}} = \frac{1}{4\pi} \int \left[1 - \left(\frac{1 - e^{-\tau_0}}{\tau_0} \right) \right] S d\Omega = (1 - \beta)S , \quad (104)$$

where the Sobolev optical depth, τ_0 , and escape probability β are given by

$$\tau_0 = \frac{k_L c}{\nu_0 |d(\mathbf{v} \cdot \hat{\mathbf{n}})/dl|} , \quad (105)$$

$$\beta = \frac{1}{4\pi} \int \left(\frac{1 - e^{-\tau_0}}{\tau_0} \right) d\Omega . \quad (106)$$

Substituting (103) and (104) into (101), the source function becomes

$$S = \frac{(1 - \epsilon)(\bar{J}_* + \bar{J}_{\text{env}}) + \epsilon B_\nu}{\epsilon + (1 - \epsilon)\beta} . \quad (107)$$

We still require the stellar and envelope contributions. The stellar contribution is

$$\bar{J}_* = \frac{1}{4\pi} \int_{\Omega_*} \left(\frac{1 - e^{-\tau_\nu^*}}{\tau_0} \right) e^{-\tau_\nu^*} I_\nu^* d\Omega , \quad (108)$$

where τ_ν^* is the (direction-dependent) optical depth to the stellar surface, $\nu = \nu_0(1 + \hat{\mathbf{n}} \cdot \mathbf{v}_0/c)$, and \mathbf{v}_0 is the velocity at the location where (107) is evaluated. Note that τ_ν^* will be non-zero only when there are intervening common point surfaces between the point of interest and the stellar surface. The stellar contribution is relatively easy to evaluate, but this is not the case for the diffuse contribution. The diffuse contribution is given by

$$\bar{J}_{\text{env}} = \frac{1}{4\pi} \int \left(\frac{1 - e^{-\tau_0}}{\tau_0} \right) I_\nu^{\text{env}} d\Omega , \quad (109)$$

$$I_\nu^{\text{env}} = \int e^{-\tau_\nu^{\text{env}}} S \kappa_L \phi_\nu [\nu_0 \hat{\mathbf{n}} \cdot (\mathbf{v} - \mathbf{v}_0)/c] d\mathbf{l} , \quad (110)$$

$$\tau_\nu^{\text{env}} = \int \kappa_L \phi_\nu [\nu_0 \hat{\mathbf{n}} \cdot (\mathbf{v} - \mathbf{v}_0)/c] d\mathbf{l} . \quad (111)$$

Note that to determine the diffuse contribution at a given point in the envelope, we must solve the transfer equation (110) for one frequency (line center) in all directions. This requires that we develop a velocity root finder that can locate all the common point surfaces. This is a great deal of work, but the even more insidious problem is that the value of the source function is now coupled to the value of the source functions at all locations on the common point surfaces. This non-local coupling of the source functions means that we can no longer simply integrate all the appropriate equations (109)–(111) to determine the source function throughout the envelope. Instead we must iterate the solution. In other words, we must perform lambda iteration to determine the value of the source function versus position. Mazzali et al. (1992) produced a 2-d Sobolev code that uses such lambda iteration. Fortunately it appears that lambda iteration converges fast enough to be a useful technique. If one is not brave enough to perform lambda iteration, a useful approximation is to assume that the star dominates the contribution to the mean intensity; i.e., assume $\bar{J}_{\text{env}} \ll \bar{J}_*$. In this case,

$$S = \frac{(1 - \epsilon)\bar{J}_* + \epsilon B_\nu}{\epsilon + (1 - \epsilon)\beta} . \quad (112)$$

It is difficult to assess how good or bad this approximation is. Typically the source function in the envelope $S \approx WB_\nu$ (Castor 1970), where W is the “dilution factor” (relative solid angle of the star). Thus, the diffuse mean

intensity $\bar{J}_{\text{env}} \approx (\Omega_{\text{cp}}/4\pi)WB_{\nu}$, while the stellar mean intensity $\bar{J}_{*} \approx WB_{\nu}$. This implies that the approximation (112) probably is good whenever the common point surfaces are small ($\Omega_{\text{cp}} \ll 4\pi$ steradians); otherwise, the diffuse contribution is probably of order the stellar contribution.

5 Determination of Disk Geometry

Now that we have developed methods for calculating IR excesses, intrinsic polarization, and spectroscopic line profiles, we want to use these calculations to test theoretical models and to determine the geometry of circumstellar disks. We saw that the slope of the IR excess determines the radial exponent, n , of our density model, but the stellar inclination angle and disk opening angle were undetermined.

By combining the IR excess with the intrinsic polarization data, we can obtain information about the disk geometry. Coté and Waters (1987) found that there is a correlation between the IR excess and the maximum optical (broad band) polarization. In a plot of polarization versus IR excesses for a randomly chosen set of stars, all observations lie below this upper limit and are distributed in a triangular-shaped region. This shape is a consequence of observing stars with random inclination angles. The stars that are nearly edge-on have maximum values for their polarization, while nearly pole-on stars have small polarization values. Although the IR excess depends on inclination angle, it does not change by more than about a factor of two. Therefore, the position of a star in this triangle diagram is an indication of its inclination angle.

This conclusion is born out by optical $H\alpha$ interferometry. Quirrenbach et al. (1997) show that stars with highly flattened images are near the upper limit in the triangle diagram, stars with intermediate flattening are in the middle, and stars with circularly symmetric images lie near the bottom of the triangle diagram. This is exactly the behavior one would expect if all Be stars have geometrically thin disks; we are simply looking at the projection of the disk on the plane of the sky. Therefore the ellipticity of the interferometric image should determine the inclination angle of the system. This inclination angle obtained from the interferometry agrees quantitatively with that inferred from the Coté and Waters triangle diagram, so the interpretation that we are viewing a thin disk at different inclination angles is quantitatively consistent with both the optical interferometry and triangle diagram. Unfortunately the interferometry does not have sufficient resolution to determine the vertical thickness of the edge-on disks; it only places an upper limit on the disk opening angle, $\Delta\theta < 20^\circ$.

To determine an actual value for the disk opening angle, we turn to spectropolarimetry. Although electron scattering is wavelength-dependent, the observed intrinsic polarization is not. This is because the stellar flux passes through the disk both prior to and after scattering. The disk contains not only

free electrons but some neutral hydrogen as well. Consequently the polarized flux is attenuated by the hydrogen bound-free opacity (as well as any other opacity sources) in the disk, and the observed polarization exhibits jumps across the hydrogen ionization edges. Shortward of each edge, the opacity decreases with decreasing wavelength ($\kappa_{\text{bf}} \propto \lambda^3$), producing a “saw-toothed” shape for the polarization spectrum. The size of the polarization Balmer jump depends on the hydrogen opacity, which is density dependent, so fitting the polarization Balmer jump essentially determines the disk density. Finally the polarization level depends on the opening angle of the disk as discussed in Sect. 4.2; however, for any given polarization level, there are two possible disk opening angles. Wood et al. (1997) applied this technique to spectropolarimetric observations of ζ Tau and found that the disk could have an opening angle of either 2.5° or 52° . Since the interferometric observations show that the circumstellar envelope must have an opening angle less than 20° , we may eliminate the thick disk solution. Combining all these observations, we conclude that the opening angle is 2.5° , which is remarkably close to the WCD model predictions. This is also approximately the scale height one would infer for a Keplerian disk, so this determination of the disk thickness cannot distinguish between WCDs and Keplerian disks.

The bad news is that a density $\rho_0 = 5 \times 10^{-11} \text{ g cm}^{-3}$ is required to match the polarization Balmer jump. This density is two orders of magnitude higher than predicted by the original WCD model calculations, which assumed the Be star mass loss rates derived by Snow (1981) using UV line profiles. This discrepancy could simply imply that Be stars have much higher mass loss rates than previously thought (recall that ionization fractions are very uncertain), or maybe additional physics plays a role in determining the disk density. As usual, the answer to these questions requires more work.

References

- Berestetskii, V. B., Lifshitz, E. M., Pitaevskii, L. P. (1971): *Landau & Lifshitz Course of Theoretical Physics*, Vol. 4, Part 1, Relativistic Quantum Theory, 1st ed., tr. J. B. Sykes & J. S. Bell (Oxford: Pergamon)
- Bjorkman, J. E., (1992): Ph.D. thesis, Univ. Wisconsin
- Bjorkman, J. E., Bjorkman, K. S. (1994): *ApJ* **436**, 818
- Bjorkman, J. E., Cassinelli, J. P. (1993): *ApJ* **409**, 429
- Bjorkman, K. S. (1989): Ph.D. thesis, Univ. Colorado
- Brown, J. C., McLean, I. S. (1977): *A&A* **57**, 141
- Cassinelli, J. P., Nordseick, K. H., Murison, M. A. (1987): *ApJ* **317**, 290
- Castor, J. I. (1970): *MNRAS* **149**, 111
- Castor, J. I., Abbott, D. C., Klein, R. I. (1975): *ApJ* **195**, 157
- Coté, J., Waters, L. B. F. M. (1987): *A&A* **176**, 93
- Friend, D. B., Abbott, D. C. (1986): *ApJ* **311**, 701
- Grady, C. A., Bjorkman, K. S., Snow, T. P. (1987): *ApJ* **320**, 376
- Grady, C. A., Bjorkman, K. S., Snow, T. P., et al. (1989): *ApJ* **339**, 403

- Groenewegen, M. A. T., Lamers, H. J. G. L. M. (1989): A&AS **79**, 359
- Hamann, W.-R. (1981): A&A **100**, 169
- Knigge, C., Woods, J. A., Drew, J. E. (1995): MNRAS **273**, 225
- Lamers, H. J. G. L. M., Cerruti-Sola, M., Perinotto, M. (1987): ApJ **314**, 726
- Landau, L. D., Lifshitz, E. M. (1975) *Course of Theoretical Physics*, Vol. 2, The Classical Theory of Fields, 4th ed., tr. M. Hamermesh (Oxford: Pergamon)
- Mazzali, P. A., Pauldrach, A. W. A., Puls, J., Plavec, M. J. (1992): A&A **254**, 241
- Mourard, D., Bosc, I., Labeyrie, A., Koechlin, L., Saha, S. (1989): Nat **342**, 520
- Owocki, S. P., Cranmer, S. R., Blondin, J. M. (1994): ApJ **424**, 887
- Press, W. H., Flannery, B. P., Teukolsky, S. A., Vetterling, W. T. (1986): *Numerical Recipes* (Cambridge: Cambridge)
- Quirrenbach, A., Hummel, C. A., Buscher, D. F., et al. (1993): ApJ **416**, L25
- Quirrenbach, A., Buscher, D. F., Mozurkewich, D., Hummel, C. A., Armstrong, J. T. (1994): A&A **283**, L13
- Quirrenbach, A., Bjorkman, K. S., Bjorkman, J. E., et al. (1997): ApJ (in press)
- Rybicki, G. B., Hummer, D. G. (1978): ApJ **219**, 654
- Shakura, N. I. Sunyaev, R. A. (1973): A&A **24**, 337
- Snow, T. P. (1981): ApJ **251**, 139
- Struve, O. (1931): ApJ **73**, 94
- Thom, C., Granes, P., Vakili, F. (1986): A&A **165**, L13
- Underhill, A., Doazan, V. (1982): *B Stars With and Without Emission Lines*, NASA SP-456
- Waters, L. B. F. M. (1986): A&A **162**, 121
- Waters, L. B. F. M., Côté, J., Lamers, H. J. G. L. M. (1987): A&A **185**, 206
- Wood, K., Bjorkman, J. E., Whitney, B. A., Code, A. D. (1996): ApJ **461**, 828
- Wood, K., Bjorkman, K. S., Bjorkman, J. E. (1997): ApJ **477**, 926

Stellar Coronae

Jürgen H.M.M. Schmitt

Max-Planck-Institut für Extraterrestrische Physik, 85748 Garching, Germany
e-mail: jhs@rosat.mpe-garching.mpg.de

Abstract. In the following chapter I will discuss recent developments in the field of X-ray astronomy of cool stars, and try to highlight some of the basic observational findings obtained with the *Einstein* and ROSAT satellites. In particular, coronae appear to exist around all cool stars with outer convection zones with a minimum surface flux agreeing with the X-ray flux observed from solar coronal holes. The overall X-ray output of cool stars can vary enormously from star to star with a total range of four orders of magnitude. The factor most important in determining the actual X-ray emission level for a given star appears to be its rotation rate. For young stars one observes a significant evolution of rotation in the first 10^8 yrs of their main sequence life times, which leads to a corresponding evolution of X-ray luminosity. I argue that magnetic fields play a very central role for the development and evolution of coronae, and consequently the theory of magnetohydrodynamics (MHD) provides the appropriate theoretical framework to describe the dynamics of coronal plasma. I describe the fundamental assumptions of MHD, and present simple models of both magnetically closed and open regions as observed on the Sun, and – by analogy – presumed to exist also on other stars.

1 Introduction

The study of coronae around other stars has recently become possible due to significant advances in astronomical instrumentation. Coronal plasma is – by definition – hot with temperatures in excess of 10^6 K, and loses the bulk of its energy at soft X-ray wavelengths. The X-ray range is therefore the most natural spectral range to study radiative emissions from stellar coronae, and in particular it is the spectral range most relevant for the overall coronal radiative energy budget.

The observational progress in the study of stellar coronae can probably be demonstrated best by considering the number of detected coronal X-ray sources as a function of time (plotted in Fig. 1). The field of X-ray astronomy as a whole started immediately after World War II in 1948 with detection of X-ray emission from the Sun. This discovery was in a way not surprising since X-ray emission was expected as a consequence of the large coronal temperatures of $\sim 2 \cdot 10^6$ K which were inferred from the identification of forbidden coronal lines (in the optical spectrum of the Sun) such as the “green” line at 5303 Å with emission from Fe XIV ! It then took almost 30 years until the first truly stellar coronal source, i.e., Capella, the brightest “persistent” coronal source, was detected in 1975. The first breakthrough

for stellar X-ray astronomy occurred in the period between 1978 and 1981 with the launch and operations of the *Einstein Observatory*. For the first time imagery was possible at soft X-ray wavelengths with a sensitivity sufficient to detect solar-like X-ray emission even at stellar distances. Quite surprisingly at the time, far more than 1000 coronal X-ray sources from stars distributed more or less throughout the Hertzsprung-Russell diagram were detected, thus demonstrating the ubiquity of stellar X-ray emission. With the advent of the ROSAT all-sky survey (RASS) the number of known coronal X-ray sources was increased by another order of magnitude. About a third of its 75000 or so sources are thought to be of coronal origin, and this sample certainly constitutes the largest known sample of active stars. As evidenced by Fig. 1, there is clearly no lack of suitable sources to study in contrast to the situation 20 years ago when less than two handfuls of coronal X-ray sources were known.

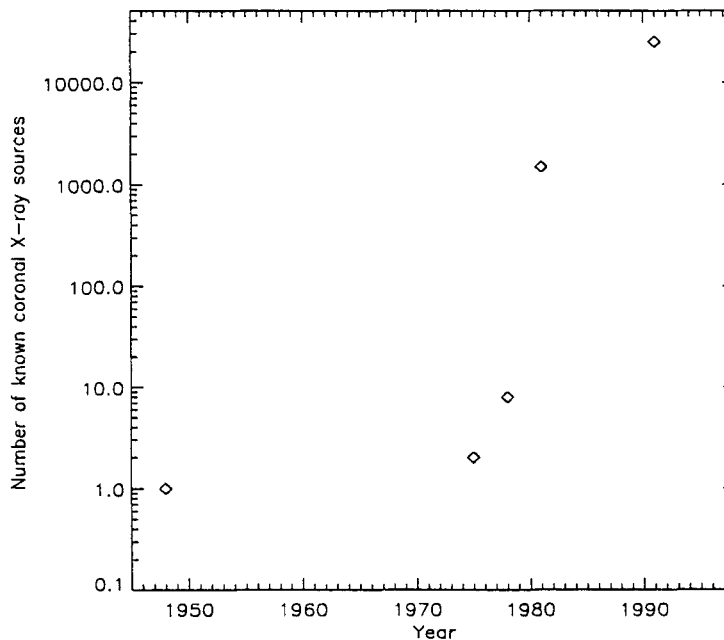


Fig. 1. Number of known *coronal* X-ray sources as function of time

Why should now anybody be surprised at the observed ubiquity of stellar X-ray emission? After all, the Sun is an X-ray source, and why should stars be any different? There are two answers to these questions, one observationally oriented and the other more theoretically oriented.

Let me consider the observations first and assume – as a working hypothesis – that all stars indeed emit X-rays at the level of the Sun, which emits (at solar maximum) $\sim 2 \times 10^{27}$ erg/sec at soft X-ray wavelengths. Given the characteristic limiting RASS flux of 2×10^{-13} erg/sec/cm², it is straightforward to compute the maximum distance at which a source emitting at solar maximum levels can still be detected as an X-ray source in the ROSAT all-sky survey. This distance is found to be 9 pc, which is tiny with respect to the dimensions of our Galaxy. A sphere around the Sun with a radius of 9 pc contains approximately 200 or so stars, but certainly not 20000 ! Therefore the initial hypothesis that all stars emit at solar maximum levels has to be fundamentally wrong. Some fraction of the stellar population emits X-rays at levels considerably above the solar maximum level and can therefore be detected over far larger volumes. Thus the real surprise was not the detection of X-ray emission from other stars, but rather the large dispersion of the observed levels of stellar X-ray emission.

This immediately leads to the other more theoretically oriented answer to the question posed above. Clearly, the level of expectation always determines the level of surprise, and the basic point is that until the early seventies the view had been prevalent (although by no means universally accepted) that acoustic heating was the most important mechanism responsible for the obviously required mechanical heating of the outer layers of the Sun. Obviously, under the assumption of radiative equilibrium there is no way the temperature can increase against the flow of radiation and energy. In the acoustic heating picture this mechanical heating is thought to originate from sound waves, which are copiously produced in the outer convection zones of cool stars. These sound waves propagate upwards into a region with diminishing density, whereupon the amplitudes of the waves grow and steepen until shocks are formed and the wave energy is dissipated. In this picture coronal emission would be an immediate consequence of the fluid turbulence in the convection zone. Specifically one predicts, first, that the level of sound generation and consequently the wave flux, which finally leads to coronal heating, depends on the eighth power of the convective velocity; and second, that the sound generation for stars occupying the same region of the HR diagram is the same. One therefore expects large differences in coronal X-ray flux between spectral types while stars of given spectral type should have essentially the same X-ray flux. These expectations are at variance with the observations I will discuss below. The observations show precisely the opposite trend: one finds relatively little changes in the emission level between spectral type, but rather large differences of up to four orders of magnitude in total X-ray output between stars of basically identical spectral type.

This finding coupled with the extensive set of spatially resolved X-ray images obtained with *Skylab* (cf. Fig. 4) in the early seventies led to the realization that for a proper description of the coronae of the Sun and those of other stars additional physical input is required. Magnetic fields are an

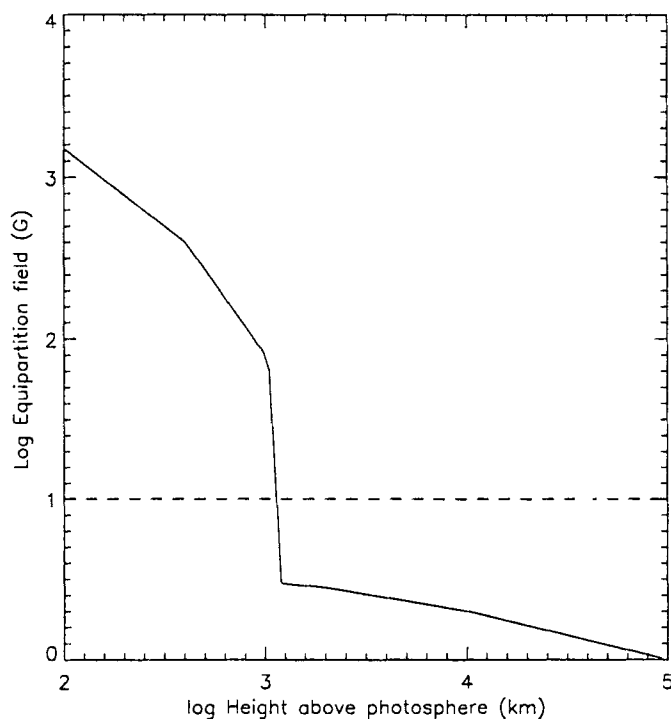


Fig. 2. Equipartition magnetic field strength as function of height above the solar photosphere; dashed line indicates typical coronal magnetic field strengths

obvious candidate for such an additional ingredient. For the case of the Sun, the importance of magnetic fields can be readily appreciated by considering the ratio β between gas and magnetic pressure, i.e., $\beta = P_{\text{gas}}/P_{\text{magnetic}}$ as a function of height (cf. Longair 1992). Given density n and temperature T as a function of height, one can specifically compute that magnetic field strength B_{equ} for which gas and magnetic pressure are equal through $B_{\text{equ}} = \sqrt{16\pi nkT}$. In Fig. 2 I plot B_{equ} as a function of height above the photosphere; because of the rapid decrease of particle density with height, B_{equ} also decreases very quickly with height. Also shown in Fig. 2 is a line indicating a field of $B_{\text{cor}} = 10$ G, which is thought to be a typical value for the solar corona. Clearly, B_{cor} exceeds the equipartition field at most heights and therefore the magnetic fields will actually control the dynamics of the coronal plasma.

Bob Rosner and collaborators have proposed a new scenario for the interpretation of solar and stellar activity. Its various physical ingredients and

Stellar Activity Flowchart

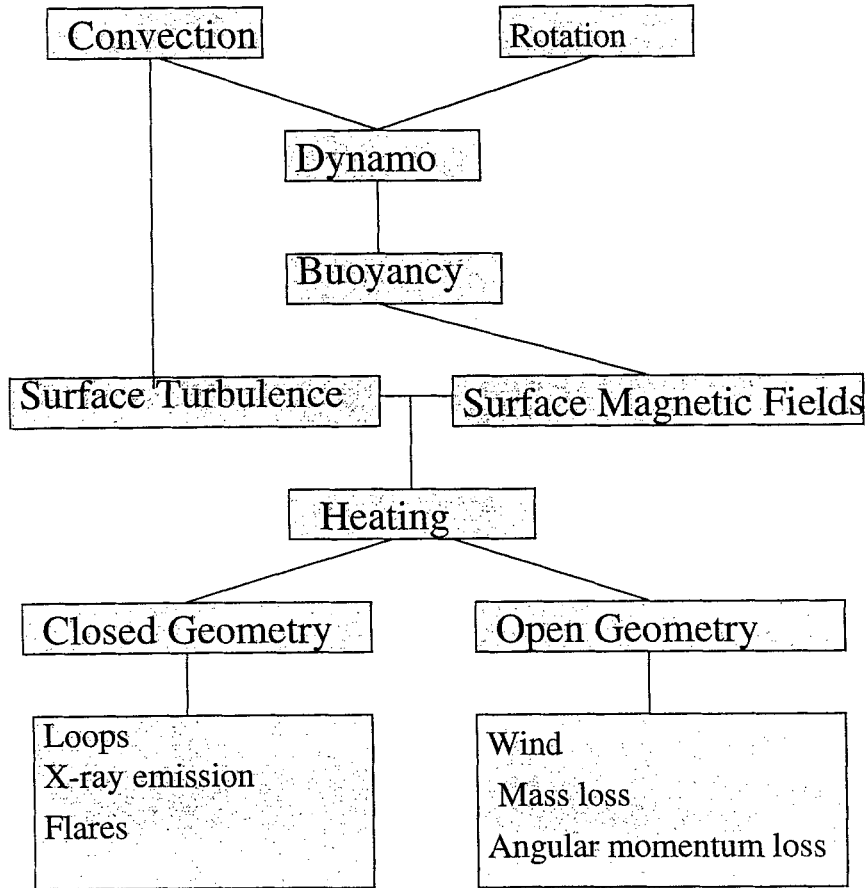


Fig. 3. New scenario for the interpretation of solar and stellar activity

their interplay are described in Fig. 3. Magnetic fields play a key role in all the processes considered. First of all, they must be produced in the stellar interiors probably by a dynamo process, which (presumably) is the result of an interaction between rotation and convection. Since all cool stars have outer convection zones and all cool stars are likely to rotate, dynamos should be operating in many if not all cool stars. In principle, stellar activity could also work with primordial magnetic fields, but magnetic cycles as observed on the

Sun and possibly other stars strongly argue against the importance of primordial fields for stellar activity. Through the process of magnetic buoyancy the magnetic fields generated in the deep interior rise to the surface, where they become visible as photospheric magnetic fields, visible, for example, as dark spots. At the same time, the outer convection zones lead to turbulence at the stellar surface, and the interaction between magnetic fields and turbulent fluid motions is thought to – somehow – give rise to heating. The results of these heating processes which are not well understood in detail depend on the magnetic field geometry. In magnetically closed geometries the coronal plasma is confined and loses the bulk of its energy by radiation, which can be diagnosed at the UV, EUV and X-ray wavelengths. In magnetically open regions on the other hand, the plasma can escape into interstellar space, thus giving rise to mass and angular momentum loss.

2 Basic Observational Results

In the following section I will review some of the basic results obtained from the X-ray observations carried out with the recent generations of X-ray satellites. I will not aim for completeness; rather I will focus on the results most relevant for the overall context of my discussion.

2.1 The Solar–Stellar Connection

To set the stage for the discussion to follow, I show in Fig. 4 a “typical” X-ray image of the (active) Sun, i.e., one of the thousands of solar X-ray images obtained with the Japanese *YOHKOH* satellite. As is well known, the X-ray emission from the Sun is highly inhomogeneous, X-ray bright regions can be located close to almost X-ray dark regions, with a brightness contrast of a few orders of magnitude. The X-ray emission is concentrated in arches and tubes, which follow the magnetic field lines and connect regions of opposite magnetic polarity. Given the complex structure and behavior of the solar corona, one may ask the question to what extent the study of stellar coronae may not be a “mission impossible”. Obviously, stellar X-ray astronomy can never compete with solar observations with respect to angular resolution, spectral coverage and signal-to-noise ratio of the data. The important point however is that in the context of solar physics one can deal with only one star. To put this in perspective, imagine the psychologist who is asked to characterize the behavior of humans and can study only one example out of a few billions available ! In addition, the solar physicist cannot really experiment with the Sun, but rather only observe what is going on. For the solar physicist there is no way to change, say, the mass, radius, age, rotation rate etc. of the Sun and study the influence of these parameters on solar activity. Strictly speaking, he cannot even tell whether the Sun behaves “normal” or not. In the stellar context one can – at least

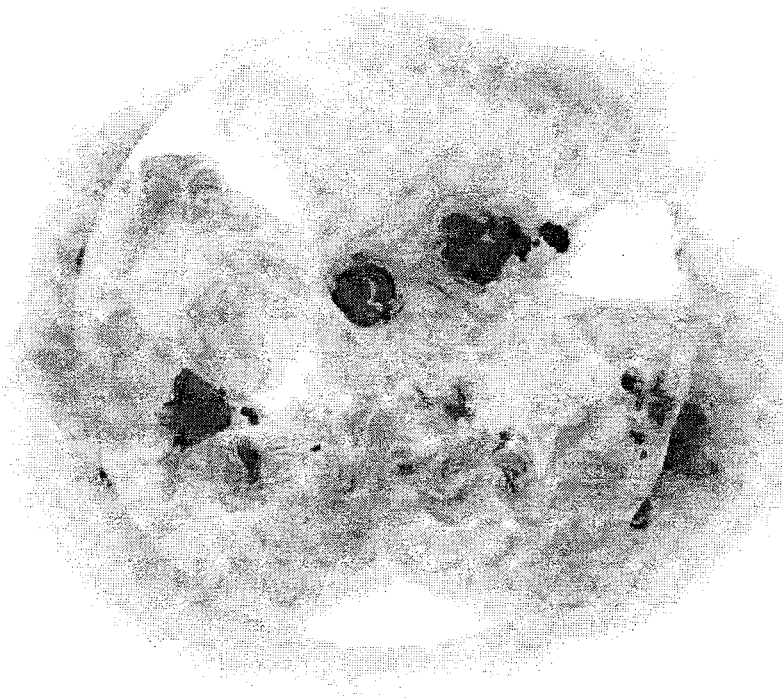


Fig. 4. YOHKOH image of the active Sun

in principle – do precisely this by selecting stars with different ages, masses, radii, rotation rates etc. and studying their coronal properties in comparison to what is known from the Sun. However, to this end the full range of stellar X-ray emission must be observed, while X-ray selected stellar samples are by necessity biased towards the intrinsically luminous X-ray emitters. Therefore the question then to what extent we can consider the Sun as a typical (or normal) star from the coronal point of view does require a careful sample selection.

2.2 Which Stars Have Coronae?

Let us first address the issue which kind of stars possess coronae and to what extent the scenario sketched in Fig. 3 finds any observational support. As is clear from Fig. 3, rotation and convection are the basic required ingredients for the whole scheme to work. All stars probably rotate at some level – it is notoriously difficult to dispose of angular momentum! However, not all stars have surface convection zones, and stellar structure theory predicts that such

surface convection zones only occur for cool stars with photospheric temperatures below about 8000 K. Therefore one can ask whether any change in the observed X-ray properties occurs for stars with surface temperatures at ~ 8000 K. Next one can ask to what extent a rotation-activity connection exists at X-ray wavelengths in the sense that larger X-ray outputs are correlated with larger rotation rates and shorter periods, and finally one can ask to what extent coronal formation is a universal phenomenon, or putting the question differently: Are there any cool stars that are truly X-ray dark ?

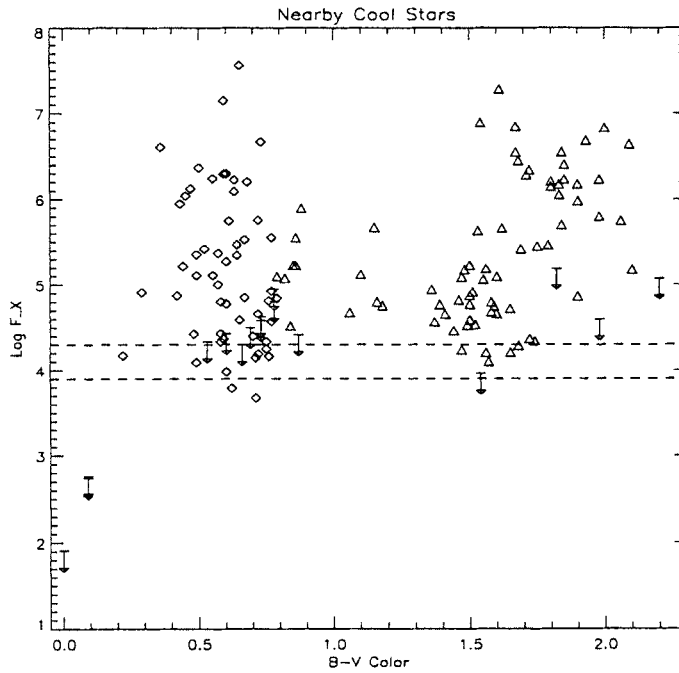


Fig. 5. Mean X-ray surface brightness F_X vs. $B - V$ color for my sample stars (including A-type stars drawn as upper limits). F and G type stars are plotted with diamonds, K and M type stars (as discussed by Schmitt et al. 1995) with upward triangles. For comparison the typical X-ray surface flux level (in the PSPC band pass) from solar coronal holes is shown by the two dashed curves. Clearly the observed solar coronal hole surface flux provides a good description of the observed stellar minimum X-ray flux

As is clear from Fig. 5, for stars classified as late A-type or F-type, the detection rate is 100 %, for stars classified as G-type, the detection rate is very large. I argue that also for the latter group of stars it is reasonable to assume the existence of coronae, since, first, all cases where all-sky survey

non-detections were reobserved in the pointing program resulted in detections, and second, my upper limits lie well above the lowest detections. The conclusion then is that coronal formation and X-ray emission are universal for stars in the spectral range A7 to G9. Combining this with the findings obtained by Schmitt et al. (1995) it follows that **all** cool dwarf stars must be surrounded by X-ray emitting coronae. The existence of truly X-ray dark cool dwarf stars can of course not be entirely excluded, but one can state with confidence that such objects must be very rare. On the other hand, for nearby A-type stars, specifically the prototypical A-star Vega, extremely sensitive upper limits are now available, which demonstrate that coronae around those stars (if at all existent) must be very different from those around cooler stars.

2.3 The Sun in Perspective

With my complete sample of solar-like stars I am now in a position to carry out a fair comparison between solar and stellar X-ray emission. Interestingly, the median of the observed X-ray luminosity distribution function at $\log L_X = 27.5$ lies actually somewhat above typical solar maximum emission levels. Therefore one must look at the Sun as a star with an activity below average, however, the observed range (between maximum and minimum) of solar soft X-ray luminosity compares well with the low luminosity part of the observed stellar X-ray luminosity distribution function, and therefore the Sun is certainly not atypical among solar-like stars. The X-ray surface fluxes and luminosities (cf. Fig. 5 and Fig. 3 in Schmitt et al. 1995) are very similar for the whole sample studied, and in fact for all cool stars when the F and G type dwarfs discussed in this paper are combined with the K and M dwarfs presented by Schmitt et al. (1995). The distribution functions for X-ray luminosity (cf. Fig. 4 in Schmitt et al. 1995) and X-ray surface flux vary smoothly over the observed range of data values with no sign of any bimodal distribution. The most natural explanation for these findings seems to be to assume that the same heating processes that are operating in the solar corona are also operating in stellar coronae.

2.4 Rotation-Activity Connection

Why do two almost identical stars differ in their coronal output by several orders of magnitude as evidenced by Fig. 5? If magnetic dynamos do indeed operate in the stellar interior, stellar rotation must play a very important role, and numerous studies have searched for relationships between activity and rotation. X-ray luminosity and rotation are indeed correlated, such that the more rapid rotators produce more X-ray output. This was first discovered for RS CVn systems by Walter and Bowyer (1981) and was generalized by Pallavicini et al. (1981) as

$$L_X = 10^{27} (v \sin i)^{1.9} . \quad (1)$$

In Fig. 6 I show a ROSAT version for the rotation-activity connection (taken from Hempelmann et al. 1995).

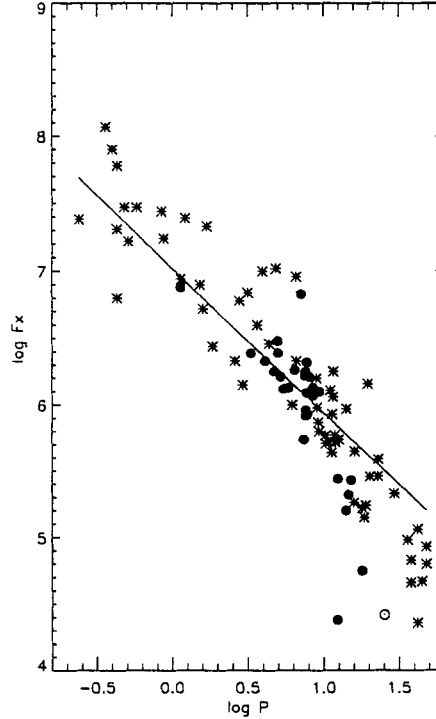


Fig. 6. Mean X-ray surface flux F_X vs. rotation period P for a (complete) sample of cool stars with photometrically determined rotation periods (from Hempelmann et al. 1995)

For stars of a given spectral type, hence given radius, the X-ray vs. rotation relationship holds only up to a certain point. Obviously, if one were to increase $v \sin i$ in (1), extremely large X-ray luminosities are obtained. What is observed instead is that for the most active stars a maximum X-ray luminosity $L_{X,\max}$ is produced such that

$$\frac{L_{X,\max}}{L_{\text{bol}}} = 10^{-3} , \quad (2)$$

where L_{bol} indicates the star's bolometric luminosity. In other words, empirically one finds that no more than 1 permille of the total stellar output can be emitted at soft X-ray wavelengths, are stars with $L_X \approx 10^{-3} \times L_{\text{bol}}$ are

called “saturated”. The interpretation of this effect is indeed surface saturation. The more rapid the rotation, the more activity is generated up to – couching this in solar terms – where the star runs out of available surface area to accommodate more active regions and plage. The saturation limit of $f_x/f_{\text{bol}} \approx 10^{-3}$ (or equivalently $L_x/L_{\text{bol}} \approx 10^{-3}$) appears to extend all the way along the main sequence from G stars to the latest M dwarfs (Fleming et al. 1993). The dependence of the saturation limit on rotation velocity has been beautifully shown by the ROSAT observations of the Pleiades (Stauffer et al. 1994) and α Per (Randich et al. 1995). Using as activity indicator L_x/L_{bol} , one finds in both clusters a more or less linear relationship between L_x/L_{bol} and the rotation velocity up to velocities of ~ 15 km/sec, at which point the L_x/L_{bol} values cluster around the saturation limit of $L_x/L_{\text{bol}} \approx 10^{-3}$.

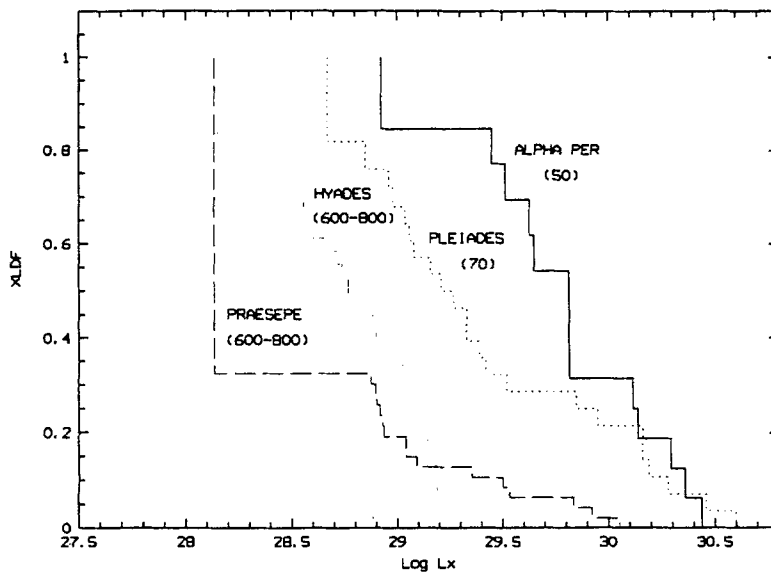


Fig. 7. Integral X-ray luminosity distributions for a number of young clusters (α Per, Pleiades, Hyades and Praesepe; data courtesy of Dr. S. Randich. Note the substantial decrease in mean X-ray luminosity with age; the Sun at solar maximum would still be below the plot scale !

A summary of the ROSAT X-ray observations is shown in Fig. 7, where – by courtesy of Dr. S. Randich (ESO) – the integral X-ray luminosity distribution functions for solar-like (i.e. G-type!) stars in a number of rather young nearby clusters are shown. The most X-ray luminous stars are found in the α Per cluster (age 50 Myrs), while the X-ray luminosities of the older

Pleiades (age 70 Myrs) and still older Hyades (age ≈ 700 Myrs) and Praesepe (age ≈ 700 Myrs) clusters are distinctly lower. It is worthwhile mentioning, however, that the X-ray luminosity of the Sun at solar maximum is still below the plot scale in Fig. 7 ! Very clearly, there is an enormous evolution in X-ray luminosity during the first few 100 Myrs main sequence life time for solar-like stars. It is generally thought that because of the rotation-activity connection this luminosity evolution is a reflection of the rotational evolution, which is observed in the period distributions of cool stars of the same age class. In Fig. 8 I plot for the α Per, Pleiades and Hyades clusters measured rotation periods as a function of color (the data are courtesy of J. Stauffer, SAO). Very obviously, the mean rotation period increases with age in a similar fashion as the mean X-ray output decreases with age. To the extent that the measured rotation periods refer to the star as a whole (and not just to the surface layer to which the actual measurements refer) one concludes that a substantial angular momentum loss must occur for main-sequence stars during the first few hundred million years. Young stars tend to rotate far more rapidly than the present Sun, and because of the rotation-activity connection such stars also have substantially increased X-ray outputs which makes such stars detectable over rather large distances.

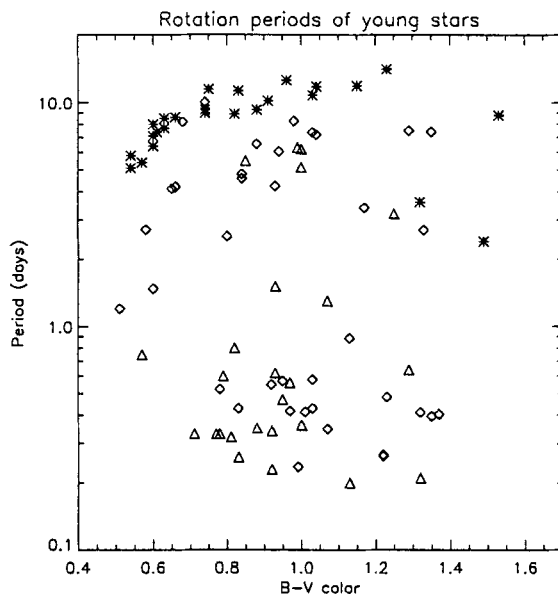


Fig. 8. Rotational period vs. B-V color for cool main-sequence stars in α Per (triangles), Pleiades (diamonds) and Hyades (asterisk). Note the substantial decrease in mean period with age. Data courtesy of Dr. J. Stauffer

2.5 Spectral Properties of X-Ray Coronae

From the Sun one observes both thermal and non-thermal X-ray emission. Non-thermal X-ray emission is observed during flares mostly although not exclusively in their impulsive phases at photon energies above ~ 20 keV. At lower photon energies the emission is always dominated by thermal emission and in the form of numerous spectral lines of highly excited atoms which allow very detailed plasma diagnostics. The typical temperatures of the quiescent coronal plasma is of the order $2\text{--}3 \cdot 10^6$ K with relatively little spread; however, during flares one observes significantly hotter plasma with temperatures of $2 \cdot 10^7$ K and higher, but this plasma is only present in transient form.

In the stellar context, the possibilities to extract spectral information from the observed X-ray data have been quite limited. In particular, essentially no data (on coronal X-ray sources) exist at photon energies > 10 keV, and consequently there is so far no direct evidence for non-thermal X-ray emission from stellar coronae, although such emission is definitely expected to occur. All of the stellar X-ray data refer to photon energies < 10 keV, and most observations are even restricted to photon energies < 2 keV with often quite moderate energy resolutions. The spectral resolution of proportional counters is such that only broad band photometry can be performed, and it is customary to describe the spectral energy distribution of the recorded photons in terms of a so-called *hardness ratio* HR defined as

$$\text{HR} = \frac{\text{Hard Rate} - \text{Soft Rate}}{\text{Soft Rate} + \text{Hard Rate}}, \quad (3)$$

where hard and soft rate are – for the case of the ROSAT PSPC – the count rates recorded above and below 0.5 keV respectively. The advantage of such an instrumental parameter is that it is independent of any modeling, which requires quite a large number of assumptions on the underlying spectrum. It is instructive to plot for the volume-limited sample of stars the observed mean X-ray surface flux F_X vs. HR (cf. Fig. 9). As is clear from Fig. 9, there is a clear correlation between F_X and HR such that stars with larger surface flux tend to have harder X-ray spectra. If one “calibrates” the PSPC hardness ratios with plasma emission codes, one finds that coronal temperatures of $\sim 1.5 \cdot 10^6$ K correspond to $\text{HR} \approx -0.9$, while temperatures of $\sim 1.0 \cdot 10^7$ K correspond to $\text{HR} \approx 0.0$. In other words, the coronal temperatures of the more active stars seem to be similar to those found during solar flares, the difference being that the latter is transient while the former appears to be persistent.

This last conclusion obviously depends on the correctness of the interpretation of the X-ray emission being thermal. Using the spectrometers on board the *Extreme Ultraviolet Explorer* (EUVE) Satellite it has become possible to record high resolution ($\lambda/\Delta\lambda \approx 200$) EUV spectra of a few of the brightest coronal X-ray sources. An example is shown in Fig. 10, where I show the EUV spectrum of the nearby star Procyon (spectral type F5 IV, $d = 3.5$ pc, $L_X \approx$

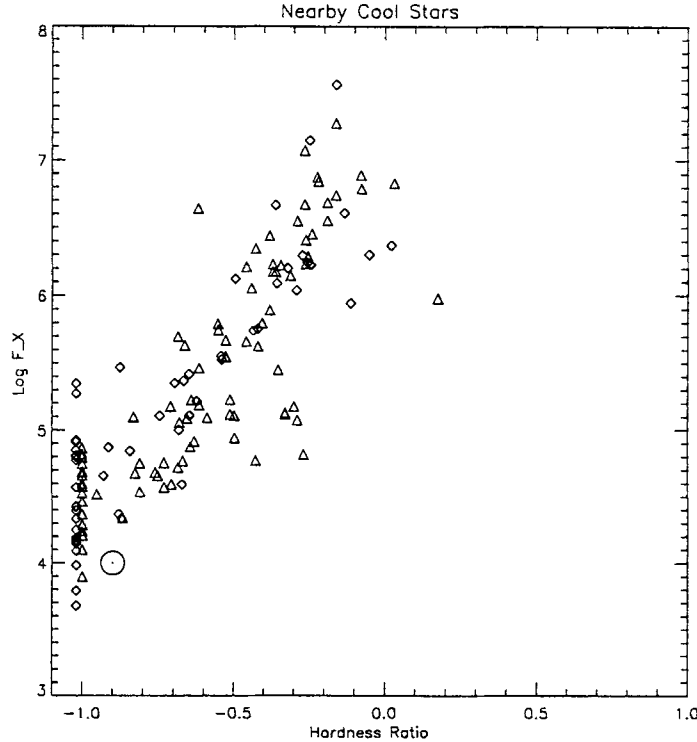


Fig. 9. Plot of X-ray luminosity L_X vs. spectral hardness between soft and hard PSPC counts for F and G stars (diamonds) and K and M stars (triangles; from Schmitt et al. 1995). The correlation between hardness and total X-ray output is obvious, but a large scatter around the regression curve is also apparent. A typical value in terms of F_X and HR for a solar coronal hole is also shown

$3 \cdot 10^{28}$ erg/sec) in the range 170 - 210 Å. Clearly, the spectrum is dominated by line emission, which turns out to be attributable to iron in the ionization stages Fe IX to Fe XIII; the highest detectable ionization stage of iron is that of Fe XVI, which is detected through weak line emission at 335 Å.

The EUV spectrum of Procyon is identical – at least for practical purposes – to that of the Sun; in Fig. 11 I plot a solar EUV spectrum taken with the Grazing Incidence Spectrometer (GIS) on board SOHO, and the extremely large similarity of the EUV spectra of the Sun and Procyon becomes evident by comparing Fig. 10 and Fig. 11, implying that the mean coronal temperatures of the Sun and Procyon must be very similar.

The EUV spectra of active stars, however, look quite different. In Fig. 12 I plot the EUV spectrum of the active star Algol ($L_X \approx 5 \cdot 10^{30}$ erg/sec) in

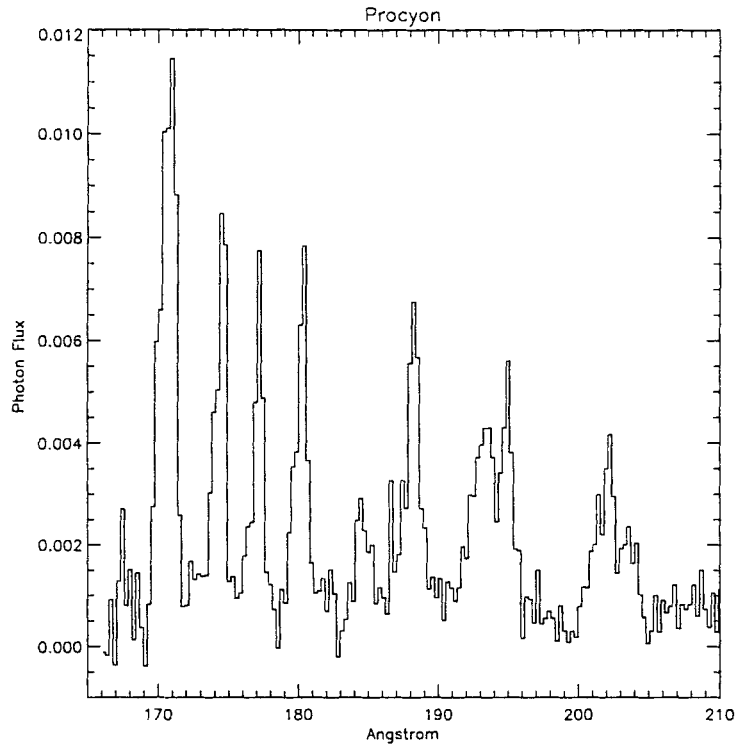


Fig. 10. EUVE medium wavelength spectrum for Procyon (in histogram representation) in the region 170 to 200 Å. Almost all the lines are due to iron in ionization stages Fe IX to Fe XIII

the range 90 - 140 Å. In the case of Algol the spectrum is again dominated by spectral lines, which can however be attributed exclusively to iron in ionization stages Fe XV to Fe XXIV. The only lines in common between Procyon and Algol are the Fe XV line at 284 Å and the Fe XVI line at 335 Å. Therefore the mean coronal temperature in Algol must significantly exceed that of Procyon and that of the Sun. This is however precisely the implication of Fig. 9, which states that large coronal X-ray surface fluxes go together with large coronal temperature. In some sense, Fig. 9 is the first case of an X-ray Hertzsprung-Russell diagram, plotting (X-ray) activity (measured in terms of surface flux) vs (X-ray) temperature.

2.6 Physical Properties of Stellar Coronae

The Role of Plasma. Most astrophysical fluids and in particular the gas in solar and stellar coronae differ from fluids encountered on the Earth or in

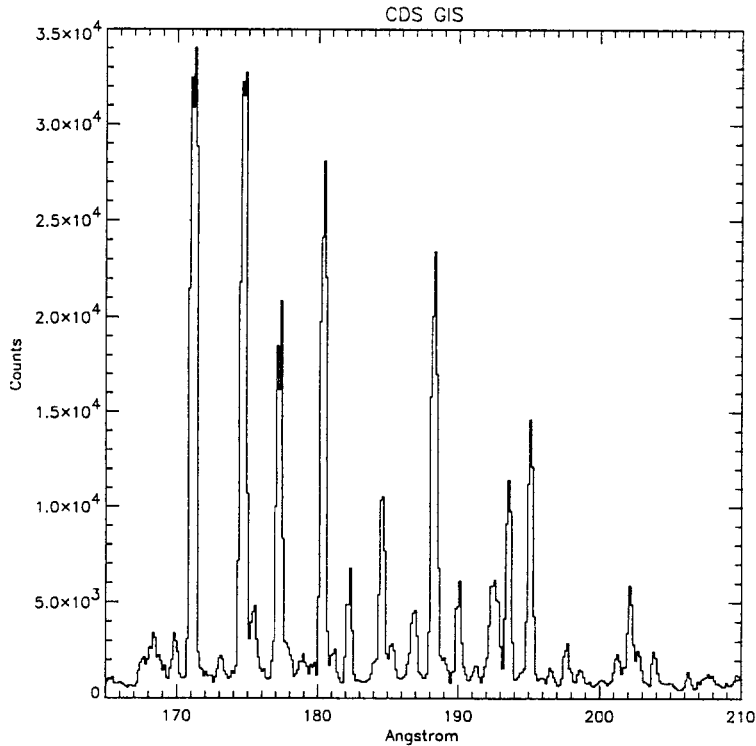


Fig. 11. CDS GIS spectrum of a quiet region the Sun (in histogram representation) in the region 170 to 200 Å. Almost all the lines are due to iron in ionization stages Fe IX to Fe XIII; note the similarity to the EUVE Procyon spectrum shown in Fig. 10

the laboratory in one very important aspect: They are usually highly or fully ionized, while the oceans, rivers, winds etc. on the Earth are not. Ionized gas is usually referred to as “plasma”, and in fact, most of the matter astrophysicists are dealing with are in plasma state. As a consequence of the ionization of the plasma, electrodynamic forces are often the most important forces acting on a plasma. Magnetohydrodynamic theory provides a description of these forces within the context of continuum mechanics; effects of *kinetic plasma physics* are not discussed in this paper. Also, the physical properties of plasma are quite different from those of neutral matter, and I will deal with those first, and then discuss the basic assumptions of magnetohydrodynamics.

Basic Plasma Properties. Since plasma is ionized, it contains copious numbers of very mobile charge carriers and is therefore expected to be a very good conductor of both electric currents and heat. For a fully ionized plasma

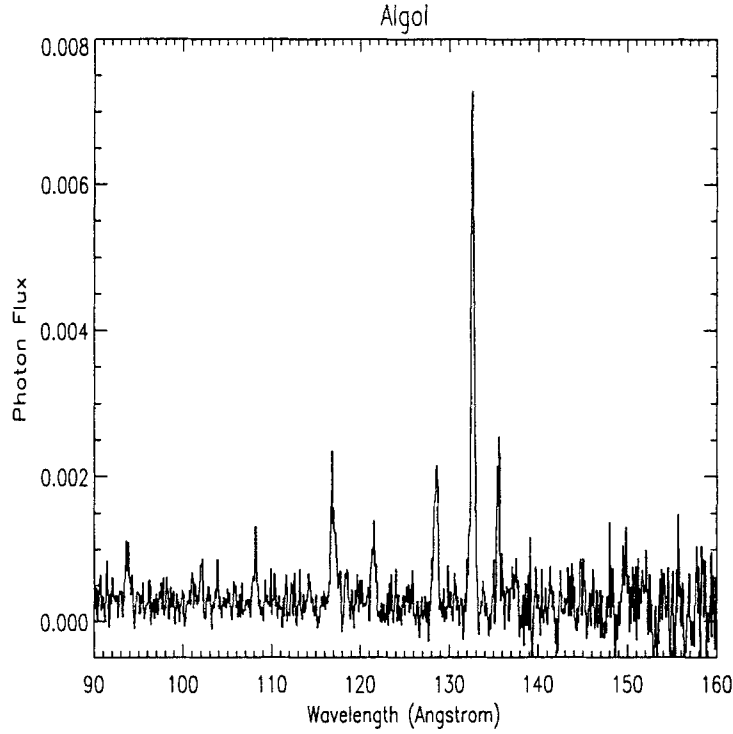


Fig. 12. EUVE short wavelength spectrum for the active star Algol (in histogram representation) in the region 170 to 200 Å. All the visible lines are due to iron in ionization stages Fe XIX to Fe XXIII

the electric conductivity σ can be expressed as

$$\sigma = \frac{n_e e^2 \tau_{ei}}{m_e} \quad (4)$$

where n_e , e , and m_e denote electron density, charge and mass as usual. τ_{ei} is the effective electron-ion collision time. If one replaces τ_{ei} by the effective electron self-collision time τ_e , which can be written according to Spitzer (1962) as

$$\tau_e = 0.266 \frac{T^{3/2}}{n_e \ln \Lambda} \quad (\text{sec}) , \quad (5)$$

one obtains results accurate to within a factor of 2. Here $\ln \Lambda$ denotes the so-called Coulomb logarithm which is a very weakly dependent function of temperature and density. Under typical coronal conditions, i.e., $6 < \log T < 7$ and $7 < \log n < 9$, $\ln \Lambda \approx 20$ with better than 10% accuracy. Putting in all

the numbers one finally obtains

$$\sigma = 1.53 \times 10^{-2} \frac{T^{3/2}}{\ln A} \quad (\text{ohm}^{-1} \text{m}^{-1}) . \quad (6)$$

Note that the unit $\text{ohm}^{-1} \text{m}^{-1}$ is the appropriate MKS unit for electric conductivity. Interestingly, the above expression for the conductivity is independent of density. Obviously, the above expression becomes meaningful only when compared to the electric conductivities of materials known from everyday experience. I have therefore compiled in Table 1 values of electric conductivity for a number of materials ranging from very good conductors to almost perfect insulators. Also given are the values for plasma under conditions encountered in the coronae of the Sun and other stars. As is clear from Table 1, hot plasma as encountered in an active star behaves – as far as electric conductivity is concerned – almost like copper ! In other words, plasma is able to conduct charges and hence currents extremely well, and therefore it is clear that it will be rather difficult to build up and maintain large gradients of electric potential in a plasma.

Table 1. Electric conductivities of some sample materials

Material	Temperature (K)	$\sigma \text{ ohm}^{-1} \text{m}^{-1}$
Plasma	2×10^6	1.4×10^5
Plasma	1×10^7	2.4×10^7
Copper	291	5.9×10^7
Mercury	291	1.0×10^6
China	291	1×10^{-12}

Good electric conductors are also good heat conductors. The reason for this is simply that the particles responsible for charge transport are also responsible for heat transport. Spitzer (1962) derives for the thermal conductivity κ_{\parallel} along the magnetic field the expression

$$\kappa_{\parallel} = 1.8 \times 10^{-5} \frac{T^{5/2}}{\ln A} \quad \text{erg/cm/sec/K} . \quad (7)$$

The conductivity perpendicular to the field is strongly suppressed. Spitzer (1962) quotes

$$\frac{\kappa_{\perp}}{\kappa_{\parallel}} = 2 \times 10^{-27} \frac{n^2}{T^3 B^2} . \quad (8)$$

The RHS of (8) is very small, and therefore κ_{\perp} is negligible for many applications. In Table 2 I have again compiled the thermal conductivities of a

number of materials and compared them to that of typical coronal plasma. As can be seen from Table 2, plasma is an extremely good heat conductor, and therefore it will be quite difficult to maintain large temperature gradients in a plasma since these will drive enormous heat fluxes to minimize temperature gradients.

Table 2. Thermal conductivities of some sample materials

Material	Temperature (K)	$\text{erg cm}^{-1} \text{sec}^{-1} \text{K}^{-1}$
Plasma	1×10^6	7.9×10^8
Plasma	1×10^7	2.3×10^{11}
Silver	273	4.2×10^7
Lead	273	3.6×10^6
Air	273	2.4×10^3
Water	273	5.4×10^4

Finally, plasma can lose energy by radiation. Very often astrophysical plasmas are optically thin, a property enormously simplifying the radiative transfer. In this case the radiation field is decoupled from the plasma, and the radiative loss function $P_{\text{rad}}(T)$, i.e., the energy lost per unit volume of plasma, takes the form

$$P_{\text{rad}}(T) = n_e n_H Q(T) . \quad (9)$$

Here $Q(T)$ denotes the so-called radiative cooling function, which has been computed by a large number of authors. In Fig. 13 I plot the radiative cooling function as calculated by Raymond and Smith (1977). As can be seen from Fig. 13, plasma at temperatures of $\sim 10^5$ K cools most efficiently. Somewhat counterintuitively to the blackbody case, plasma at larger temperatures cools less efficiently, or putting it differently, the same amount of emission measure of plasma will lose less and less energy by radiation the hotter its temperature. A useful parametrisation for the energy losses in the temperature range $10^5 K < T < 10^7 K$ is given by

$$Q(T) = 10^{-22} T_6^{-1/2} \quad (\text{erg cm}^3) \quad (10)$$

where T_6 denotes the temperature in units of millions of degrees.

The Role of Magnetic Fields. The Sun is - naturally - the only star where detailed structural studies of photospheric magnetic fields are possible. The magnetic fields in the solar photosphere are found to be compressed into

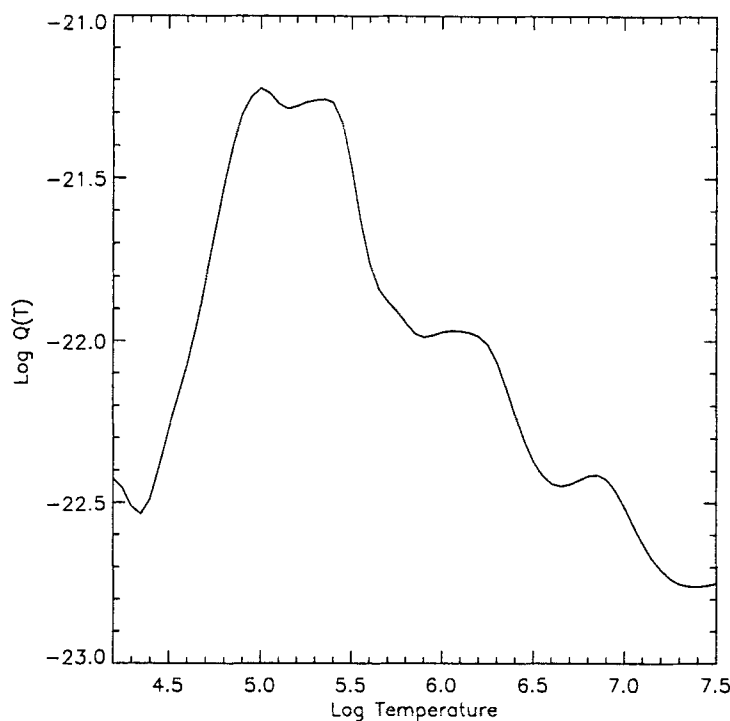


Fig. 13. Radiative loss function $Q(T)$ (in units of erg cm^3) versus temperature T

rather small flux tubes with magnetic field strengths of ~ 1500 G and filling factors well below the percent level; the photospheric gas outside these flux tubes appears to be essentially field-free. Little is known about the magnetic field structure in other stars. Combining the few measurements of magnetic field strength and filling factor with the Doppler images of rapidly rotating active stars, it is suggestive to assume that the essential difference between the solar photosphere and that of an active late-type star is not the strength of the magnetic field, but rather its filling factor. In fact, all the available evidence suggests that magnetic fields must cover not one percent but significant fractions of surfaces of the most active stars.

Magnetohydrodynamics. The Earth's surface, i.e., the site of our everyday life, is an electrically neutral environment, where electrodynamic and hydrodynamic phenomena are completely decoupled. As a consequence, for example, the reception of radio or television is – at least to a large extent – independent of the prevailing weather condition. Physically this means that the

equations describing electrodynamic phenomena, i.e., Maxwell's equations, and the hydrodynamic equations are decoupled, and can be solved separately. However, most astrophysical plasmas and in particular the plasma in stellar coronae are highly ionized and therefore highly conducting. In such an environment electrodynamic and hydrodynamic phenomena are closely coupled and the appropriate framework for the theoretical description of such plasmas is known as Magnetohydrodynamics (MHD).

Maxwell's Equations. Let us first recall the set of Maxwell's equations, which describe how the electric field \mathbf{E} and the magnetic field (or more precisely the magnetic induction) \mathbf{B} are generated from currents \mathbf{j} and charges ρ_c :

$$\nabla \times \frac{\mathbf{B}}{\mu} = \mathbf{j} + \epsilon \frac{\partial \mathbf{E}}{\partial t} \quad (11)$$

$$\nabla \cdot \mathbf{B} = 0 \quad (12)$$

$$\nabla \times \mathbf{E} = -\frac{\partial \mathbf{B}}{\partial t} \quad (13)$$

$$\nabla \cdot \mathbf{E} = \frac{\rho_c}{\epsilon} \quad (14)$$

Here the constants μ and ϵ denote magnetic permeability and electric permittivity of free space. Maxwell's equations, first, specify how the sources of electric fields, i.e., free charges and time-variable electric fields, produce magnetic fields, and second, specify, that magnetic fields must be free of monopoles, and are in turn produced by currents and time-variable electric fields.

Hydrodynamic Equations. In ordinary hydrodynamics one describes the bulk properties of the plasma, i.e., density, pressure, temperature and velocity, by the following set of equations:

$$\frac{\partial \rho}{\partial t} + \nabla \cdot (\rho \mathbf{v}) = 0 \quad (15)$$

$$\rho \left(\frac{\partial \mathbf{v}}{\partial t} + \mathbf{v} \cdot \nabla \mathbf{v} \right) = -\nabla p + \rho \mathbf{g} \quad (16)$$

$$p = 2 \frac{\rho}{m_H} kT \quad (17)$$

Here p , T , and ρ denote pressure, temperature and density of the plasma respectively, \mathbf{g} specifies the external gravity acting on the plasma. The first two equations are of course simply the conservation equations for mass and momentum, while the third equation is the equation of state which one always assumes to be that of an ideal gas. In order to close the above set of hydrodynamical equations, one needs an energy equation; often it is possible to capture the essential physics of a given problem by assuming isothermality, i.e., $T = \text{const.}$

Magnetohydrodynamic Equations (MHD). Just as in ordinary hydrodynamics, one continues to describe the plasma as a single-species fluid, governed by the above derived hydrodynamic equations. However, the presence of charges in the plasma leads to the appearance of an additional force, i.e., the Lorentz force in the momentum equation, and also Maxwell's equations are altered in the following way to arrive at the set of magnetohydrodynamic equations describing *non-relativistic MHD*. One first assumes all plasma motions to be non-relativistic and obey $v \ll c$. As a consequence, the displacement current in Ampere's law can be neglected and one writes

$$\nabla \times \frac{\mathbf{B}}{\mu} = \mathbf{j} . \quad (18)$$

Because $\nabla \cdot \mathbf{B} = 0$ still holds, one deduces

$$\nabla \cdot \mathbf{j} = 0 \quad (19)$$

which implies that there cannot be any substantial accumulation of charge and that currents flow in closed circuits. Ohm's law relates the electric field strength \mathbf{E} to the current density \mathbf{j} through

$$\mathbf{j} = \sigma \cdot \mathbf{E} \quad (20)$$

where σ denotes the electric conductivity. In the form (20) Ohm's law refers to the frame comoving with the plasma, i.e., the frame where $\mathbf{v} = 0$. Lorentz transformation of the electric field \mathbf{E}_{com} into the field \mathbf{E}_{ob} in the observer frame yields (in first order in v/c)

$$\mathbf{E}_{\text{ob}} = \mathbf{E}_{\text{com}} + \mathbf{v} \times \mathbf{B} \quad (21)$$

and thus Ohm's law becomes

$$\mathbf{j} = \sigma(\mathbf{E} + \mathbf{v} \times \mathbf{B}) \quad (22)$$

which clearly does provide a coupling between the electrodynamic and hydrodynamic plasma properties. I will show below that the $\mathbf{v} \times \mathbf{B}$ term usually dominates the electric fields in the observer's frame.

The other coupling comes through the Lorentz force. It is well known that currents flowing in a magnetic field feel a force (Biot-Savart's law), and one writes analogously for the force density

$$\mathbf{F}_{\text{Lor}} = \mathbf{j} \times \mathbf{B} \quad (23)$$

so that the MHD momentum equation becomes

$$\rho \left(\frac{\partial \mathbf{v}}{\partial t} + \mathbf{v} \cdot \nabla \mathbf{v} \right) = -\nabla p + \rho \mathbf{g} + \mathbf{j} \times \mathbf{B} \quad (24)$$

which provides yet another coupling between the electrodynamics and hydrodynamics of a plasma.

As I already demonstrated above, the electrical conductivity of plasma is often quite large. In the limit $\sigma = \infty$, Ohm's law would lead to infinitely large current densities. This can only be avoided by demanding

$$\mathbf{E} + \mathbf{v} \times \mathbf{B} = 0 \quad (25)$$

which implies that there are no electric fields in the plasma rest frame, or putting it differently, the electric fields due to the current term are totally negligible. The infinite conductivity limit is also known as the *ideal MHD approximation*.

An extremely important equation in any MHD context is the so-called induction equation which relates magnetic field strength to fluid velocity. If one combines Faraday's law with Ohm's law, one obtains

$$\frac{\partial \mathbf{B}}{\partial t} = \nabla \times (\mathbf{v} \times \mathbf{B}) - \frac{1}{\sigma \mu} \nabla \times (\nabla \times \mathbf{B}) \quad (26)$$

which can be rewritten using the vector identity $\nabla \times (\nabla \times \mathbf{B}) = \nabla(\nabla \cdot \mathbf{B}) - \Delta \mathbf{B}$. Here $\eta = \frac{1}{\sigma \mu}$ denotes the magnetic diffusivity. In ideal MHD the induction equation simplifies to

$$\frac{\partial \mathbf{B}}{\partial t} = \nabla \times (\mathbf{v} \times \mathbf{B}) \quad (27)$$

which implies that the specification of the magnetic field distribution $\mathbf{B}(\mathbf{x}, t=0)$ and the velocity field $\mathbf{v}(\mathbf{x}, t)$ determines the magnetic field distribution at all later times (kinematic theory). Of course, because of the Lorentz force in the momentum equation, the magnetic field does influence the velocity field, and therefore MHD theory is intrinsically non-linear.

A few Comments. A few comments on the basic assumptions and concepts of MHD seem to be in order in this context. According to the MHD version of Ampere's law, currents are the only sources of magnetic fields. For a current to flow, however, one requires that the velocity difference between electrons and ions, i.e., the drift velocity between negative and positive charges $\mathbf{v}_{\text{drift}} = \mathbf{v}_{\text{el}} - \mathbf{v}_{\text{ion}}$, must be non-zero. This seems to violate our assumption that the whole plasma can be treated as a single species fluid and can be characterized by a single velocity. We therefore have to ask ourselves how large are the required drift speeds under typical astrophysical circumstances.

By order of magnitude one can estimate the required drift velocities. The current is determined by the curl of the magnetic field and therefore $j \approx \frac{B}{L\mu}$, where L is a characteristic size scale of the MHD system under consideration. On the other hand, the current can also be expressed through the drift speed v_{drift} as $j = n_{\text{electron}} e v_{\text{drift}}$ (which implicitly assumes $n_{\text{electron}} = n_{\text{ion}}$), and combining these two equations and eliminating j results in the estimate

$$v_{\text{drift}} = \frac{B}{L\mu n_{\text{el}} e} \quad (28)$$

It is quite instructive to evaluate (28) for a few cases. For example, using $B = 1000$ G, $L = 2 \times 10^{10}$ cm and $n = 10^{23}$ cm $^{-3}$ as typical parameters for a sunspot, one obtains $v_{\text{drift}} \approx 2.5 \times 10^{-12}$ cm/sec; using $B = 10$ G, $L = 2 \times 10^9$ cm and $n = 2 \times 10^9$ cm $^{-3}$ as typical parameters for a solar coronal active region, one finds $v_{\text{drift}} \approx 10$ cm/sec. In both cases the required drift speeds are ridiculously small and most certainly not measurable. Hence the MHD assumptions are well justified. Note that in (28), the required drift velocity is inversely proportional to the size scale L of the system. Astrophysical systems are, almost by definition, large, and therefore tend to obey the MHD approximation.

If one evaluates in the same fashion as above the terms in the force equation, one finds that the $\mathbf{j} \times \mathbf{B}$ term dominates under coronal conditions. In order to achieve force balance, it is therefore important to satisfy the relation

$$\mathbf{j} \times \mathbf{B} = (\nabla \times \mathbf{B}) \times \mathbf{B} = 0 \quad (29)$$

and magnetic field configuration satisfying (29) are called force-free. Magnetic field configurations satisfying the even more restricted equation

$$\nabla \times \mathbf{B} = 0 \quad (30)$$

are current-free and potential.

Returning now to my previous examples, one can calculate the required current j_{cor} , yielding the prescribed magnetic field strengths and length scales. Using Ampere's law, one finds $j_{\text{cor}} = 4.0 \cdot 10^{-5}$ A m $^{-2}$, and with Ohm's law and assuming Spitzer conductivities the associated electric field strength necessary to drive the currents can be calculated as $E_{\text{cor}} = 2.8 \cdot 10^{-10}$ V m $^{-1}$. This value needs to be compared to the electric fields obtained from Lorentz transformations from the plasma rest frame to the observer's frame, i.e., $\mathbf{E} = -\mathbf{v} \times \mathbf{B}$, which gives $E_{\text{cor,Lo}} = 1.0$ V m $^{-1}$ if typical plasma speeds of $v \approx 1$ km sec $^{-1}$ are assumed. Clearly, $E_{\text{cor,Lo}} \gg E_{\text{cor}}$ by quite a few orders of magnitude, so that changing the input parameters B , L or v will not change the conclusion. Therefore the magnetic field is basically given by *magnetostatics*, and the electric fields in the observer frame result from Lorentz transforming via $\mathbf{v} \times \mathbf{B}$; thus both currents and electric fields are *derived* quantities, which can be calculated (if desired) from the magnetic and velocity fields.

3 Magnetically Closed Regions

In the following section I will consider some MHD models of regions relevant to solar and stellar coronae. Let me first consider stationary MHD models of regions with magnetically closed topology, i.e., the prototypical X-ray emitting hot loops. In such regions one observes – at least outside flares – no substantial plasma velocities. The dynamic pressure in the force equation can

therefore be neglected by setting $\mathbf{v} \approx 0$, which satisfies the mass conservation equation trivially. The force equation then becomes

$$-\frac{\nabla p}{\rho} + \mathbf{g} + \mathbf{j} \times \mathbf{B} = 0. \quad (31)$$

Because of its definition the Lorentz force has no component *along* the magnetic field; multiplying (31) with \mathbf{B} , one obtains

$$\mathbf{B} \cdot \left(-\frac{\nabla p}{\rho} + \mathbf{g}\right) = 0, \quad (32)$$

which implies that hydrostatic equilibrium must prevail *along* a magnetic field line. Consequently, the gas pressure along a field line will remain constant if the characteristic scale size of the system is less than the pressure scale height $\Lambda_p = \frac{2kT}{gm_H}$. For the simplest loop models it is customary to assume $p = \text{const}$, an assumption which approximately satisfies the force equation.

The temperature structure of a magnetically closed region must therefore be determined by the only remaining equation, i.e., the energy equation. Here one assumes that at any given point along the magnetic loop there is a local energy balance between energy losses through conduction and radiative cooling and energy gains by some unspecified heating mechanism. Specifically one writes

$$\nabla F_{\text{cond}} + P_{\text{rad}} + H = 0, \quad (33)$$

where F_{cond} , P_{rad} and H denote the conductive flux, the radiative cooling rate and the volumetric heating rate respectively. I assume the "classical" form of the conductive flux through

$$\nabla F_{\text{cond}} = A\kappa_o T^{5/2} \frac{dT}{ds}, \quad (34)$$

where A denotes the loop cross section, and κ_o the Spitzer conductivity (cf. (7)). The radiative cooling is given as in Fig. 13, and can be expressed in terms of pressure through

$$P_{\text{rad}} = \frac{p^2}{4k^2 T^2} Q(T), \quad (35)$$

where I have assumed $n_H = n_e$ for simplicity; for a fully ionized gas with solar abundances $n_H = 0.85 n_e$ holds. In order to make analytical progress, I assume that the loop cross section A , the cooling function Q and the heating H have temperature dependences of the following form:

$$A(T) = A_0 T^\alpha \quad Q(T) = \chi T^\gamma \quad H(T) = H_0 T^\beta, \quad (36)$$

where the parameters α , β and γ can be arbitrarily chosen. In (36) the case $\alpha = 0$ describes the (canonical) case of a loop with constant cross section, $\gamma = \frac{1}{2}$ gives the (canonical) cooling function for plasma in the temperature range $2-8 \cdot 10^6$ K, and $\beta = 0$ assumes constant heating per unit volume, while

$\beta = -1$ corresponds to constant heating per unit mass. These temperature dependences are admittedly rather arbitrary, their main justification being the analytical solvability of the resulting equations. With these definitions the energy equation finally reads

$$\frac{d}{ds} \left(\kappa_0 T^{\alpha+5/2} \frac{dT}{ds} \right) - \frac{p^2 \chi}{4k^2} T^{\gamma+\alpha-2} + H_0 T^{\beta+\alpha} = 0, \quad (37)$$

which is a second order ordinary differential equation determining the temperature T as a function of the length s along the loop.

Loop Scaling Laws. I now proceed with the solution of the energy equation (37). In order to arrive at a physically meaningful solution, appropriate boundary conditions must be imposed. The choice of the boundary conditions becomes more apparent, if equation (37) is rewritten in terms of the variables F_{cond} and T through

$$\frac{1}{2} \frac{dF_{\text{cond}}^2}{dT} - \frac{p^2 \chi \kappa_0}{4k^2} T^{\gamma+2\alpha+1/2} + H_0 T^{\beta+2\alpha+5/2} = 0. \quad (38)$$

The important point now is that at the top of the loop the temperature is assumed to become maximal, and therefore the conductive flux must vanish there. Furthermore, at the bottom of the loop, the conductive flux becomes also very small because of the $T^{5/2}$ dependence of the thermal conductivity. Thus formally one requires the boundary conditions

$$F_{\text{cond}}(T_{\text{max}}) = F_{\text{cond}}(T_{\text{min}}) = 0 \quad (39)$$

where T_{max} and T_{min} denote the temperature at loop top and bottom respectively. Physically the boundary condition (38) means that the loop is *thermally isolated* and that the overall energy budget of the loop is only given by radiation and heating; conduction only *redistributes* the energy deposited by the heating process but it cannot make any energy leave the system.

With the boundary conditions (39) the loop energy equation (35) can be integrated once. The first term can be integrated trivially and vanishes because of the choice of boundary conditions. The other two terms are functions of T alone – note that $p = \text{const}$ is assumed! – and thus performing the integration must result in a relation between the remaining parameters H_0 , T_{max} , T_{min} and p . If the temperatures at loop top and bottom are assumed to differ substantially, i.e., $T_{\text{max}} \gg T_{\text{min}}$, the contributions arising from T_{min} can be ignored altogether. In practice, this last assumption is satisfied extremely well since one typically chooses $T_{\text{min}} = 20000 \text{ K}$, i.e., a temperature where hydrogen becomes fully ionized, and $T_{\text{max}} = 10^6 \text{ K}$ or greater, i.e., a coronal temperature.

Working out the algebra, one then obtains a scaling relation between H_0 , T_{max} and p of the form

$$H_0 = \frac{p^2 \chi}{4k^2} \frac{7/2 + 2\alpha + \beta}{3/2 + 2\alpha + \gamma} T_{\text{max}}^{\gamma-\beta-2}. \quad (40)$$

As a consequence of (40), the normalization of the heating function $H(T)$ cannot be arbitrarily chosen; once T_{\max} and p are known – and both of these parameters can be inferred from observations – the heating function $H(T)$ is fixed at least within the considered parametric framework.

Putting the obtained expression for H_0 back in the differential equation for the conductive flux (38), I can integrate the energy equation once between T_{\min} and T to obtain

$$\frac{1}{2} F_{\text{cond}}^2 = \frac{p^2 \chi \kappa_0 T^{\gamma+2\alpha+3/2}}{4k^2(3/2 + \gamma + 2\alpha)} \left(1 - \left(\frac{T}{T_{\max}} \right)^{2+\beta-\gamma} \right), \quad (41)$$

an equation determining the conductive flux and hence the temperature gradient at any point along the loop. Taking the square root, reexpressing F_{cond} with dT/ds , and introducing a non-dimensional temperature variable $\tau = \frac{T}{T_{\max}}$ one obtains

$$\frac{d\tau}{\tau^{\gamma/2-7/4}(1-\tau^{\beta-\gamma+2})^{1/2}} T_{\max}^{(11/4-\gamma/2)} = p \left(\frac{\chi}{2k^2 \kappa_0 (3/2 + \gamma + 2\alpha)} \right)^{1/2} ds. \quad (42)$$

The integral on the LHS of (42) must be evaluated between 0 and 1 and can be expressed in terms of the Γ -function through

$$I_{\beta,\gamma} = \int_0^1 \frac{d\tau}{\tau^{\gamma/2-7/4}(1-\tau^{\beta-\gamma+2})^{1/2}} = \frac{\sqrt{\pi}}{2 + \beta - \gamma} \frac{\Gamma(\frac{11-2\gamma}{8+4\beta-4\gamma})}{\Gamma(\frac{15+2\beta-4\gamma}{8+4\beta-4\gamma})}, \quad (43)$$

while the RHS of (43) is integrated trivially. Since $I_{\beta,\gamma}$ is dimensionless and of order unity for all reasonable values of the parameters α , β and γ , one obtains a second loop scaling law relating the physical parameters p , L , and T_{\max} in the form

$$T_{\max}^{(11/4-\gamma/2)} I_{\beta,\gamma} \left(\frac{2k^2 \kappa_0 (3/2 + \gamma + 2\alpha)}{\chi} \right)^{1/2} = p \cdot L. \quad (44)$$

This scaling law (44) asserts that the pressure p , the peak temperature T_{\max} , and the length L of a magnetically closed region cannot be independently chosen. The important point now is that in the case of the Sun all three physical parameters in the scaling law (44) can be directly measured. Hence the scaling law (44) can be verified (or falsified !) by observations. In general it is the case that the measured loop lengths show good agreement with those “predicted” from the knowledge of T_{\max} and p .

The other remarkable point about the scaling law (44) is that it is quite robust with respect to the parameters α , β and γ . In fact, the parameters α and β , which describe the dependence of loop cross section and heating on temperature, only enter the normalization of the scaling law. Only the parameter γ , which describes the temperature dependence of the radiative

cooling and is thus given by atomic physics, enters into the physical quantities. Using the canonical value of $\gamma = -\frac{1}{2}$, one obtains the “standard” form of the loop scaling law

$$T_{\max}^3 \sim p \cdot L , \quad (45)$$

which, as we have seen, is independent of loop cross section and heating at least in the frame work of our analytical model, and rather insensitive to the precise form of the cooling function. This robustness is of course responsible for the great success of the scaling law (44), on the other hand it is also in some sense a curse. One would have naively assumed that a precise determination of the temperature structure along the loop would determine the heating function and thus reveal the nature of the underlying heating mechanism; however, the temperature structure is more or less independent of the precise spatial variation of the heating function because of the high efficiency of thermal conduction. Therefore, one can gain only little insight into the heating mechanism, but at least the observations clearly indicate that the basic assumptions, i.e., a magnetically confined static plasma in energy equilibrium between heating and cooling, capture the essential physics of a hot X-ray emitting loop.

3.1 Magnetically Open Regions

I consider next the modeling of magnetically open regions. First I will show that such regions must deviate from hydrostatic equilibrium and that flows (i.e., winds) must exist. Next, I will construct simple wind models, and emphasize the important physics of such thermally driven winds.

Impossibility of a Static Corona. In magnetically open regions a corona cannot be maintained in hydrostatic or magnetostatic equilibrium. In order to demonstrate this let me assume a purely radial field geometry such that

$$\mathbf{B} = B_r(r) \mathbf{e}_r \quad (46)$$

is the only relevant magnetic field component. Since I of course demand $\nabla \cdot \mathbf{B} = 0$, one finds the radial dependence of $B_r(r)$:

$$B_r(r) \sim \frac{1}{r^2} . \quad (47)$$

Such a field configuration is obviously current-free, and therefore also force-free and consequently the Lorentz force does not contribute in the force equation. Since I am looking for static solutions, I of course set $v = 0$, and only need to solve the equation of hydrostatic equilibrium:

$$\frac{dP}{dr} = -\frac{\rho G M_{\text{star}}}{r^2} , \quad (48)$$

where M_{star} denotes the mass of the star and G the constant of gravitation as usual. The total mass in the corona is assumed to be so small that it does not contribute to the overall mass and gravity of the star. For the energy equation I appeal to the large thermal conductivity of plasma and assume $T = \text{const}$, which clearly implies $F_{\text{cond}} = 0$; I note that results do not sensitively depend on this choice as long as F_{cond} is sufficiently small. With this assumption and using the ideal gas law, the equation of hydrostatic equilibrium can be readily expressed in terms of the particle density n :

$$\frac{d \ln(n)}{dx} = -\frac{r_0}{H} \frac{1}{x^2}, \quad (49)$$

where r_0 is a reference level at which some initial density n_0 and temperature T_0 are obtained. The variable x is a dimensionless radial variable and H the scale height:

$$x = \frac{r}{r_0} \quad H = \frac{2kT_0 r_0^2}{GM_{\text{star}} m_{\text{H}}}. \quad (50)$$

Equation (49) can be readily integrated and has the solution

$$n = n_0 \exp\left(-\frac{r_0}{H} \left(1 - \frac{r_0}{r}\right)\right), \quad (51)$$

which satisfies the boundary condition $n(r_0) = n_0$ by construction. The important feature of this solution is that it approaches a finite value $n_0 \exp(-\frac{r_0}{H})$ as r approaches infinity. Since T is constant, the asymptotic pressure is therefore also constant. The ratio between initial and asymptotic pressure is then determined by the ratio

$$\frac{r_0}{H} = \frac{GM_{\text{star}} m_{\text{H}}}{2kT_0 r_0} = 7.7, \quad (52)$$

where the numerical value of 7.7 applies to solar conditions. As is clear from (52), the asymptotic pressure solely depends on coronal temperature and radius, both of which are rather well known at least for the Sun. Using characteristic values for p_0 , one then finds asymptotic pressures which exceed the pressure inferred for the interstellar medium by many orders of magnitude. It is therefore difficult to avoid the conclusion that the ISM pressure is not sufficient to confine the solar corona and that the corona must expand into the ISM *in violation of my initial assumption of hydrostatic equilibrium*.

Coronal Winds. As demonstrated in the previous section, a magnetically open region cannot be maintained in hydrostatic equilibrium. It is therefore invalid to assume $v = 0$, instead I now assume a stationary, spherically symmetric flow field $v(r)$ satisfying the mass conservation equation

$$\frac{d}{dr}(r^2 \rho v) = 0 \quad (53)$$

and the force equation

$$\rho v \frac{dv}{dr} = -\frac{dP}{dr} - \frac{\rho G M_{\odot}}{r^2} . \quad (54)$$

For the energy equation I assume again $T(r) = T_0 = \text{const}$, which implies the operation of a suitable heating mechanism to produce the assumed isothermality. At any rate, as in the case of a static corona, the high thermal conductivity of the coronal plasma ensures that large temperature gradients cannot be maintained.

The mass conservation equation can be easily integrated with the mass loss rate \dot{M} as integration constant:

$$4\pi\rho v r^2 = \dot{M} . \quad (55)$$

Mass conservation implies that in a stationary wind density and velocity cannot be independently chosen. Using then the ideal gas law and (55) in the force equation, one can first replace the pressure gradient with a density gradient, which in turn can be expressed in terms of a velocity gradient. Collecting terms, one obtains a non-linear ordinary differential equation for the velocity field $v(r)$:

$$\frac{dv^2}{dr} = -\frac{2GM}{r^2} \frac{1 - \frac{4kT_0 r}{m_H G M}}{1 - \frac{2kT_0}{m_H v^2}} . \quad (56)$$

The term on the right hand side of (56) can be recognized as the ratio of the thermal and potential energy in the nominator, and the ratio between thermal and kinetic energy in the denominator. The thermal energy stays constant by the assumption of isothermality, while the potential energy approaches zero as r approaches ∞ . Therefore the nominator $f(r)$ in (56)

$$f(r) = 1 - \frac{4kT_0 r}{m_H G M} \quad (57)$$

will change sign at the so-called critical radius r_c given by

$$r_c = \frac{m_H G M}{4kT_0} . \quad (58)$$

For a typical temperature of a solar coronal hole (i.e., $T_0 \approx 1.5 \cdot 10^6$ K) one finds $r_c = 3.84 R_{\odot}$. A regular solution of the wind equation (56) must therefore satisfy additional conditions at the critical point r_c :

$$\text{Case A :} \quad \left. \frac{dv}{dr} \right|_{r_c} = 0 , \quad (59)$$

or, alternatively, the denominator must also vanish at the critical radius, which in turn imposes a condition on the velocity v_c at the critical point:

$$\text{Case B :} \quad v_c^2 = \frac{2kT_0}{m_H} . \quad (60)$$

These two types of solution have very different properties. In **Case A** solutions there is no acceleration at the critical point; therefore the maximal velocity will be reached at the critical point, and if the flow is subsonic near the surface regions (an implicitly made assumption), the flow will remain subsonic at all radii. On the other hand, in **Case B** there is acceleration at the critical point, and the critical velocity v_c is immediately recognized as the isothermal sound speed. Hence in the type **B** solutions the flow changes from being subsonic for radii $r < r_c$ to being supersonic for radii $r > r_c$. Solutions of type **A** are known as “breeze” solutions, while solutions of type **B** are called “wind” solutions.

It is instructive to cast the wind equation (56) into dimensionless form by introducing the variables:

$$\hat{r} = \frac{r}{r_c} \quad \hat{v} = \frac{v}{v_c} . \quad (61)$$

In terms of the variables \hat{r} and \hat{v} the wind equation reads

$$\frac{d\hat{v}^2}{d\hat{r}} \left(1 - \frac{1}{\hat{v}^2}\right) = -\frac{4}{\hat{r}^2} (1 - \hat{r}) . \quad (62)$$

The last equation can be analytically integrated with the solution

$$\hat{v}^2 - \ln \hat{v}^2 = 4 \ln(\hat{r}) + \frac{4}{\hat{r}} + C . \quad (63)$$

with an arbitrary integration constant C . For the critical solution one of course demands

$$\hat{r}_c = 1 \quad \hat{v}_c = 1 , \quad (64)$$

therefore the choice $C = -3$ yields precisely the critical solution. If $C < -3$, one obtains breeze solutions, while the choice $C > -3$ leads to double-valued solutions which are rejected on physical grounds.

In order to illustrate wind and breeze solutions, I plot in Fig. 14 the run of velocity (expressed in terms of \hat{v}) as a function of radial distance (expressed in terms of \hat{r}) for a couple of subsonic breeze solutions and the critical wind solution; the breeze solutions are plotted as dotted line, the critical wind solution is plotted as a solid line. As is clear from Fig. 14, the different solutions differ only little in the subsonic part, but differ dramatically in the supersonic regime. I emphasize that no other solutions of the wind equation exist such that the velocity approaches zero at the inner wind boundary.

With the help of the solution (63), one can determine the asymptotic solution properties. On the right hand side of (63), the $\ln(\hat{r})$ term will always dominate asymptotically, however, we obtain different dependences for the velocity terms on the left hand side of (63). For the critical solution the \hat{v}^2 term dominates, so that asymptotically

$$\hat{v} \sim 2v_c (\ln \hat{r})^{1/2} . \quad (65)$$

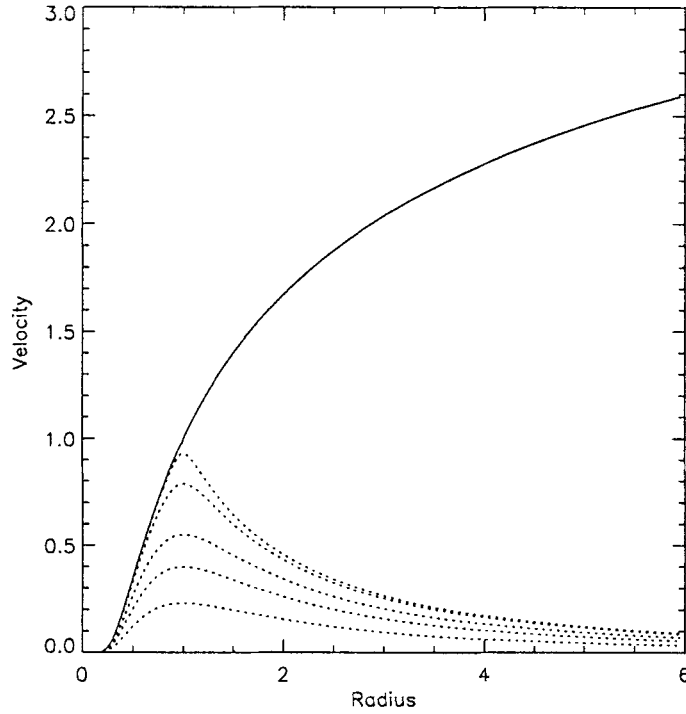


Fig. 14. \hat{v} vs. \hat{r} for breeze solutions (dotted lines) and the critical wind solution (solid line). All other wind solutions do not satisfy appropriate conditions at the inner wind boundary

On the other hand, for the breeze solution the $\ln \hat{v}^2$ term dominates, so that asymptotically

$$v \sim \frac{1}{r^2} . \quad (66)$$

Obviously, both asymptotic solutions are unphysical. The wind solution goes to infinity (albeit only logarithmically), clearly a not particularly desirable property, while the breeze solution results in a constant asymptotic density and hence pressure, which leads to a mismatch between asymptotic and interstellar medium pressure as in the static corona model. In both cases, this unphysical behavior is a consequence of the assumption $T_o = \text{const}$, which implies heating at very large distances from the stellar surface. It can be shown, however, that by using a more realistic energy equation internally consistent wind solutions, which approach a finite velocity at infinity, and internally consistent breeze solutions with zero pressure at infinity can be constructed.

4 The Angular Momentum Problem

In order to estimate the angular momentum of a star, let us model the star as a sphere of radius R , with a radial density variation $\rho(r)$, and rotating rigidly with some angular velocity Ω . The angular momentum vector is parallel to the rotation axis and has a magnitude

$$J = 2 \int_0^R r^4 \rho(r) dr \int_0^{2\pi} \int_0^{\pi/2} \Omega \sin^3 \psi d\psi = \frac{8\pi\Omega}{3} \int_0^R r^4 \rho(r) dr. \quad (67)$$

For the special case $\rho = \text{const}$ the remaining integral in (67) can be evaluated as

$$J = \frac{2}{5} M_{\text{star}} R^2 \Omega = K M_{\text{star}} R^2 \Omega \quad (68)$$

where M_{star} as before is the total mass of the star under consideration. Obviously, the approximation $\rho = \text{const}$ is rather poor for a real star and will overestimate the total angular momentum; however, the basic functional dependence of J on M_{star} , R and Ω remains the same, except that the constant K has a value of $\approx \frac{1}{13}$ instead of the value $\frac{2}{5}$ obtained for a rigid body.

With these numbers we can now determine the total angular momentum of the Sun. Using $R = 7 \cdot 10^{10}$ cm, $M = 2 \cdot 10^{33}$ g, and $\Omega = 2.5 \cdot 10^{-6}$ sec $^{-1}$ results in a value of $J_{\odot} = 9.8 \cdot 10^{48}$ g cm 2 sec $^{-1}$. As demonstrated earlier, younger stars can rotate considerably faster than the present age Sun, but for the discussion to follow I will adopt $J = 10^{49}$ g cm 2 sec $^{-1}$ as a typical value for a stellar angular momentum. From observations one knows that a significant fraction of the stellar angular momentum is lost on a time scale of 10^9 yrs and possibly even as short as 10^8 yrs. In the absence of magnetic fields, this angular momentum must be carried away by a mass flow. If one assumes that each mass element leaving the star carries with it its rigid body angular momentum per unit mass at the stellar surface, an angular momentum loss rate of

$$\dot{J} = R_{\text{star}}^2 \Omega \dot{M} \quad (69)$$

is obtained. This last expression (69) will clearly overestimate the actual angular momentum losses since it applies only at the equatorial regions. Proceeding now to compute the angular momentum loss time scale one finds

$$\tau_J \equiv \frac{J}{\dot{J}} = \frac{2}{5} \frac{M}{\dot{M}} \approx 10^{13} \text{ yrs} \quad (70)$$

with the numerical value resulting from assuming a solar value for the mass loss rate, i.e., $\dot{M}_{\odot} = 1.5 \cdot 10^{12}$ g sec $^{-1}$. The angular momentum time scale in (70) is of course absurdly long, and exceeds the presumed age of the universe by a few orders of magnitude! Even more importantly, (70) implies that a significant fraction of the total angular momentum can only be lost if a significant fraction of the mass is lost at the same time. This violates, however, both observations as well as stellar evolution theory, and one therefore concludes that mass loss cannot be the dominant contributor to the observed angular momentum loss of cool stars like the Sun.

5 Magnetized Coronal Wind

In a landmark paper Weber and Davis (1967) pointed out the fact that a **magnetized** wind can in fact solve the angular problem as posed in the previous section. Since the coronal plasma is magnetized, it has to be described with the magnetohydrodynamic rather than hydrodynamic equations. Let me therefore assume a stationary and isothermal wind as in the case of a Parker wind; in addition, I assume that the underlying star is rotating rigidly with an angular velocity Ω and is the source of the magnetic field permeating the wind. Furthermore all physical variables are assumed to have only radial dependence, and I envisage a stationary flow only in the equatorial plane. The MHD equations governing this wind are given by the mass conservation equation

$$\nabla \cdot (\rho \mathbf{v}) = 0 \quad (71)$$

the force equation

$$\rho \mathbf{v} \cdot \nabla \mathbf{v} = -\nabla(p + \frac{B^2}{2\mu}) + \mathbf{B} \cdot \nabla \mathbf{B} - \frac{GM\rho}{r^2} \hat{\mathbf{e}}_r . \quad (72)$$

I of course demand

$$\nabla \cdot \mathbf{B} = 0 \quad (73)$$

as usual and the stationary induction equation becomes

$$(\nabla \times \mathbf{B}) \times \mathbf{B} = 0 . \quad (74)$$

Both the magnetic field and velocity field are assumed to have only radial and azimuthal components which are just as all the other physical variables functions of r only:

$$\mathbf{v} = v_\phi \hat{\mathbf{e}}_\phi + u_r \hat{\mathbf{e}}_r \quad \mathbf{B} = B_\phi \hat{\mathbf{e}}_\phi + B_r \hat{\mathbf{e}}_r . \quad (75)$$

Next I try to express these equations in conservation form. Trivially one obtains

$$\frac{\partial}{\partial r}(r^2 \rho v) = 0 \quad (76)$$

as in the non-magnetic case, and also

$$\frac{\partial}{\partial r}(r^2 B_r) = 0 . \quad (77)$$

Among the three components of the induction equation only the ϕ -component is non-trivial:

$$\frac{\partial}{\partial r} r (u_r B_\phi - v_\phi B_r) = 0 . \quad (78)$$

Finally, the ϕ -component of the force equation can be expressed as

$$\frac{\partial}{\partial r} \left((\rho u_r r^2)(r v_\phi) - \frac{(r^2 B_r)}{\mu} (r B_\phi) \right) = 0 . \quad (79)$$

The radial component of the force equation is the only remaining equation. Even in the nonmagnetic case it cannot be written in conservation form; it now becomes rather complicated because of the magnetic field related terms. Therefore four equations are available in conservation form (requiring the specification of four constants of motion) as well as the radial component of the force equation to determine the radial and azimuthal components of magnetic field and velocity and density; note that density and temperature determine pressure through (17). Thus mathematically one has five equations to determine five unknown functions of radial distance r .

The first two conservation equations can be readily integrated to yield

$$(r^2 \rho v) = \frac{\dot{M}}{4\pi} , \quad (80)$$

with the first integration constant being determined by the total mass loss \dot{M} , and

$$B_r = B_o \frac{r_o^2}{r^2} , \quad (81)$$

where B_o specifies the radial field at some reference level r_o . Alternatively, the product $B_o r_o^2$ can be thought of the total magnetic flux leaving the star which naturally needs to be conserved. The ϕ -component of the induction equation can be integrated to yield

$$r (u_r B_\phi - v_\phi B_r) = -r_o^2 \Omega B_o , \quad (82)$$

where it has been assumed that at the reference level r_o , first, the azimuthal plasma speed is given by the solid body rotation value

$$v_\phi(r_o) = r_o \Omega , \quad (83)$$

with Ω denoting the angular velocity of the star, and second, that the radial velocity $u_r(r_o)$ is sufficiently small so that the inequality

$$v_\phi(r_o) B_o \gg u_r(r_o) B_\phi(r_o) \quad (84)$$

is satisfied. Finally, the ϕ -component of the force equation is integrated in the following form:

$$\left((\rho u_r r^2) (r v_\phi) - \frac{(r^2 B_r)}{\mu} (r B_\phi) \right) = L \cdot \frac{\dot{M}}{4\pi} , \quad (85)$$

with the integration constant L to be interpreted momentarily. Using (80), this last expression can be written as

$$r v_\phi - \frac{r B_r B_\phi}{\mu \rho u_r} = L . \quad (86)$$

Since the product $(r v_\phi)$ represents the *angular momentum* per unit mass of the outflowing plasma, it is suggestive to interpret L as the total angular

momentum contained in plasma **and** fields, which again and not surprisingly is conserved. One might naively assume that the total angular momentum per unit mass L can be arbitrarily specified. However, this is not the case as can be seen as follows: If the product rB_ϕ is eliminated from the force equation (86) by substituting from the induction equation (82) in terms of (r, v_ϕ) , one can solve for the azimuthal velocity field $v_\phi(r)$. It is customary to introduce the so-called radial Alfvénic Mach number M_A defined as

$$M_A^2 = \frac{\mu \rho u_r^2}{B_r^2} , \quad (87)$$

and with this definition the azimuthal flow field $v_\phi(r)$ is given by

$$v_\phi = r \Omega \frac{\frac{LM_A^2}{r^2 \Omega} - 1}{M_A^2 - 1} , \quad (88)$$

which expresses $v_\phi(r)$ in terms of constants, the radial distance r and the yet unknown function $M_A^2(r)$. Recalling the definition of the Alfvénic Mach number, I can write

$$M_A^2 = \frac{\mu \rho u_r^2}{B_r^2} = \mu \left(\frac{u_r \rho r^2}{r^2 B_r} \right)^2 \frac{1}{\rho} \sim \frac{1}{\rho} \quad (89)$$

since all the other terms are constants. If I am now allowed to appeal to intuition and argue that the plasma density must be monotonically decreasing outwards, it is clear that M_A^2 will attain its smallest value at the inner boundary r_0 and approach infinity as r approaches infinity. If $M_A(r_0) < 1$ there will therefore exist a so-called Alfvén-critical radius r_A at which

$$M_A^2(r_A) = 1 , \quad (90)$$

where the denominator of (88) changes sign. In order to illustrate the radial dependence of the Alfvénic Mach number, I have calculated $M_A^2(r)$ for a model wind with the solar mass loss rate (i.e., $\dot{M}_\odot = 1.5 \cdot 10^{12} \text{ g sec}^{-1}$), a mean radial surface field of 0.5 G, and using for the radial flow field somewhat unrealistically a critical Parker wind solution *without* any magnetic field effects. The resulting curve $M_A^2(r)$ is shown in Fig. 15 as solid line; the Alfvén critical point r_A lies at about 17 solar radii, i.e., much further out than the (thermal) critical point.

Obviously, if the azimuthal flow field $v_\phi(r)$ is to be regular at r_A , the nominator of (88) must also vanish at the Alfvén critical point, i.e., implying that the condition

$$L = r_A^2 \Omega \quad (91)$$

holds. Therefore, as advertised earlier, the (mathematical) integration constant L , which represents (physically) the total angular momentum per unit mass **can in fact not be arbitrarily specified**, rather it is determined, first, by the rotation rate of the star Ω , and second, by the radius r_A , at

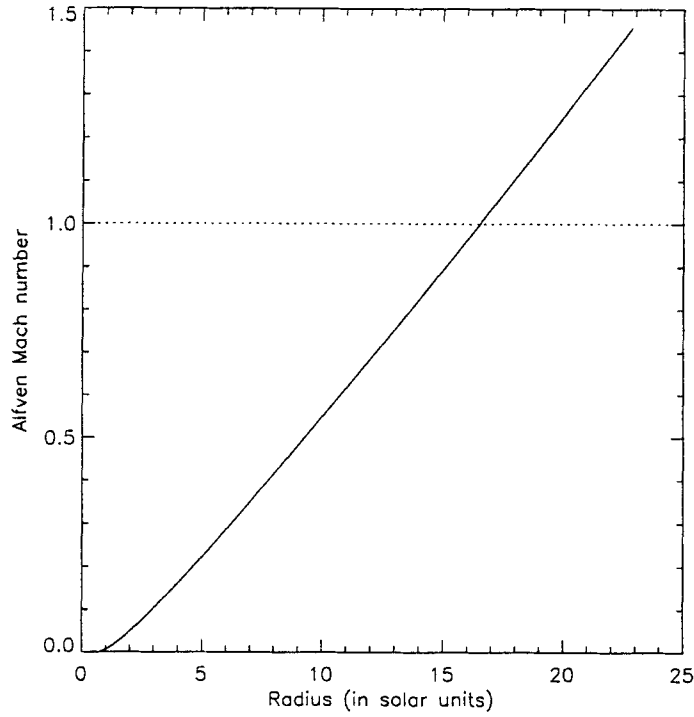


Fig. 15. Alfvénic Mach number M_A^2 vs. radius r for a solar-like coronal wind. Intersection between solid and dotted line gives Alfvén critical point

which the radial outflow becomes super-Alfvénic. To illustrate the radial dependence of the azimuthal flow field I have calculated $v_\phi(r)$ for the above model using the solar rotation rate of $\Omega = 2.5 \cdot 10^{-6} \text{ sec}^{-1}$. The resulting curve $v_\phi(r)$ is plotted in Fig. 16.

Finally, I return to the angular momentum loss of a magnetized wind. The total angular momentum per unit mass L , given by (91), is that of a rigidly rotating body with radius r_A ! Since $r_A > R_{\text{star}}$, the angular momentum loss rates will be much higher. In fact, comparing (69) and (91), one finds

$$\frac{\dot{J}_{\text{magnetic}}}{\dot{J}_{\text{non-magnetic}}} = \frac{r_{\text{Alfvén}}^2}{R_{\text{star}}^2} . \quad (92)$$

Unfortunately, the value of $r_{\text{Alfvén}}/R_{\text{star}}$ is not known even for the Sun, where it may reach 50, and we have no idea about the stellar case. For young stars one may expect larger magnetic fluxes also in open regions and hence even larger Alfvénic Mach numbers. In order to reach an angular momentum loss time scale of $\tau_j \approx 10^8 \text{ yrs}$ as required by the observations, one needs the

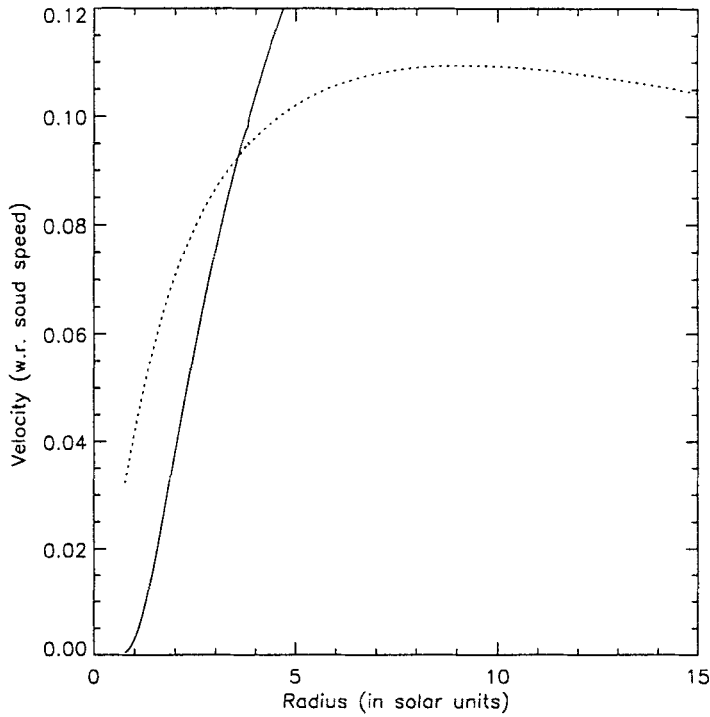


Fig. 16. Azimuthal flow field v_ϕ vs. radius r (normalized w.r.t. isothermal sound speed) for a solar-like coronal wind assuming the solar surface rotation rate (dotted line). For comparison the assumed radial flow field (scaled by 0.1) is also shown (solid line); see text for details

Alfvénic point to be located at about 300 stellar radii, which is certainly within reach of the model presented here. At any rate, my above discussion should have made it abundantly clear that *without the presence of a hot magnetized corona* it is next to impossible to understand the angular momentum loss of late-type stars observed during their main sequence careers.

References

- Fleming, T. A., Giampapa, M. S., Schmitt, J. H. M. M., Bookbinder, J. A. (1993): *ApJ* **410**, 387
 Hempelmann, A., Schmitt, J. H. M. M., Schultz, M., Rüdiger, G., Stepień, K. (1995): *A&A* **294**, 515
 Longair, M. S. (1992): in *High Energy Astrophysics*, Vol.1, Cambridge University Press

- Pallavicini, R. et al. (1981) ApJ **248**, 279.
- Randich, S., Schmitt, J. H. M. M., Prosser, C. F., Stauffer, J. R. (1996): A&A **305**, 785
- Raymond, J., Smith, B. (1977): ApJS **35**, 419
- Schmitt, J. H. M. M., Fleming, T. A., Giampapa, M. S. (1995): ApJ **450**, 392
- Spitzer, L. Jr. (1962): *Physics of Fully Ionized Gases*, Interscience Publishers John Wiley
- Stauffer, J. R., Cailault, J.-P., Gagné, M., Prosser, C. F., Hartmann, L. W. (1994): ApJS **91**, 625.
- Walter, F. M., Bowyer, S. (1981): ApJ **245**, 671.
- Weber, E. J., Davis, L. Jr. (1967): ApJ **148**, 217

Atmospheres and Interior Models

J.P. De Greve

Astronomy Group, Vrije Universiteit Brussel,
Pleinlaan 2, B-1050 Brussels, Belgium
e-mail: jpdgreve@vnet3.vub.ac.be

1 Why?

There are several reasons to dedicate part of a Summer School on Stellar Atmospheres to stellar structure and evolution. First of all (and certainly not the least) it is where my personal interest lies. And being responsible for the 1996 edition of the School it was an opportunity I couldn't miss. I'm modelling the structure and evolution of stars, and it's fun.

But there is also the physical reality. Atmospheres, although often largely defined by the local physical circumstances, depend on the interior processes for their macroscopic as well as their microscopic behaviour, certainly on the medium and long term timescales. Atmospheres are the fingerprints of the interior. To emphasize the need of knowledge of the interior to understand the atmospheres, allow me to simplify the situation in JP's Two Trivial Theorems:

- a) There is no atmosphere without interior (actual or in the past).
- b) Different atmospheres reflect different interiors.

The above statements merely state the strong existing links between the atmosphere and the stellar interior. Atmospheres are observed because of escaping radiation. That energy comes essentially from the interior. Moreover, the composition of the atmosphere is by and large the result of stellar evolution. The fractions of the various elements in the outer layers, even when unmodified by mixing or mass loss, are the result of the yields of previous generations of stars. Large scale phenomena (both structural and temporal), linked to specific evolutionary stages, alter the chemical composition, and hence the whole structure of the atmosphere. Drastic examples of such changes can be found in interacting binaries, planetary nebulae, etc.

Finally, it is instructive to point out some of the similarities and differences between the stellar interior and the atmosphere.

Both parts of the star are made out of gas, but the interior part is totally (or almost) ionized, whereas the atmosphere is more complex in containing partially ionized constituents and neutral gas as well. The inner part is dominated by the energy production (either from nuclear or from gravitational contraction), the atmosphere is not (apart from eventual shocks, recombination processes, etc., that do not really contribute to the overall energy

generation). The interior is opaque, while the atmosphere can be considered as transparent (apart from clumps, clouds, rings, dust,...). This opacity difference is of course linked to the high interior density versus the low density in the outer layers. As a consequence, in treating the gas mass is an important parameter for the interior, while radius (or optical depth) is a better parameter at the outside of the star. The interior tells the most important part of its story through long term variations, whereas the atmosphere reveals intriguing processes through short term variations.

2 Recipe and Ingredients

2.1 Equations

The structure of a star in hydrostatic equilibrium is given by the well known four structure equations (in Lagrangian coordinates):

Mass conservation:

$$\frac{\partial r}{\partial m} = \frac{1}{4\pi r^2 \rho} . \quad (1)$$

Hydrostatic equilibrium:

$$\frac{\partial P}{\partial m} = -\frac{Gm}{4\pi r^4} - \frac{1}{4\pi r^4} \frac{\partial^2 r}{\partial t^2} . \quad (2)$$

Energy conservation:

$$\frac{\partial L}{\partial m} = \epsilon_n - \epsilon_\nu - c_P \frac{\partial T}{\partial t} + \frac{\delta}{\rho} \frac{\partial \rho}{\partial t} . \quad (3)$$

Energy transport:

$$\frac{\partial T}{\partial m} = -\frac{GmT}{4\pi r^4 P} \nabla \quad (4)$$

with $\nabla = \nabla_r$ in the case of radiative transport and $\nabla = \nabla_{ad}$ in the case of convective transport.

It is convenient to transform these relations further with respect to the relative mass: $\mu = 1 - m(r)/M$.

2.2 Ingredients

To solve the equations we need to describe a number of properties of stellar material hidden behind various symbols like $r, \epsilon_n, \epsilon_\nu, \kappa, c_P, \nabla_{ad}, \delta$.

We assume them to be known functions of P, T and the chemical composition functions $X_i(m, t)$.

$\rho = \rho(P, T, X_i)$ (equation of state)

$\nabla_{ad} = \nabla_{ad}(P, T, X_i)$

$$\delta = \delta(P, T, X_i)$$

$$\kappa = \kappa(P, T, X_i) \text{ (Rosseland mean of the opacity, including conduction)}$$

$$\epsilon = \epsilon(P, T, X_i)$$

Finally, we have to define the boundary conditions in the center and at the border of the star.

In the center we obviously have $r(\mu = 1) = 0$ and, because of the conservation of energy, also $L_r(\mu = 1) = 0$.

At the surface we assume the Eddington approximation for the temperature $T^4 = L/(8\pi\sigma r^2)$, defined at $r = R_{\text{eff}}$, together with P defined through the equation of state at $r = R_{\text{eff}}$. The independent variables are m and t . All in all we deal with a two-boundary (at $m=0$ and $m=M$) initial value (at $t = t_0$) problem of solving four non-linear, partial differential equations.

2.3 Shooting (a Solution)

a) Occam's razor does not work.....

It is obvious that in this case Occam's razor will not work. The simplest approach will not lead to a solution. Indeed, simply integrating the equations towards the surface from the estimated central values T_c and ρ_c , to meet the surface boundary conditions, will not work. The difference between the values of T and P obtained through integration and the outer boundary values lead to a correction on the estimated values of T_c and ρ_c . But small changes in the center produce huge variations further out in the star leading to divergence. The reverse, integrating from the outside inward to the center suffers from the same problem.

b) But Schwarzschild's razor sometimes does.....

A way out is avoiding too large variations, by integrating less far. This method is the Schwarzschild method, which can be used when the stars have a fairly simple structure. This is especially the case at the onset of the evolution (example: start of the main sequence evolution for a star of $5 M_\odot$). The equations are integrated from the center outwards and from the border inwards to a point inside the star, called the fitting point. Iteratively one then tries to match the two solutions at the predefined layer M_{fit} (Schwarzschild 1958).

c) And Henyey's shaver always works, but how clean?

When stars have a more complicated structure (i.e. varying chemical profile, shell sources, ...) the foregoing method fails because of numerical instabilities. The required stability can be obtained by a method developed by Henyey et al. (1959, 1964). This method is now widely applied in most of the existing evolution codes. The star is divided into a number of layers (zones) in such a way that the variables (or a power or combination of them) vary linear on the interval between zoning points (Fig. 1). The structure equations are now replaced by difference equations. The outermost interval is the atmosphere, which is integrated inwards towards a fitpoint. That is the layer

where inner and outer solution must match. Iteration is performed until the required convergence is obtained.

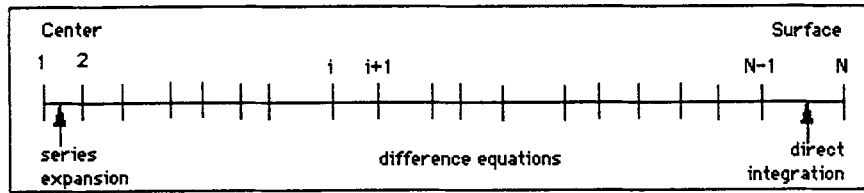


Fig. 1. The mass layer distribution (zoning) in the Henyey iteration method

An example of a difference equation is the one that follows from the partial differential equation for the conservation of mass (in the absence of mass flows):

$$\frac{r_{j+1} - r_j}{M_{j+1} - M_j} = \left[-\frac{M}{4\pi r^2 \rho} \right]_{j+\frac{1}{2}} \quad (5)$$

with the subscripts denoting values on the grid points $(j, j+1)$ or some average in between two grid points $(j+1/2)$. The linearization of the structure equations introduces a truncation error, which is difficult to follow. The truncation error in the above equation is

$$-(M_{j+1} - M_j)^{\frac{3}{24}} y''' . \quad (6)$$

Precise zoning is required to keep it small.

d) The best of two worlds: the multiple fitting method.

In a paper by Wilson (1981) a method was proposed that combines the stability of the Henyey method with the accuracy of the Schwarzschild integration. In this method a generalized Newton iteration is performed on the condition equations at the fit points. Instead of one fitpoint, one chooses N fitpoints, one of them serving as main fitpoint, where inward and outward solution meet (Fig. 2). In between two fitpoints the structure equations are integrated (inward from the surface, and outward from the center). From the center to the first fitpoint series expansions are used. The truncation error is controlled with a predictor-corrector method.

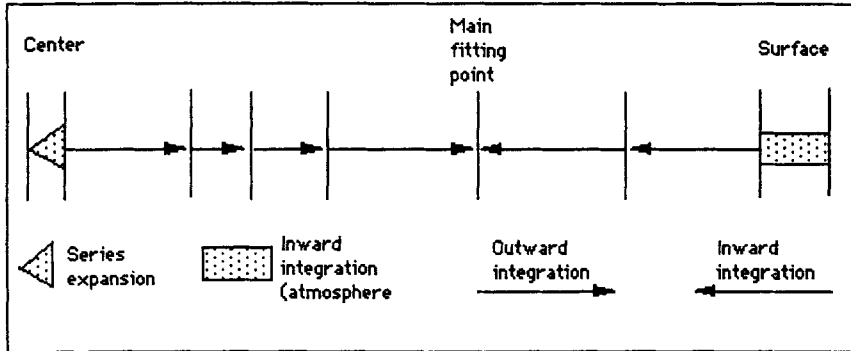


Fig. 2. The mass layer distribution (fitting points) in the multiple fitting method

3 Evolution: From Wherefrom to Whereto, but Most of All: Why?

3.1 Masses Make All the Difference

We can divide the evolution of stars into three groups, according to the mass, though other classifications are possible. The three groups are the low mass stars, the intermediate mass stars, and the high mass stars. For each group the mass limit is influenced by the treatment of the interior, more specifically the amount of overshooting applied in the models (cf. Sect. 3.3.3). We will give values for convective cores determined by the Schwarzschild criterion (cf. Sect. 3.3.1) and, between brackets, for overshooting characterized by $\alpha=0.2$ (where α denotes the fraction of the local pressure scale height by which the convective core extends beyond the classical Schwarzschild core).

The low mass stars are defined as stars with mass smaller than $2.3 M_{\odot}$ ($M < 1.6$ to $1.8 M_{\odot}$). After core hydrogen burning these stars develop a helium core with degenerated electrons. The degeneracy is lifted by the onset of helium burning through a helium flash. The intermediate mass stars are stars with masses ranging between 2.3 and $9 M_{\odot}$ (1.6 to $1.8 M_{\odot}$ and $6 M_{\odot}$). In these stars helium is ignited in non-degenerate conditions, but after the stage of core helium burning a highly electron-degenerated carbon-oxygen core develops. Finally, the massive star group consists of stars more massive than $9 M_{\odot}$ ($6 M_{\odot}$). In these stars electron degeneracy does not occur. At cen-

tral temperatures exceeding $6 \cdot 10^8 \text{K}$ they produce Ne and Mg after quiescent carbon ignition.

Apart from this mass distinction, we can also separate the (early) evolution of the stars according to the threshold value of the central temperature of $2 \cdot 10^7 \text{K}$ on the main sequence (corresponding to a mass of about $1.3 M_\odot$). For temperatures below this, the proton-proton cycle is the more active nuclear burning source, while for larger temperatures the CNO cycle will dominate. In small stars the core will contract faster and more pronounced because the energy production rate $\epsilon \approx \rho X^2 T^n$, whereas in massive stars this is $\epsilon \approx \rho X Z_{\text{CNO}} T^n$.

There are also structural differences between small and large masses in the outer layers of the stars. For low masses the hydrogen (and helium) ionization zone reduce the adiabatic gradient and hence, convective zones occur in the outer envelope. For larger masses (i.e. with effective temperature on the main sequence exceeding 8300K , or $M > 1.7 M_\odot$), the ionization zones are very thin and the outer layers remain in radiative equilibrium.

3.2 Timescales

For the central hydrogen burning stage the timescale can be estimated as $t_H = E_H/L$.

The energy produced through nuclear burning is proportional to the amount of hydrogen, which in order of magnitude can be approximated by the mass of the star. The luminosity is proportional to M^n (mass-luminosity relation). On average $n=3.5$, in the range 1 to $10 M_\odot$ it is about 3.9 , in the range 1 to $40 M_\odot$ one obtains a value of 3.35 . The estimate for the timescale of core hydrogen burning then becomes $t_H \sim M/L \sim M^{1-n} \sim M^{-2.5}$.

The relation shows that the hydrogen burning timescale strongly decreases towards larger M -values.

Comparison of the estimates derived with the above relation with the timescales derived from model calculations (Meynet et al. 1994) shows that the estimates must be used cautiously. Table 1 gives the ratio of the calculated timescales to the mass power, $t_H/M^{-2.5}$. This ratio clearly varies over two orders of magnitude in the range 3 to $120 M_\odot$.

Table 1. Timescales t_H for core hydrogen burning (Meynet et al. 1994) and the ratio $t_H/M^{-2.5}$. The number between brackets denotes the power of ten

M/M_\odot	0.8	1	3	40	120
$t_H/10^6 \text{yr}$	25027.9	9961.7	352.5	4.3	2.6
$t_H/M^{-2.5}$	1.4 (4)	9.9 (3)	5.5 (3)	4.3 (4)	4.1 (5)

3.3 Convection and Other Mixings

3.3.1. Stability against convection and mixing

One of the important but still poorly known aspects of stellar structure is the extension of convection inside a star, and the associated mixing. The standard theory of convection is known as the Mixing Length Theory (Böhm-Vitense 1958). In this framework the boundary of a convective region is determined by a local criterion.

We call a medium unstable when small random motions of matter are amplified and evolve into large scale motions. Stability against convective motion is usually investigated using a model of rising blobs of matter, transporting heat and kinetic energy. In this model the buoyancy force, responsible for the motion of the bubble, is evaluated (and as the border is determined only by the vanishing of the buoyancy force, it implies that the inertia of the convective elements is neglected). Four conditions determine the rise of the bubble:

a) The difference in mean molecular weight between the bubble and the surrounding medium, resulting from the μ -gradient in the medium:

$$\Delta\mu + \mu \frac{d\ln\mu}{d\ln P} \frac{d\ln P}{dr} \Delta r = 0 . \quad (7)$$

b) The adiabatic displacement of the bubble, allowing for a small but non-negligible heat loss during the rise:

$$\frac{d\Delta T}{dt} + T \frac{d\ln P}{dr} (\nabla - \nabla_{ad}) \frac{d\Delta r}{dt} + \lambda \Delta T = 0 . \quad (8)$$

c) The perfect gas equation under the assumption of continuous pressure equilibrium between bubble and medium:

$$\chi_\rho \frac{\Delta\rho}{\rho} + \chi_T \frac{\Delta T}{T} + \chi_\mu \frac{\Delta\mu}{\mu} = 0 . \quad (9)$$

d) The equation of motion due to buoyancy, with g being the local acceleration:

$$\rho \frac{d^2 r}{dt^2} + g \Delta\rho = 0 . \quad (10)$$

The equations are homogeneous, and can be linearized because the Δ 's are small. The trivial solution is of course the one with all variations $\Delta = 0$, but we look specifically for a solution in which all quantities vary with the same phase ω (real or complex), for example $\Delta r = A_r e^{\omega t}$. A negative value of ω implies a stable medium in which the disturbances die out rapidly, a positive ω implies an unstable medium in which the disturbances are amplified. We will obtain nontrivial solutions if the determinant from the coefficients A_T , A_ρ , A_μ , A_r is zero, resulting in the following condition for ω :

$$\omega^3 + \omega^2 \lambda + \omega \left[g \frac{\chi_T}{\chi_\rho} \frac{d \ln P}{dr} \left(\nabla - \nabla_{ad} + \frac{\chi_\mu}{\chi_T} \frac{d \ln \mu}{d \ln P} \right) \right] + \left[\lambda g \frac{\chi_\mu}{\chi_\rho} \frac{d \ln P}{dr} \frac{d \ln \mu}{d \ln P} \right] = 0 . \quad (11)$$

In the absence of heat loss ($\lambda = 0$) we obtain

$$\omega^2 = -g \frac{\chi_T}{\chi_\rho} \frac{d \ln P}{dr} \left(\nabla - \nabla_{ad} + \frac{\chi_\mu}{\chi_T} \frac{d \ln \mu}{d \ln P} \right) . \quad (12)$$

We have a medium that is unstable against convection if ω^2 is positive. Because $d \ln P / dr$ is negative and χ_T and χ_ρ are positive, we have

$$\nabla > \nabla_{ad} - \frac{\chi_\mu}{\chi_T} \frac{d \ln \mu}{d \ln P} \quad (13)$$

(note that $\chi_\mu < 0$). If there is some heat loss during the rise of the bubble, then we have an unstable medium if $\text{re}(\omega) > 0$. This is obtained for the following three conditions:

$$\begin{aligned} \frac{d \ln \mu}{d \ln r} &> 0 \\ \nabla &> \nabla_{ad} - \frac{\chi_\mu}{\chi_T} \frac{d \ln \mu}{d \ln P} \\ \nabla &> \nabla_{ad} . \end{aligned}$$

The first condition describes the onset of a Rayleigh–Taylor instability, the second is the Ledoux criterion, the third the Schwarzschild criterion. Remark that for $d \ln \mu / d \ln r = 0$ the Ledoux and the Schwarzschild criterion become identical.

In practice one uses the radiative and the adiabatic gradient, hence, adopting the Schwarzschild criterion, convection sets in if

$$\nabla_r = \frac{3}{16\pi acG} \frac{\kappa P}{T^4} \frac{L_r}{M_r} > \nabla_{ad} . \quad (14)$$

In the outer layers of the star the ratio L_r / M_r remains constant, whereas the adiabatic gradient decreases in regions of partial ionization. This means that these regions can become convectively unstable.

Because of the simplified way to determine the border of a convective region, and especially the existence of the nonzero velocity of the elements at the edge, additional mixing processes may occur at the border, such as semiconvection and overshooting, which will be discussed in the following sections.

3.3.2. Semiconvection

Semiconvection is a slow form of mixing occurring in a zone intermediate between the convective core and the surface, a region with decreasing mean molecular weight.

In massive stars semiconvection occurs because the radiation pressure dominates the pressure and the electron scattering the opacity. In luminous

stars the high radiation pressure leads to a tendency for the convective core to grow (with increasing mass) and to expand (with evolution). A discontinuity appears at the border of the convective core. Because of the dominant electron scattering (opposed to Kramers bound-free absorption) radiative equilibrium cannot be maintained outside the formal convective core (Schwarzschild and Harm 1965). A second type of semiconvection occurs during core He-burning (Schwarzschild 1970, Paczynski 1971, Castellani et al. 1971 a, b). It results from the increasing opacity in the convective core as the carbon abundance increases, implying an increasing radiative temperature gradient. This type of semiconvection only shows up in stars with masses up to $5 M_{\odot}$. Finally, at the end of helium burning the core may show an oscillatory growth, called “Breathing Convection” (Castellani et al. 1985).

In these zones mixing should occur to smooth out the gradient in molecular weight. However, we would thus change the chemical composition, and the radiative gradient would decrease below the adiabatic.

We thus face a dilemma: If no mixing is applied, the region outside the core is unstable against convection, if mixing is applied, the region becomes stable, and hence no homogenization should take place.

One way of dealing with this is to install a so-called neutrality condition in that region (i.e. $\nabla_r = \nabla_{ad}$) through suitable mixing that involves a redistribution of the chemical elements over a finite region to smooth out the gradient in mean molecular weight.

Because the fluxes of heat and kinetic energy are extremely small, and the energy transport is essentially radiative, semiconvection is a diffusion problem. Hence, we can adopt a diffusion coefficient that is proportional to the difference of the gradients $\nabla_r - \nabla_{ad}$

$$\sigma_{sc} = \Lambda v_s (\nabla_r - \nabla_{ad}) \text{ if } \nabla_r > \nabla_{ad} \quad (15)$$

$$\sigma_{sc} = 0 \text{ if } \nabla_r \leq \nabla_{ad} \quad (16)$$

with v_s , the adiabatic sound velocity, and Λ a typical length scale.

3.3.3. Convective overshoot

This process comes from the difference between the condition for the border of the convective core (zero acceleration) and the nonzero velocity of the elements at that moment. In principle the varying molecular weight gradient assures an almost immediate stop of the elements (Saslow and Schwarzschild 1965), but Shaviv and Salpeter (1973) showed that the overshoot distance can amount to a nonnegligible fraction of the pressure scale height. The buoyancy force F_b is proportional to the difference of the temperature gradients. Below the boundary that difference is very small and positive. Above, the radiative gradient becomes much smaller than the adiabatic in a distance of one scale height. Hence a drastic change from small and positive F_b to a large and negative value takes place over a short distance, bringing the penetrating

element to an immediate stop. However, if we consider the temperature excess ΔT of the rising bubbles over the surroundings, we remark that below the boundary $\Delta T \geq 0$ while above it $\Delta T < 0$. This means that the convective flux F_{conv} becomes negative (being proportional to $v \Delta T$): $F_{\text{conv}} < 0$.

Because $F_{\text{tot}} = F_{\text{conv}} + F_r$ is constant, we have an increase of F_r and hence $\nabla = -(3/4ac)(\kappa\rho/T^3)F_r$ will increase. As a consequence the absolute value of $\nabla_r - \nabla_{\text{ad}}$ decreases and the buoyancy force will change less drastic. The elements coming through the border will decelerate less strongly and a better penetration in the radiative zone is obtained.

In most treatments of the overshoot an ad hoc approach is used. The boundary of the overshoot region is linked to the gas pressure, through the pressure scale height $H = \mathcal{R}T/\mu g$. The boundary of the convective core is then the region where

$$P_{\text{ov}} = P_{\text{Schw}} e^{-\alpha} \quad (17)$$

with P_{ov} the pressure at the overshoot boundary, and P_{Schw} the pressure at the convective core boundary determined by the Schwarzschild criterion.

$\alpha = 0$: The convective core is identical to the ‘‘Schwarzschild’’ core

$\alpha = 1$: The core boundary is at a location where the pressure is a factor e lower (i.e. one scale height outwards).

Other approaches of the overshoot, such as diffusive mixing including the concept of most effective scale length (Deng et al. 1996a,b) or time-dependent compressible convection (Freytag et al. 1996), have been published in the recent year (see also the review by Zahn 1992).

The influence of semiconvection and overshoot on the internal structure is shown in Table 2 (from Aubert et al. 1996), giving the mass of the core at various evolutionary stages, for various combinations of convection, overshooting and semiconvection. Models are given for the two different criteria for convective instability (Ledoux and Schwarzschild). Although for a $20 M_{\odot}$ star the differences remain relatively small for the hydrogen exhausted core (max. $1.4 M_{\odot}$ or 25 %), they can be as large as a factor 2 for the carbon exhausted core.

3.4 Dredge-Up Phases in the Life of a Star

During the evolution there are particular phases that are interesting with regard to the composition of the atmosphere. Such phases can occur each time an outer convective zone descends deeply inward the star. When this zone reaches layers of former nuclear burning, the products of that process are mixed in and brought to the surface. Such a process is called a dredge-up.

a) Climbing the giant branch: the first dredge-up.

When the star reaches the left side of the Hertzsprung–Russell diagram after core hydrogen burning, it moves upward along the Hayashi track. During that phase the outer convective zone grows inward. In a $3 M_{\odot}$ model

Table 2. Core masses at various evolutionary (nuclear exhausted) stages, for different combinations of convection, overshooting and semiconvection (Table from Aubert et al. 1996)

Convection Criterion	Oversh.	Semiconv.	M_α (H-exh)	M_{CO} (He-exh)	M_{ONe} (C-exh)	Ref.
Ledoux	No	No	5.7	2.2	2.0	1
Ledoux	Yes	Yes	6.2	3.7	3.5	1
Schwarzschild	No	No	6.0	3.8	3.7	2
Schwarzschild	Yes	No	7.1	5.1	≈ 4.0	3
Schwarzschild	No	No	6.1	4.7	3.8	4

Ref.: 1: Woosley and Weaver (1988); 2: Nomoto and Hashimoto (1988);
3: Meynet and Arnould (1993); 4: Aubert et al. (1996).

($Z=0.02$, $X=0.70$, Mowlavi 1995) it reaches down to almost $0.4 M_\odot$. During the previous core hydrogen burning the convective core extended outward to $0.58 M_\odot$. Hence, products of CNO-burning are brought up to the surface when the star evolves to the top of the red giant branch.

A similar behaviour was found in a $6 M_\odot$ star with the same composition, but not in the $3 M_\odot$ star with lower metallicity ($Z=0.001$, Mowlavi 1995).

b) The second dredge-up.

A new opportunity to bring nuclear burning products to the surface occurs in intermediate mass stars after core helium burning when a new approach of the Hayashi boundary causes the outer convective zone once more to move deeply inward to reach the chemical discontinuity between the hydrogen-rich outer layers and the helium-rich region above the helium-burning shell. The resulting mixing increases the helium and nitrogen content of the envelope.

c) The third dredge-up.

This phase occurs in asymptotic giant branch stars of more than $2 M_\odot$, when the outer convection zone merges with the convection zone between the hydrogen and the helium burning shell, which occurs during a thermal pulse of the latter (cf. Sect. 4).

3.5 Anchored Shell Sources (the Node Theorem for Active Shell Sources)

After core hydrogen burning a hydrogen shell source develops at the border of the contracting core. Active shell sources tend to remain at the same distance from the center (by active we mean that it contributes significantly to the total energy production of the star). This characteristic is known as the node theorem (Fig. 3).

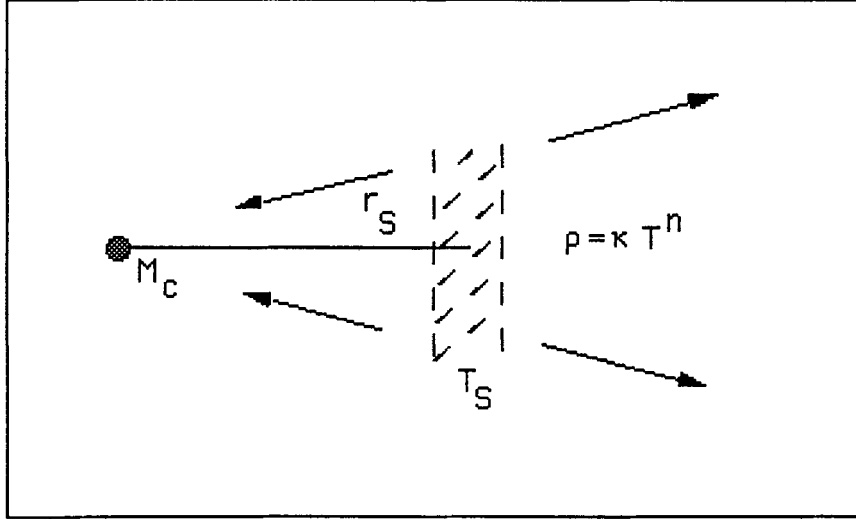


Fig. 3. The node theorem: an active shell with temperature T_c at a distance r_c from the center, outside a core mass M_c . A polytropic relation is applied to the envelope

Consider a shell S at a distance r_s from the center, with temperature T_s . The central mass underneath the shell is M_c .

Assume that the shell source region can be considered as an ideal gas with radiation and that the star is in hydrostatic equilibrium. Moreover we adopt a polytropic expression for the envelope, $\rho = kT^n$. This is valid if $P_g/P_r \approx$ constant, which means that the shell must be active. The proper value of n here is 3. We can then write

$$P = \frac{N_o k \rho T}{\mu} + \frac{1}{3} a T^4 \quad (18)$$

or

$$\frac{dP}{dr} = \frac{dP}{dT} \frac{dT}{dr} = \frac{N_o k}{\beta \mu} \kappa^{n+1} \rho \frac{dT}{dr} \quad (19)$$

with $\beta = P_g/P_{tot}$.

Hydrostatic equilibrium leads to

$$\frac{dP_s}{dr} = - \frac{GM_c}{r_s^2 \rho_s} . \quad (20)$$

After combining the two equations and integrating the temperature one obtains

$$T_S = \beta \frac{\mu}{N_o k} \frac{GM_c}{\kappa^{n+1}} \frac{1}{r_S} + \text{constant} \quad (21)$$

or

$$T_S \sim \frac{1}{r_S} . \quad (22)$$

When the shell is moved to the center the shell temperature rises. This causes an increase in the nuclear energy production, resulting in a rising gas pressure. The increase in gas pressure moves the shell outwards again. Inversely, if the shell is moved outward, its temperature drops, the nuclear energy production decreases, with a corresponding decrease in gas pressure, moving the shell back inwards. Hence, a shell tends to remain at a fixed position.

Shell \rightarrow Center : $T_S \uparrow \Rightarrow \epsilon_{\text{nuc}} \uparrow \Rightarrow P_S \uparrow \Rightarrow r_S \uparrow$

Shell \rightarrow Out : $T_S \downarrow \Rightarrow \epsilon_{\text{nuc}} \downarrow \Rightarrow P_S \downarrow \Rightarrow r_S \downarrow$.

When a shell source develops, the core becomes inert (apart from a small contribution from gravitational contraction). Volume changes are reversed at the boundaries of the active shell. In the post core hydrogen burning stage this results in an expansion of the outer envelope, balancing the contraction of the inert helium core. The star rapidly develops into a red giant.

3.6 Mass Motions of Different Shells

Shell sources may be active or non-active for some time. Because of the different temperature ranges required for each burning, neighbouring shell sources can influence each other. And because of the different temperature dependence of the reactions, the shell sources generally move with different mass “velocities” (\dot{M}_S) through the mass.

Denoting X_i the mass concentration of the reacting element i ahead of the shell source, and ϵ_i the energy released per gram of mass burned, then the mass velocity is given by $\dot{M}_S = L_i / (\epsilon_i X_i)$. The relative motion of the hydrogen and helium shell sources through the mass is then given by

$$\frac{\dot{M}_H}{\dot{M}_{\text{He}}} = \frac{L_H}{L_{\text{He}}} \frac{\epsilon_{\text{He}}}{\epsilon_H} \frac{X_{\text{He}}}{X_H} . \quad (23)$$

Note that roughly equal velocities of the shells (and hence a stationary situation) are obtained for $L_H \approx 7L_{\text{He}}$, since $X_H \approx 0.7$, $X_{\text{He}} \approx 1$ and $\epsilon_H/\epsilon_{\text{He}} \approx 10$.

While the shell is burning outwards, it tends to concentrate on gradually smaller mass ranges. Changes become more rapid (changes are defined here by the time interval it takes to shift the very steep chemical profile over a range that is comparable to its extension). If the shell is thermally unstable, the

assumption of complete equilibrium has to be abandoned. Such instabilities differ from perturbations of the central nuclear burning region by

- a) different geometry
- b) different reaction of the density to an expansion.

The expansion of a thin shell source will not stabilize it, but will enforce the liberation of energy by heating. This means that the shell source reacts just as if the equation of state were $r \sim 1/T$, reflecting an instable situation.

The pulse instability was first found by Schwarzschild and Harm (1965) for a helium shell source in a star of $1 M_{\odot}$. In a study of a $5 M_{\odot}$ star Weigert (1966) found the same instability in a two-shell source model. He also found that the instability leads to nearly periodic relaxation oscillations, called thermal pulses.

4 Thermal Pulses or Secular Stabilities of Shell Sources

How can we explain the strange behaviour described in the foregoing section? We therefore need to consider the difference between density changes in the core and in the shell.

4.1 Density Changes of a Nuclear Burning Zone

We consider two different situations, a nuclear burning core and a nuclear burning shell. For the spherical core we have $m \sim \rho r^3$, and a radial expansion (at constant mass, $dm = 0$) therefore leads to $d\rho/\rho = -3dr/r$. Now consider a shell at a distance r_0 from the center, with thickness D ($r = r_0 + D$). If the shell expands we have $dr = dD$ ($r_0 \approx \text{constant}$) and hence, $d\rho/\rho = -dD/D = -r/D dr/r$.

If we assume that the changes near the boundary are homologous (i.e. $r+dx = r(1+x)$), we obtain different proportionality constants for the changes of the density with radius in the core and in a shell:

Central: 3	Shell: r/D
------------	--------------

4.2 Shell Perturbation and Pressure Change

Consider the change of pressure in the shell source as a hydrostatic reaction to the lift of the layers above (again we assume homology for simplicity).

Assume that the shell expands to get rid of the perturbation: $dD/D > 0$. This causes a corresponding change of the density $d\rho/\rho < 0$, but only a very small increase dr/r of the radius if the shell thickness is small compared to the distance to the center ($D/r \ll 1$).

As a result the layers are hardly lifted and therefore the weight of these layers remains constant. In that case hydrostatic equilibrium tells us that there is no decrease in pressure ($dP/P \approx 0$).

Indeed, the homology relation $dP/P = -4dr/r$ and $d\rho/\rho = -r/D dr/r$ combine to $dP/P = 4D/r d\rho/\rho$.

Using the equation of state in the form $d\rho/\rho = \alpha dP/P - \delta dT/T$, we find that $d\rho/\rho = -\delta dT/T$, since dP/P goes to zero for small values of D/r .

Hence we obtain a result that is similar to an equation of state of the type $\rho \sim 1/T$. The expansion of the helium shell leads to an increase of its temperature. This secular instability of the shell results in nearly periodic relaxation oscillations.

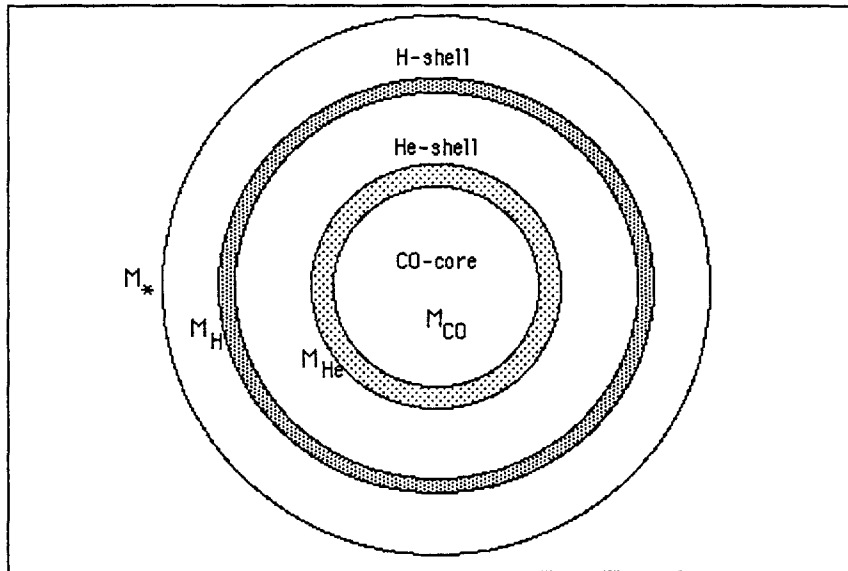


Fig. 4. Structure of a star with two active shell sources outside an inert Carbon-Oxygen core

More precisely, when we have two active shell sources (helium and hydrogen) surrounding an inert CO-core, a thermal pulse evolves through the following sequence of events (Fig. 4). In the helium burning shell the energy production rises steeply as the energy rate is proportional to T^5 . This causes an increase of the pressure in the inner shell region, pushing the H-shell outwards. The H-shell dies out, and the total energy production decreases below the amount L that is lost at the surface. The difference is then produced by contraction of that region (interpulse phase). The H-shell goes down, heats up and finally ignites again.

As model calculations show, a shortlived convective shell develops above the helium shell during the thermal runaway. This shell mixes helium burning products into the intershell region, and at the same time it brings helium-enriched intershell matter into the nuclear burning region. For a $5 M_{\odot}$ star Kippenhahn and Weigert (1967) found a lifetime of ~ 70 years for the thermal runaway, whereas the convective shell only exists in the first 50 years. The time between two pulses increases gradually, from 3200 years for the first, to 4300 years for the sixth pulse in their models. The first pulse occurs when the helium shell has reached $m/M=0.1597$, while the hydrogen shell is at $m/M=0.1603$. It is the latter that provides almost all the surface luminosity, which is only little affected by the pulses. In small mass stars ($\sim 0.6 M_{\odot}$) the period between pulses may reach hundreds of thousands of years. The pulse amplitude grows with each successive event.

For the atmospheric conditions it is interesting to see that the outer convection zone reaches almost to the H-He discontinuity, retreats upwards at each pulse and moves back to the discontinuity in the interpulse phase. If the outer convection zone descends below the discontinuity and merges with the shortlived convection zone above the helium shell a third dredge-up phase occurs ($M > 2 M_{\odot}$). Intershell matter from carbon synthesis can be dredged up to the surface. The observed differences between oxygen-rich giants and carbon-rich giants can probably be explained through this process.

5 Cepheids

(as an Answer to the Request of T. Le Bertre)

5.1 The Period-Density Relation

Intermediate mass stars may pulsate with periods between 2 and 40 days during the phase of core helium burning. In this phase we call them Cepheids (in the case of low mass stars: RR Lyrae variables), representing variable stars (with variations in radial velocity, radius and effective temperature). Maximum luminosity and minimum radius have a time lag, the maximum luminosity corresponds with the largest contraction velocity.

In modelling such pulsations astrophysicists get a better understanding of the stellar interior. The observed radial pulsations result from sound waves that resonate in the interior. An estimate of the pulsation period can be obtained by evaluating the crossing time of a sound wave through a star with radius R and average density ρ . In such a star the adiabatic sound velocity is given by (Carroll and Ostlie 1996)

$$v_s = \sqrt{\frac{\gamma P}{\rho}} \quad (24)$$

with γ the ratio of specific heats $\gamma = c_P/c_V = (d \ln P / d \ln \rho)_{\text{ad}}$.

The pressure follows from hydrostatic equilibrium, assuming a constant density (!):

$$\frac{dP}{dr} = -\frac{4}{3}\pi G\rho^2 r . \quad (25)$$

Integrating from $P = 0$ ($r = R$) we obtain:

$$P(r) = \frac{2}{3}\pi G\rho^2 (R^2 - r^2) . \quad (26)$$

The pulsation period can then be estimated as

$$\Pi \approx 2 \int_0^R \frac{dr}{v_s} \approx \sqrt{\frac{3\pi}{2\gamma G\rho}} . \quad (27)$$

If we take $M = 5 M_\odot$ and a radius of $R = 50 R_\odot$ (representing a typical Cepheid), we obtain $\Pi \approx 10$ days.

5.2 The Valve Mechanism

In order for pulsations to work one has the following basic equation

$$\oint \frac{dQ\Delta T}{T_0} > 0 \quad (28)$$

with ΔT the cyclic variation of the temperature (i.e. the deviation from T_0). One can explain the equation as follows:

In order to perform work against the surroundings, heat has to be absorbed at high temperature, and has to be emitted at low temperature. For a pulsation each small gas element has to absorb energy during compression (when the temperature is high) and to emit heat during the expansion (when the temperature is low).

The process above shows similarities to the process in an explosion motor with valves.

In a star the energy flux in the atmosphere is constant. During maximum compression the heat leakage has to be small, and during expansion it has to be large. The change of the leakage can be produced by the opacity changes during compression (large κ 's are needed) and expansion (small κ 's are needed).

5.3 The Kappa Mechanism (Baker and Kippenhahn 1962)

The pulsation is driven by the opacity, which is modified by changing ionization states. The mechanism can only work in a state of partial ionization.

Indeed, adopting a fully ionized gas and Kramers opacity, the kappa mechanism will not work as ρ and κ vary in the opposite way during compression and expansion.

However, in an ionization zone (H^- , He, He^+) the mechanical energy of a compression will be used to increase the ionization, with only a slow rise of the temperature. This means that the third adiabatic coefficient $\gamma_3 = \rho/T \, dT/d\rho + 1$ is only slightly larger than 1. If we put $\gamma_3 - 1 = 1$, the Kramers opacity reduces to $\kappa \approx \rho^{1-3.5\lambda}$.

For a positive power κ increases for compression and decreases for expansion. Hence, the condition for pulsation becomes $1 - 3.5\lambda > 0$ or $\lambda < 2/7 \approx 0.38$.

If this condition is fulfilled, the kappa mechanism evolves through the following cycle:

The ionization zones compresses adiabatically, increasing κ . Because of the energy increase (from the larger absorption) the pressure starts to increase. This results in an adiabatic expansion. At the end of it an accelerating phase of energy release follows the decrease of κ . At the end of it the maximum luminosity coincides with the maximum contraction velocity.

Let us now examine the conditions of the ionization zones. For the hydrogen and helium ionization zone the temperature range is about 10^4 K, while for the He^+ zone it is about $2 \cdot 10^4$ K. Stars hotter than type G have zones that are too far outside and too thin, so their heat capacity is insufficient to drive the pulsations. In stars earlier than type A the He^+ zone is too far out and too shallow.

On the other hand, if the zones are too far inside the star, damping by the thick outer layers will suppress the starting pulsations.

Summarizing, the pulsations can occur when the ionization zones have a good heat capacity and when they are not too far inside. Figure 5 shows the relative location of the shells for different masses of the star (according to Carroll and Ostlie 1996).

6 Massive Stars ($M > 9 M_\odot$)

We recall some of the characteristics of this group of stars. They evolve through quiet phases of nuclear burning beyond helium. In the HR-diagram their location is bounded by a luminosity boundary, the Humphreys-Davidson limit (for effective temperatures < 4 dex the bolometric magnitude does not exceed -9.5 to -10). Hot stars with $M_{bol} = -10$ to -11 exist, but no cool stars. Stars with masses exceeding $15 M_\odot$ show signs of strong stellar winds. These winds are large enough to cause a substantial mass decrease, thereby removing the outer layers of the star. As a result the initial convective core appears at the surface and enhancements in He, C, N, Ne and O appear in the spectrum. This is shown in Table 3 reflecting the results of calculations of Maeder (1990) for various masses. The $85 M_\odot$ star leaves a remnant of $43.5 M_\odot$ after core hydrogen burning, with a hydrogen by mass fraction of 0.25 at the surface.

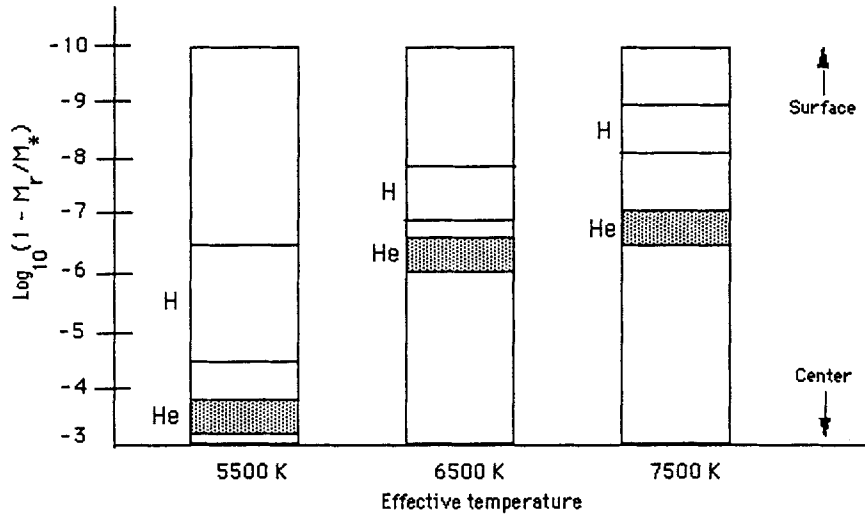


Fig. 5. Relative location of hydrogen and helium ionization zones for different effective temperatures (adapted from Carroll and Ostlie 1996). The vertical axis displays the logarithm of the fraction of the star's mass that lies above each point in the star

With models of stellar evolution generic relations have been established between massive O, B stars, LBVs, blue and red supergiants and WR stars, as outlined in Fig. 6 (Langer 1996).

As mentioned earlier overshooting increases the size of the convective core, causing an increase of the main sequence lifetime, and a widening of the main sequence band in the HR diagram. On the other hand a strong stellar wind mass loss may lead to a decrease of the surface hydrogen abundance, even causing a rightward evolution in the HR diagram.

6.1 Mass Loss by Stellar Wind

I will only discuss aspects relevant to stellar evolution, as the stellar wind topic has been extensively treated in foregoing chapters. Mass loss in massive stars deeply affects the stellar structure of the star: effective temperature, luminosity, chemical abundances at the surface etc. The more massive the star is the more mass it loses. Following Maeder (1994) we combine the average observed mass loss rate with the mass-luminosity relation and the evolutionary timescale from model calculations to yield the fraction of mass lost by evolution:

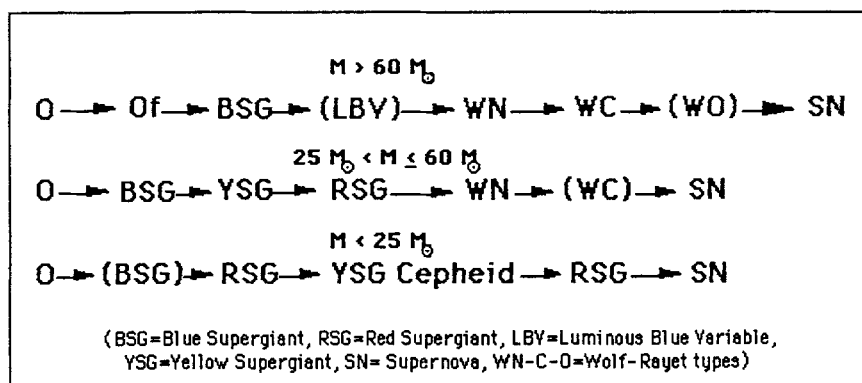


Fig. 6. Generic relations between luminous stars, according to Langer (1996, upper), Maeder (middle), Langer (1996, lower scenario)

$$\frac{\delta M}{M} = \frac{\langle \dot{M} \rangle}{M} t_{ev} \quad (29)$$

a) Mass loss rate (Nieuwenhuyzen and de Jager 1990)

$$M = -10^{-7.93} \frac{L^{1.64} M^{0.16}}{T_{\text{eff}}^{1.61}} M_{\odot}/\text{yr} . \quad (30)$$

b) Evolutionary timescale (Maeder 1994, solar abundances):

$$t_{\text{ev}} = 10^{7.87} M^{-0.72} \text{ yr} . \quad (31)$$

c) Mass-luminosity relation (Maeder 1994):

$$L = 10^{1.83} M^{2.17} L_{\odot} . \quad (32)$$

Combining this we obtain

$$\frac{\delta M}{M} \sim M^2. \quad (33)$$

The above result is of course model dependent, and hence subject to the metallicity. (Note: The increase of the convective core mass with initial stellar mass is proportional to M).

Calculations of stellar evolution with stellar wind mass loss have been performed with various parametrizations, all essentially based on the luminosity. Some examples are:

Table 3. Remnant masses and main sequences lifetimes for a massive star of 20 M_{\odot} with stellar wind mass loss according to (30)

N	t_{ms} in 10^6 yrs (end main sequence)	M/ M_{\odot}
0	6.14	20.0
100	6.88	17.9
300	7.92	14.0
1000	11.39	6.4

$$\log(-\dot{M}) = m + n \log L \quad (34)$$

or

$$-\dot{M} = \frac{NL}{c^2} \quad (35)$$

(de Loore et al. 1976)

$$\log(-\dot{M}) = 1.42 \log L + 0.61 \log R - 0.99 \log M - 12.79 \quad (36)$$

(Lamers 1981)

$$\log(-\dot{M}) = 1.24 \log L + 0.81 \log R + 0.16 \log M - 14.02 \quad (37)$$

(de Jager et al. 1988) and for WR stars,

$$\log(-\dot{M}) = \alpha 10^{-7} M^{2.5} . \quad (38)$$

(with $\alpha = 0.6$ to 1, Langer 1989).

The influence of the wind on the evolution in the main sequence can easily be demonstrated with (35). Results for 4 values of the wind parameter N are shown in Table 4 for a 20 M_{\odot} star. The main sequence lifetime increases with increasing wind, while the remnant mass at the end of the main sequence decreases substantially. In the HR diagram stars with stronger winds evolve at lower luminosity.

6.2 Effects on the Position in the HRD

The mass loss by stellar wind is an energy loss to the star. This loss will affect the outer characteristics, i.e. its effective temperature and luminosity. An increased mass loss will move the red points of the main sequence evolutionary tracks (Terminal Age Main Sequence or TAMS) to the right. Hence

Table 4. Mass of the helium core (in M_{\odot}) of a $60 M_{\odot}$ star for three different wind regimes

	$\dot{M} = 0$	Weak \dot{M}	Strong \dot{M}
start He-burning	20	17.5	15
end He-burning	21.7	21.9	20

the main sequence band will widen (de Loore et al. 1976). The mass loss rate is calculated as a simple luminosity depending function: $\dot{M} = NL/c^2$.

A very large mass loss rate moves the TAMS back to the left. For increasing mass loss rates the final masses decrease and trivially the main sequence lifetimes increase (because the central temperature increases slower). This mass decrease removes the outer layers, and after some time the boundary of the initial convective core may appear at the surface. During the further evolution the outer layers become more and more helium enriched ($N(H)/N(He)$ goes down).

When the hydrogen abundance by weight at the surface, X_{atm} , drops below 0.4 - 0.3, the opacity in the outer layers changes drastically (the effect is temperature dependent, for lower temperatures the effect occurs at $X_{\text{atm}} \approx 0.4$, for high temperatures at $X_{\text{atm}} \approx 0.3$). The outer layers contract rapidly while the luminosity remains about the same. Hence, T_{eff} increases and the star moves to the blue part of the HRD.

Also more advanced stages are strongly affected by the strength of the stellar wind. This is shown in Table 4, giving the mass of the helium core of a massive star at the beginning and the end of helium burning for three different wind regimes.

6.3 The Effect of Overshooting

Overshooting of the convective core (cf. Sect. 3.3.3) is the second mechanism, influencing the structure of massive stars, and competing with the stellar wind mass loss. Using the parameter α , defined as the fraction of the pressure scale height, for the amount of overshooting, we have the following effects in the HRD: larger values of α result in higher main sequence luminosity, very high values move the TAMS to the right. Table 5 shows how the initial mass of the convective core is affected for different initial masses and different values of α .

6.4 Internal Mixing

Maeder (1987) estimated the mixing timescale for massive stars. As most mixing mechanisms are dissipative, the diffusion coefficient depends on the

Table 5. Mass of the convective core for initial masses 20 to 100 M_{\odot} , and different amounts of overshooting $\alpha = l/H_p$. All masses are in M_{\odot}

Mass	M_{Schw}		M_{ov}		
	$\alpha = 0$	$\alpha = 0.25$	$\alpha = .50$	$\alpha = 1.00$	$\alpha = 1.50$
100	78	80	83	87	92
80	58	61	64	68	72
60	43	43	45	49	52
40	24	26	28	31	34
30	16	18	19	22	24
20	9	11	12	14	15

viscosity coefficient ν . In general the characteristic time of mixing is (Schatzmann 1977)

$$t_{\text{mix}} = \frac{4}{\pi^2} \left(\int_0^R \frac{d}{\sqrt{D}} \right)^2 \quad (39)$$

which is approximately

$$t_{\text{mix}} \approx 0.4 \frac{R^2}{\langle D \rangle} \quad (40)$$

with $\langle D \rangle$ an appropriate average.

In massive stars the viscosity ν is essentially radiative

$$\nu = \frac{4}{15} \frac{aT^4}{(c\kappa\rho^2)} \quad (41)$$

Taking $T \approx \mu m_H/k$ GM/R gives t_{mix} as

$$t_{\text{mix}} \approx 0.1 \frac{c}{a} \left(\frac{k}{\mu} m_H G \right)^4 \frac{\kappa}{Re_*} M^2 \quad (42)$$

with $Re_* = D/\nu$ a factor of the order of 10^2 .

We see that the timescale of mixing decreases rapidly with increasing mass, faster than the evolutionary timescale given earlier. This suggests that massive stars are close to a partial mixing stage or, as was suggested by Maeder (1987), may even evolve close to homogeneity.

6.5 Radius Correction for Hydrostatic Stars

Computer codes usually use hydrostatic atmospheres, with no line formation processes. The models therefore do not give spectroscopic information, but serve to calculate the absolute dimensions of the star in a simplified way. This

saves computer memory and calculation time. For a large range of masses, and large parts of the evolution this approximation is quite satisfactory. However, for massive stars such as WR stars this is inaccurate. These stars have extended, dynamic atmospheres, and therefore a different radius. A procedure to correct hydrostatic radii for the effect of dynamic, outflowing winds was developed by de Loore et al. (1982). They combined three relations,

a) the optical depth:

$$d\tau = -\kappa\rho dr \quad . \quad (43)$$

b) the continuity law:

$$\dot{M} = -4\pi r^2 v(r) \quad . \quad (44)$$

c) the velocity law:

$$v(r) = v_\infty \left(1 - \frac{R_\star}{r}\right)^\beta \quad . \quad (45)$$

into

$$d\tau = \kappa \frac{\dot{M}}{4\pi r^2 v_\infty \left(1 - \frac{R_\star}{r}\right)^\beta} \quad . \quad (46)$$

Adopting electron scattering as the dominant absorption source we can write $\kappa = \sigma_{\text{el}} = 0.22 (1+X)$. Integrating the luminosity part from 0 to τ and the radius part correspondingly from ∞ to r , we obtain after some calculations an expression for the radius at $\tau = 2/3$:

$$R_{\text{eff}} = R + \frac{3\kappa|\dot{M}|}{8\pi v_\infty} \quad . \quad (47)$$

For $\tau = 1$ we get a difference of $< 10\%$. Taking $v_\infty = 3000$ km/s we get

$$R_{\text{eff}} = R + 7.97 \cdot 10^4 |\dot{M}| \quad . \quad (48)$$

The corresponding effective temperature is

$$\log T_{\text{eff}} = 3.76 + 0.25 \log \frac{L}{L_\odot} - 0.5 \log R_{\text{eff}} \quad . \quad (49)$$

For WR stars we obtain shifts of $\Delta \log T_{\text{eff}} \approx 0.3 - 0.6$.

Recently, Heger and Langer (1996) calculated new models for WR stars including a grey optically thick, stationary outflowing wind. They show that the radius of the sonic point is almost identical to the radius of a helium star with the same mass but without mass loss. Such small radii are confirmed by recent studies of very close WR + O systems (Moffat and Marchenko 1996).

6.6 New Models for Massive Stars

In the standard method the structure equations are solved with the boundary conditions at the center and at the surface. The latter are provided by the outer layer calculations (“atmosphere”). These outer layers are treated as hydrostatic plane parallel grey atmospheres in the Eddington approximation.

For phases with mass loss this phenomenon, described by \dot{M} , is added to the evolution as a stepwise decrease of the mass according to some empirical relation (cf. Sect. 6.1).

A better approach is to combine stellar structure and atmosphere models, using for the latter spherically expanding non-LTE atmospheres including line blanketing (Costar: Schaerer et al. 1996). Such models not only describe the internal evolution, but also the detailed spectral evolution (continuum and line spectra).

Models have recently be calculated for the main sequence evolution for 40, 60 and 85 M_{\odot} . The HRD evolution (and hence also the inner structure) is nearly identical to the “standard” models. The 85 M_{\odot} evolves close to the Eddington limit, and shows larger differences than the 40 and 60 M_{\odot} cases.

References

- Aubert, O., Prantzos, N., Bareffe, I. (1996) *A&A* **312**, 845
 Baker, N., Kippenhahn, R. (1962) *Z. Astrophys.* **54**, 114
 Böhm-Vitense, E. (1958): *Z. Astrophys.* **46**, 108
 Carroll, B. W., Ostlie, D. A. (1996): *An Introduction to Modern Astrophysics*, Addison-Wesley, Reading, Massachusetts
 Castellani, V., Giannone, P., Renzini, A. (1971a): *Ap&SS* **10**, 340
 Castellani, V., Giannone, P., Renzini, A. (1971b): *Ap&SS* **10**, 355
 Castellani, V., Chieffi, A., Pulone, L., Tornambé, A. (1985): *A&AS* **100**, 47
 de Jager, C., Nieuwenhuijzen, H., van der Hucht, K. A. (1988): *A&AS* **72**, 259
 de Loore, C., De Greve, J. P., Lamers, H. J. G. L. M. (1976): *A&A* **61**, 251
 de Loore, C., Hellings, H., Lamers, H. J. G. L. M. (1982): in *Wolf-Rayet Stars: Observations, Physics and Evolution*, ed. C. de Loore and A. Willis, Reidel, Dordrecht, p. 53
 Deng, L., Bressan, A., Chiosi, C. (1996a): *A&A* **313**, 145
 Deng, L., Bressan, A., Chiosi, C. (1996b): *A&A* **313**, 159
 Freytag, B., Ludwig, H.-G., Steffen, M. (1996): *A&A* **313**, 497
 Heger, A., Langer, N. (1996): *A&A* **315**, 421
 Henyey, L. G., Wilets, L., Böhm, K. H., Lelevier, R., Levée, R. D. (1959): *ApJ* **129**, 628
 Henyey, L. G., Forbes, G. E., Gould, N. L. (1964): *ApJ* **139**, 306
 Kippenhahn, R., Weigert, A. (1967): *Z. Astrophys.* **65**, 221
 Lamers, H. J. G. L. M. (1981): *ApJ* **245**, 593
 Langer, N. (1989): *A&A* **220**, 135
 Langer, N. (1996): preprint
 Maeder, A. (1987): *A&A* **178**, 159
 Maeder, A. (1990): *A&AS* **84**, 139

- Maeder, A. (1994): *Physical Processes in Astrophysics*, Springer, p.12
- Meynet, G., Arnould, M. (1993) in *Nuclei in the Cosmos*, eds. F. Cappelero and K. Wisliak, Inst. of Phys., p. 503
- Meynet, G., Maeder, A., Schaller, G., Schaerer, D., Charbonnel, C. (1994): A&AS **103**, 97
- Moffat, A. F. J., Marchenko, S. V. (1996): A&A **305**, L29
- Mowlavi, N. (1995): Ph.D. thesis, U.L.B., Brussels
- Nieuwenhuijzen, H., de Jager, C. (1990): A&A **231**, 134
- Nomoto, K., Hashimoto, M. (1988): Phys. Rep. **163**, 13
- Paczynski, B. (1971): Acta Astron. **21**, 417
- Saslow, W. C., Schwarzschild, M. (1965): ApJ **142**, 1468
- Schaerer, D., de Koter, A., Schmutz, W., Maeder, A. (1996): A&A **312**, 475
- Schatzmann, A. (1977): A&A **56**, 211
- Schwarzschild, M. (1958): *Structure and Evolution of Stars*, Princeton University Press, Princeton
- Schwarzschild, M. (1970): QJRAS **11**, 12
- Schwarzschild, M., Harm, R. (1965): ApJ **142**, 855
- Shaviv, G., Salpeter, E. E. (1973): ApJ **184**, 191
- Weigert, A. (1966): Z. Astrophys. **64**, 395
- Wilson, R. E. (1981): A&A **99**, 43
- Woosley, S., Weaver, T. (1988): Phys. Rep. **163**, 79
- Zahn, J. P. (1992): A&A **265**, 115

Atmospheres and Interior Models

J.P. De Greve

Astronomy Group, Vrije Universiteit Brussel,
Pleinlaan 2, B-1050 Brussels, Belgium
e-mail: jpdgreve@vnet3.vub.ac.be

1 Why?

There are several reasons to dedicate part of a Summer School on Stellar Atmospheres to stellar structure and evolution. First of all (and certainly not the least) it is where my personal interest lies. And being responsible for the 1996 edition of the School it was an opportunity I couldn't miss. I'm modelling the structure and evolution of stars, and it's fun.

But there is also the physical reality. Atmospheres, although often largely defined by the local physical circumstances, depend on the interior processes for their macroscopic as well as their microscopic behaviour, certainly on the medium and long term timescales. Atmospheres are the fingerprints of the interior. To emphasize the need of knowledge of the interior to understand the atmospheres, allow me to simplify the situation in JP's Two Trivial Theorems:

- a) There is no atmosphere without interior (actual or in the past).
- b) Different atmospheres reflect different interiors.

The above statements merely state the strong existing links between the atmosphere and the stellar interior. Atmospheres are observed because of escaping radiation. That energy comes essentially from the interior. Moreover, the composition of the atmosphere is by and large the result of stellar evolution. The fractions of the various elements in the outer layers, even when unmodified by mixing or mass loss, are the result of the yields of previous generations of stars. Large scale phenomena (both structural and temporal), linked to specific evolutionary stages, alter the chemical composition, and hence the whole structure of the atmosphere. Drastic examples of such changes can be found in interacting binaries, planetary nebulae, etc.

Finally, it is instructive to point out some of the similarities and differences between the stellar interior and the atmosphere.

Both parts of the star are made out of gas, but the interior part is totally (or almost) ionized, whereas the atmosphere is more complex in containing partially ionized constituents and neutral gas as well. The inner part is dominated by the energy production (either from nuclear or from gravitational contraction), the atmosphere is not (apart from eventual shocks, recombination processes, etc., that do not really contribute to the overall energy

generation). The interior is opaque, while the atmosphere can be considered as transparent (apart from clumps, clouds, rings, dust,...). This opacity difference is of course linked to the high interior density versus the low density in the outer layers. As a consequence, in treating the gas mass is an important parameter for the interior, while radius (or optical depth) is a better parameter at the outside of the star. The interior tells the most important part of its story through long term variations, whereas the atmosphere reveals intriguing processes through short term variations.

2 Recipe and Ingredients

2.1 Equations

The structure of a star in hydrostatic equilibrium is given by the well known four structure equations (in Lagrangian coordinates):

Mass conservation:

$$\frac{\partial r}{\partial m} = \frac{1}{4\pi r^2 \rho} . \quad (1)$$

Hydrostatic equilibrium:

$$\frac{\partial P}{\partial m} = -\frac{Gm}{4\pi r^4} - \frac{1}{4\pi r^4} \frac{\partial^2 r}{\partial t^2} . \quad (2)$$

Energy conservation:

$$\frac{\partial L}{\partial m} = \epsilon_n - \epsilon_\nu - c_P \frac{\partial T}{\partial t} + \frac{\delta}{\rho} \frac{\partial \rho}{\partial t} . \quad (3)$$

Energy transport:

$$\frac{\partial T}{\partial m} = -\frac{GmT}{4\pi r^4 P} \nabla \quad (4)$$

with $\nabla = \nabla_r$ in the case of radiative transport and $\nabla = \nabla_{ad}$ in the case of convective transport.

It is convenient to transform these relations further with respect to the relative mass: $\mu = 1 - m(r)/M$.

2.2 Ingredients

To solve the equations we need to describe a number of properties of stellar material hidden behind various symbols like $r, \epsilon_n, \epsilon_\nu, \kappa, c_P, \nabla_{ad}, \delta$.

We assume them to be known functions of P, T and the chemical composition functions $X_i(m, t)$.

$\rho = \rho(P, T, X_i)$ (equation of state)

$\nabla_{ad} = \nabla_{ad}(P, T, X_i)$

$$\delta = \delta(P, T, X_i)$$

$$\kappa = \kappa(P, T, X_i) \text{ (Rosseland mean of the opacity, including conduction)}$$

$$\epsilon = \epsilon(P, T, X_i)$$

Finally, we have to define the boundary conditions in the center and at the border of the star.

In the center we obviously have $r(\mu = 1) = 0$ and, because of the conservation of energy, also $L_r(\mu = 1) = 0$.

At the surface we assume the Eddington approximation for the temperature $T^4 = L/(8\pi\sigma r^2)$, defined at $r = R_{\text{eff}}$, together with P defined through the equation of state at $r = R_{\text{eff}}$. The independent variables are m and t . All in all we deal with a two-boundary (at $m=0$ and $m=M$) initial value (at $t = t_0$) problem of solving four non-linear, partial differential equations.

2.3 Shooting (a Solution)

a) Occam's razor does not work.....

It is obvious that in this case Occam's razor will not work. The simplest approach will not lead to a solution. Indeed, simply integrating the equations towards the surface from the estimated central values T_c and ρ_c , to meet the surface boundary conditions, will not work. The difference between the values of T and P obtained through integration and the outer boundary values lead to a correction on the estimated values of T_c and ρ_c . But small changes in the center produce huge variations further out in the star leading to divergence. The reverse, integrating from the outside inward to the center suffers from the same problem.

b) But Schwarzschild's razor sometimes does.....

A way out is avoiding too large variations, by integrating less far. This method is the Schwarzschild method, which can be used when the stars have a fairly simple structure. This is especially the case at the onset of the evolution (example: start of the main sequence evolution for a star of $5 M_{\odot}$). The equations are integrated from the center outwards and from the border inwards to a point inside the star, called the fitting point. Iteratively one then tries to match the two solutions at the predefined layer M_{fit} (Schwarzschild 1958).

c) And Henyey's shaver always works, but how clean?

When stars have a more complicated structure (i.e. varying chemical profile, shell sources, ...) the foregoing method fails because of numerical instabilities. The required stability can be obtained by a method developed by Henyey et al. (1959, 1964). This method is now widely applied in most of the existing evolution codes. The star is divided into a number of layers (zones) in such a way that the variables (or a power or combination of them) vary linear on the interval between zoning points (Fig. 1). The structure equations are now replaced by difference equations. The outermost interval is the atmosphere, which is integrated inwards towards a fitpoint. That is the layer

where inner and outer solution must match. Iteration is performed until the required convergence is obtained.

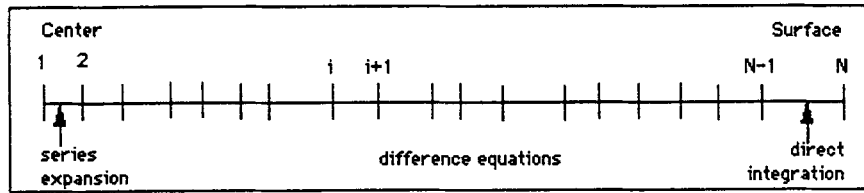


Fig. 1. The mass layer distribution (zoning) in the Henyey iteration method

An example of a difference equation is the one that follows from the partial differential equation for the conservation of mass (in the absence of mass flows):

$$\frac{r_{j+1} - r_j}{M_{j+1} - M_j} = \left[-\frac{M}{4\pi r^2 \rho} \right]_{j+\frac{1}{2}} \quad (5)$$

with the subscripts denoting values on the grid points $(j, j+1)$ or some average in between two grid points $(j+1/2)$. The linearization of the structure equations introduces a truncation error, which is difficult to follow. The truncation error in the above equation is

$$-(M_{j+1} - M_j)^{\frac{3}{24}} y''' . \quad (6)$$

Precise zoning is required to keep it small.

d) The best of two worlds: the multiple fitting method.

In a paper by Wilson (1981) a method was proposed that combines the stability of the Henyey method with the accuracy of the Schwarzschild integration. In this method a generalized Newton iteration is performed on the condition equations at the fit points. Instead of one fitpoint, one chooses N fitpoints, one of them serving as main fitpoint, where inward and outward solution meet (Fig. 2). In between two fitpoints the structure equations are integrated (inward from the surface, and outward from the center). From the center to the first fitpoint series expansions are used. The truncation error is controlled with a predictor-corrector method.

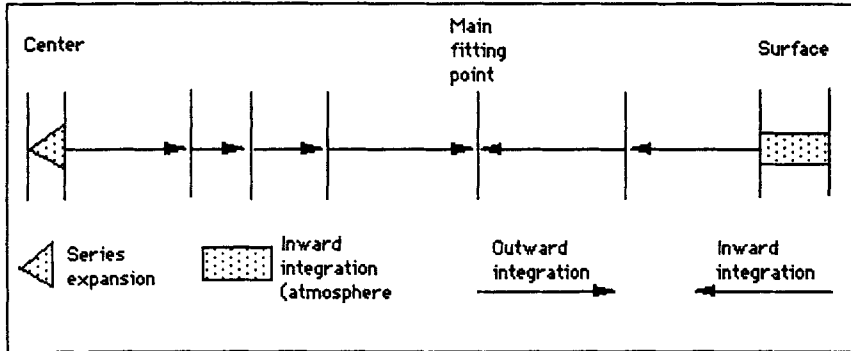


Fig. 2. The mass layer distribution (fitting points) in the multiple fitting method

3 Evolution: From Wherefrom to Whereto, but Most of All: Why?

3.1 Masses Make All the Difference

We can divide the evolution of stars into three groups, according to the mass, though other classifications are possible. The three groups are the low mass stars, the intermediate mass stars, and the high mass stars. For each group the mass limit is influenced by the treatment of the interior, more specifically the amount of overshooting applied in the models (cf. Sect. 3.3.3). We will give values for convective cores determined by the Schwarzschild criterion (cf. Sect. 3.3.1) and, between brackets, for overshooting characterized by $\alpha=0.2$ (where α denotes the fraction of the local pressure scale height by which the convective core extends beyond the classical Schwarzschild core).

The low mass stars are defined as stars with mass smaller than $2.3 M_{\odot}$ ($M < 1.6$ to $1.8 M_{\odot}$). After core hydrogen burning these stars develop a helium core with degenerated electrons. The degeneracy is lifted by the onset of helium burning through a helium flash. The intermediate mass stars are stars with masses ranging between 2.3 and $9 M_{\odot}$ (1.6 to $1.8 M_{\odot}$ and $6 M_{\odot}$). In these stars helium is ignited in non-degenerate conditions, but after the stage of core helium burning a highly electron-degenerated carbon-oxygen core develops. Finally, the massive star group consists of stars more massive than $9 M_{\odot}$ ($6 M_{\odot}$). In these stars electron degeneracy does not occur. At cen-

tral temperatures exceeding $6 \cdot 10^8 \text{K}$ they produce Ne and Mg after quiescent carbon ignition.

Apart from this mass distinction, we can also separate the (early) evolution of the stars according to the threshold value of the central temperature of $2 \cdot 10^7 \text{K}$ on the main sequence (corresponding to a mass of about $1.3 M_{\odot}$). For temperatures below this, the proton-proton cycle is the more active nuclear burning source, while for larger temperatures the CNO cycle will dominate. In small stars the core will contract faster and more pronounced because the energy production rate $\epsilon \approx \rho X^2 T^n$, whereas in massive stars this is $\epsilon \approx \rho X Z_{\text{CNO}} T^n$.

There are also structural differences between small and large masses in the outer layers of the stars. For low masses the hydrogen (and helium) ionization zone reduce the adiabatic gradient and hence, convective zones occur in the outer envelope. For larger masses (i.e. with effective temperature on the main sequence exceeding 8300K , or $M > 1.7 M_{\odot}$), the ionization zones are very thin and the outer layers remain in radiative equilibrium.

3.2 Timescales

For the central hydrogen burning stage the timescale can be estimated as $t_{\text{H}} = E_{\text{H}}/L$.

The energy produced through nuclear burning is proportional to the amount of hydrogen, which in order of magnitude can be approximated by the mass of the star. The luminosity is proportional to M^n (mass-luminosity relation). On average $n=3.5$, in the range 1 to $10 M_{\odot}$ it is about 3.9, in the range 1 to $40 M_{\odot}$ one obtains a value of 3.35. The estimate for the timescale of core hydrogen burning then becomes $t_{\text{H}} \sim M/L \sim M^{1-n} \sim M^{-2.5}$.

The relation shows that the hydrogen burning timescale strongly decreases towards larger M -values.

Comparison of the estimates derived with the above relation with the timescales derived from model calculations (Meynet et al. 1994) shows that the estimates must be used cautiously. Table 1 gives the ratio of the calculated timescales to the mass power, $t_{\text{H}}/M^{-2.5}$. This ratio clearly varies over two orders of magnitude in the range 3 to $120 M_{\odot}$.

Table 1. Timescales t_{H} for core hydrogen burning (Meynet et al. 1994) and the ratio $t_{\text{H}}/M^{-2.5}$. The number between brackets denotes the power of ten

M/M_{\odot}	0.8	1	3	40	120
$t_{\text{H}}/10^6 \text{yr}$	25027.9	9961.7	352.5	4.3	2.6
$t_{\text{H}}/M^{-2.5}$	1.4 (4)	9.9 (3)	5.5 (3)	4.3 (4)	4.1 (5)

3.3 Convection and Other Mixings

3.3.1. Stability against convection and mixing

One of the important but still poorly known aspects of stellar structure is the extension of convection inside a star, and the associated mixing. The standard theory of convection is known as the Mixing Length Theory (Böhm-Vitense 1958). In this framework the boundary of a convective region is determined by a local criterion.

We call a medium unstable when small random motions of matter are amplified and evolve into large scale motions. Stability against convective motion is usually investigated using a model of rising blobs of matter, transporting heat and kinetic energy. In this model the buoyancy force, responsible for the motion of the bubble, is evaluated (and as the border is determined only by the vanishing of the buoyancy force, it implies that the inertia of the convective elements is neglected). Four conditions determine the rise of the bubble:

a) The difference in mean molecular weight between the bubble and the surrounding medium, resulting from the μ -gradient in the medium:

$$\Delta\mu + \mu \frac{d\ln\mu}{d\ln P} \frac{d\ln P}{dr} \Delta r = 0 . \quad (7)$$

b) The adiabatic displacement of the bubble, allowing for a small but non-negligible heat loss during the rise:

$$\frac{d\Delta T}{dt} + T \frac{d\ln P}{dr} (\nabla - \nabla_{ad}) \frac{d\Delta r}{dt} + \lambda \Delta T = 0 . \quad (8)$$

c) The perfect gas equation under the assumption of continuous pressure equilibrium between bubble and medium:

$$\chi_\rho \frac{\Delta\rho}{\rho} + \chi_T \frac{\Delta T}{T} + \chi_\mu \frac{\Delta\mu}{\mu} = 0 . \quad (9)$$

d) The equation of motion due to buoyancy, with g being the local acceleration:

$$\rho \frac{d^2 r}{dt^2} + g \Delta\rho = 0 . \quad (10)$$

The equations are homogeneous, and can be linearized because the Δ 's are small. The trivial solution is of course the one with all variations $\Delta = 0$, but we look specifically for a solution in which all quantities vary with the same phase ω (real or complex), for example $\Delta r = A_r e^{\omega t}$. A negative value of ω implies a stable medium in which the disturbances die out rapidly, a positive ω implies an unstable medium in which the disturbances are amplified. We will obtain nontrivial solutions if the determinant from the coefficients A_T , A_ρ , A_μ , A_r is zero, resulting in the following condition for ω :

$$\omega^3 + \omega^2 \lambda + \omega \left[g \frac{\chi_T}{\chi_\rho} \frac{d \ln P}{dr} \left(\nabla - \nabla_{ad} + \frac{\chi_\mu}{\chi_T} \frac{d \ln \mu}{d \ln P} \right) \right] + \left[\lambda g \frac{\chi_\mu}{\chi_\rho} \frac{d \ln P}{dr} \frac{d \ln \mu}{d \ln P} \right] = 0 . \quad (11)$$

In the absence of heat loss ($\lambda = 0$) we obtain

$$\omega^2 = -g \frac{\chi_T}{\chi_\rho} \frac{d \ln P}{dr} \left(\nabla - \nabla_{ad} + \frac{\chi_\mu}{\chi_T} \frac{d \ln \mu}{d \ln P} \right) . \quad (12)$$

We have a medium that is unstable against convection if ω^2 is positive. Because $d \ln P / dr$ is negative and χ_T and χ_ρ are positive, we have

$$\nabla > \nabla_{ad} - \frac{\chi_\mu}{\chi_T} \frac{d \ln \mu}{d \ln P} \quad (13)$$

(note that $\chi_\mu < 0$). If there is some heat loss during the rise of the bubble, then we have an unstable medium if $\text{re}(\omega) > 0$. This is obtained for the following three conditions:

$$\begin{aligned} \frac{d \ln \mu}{d \ln r} &> 0 \\ \nabla &> \nabla_{ad} - \frac{\chi_\mu}{\chi_T} \frac{d \ln \mu}{d \ln P} \\ \nabla &> \nabla_{ad} . \end{aligned}$$

The first condition describes the onset of a Rayleigh–Taylor instability, the second is the Ledoux criterion, the third the Schwarzschild criterion. Remark that for $d \ln \mu / d \ln r = 0$ the Ledoux and the Schwarzschild criterion become identical.

In practice one uses the radiative and the adiabatic gradient, hence, adopting the Schwarzschild criterion, convection sets in if

$$\nabla_r = \frac{3}{16\pi acG} \frac{\kappa P}{T^4} \frac{L_r}{M_r} > \nabla_{ad} . \quad (14)$$

In the outer layers of the star the ratio L_r / M_r remains constant, whereas the adiabatic gradient decreases in regions of partial ionization. This means that these regions can become convectively unstable.

Because of the simplified way to determine the border of a convective region, and especially the existence of the nonzero velocity of the elements at the edge, additional mixing processes may occur at the border, such as semiconvection and overshooting, which will be discussed in the following sections.

3.3.2. Semiconvection

Semiconvection is a slow form of mixing occurring in a zone intermediate between the convective core and the surface, a region with decreasing mean molecular weight.

In massive stars semiconvection occurs because the radiation pressure dominates the pressure and the electron scattering the opacity. In luminous

stars the high radiation pressure leads to a tendency for the convective core to grow (with increasing mass) and to expand (with evolution). A discontinuity appears at the border of the convective core. Because of the dominant electron scattering (opposed to Kramers bound-free absorption) radiative equilibrium cannot be maintained outside the formal convective core (Schwarzschild and Harm 1965). A second type of semiconvection occurs during core He-burning (Schwarzschild 1970, Paczynski 1971, Castellani et al. 1971 a, b). It results from the increasing opacity in the convective core as the carbon abundance increases, implying an increasing radiative temperature gradient. This type of semiconvection only shows up in stars with masses up to $5 M_{\odot}$. Finally, at the end of helium burning the core may show an oscillatory growth, called “Breathing Convection” (Castellani et al. 1985).

In these zones mixing should occur to smooth out the gradient in molecular weight. However, we would thus change the chemical composition, and the radiative gradient would decrease below the adiabatic.

We thus face a dilemma: If no mixing is applied, the region outside the core is unstable against convection, if mixing is applied, the region becomes stable, and hence no homogenization should take place.

One way of dealing with this is to install a so-called neutrality condition in that region (i.e. $\nabla_r = \nabla_{ad}$) through suitable mixing that involves a redistribution of the chemical elements over a finite region to smooth out the gradient in mean molecular weight.

Because the fluxes of heat and kinetic energy are extremely small, and the energy transport is essentially radiative, semiconvection is a diffusion problem. Hence, we can adopt a diffusion coefficient that is proportional to the difference of the gradients $\nabla_r - \nabla_{ad}$

$$\sigma_{sc} = \Lambda v_s (\nabla_r - \nabla_{ad}) \text{ if } \nabla_r > \nabla_{ad} \quad (15)$$

$$\sigma_{sc} = 0 \text{ if } \nabla_r \leq \nabla_{ad} \quad (16)$$

with v_s , the adiabatic sound velocity, and Λ a typical length scale.

3.3.3. Convective overshoot

This process comes from the difference between the condition for the border of the convective core (zero acceleration) and the nonzero velocity of the elements at that moment. In principle the varying molecular weight gradient assures an almost immediate stop of the elements (Saslow and Schwarzschild 1965), but Shaviv and Salpeter (1973) showed that the overshoot distance can amount to a nonnegligible fraction of the pressure scale height. The buoyancy force F_b is proportional to the difference of the temperature gradients. Below the boundary that difference is very small and positive. Above, the radiative gradient becomes much smaller than the adiabatic in a distance of one scale height. Hence a drastic change from small and positive F_b to a large and negative value takes place over a short distance, bringing the penetrating

element to an immediate stop. However, if we consider the temperature excess ΔT of the rising bubbles over the surroundings, we remark that below the boundary $\Delta T \geq 0$ while above it $\Delta T < 0$. This means that the convective flux F_{conv} becomes negative (being proportional to $v \Delta T$): $F_{\text{conv}} < 0$.

Because $F_{\text{tot}} = F_{\text{conv}} + F_r$ is constant, we have an increase of F_r and hence $\nabla = -(3/4ac)(\kappa\rho/T^3)F_r$ will increase. As a consequence the absolute value of $\nabla_r - \nabla_{\text{ad}}$ decreases and the buoyancy force will change less drastic. The elements coming through the border will decelerate less strongly and a better penetration in the radiative zone is obtained.

In most treatments of the overshoot an ad hoc approach is used. The boundary of the overshoot region is linked to the gas pressure, through the pressure scale height $H = \mathcal{R}T/\mu g$. The boundary of the convective core is then the region where

$$P_{\text{ov}} = P_{\text{Schw}} e^{-\alpha} \quad (17)$$

with P_{ov} the pressure at the overshoot boundary, and P_{Schw} the pressure at the convective core boundary determined by the Schwarzschild criterion.

$\alpha = 0$: The convective core is identical to the ‘‘Schwarzschild’’ core

$\alpha = 1$: The core boundary is at a location where the pressure is a factor e lower (i.e. one scale height outwards).

Other approaches of the overshoot, such as diffusive mixing including the concept of most effective scale length (Deng et al. 1996a,b) or time-dependent compressible convection (Freytag et al. 1996), have been published in the recent year (see also the review by Zahn 1992).

The influence of semiconvection and overshoot on the internal structure is shown in Table 2 (from Aubert et al. 1996), giving the mass of the core at various evolutionary stages, for various combinations of convection, overshooting and semiconvection. Models are given for the two different criteria for convective instability (Ledoux and Schwarzschild). Although for a $20 M_{\odot}$ star the differences remain relatively small for the hydrogen exhausted core (max. $1.4 M_{\odot}$ or 25 %), they can be as large as a factor 2 for the carbon exhausted core.

3.4 Dredge-Up Phases in the Life of a Star

During the evolution there are particular phases that are interesting with regard to the composition of the atmosphere. Such phases can occur each time an outer convective zone descends deeply inward the star. When this zone reaches layers of former nuclear burning, the products of that process are mixed in and brought to the surface. Such a process is called a dredge-up.

a) Climbing the giant branch: the first dredge-up.

When the star reaches the left side of the Hertzsprung–Russell diagram after core hydrogen burning, it moves upward along the Hayashi track. During that phase the outer convective zone grows inward. In a $3 M_{\odot}$ model

Table 2. Core masses at various evolutionary (nuclear exhausted) stages, for different combinations of convection, overshooting and semiconvection (Table from Aubert et al. 1996)

Convection Criterion	Oversh.	Semiconv.	M_α (H-exh)	M_{CO} (He-exh)	M_{ONe} (C-exh)	Ref.
Ledoux	No	No	5.7	2.2	2.0	1
Ledoux	Yes	Yes	6.2	3.7	3.5	1
Schwarzschild	No	No	6.0	3.8	3.7	2
Schwarzschild	Yes	No	7.1	5.1	≈ 4.0	3
Schwarzschild	No	No	6.1	4.7	3.8	4

Ref.: 1: Woosley and Weaver (1988); 2: Nomoto and Hashimoto (1988);
3: Meynet and Arnould (1993); 4: Aubert et al. (1996).

($Z=0.02$, $X=0.70$, Mowlavi 1995) it reaches down to almost $0.4 M_\odot$. During the previous core hydrogen burning the convective core extended outward to $0.58 M_\odot$. Hence, products of CNO-burning are brought up to the surface when the star evolves to the top of the red giant branch.

A similar behaviour was found in a $6 M_\odot$ star with the same composition, but not in the $3 M_\odot$ star with lower metallicity ($Z=0.001$, Mowlavi 1995).

b) The second dredge-up.

A new opportunity to bring nuclear burning products to the surface occurs in intermediate mass stars after core helium burning when a new approach of the Hayashi boundary causes the outer convective zone once more to move deeply inward to reach the chemical discontinuity between the hydrogen-rich outer layers and the helium-rich region above the helium-burning shell. The resulting mixing increases the helium and nitrogen content of the envelope.

c) The third dredge-up.

This phase occurs in asymptotic giant branch stars of more than $2 M_\odot$, when the outer convection zone merges with the convection zone between the hydrogen and the helium burning shell, which occurs during a thermal pulse of the latter (cf. Sect. 4).

3.5 Anchored Shell Sources (the Node Theorem for Active Shell Sources)

After core hydrogen burning a hydrogen shell source develops at the border of the contracting core. Active shell sources tend to remain at the same distance from the center (by active we mean that it contributes significantly to the total energy production of the star). This characteristic is known as the node theorem (Fig. 3).

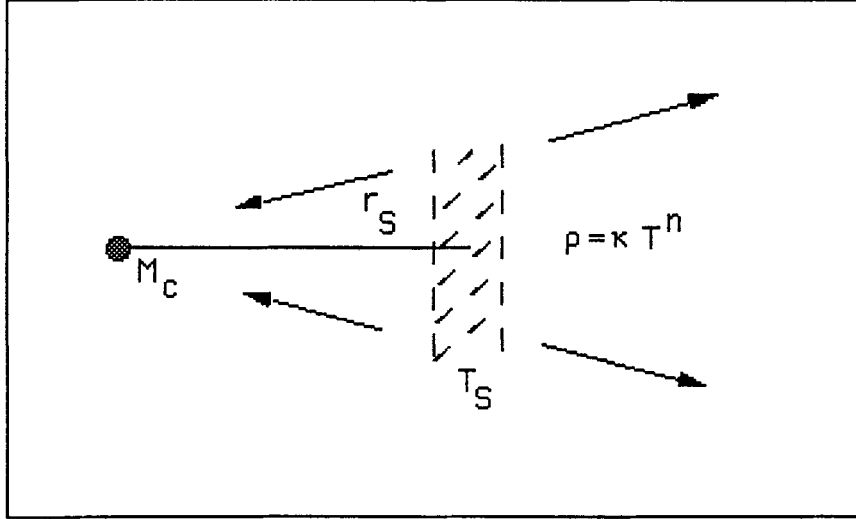


Fig. 3. The node theorem: an active shell with temperature T_c at a distance r_c from the center, outside a core mass M_c . A polytropic relation is applied to the envelope

Consider a shell S at a distance r_s from the center, with temperature T_s . The central mass underneath the shell is M_c .

Assume that the shell source region can be considered as an ideal gas with radiation and that the star is in hydrostatic equilibrium. Moreover we adopt a polytropic expression for the envelope, $\rho = kT^n$. This is valid if $P_g/P_r \approx$ constant, which means that the shell must be active. The proper value of n here is 3. We can then write

$$P = \frac{N_o k \rho T}{\mu} + \frac{1}{3} a T^4 \quad (18)$$

or

$$\frac{dP}{dr} = \frac{dP}{dT} \frac{dT}{dr} = \frac{N_o k}{\beta \mu} \kappa^{n+1} \rho \frac{dT}{dr} \quad (19)$$

with $\beta = P_g/P_{tot}$.

Hydrostatic equilibrium leads to

$$\frac{dP_s}{dr} = - \frac{GM_c}{r_s^2 \rho_s} . \quad (20)$$

After combining the two equations and integrating the temperature one obtains

$$T_S = \beta \frac{\mu}{N_0 k} \frac{GM_c}{\kappa^{n+1}} \frac{1}{r_S} + \text{constant} \quad (21)$$

or

$$T_S \sim \frac{1}{r_S} . \quad (22)$$

When the shell is moved to the center the shell temperature rises. This causes an increase in the nuclear energy production, resulting in a rising gas pressure. The increase in gas pressure moves the shell outwards again. Inversely, if the shell is moved outward, its temperature drops, the nuclear energy production decreases, with a corresponding decrease in gas pressure, moving the shell back inwards. Hence, a shell tends to remain at a fixed position.

Shell \rightarrow Center : $T_S \uparrow \Rightarrow \epsilon_{\text{nuc}} \uparrow \Rightarrow P_S \uparrow \Rightarrow r_S \uparrow$

Shell \rightarrow Out : $T_S \downarrow \Rightarrow \epsilon_{\text{nuc}} \downarrow \Rightarrow P_S \downarrow \Rightarrow r_S \downarrow$.

When a shell source develops, the core becomes inert (apart from a small contribution from gravitational contraction). Volume changes are reversed at the boundaries of the active shell. In the post core hydrogen burning stage this results in an expansion of the outer envelope, balancing the contraction of the inert helium core. The star rapidly develops into a red giant.

3.6 Mass Motions of Different Shells

Shell sources may be active or non-active for some time. Because of the different temperature ranges required for each burning, neighbouring shell sources can influence each other. And because of the different temperature dependence of the reactions, the shell sources generally move with different mass “velocities” (\dot{M}_S) through the mass.

Denoting X_i the mass concentration of the reacting element i ahead of the shell source, and ϵ_i the energy released per gram of mass burned, then the mass velocity is given by $\dot{M}_S = L_i / (\epsilon_i X_i)$. The relative motion of the hydrogen and helium shell sources through the mass is then given by

$$\frac{\dot{M}_H}{\dot{M}_{\text{He}}} = \frac{L_H}{L_{\text{He}}} \frac{\epsilon_{\text{He}}}{\epsilon_H} \frac{X_{\text{He}}}{X_H} . \quad (23)$$

Note that roughly equal velocities of the shells (and hence a stationary situation) are obtained for $L_H \approx 7L_{\text{He}}$, since $X_H \approx 0.7$, $X_{\text{He}} \approx 1$ and $\epsilon_H/\epsilon_{\text{He}} \approx 10$.

While the shell is burning outwards, it tends to concentrate on gradually smaller mass ranges. Changes become more rapid (changes are defined here by the time interval it takes to shift the very steep chemical profile over a range that is comparable to its extension). If the shell is thermally unstable, the

assumption of complete equilibrium has to be abandoned. Such instabilities differ from perturbations of the central nuclear burning region by

- a) different geometry
- b) different reaction of the density to an expansion.

The expansion of a thin shell source will not stabilize it, but will enforce the liberation of energy by heating. This means that the shell source reacts just as if the equation of state were $r \sim 1/T$, reflecting an instable situation.

The pulse instability was first found by Schwarzschild and Harm (1965) for a helium shell source in a star of $1 M_{\odot}$. In a study of a $5 M_{\odot}$ star Weigert (1966) found the same instability in a two-shell source model. He also found that the instability leads to nearly periodic relaxation oscillations, called thermal pulses.

4 Thermal Pulses or Secular Stabilities of Shell Sources

How can we explain the strange behaviour described in the foregoing section? We therefore need to consider the difference between density changes in the core and in the shell.

4.1 Density Changes of a Nuclear Burning Zone

We consider two different situations, a nuclear burning core and a nuclear burning shell. For the spherical core we have $m \sim \rho r^3$, and a radial expansion (at constant mass, $dm = 0$) therefore leads to $d\rho/\rho = -3dr/r$. Now consider a shell at a distance r_0 from the center, with thickness D ($r = r_0 + D$). If the shell expands we have $dr = dD$ ($r_0 \approx \text{constant}$) and hence, $d\rho/\rho = -dD/D = -r/D dr/r$.

If we assume that the changes near the boundary are homologous (i.e. $r+dx = r(1+x)$), we obtain different proportionality constants for the changes of the density with radius in the core and in a shell:

Central: 3	Shell: r/D
------------	--------------

4.2 Shell Perturbation and Pressure Change

Consider the change of pressure in the shell source as a hydrostatic reaction to the lift of the layers above (again we assume homology for simplicity).

Assume that the shell expands to get rid of the perturbation: $dD/D > 0$. This causes a corresponding change of the density $d\rho/\rho < 0$, but only a very small increase dr/r of the radius if the shell thickness is small compared to the distance to the center ($D/r \ll 1$).

As a result the layers are hardly lifted and therefore the weight of these layers remains constant. In that case hydrostatic equilibrium tells us that there is no decrease in pressure ($dP/P \approx 0$).

Indeed, the homology relation $dP/P = -4dr/r$ and $d\rho/\rho = -r/D dr/r$ combine to $dP/P = 4D/r d\rho/\rho$.

Using the equation of state in the form $d\rho/\rho = \alpha dP/P - \delta dT/T$, we find that $d\rho/\rho = -\delta dT/T$, since dP/P goes to zero for small values of D/r .

Hence we obtain a result that is similar to an equation of state of the type $\rho \sim 1/T$. The expansion of the helium shell leads to an increase of its temperature. This secular instability of the shell results in nearly periodic relaxation oscillations.

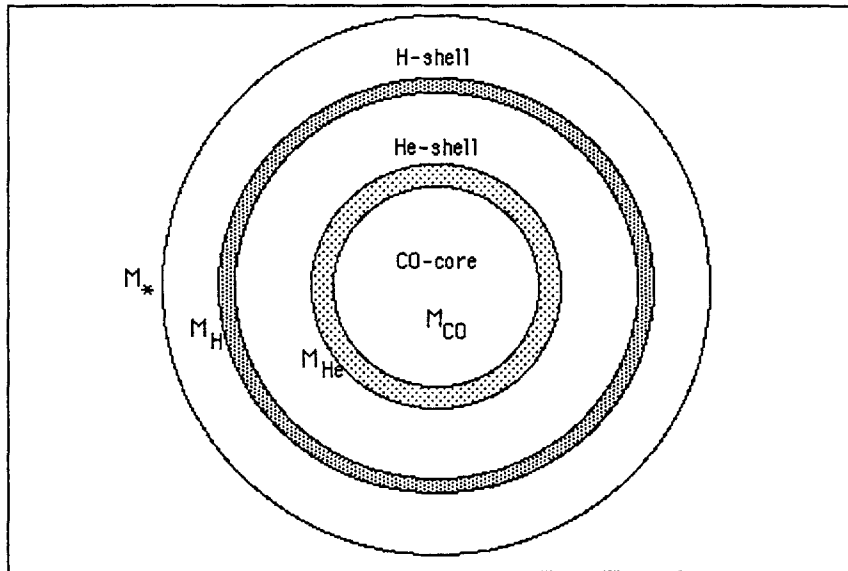


Fig. 4. Structure of a star with two active shell sources outside an inert Carbon-Oxygen core

More precisely, when we have two active shell sources (helium and hydrogen) surrounding an inert CO-core, a thermal pulse evolves through the following sequence of events (Fig. 4). In the helium burning shell the energy production rises steeply as the energy rate is proportional to T^5 . This causes an increase of the pressure in the inner shell region, pushing the H-shell outwards. The H-shell dies out, and the total energy production decreases below the amount L that is lost at the surface. The difference is then produced by contraction of that region (interpulse phase). The H-shell goes down, heats up and finally ignites again.

As model calculations show, a shortlived convective shell develops above the helium shell during the thermal runaway. This shell mixes helium burning products into the intershell region, and at the same time it brings helium-enriched intershell matter into the nuclear burning region. For a $5 M_{\odot}$ star Kippenhahn and Weigert (1967) found a lifetime of ~ 70 years for the thermal runaway, whereas the convective shell only exists in the first 50 years. The time between two pulses increases gradually, from 3200 years for the first, to 4300 years for the sixth pulse in their models. The first pulse occurs when the helium shell has reached $m/M=0.1597$, while the hydrogen shell is at $m/M=0.1603$. It is the latter that provides almost all the surface luminosity, which is only little affected by the pulses. In small mass stars ($\sim 0.6 M_{\odot}$) the period between pulses may reach hundreds of thousands of years. The pulse amplitude grows with each successive event.

For the atmospheric conditions it is interesting to see that the outer convection zone reaches almost to the H-He discontinuity, retreats upwards at each pulse and moves back to the discontinuity in the interpulse phase. If the outer convection zone descends below the discontinuity and merges with the shortlived convection zone above the helium shell a third dredge-up phase occurs ($M > 2 M_{\odot}$). Intershell matter from carbon synthesis can be dredged up to the surface. The observed differences between oxygen-rich giants and carbon-rich giants can probably be explained through this process.

5 Cepheids

(as an Answer to the Request of T. Le Bertre)

5.1 The Period-Density Relation

Intermediate mass stars may pulsate with periods between 2 and 40 days during the phase of core helium burning. In this phase we call them Cepheids (in the case of low mass stars: RR Lyrae variables), representing variable stars (with variations in radial velocity, radius and effective temperature). Maximum luminosity and minimum radius have a time lag, the maximum luminosity corresponds with the largest contraction velocity.

In modelling such pulsations astrophysicists get a better understanding of the stellar interior. The observed radial pulsations result from sound waves that resonate in the interior. An estimate of the pulsation period can be obtained by evaluating the crossing time of a sound wave through a star with radius R and average density ρ . In such a star the adiabatic sound velocity is given by (Carroll and Ostlie 1996)

$$v_s = \sqrt{\frac{\gamma P}{\rho}} \quad (24)$$

with γ the ratio of specific heats $\gamma = c_P/c_V = (d \ln P / d \ln \rho)_{ad}$.

The pressure follows from hydrostatic equilibrium, assuming a constant density (!):

$$\frac{dP}{dr} = -\frac{4}{3}\pi G\rho^2 r . \quad (25)$$

Integrating from $P = 0$ ($r = R$) we obtain:

$$P(r) = \frac{2}{3}\pi G\rho^2 (R^2 - r^2) . \quad (26)$$

The pulsation period can then be estimated as

$$\Pi \approx 2 \int_0^R \frac{dr}{v_s} \approx \sqrt{\frac{3\pi}{2\gamma G\rho}} . \quad (27)$$

If we take $M = 5 M_\odot$ and a radius of $R = 50 R_\odot$ (representing a typical Cepheid), we obtain $\Pi \approx 10$ days.

5.2 The Valve Mechanism

In order for pulsations to work one has the following basic equation

$$\oint \frac{dQ\Delta T}{T_0} > 0 \quad (28)$$

with ΔT the cyclic variation of the temperature (i.e. the deviation from T_0). One can explain the equation as follows:

In order to perform work against the surroundings, heat has to be absorbed at high temperature, and has to be emitted at low temperature. For a pulsation each small gas element has to absorb energy during compression (when the temperature is high) and to emit heat during the expansion (when the temperature is low).

The process above shows similarities to the process in an explosion motor with valves.

In a star the energy flux in the atmosphere is constant. During maximum compression the heat leakage has to be small, and during expansion it has to be large. The change of the leakage can be produced by the opacity changes during compression (large κ 's are needed) and expansion (small κ 's are needed).

5.3 The Kappa Mechanism (Baker and Kippenhahn 1962)

The pulsation is driven by the opacity, which is modified by changing ionization states. The mechanism can only work in a state of partial ionization.

Indeed, adopting a fully ionized gas and Kramers opacity, the kappa mechanism will not work as ρ and κ vary in the opposite way during compression and expansion.

However, in an ionization zone (H^- , He, He^+) the mechanical energy of a compression will be used to increase the ionization, with only a slow rise of the temperature. This means that the third adiabatic coefficient $\gamma_3 = \rho/T \, dT/d\rho + 1$ is only slightly larger than 1. If we put $\gamma_3 - 1 = 1$, the Kramers opacity reduces to $\kappa \approx \rho^{1-3.5\lambda}$.

For a positive power κ increases for compression and decreases for expansion. Hence, the condition for pulsation becomes $1 - 3.5\lambda > 0$ or $\lambda < 2/7 \approx 0.38$.

If this condition is fulfilled, the kappa mechanism evolves through the following cycle:

The ionization zones compresses adiabatically, increasing κ . Because of the energy increase (from the larger absorption) the pressure starts to increase. This results in an adiabatic expansion. At the end of it an accelerating phase of energy release follows the decrease of κ . At the end of it the maximum luminosity coincides with the maximum contraction velocity.

Let us now examine the conditions of the ionization zones. For the hydrogen and helium ionization zone the temperature range is about 10^4 K, while for the He^+ zone it is about $2 \cdot 10^4$ K. Stars hotter than type G have zones that are too far outside and too thin, so their heat capacity is insufficient to drive the pulsations. In stars earlier than type A the He^+ zone is too far out and too shallow.

On the other hand, if the zones are too far inside the star, damping by the thick outer layers will suppress the starting pulsations.

Summarizing, the pulsations can occur when the ionization zones have a good heat capacity and when they are not too far inside. Figure 5 shows the relative location of the shells for different masses of the star (according to Carroll and Ostlie 1996).

6 Massive Stars ($M > 9 M_\odot$)

We recall some of the characteristics of this group of stars. They evolve through quiet phases of nuclear burning beyond helium. In the HR-diagram their location is bounded by a luminosity boundary, the Humphreys-Davidson limit (for effective temperatures < 4 dex the bolometric magnitude does not exceed -9.5 to -10). Hot stars with $M_{bol} = -10$ to -11 exist, but no cool stars. Stars with masses exceeding $15 M_\odot$ show signs of strong stellar winds. These winds are large enough to cause a substantial mass decrease, thereby removing the outer layers of the star. As a result the initial convective core appears at the surface and enhancements in He, C, N, Ne and O appear in the spectrum. This is shown in Table 3 reflecting the results of calculations of Maeder (1990) for various masses. The $85 M_\odot$ star leaves a remnant of $43.5 M_\odot$ after core hydrogen burning, with a hydrogen by mass fraction of 0.25 at the surface.

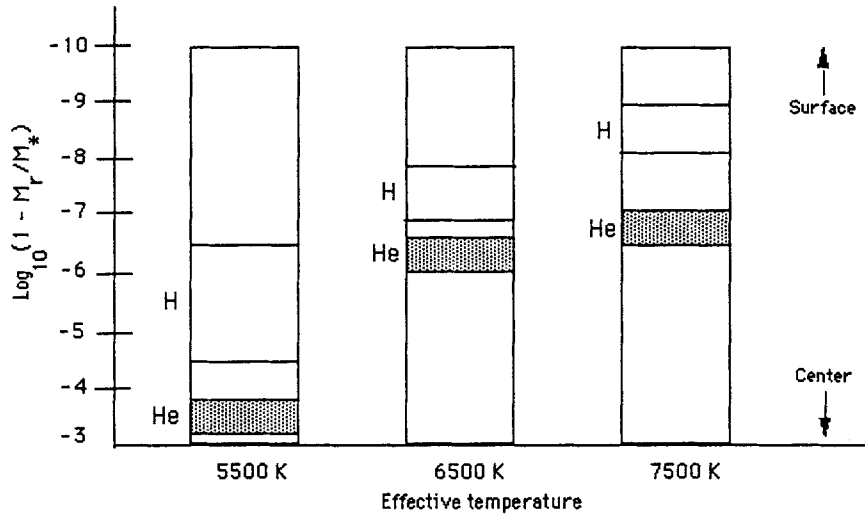


Fig. 5. Relative location of hydrogen and helium ionization zones for different effective temperatures (adapted from Carroll and Ostlie 1996). The vertical axis displays the logarithm of the fraction of the star's mass that lies above each point in the star

With models of stellar evolution generic relations have been established between massive O, B stars, LBVs, blue and red supergiants and WR stars, as outlined in Fig. 6 (Langer 1996).

As mentioned earlier overshooting increases the size of the convective core, causing an increase of the main sequence lifetime, and a widening of the main sequence band in the HR diagram. On the other hand a strong stellar wind mass loss may lead to a decrease of the surface hydrogen abundance, even causing a rightward evolution in the HR diagram.

6.1 Mass Loss by Stellar Wind

I will only discuss aspects relevant to stellar evolution, as the stellar wind topic has been extensively treated in foregoing chapters. Mass loss in massive stars deeply affects the stellar structure of the star: effective temperature, luminosity, chemical abundances at the surface etc. The more massive the star is the more mass it loses. Following Maeder (1994) we combine the average observed mass loss rate with the mass-luminosity relation and the evolutionary timescale from model calculations to yield the fraction of mass lost by evolution:

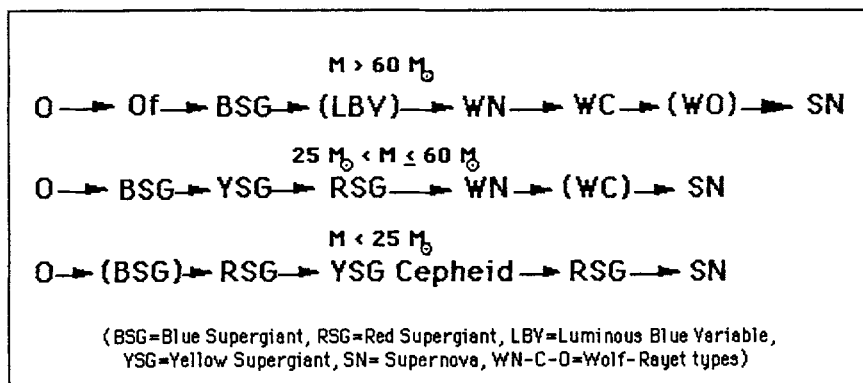


Fig. 6. Generic relations between luminous stars, according to Langer (1996, upper), Maeder (middle), Langer (1996, lower scenario)

$$\frac{\delta M}{M} = \frac{\langle \dot{M} \rangle}{M} t_{ev} . \quad (29)$$

a) Mass loss rate (Nieuwenhuyzen and de Jager 1990)

$$M = -10^{-7.93} \frac{L^{1.64} M^{0.16}}{T_{\text{eff}}^{1.61}} M_{\odot}/\text{yr} . \quad (30)$$

b) Evolutionary timescale (Maeder 1994, solar abundances):

$$t_{\text{ev}} = 10^{7.87} \text{M}^{-0.72} \text{ yr} . \quad (31)$$

c) Mass-luminosity relation (Maeder 1994):

$$L = 10^{1.83} M^{2.17} L_{\odot} . \quad (32)$$

Combining this we obtain

$$\frac{\delta M}{M} \sim M^2. \quad (33)$$

The above result is of course model dependent, and hence subject to the metallicity. (Note: The increase of the convective core mass with initial stellar mass is proportional to M).

Calculations of stellar evolution with stellar wind mass loss have been performed with various parametrizations, all essentially based on the luminosity. Some examples are:

Table 3. Remnant masses and main sequences lifetimes for a massive star of 20 M_{\odot} with stellar wind mass loss according to (30)

N	t_{ms} in 10^6 yrs (end main sequence)	M/ M_{\odot}
0	6.14	20.0
100	6.88	17.9
300	7.92	14.0
1000	11.39	6.4

$$\log(-\dot{M}) = m + n \log L \quad (34)$$

or

$$-\dot{M} = \frac{NL}{c^2} \quad (35)$$

(de Loore et al. 1976)

$$\log(-\dot{M}) = 1.42 \log L + 0.61 \log R - 0.99 \log M - 12.79 \quad (36)$$

(Lamers 1981)

$$\log(-\dot{M}) = 1.24 \log L + 0.81 \log R + 0.16 \log M - 14.02 \quad (37)$$

(de Jager et al. 1988) and for WR stars,

$$\log(-\dot{M}) = \alpha 10^{-7} M^{2.5} . \quad (38)$$

(with $\alpha = 0.6$ to 1, Langer 1989).

The influence of the wind on the evolution in the main sequence can easily be demonstrated with (35). Results for 4 values of the wind parameter N are shown in Table 4 for a 20 M_{\odot} star. The main sequence lifetime increases with increasing wind, while the remnant mass at the end of the main sequence decreases substantially. In the HR diagram stars with stronger winds evolve at lower luminosity.

6.2 Effects on the Position in the HRD

The mass loss by stellar wind is an energy loss to the star. This loss will affect the outer characteristics, i.e. its effective temperature and luminosity. An increased mass loss will move the red points of the main sequence evolutionary tracks (Terminal Age Main Sequence or TAMS) to the right. Hence

Table 4. Mass of the helium core (in M_{\odot}) of a $60 M_{\odot}$ star for three different wind regimes

	$\dot{M} = 0$	Weak \dot{M}	Strong \dot{M}
start He-burning	20	17.5	15
end He-burning	21.7	21.9	20

the main sequence band will widen (de Loore et al. 1976). The mass loss rate is calculated as a simple luminosity depending function: $\dot{M} = NL/c^2$.

A very large mass loss rate moves the TAMS back to the left. For increasing mass loss rates the final masses decrease and trivially the main sequence lifetimes increase (because the central temperature increases slower). This mass decrease removes the outer layers, and after some time the boundary of the initial convective core may appear at the surface. During the further evolution the outer layers become more and more helium enriched ($N(H)/N(He)$ goes down).

When the hydrogen abundance by weight at the surface, X_{atm} , drops below 0.4 - 0.3, the opacity in the outer layers changes drastically (the effect is temperature dependent, for lower temperatures the effect occurs at $X_{\text{atm}} \approx 0.4$, for high temperatures at $X_{\text{atm}} \approx 0.3$). The outer layers contract rapidly while the luminosity remains about the same. Hence, T_{eff} increases and the star moves to the blue part of the HRD.

Also more advanced stages are strongly affected by the strength of the stellar wind. This is shown in Table 4, giving the mass of the helium core of a massive star at the beginning and the end of helium burning for three different wind regimes.

6.3 The Effect of Overshooting

Overshooting of the convective core (cf. Sect. 3.3.3) is the second mechanism, influencing the structure of massive stars, and competing with the stellar wind mass loss. Using the parameter α , defined as the fraction of the pressure scale height, for the amount of overshooting, we have the following effects in the HRD: larger values of α result in higher main sequence luminosity, very high values move the TAMS to the right. Table 5 shows how the initial mass of the convective core is affected for different initial masses and different values of α .

6.4 Internal Mixing

Maeder (1987) estimated the mixing timescale for massive stars. As most mixing mechanisms are dissipative, the diffusion coefficient depends on the

Table 5. Mass of the convective core for initial masses 20 to 100 M_{\odot} , and different amounts of overshooting $\alpha = l/H_p$. All masses are in M_{\odot}

Mass	M_{Schw}		M_{ov}		
	$\alpha = 0$	$\alpha = 0.25$	$\alpha = .50$	$\alpha = 1.00$	$\alpha = 1.50$
100	78	80	83	87	92
80	58	61	64	68	72
60	43	43	45	49	52
40	24	26	28	31	34
30	16	18	19	22	24
20	9	11	12	14	15

viscosity coefficient ν . In general the characteristic time of mixing is (Schatzmann 1977)

$$t_{\text{mix}} = \frac{4}{\pi^2} \left(\int_0^R \frac{d}{\sqrt{D}} \right)^2 \quad (39)$$

which is approximately

$$t_{\text{mix}} \approx 0.4 \frac{R^2}{\langle D \rangle} \quad (40)$$

with $\langle D \rangle$ an appropriate average.

In massive stars the viscosity ν is essentially radiative

$$\nu = \frac{4}{15} \frac{aT^4}{(c\kappa\rho^2)} \quad (41)$$

Taking $T \approx \mu m_H/k$ GM/R gives t_{mix} as

$$t_{\text{mix}} \approx 0.1 \frac{c}{a} \left(\frac{k}{\mu} m_H G \right)^4 \frac{\kappa}{Re_*} M^2 \quad (42)$$

with $Re_* = D/\nu$ a factor of the order of 10^2 .

We see that the timescale of mixing decreases rapidly with increasing mass, faster than the evolutionary timescale given earlier. This suggests that massive stars are close to a partial mixing stage or, as was suggested by Maeder (1987), may even evolve close to homogeneity.

6.5 Radius Correction for Hydrostatic Stars

Computer codes usually use hydrostatic atmospheres, with no line formation processes. The models therefore do not give spectroscopic information, but serve to calculate the absolute dimensions of the star in a simplified way. This

saves computer memory and calculation time. For a large range of masses, and large parts of the evolution this approximation is quite satisfactory. However, for massive stars such as WR stars this is inaccurate. These stars have extended, dynamic atmospheres, and therefore a different radius. A procedure to correct hydrostatic radii for the effect of dynamic, outflowing winds was developed by de Loore et al. (1982). They combined three relations,

a) the optical depth:

$$d\tau = -\kappa\rho dr \quad . \quad (43)$$

b) the continuity law:

$$\dot{M} = -4\pi r^2 v(r) \quad . \quad (44)$$

c) the velocity law:

$$v(r) = v_\infty \left(1 - \frac{R_\star}{r}\right)^\beta \quad . \quad (45)$$

into

$$d\tau = \kappa \frac{\dot{M}}{4\pi r^2 v_\infty \left(1 - \frac{R_\star}{r}\right)^\beta} \quad . \quad (46)$$

Adopting electron scattering as the dominant absorption source we can write $\kappa = \sigma_{\text{el}} = 0.22 (1+X)$. Integrating the luminosity part from 0 to τ and the radius part correspondingly from ∞ to r , we obtain after some calculations an expression for the radius at $\tau = 2/3$:

$$R_{\text{eff}} = R + \frac{3\kappa|\dot{M}|}{8\pi v_\infty} \quad . \quad (47)$$

For $\tau = 1$ we get a difference of $< 10\%$. Taking $v_\infty = 3000$ km/s we get

$$R_{\text{eff}} = R + 7.97 \cdot 10^4 |\dot{M}| \quad . \quad (48)$$

The corresponding effective temperature is

$$\log T_{\text{eff}} = 3.76 + 0.25 \log \frac{L}{L_\odot} - 0.5 \log R_{\text{eff}} \quad . \quad (49)$$

For WR stars we obtain shifts of $\Delta \log T_{\text{eff}} \approx 0.3 - 0.6$.

Recently, Heger and Langer (1996) calculated new models for WR stars including a grey optically thick, stationary outflowing wind. They show that the radius of the sonic point is almost identical to the radius of a helium star with the same mass but without mass loss. Such small radii are confirmed by recent studies of very close WR + O systems (Moffat and Marchenko 1996).

6.6 New Models for Massive Stars

In the standard method the structure equations are solved with the boundary conditions at the center and at the surface. The latter are provided by the outer layer calculations (“atmosphere”). These outer layers are treated as hydrostatic plane parallel grey atmospheres in the Eddington approximation.

For phases with mass loss this phenomenon, described by \dot{M} , is added to the evolution as a stepwise decrease of the mass according to some empirical relation (cf. Sect. 6.1).

A better approach is to combine stellar structure and atmosphere models, using for the latter spherically expanding non-LTE atmospheres including line blanketing (Costar: Schaerer et al. 1996). Such models not only describe the internal evolution, but also the detailed spectral evolution (continuum and line spectra).

Models have recently been calculated for the main sequence evolution for 40, 60 and 85 M_{\odot} . The HRD evolution (and hence also the inner structure) is nearly identical to the “standard” models. The 85 M_{\odot} evolves close to the Eddington limit, and shows larger differences than the 40 and 60 M_{\odot} cases.

References

- Aubert, O., Prantzos, N., Bareffe, I. (1996) *A&A* **312**, 845
 Baker, N., Kippenhahn, R. (1962) *Z. Astrophys.* **54**, 114
 Böhm-Vitense, E. (1958): *Z. Astrophys.* **46**, 108
 Carroll, B. W., Ostlie, D. A. (1996): *An Introduction to Modern Astrophysics*, Addison-Wesley, Reading, Massachusetts
 Castellani, V., Giannone, P., Renzini, A. (1971a): *Ap&SS* **10**, 340
 Castellani, V., Giannone, P., Renzini, A. (1971b): *Ap&SS* **10**, 355
 Castellani, V., Chieffi, A., Pulone, L., Tornambé, A. (1985): *A&AS* **100**, 47
 de Jager, C., Nieuwenhuijzen, H., van der Hucht, K. A. (1988): *A&AS* **72**, 259
 de Loore, C., De Greve, J. P., Lamers, H. J. G. L. M. (1976): *A&A* **61**, 251
 de Loore, C., Hellings, H., Lamers, H. J. G. L. M. (1982): in *Wolf-Rayet Stars: Observations, Physics and Evolution*, ed. C. de Loore and A. Willis, Reidel, Dordrecht, p. 53
 Deng, L., Bressan, A., Chiosi, C. (1996a): *A&A* **313**, 145
 Deng, L., Bressan, A., Chiosi, C. (1996b): *A&A* **313**, 159
 Freytag, B., Ludwig, H.-G., Steffen, M. (1996): *A&A* **313**, 497
 Heger, A., Langer, N. (1996): *A&A* **315**, 421
 Henyey, L. G., Wilets, L., Böhm, K. H., Lelevier, R., Levée, R. D. (1959): *ApJ* **129**, 628
 Henyey, L. G., Forbes, G. E., Gould, N. L. (1964): *ApJ* **139**, 306
 Kippenhahn, R., Weigert, A. (1967): *Z. Astrophys.* **65**, 221
 Lamers, H. J. G. L. M. (1981): *ApJ* **245**, 593
 Langer, N. (1989): *A&A* **220**, 135
 Langer, N. (1996): preprint
 Maeder, A. (1987): *A&A* **178**, 159
 Maeder, A. (1990): *A&AS* **84**, 139

- Maeder, A. (1994): *Physical Processes in Astrophysics*, Springer, p.12
- Meynet, G., Arnould, M. (1993) in *Nuclei in the Cosmos*, eds. F. Cappelero and K. Wisliak, Inst. of Phys., p. 503
- Meynet, G., Maeder, A., Schaller, G., Schaerer, D., Charbonnel, C. (1994): A&AS **103**, 97
- Moffat, A. F. J., Marchenko, S. V. (1996): A&A **305**, L29
- Mowlavi, N. (1995): Ph.D. thesis, U.L.B., Brussels
- Nieuwenhuijzen, H., de Jager, C. (1990): A&A **231**, 134
- Nomoto, K., Hashimoto, M. (1988): Phys. Rep. **163**, 13
- Paczynski, B. (1971): Acta Astron. **21**, 417
- Saslow, W. C., Schwarzschild, M. (1965): ApJ **142**, 1468
- Schaerer, D., de Koter, A., Schmutz, W., Maeder, A. (1996): A&A **312**, 475
- Schatzmann, A. (1977): A&A **56**, 211
- Schwarzschild, M. (1958): *Structure and Evolution of Stars*, Princeton University Press, Princeton
- Schwarzschild, M. (1970): QJRAS **11**, 12
- Schwarzschild, M., Harm, R. (1965): ApJ **142**, 855
- Shaviv, G., Salpeter, E. E. (1973): ApJ **184**, 191
- Weigert, A. (1966): Z. Astrophys. **64**, 395
- Wilson, R. E. (1981): A&A **99**, 43
- Woosley, S., Weaver, T. (1988): Phys. Rep. **163**, 79
- Zahn, J. P. (1992): A&A **265**, 115

Subject Index

- Absorption 9, 10, 21, 43–45, 96, 113, 224
 - profile 21, 22, 25, 200, 203
- Abundance 40, 61, 63, 104, 123, 136, 207, 327, 332, 334, 338
- Accelerated Lambda Iteration *see* ALI
- Acceleration of convergence 36, 37, 51
- Accretion disk 2, 57, 239, 241–250
- Accretion rate 247–249
- Active accretion disk 248, 249
- AFGL 1085 128
- AGB star 69, 85, 92, 95, 123, 133–154, 327
- Alfvénic Mach number 312, 313
- Alfvén wave driven wind 86, 87
- Algol 290, 293
- Algonquin Radio Observatory 227
- ALI 34–39, 51, 267
- α Cam 212
- α disk 246
- $\alpha^{1,2}$ Her 137
- α Per cluster 287, 288
- Amorphous carbon 111, 121, 138, 142
- Amorphous silicate 150
- Ampère’s law 298, 299
- Angular momentum loss 282, 283, 288, 309–314
 - disk 242, 246
- Approximate lambda operator 35, 38
- Approximate-Operator Iteration *see* ALI
- ARO 227
- Asymmetry wind 8, 140, 141, 148, 149, 203, 214, 217, 233
- Asymptotic Giant Branch *see* AGB star
- ATCA 227, 228
- ATLAS 50
- Auger ionization 181
- ζ Aur 90
- Australia Telescope Compact Array 227, 228
- Back scattering 195–197, 219–221
- Backwarming 49–56, 63
 - due to dust 120, 126
- Balmer jump 275
- Balmer progression 190
- Be star 192, 239–241, 250, 252, 258, 259, 263, 266, 274, 275
- Beals classification 190–192
- β law 172, 174–178, 205–207, 210–214, 226, 252
- β Peg 139
- Bi-stability jump 181
- Biot-Savart’s law 298
- Bipolar jets 249, 265
- Black trough 208–210, 215, 220–223
- Blue edge 198, 208–210, 215, 220–223, 258
- Boltzmann equation 3, 6, 50
- Break-up velocity 243
- Breathing convection 325
- Breeze 307, 308
- Bremsstrahlung 45, 223
- Bumps 217
- CAK theory 159, 165, 171
- α Cam 212
- Canada-France-Hawaii Telescope 140, 232
- Capella 277
- η Car 239
- Carbon (amorphous) 111, 121, 138, 142
- Carbon-oxygen core 134–137, 321, 327
- Carbon-rich star 101, 102, 104, 136, 142–144, 146, 148, 153, 154, 332
- Cayrel mechanism 56
- CCP7 58, 203
- Centrifugal force 253, 255, 256
- μ Cep 140, 141
- Cepheids 332–334
- o Cet 90, 136
- CFHT 140, 232
- Charge conservation 44, 45
- Chemical equilibrium 99–102, 106
- Chemistry 92–107, 111, 116, 117, 145, 146

- Chromosphere 93, 98
 Clumping *see* Inhomogeneity
 CNO cycle 322, 327
 Codes 40, 41, 50, 52, 58, 61
 Collisional transition 6, 7, 23, 38, 44, 45
 Column depth 206, 207
 Common direction surface *see* Isovelocity contours
 Common point surface 272–274
 Common velocity surface *see* Isovelocity contours
 Comoving frame 177, 178, 201, 203
 Complete linearization 51, 52
 Complete redistribution 22, 26, 199
 Conduction 4, 301
 Continuity equation 3, 70, 97, 112, 189
 – disk 242, 247, 250–252
 – dust formation 107
 – MHD 297, 305, 310
 – stellar evolution 318, 320, 340
 Continuum diagnostics 223–231
 Convection 4, 5, 40, 281, 283, 323–327
 Convection zone 84, 85, 136, 279, 281–283, 322, 326, 327, 332
 Convective core 325, 327, 335, 338
 Cooling process *see* Radiative cooling
 Cooling region 47, 49, 52, 53, 55
 Copernicus 192, 215
 Core helium burning 325, 327, 332
 Core hydrogen burning 321, 322, 327, 329, 334
 Core mass 327
 Core-halo models 41, 212
 Coriolis force 253
 Corona 84, 277–314
 – acoustic heating 279
 – mechanical heating 279
 – Sun *see* Sun
 Coronal hole *see* Magnetically open region
 Coronal line 277, 290–293
 Coronal wind 84, 87, 124, 305, 307, 308, 310, 311, 313
 Corotation 87, 184, 223, 249
 Costar 341
 Coulomb logarithm 293
 Critical cluster size 105, 106
 Critical point 72–83, 114
 – Alfvénic 312, 313
 – coronal wind 306, 307
 – isothermal wind 73, 74, 76, 79
 – line driven wind 171
 – r^{-2} force wind 82, 83
 CRL 2688 140
 Cyg OB2 No. 9 229–231
 DAC 178, 208, 210, 215–217, 221–223
 Damping parameter 22
 Deep Near-Infrared Survey 152
 Deferred corrections method 35
 δ Ori 188
 DENIS 152
 Density
 – coronal wind 308
 – disk 243, 244, 248, 257, 259, 260, 264, 266, 275
 – dust driven wind 120
 – from continuum observations 224, 226, 227
 – isothermal wind 76, 77, 79
 – late-type star wind 92, 125
 – line driven wind 175, 189, 218
 – nonmonotonic 219
 – wind 84
 Departure coefficient 211–213
 Destruction probability 23, 24, 26, 27
 DETAIL/SURFACE 41
 Detailed balance 6, 7
 Dichroic absorption 264, 265
 Dielectronic recombination 198
 Diffuse Interstellar Band 139
 Diffusion approximation 19, 20, 32, 42, 47, 266
 Dilution factor 166, 273
 Discontinuous Finite Element method 30, 42
 Discrete absorption component *see* DAC
 Discrete ordinates method 266, 267
 Disk 198, 239–275
 – formation 258
 – geometry 274–275
 – *see also* α disk
 – *see also* Accretion disk
 – *see also* Keplerian disk
 – *see also* Reprocessing disk

- Distribution function 3, 5, 6, 8, 15
- Doppler profile 21, 22, 25
- Dredge-up 136, 326, 327, 332
- Drift velocity (MHD) 299, 300
- Dust 91, 94–129, 141, 142, 144, 145, 148–150, 239
 - formation 84, 91, 93–98, 102–105, 107, 109–111, 117, 119, 123–128, 137, 149, 150
 - grain size 109–111, 114
 - scattering 113, 139, 140, 264
- Dust driven wind 70, 82, 84–87, 110–123, 149, 150
- Dynamo process 281, 282, 285

- Eddington approximation 46, 47, 319, 341
- Eddington factor 16, 19, 34
- Eddington limit 341
- Eddington luminosity 119, 123
- Eddington-Barbier relation 14, 37, 48
- Effective gravity 43
- Einstein coefficient 21, 23, 45
- Einstein Observatory 278
- Electric conductivity 293, 294
- Electron scattering 43, 45, 160, 166, 264–266, 325
- Emission 7, 9, 10, 21, 44, 45, 96
 - profile 22
- Emission line 56, 193, 198, 210–215, 228, 229, 231, 233, 239, 240, 274
- Energy density *see* Mean intensity
- Energy dissipation 246, 248, 249
- Energy distribution *see* Spectral energy distribution
- Energy equation 4, 71, 81, 297
 - coronal wind 295, 305, 306, 308
 - disk 244
 - late-type star wind 95, 115
 - line driven wind 72
 - magnetically closed region 301–303
 - stellar evolution 318, 325
- Energy flux *see* Flux
- Energy loss in wind 161
- Energy production 317, 318, 322, 327, 329, 331
- Enthalpy 71, 72, 115
- ϵ Ori 188

- Equation of motion *see* Momentum equation
- Equation of state 96, 112, 243, 297
 - stellar evolution 318, 319, 331
- Equipartition magnetic field 280
- Equivalent two-level atom *see* Two-level atom
- Escape probability 20, 26–29, 36, 198, 200, 270, 272
- η Car 239
- EUVE 289, 291–293
- Excitation equation 6
- Extreme ultraviolet 50, 208, 289–293
- Extreme Ultraviolet Explorer 289, 291–293

- Far Infra-Red and Submillimeter Space Telescope 152
- Faraday's law 299
- Feautrier method 30, 31, 33, 34, 37, 116, 262
- Finite disk correction 173–178
- Finite homogeneous slab 14
- FIRST 152
- Fit diagram 63, 64
- Flux 9, 15, 20, 43, 46
- Forbidden line 13, 277
- Force equation *see* Momentum equation
- Force multiplier 167
 - metallicity dependence 167
 - parameters 166, 167
- Formal solution 14, 17, 19, 29–32, 199, 225, 260, 261, 271
- Fornax cluster 233
- Free-free transition 45, 223–226, 228, 262–264

- Galactic Centre 231
- Galactic evolution 133, 188
- γ -rays 189
- Gas pressure 43, 71, 72, 75–77, 79, 259
- Gaunt factor 224, 226
- Grain formation *see* Dust - formation
- Grey model 40, 41, 46–50, 340
 - two step 48–50, 55
- Grid of models 39, 51, 53, 167
- Grid-fitting 62

- H α line 56, 210, 211, 213–215, 228, 229, 233, 240
- interferometry 239, 274
- Hardness ratio X-rays 289, 290
- HD 14947 212
- HD 160529 231, 232
- HD 64760 222
- Heating process 282, 285, 303, 304
- *see also* Backwarming
- Heating region 47–49, 53, 56
- Helium flash 134, 135, 321
- Helium line 193, 210, 212, 231
- Helix Nebula 140
- Heney method 319, 320
- $\alpha^{1,2}$ Her 137
- High mass star 134, 321, 334
- High spatial resolution 93, 139–141, 146–149, 228, 230
- Hipparcos 65
- Hopf function 47
- Horizontal branch 134
- Hubble Space Telescope 239
- Humphreys-Davidson limit 334
- Hyades cluster 287, 288
- Hydrodynamical equation *see* Continuity equation, Momentum equation, Energy equation
- Hydrostatic equilibrium
- atmosphere 4, 42, 43, 45, 47, 50, 64, 76
- corona 304
- stellar evolution 318, 328, 339
- Ideal MHD approximation 299
- Inclination angle disk 274
- Induction equation 299, 310
- Infrared Astronomical Satellite *see* IRAS
- Infrared excess 93, 94, 124, 142, 224–228, 230
- disk 240, 249, 262–264, 274
- Infrared observations 227, 231
- early-type star 223, 224, 229
- late-type star 141–145, 149–154
- Infrared Space Observatory *see* ISO
- Infrared Spatial Interferometer 150
- Inhomogeneity 62, 140, 149, 184, 214, 217, 219, 220, 228, 229, 233
- Instability
- line driven wind 177–181, 214, 218, 219, 221–223
- star 136, 137, 323–326, 329–331
- stellar evolution 329
- Instituto de Radioastronomia
- Millimetrica 227
- Instrumental broadening 61, 62
- Intermediate mass star 134, 135, 321, 327, 332
- International Ultraviolet Explorer *see* IUE
- Interstellar medium 1, 2, 133, 138, 150, 188, 305
- Ionization 6, 206, 208
- IRAM 227
- IRAS 91, 93, 142–145, 151, 152, 227, 263
- IRC +10216 101, 119–122, 128, 140, 141, 148–150, 152
- Iron-peak elements 52, 53, 169, 170
- Irregular variables 137
- ISI 150
- ISO 151, 152, 227, 232
- Isothermal wind 72–79, 81, 83, 169–173
- Isovelocity contours 194, 196, 198, 200, 271, 272
- IUE 192, 215, 217
- Jacobi matrix 38, 51
- κ mechanism 136, 333, 334
- Keplerian disk 242–244, 246, 254, 275
- Kernel function 17, 18, 28, 33, 34
- Kiel code 40
- Kinetic equilibrium 99, 100, 102
- Kinetic theory 3–5, 7, 15
- Kirchhoff's law 10, 116
- Laboratory studies 150
- Lambda iteration 273
- Lambda operator 17, 18, 35
- Laws of stellar winds 83
- LBV 135, 187, 224, 227, 231, 232, 239, 335
- Ledoux criterion 324, 326, 327
- Light curve 127, 128, 136, 143, 149
- Limb-darkening 61
- Line blanketing 41, 51–56, 63, 208

- Line driven wind 70, 85, 87, 159–184, 189, 218, 252, 255
 Line transition *see* Radiative transition, Two-level atom
 Line-of-sight velocity 195
 Linearization 38, 51, 52
 Local operator 36
 Local thermodynamic equilibrium *see* LTE
 Long-period variable star *see* LPV
 Loop *see* Magnetically closed region
 Lorentz force 298
 Lorentz profile 22
 Low mass star 134, 135, 322, 332
 LPV 89, 91, 112, 118, 124, 126, 128, 136, 143
 LTE 5, 7, 40, 46, 50, 99
 – breakdown 5–7, 25, 50, 99, 189
 – population ratio 23
 – *see also* Thermodynamic equilibrium
 Luminous Blue Variable *see* LBV

 Mach number 76
 Macroturbulence 62
 Magnetic field 279, 281, 282, 295
 – and stellar wind 86, 87
 – disk 249
 – dynamo *see* Dynamo process
 – filling factor 296
 – force-free 300, 304
 – primordial 281
 Magnetic pressure 280
 Magnetic rotating wind 86, 87
 Magnetically closed region 282, 300–304
 Magnetically open region 282, 304–308, 310, 313
 Magnetohydrodynamics 292–314
 MALI 41
 Maser 140, 146–148
 Mass continuity equation *see* Continuity equation
 Mass discrepancy hot stars 65
 Mass loss mechanism 84–87, 90, 92, 137, 282
 Mass loss rate 79, 81, 83, 84, 89
 – Alfvén wave driven wind 86
 – Be star 275
 – coronal wind 311
 – disk 251, 252
 – dust driven wind 85, 118, 119, 123
 – early-type star 69, 159, 182, 208
 – fit formula 336
 – from continuum observations 223, 226–229, 231
 – from H α 213, 214, 223, 228, 229
 – from P Cygni profile 188, 207, 208, 211, 214, 223, 229, 233
 – isothermal wind 73, 74, 77, 79
 – late-type star 91–93, 137, 139, 143–146, 150
 – line driven wind 163, 171, 173–176, 180, 182, 218
 – magnetic rotating wind 87
 – r^{-2} force wind 81, 82
 – sound wave driven wind 86
 – Sun 69, 77
 – Wolf-Rayet star 183
 Mass-luminosity relation 65, 322, 336
 Massive star *see* High mass star
 Maxwell distribution 5, 6
 Maxwell's equations 297, 298
 Mean free path 9, 26
 Mean intensity 8, 9, 13, 15, 17, 18, 23, 27, 28, 31, 33, 42, 48, 116
 MEGA Campaign 222
 MERLIN 147
 Metallicity 40, 143, 327
 Meteorite 150
 MHD *see* Magnetohydrodynamics
 Microturbulence 40, 43, 57, 63
 Mie theory 114
 Mira star 85, 89–91, 126, 136, 143, 147
 Mixing 323, 338–339
 Mixing length 5, 40, 57, 323
 Model atmosphere 20, 39–56
 Molecule
 – Al₂O₃ 144
 – (Al₂O₃)_n 104
 – AlCl 103
 – AlF 103
 – AlO 104
 – C 101
 – C₂ 136
 – C₂H 101, 104
 – C₂H₂ 101, 104, 136, 148
 – C₂S 103

- C_3H_2 103, 148
- C_3N 103
- C_3S 103
- C_8H 148
- C_n 104
- C_nH 103, 148
- CH_3CN 103
- CN 101, 103, 136
- CO 101-103, 136, 142, 145, 146, 148
- CO_2 151
- CS 103, 148
- Cyanopolyynes 145
- $(Fe)_n$ 104
- H 101
- H_2 95, 101, 103, 145
- H_2O 103, 136, 145, 146, 148, 151
- H_2S 103, 148
- HC_nN 103
- $HC_{2n+1}N$ 145, 148
- HCN 101, 103, 136, 145, 148
- HCO^+ 103
- HNC 103
- $HSiC_2$ 103
- Hydrocarbons 103
- KCl 103
- MgO 104
- $(MgO)_n$ 104
- MgS 142
- N_2 101, 148
- $NaCl$ 103
- NH_3 103
- OCS 103, 148
- OH 103, 145-147, 151
- $PACs$ 104
- $PAHs$ 104, 105, 107
- Polyaromatic Hydrocarbons 104, 105, 107
- SiC 103, 142, 150
- $(SiC)_n$ 104
- SiC_2 103, 148
- SiO 103, 104, 145, 148, 149, 151
- $(SiO)_n$ 104
- SiS 103, 148
- SO 103, 148
- SO_2 103, 148
- TiC 150
- TiO 136
- VO 136
- YO 136
- ZrO 136
- Momentum density photons 9
- Momentum equation 4, 70, 71, 80, 114
- coronal wind 124
- disk 242, 247, 250, 251, 253, 255
- isothermal wind 72-75, 78
- late-type star 112
- line driven wind 169-172, 174
- MHD 297, 298, 301, 306, 307, 310, 311
- r^{-2} force wind 81, 82
- stellar evolution 323
- Momentum transfer
- dust-gas 85, 90, 95, 113, 118, 119, 126
- efficiency factor 163
- photons-gas 159-163, 193, 252
- Monte Carlo method 52, 203, 266, 267, 269, 270
- μ Cep 140, 141
- MULTI 41
- Multi Element Radio Linked Interferometer Network 147
- Multilevel atom 37-39
- Multiple scattering 219-221, 266, 270
- Natural broadening 22
- Ng acceleration 37
- NGC 7293 140
- Node theorem 327-329
- Non-CE 106
- Non-KE 99, 100
- Non-LTE 5-7, 20, 40, 44, 50, 51, 53, 55, 99, 106, 189
- Non-LTE model 40, 53, 211, 212
- Non-resonance line 193
- Nonmonotonic wind 219-221
- Nonthermal radio emission 229-231
- Nonthermal X-rays 289
- Number conservation 44
- Numerical aspects 2, 6, 16, 29-34, 58, 60
- chemistry 97
- disk 260-262, 267, 271
- dust formation 104, 110
- line blanketing 52-54
- model atmosphere 51-52, 58

- P Cygni profile 198–203, 213, 221, 261, 271
- pulsation 124
- radiative transfer 18, 29–39
- statistical equilibrium 44
- stellar evolution 319–321, 325, 326
- time-scale 100
- *see also* Acceleration of convergence
- *see also* ALI
- ODF *see* Opacity distribution function
- OH/IR 26.5+0.6 149
- OH/IR sources 143, 147
- Ohm's law 298
- Olivine 151
- o Cet 90, 136
- Opacity *see* Absorption
- Opacity distribution function 52–54, 96
- Opacity sampling 52–54, 97
- Opening angle *see* Scale height disk
- Operator Perturbation *see* ALI
- Operator splitting 35
- Optical depth 12, 27
- P Cygni profile 199, 202
- δ Ori 188
- ϵ Ori 188
- ζ Ori 188
- OS *see* Opacity sampling
- Outflow disk 250–260
- Overshooting 321, 325–327, 335, 338
- Oxygen-rich star 101–102, 104, 136, 142–144, 146, 148, 151, 153, 154, 332
- P Cyg 187, 192, 232
- P Cygni profile 94, 178, 208, 211, 214, 233
 - disk 240
 - doublets 203
 - early-type star 187, 188, 208, 217
 - late-type star 92
 - nonmonotonic wind 219, 223, 229
 - theory 195–203, 207, 208
 - *see also* Beals classification
 - *see also* Black trough
 - *see also* Blue edge
 - *see also* DAC
- PAM 40
- Parker wind 310
- Partial redistribution 22, 26
- Partition function 6, 44
- β Peg 139
- ξ Per 208–210, 215–217, 221
- Planck function 5, 7, 10, 47
- Plane-parallel atmosphere 2–66, 198, 341
- Planetary nebula 13, 65, 133, 137, 140, 144, 239, 317
- Pleiades cluster 287, 288
- Polarization 8, 140, 141, 240, 264–270, 275
- Population synthesis 1
- Post-AGB star 239
- Praesepe cluster 287, 288
- Preconditioning 38, 39
- Pressure scale height 325, 338
- Procyon 289–292
- Proton-proton cycle 322
- Pulsation 62, 89, 92, 118, 123, 124, 126, 136, 139, 330, 333
- Pulsation driven wind 85–87
- ζ Pup 90, 163, 169, 214, 215, 222, 224–226, 229
- Pyroxene 151
- R CrB star 89, 90, 102
- R For 128
- R Scl 90
- Radiation force 160, 165–167, 169, 170, 173, 179
 - disk 251, 254–256
- Radiation pressure 43, 81, 84–86, 159, 164, 165
- Radiation stress tensor 9, 15
- Radiative cooling 295, 296, 301, 303
- Radiative equilibrium 4, 41, 43, 45–48, 50, 55, 115, 118, 244, 248, 259, 279, 322
- Radiative transfer 7–39, 46, 95, 111, 116, 260, 266, 270, 274
- Radiative transfer equation 5, 11–15, 17, 19, 29–32, 42, 45, 116
 - boundary conditions 32
 - continuum 225
 - differential 32–34
 - disk 260–264, 270, 271, 273
 - first order 16, 30, 42

- integral 32-34
- kernel function 17, 18, 28, 33, 34
- moments 15
- P Cygni profile 199, 202
- second order 16, 30, 31, 42
- Radiative transition 6, 7, 23, 38, 44, 45
- Radiatively driven wind *see* Dust driven wind, Line driven wind
- Radio excess 224-231
- Radio observations 92, 145, 149, 208, 223, 224, 227-231
- Radius correction 339-340
- Ram pressure 257, 259
- Rate equations *see* Statistical equilibrium
- Rayleigh scattering 45, 265
- Rayleigh-Jeans limit 47, 48, 245, 262
- Rayleigh-Taylor instability 324
- Recombination line *see* Emission line
- Red Giant Branch 134, 327
- Red supergiant 134, 136, 335
- Reddening due to dust 91, 102, 152
- Reprocessing disk 246, 248, 249
- Resonance line
 - optical 140
 - theory 22, 23, 195-198, 202, 204-206, 210, 220, 270, 272
 - UV 181, 182, 187, 188, 192, 193, 195, 199, 203, 204, 206, 208, 209, 211, 216, 220, 232, 240
- RGB 134, 327
- ρ^2 process 192, 193, 198, 210, 212, 214, 228, 231, 233
- ROSAT 278, 279, 286, 287, 289
- Rosseland mean opacity 12, 20, 46, 319
- Rotation-activity connection 281, 283-288
- Rotation-DAC connection 222
- Rotational broadening 61
- RR Lyrae variable 332
- RS CVn star 285
- RSG 134, 136, 335
- Rybicki method 34
- S Sct 146
- Saha equation 6, 50
- Saha-Boltzmann factor 211
- Scale height 202, 325, 338
- Scale height disk 244, 245, 248, 258, 264, 266, 274, 275
- Scattering *see* Dust, Electron scattering, Resonance line
- Schwarzschild criterion 321, 324, 326, 327
- SEI 203, 270, 271
- Self-collision time 293
- Semi-infinite atmosphere 14, 17, 24, 30, 32
- Semi-regular variables 90, 136
- Semiconvection 324-327
- SEST 227
- 9 Sge 209
- 9 Sgr 229
- Shear stress 247-249
- Shell around late-type star 91-129, 137, 139-154
- Shell burning 134, 135, 327-332
- Shock
 - corona 124, 279
 - disk 241, 249, 256-260
 - wind 89, 99, 126, 179-181, 208, 219, 230, 231
- Silicate (amorphous) 150
- Skylab 279
- SN 1987a 1, 90
- Sobolev approximation 41, 165, 176, 178, 198, 200-203, 212, 218, 220, 270-272
 - generalized 272
- Sobolev length 202
- Sobolev optical depth 201, 203, 204, 207, 211, 272
- Sobolev with exact integration *see* SEI
- SOHO 290, 292
- Sonic point 73, 100, 111, 205, 252, 253, 255-257, 307, 340
- Sound wave driven wind 85-87
- Source function 12, 13, 15, 19, 23, 33
 - continuum 223
 - disk 262, 271-273
 - linear 14, 23, 29
 - P Cygni profile 200
 - two-level atom 22, 24, 25, 27, 28
- Specific intensity 8, 12, 15, 17, 18
- Spectral energy distribution 263

- disk 245, 248, 249
- dust shell model 121, 122
- Spectral features 141, 142, 144
- Spectral index 226, 229–231, 263
- Spectropolarimetry 274, 275
- Spectroscopic diagnostics 57–66, 97, 137–139, 189–223, 231, 270, 274–275
- Spectrum synthesis 58, 60, 61, 122
- Stagnation point disk 258
- Stark broadening 22
- Static corona 304
- Statistical equilibrium 4, 22, 43–45, 100, 108
- Stellar evolution 1, 20, 57, 65, 66, 69, 134, 136, 317–341
 - mass loss 70, 133, 134, 188, 334–338
- Stokes parameters 8, 264, 268
- Streamline 252–254, 256, 257
- Streamtube 250, 252
- Sun 1, 279, 280, 282, 303, 305
 - corona 13, 277, 279, 280, 282, 283, 285, 287, 289, 300, 313
 - coronal hole 86, 284, 290, 306
 - extreme ultraviolet 290, 292
 - magnetic field 295
 - transition region 4, 13
 - wind 69, 72, 77
- Superionization 177, 181, 259
- Superlevel 52
- Superline 52, 54
- Surface cooling 49, 52, 53
- Surface heating 49, 56
 - *see also* Backwarming
- Surface temperature 56
- Swedish-ESO Submillimeter Telescope 227
- Synchrotron emission 230, 264
- SYNSPEC 61
- SYNTHE 61

- T Tau 241
- T Tauri star 240, 249
- TAMS 337
- ζ Tau 275
- Temperature
 - corona 277, 289, 291, 293, 295
 - disk 244, 245, 248, 259, 260, 264
 - dust 103, 104, 106, 116, 120
 - dust driven wind 120
 - from continuum observations 227
 - late-type star wind 93, 95, 115, 116, 125, 126
 - line blanketing 53–56, 63
 - line driven wind 181
 - magnetically closed region 301, 304
 - model atmosphere 20, 46–50
 - r^{-2} force wind 82
 - stellar evolution 319, 322, 329, 334
 - surface 48
 - wind 79, 80
 - *see also* Grey model
- Terminal Age Main Sequence 337
- Terminal velocity
 - coronal wind 307, 308
 - disk 240, 252, 258, 259
 - dust driven wind 122
 - early-type star wind 159, 181, 182
 - from P Cygni profile 198, 205, 209, 210, 219, 232
 - isothermal wind 75
 - late-type star wind 92
 - line driven wind 161, 173, 175, 177, 180, 181, 183
 - *see also* Blue edge
- Thermal conductivity 294, 295
- Thermal pulse 135, 136, 327, 330–332
- Thermalization depth 25, 26, 28
- Thermodynamic equilibrium 5, 10, 19, 104
 - *see also* LTE
 - *see also* Non-LTE
- Thermodynamics 71, 115
- Thomson scattering 43, 160
- Time-dependent hydrodynamics 124, 125, 180, 218, 220–223, 257, 258
- Time-scale
 - DAC 217
 - stellar evolution 322, 332, 336–339
 - wind 97–100, 105, 109, 116, 181
- TLUSTY 40, 61
- TMSS 152
- Transfer *see* Radiative transfer
- Transition *see* Collisional, Radiative transition, Two-level atom
- Triple-α reaction 134
- Turbulence
 - atmosphere 43

- corona 282
- disk 249, 271, 272
- wind 209, 210, 221
- Two-level atom 20–29, 34, 35, 200, 272
- equivalent 27
- Two-Micron All Sky Survey 152
- Two-Micron Sky Survey 152
- 2MASS 152

- U Hya 145
- Ultraviolet excess 249
- Unified models 41, 57, 212, 225

- V 846 Cen 90
- Valve mechanism 333
- Van der Waals broadening 22
- Variability 126–129, 146, 147, 150, 178, 183, 184, 210, 215, 218, 221, 229, 230, 233
- Variable Eddington factor 34, 42
- Vega 285
- Velocity
 - Alfvén wave driven wind 86
 - coronal wind 307, 308
 - disk 242, 243, 247, 248, 257
 - dust driven wind 120, 123
 - early-type star wind 205, 206
 - from continuum observations 223, 226, 227
 - from P Cygni profile 206, 208, 214, 233
 - isothermal wind 73, 75–79
 - late-type star wind 91, 92, 125, 126, 139, 145
 - line driven wind 171–174, 176, 178, 180, 218
 - magnetic rotating wind 87
 - nonmonotonic 219–221
 - r^{-2} force wind 81–83
 - wind 81, 83, 84
 - Wolf-Rayet star wind 340
 - *see also* β law
 - *see also* Terminal velocity
- Velocity-excitation relation 190
- Very Large Array 147, 148, 227
- Very Long Baseline Interferometry 147, 148
- Virgo cluster 233
- Viscosity 246–248

- VLA 147, 148, 227
- VLBI 147, 148
- Voigt profile 22, 25

- Wave dissipation 93
- WCD *see* Wind-compressed disk
- WCZ *see* Wind-compressed zone
- Wien limit 47, 48, 245
- Wind equation *see* Momentum equation
- Wind momentum 182, 184
- Wind performance number 163, 169
- Wind-compressed disk 214, 256–259, 275
- Wind-compressed zone 214, 229
- Wolf-Rayet star 89, 90, 135, 163, 182–184, 187, 190, 217, 224, 227, 335, 337, 340
- WR 140 90

- X-ray luminosity 285–287, 290
- X-rays 177, 181, 208, 259, 277–291, 300, 304
- ξ Per 208–210, 215–217, 221

- YOHKOH 282, 283
- Young stellar object 239, 249, 265, 267

- ζ Aur 90
- ζ Ori 188
- ζ Pup 90, 163, 169, 214, 215, 222, 224–226, 229
- ζ Tau 275
- Zoning 320

New Series m: Monographs

- Vol. m 2: P. Busch, P. J. Lahti, P. Mittelstaedt, *The Quantum Theory of Measurement*. XIII, 165 pages. 1991. Second Revised Edition: XIII, 181 pages. 1996.
- Vol. m 3: A. Heck, J. M. Perchang (Eds.), *Applying Fractals in Astronomy*. IX, 210 pages. 1991.
- Vol. m 4: R. K. Zeytounian, *Mécanique des fluides fondamentale*. XV, 615 pages, 1991.
- Vol. m 5: R. K. Zeytounian, *Meteorological Fluid Dynamics*. XI, 346 pages. 1991.
- Vol. m 6: N. M. J. Woodhouse, *Special Relativity*. VIII, 86 pages. 1992.
- Vol. m 7: G. Morandi, *The Role of Topology in Classical and Quantum Physics*. XIII, 239 pages. 1992.
- Vol. m 8: D. Funaro, *Polynomial Approximation of Differential Equations*. X, 305 pages. 1992.
- Vol. m 9: M. Namiki, *Stochastic Quantization*. X, 217 pages. 1992.
- Vol. m 10: J. Hoppe, *Lectures on Integrable Systems*. VII, 111 pages. 1992.
- Vol. m 11: A. D. Yaghjian, *Relativistic Dynamics of a Charged Sphere*. XII, 115 pages. 1992.
- Vol. m 12: G. Esposito, *Quantum Gravity, Quantum Cosmology and Lorentzian Geometries*. Second Corrected and Enlarged Edition. XVIII, 349 pages. 1994.
- Vol. m 13: M. Klein, A. Knauf, *Classical Planar Scattering by Coulombic Potentials*. V, 142 pages. 1992.
- Vol. m 14: A. Lerda, *Anyons*. XI, 138 pages. 1992.
- Vol. m 15: N. Peters, B. Rogg (Eds.), *Reduced Kinetic Mechanisms for Applications in Combustion Systems*. X, 360 pages. 1993.
- Vol. m 16: P. Christe, M. Henkel, *Introduction to Conformal Invariance and Its Applications to Critical Phenomena*. XV, 260 pages. 1993.
- Vol. m 17: M. Schoen, *Computer Simulation of Condensed Phases in Complex Geometries*. X, 136 pages. 1993.
- Vol. m 18: H. Carmichael, *An Open Systems Approach to Quantum Optics*. X, 179 pages. 1993.
- Vol. m 19: S. D. Bogan, M. K. Henders, *Interface Effects in Elastic Wave Scattering*. XII, 182 pages. 1994.
- Vol. m 20: E. Abdalla, M. C. B. Abdalla, D. Dalmazi, A. Zadra, *2D-Gravity in Non-Critical Strings*. IX, 319 pages. 1994.
- Vol. m 21: G. P. Berman, E. N. Bulgakov, D. D. Holm, *Crossover-Time in Quantum Boson and Spin Systems*. XI, 268 pages. 1994.
- Vol. m 22: M.-O. Hongler, *Chaotic and Stochastic Behaviour in Automatic Production Lines*. V, 85 pages. 1994.
- Vol. m 23: V. S. Viswanath, G. Müller, *The Recursion Method*. X, 259 pages. 1994.
- Vol. m 24: A. Ern, V. Giovangigli, *Multicomponent Transport Algorithms*. XIV, 427 pages. 1994.
- Vol. m 25: A. V. Bogdanov, G. V. Dubrovskiy, M. P. Krutikov, D. V. Kulginov, V. M. Strelchenya, *Interaction of Gases with Surfaces*. XIV, 132 pages. 1995.
- Vol. m 26: M. Dineykhani, G. V. Efimov, G. Ganbold, S. N. Nedelko, *Oscillator Representation in Quantum Physics*. IX, 279 pages. 1995.
- Vol. m 27: J. T. Ottesen, *Infinite Dimensional Groups and Algebras in Quantum Physics*. IX, 218 pages. 1995.
- Vol. m 28: O. Piguet, S. P. Sorella, *Algebraic Renormalization*. IX, 134 pages. 1995.
- Vol. m 29: C. Bendjaballah, *Introduction to Photon Communication*. VII, 193 pages. 1995.
- Vol. m 30: A. J. Greer, W. J. Kossler, *Low Magnetic Fields in Anisotropic Superconductors*. VII, 161 pages. 1995.
- Vol. m 31: P. Busch, M. Grabowski, P. J. Lahti, *Operational Quantum Physics*. XI, 230 pages. 1995.
- Vol. m 32: L. de Broglie, *Diverses questions de mécanique et de thermodynamique classiques et relativistes*. XII, 198 pages. 1995.
- Vol. m 33: R. Alkofer, H. Reinhardt, *Chiral Quark Dynamics*. VIII, 115 pages. 1995.
- Vol. m 34: R. Jost, *Das Märchen vom Elfenbeinernen Turm*. VIII, 286 pages. 1995.
- Vol. m 35: E. Elizalde, *Ten Physical Applications of Spectral Zeta Functions*. XIV, 228 pages. 1995.
- Vol. m 36: G. Dunne, *Self-Dual Chern-Simons Theories*. X, 217 pages. 1995.
- Vol. m 37: S. Childress, A.D. Gilbert, *Stretch, Twist, Fold: The Fast Dynamo*. XI, 410 pages. 1995.
- Vol. m 38: J. González, M. A. Martín-Delgado, G. Sierra, A. H. Vozmediano, *Quantum Electron Liquids and High- T_c Superconductivity*. X, 299 pages. 1995.
- Vol. m 39: L. Pittner, *Algebraic Foundations of Non-Commutative Differential Geometry and Quantum Groups*. XII, 469 pages. 1996.
- Vol. m 40: H.-J. Borchers, *Translation Group and Particle Representations in Quantum Field Theory*. VII, 131 pages. 1996.
- Vol. m 41: B. K. Chakrabarti, A. Dutta, P. Sen, *Quantum Ising Phases and Transitions in Transverse Ising Models*. X, 204 pages. 1996.
- Vol. m 42: P. Bouwknegt, J. McCarthy, K. Pilch, *The \mathbb{W}_3 Algebra. Modules, Semi-infinite Cohomology and BV Algebras*. XI, 204 pages. 1996.
- Vol. m 43: M. Schottenloher, *A Mathematical Introduction to Conformal Field Theory*. VIII, 142 pages. 1997.
- Vol. m 44: A. Bach, *Indistinguishable Classical Particles*. VIII, 157 pages. 1997.
- Vol. m 45: M. Ferrari, V. T. Granik, A. Imam, J. C. Nadeau (Eds.), *Advances in Doublet Mechanics*. XVI, 214 pages. 1997.
- Vol. m 46: M. Camenzind, *Les noyaux actifs de galaxies*. XVIII, 218 pages. 1997.
- Vol. m 47: L. M. Zubov, *Nonlinear Theory of Dislocations and Disclinations in Elastic Body*. VI, 205 pages. 1997.
- Vol. m 48: P. Kopietz, *Bosonization of Interacting Fermions in Arbitrary Dimensions*. XII, 259 pages. 1997.
- Vol. m 49: M. Zak, J. B. Zbilut, R. E. Meyers, *From Instability to Intelligence. Complexity and Predictability in Nonlinear Dynamics*. XIV, 552 pages. 1997.
- Vol. m 50: J. Ambjørn, M. Carfora, A. Marzuoli, *The Geometry of Dynamical Triangulations*. VI, 197 pages. 1997.
- Vol. m 51: G. Landi, *An Introduction to Noncommutative Spaces and Their Geometries*. XI, 200 pages. 1997.

Lecture Notes in Physics

For information about Vols. 1–461

please contact your bookseller or Springer-Verlag

- Vol. 462: M. Meneguzzi, A. Pouquet, P.-L. Sulem (Eds.), Small-Scale Structures in Three-Dimensional Hydrodynamic and Magnetohydrodynamic Turbulence. Proceedings, 1995. IX, 421 pages. 1995.
- Vol. 463: H. Hippelein, K. Meisenheimer, H.-J. Röser (Eds.), Galaxies in the Young Universe. Proceedings, 1994. XV, 314 pages. 1995.
- Vol. 464: L. Ratke, H. U. Walter, B. Feuerbach (Eds.), Materials and Fluids Under Low Gravity. Proceedings, 1994. XVIII, 424 pages. 1996.
- Vol. 465: S. Beckwith, J. Staude, A. Quetz, A. Natta (Eds.), Disks and Outflows Around Young Stars. Proceedings, 1994. XII, 361 pages. 1996.
- Vol. 466: H. Ebert, G. Schütz (Eds.), Spin – Orbit-Influenced Spectroscopies of Magnetic Solids. Proceedings, 1995. VII, 287 pages. 1996.
- Vol. 467: A. Steinchen (Ed.), Dynamics of Multiphase Flows Across Interfaces. 1994/1995. XII, 267 pages. 1996.
- Vol. 468: C. Chiuderi, G. Einaudi (Eds.), Plasma Astrophysics. 1994. VII, 326 pages. 1996.
- Vol. 469: H. Grosse, L. Pittner (Eds.), Low-Dimensional Models in Statistical Physics and Quantum Field Theory. Proceedings, 1995. XVII, 339 pages. 1996.
- Vol. 470: E. Martí'nez-González, J. L. Sanz (Eds.), The Universe at High- z , Large-Scale Structure and the Cosmic Microwave Background. Proceedings, 1995. VIII, 254 pages. 1996.
- Vol. 471: W. Kundt (Ed.), Jets from Stars and Galactic Nuclei. Proceedings, 1995. X, 290 pages. 1996.
- Vol. 472: J. Greiner (Ed.), Supersoft X-Ray Sources. Proceedings, 1996. XIII, 350 pages. 1996.
- Vol. 473: P. Weingartner, G. Schurz (Eds.), Law and Prediction in the Light of Chaos Research. X, 291 pages. 1996.
- Vol. 474: Aa. Sandqvist, P. O. Lindblad (Eds.), Barred Galaxies and Circumnuclear Activity. Proceedings of the Nobel Symposium 98, 1995. XI, 306 pages. 1996.
- Vol. 475: J. Klamut, B. W. Veal, B. M. Dabrowski, P. W. Klamut, M. Kazimierski (Eds.), Recent Developments in High Temperature Superconductivity. Proceedings, 1995. XIII, 362 pages. 1996.
- Vol. 476: J. Parisi, S. C. Müller, W. Zimmermann (Eds.), Nonlinear Physics of Complex Systems. Current Status and Future Trends. XIII, 388 pages. 1996.
- Vol. 477: Z. Petru, J. Przystawa, K. Rapcewicz (Eds.), From Quantum Mechanics to Technology. Proceedings, 1996. IX, 379 pages. 1996.
- Vol. 478: G. Sierra, M. A. Martín-Delgado (Eds.), Strongly Correlated Magnetic and Superconducting Systems. Proceedings, 1996. VIII, 323 pages. 1997.
- Vol. 479: H. Latal, W. Schweiger (Eds.), Perturbative and Nonperturbative Aspects of Quantum Field Theory. Proceedings, 1996. X, 430 pages. 1997.
- Vol. 480: H. Flyvbjerg, J. Hertz, M. H. Jensen, O. G. Mouritsen, K. Sneppen (Eds.), Physics of Biological Systems. From Molecules to Species. X, 364 pages. 1997.
- Vol. 481: F. Lenz, H. Griefshammer, D. Stoll (Eds.), Lectures on QCD. VII, 276 pages. 1997.
- Vol. 482: X.-W. Pan, D. H. Feng, M. Vallières (Eds.), Contemporary Nuclear Shell Models. Proceedings, 1996. XII, 309 pages. 1997.
- Vol. 483: G. Trottet (Ed.), Coronal Physics from Radio and Space Observations. Proceedings, 1996. XVII, 226 pages. 1997.
- Vol. 484: L. Schimansky-Geier, T. Pöschel (Eds.), Stochastic Dynamics. XVIII, 386 pages. 1997.
- Vol. 485: H. Friedrich, B. Eckhardt (Eds.), Classical, Semi-classical and Quantum Dynamics in Atoms. VIII, 341 pages. 1997.
- Vol. 486: G. Chavent, P. C. Sabatier (Eds.), Inverse Problems of Wave Propagation and Diffraction. Proceedings, 1996. XV, 379 pages. 1997.
- Vol. 487: E. Meyer-Hofmeister, H. Spruiik (Eds.), Accretion Disks – New Aspects. Proceedings, 1996. XIII, 356 pages. 1997.
- Vol. 488: B. Apagyi, G. Endrédi, P. Lévy (Eds.), Inverse and Algebraic Quantum Scattering Theory. Proceedings, 1996. XV, 385 pages. 1997.
- Vol. 489: G. M. Simnett, C. E. Alissandrakis, L. Vlahos (Eds.), Solar and Heliospheric Plasma Physics. Proceedings, 1996. VIII, 278 pages. 1997.
- Vol. 490: P. Kutler, J. Flores, J.-J. Chattot (Eds.), Fifteenth International Conference on Numerical Methods in Fluid Dynamics. Proceedings, 1996. XIV, 653 pages. 1997.
- Vol. 491: O. Boratav, A. Eden, A. Erzan (Eds.), Turbulence Modeling and Vortex Dynamics. Proceedings, 1996. XII, 245 pages. 1997.
- Vol. 492: M. Rubí, C. Pérez-Vicente (Eds.), Complex Behaviour of Glassy Systems. Proceedings, 1996. IX, 467 pages. 1997.
- Vol. 493: P. L. Garrido, J. Marro (Eds.), Fourth Granada Lectures in Computational Physics. XIV, 316 pages. 1997.
- Vol. 494: J. W. Clark, M. L. Ristig (Eds.), Theory of Spin Lattices and Lattice Gauge Models. Proceedings, 1996. XI, 194 pages. 1997.
- Vol. 496: F. Lenz, H. Griefshammer, D. Stoll (Eds.), Lectures on QCD. VII, 483 pages. 1997.
- Vol. 497: J.P. De Greve, R. Blomme, H. Hensberge (Eds.), Stellar Atmospheres: Theory and Observations. VIII, 352 pages. 1997.